





# **N<sub>2</sub> Fixation by Chromium and Rhenium PNP Pincer Complexes**

**Dissertation**

zur Erlangung des mathematisch-naturwissenschaftlichen Doktorgrades

„Doctor rerum naturalium“

der Fakultät für Anorganische Chemie

der Georg-August-Universität Göttingen

im Promotionsprogramm der „Georg-August University School of Science“  
(GAUSS)

vorgelegt von

**M. Sc. Maximilian Fritz**

geboren in Wiesbaden

**Göttingen, 2021**

## Betreuungsausschuss

**Prof. Dr. Sven Schneider**

Institut für Anorganische Chemie, Georg-August-Universität Göttingen

**Prof. Dr. Inke Siewert**

Institut für Anorganische Chemie, Georg-August-Universität Göttingen

**Dr. Markus Finger**

Institut für Anorganische Chemie, Georg-August-Universität Göttingen

## Mitglieder der Prüfungskommission

Referent: **Prof. Dr. Sven Schneider**

Institut für Anorganische Chemie, Georg-August-Universität Göttingen

Korreferent: **Prof. Dr. Inke Siewert**

Institut für Anorganische Chemie, Georg-August-Universität Göttingen

Weitere Mitglieder der Prüfungskommission:

**Prof. Dr. Franc Meyer**

Institut für Anorganische Chemie, Georg-August-Universität Göttingen

**Prof. Dr. Manuel Alcarazo**

Institut für Organische und Biomolekulare Chemie, Georg-August-Universität Göttingen

**Dr. Daniel Janßen-Müller**

Institut für Organische und Biomolekulare Chemie, Georg-August-Universität Göttingen

**Dr. Michael John**

Institut für Organische und Biomolekulare Chemie, Georg-August-Universität Göttingen

Tag der mündlichen Prüfung: 25.11.2021

# Acknowledgments

Mein besonderer Dank ist an Prof. Dr. Sven Schneider gerichtet, der es mir ermöglicht hat, die vorliegende Arbeit in seiner Arbeitsgruppe anfertigen zu dürfen. Ich bedanke mich für die Vergabe von einem hochspannenden Forschungsprojekt, für den stetigen, wissenschaftlichen Austausch und für die Unterstützung bei der Präsentation von Forschungsergebnissen auf etlichen Konferenzen.

Weiterhin geht mein Dank an Prof. Dr. Inke Siewert für die Übernahme der Zweitkorrektur sowie an den Rest der Prüfungskommission, bestehend aus Prof. Dr. Franc Meyer, Prof. Dr. Manuel Alcarazo, Dr. Daniel Janßen-Müller und Dr. Michael John, die sich die Zeit für mich und meine Arbeit nehmen.

Dr. Christian Würtele danke ich für die Einführung am Diffraktometer und die Weitergabe von seinem Wissen. Ich bedanke mich bei Dr. Markus Finger für die DFT Rechnungen in dem ersten Hauptkapitel dieser Arbeit. Für zahlreiche SQUID Messungen danke ich Dr. Serhiy Demeshko. Ich danke Dr. Sebastian Dechert für sämtliche Raman-Messungen. Dr. Claudia Stückl sei gedankt für die EPR-Messungen.

Vielen Dank an Prof. Dr. Vera Krewald und Severine Rupp für die (TD)-DFT Rechnungen in dem zweiten Hauptkapitel dieser Arbeit.

Ich danke Dr. Bastian Schluschaß, Dr. Josh Abbenseth, Dr. Markus Finger, Dr. Richt van Alten und Dr. Kirsten Höwler für das Korrekturlesen dieser Arbeit. Danke an den gesamten AK Schneider für die einzigartige Zeit! Katharina Wenderoth, ich danke dir für die Bereitstellung sämtlicher Rheniumkomplexe, besonders während meiner Schreibphase. Ich danke Sebastian Kopp für seine Unterstützung in der Arbeitsgruppe, ohne die die Gruppe im Chaos enden würde.

Vielen Dank an meine Abteilungspraktikanten (Niels Benjamin Paul und Leonard Hartung) und an meine Bachelorstudenten (Paul Julius Weiß und Johannes Müller) für die vielen wichtigen Ergebnisse.

Ich bedanke mich bei Dr. Claudia Stückl und Dalila Griffin für die Unterstützung bei administrativen Angelegenheiten. Danke an sämtliche Leute aus den Serviceabteilungen und den Hausmeistern!

Mein unermesslicher Dank geht an meine lieben Eltern Heike Brosinger-Fritz und Dr. Bernhard Fritz und meine Schwester Dr. Eva-Corinna Fritz, die mich seit dem Studienbeginn in jeglicher Hinsicht unterstützt und mir somit eine unvergessliche Zeit ermöglicht haben. Danke!

Am Ende möchten ich meiner Herzallerliebsten Dr. Kirsten „Dr. Maus!“ Höwler für ihre unermüdliche Unterstützung danken. Jeder Moment mit dir ist einzigartig und ich freue mich riesig auf das, was uns zukünftig erwartet!

# Table of content

Acknowledgments.....	I
Table of content .....	II
List of abbreviations.....	VI
<b>1 Introduction .....</b>	<b>1</b>
1.1 N <sub>2</sub> activation in transition metal complexes .....	1
1.1.1 General aspects .....	1
1.1.2 N <sub>2</sub> as a ligand in transition metal complexes.....	2
1.1.3 Electronic structures of N <sub>2</sub> bridged dinitrogen complexes.....	2
1.1.4 Robin-Day classification of N <sub>2</sub> bridged dinuclear complexes .....	4
1.1.5 Thermal and photochemical N <sub>2</sub> cleavage into terminal nitride complexes.....	8
1.2 Functionalization of N <sub>2</sub> derived nitrides species.....	13
1.2.1 The bonding situation in transition metal nitride (M≡N) and imido (M≡N-R / M=N-R) complexes.....	13
1.2.2 Nitride functionalization via N-C bond formation.....	14
1.2.3 N-H bond formation in nitride complexes and ammonia production .....	18
1.3 Chromium mediated N <sub>2</sub> -activation and functionalization.....	20
1.3.1 Examples of low-valent, N <sub>2</sub> bridged multinuclear chromium complexes.....	21
1.3.2 Reactivity of chromium N <sub>2</sub> complexes .....	23
1.3.3 Chromium mediated N-N bond cleavage.....	25
1.3.4 Cr vs. Mo in N <sub>2</sub> activation.....	27
1.4 Scope of this Work.....	28
1.4.1 Results and Discussion I.....	28
1.4.2 Results and Discussion II .....	28
<b>2 Results and Discussion I .....</b>	<b>30</b>
2.1 An N <sub>2</sub> bridged dichromium complex.....	30
2.1.1 Synthetic access of dinitrogen complex [(μ-N <sub>2</sub> ) {Cr( <sup>t</sup> BuPNP <sup>o</sup> )} <sub>2</sub> ] (3).....	30
2.1.2 The electronic structure of [(μ-N <sub>2</sub> ) {Cr( <sup>t</sup> BuPNP <sup>o</sup> )} <sub>2</sub> ] (3).....	34
2.2 [(μ-N <sub>2</sub> ) {Cr( <sup>t</sup> BuPNP <sup>o</sup> )}] (3) as a reductive precursor complex .....	38
2.2.1 The reactivity of [(μ-N <sub>2</sub> ) {Cr( <sup>t</sup> BuPNP <sup>o</sup> )}] (3) towards CO .....	38
2.2.2 The reactivity of [(μ-N <sub>2</sub> ) {Cr( <sup>t</sup> BuPNP <sup>o</sup> )} <sub>2</sub> ] (3) towards <sup>t</sup> Bu-NC.....	44
2.3 Attempts of N <sub>2</sub> cleavage.....	47
2.4 Conclusion.....	49
<b>3 Results and Discussion II.....</b>	<b>50</b>
3.1 Electro- and photosynthesis of octahedral Re <sup>V</sup> nitride complexes .....	50
3.1.1 Synthesis of [ReX <sub>3</sub> ( <sup>Pr</sup> PN <sup>H</sup> P)] (X = Cl, Br, I) and electrochemical evaluation.....	50
3.1.2 Synthesis and characterization of [(μ-N <sub>2</sub> ) {ReX <sub>2</sub> ( <sup>Pr</sup> PN <sup>H</sup> P)} <sub>2</sub> ] (X = Cl, Br, I) .....	54
3.1.3 Photochemical properties of dinitrogen complexes 11 <sup>Cl</sup> , 11 <sup>Br</sup> and 11 <sup>I</sup> .....	61
3.1.4 TD-DFT of 11 <sup>Cl</sup> and 11 <sup>Br</sup> .....	65
3.1.5 Light-supported electrolysis of 11 <sup>Br</sup> and 11 <sup>I</sup> under N <sub>2</sub> atmosphere.....	66

3.1.6	Concluding remarks.....	70
3.2	Rhenium-mediated <i>N</i> -transfer to benzonitrile .....	71
3.2.1	Acylation of nitride 13 <sup>Br</sup> .....	71
3.2.2	Electrochemical evaluation and reactivity under reductive conditions .....	74
3.2.3	Benzamide production mediated by a rhenium imido complex via PCET.....	82
3.2.4	Electrochemical benzamide formation via PCET.....	85
3.2.5	Nitride transfer forming benzonitrile via PCET.....	88
3.2.6	Concluding remarks.....	90
3.3	The electronic structure of the redox series (11 <sup>Br</sup> , 11 <sup>Br+</sup> , 11 <sup>Br2+</sup> ) .....	92
3.3.1	Synthesis and characterization of 11 <sup>Br</sup> .....	92
3.3.2	Synthesis and characterization of 11 <sup>Br+</sup> .....	93
3.3.3	Synthesis and characterization of 11 <sup>Br2+</sup> .....	96
3.3.4	The redox series [( $\mu$ -N <sub>2</sub> ) {ReBr <sub>2</sub> ( <sup>Br</sup> PN <sup>H</sup> P)} <sub>2</sub> ] <sup>0/+ / 2+</sup> : Discussion of trends.....	98
3.3.5	Concluding remarks.....	100
3.4	Conclusion and Outlook.....	101
<b>4</b>	<b>Experimental.....</b>	<b>104</b>
4.1	General synthesis and materials .....	104
4.2	Analytical methods .....	104
4.2.1	Crystallographic details.....	104
4.2.2	Cyclic voltammetry .....	105
4.2.3	Electron paramagnetic resonance .....	105
4.2.4	Elemental analysis .....	105
4.2.5	Irradiation.....	105
4.2.6	Nuclear magnetic resonance .....	106
4.2.7	Mass spectrometry .....	106
4.2.8	UVvis spectroscopy.....	106
4.2.9	IR spectroscopy.....	106
4.2.10	Resonance Raman spectroscopy .....	106
4.2.11	Magnetic measurements .....	106
4.2.12	Quantum yield determination of 11 <sup>Br</sup> .....	107
4.2.13	Rate constant determination for halide loss of 10 <sup>Cl/Br/1</sup> upon reduction and isomerization of 15 <sup>BArF</sup> upon reduction .....	108
4.3	Synthesis.....	109
4.3.1	Synthesis of [CrCl <sub>2</sub> ( <sup>ABu</sup> PNP)] (1).....	109
4.3.2	Synthesis of [CrCl <sub>2</sub> ( <sup>ABu</sup> PNP <sup>''</sup> )] (1 <sup>''</sup> ) .....	110
4.3.3	Synthesis of [CrCl( <sup>ABu</sup> PNP)] (2).....	111
4.3.4	Synthesis of [CrCl( <sup>ABu</sup> PNP <sup>''</sup> )] 2 <sup>''</sup> .....	112
4.3.5	Synthesis of [CrN <sub>3</sub> ( <sup>ABu</sup> PNP <sup>''</sup> )] (9).....	113
4.3.6	Synthesis of [( $\mu$ -N <sub>2</sub> ) {Cr( <sup>ABu</sup> PNP <sup>''</sup> )} <sub>2</sub> ] (3) .....	114
4.3.7	Synthesis of [{Cr(CO) <sub>2</sub> ( <sup>ABu</sup> PNP <sup>''</sup> )}( $\mu$ -CO) {Cr( <sup>ABu</sup> PNP <sup>''</sup> )}] (4) .....	115
4.3.8	Synthesis of [{Cr(CO) <sub>2</sub> ( <sup>ABu</sup> PNP <sup>''</sup> )}( $\mu$ -N <sub>2</sub> ) {Cr( <sup>ABu</sup> PNP <sup>''</sup> )}] (5).....	116
4.3.9	Synthesis of K[Cr(CO) <sub>2</sub> ( <sup>ABu</sup> PNP <sup>''</sup> )] (6).....	117
4.3.10	Synthesis of [{Cr(CN)( <sup>ABu</sup> PNP <sup>''</sup> )}( $\mu$ -CN) {Cr( <sup>ABu</sup> PNP <sup>''</sup> )}] (7).....	118

4.3.11	Synthesis of $[\text{ReBr}_3(\text{}^{\text{Ar}}\text{PN}^{\text{HP}})]$ (10 <sup>Br</sup> ).....	119
4.3.12	Synthesis of $[\text{ReI}_3(\text{}^{\text{Ar}}\text{PN}^{\text{HP}})]$ (10 <sup>I</sup> ).....	120
4.3.13	Synthesis of $[(\mu\text{-N}_2)\{\text{ReBr}_2(\text{}^{\text{Ar}}\text{PN}^{\text{HP}})\}_2]$ (11 <sup>Br</sup> ).....	121
4.3.14	Synthesis of $[\text{ReBr}(\text{N}_2)_2(\text{}^{\text{Ar}}\text{PN}^{\text{HP}})]$ (12).....	123
4.3.15	Synthesis of $[(\mu\text{-N}_2)\{\text{ReI}_2(\text{}^{\text{Ar}}\text{PN}^{\text{HP}})\}_2]$ (11 <sup>I</sup> ).....	124
4.3.16	Synthesis of $[\text{ReBr}_2\text{N}(\text{}^{\text{Ar}}\text{PN}^{\text{HP}})]$ (13 <sup>Br</sup> ).....	126
4.3.17	Synthesis of $[\text{ReI}_2\text{N}(\text{}^{\text{Ar}}\text{PN}^{\text{HP}})]$ (13 <sup>I</sup> ).....	129
4.3.18	Synthesis of $[\text{ReBrN}(\text{}^{\text{Ar}}\text{PNP})]$ (14 <sup>Br</sup> ).....	131
4.3.19	Synthesis of $[\text{ReIN}(\text{}^{\text{Ar}}\text{PNP})]$ (14 <sup>I</sup> ).....	132
4.3.20	Synthesis of $[(\mu\text{-N}_2)\{\text{ReBr}_2(\text{}^{\text{Ar}}\text{PN}^{\text{HP}})\}_2][\text{BPh}_4]$ (11 <sup>Br+</sup> ).....	133
4.3.21	Synthesis of $[(\mu\text{-N}_2)\{\text{ReBr}_2(\text{}^{\text{Ar}}\text{PN}^{\text{HP}})\}_2][\text{Al}(\text{OC}(\text{CF}_3)_3)_4]_2$ (11 <sup>Br2+</sup> ).....	134
4.3.22	Synthesis of $[\text{ReBr}_2\{\text{N}(\text{CO})\text{C}_6\text{H}_5\}(\text{}^{\text{Ar}}\text{PN}^{\text{HP}})][\text{BArF}_{24}]$ (15 <sup>BArF</sup> ).....	135
4.3.23	Synthesis of $[\text{ReBr}_2\{\text{N}(\text{CO})\text{C}_6\text{H}_5\}(\text{}^{\text{Ar}}\text{PN}^{\text{HP}})]$ (16).....	137
4.3.24	Synthesis of $[\text{ReBr}\{\text{NH}_2(\text{CO})\text{C}_6\text{H}_4\}(\text{}^{\text{Ar}}\text{PNP})]$ (17).....	138
4.3.25	Synthesis $[\text{ReBr}_2\{\text{NH}(\text{CO})\text{C}_6\text{H}_5\}(\text{}^{\text{Ar}}\text{PN}^{\text{HP}})]$ (18).....	139
4.3.26	Synthesis of $[\text{ReBr}_2(\text{}^{\text{Ar}}\text{PNP})]$ (19 <sup>Br</sup> ).....	140
4.4	Nitride transfer reactions via PCET and protonation.....	141
4.4.1	Benzonitrile formation via PCET starting from nitride complex 13 <sup>Br</sup> .....	141
4.4.2	Benzamide formation via PCET starting from imido complex 15 <sup>BArF</sup> .....	145
4.4.3	Electrochemical benzamide formation mediated by 15 <sup>BArF</sup> using LutHOTf.....	147
4.4.4	Electrochemical benzamide formation mediated by 15 <sup>BArF</sup> using LutHBr.....	150
4.4.5	Benzonitrile formation by protonolysis of 18.....	152
4.4.6	Benzonitrile formation by protonolysis of 17.....	153
<b>5</b>	<b>References.....</b>	<b>155</b>
<b>6</b>	<b>Appendix.....</b>	<b>175</b>
6.1	Spectroscopic results.....	175
6.1.1	$[\text{CrCl}_2(\text{}^{\text{tBu}}\text{PNP})]$ (1).....	175
6.1.2	$[\text{CrCl}(\text{}^{\text{tBu}}\text{PNP})]$ (2).....	176
6.1.3	$[\text{CrCl}_2(\text{}^{\text{tBu}}\text{PNP}^{\text{''}})]$ (1 <sup>''</sup> ).....	177
6.1.4	$[\text{CrCl}(\text{}^{\text{tBu}}\text{PNP}^{\text{''}})]$ (2 <sup>''</sup> ).....	178
6.1.5	$[(\mu\text{-N}_2)\{\text{Cr}(\text{}^{\text{tBu}}\text{PNP}^{\text{''}})\}_2]$ (3).....	179
6.1.6	$[\{\text{Cr}(\text{CO})_2(\text{}^{\text{tBu}}\text{PNP}^{\text{''}})\}(\mu\text{-CO})\{\text{Cr}(\text{}^{\text{tBu}}\text{PNP}^{\text{''}})\}]$ (4).....	180
6.1.7	$[\{\text{Cr}(\text{CO})_2(\text{}^{\text{tBu}}\text{PNP}^{\text{''}})\}(\mu\text{-N}_2)\{\text{Cr}(\text{}^{\text{tBu}}\text{PNP}^{\text{''}})\}]$ (5).....	181
6.1.8	$\text{K}[\text{Cr}(\text{CO})_2(\text{}^{\text{tBu}}\text{PNP}^{\text{''}})]$ (6).....	181
6.1.9	$[\{\text{Cr}(\text{CN})(\text{}^{\text{tBu}}\text{PNP}^{\text{''}})\}(\mu\text{-CN})\{\text{Cr}(\text{}^{\text{tBu}}\text{PNP}^{\text{''}})\}]$ (7).....	183
6.1.10	$[\text{Cr}(\text{CN}^{\text{tBu}})_4(\text{}^{\text{tBu}}\text{PNP}^{\text{''}})]$ (8).....	184
6.1.11	$[\text{CrN}_3(\text{}^{\text{tBu}}\text{PNP}^{\text{''}})]$ (9).....	184
6.1.12	$[\text{ReCl}_3(\text{}^{\text{Ar}}\text{PN}^{\text{HP}})]$ (10 <sup>Cl</sup> ).....	185
6.1.13	$[\text{ReBr}_3(\text{}^{\text{Ar}}\text{PN}^{\text{HP}})]$ (10 <sup>Br</sup> ).....	185
6.1.14	$[\text{ReI}_3(\text{}^{\text{Ar}}\text{PN}^{\text{HP}})]$ (10 <sup>I</sup> ).....	186
6.1.15	$[(\mu\text{-N}_2)\{\text{ReBr}_2(\text{}^{\text{Ar}}\text{PN}^{\text{HP}})\}_2]$ (11 <sup>Br</sup> ).....	189
6.1.16	$[\text{ReBr}(\text{N}_2)_2(\text{}^{\text{Ar}}\text{PN}^{\text{HP}})]$ (12).....	191
6.1.17	$[(\mu\text{-N}_2)\{\text{ReI}_2(\text{}^{\text{Ar}}\text{PN}^{\text{HP}})\}_2]$ (11 <sup>I</sup> ).....	192



6.1.18	[ReI <sub>2</sub> N( <sup><i>t</i></sup> PrPN <sup>H</sup> HP)] (13 <sup>I</sup> ) .....	194
6.1.19	[ReBrN( <sup><i>t</i></sup> PrPNP)] (14 <sup>Br</sup> ).....	195
6.1.20	[ReIN( <sup><i>t</i></sup> PrPNP)] (14 <sup>I</sup> ).....	196
6.1.21	[( $\mu$ -N <sub>2</sub> ){ReBr <sub>2</sub> ( <sup><i>t</i></sup> PrPN <sup>H</sup> HP)} <sub>2</sub> ]BPh <sub>4</sub> (11 <sup>Br+</sup> ) .....	197
6.1.22	[( $\mu$ -N <sub>2</sub> ){ReBr <sub>2</sub> ( <sup><i>t</i></sup> PrPN <sup>H</sup> HP)} <sub>2</sub> ][Al(OC(CF <sub>3</sub> ) <sub>3</sub> ) <sub>4</sub> ] (11 <sup>Br2+</sup> ) .....	198
6.1.23	[ReBr <sub>2</sub> {N(CO)C <sub>6</sub> H <sub>5</sub> }( <sup><i>t</i></sup> PrPN <sup>H</sup> HP)][BArF <sub>24</sub> ] (15 <sup>BArF</sup> ) .....	199
6.1.24	[Re <sup>IV</sup> Br <sub>2</sub> {N(CO)C <sub>6</sub> H <sub>5</sub> }( <sup><i>t</i></sup> PrPN <sup>H</sup> HP)] (16).....	203
6.1.25	[ReBr{NH <sub>2</sub> (CO)C <sub>6</sub> H <sub>4</sub> }( <sup><i>t</i></sup> PrPNP)] (17).....	204
6.1.26	[ReBr <sub>2</sub> {NH(CO)C <sub>6</sub> H <sub>5</sub> }( <sup><i>t</i></sup> PrPN <sup>H</sup> HP)] (18).....	206
6.1.27	[ReBr <sub>2</sub> ( <sup><i>t</i></sup> PrPNP)] (23) .....	208
6.2	Crystallographic details .....	209
6.2.1	[CrCl <sub>2</sub> ( <sup><i>t</i></sup> BuPNP)] (1) .....	209
6.2.2	[CrCl( <sup><i>t</i></sup> BuPNP)] (2) .....	210
6.2.3	[CrCl( <sup><i>t</i></sup> BuPNP <sup>''</sup> )] (2 <sup>''</sup> ) .....	211
6.2.4	[( $\mu$ -N <sub>2</sub> ){Cr( <sup><i>t</i></sup> BuPNP <sup>''</sup> )} <sub>2</sub> ] (3).....	212
6.2.5	[( $\mu$ -CO){Cr(CO) <sub>2</sub> ( <sup><i>t</i></sup> BuPNP <sup>''</sup> )}{Cr( <sup><i>t</i></sup> BuPNP <sup>''</sup> )}] (4).....	213
6.2.6	[{Cr(CO) <sub>2</sub> ( <sup><i>t</i></sup> BuPNP <sup>''</sup> )}( $\mu$ -N <sub>2</sub> ){Cr( <sup><i>t</i></sup> BuPNP <sup>''</sup> )}] (5) .....	214
6.2.7	[Cr(CO) <sub>2</sub> ( <sup><i>t</i></sup> BuPNP <sup>''</sup> )]K(18c6) (6) .....	215
6.2.8	[{Cr(CN)( <sup><i>t</i></sup> BuPNP <sup>''</sup> )}( $\mu$ -CN){Cr( <sup><i>t</i></sup> BuPNP <sup>''</sup> )}] (7) .....	216
6.2.9	[Cr(CN <sup><i>t</i></sup> Bu) <sub>4</sub> ( $\chi^2$ - <sup><i>t</i></sup> BuPNP <sup>''</sup> )] (8) .....	217
6.2.10	[CrN <sub>3</sub> ( <sup><i>t</i></sup> BuPNP <sup>''</sup> )] (9) .....	218
6.2.11	[ReBr <sub>3</sub> ( <sup><i>t</i></sup> PrPN <sup>H</sup> HP)] (10 <sup>Br</sup> ) .....	219
6.2.12	[ReI <sub>3</sub> ( <sup><i>t</i></sup> PrPN <sup>H</sup> HP)] (10 <sup>I</sup> ).....	220
6.2.13	[( $\mu$ -N <sub>2</sub> ){ReBr <sub>2</sub> ( <sup><i>t</i></sup> PrPN <sup>H</sup> HP)} <sub>2</sub> ] (11 <sup>Br</sup> ).....	221
6.2.14	[( $\mu$ -N <sub>2</sub> ){ReI <sub>2</sub> ( <sup><i>t</i></sup> PrPN <sup>H</sup> HP)} <sub>2</sub> ] (11 <sup>I</sup> ) .....	222
6.2.15	[ReBr(N <sub>2</sub> ) <sub>2</sub> ( <sup><i>t</i></sup> PrPN <sup>H</sup> HP)] (12).....	223
6.2.16	[ReI <sub>2</sub> N( <sup><i>t</i></sup> PrPN <sup>H</sup> HP)] (13 <sup>I</sup> ) .....	224
6.2.17	[ReBrN( <sup><i>t</i></sup> PrPNP)] (14 <sup>Br</sup> ).....	225
6.2.18	[ReIN( <sup><i>t</i></sup> PrPNP)] (14 <sup>I</sup> ).....	226
6.2.19	[ReBr <sub>2</sub> {N(CO)C <sub>6</sub> H <sub>5</sub> }( <sup><i>t</i></sup> PrPN <sup>H</sup> HP)][BArF <sub>24</sub> ] (15 <sup>BArF</sup> ) .....	227
6.2.20	[ReBr <sub>2</sub> {N(CO)C <sub>6</sub> H <sub>5</sub> }( <sup><i>t</i></sup> PrPN <sup>H</sup> HP)] (16).....	228
6.2.21	[ReBr{NH <sub>2</sub> (CO)C <sub>6</sub> H <sub>4</sub> }( <sup><i>t</i></sup> PrPNP)] (17).....	229
6.2.22	[ReBr <sub>2</sub> {NH(CO)C <sub>6</sub> H <sub>5</sub> }( <sup><i>t</i></sup> PrPN <sup>H</sup> HP)] (18).....	230
6.2.23	[( $\mu$ -N <sub>2</sub> ){ReBr <sub>2</sub> ( <sup><i>t</i></sup> PrPN <sup>H</sup> HP)} <sub>2</sub> ]BPh <sub>4</sub> (11 <sup>Br+</sup> ) .....	231
6.2.24	[( $\mu$ -N <sub>2</sub> ){ReBr <sub>2</sub> ( <sup><i>t</i></sup> PrPN <sup>H</sup> HP)} <sub>2</sub> ]OTf <sub>2</sub> (11 <sup>Br2+</sup> ).....	232
6.2.25	[ReBr <sub>2</sub> ( <sup><i>t</i></sup> PrPNP)] (23) .....	233
6.3	DFT calculations .....	234
6.3.1	Computational details of 3, 3-CO, 3-(CO) <sub>2</sub> , 4 and 5.....	234
6.3.2	TD-DFT calculations for [( $\mu$ -N <sub>2</sub> ){ReCl <sub>2</sub> ( <sup><i>t</i></sup> PrPN <sup>H</sup> HP)} <sub>2</sub> ] 11 <sup>Cl</sup> .....	239
6.3.3	TD-DFT calculations for [( $\mu$ -N <sub>2</sub> ){ReBr <sub>2</sub> ( <sup><i>t</i></sup> PrPN <sup>H</sup> HP)} <sub>2</sub> ] 11 <sup>Br</sup> .....	241
6.3.4	DFT calculations of PCET on nitride complex 10 <sup>Br</sup> .....	245
7	<b>Curriculum vitae</b> .....Fehler! Textmarke nicht definiert.	

## List of abbreviations

<b>ATP</b>	Adenosine triphosphate
<b>Cp<sup>+</sup></b>	Trimethylsilyl cyclopentadienyl, (C <sub>5</sub> H <sub>4</sub> SiMe <sub>3</sub> ) <sup>+</sup>
<b>Cp<sup>*</sup></b>	Pentamethylcyclopentadienyl
<b>CPE</b>	Controlled Potential Electrolysis
<b>CV</b>	Cyclic voltammetry
<b>DCM</b>	Dichloromethane
<b>Dmpe</b>	1,2-Bis(dimethylphosphino)ethane
<b>EPR</b>	Electron paramagnetic resonance
<b>ESI</b>	Electron Spray Ionization
<b>Fc</b>	Ferrocene
<b>Fc<sup>*</sup></b>	Decamethylferrocene
<b>HMDSO</b>	Hexamethyldisiloxane
<b>IC</b>	Interconfigurational
<b>IR</b>	Infrared
<b>IVCT</b>	Intervalence charge transfer
<b>LIFDI</b>	Liquid Injected Field Desorption Ionization
<b>MCD</b>	Magnetic circular dichroism
<b>MeCN</b>	acetonitrile
<b>NaBARF<sub>24</sub></b>	Sodium tetrakis(3,5-bis(trifluoromethyl)phenyl)borate
<b>dipp<sup>+</sup>Nacnac</b>	[{(C <sub>6</sub> H <sub>3</sub> (CH(CH <sub>3</sub> ) <sub>2</sub> )NCCCH <sub>3</sub> ) <sub>2</sub> CH}] <sup>+</sup> , 2,4-bis(2,6-dimethylphenylimino)-3-methyl-pent-3-yl)
<b>NaHMDS</b>	Natrium(hexamethyldisilazide)
<b>NMR</b>	Nuclear magnetic resonance
<b>(<sup>Pr</sup>P<sup>H</sup>P)</b>	HN{CH <sub>2</sub> CH <sub>2</sub> P(CH(CH <sub>3</sub> ) <sub>2</sub> ) <sub>2</sub> } <sub>2</sub>
<b>(<sup>Pr</sup>PNP)</b>	N{CH <sub>2</sub> CH <sub>2</sub> P(CH(CH <sub>3</sub> ) <sub>2</sub> ) <sub>2</sub> } <sub>2</sub> <sup>-</sup>
<b>(<sup>Bu</sup>P<sup>H</sup>P)</b>	HN{CH <sub>2</sub> CH <sub>2</sub> P(C(CH <sub>3</sub> ) <sub>3</sub> ) <sub>2</sub> } <sub>2</sub>
<b>(<sup>Bu</sup>P=N=P)</b>	N{CHCHP(C(CH <sub>3</sub> ) <sub>3</sub> ) <sub>2</sub> } <sub>2</sub>
<b>(<sup>Bu</sup>PNP)</b>	N{CH <sub>2</sub> CH <sub>2</sub> P(C(CH <sub>3</sub> ) <sub>3</sub> ) <sub>2</sub> } <sub>2</sub> <sup>-</sup>
<b>(<sup>Pr</sup>P=N<sup>H</sup>P)</b>	N{CHCH <sub>2</sub> P(CH(CH <sub>3</sub> ) <sub>2</sub> ) <sub>2</sub> } {CH <sub>2</sub> CH <sub>2</sub> P(CH(CH <sub>3</sub> ) <sub>2</sub> ) <sub>2</sub> }
<b>(PPPP)</b>	P{CH <sub>2</sub> CH <sub>2</sub> P(CH(CH <sub>3</sub> ) <sub>2</sub> ) <sub>2</sub> } <sub>3</sub>
<b>PDI</b>	Bis(2,6-diimine-pyridine)
<b>P<sub>3</sub>B</b>	tris(o-diisopropylphosphinophenyl)-borane
<b><sup>Pr</sup>PONOP</b>	2,6-bis(diisopropylphosphinito)pyridine
<b>Pyr</b>	Pyrazine
<b>RT</b>	room temperature
<b>Salen</b>	N,N'-Ethylenebis(salicylimine)
<b>SOC</b>	Spin-orbit coupling
<b>SQUID</b>	Superconducting quantum interference device
<b>TIP</b>	Temperature independent paramagnetism
<b>TP</b>	Tris(pyrazolyl)borate, [HB(C <sub>3</sub> N <sub>2</sub> H <sub>3</sub> ) <sub>3</sub> ] <sup>-</sup>
<b>Tpy</b>	2,2';6',2''-terpyridine
<b>THF</b>	Tetrahydrofuran
<b>TMS</b>	Trimethylsilyl
<b>UV<sub>vis</sub></b>	Ultra Violet visible light
<b>ZFS</b>	Zero-field splitting

# 1 Introduction

## 1.1 N<sub>2</sub> activation in transition metal complexes

### 1.1.1 General aspects

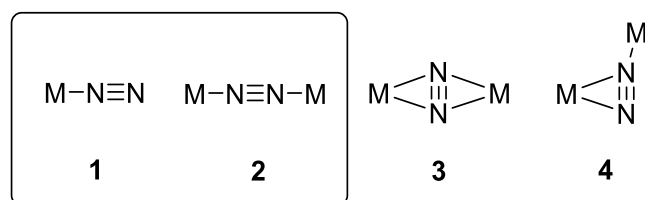
Ammonia is the most important nitrogen precursor molecule for the synthesis of nitrogenous compounds which is produced within the Haber-Bosch process by the conversion of dinitrogen and hydrogen, catalyzed by a heterogenous iron-based catalyst. The Haber-Bosch process operates at an impressive industrial scale, for example in 2019, 182 million tons of ammonia have been produced. 4% of the global generated methane and about 60% of the global H<sub>2</sub> resources are required for this process that exhausts 0.5 gigatons CO<sub>2</sub> per year equating to 3% of global CO<sub>2</sub> emissions. The forcing conditions, under which ammonia is formed (450 °C, 100 Bar), reflect the inertness of the N<sub>2</sub> molecule: it has a very strong N-N triple bond (941 kJ mol<sup>-1</sup>), a high ionization potential (15.6 eV) and low electron (-1.9 eV) and proton affinities (5.1 eV) which challenges functionalization. In contrast, nature evolved pathways to functionalize atmospheric N<sub>2</sub> into ammonia under ambient conditions using nitrogenase as biocatalyst. This anticipates a higher efficiency, however, 16 molecules ATP and eight H<sup>+</sup>/e<sup>-</sup> are required to convert one dinitrogen molecule into two molecules ammonia, corresponding to an overpotential of 117 kcal mol<sup>-1</sup> being significantly higher than the overpotential generated in the Haber-Bosch process (14 kcal mol<sup>-1</sup>).<sup>1-5</sup>

The costs and ecologic concerns, that are associated with the Haber-Bosch process, fueled the search of alternative pathways to surrogate ammonia as nitrogen precursor for the formation of nitrogenous fine chemicals. Transition metal complexes, as obtained by N-N bond homolysis, play a key role in this field as they mimic the rate-determining step in the Haber-Bosch process, which is the dissociative absorption of dinitrogen on the metal surface.<sup>4</sup> Note, transition metal mediated N-N bond cleavage often has a low kinetic barrier and proceeds at room temperature.<sup>2</sup> This approach is therefore highly attractive because N<sub>2</sub> fixation is facilitated at ambient conditions, and moreover, N<sub>2</sub> derived nitride species exhibit nucleophilic character opening the gate for reactivity with mild, organic electrophiles by N-C bond formation.

The application of transition metal complexes in dinitrogen fixation provides additional, beneficial aspects worth to mention: The possibility to apply a broad array of spectroscopic methods helps to explore the electronic structure of key species and provide insight into molecular processes in solution which is less accessible for heterogenous materials. Furthermore, the molecular modularity allows for a precise fine-tuning of electronic effects to tailor well-defined functional complexes.

### 1.1.2 N<sub>2</sub> as a ligand in transition metal complexes

The bonding situation of a dinitrogen ligand in transition metal complexes can be described as a combination of  $\sigma$ -donor/ $\pi$ -acceptor interactions with the d-orbitals of the transition metal complexes. There are four common binding modes, how dinitrogen can interact as a ligand with a transition metal ion (Figure 1.1), which can be classified into the terminal end-on binding mode (1), the dinuclear end-on (2), dinuclear side-on (3) and dinuclear end-on (4), whereby the first two modes are the most frequently encountered (Figure 1.1). In these different binding modes, the dinitrogen ligand exhibits different degrees of activation, ranging from the electronically neutral ligand form (N<sub>2</sub><sup>0</sup>) to (multiple) reduced forms such as the diazenide (N<sub>2</sub><sup>2-</sup>) or hydrazide the form (N<sub>2</sub><sup>4-</sup>). The extend of activation depends on the degree of backbonding of the metal d-orbital into the N-N  $\pi^*$ -orbital and can be quantified by the N-N bond length and the N-N stretching frequency which are inversed proportional to Badger's rule.<sup>1,2</sup>



	Spin state	$d_{\text{N-N}}$ [Å]	$\nu$ [cm <sup>-1</sup> ]
N≡N (free)	$S = 0$	1.10	2331
[N≡N] <sup>-</sup>	$S = 1/2$	n.a.	n.a.
Free H <sub>2</sub> N <sub>2</sub>		1.25	1.583 ( <i>trans</i> ) / 1.529 ( <i>cis</i> )
N=N <sup>2-</sup>	$S = 1$	1.20 – 1.35	1200 – 1700
[N=N] <sup>3-</sup>	$S = 1/2$	1.40	989 – 1040
Free H <sub>4</sub> N <sub>2</sub>		1.45	885
N-N <sup>4-</sup>	$S = 0$	1.40 – 1.60	700 – 1100

**Figure 1.1 Top:** N<sub>2</sub> binding modes in transition metal complexes. **Bottom:** Different dinitrogen redox states in transition metal complexes including bond metrics and stretching vibrations.<sup>1,2</sup>

The terminal binding mode features a low degree of activation. Consequently, there are only slight deviations in the N-N bond length and the corresponding stretching vibration compared to free dinitrogen. In such cases, the dinitrogen ligand is considered as electronically neutral. Towards dinuclear modes 2 – 4, the degree of activation is generally higher due to  $\pi$ -backbonding from two metal centers and the N<sub>2</sub> ligand has reduced character.

### 1.1.3 Electronic structures of N<sub>2</sub> bridged dinitrogen complexes

In the following, the bonding interaction between the dinitrogen ligand and a transition metal fragment will be discussed in detail within a molecular orbital scheme (Figure 1.2) that mostly relies on N<sub>2</sub> binding mode 2 presented in Figure 1.1. The bonding can be described by  $\sigma$ - and  $\pi$ -interactions between the metal centers and the N<sub>2</sub> ligand. In an example of an  $S_6$ -

symmetric complex, the linear combination of the dinitrogen  $\pi/\pi^*$ -orbitals with the metal  $d_{yz}$  and  $d_{xz}$ -orbitals generates four degenerate molecular orbitals with  $\pi$ -symmetry with 0, 1, 2 and 3 nodal planes ( $1e_u$ ,  $1e_g$ ,  $2e_u$ ,  $2e_g$ , respectively). The molecular orbital with  $\sigma$ -symmetry ( $a_u$ ) is derived by the linear combination of the metal  $d_{z^2}$  orbital with the dinitrogen  $\sigma^*$ -orbital, whereby the metal  $d_{xz}$  and  $d_{x^2y^2}$ -orbitals are non-bonding. In presence of a fourth ligand on the metal center ( $L_4M-N_2-M_4L$ ) in  $D_{4h}$ -symmetry, the molecular orbital scheme is nearly unchanged with the exception that the  $d_{xy}$ ,  $d_{xz}$  and  $d_{yz}$ -orbitals are degenerate and the non-bonding  $b_{1u}/b_{1g}$  molecular orbitals are energetically in between the  $1e_g$  and  $2e_u$  orbital.<sup>1,2</sup>

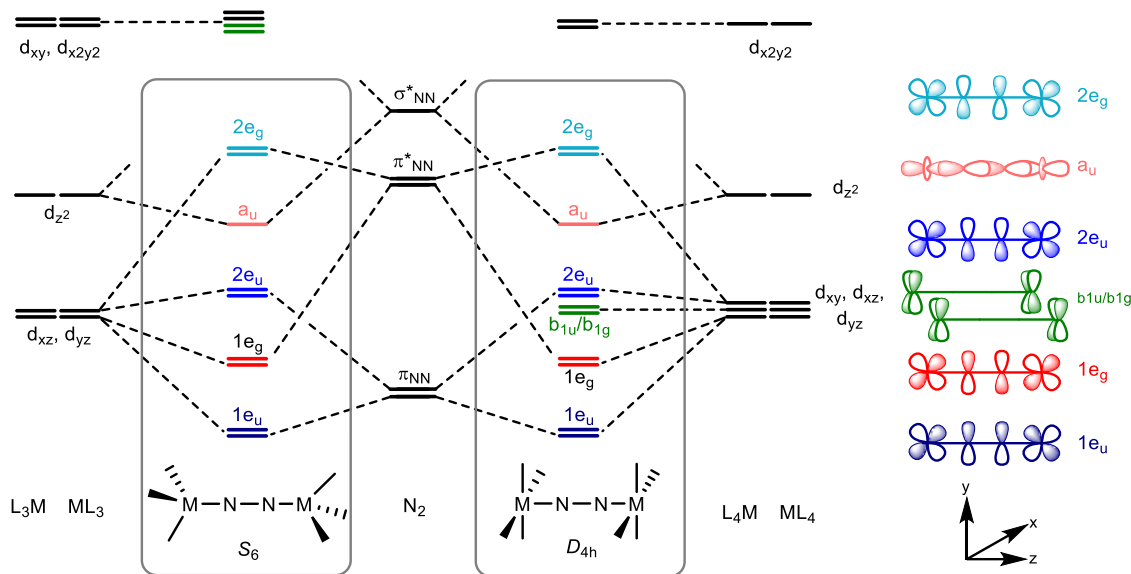


**Figure 1.2** Molecular orbital scheme of an  $L_3M-N_2-ML_3$  complex in  $S_6$ -symmetry and an  $L_4M-N_2-ML_4$  complex in  $D_{4h}$ -symmetry.<sup>1,2</sup>

This bonding model is in full agreement with a redox series of  $N_2$  bridged dimolybdenum complexes  $[(\mu-N_2)\{Mo(NR^tBu)_3\}_2]$  ( $II^{0+/2+}$ ) ( $R = 3,5$ -dimethylphenyl), reported by Cummins (Figure 1.3).<sup>6</sup> The neutral species, derived from  $N_2$  binding with tris amide complex  $[Mo(NR^tBu)_3]$  (**I**) at low temperatures, has ten  $\pi$ -electrons among the M-N-N-M manifold, derived from two  $d^3$  configured molybdenum centers and four electrons from the dinitrogen  $\pi$ -orbitals. Resultantly, the  $1e_u$  and the  $1e_g$ -orbitals are both fully occupied and the  $2e_u$  is filled with two unpaired electrons, establishing an electron triplet. The mono oxidized complex **II**<sup>+</sup> has nine  $\pi$ -electrons among the M-N-N-M manifold and the  $2e_u$  orbital is singly occupied, corresponding to an electron doublet. Further oxidation to **II**<sup>2+</sup> leads to complete depopulation which introduces a diamagnetic complex with eight  $\pi$ -electrons among the M-N-N-M manifold. Since the  $2e_u$  orbital has Mo-N antibonding and N-N bonding character, N-N bond elongation and a shift of the N-N stretching vibration to lower energy is observed upon successive depopulation of the  $2e_u$ -orbitals. An analogous trend was observed for a related redox series reported by Chirik.<sup>7</sup> Importantly, despite stronger degree of activation of the mono- and doubly-oxidized species **II**<sup>+</sup> and **II**<sup>2+</sup>, these two redox isomers are thermally stable complexes and only the redox neutral complex **II** undergoes N-N bond cleavage into

terminal nitrides. The association of a  $\pi^{10}$  electron configuration with N-N bond homolysis will be discussed in subchapter 1.1.5.

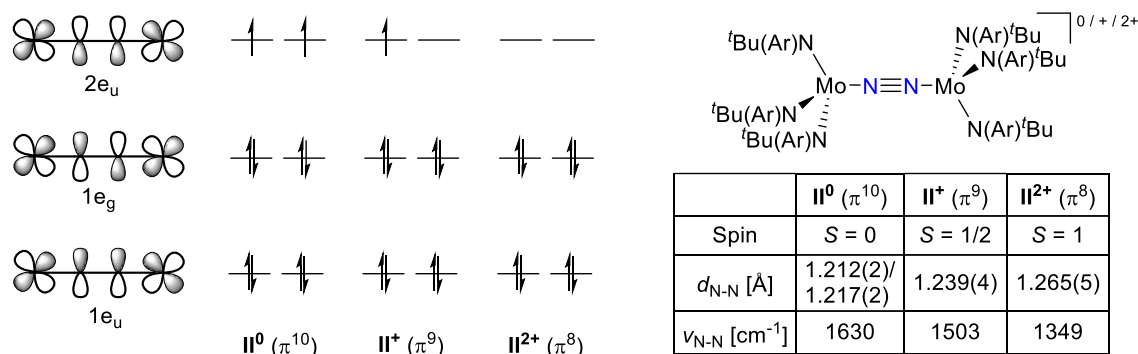


**Figure 1.3** Redox series based on  $[(\mu\text{-N}_2)\{\text{Mo}(\text{NR}^t\text{Bu})_3\}_2]$  **Mo<sup>0/+2+</sup>** reported by Cummins.<sup>6,8</sup>

Another group 6 redox series  $[(\mu\text{-N}_2)\{\text{WCl}(\text{P}^t\text{Bu})\text{PNP}\}_2]$  (**W<sup>0/+2+</sup>**) was reported by Schneider (Figure 1.4).<sup>9</sup> The redox neutral congener **W<sup>0</sup>** features a  $\pi^8\delta^4$  electron configuration in which the non-bonding  $\delta$ -orbitals are fully occupied ( $b_{1u} / b_{1g}$ ) resulting in an overall electron singlet ( $S = 0$ ). Hence, stepwise oxidation to **W<sup>+</sup>** and **W<sup>2+</sup>** has no significant influence on the degree of  $\text{N}_2$ -activation due to their non-bonding character as indicated in retained N-N bond lengths and stretching vibrations of the  $\text{N}_2$  ligand. The same trend of the N-N bond lengths and stretching vibrations was observed in the analogous molybdenum based redox series.<sup>10</sup> Importantly, none of these redox isomers undergoes N-N bond cleavage.

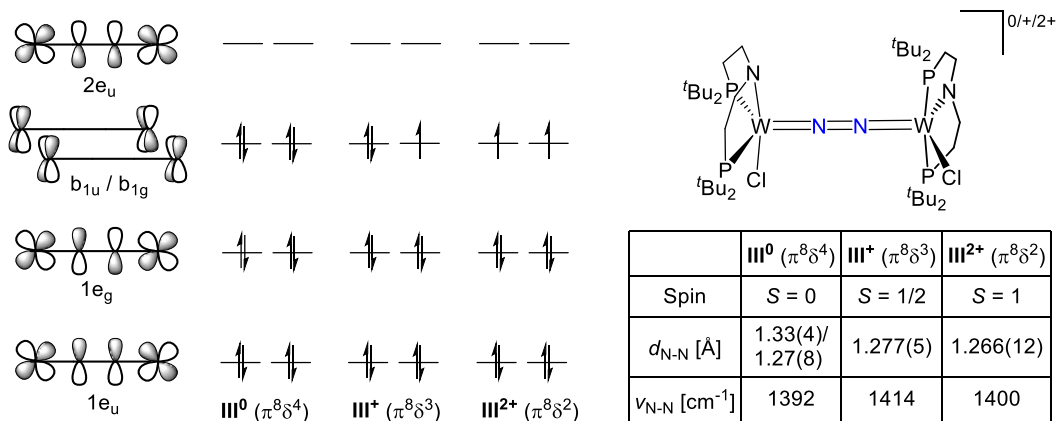


**Figure 1.4** Redox series based on  $[(\mu\text{-N}_2)\{\text{WCl}(\text{P}^t\text{Bu})\text{PNP}\}_2]$  (**W<sup>0/+2+</sup>**) reported by Schneider.<sup>9</sup>

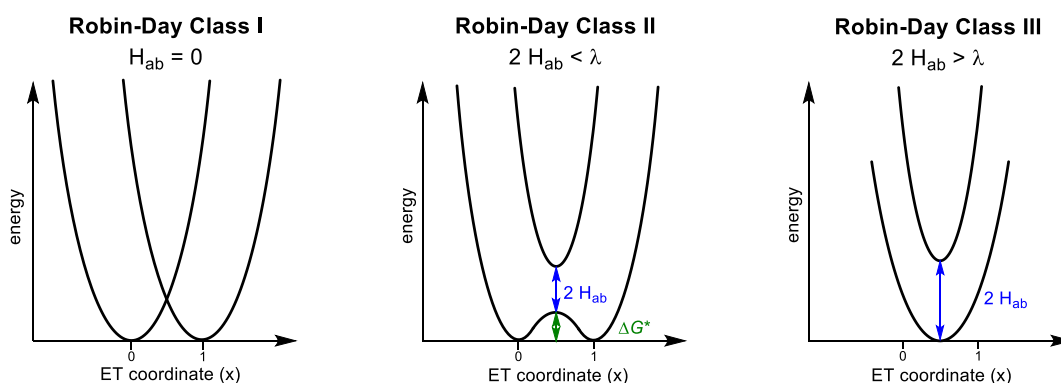
### 1.1.4 Robin-Day classification of $\text{N}_2$ bridged dinuclear complexes

The examination of mixed-valent complexes is of huge interest in order to understand electron transfer process in multinuclear transition metal complexes, for instance in metalloenzymes.<sup>11,12</sup> This research field commenced with the groundbreaking contributions from Creutz and Taube who initially examined the mixed-valent pyrazine-based diruthenium complex  $[(\mu\text{-Pyr})\{\text{Ru}(\text{NH}_3)_5\}_2]^{5+}$ <sup>13,14</sup> and later group 8 dinitrogen-bridged complexes  $[(\mu\text{-N}_2)\{\text{M}(\text{NH}_3)_5\}_2]^{5+}$  ( $\text{M} = \text{Ru}, \text{Os}$ ).<sup>15,16</sup> From then, the field of mixed-valent, dinuclear transition metal complexes has rapidly evolved and intensively reviewed.<sup>17-24</sup> Note, mixed-

valent organic compounds are another important branch in this research field, which is not of relevance for this work.<sup>25</sup>

Mixed-valent transition metal complexes are composed of at least two redox centers adapting different oxidation states, being connected by a bridging ligand that is suitable for electronic interactions. Classical examples are (poly)pyridyl- or dinitrogen ligands or organic, aromatic linker. The core of discussion in mixed-valent complexes is the question of how far the charge is (de)localized over the metal centers. Importantly, the examination of so-called inter-valence-charge-transfer (IVCT) bands is a particular characteristic, spectroscopic tool for mixed-valent complexes whose appearance strongly correlates with the nature of the electronic interaction, as discussed in detail below. These bands are typically low-energy transitions and therefore occur in the near-IR region.

The Robin-Day classification<sup>26</sup> differentiates three primary classes, as illustrated in Scheme 1.1. This classification is coined by the extent of the electronic coupling between the redox centers, expressed by the electronic coupling parameter “ $H_{ab}$ ”, and the reorganization energy “ $\lambda$ ” that is associated with electron transfer: There is no electronic coupling in class I complexes ( $H_{ab} = 0$ ) between both metal centers, that are represented by two diabatic potential surfaces, centered at  $x = 0$  and  $1$  at the dimensionless reaction coordinate (Scheme 1.1, left). This can be the case when the metal centers are spatially separated or if the electronic interaction is spin or symmetry forbidden. The unpaired electron is in this case fully localized and no IVCT band is expected.



**Scheme 1.1** Potential surfaces for complexes belonging to Robin-Day classes I, II and III.<sup>22–24,27</sup>

The situation is significantly different for class II complexes: At the intersection of both diabatic surfaces at  $x = 0.5$ , both wave functions can mix, thus giving rise to two adiabatic surfaces (Scheme 1.1, middle). The energetic separation is defined by the electronic coupling parameter “ $2 H_{ab}$ ”, which is significantly lower than the Marcus reorganization energy in class II complexes ( $2 H_{ab} < \lambda$ ). The electronic ground state is expressed by an adiabatic double-well curve with a sizable thermal barrier for electron transfer leading to partial delocalization of the unpaired electron. Vertical transitions between the adiabatic surfaces are possible and thus, IVCT bands can be expected. However, as the electronic coupling parameter  $H_{ab}$  scales with the band intensity, IVCT bands of class II complexes are typically less intensive

( $\epsilon_{\max} \leq 5000 \text{ M}^{-1} \text{ cm}^{-1}$ ), show a solvent dependence and feature large line-widths ( $\Delta\nu_{1/2} \geq 2000 \text{ cm}^{-1}$ ). Other molecular properties that are characteristic for valence localization are deviations in the geometry around the metal centers or the appearance of the symmetric stretching vibration of the bridging ligand, which is particularly conclusive in  $\text{N}_2$  bridged, mixed-valent complexes.

In case of strong electronic coupling ( $2 H_{ab} > \lambda$ ), the ground state adiabatic surface shows only one minimum at  $x = 0.5$  and there is effectively no thermal barrier for electron transfer (Scheme 1.1, right). Thus, the system can be described as fully delocalized and both metal centers possess formally the same oxidation state. The ICVT bands are typically strong ( $\epsilon_{\max} \geq 5000 \text{ M}^{-1} \text{ cm}^{-1}$ ), show no solvent dependence and possess narrow line widths ( $\Delta\nu_{1/2} \leq 2000 \text{ cm}^{-1}$ ). Moreover, especially in case of strong electronic coupling, cut-off effects can occur leading to asymmetric shaped IVCT bands. In contrast to class II, class III mixed-valent complexes neither show a symmetric stretching vibration nor differences in the geometry between the redox centers.<sup>22–24,27</sup>

Importantly, the interpretation of IVCT bands can be perturbed by superimposing interconfigurational (IC) bands. This phenomenon is observed in mixed-valent complexes that contain heavy metals, where spin-orbit coupling leads to splitting of the electronic ground state.<sup>22–24,27</sup> Generally, it is emphasized that the borders of the Robin-Day classes are blurred in some cases, prohibiting a clear assignment, as discussed below.<sup>23</sup>

In the following, examples of mixed-valent, dinuclear compounds are shown, which have been assigned to the Robin-Day classification. There are almost no examples of dinuclear  $\text{N}_2$  complexes belonging to class I. Field reported the asymmetric, dinitrogen complex  $[(\mu\text{-N}_2)\{\text{Fe}^{\text{I}}\text{H}(\text{PPPP})\}\{\text{Fe}^{\text{II}}\text{H}(\text{PPPP})\}]$  (**IV**), in which the metal centers possess oxidation states  $\text{Fe}^{\text{II}}/\text{Fe}^{\text{I}}$ .<sup>28</sup> Based on different ligand signal sets in the  $^1\text{H}$  and  $^{31}\text{P}$  NMR signature, this complex was assigned to class I (IR/UVvis spectroscopy was not reported).<sup>29</sup> Robin-Day class II is most common among mixed-valent  $\text{N}_2$  complexes. Schneider reported a series of molybdenum based  $\text{N}_2$  complexes, including  $[(\mu\text{-N}_2)\{\text{MoCl}(\text{t}^{\text{Bu}}\text{PNP})\}_2]^+$  (**V**) where the metal centers possess the oxidation states  $\text{Mo}^{\text{IV}}/\text{Mo}^{\text{III}}$ .<sup>10</sup> NMR characterization revealed  $C_2$ -symmetry in solution, indicating valence delocalization on the slow NMR time scale. However, room temperature EPR spectroscopy showed an isotropic signal with significant  $^{95/97}\text{Mo}$  and  $^{31}\text{P}$  (to two phosphorous atoms) hyperfine coupling. In combination with significant structural differences in bond lengths between the metal centers ( $d_{\text{Mo-Cl}} = 2.3519(11), 2.4515(11) \text{ \AA}$ ), class II was suggested.<sup>10</sup> Another class II representative was reported by Holland.<sup>29</sup> Within a nacnac ligand framework, the iron centers in the dinuclear complex  $[(\mu\text{-N}_2)\{\text{Fe}(\text{t}^{\text{Pr}}\text{nacnac})\}_2]^+$  (**VI**) adopt oxidation states  $\text{Fe}^{\text{I}}/\text{Fe}^{\text{I}}$ . This assignment is based on Mößbauer spectroscopy, where the obtained spectra could be fitted by two overlapping quadrupole doublets with identical intensity but significantly different isotopic shifts ( $\delta = 0.63, 0.49 \text{ mm s}^{-1}$ ). Importantly, valence localization of **VI** is resolved on



the IR time scale ( $\nu = 1749 \text{ cm}^{-1}$ ). However, analogous to the former example, the charge is delocalized on the slow NMR time scale, as judged by  $D_{2d}$  or  $D_{2h}$ -symmetry in solution.

A series of mixed-valent dioxmium complexes was published by Mayer that could not be definitely assigned to one single of the three Robin-Day classes.<sup>30</sup> One representative of these complexes,  $[(\mu\text{-N}_2)\{\text{OsCl}_2(\text{tpy})\}_2]^+$  **VII**, is shown in Figure 1.5 (top middle).<sup>31</sup> Comparing the Os-Cl bond length, significant differences can be observed between the metal centers ( $d_{\text{Os-Cl}} = 2.352(3), 2.371(3)$  vs.  $2.401(3), 2.402(3)$  Å). Another strong argument for valence localization is the appearance of an intense stretching vibration in the IR spectrum at  $\nu = 2012 \text{ cm}^{-1}$ . By contrast, the examination of the near-IR region revealed five bands, which were assigned to three IVCT ( $3175 \text{ cm}^{-1}, 4720 \text{ cm}^{-1}, 5250 \text{ cm}^{-1}$ ) and two IC bands ( $6610 \text{ cm}^{-1}, 10000 \text{ cm}^{-1}$ ). As a major characteristic for class III complexes, the IVCT bands are intense, narrow and do not show solvent dependence. These observations prompted the authors to introduce the “class II-III” to the Robin-Day classification scheme.<sup>31</sup>

Class III was defined for the mixed-valent dimolybdenum complex  $[(\mu\text{-N}_2)\{\text{Mo}(\text{NAr}^t\text{Bu})_2\}_2]^+$  (Ar = 3,5-dimethylphenyl) **I**<sup>+</sup>, that showed no significant structural differences between the metal centers. Moreover, the N-N stretching vibration is only Raman and not IR active. The absence of diagnostic bands in the near-IR region did not allow for further spectroscopic confirmation. The unpaired electron was proposed to be located in a molecular orbital that is delocalized across the M-N-N-M vector.<sup>6</sup> An older example is given by dioxmium complex  $[(\mu\text{-N}_2)\{\text{Os}(\text{NH}_3)_5\}_2]^+$  **VIII**. Full delocalization is suggested based on the absence of a diagnostic N-N stretching vibration in the IR spectrum, and the absence of an interconfigurational (IC) band, which is a spectroscopic marker for valence-localized  $\text{Os}^{\text{II/III}}$  compounds.<sup>15,16</sup>

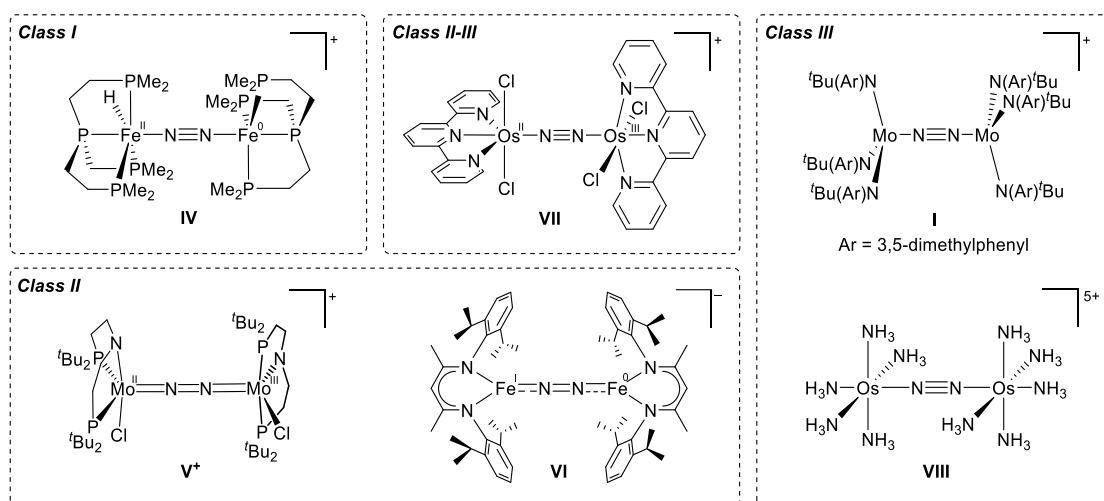
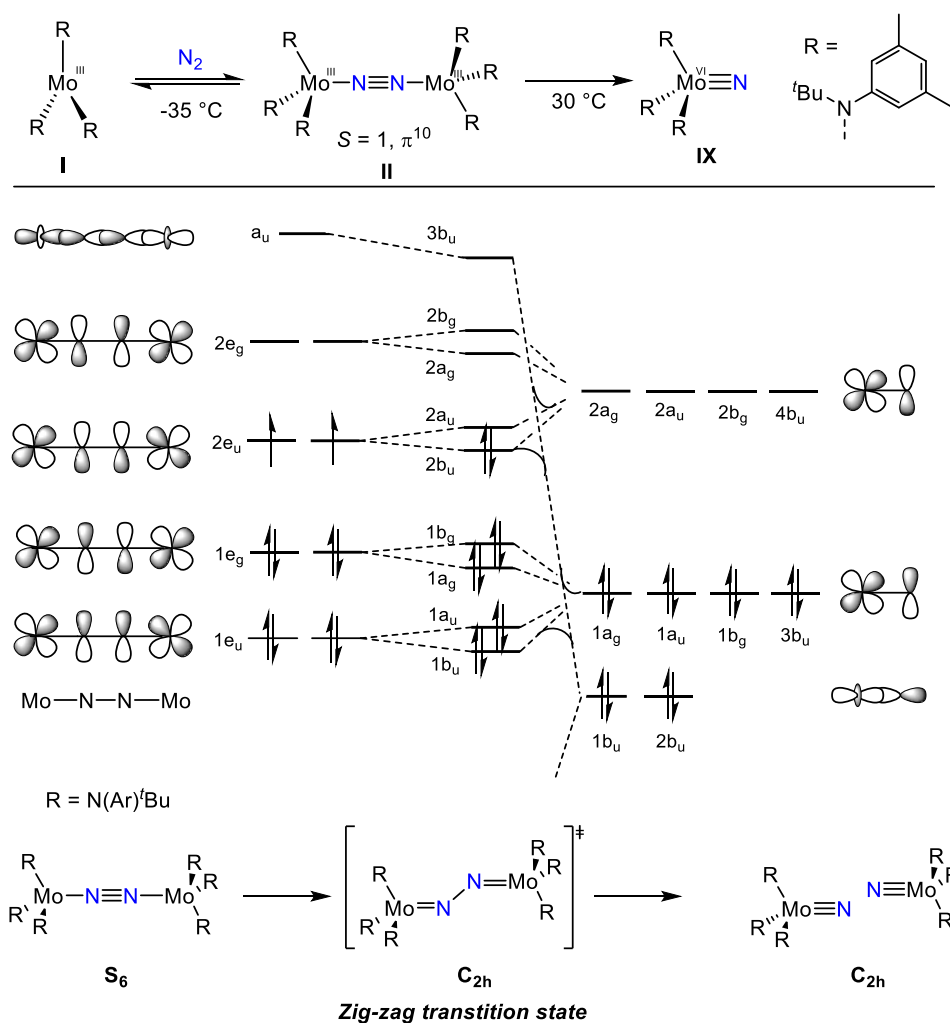


**Figure 1.5** Mixed-valent transition metal complexes assigned to the Robin-Day classification including formal oxidation states.<sup>6,10,15,28–30</sup>

### 1.1.5 Thermal and photochemical N<sub>2</sub> cleavage into terminal nitride complexes

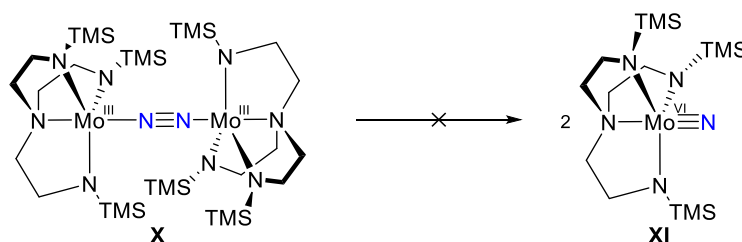
As mentioned earlier, N-N bond scission into terminal nitride species is associated with a  $\pi^{10}$  electron configuration in dinuclear N<sub>2</sub> complexes. This observation can be rationalized by the molecular orbital scheme depicted in Scheme 1.2 that applies to molybdenum complex  $[(\mu\text{-N}_2)\{\text{Mo}(\text{NR}'\text{Bu})_3\}_2]$  **II**<sup>0</sup> (R = 3,5-dimethylphenyl). As introduced in Figure 1.3, the HOMO consists of two degenerate 2e<sub>u</sub>-orbitals that are occupied by two unpaired electrons. As bond homolysis along the M-N-N-M vector is symmetry forbidden, the symmetry is broken within a zig-zag transition state, where the degeneracy of the 2e<sub>u</sub>-orbitals of **II**<sup>0</sup> is canceled out. Hence, mixing of the 2b<sub>u</sub>-orbital with the 3b<sub>u</sub>-orbital leads to destabilization of the N-N bond, as the 3b<sub>u</sub>-orbital has strong N-N antibonding character, which then finally leads to N-N bond cleavage giving rise to closed shell nitride complexes **IX**. The thermodynamic driving force is the formation of the stable Mo-N triple bonds which is particularly favored by a  $\pi^{10}$  electron configuration explaining the thermal persistence of **II**<sup>+</sup> ( $\pi^9$ ) and **II**<sup>2+</sup> ( $\pi^8$ ) with respect to N<sub>2</sub> cleavage.<sup>1,2,32</sup>



**Scheme 1.2** Molecular orbital scheme of thermal N<sub>2</sub> splitting into terminal nitrides.<sup>21</sup>

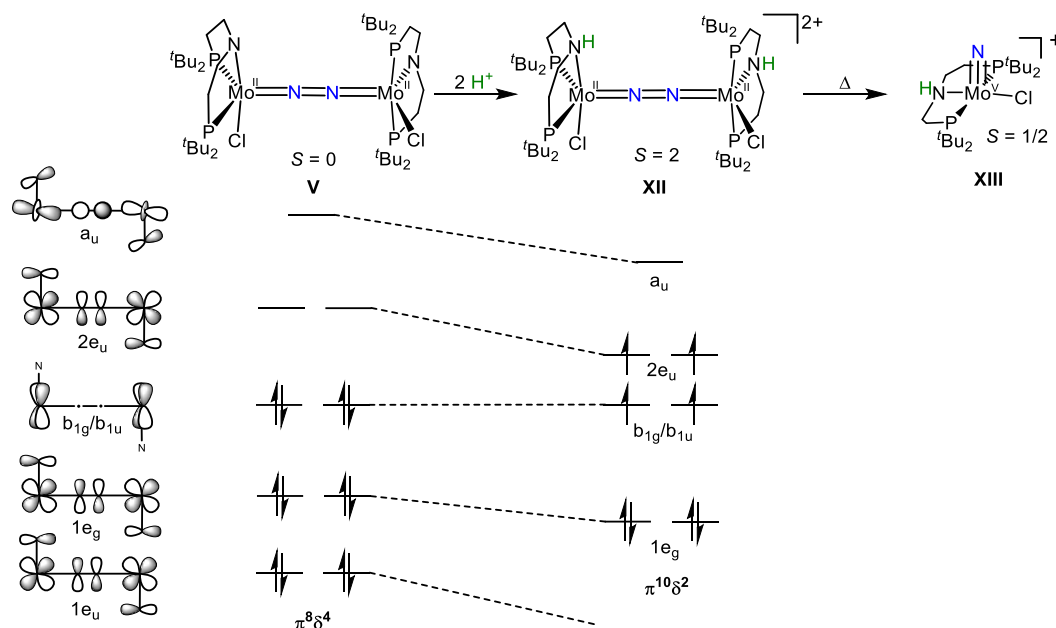
The computed kinetic barrier of 21 kcal mol<sup>-1</sup> explains facile N<sub>2</sub> cleavage at room temperature.<sup>32</sup> It is important to note that the thermodynamics of N<sub>2</sub> cleavage underlie

structural constraints: An analogous dinuclear, isoelectronic Mo<sup>III</sup> dinitrogen complex  $[(\mu\text{-N}_2)\{\text{Mo}(\text{PhNCH}_2\text{CH}_2)_3\text{N}\}_2]$  **X**, in which the metal centers are coordinated by tetradentate triamidoamine ligands, is thermally stable and does not split into the respective nitrides  $[\text{MoN}(\text{PhNCH}_2\text{CH}_2)_3\text{N}]_2$  **XI** despite  $\pi^{10}$  electron configuration (Scheme 1.3). A theoretical investigation revealed that splitting is thermodynamically uphill by +10 kcal mol<sup>-1</sup> which was rationalized by the presence of a  $\sigma$ -donating ligand in *trans*-position to the N<sub>2</sub> bridge. This *trans*-effect destabilizes the a<sub>u</sub> orbital and N<sub>2</sub> cleavage is consequently getting kinetically and thermodynamically unfavored.<sup>1,2,6,32,33</sup>



**Scheme 1.3** Thermal stability of complex **X** towards N<sub>2</sub> cleavage into nitride complex **XI**.<sup>32,33</sup>

Schneider reported an example how ligand effects dictate the thermodynamics of N<sub>2</sub> cleavage (Scheme 1.4).<sup>34</sup>  $[(\mu\text{-N}_2)\{\text{MoCl}(\text{}^t\text{BuPNP})\}_2]$  **V** is an N<sub>2</sub> bridged dimolybdenum complex in square pyramidal coordination sphere that possesses a singlet ground state with a  $\pi^8\delta^4$  electron configuration. Thermal splitting was computed with a huge barrier ( $\Delta G^\ddagger = 37$  kcal mol<sup>-1</sup>) in line with the observed high thermal stability caused by strong  $\pi$ -donation of the amide PNP pincer ligands that lifts the energies of the 2e<sub>u</sub> and a<sub>u</sub>-orbitals (Scheme 1.4).<sup>34</sup> Importantly, N<sub>2</sub> splitting into nitride  $[\text{MoNCl}(\text{}^t\text{BuPN}^{\text{H}}\text{P})]^+$  **XII** is triggered upon protonation. As derived by DFT computations, the electronic structure of **V** drastically changes in presence of acid: the amide groups in the ligand backbone are getting protonated and resultantly strong  $\pi$  donation is depleted. The 2e<sub>u</sub> and a<sub>u</sub>-orbitals drop in energy and an intermediate spin ( $S = 2$ )  $\pi^{10}\delta^2$  electron configuration is favored. The doubly protonated species  $[(\mu\text{-N}_2)\{\text{MoCl}(\text{}^t\text{BuPN}^{\text{H}}\text{P})\}_2]^{2+}$  **XII** has a significantly lower barrier for N<sub>2</sub> cleavage ( $\Delta G^\ddagger = 21$  kcal mol<sup>-1</sup>) and splitting into nitrides is facilitated via a zig-zag transition state at room temperature.<sup>34</sup> Importantly, the acid counter anion controls the selectivity between dinitrogen splitting and proton reduction, which was examined with the analogous tungsten complex.<sup>9</sup> The versatile applicability of particularly molybdenum-based transition metal complexes demonstrate their key role in N<sub>2</sub> fixation and functionalization.<sup>35-40</sup>

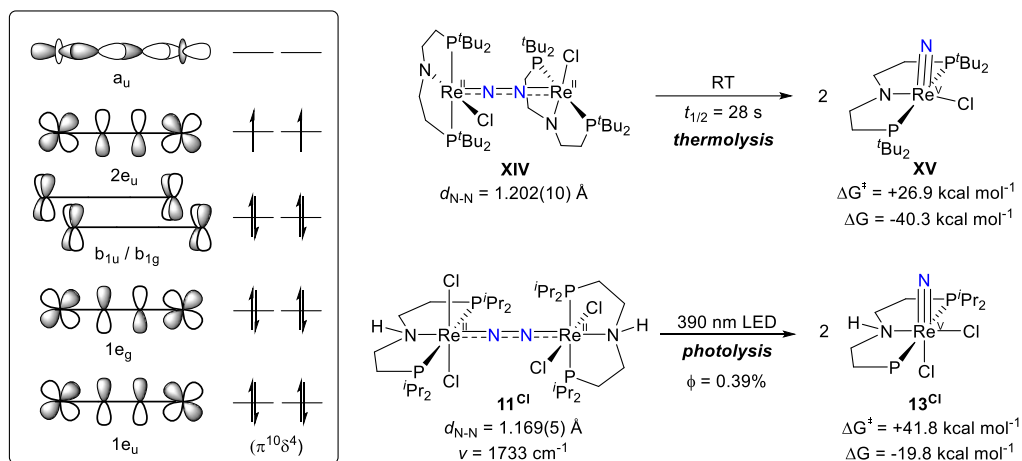


**Scheme 1.4** Molybdenum mediated  $\text{N}_2$  cleavage triggered by protonation.<sup>34</sup>

Another example where coordinative aspects control the thermodynamics of  $\text{N}_2$  cleavage is delivered by the comparison of the two structurally and isoelectronic dirhenium complexes  $[(\mu\text{-N}_2)\{\text{ReCl}(\text{}^t\text{BuPNP})\}_2]$  **XIV** and  $[(\mu\text{-N}_2)\{\text{ReCl}_2(\text{}^i\text{PrPN}^{\text{H}}\text{P})\}_2]$  **11<sup>Cl</sup>** reported by Schneider (Scheme 1.5).<sup>41–43</sup> In these two complexes, the coordination sphere around the rhenium centers is coined by the sterics of the phosphorous substituents. The sterically demanding  ${}^t\text{Bu}$ -groups favor square pyramidal coordination geometry (**XIV**), while the less bulky  ${}^i\text{Pr}$  groups prefer octahedral coordination (**11<sup>Cl</sup>**). Both complexes have an idealized  $C_2$ -symmetry in solution and in the solid state with similar N-N bond length ( $d_{\text{N-N}} = 1.169(5)$  Å (**11<sup>Cl</sup>**), 1.202(10) Å (**XIV**)). The stretching vibration of the bridging dinitrogen ligand in **11<sup>Cl</sup>** occurs at 1733  $\text{cm}^{-1}$  in the rRaman spectrum. As judged by DFT computations, both complexes can be described as electron triplets ( $S = 1$ ) with a  $\pi^{10}\delta^4$  electron configuration favoring  $\text{N}_2$  cleavage.<sup>2,41,43</sup>

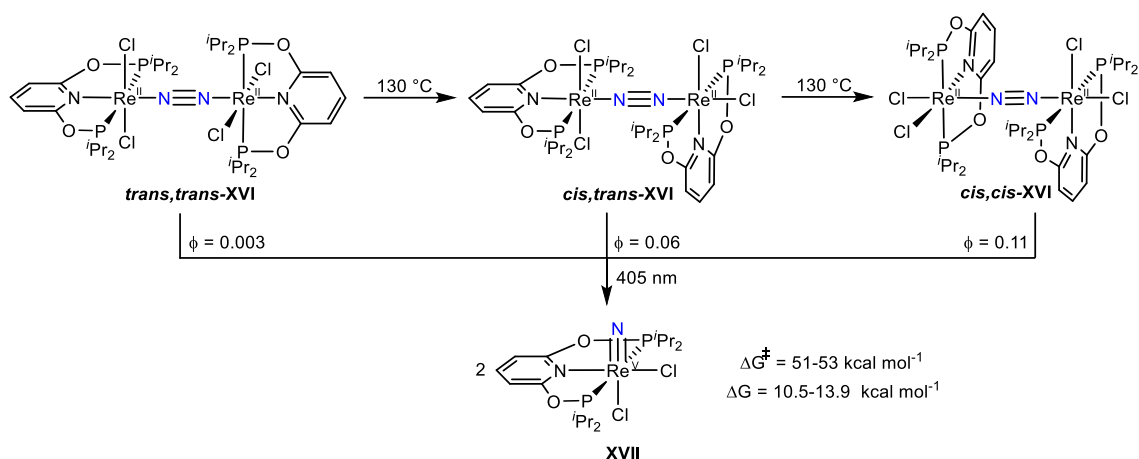
The thermal stability of both dinitrogen complexes is fundamentally different. The  ${}^t\text{Bu}$  congener **XIV** is unstable at room temperature and selectively splits into the five-coordinate  $\text{Re}^{\text{V}}$  nitride species  $[\text{ReClN}(\text{}^t\text{BuPNP})]$  **XV**. In sharp contrast, isopropyl-substituted **11<sup>Cl</sup>** is thermally persistent towards heating overnight at 60 °C. However, being exposed to a 390 nm LED lamp selectively generates the corresponding 6-coordinate, octahedral  $\text{Re}^{\text{V}}$  nitride  $[\text{ReCl}_2\text{N}(\text{}^t\text{BuPN}^{\text{H}}\text{P})]$  **13<sup>Cl</sup>**.<sup>43</sup> These observations are decently reproduced by DFT calculations that predict a huge difference in the kinetic barriers for  $\text{N}_2$  cleavage ( $\Delta G^\ddagger = 26.9$  kcal mol<sup>-1</sup> (**XIV**) vs. 41.8 kcal mol<sup>-1</sup> (**11<sup>Cl</sup>**), Scheme 1.5) caused by a *trans*-ligand to the  $\text{N}_2$  bridge in **11<sup>Cl</sup>** that lifts the energetics of the  $3b_u$ -orbitals (Scheme 1.2). While the detailed photolysis mechanism is yet to be explored, it is assumed that electronic excitation triggers a metal-ligand charge transfer (MLCT) process, that shifts electrons from the non-bonding  $\delta$ -orbitals ( $b_{1u}/b_{1g}$ ) into the strongly antibonding  $\pi^*-\pi^*-\pi^*$ -orbital ( $2e_g$ ). An increase

of flexibility along the Re-N-N-Re core allows for a zig-zag distortion that introduces N-N bond cleavage.<sup>43</sup> Furthermore, the coordination geometry has a huge impact on the overall thermodynamics of the splitting products **XV** and **13<sup>Cl</sup>** which differ by  $\sim 20$  kcal mol<sup>-1</sup>. How that affects the reactivity, will be discussed in subchapter 1.2.2.



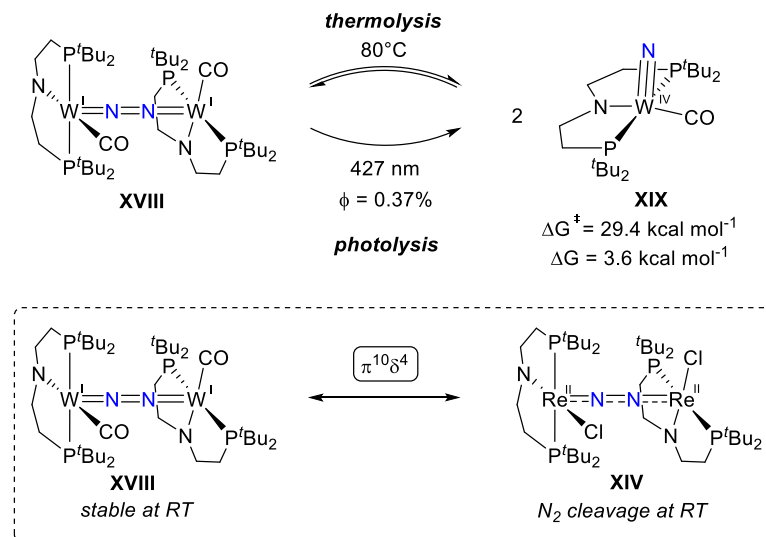
**Scheme 1.5** Rhenium N<sub>2</sub> bridged dinuclear complexes with a  $\pi^{10}\delta^4$  electron configuration that split into nitrides.<sup>41–43</sup>

A thematically similar contribution was provided by Miller (Scheme 1.6). An N<sub>2</sub> bridged dirhenium complex  $[(\mu\text{-N}_2)\{\text{Re}^{\text{II}}\text{Cl}_2(\text{P}^{\text{t}}\text{PONOP})\}_2]$  **XVI** was reported, where the rhenium atoms are octahedrally coordinated by a PONOP pincer ligand. In analogy to  $[(\mu\text{-N}_2)\{\text{Re}^{\text{II}}\text{Cl}_2(\text{P}^{\text{t}}\text{PN}^{\text{H}}\text{P})\}_2]$  **11<sup>Cl</sup>**, a diagnostic rRaman shift of 1776 cm<sup>-1</sup> was observed indicating a comparable degree of activation and DFT computations confirmed an electron triplet ( $S = 1$ ). Given the structural similarities to **11<sup>Cl</sup>** including a *trans*-ligand of the N<sub>2</sub> bridge, thermal N<sub>2</sub> cleavage is not observed in this case, which is consistent with a high computed kinetic barrier (51 – 53 kcal mol<sup>-1</sup>). However, high temperatures (toluene, 130 °C) induce isomerization, where the initial *trans-trans*-isomer is arranged via the *cis,trans* into the *cis,cis*-isomer. Importantly, all isomers are photo-active and split into the corresponding six-coordinate nitride species  $[\text{Re}^{\text{V}}\text{Cl}_2\text{N}(\text{P}^{\text{t}}\text{PONOP})]$  **XVII** under exposure to an LED (405 nm), albeit with significant different quantum yields that differ in orders of magnitudes ( $\Phi = 0.003, 0.06, 0.11$ ). Notably, the *trans,trans*-isomer, isostructural to **10<sup>Cl</sup>**, shows effectively no photolysis, while **10<sup>Cl</sup>** forms the corresponding nitride within hours. Interestingly, nitride formation is endergonic (10.5 – 13.9 kcal mol<sup>-1</sup>) for all isomers.<sup>44</sup>



**Scheme 1.6** Thermal isomerization of N<sub>2</sub> bridged dirhenium complexes and photolytic N<sub>2</sub> cleavage reported by Miller.<sup>44</sup>

The tungsten-based dinitrogen complex  $[(\mu\text{-N}_2)\{\text{W}^{\text{I}}\text{CO}(\text{t}^{\text{Bu}}\text{PNP})\}_2]$  **XVIII** is capable of both thermal and photolytic N<sub>2</sub> cleavage as recently published by Schneider (Scheme 1.7). Structurally closely related and isoelectronic ( $\pi^{10}\delta^4$ ) to rhenium complex  $[(\mu\text{-N}_2)\{\text{Re}^{\text{II}}\text{Cl}(\text{t}^{\text{Bu}}\text{PNP})\}_2]$  **XIV**, the metal centers are square pyramidal coordinated and connected via N<sub>2</sub> linkage. The pincer ligands are twisted about 90° resulting an idealized C<sub>2</sub>-symmetry in solution. Magnetic characterization by SQUID magnetometry and DFT calculations suggest an electronic triplet ground state analogous to **XIV**.



**Scheme 1.7** Tungsten mediated N<sub>2</sub> cleavage via thermolysis and photolysis.<sup>45</sup>

However, despite absence of a *trans*-ligand towards the N<sub>2</sub> bridge, the compound is thermally stable at room temperature. At elevated temperatures, however, the N-N triple bond is cleaved via equilibrium to  $[\text{WN}(\text{CO})(\text{t}^{\text{Bu}}\text{PNP})]$  **XIX**, as N<sub>2</sub> cleavage is nearly thermo-neutral ( $\Delta G = +3.6 \text{ kcal mol}^{-1}$ ) with an accessible barrier at high temperatures ( $\Delta G^\ddagger = 29.4 \text{ kcal mol}^{-1}$ ). Consequently, nitride coupling to the parent dinitrogen complex is achieved after heating nitride **XIX** for several hours. The increased barrier for N<sub>2</sub> cleavage

of **XVIII** compared to the isoelectronic rhenium complex **XIV** is proposed to be a consequence of the strong  $\pi$ -accepting carbonyl ligands withdrawing electron density from the W-N-N-W core. Importantly, quantitative nitride formation can be obtained by exposure to light with a wavelength of 427 nm. A quantum yields of about 0.37% is reported that is close to  $[(\mu\text{-N}_2)\{\text{Re}^{\text{I}}\text{Cl}_2(\text{P}^{\text{r}}\text{PN}^{\text{H}}\text{P})\}_2] \mathbf{11}^{\text{Cl}}$  (0.39%). Generally, photolytic  $\text{N}_2$  cleavage has been observed in some  $\text{N}_2$  bridged complexes,<sup>2,46–48</sup> however, relatively little is known about the splitting mechanism and the excited state dynamics.<sup>49–51</sup>

## 1.2 Functionalization of $\text{N}_2$ derived nitrides species

Transition metal nitride and imide complexes are key species in *N*-functionalization, therefore, it is of huge interest to explore their reactivity with regard to *N*-transfer and to understand their electronic structure. Nitride complexes have preceded to be synthetically accessible by N-N bond cleavage, but there are also alternative pathways including the application of azide sources or the oxidation of ammonia. Transition metal imido complexes can be synthesized directly by reacting nitride complexes with nucleophiles or electrophiles or from the reaction with organic azides.<sup>52,53</sup>

### 1.2.1 The bonding situation in transition metal nitride ( $\text{M}\equiv\text{N}$ ) and imido ( $\text{M}\equiv\text{N}-\text{R}$ / $\text{M}=\text{N}-\text{R}$ ) complexes

Transition metal nitride and imido complexes share an isoelectronic relationship that is mostly valid in the case of a linear M-N-R moiety, expressed by a bond angle of approximately  $180^\circ$  (Figure 1.6, left, A and B). The bonding situation is exemplified for an octahedral coordination sphere in Figure 1.6, right. The nitrogen  $p_z$  orbital can overlap with the d-orbitals in  $\sigma$ -symmetry whereas the nitrogen  $p_x$  and  $p_y$  orbital can interact with the  $d_{xz}$  and  $d_{yz}$ -orbitals with  $\pi$ -symmetry, respectively, giving rise to one  $\sigma$ - and two  $\pi$ -bonds which assemble the  $\text{M}\equiv\text{N}$  triple bond (Figure 1.6, right). Consequently, transition metal nitride or imido complexes predominantly occur in high oxidation states to avoid the occupation of M-N antibonding orbitals. The high degree of covalency of especially transition metal nitride complexes is expressed by short M-N bond lengths of about 1.65 Å, whereby corresponding imido complexes commonly show slight elongation towards 1.70 Å. A reduction of the  $\text{M}\equiv\text{N}-\text{R}$  bond order is expected when either the metal possesses a lower oxidation state or in presence of multiple, competing  $\pi$ -donating ligands donating into the same metal d-orbital. In these cases, the M-N bond exhibits double bond character which coincides with M-N bond elongation (1.75 Å) and deviations of the linearity of the organic imido substituent caused by a localized lone pair on the nitrogen atom (Figure 1.6, left, C). Regardless of the actual bonding situation, metal imido bonds and metal nitride bonds are frequently denoted as double and triple bonds, respectively, to simplify the assignment of formal oxidation states. Importantly, the oxidation state formalism has to be handled with care in highly covalent bonding situations, as it is the case especially in  $\text{M}\equiv\text{N}$  triple bonds: a formal triply

charged  $N^{3-}$  unit suggest to be a highly nucleophilic, however, the covalent bonding situation in a  $M\equiv N$  bond often result in thermodynamic (over)stabilization that leads to chemical inertness.<sup>52–58</sup>

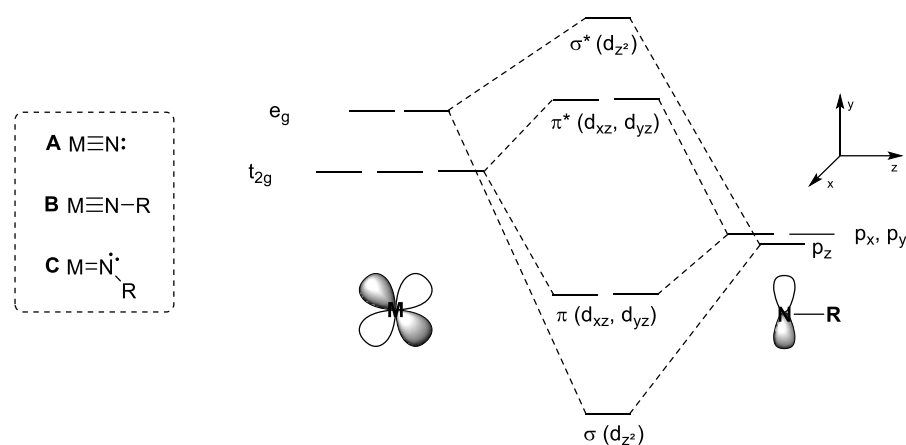


**Figure 1.6 Left:** Formalism of a transition metal nitride and imido bond. **Right:** Molecular orbital scheme of octahedral transition metal imido complexes.<sup>52,57</sup>

The reactivity of transition metal nitride and imido complexes is governed by the energetics of the  $\pi^*$ -orbital relative to the metal d or the nitrogen p-orbitals: Early to mid-transition metals possess high-lying d-orbitals, resulting in strong polarization of the  $M\equiv N$  triple bond and nucleophilic reactivity is expected (Figure 1.7, left). In contrast, late transition metals have low lying d-orbitals and the  $\pi^*$ -orbital has rather nitrogen character that induces electrophilic nitride reactivity (Figure 1.7, right).<sup>2</sup> In this regard, typical reactivity of molybdenum nitride complexes include reactions with electrophiles such as alkyl triflates. By contrast, osmium nitrides have ambiphilic character: nitride complexes can serve as a nucleophile as observed by reaction with alkyl triflates, however, reactivity with Grignard reagents clearly demonstrates electrophilic behavior.<sup>2,52–56</sup>

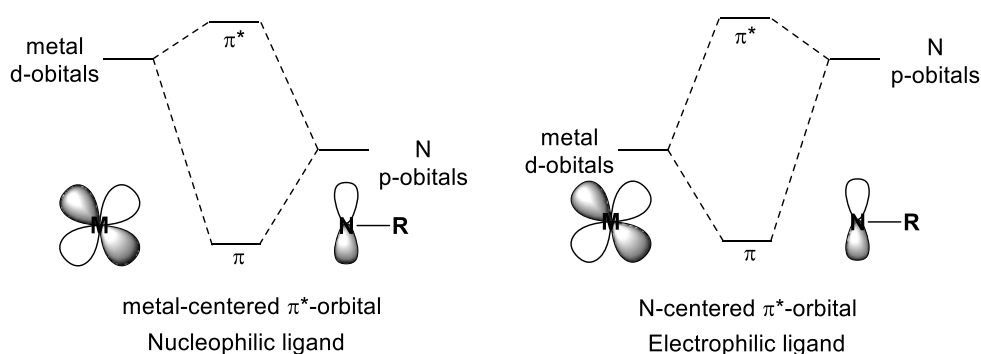


**Figure 1.7** Nucleophilic vs. electrophilic transition metal nitride ligands.<sup>52</sup>

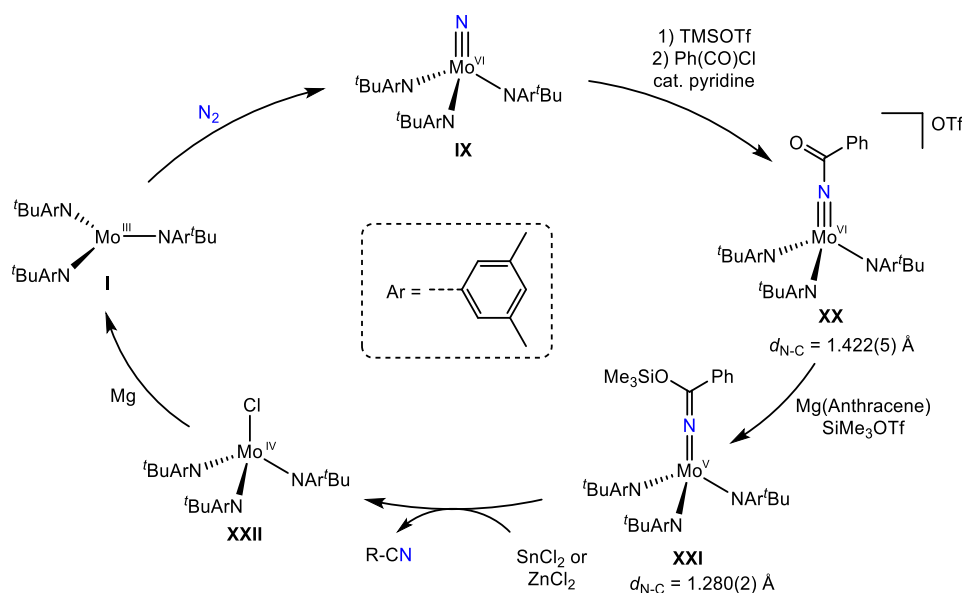
### 1.2.2 Nitride functionalization via N-C bond formation

N-C bond formation of transition metal nitride complexes with organic substrates into imido species is a highly attractive transformation for building up organic, nitrogenous molecules. To date, there are numerous transition metal imido complexes ( $M=N-R$ ) across the d-block



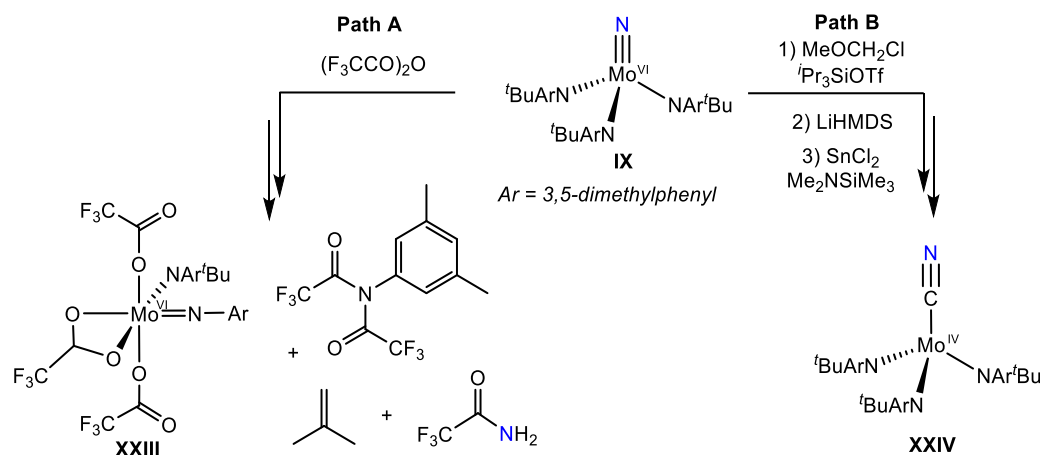
in the periodic table,<sup>52,55,67–70,59–66</sup> however, only minor examples originate from atmospheric dinitrogen. In other words, only a handful transition metal platforms can generate reactive nitride species from atmospheric N<sub>2</sub> that allow for follow-up chemistry within a synthetic cycle including simultaneous product release and recovery of the starting material on the metal side.

Seminal works by Cummins present the conversion of atmospheric dinitrogen into benzonitrile (Scheme 1.8). The synthetic cycle is initiated by N<sub>2</sub> fixation of [Mo<sup>III</sup>(NR<sup>t</sup>Bu)<sub>3</sub>] **I** forming [Mo<sup>VI</sup>N(NR<sup>t</sup>Bu)<sub>3</sub>] **IX** via N-N bond homolysis. While no direct reactivity with benzoyl chloride was observed, conversion of **IX** with trimethyl silyl triflate and subsequently with benzoyl chloride provides benzoyl imido complex [Mo<sup>VI</sup>{N(CO)C<sub>6</sub>H<sub>5</sub>} (NR<sup>t</sup>Bu)<sub>3</sub>]OTf **XX**. The N-C bond length indicates single bond character ( $d_{\text{C-N}} = 1.4225 \text{ \AA}$ ), which significantly contracts by further reduction with magnesium anthracene and addition of trimethylsilyl triflate that delivers ketimido species [Mo<sup>V</sup>N(CO(TMS))Ph(NR<sup>t</sup>Bu)<sub>3</sub>] **XXI** formally having a C=N double bond ( $d_{\text{C-N}} = 1.280(2) \text{ \AA}$ ). Benzonitrile is then liberated by the addition of tin or zinc(II)chloride to obtain the tetrahedral coordinated [Mo<sup>IV</sup>Cl(NR<sup>t</sup>Bu)<sub>3</sub>] **XXII** that fixes N<sub>2</sub> under reductive conditions to close a five-step synthetic cycle.<sup>71,72</sup>



**Scheme 1.8** 5-step synthetic cycle from dinitrogen to benzonitrile.<sup>71,72</sup>

An analogous 5-step synthetic cycle was reported within a hetero-dinuclear Nb/Mo platform that produces nitriles from N<sub>2</sub> and benzoyl chloride (not shown).<sup>73</sup> The versatility of [Mo<sup>VI</sup>N(NR<sup>t</sup>Bu)<sub>3</sub>] **IX** to undergo N-transfer is represented by stoichiometric reactions that produce trifluoroaceticamide<sup>61</sup> and molybdenum imido complex **XXIII** (Scheme 1.9, Path A). Synthetic access from dinitrogen N<sub>2</sub> into cyanide (**XXIV**) was demonstrated in another example (Scheme 1.9, Path B).<sup>74</sup> The synthesis of amides and nitriles is generally of huge interest for pharmaceutical and agrochemical applications, functional polymers or for the synthesis of N-heterocycles.<sup>75–80</sup>



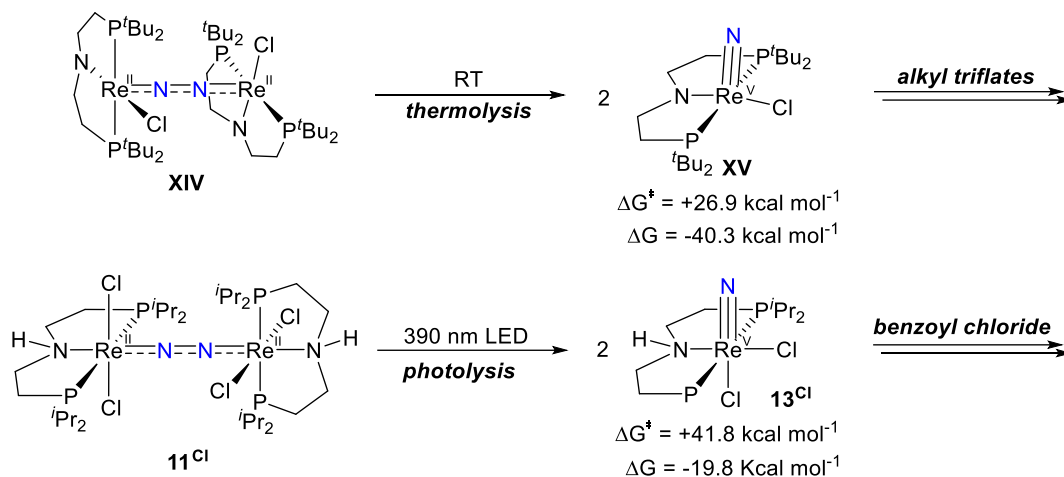
**Scheme 1.9** Acylation of Cummins  $\text{Mo}^{\text{VI}}$  nitride using trifluoromethyl acetic anhydride.<sup>61,74</sup>

These examples should be rated as proof of concept to achieve *N*-functionalization from atmospheric  $\text{N}_2$ , as these multistep synthetic cycles are far from a catalytic application. While catalytic formation of  $\text{N}(\text{SiMe}_3)_3$ <sup>81</sup> and  $\text{N}(\text{BCy}_2)_3$ <sup>82</sup> has been reported, there is to date no example for catalytic N-C bond formation into nitrogenous compounds such as amines, amides or nitriles. The reason for that is presumably a compatibility issue: The formation of a  $\text{M}\equiv\text{N}$  triple bond offers a decent driving force for (thermal) homolytic  $\text{N}_2$  cleavage, however, thermodynamic overstabilization of the respective nitride species is often encountered.<sup>2</sup> Strong electrophilic substrates are required to compensate the chemical inertness causing incompatibility towards the chemical reductant used for  $\text{N}_2$  fixation.

The major challenge to circumvent this incompatibility issue is to find a strategy how to enhance nitride nucleophilicity to operate with mild electrophiles having sufficient negative reduction potentials to coexist with chemical reductants.<sup>83</sup> Recently, the examination of computed thermodynamic and kinetic data of  $\text{N}_2$  cleavage for different linear  $\text{N}_2$  bridged complexes including the respective nitride complex revealed a Marcus-type free energy relationship: The correlation showed, that low kinetic barriers for  $\text{N}_2$  cleavage are associated with a high thermodynamic (over)stabilization of the splitting products. Inversely, high kinetic barriers are associated with less thermodynamic stabilized nitride species. Reactive nitride species that are located in the thermoneutral regime exhibit prohibitively high barriers around  $\sim 40 \text{ kcal mol}^{-1}$  being inaccessible at room temperature.<sup>2</sup> Photolytic  $\text{N}_2$  cleavage plays a key role in this respect, because it has been shown that high kinetic barriers can become accessible, as introduced in subchapter 1.1.5.

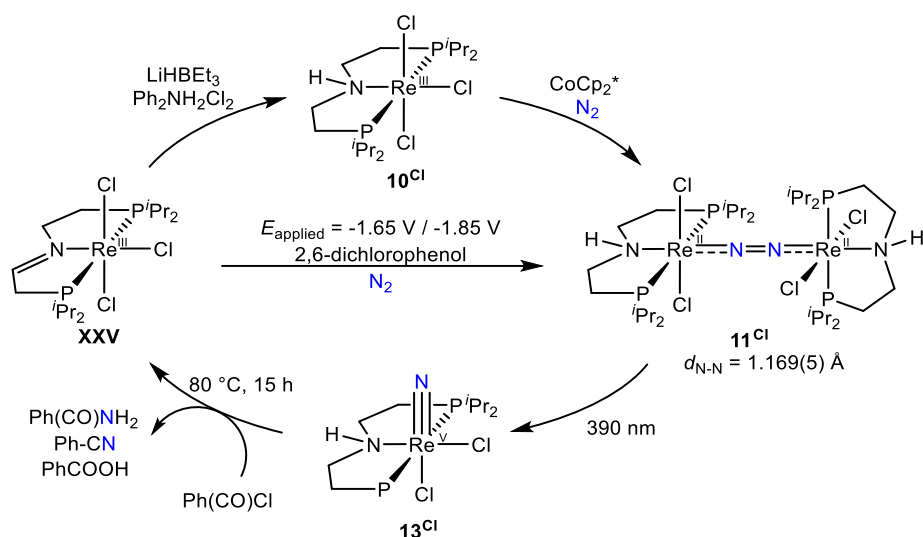
This concept is nicely resembled by the comparison of the rhenium based  $\text{N}_2$  complexes  $[(\mu\text{-N}_2)\{\text{Re}^{\text{II}}\text{Cl}(\text{t}^i\text{BuPNP})\}_2]$  **XIV** and  $[(\mu\text{-N}_2)\{\text{Re}^{\text{II}}\text{Cl}_2(\text{t}^i\text{BuPN}^{\text{H}}\text{P})\}_2]$  **11<sup>Cl</sup>** and the reactivity of their  $\text{N}_2$  splitting products  $[\text{Re}^{\text{V}}\text{ClN}(\text{t}^i\text{BuPNP})]$  **XV** and  $[\text{Re}^{\text{V}}\text{Cl}_2\text{N}(\text{t}^i\text{BuPN}^{\text{H}}\text{P})]$  **13<sup>Cl</sup>**, respectively (Scheme 1.10). As mentioned earlier (subchapter 1.1.5), both complexes exhibit analogous electronic structures, however, the thermodynamics are fundamentally different. While nitride **XV** is derived by thermolysis, **13<sup>Cl</sup>** is only accessible by photolysis, whereby the latter is far less thermodynamically stabilized ( $\Delta G = -40.3 \text{ kcal mol}^{-1}$  (**XV**) vs.  $-19.8 \text{ kcal mol}^{-1}$

( $13^{\text{Cl}}$ ). This thermodynamic gap has a tremendous effect on the reaction behavior: The five-coordinate nitride species **XV** is a reluctant nucleophile and requires strong electrophile such as alkyl triflates for N-C bond formation.<sup>84,85</sup> The six-coordinate nitride  $13^{\text{Cl}}$  is more nucleophilic and reacts with the much weaker electrophile benzoyl chloride, albeit at elevated temperatures. The destabilizing role of a *trans*-ligand to the nitride is suggested to account for the enhanced nucleophilicity.



**Scheme 1.10** Reactivity of thermolysis derived nitrides vs. photolysis derived nitrides.<sup>41–43</sup>

Nitride transfer is facilitated in a 4-step synthetic cycle (Scheme 1.11). (Electro)chemical reduction of  $[\text{Re}^{\text{III}}\text{Cl}_3(\text{P}^{\text{Pr}}\text{N}^{\text{H}}\text{P})]$   $10^{\text{Cl}}$  under an atmosphere of dinitrogen leads to  $\text{N}_2$  fixation generating dinuclear complex  $[(\mu\text{-N}_2)\{\text{Re}^{\text{II}}\text{Cl}_2(\text{P}^{\text{Pr}}\text{N}^{\text{H}}\text{P})\}_2]$   $11^{\text{Cl}}$  which can be photolyzed to  $[\text{Re}^{\text{V}}\text{Cl}_2\text{N}(\text{P}^{\text{Pr}}\text{N}^{\text{H}}\text{P})]$   $13^{\text{Cl}}$  using a light source ( $\lambda \geq 305$ ). This complex is inert at ambient conditions but can be reacted with benzoyl chloride at elevated temperatures to form the octahedral imine complex  $[\text{Re}^{\text{III}}\text{Cl}_3(\text{P}^{\text{Pr}}\text{P}=\text{N})]$  **XXV**. Unlike the Cummins' system, no imido intermediates were observed (Scheme 1.8). Imine complex **XXV** features a partially oxidized ligand backbone as it serves as a  $2\text{H}^+/2\text{e}^-$  donor in this reaction to form benzamide in high yields by metal-ligand cooperativity, which, in presence of benzoyl bromide, is converted into benzonitrile and benzoic acid. Ligand re-reduction can occur either chemically by the reaction with diphenyl ammonium chloride and lithium triethyl borohydride or electrochemically in presence of 2,6-dichlorophenol that recovers  $[\text{Re}^{\text{III}}\text{Cl}_3(\text{P}^{\text{Pr}}\text{N}^{\text{H}}\text{P})]$   $10^{\text{Cl}}$ . Importantly, ligand reduction from imine complex  $[\text{Re}^{\text{III}}\text{Cl}_3(\text{P}^{\text{Pr}}\text{P}=\text{N}^{\text{H}}\text{P})]$  **XXV** to rhenium trichloride complex  $10^{\text{Cl}}$  and subsequent  $\text{N}_2$  reduction to  $11^{\text{Cl}}$  can be performed in one pot to close a 3-step synthetic cycle. Unfortunately, photolysis of the reaction mixture obtained nitride complex  $[\text{Re}^{\text{V}}\text{Cl}_2\text{N}(\text{P}^{\text{Pr}}\text{N}^{\text{H}}\text{P})]$   $13^{\text{Cl}}$  only with a poor yield of 14%.<sup>43</sup>



**Scheme 1.11** Rhenium mediated 3-step synthetic cycle that forms benzonitrile.<sup>43</sup>

Compared to the Cummins' system (Scheme 1.8) the benefits are obvious: The reduction potential required for  $\text{N}_2$  reduction is lowered, allowing the usage of decamethyl cobaltocene instead of magnesium. Increased nitride reactivity allows for direct reactivity with benzoyl chloride, without the addition of trimethylsilyl triflate. Maybe most meaningful, parts of the synthetic cycle can be performed electrochemically, which is generally a highly attractive approach because it is associated with selectivity increase by fine-adjustment of required reduction potentials.

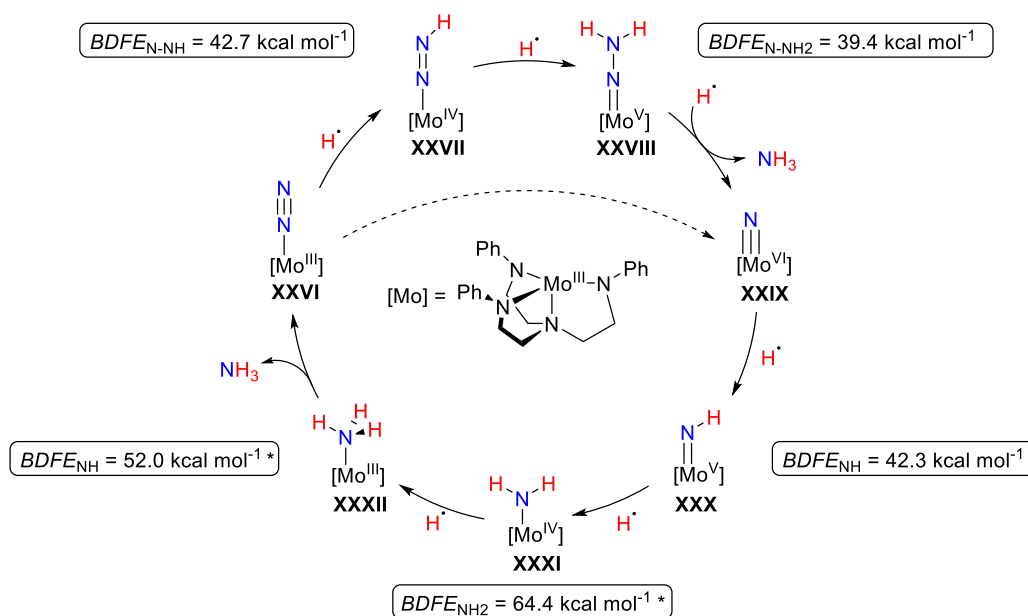
Nevertheless, what the system still restricts from catalysis is the mismatch of the reduction potential required for  $\text{N}_2$  activation ( $E_{1/2} = -1.85 \text{ V}$ ) being more negative compared to benzoyl chloride ( $E_{p,c} \sim -1.6 \text{ V}$ ).<sup>83,86</sup> Furthermore, elevated temperatures are required and the usage of high-energy wavelength, which are at the edge of UV light. Acyl halides have shown to undergo photolysis<sup>87,88</sup> forming benzoyl radicals, which have sufficient long lifetimes for bimolecular reactivity.<sup>89-91</sup>

### 1.2.3 N-H bond formation in nitride complexes and ammonia production

N-H bond formation is embedded in the world's largest industrial process, the Haber-Bosch process, that transforms  $\text{N}_2$  and  $\text{H}_2$  to ammonia. With the intention to gain a deeper understanding of this process, where  $6\text{H}^+/6\text{e}^-$  are transferred per dinitrogen molecule, researchers started almost 50 years ago to design transition metal complexes serving a model compounds. Seminal works of Chatt in 1975 report the formation of stoichiometric amounts of ammonia and hydrazine by protonation of terminal  $\text{N}_2$  ligands in octahedral  $\text{Mo}^0$  complexes.<sup>92</sup> The first report of catalytic conversion of atmospheric dinitrogen was published 30 years later by Schrock in 2003.<sup>93</sup> The generation of hydrogen atoms was facilitated by the proton-coupled-electron-transfer (PCET) reagent  $\text{CrCp}^*/\text{lutidinium BArF}_{24}$ . To date, homogenous state-of-the-art catalysts are based on molybdenum that transform dinitrogen

to ammonia with turnover numbers above 4000 using an *in situ* formed samarium diiodide/H<sub>2</sub>O complex as reduction and protonation reagent.<sup>94</sup>

The Chatt cycle, also called Schrock-cycle, is the most frequently used model that describes the mechanism of catalytic ammonia formation, that has been computed based on Chatt-type complexes<sup>95</sup> as well as for the Schrock-system, which is illustrated in Scheme 1.12.<sup>96</sup> On the Mo<sup>III</sup> stage, dinitrogen is bound forming the terminal N<sub>2</sub> complex [Mo<sup>III</sup>]-N≡N **XXVI**. In the “distal” pathway, hydrogen atoms are stepwise transferred onto the N<sub>β</sub> atom, which initially forms diazene species [Mo<sup>IV</sup>]-N=N-H **XXVII** and then hydrazide species [Mo<sup>V</sup>]-N=NH<sub>2</sub> **XXVIII**. The bond strengths of the first two N-H bonds are weak about ~40 kcal mol<sup>-1</sup> as derived by computational analysis. The transfer of a third hydrogen atom finally leads to the release of ammonia and the formation of a terminal nitride species [Mo<sup>VI</sup>]=N **XXIX**. Three subsequent HAT steps are forming parent imido species [Mo<sup>V</sup>]=N-H **XXX**, amide species [Mo<sup>IV</sup>]-NH<sub>2</sub> **XXXI** and ammine complex [Mo<sup>III</sup>]-NH<sub>3</sub> **XXXII**. The second equivalent ammonia is released, dinitrogen is coordinated and the catalytic cycle is closed. Note, within these three steps, the first N-H bond is by far the weakest (BDFE<sub>NH</sub> = 42.3 kcal mol<sup>-1</sup>), whereas the second (BDFE<sub>NH<sub>2</sub></sub> = 64.4 kcal mol<sup>-1</sup>) and third (BDFE<sub>NH<sub>3</sub></sub> = 52.0 kcal mol<sup>-1</sup>) N-H bonds significantly stronger.



**Scheme 1.12** The Schrock cycle including thermodynamic parameters.<sup>96</sup> \*values calculated for  $S = 1$ . The corresponding values of calculated  $S = 0$  species are 2-4 kcal mol<sup>-1</sup> lower and are not displayed for clarity reasons.

It is part of an ongoing debate whether the hydrogen-atom donating species of the CrCp\*<sub>2</sub>/lutidinium BArF<sub>24</sub> PCET couple is a protonated metallocene or a reduced pyridinyl radical species. However, in either case, sufficient weak C-H ( $BDFE_{C-H} = \sim 30 \text{ kcal mol}^{-1}$ )<sup>97</sup> or N-H ( $BDFE_{N-H} = \sim 35 \text{ kcal mol}^{-1}$ )<sup>96</sup> bonds are provided suitable for ammonia production.

An alternative mechanistic scenario is the “alternating pathway” (not shown), where the hydrogen atoms are transferred sequentially to the  $N_\alpha$  and  $N_\beta$  atom. A third suggested pathway implicates initial N-N bond homolysis directly into terminal nitrides species (Scheme 1.12, dashed arrow). As dinitrogen splitting via N-N bond homolysis has been observed for several  $N_2$  bridged dinuclear transition metal complexes,<sup>1,2,81</sup> the examination of the N-H bond strengths of the three last steps within the Chatt cycle are of particular interest with regard to nitride reduction to ammonia or the reversed reaction, ammonia oxidation to nitrides. Table 1.1 contains N-H<sub>x</sub> (x = 1, 2, 3) bond strengths of selected examples of transition metal imido, amido and ammine complexes. Caused by the low stability of especially the parent imido species, most of these data are derived computationally.

**Table 1.1:** Computed N-H BDFE's of selected transition metal complexes.

Entry	Complex	Solvent	BDFE <sub>N-H</sub> (kcal mol <sup>-1</sup> )		
			NH <sub>3</sub>	NH <sub>2</sub>	NH
1	[Mo{NH <sub>x</sub> }(( <sup>Ph</sup> NCH <sub>2</sub> CH <sub>2</sub> ) <sub>3</sub> N)] <sup>96</sup>	-	52	64	<b>42</b>
2	[Mo{NH <sub>x</sub> }(Py) <sub>5</sub> ] <sup>98</sup>	MeCN	68	65	<b>64</b>
3	[Mn{NH <sub>x</sub> }(salen)] <sup>99</sup>	Gas phase	85	84	<b>60</b>
4	[ReCl <sub>2</sub> {NH <sub>x</sub> }( <i>cis</i> -PONOP)] <sup>44</sup>	THF	-	78	<b>43</b>
5	[(Fe{NH <sub>x</sub> }(P <sub>3</sub> B)] <sup>100</sup>	Et <sub>2</sub> O	-	80	<b>65</b>
6	[Ir{NH <sub>x</sub> }( <sup>t</sup> BuP=N=P)] <sup>101</sup>	Gas phase	-	82	<b>71</b>

One trend being consistent throughout the six entries is a weak, first N-H bond compared to the second or third. These bond strengths clearly demonstrate that the formation of the first N-H bond is a thermodynamic bottleneck favoring hydrogen evolution ( $BDFE_{H-H} = 97.2$  kcal mol<sup>-1</sup>).<sup>102,103</sup> Indeed, hydrogen evolution is suggested as a decomposition pathway of *in situ* generated parent imido complexes besides disproportionation.<sup>97,101,104,105</sup> By contrast, high oxidation states stabilize M=N-H imido species, which commonly feature a d<sup>2</sup> electron configuration or lower.<sup>102,106,115–117,107–114</sup> Species with weak N-H bonds are particularly challenging for catalytic applications, because PCET reagents are required with even lower bond strength that tend to release hydrogen.<sup>118–120</sup>

### 1.3 Chromium mediated N<sub>2</sub>-activation and functionalization

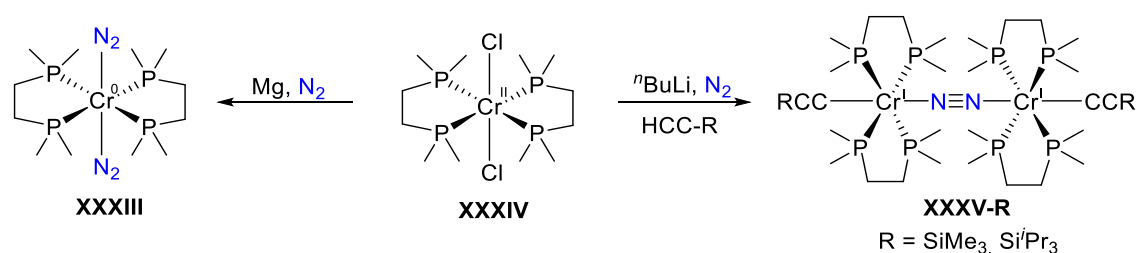
The field of chromium mediated dinitrogen activation and functionalization has attracted a lot of attention in the last two decades, but compared to its heavier homologue molybdenum, it is less explored. Compared to molybdenum, chromium complexes have shown to behave different in N<sub>2</sub> chemistry: For instance, to date only two examples report N-N bond cleavage while there are numerous examples based on molybdenum.<sup>2,8,35–38,121</sup> This chapter provides an overview about the development of chromium N<sub>2</sub> chemistry and for which reaction types

chromium dinitrogen complexes are often employed for. Finally, it is discussed, which key properties might account for the different reactivity compared to molybdenum.

### 1.3.1 Examples of low-valent, N<sub>2</sub> bridged multinuclear chromium complexes

The first reports of chromium mediated dinitrogen activation were contributed by Karsch<sup>122</sup> and Sobota<sup>123</sup> in 1977. However, thermal instability of these and other examples<sup>124–126</sup> hampered comprehensive characterization and anticipated an inherent instability of the class of chromium N<sub>2</sub> complexes for a long time. This misconception was countered by Chatt who reported the thermally stable complex [Cr<sup>0</sup>(N<sub>2</sub>)<sub>2</sub>(dmpe)<sub>2</sub>] **XXXIII** bearing bidentate dmpe ligands, synthesized from the precursor [Cr<sup>II</sup>Cl<sub>2</sub>(dmpe)<sub>2</sub>] **XXXIV** under N<sub>2</sub> atmosphere using elemental magnesium.<sup>127</sup> A *trans*-coordination mode of the dinitrogen ligands was found in **XXXIII**, with a modest degree of activation near to free dinitrogen ( $\nu = 1932, 2331 \text{ cm}^{-1}$ ) (Scheme 1.13).

Reacting the precursor [CrCl<sub>2</sub>(dmpe)<sub>2</sub>] **XXXIV** under N<sub>2</sub> atmosphere in presence of different acetylides gives rise to the dinuclear N<sub>2</sub> bridged complexes [( $\mu$ -N<sub>2</sub>){Cr<sup>I</sup>(CCR)(dmpe)<sub>2</sub>}<sub>2</sub>] (R = SiMe<sub>3</sub>, Si<sup>i</sup>Pr<sub>3</sub>) (**XXXV-R**). Due to  $\pi$ -backbonding by two metal centers, the N-N bond is significantly elongated ( $d_{\text{N-N}} = \sim 1.18 \text{ \AA}$ ) which is consistent with a rRaman shift of 1680 cm<sup>-1</sup>. In these complexes, the metal centers possess low-spin configuration ( $S = 1/2$ ), as derived from magnetic measurements. The electronic structures of these complex molecules have been interpreted differently. Berben proposed a model for [( $\mu$ -N<sub>2</sub>){Cr<sup>I</sup>(CCSiMe<sub>3</sub>)(dmpe)<sub>2</sub>}<sub>2</sub>] **XXXV-SiMe<sub>3</sub>** that includes two antiferromagnetically coupled Cr<sup>I</sup> centers ( $J_{\text{Cr-Cr}} = 0.91 \text{ cm}^{-1}$ ).<sup>128</sup> In contrast, Shores defined for the analogous complex [( $\mu$ -N<sub>2</sub>){CrCl<sub>2</sub>(CCSi<sup>i</sup>Pr<sub>3</sub>)(dmpe)<sub>2</sub>}<sub>2</sub>] **XXXV-SiMe<sub>3</sub>** an overall  $S = 1$  ground state that is stabilized by axial zero-field splitting ( $D = 8.34 \text{ cm}^{-1}$ ).<sup>129</sup>



**Scheme 1.13** Dinitrogen activation in Chatt-type chromium complexes.<sup>127–129</sup>

Dinitrogen activation in low-valent dichromium complexes was intensively explored by Theopold (Figure 1.8). Stabilized by a nacnac ligand with steric encumbering 2,6-diisopropylphenyl substituents, dinitrogen activation is facilitated forming [( $\mu$ -N<sub>2</sub>){Cr<sup>I</sup>(<sup>IPr</sup>nacnac)}<sub>2</sub>] **XXXVI**. The side-on binding motif is generally underrepresented and moreover, it is to date the only example related to chromium N<sub>2</sub> chemistry. The authors address an ambiguity concerning the oxidation states: A Cr<sup>I</sup>-N<sub>2</sub><sup>0</sup>-Cr<sup>I</sup> situation is proposed, however, the authors state that divalent chromium with a doubly reduced N<sub>2</sub> ligand (Cr<sup>II</sup>-N<sub>2</sub><sup>2-</sup>-Cr<sup>II</sup>) cannot be excluded.<sup>130</sup>

$[(\mu\text{-N}_2)\{\text{Cr}(\text{Bu}_2\text{MeTp})\}_2]$  **XXXVII** is another example of a low-valent, formally  $\text{Cr}^{\text{I}}$  complex, where the metal center is tethered by a rigid, steric encumbering Tp ligand in which the bridging dinitrogen is bound in bridging end-on mode. Based on the bond N-N length of  $d_{\text{N-N}} = 1.213(5)$  Å and an observed effective magnetic moment of  $\mu_{\text{eff}} = 3.9 \mu_{\text{B}}$  in solution, antiferromagnetically coupled  $\text{Cr}^{\text{I}}$  is suggested.<sup>131</sup>

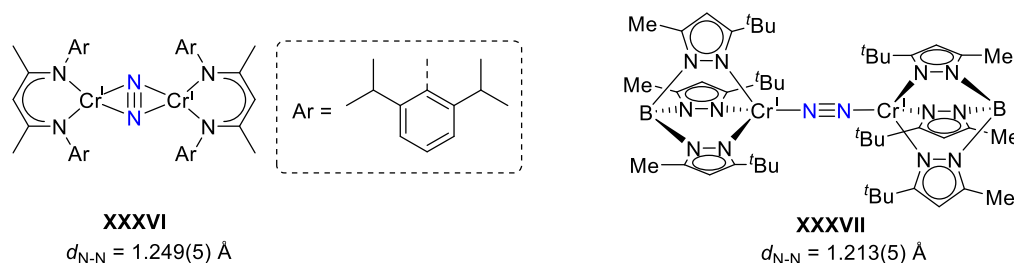


**Figure 1.8** Dinitrogen activation with a nacnac coordinated chromium complex including N-N bond lengths.<sup>130</sup>

The field of low-valent, chromium(I) dinitrogen complexes was extended by contributions from Zhang and Xi in 2019. In the reported series, a bidentate ligand was utilized composed of a donating phosphine and cyclopentadienyl unit with varied substituents on the phosphorous atom (Figure 1.9). Importantly, depending on the steric bulk of the P-substituents, the nuclearity can be controlled: With phenyl substituents, the formation of a trinuclear complex is favored in which the three complex fragments are connected by bridging dinitrogen ligands (**XXXVIII**). The flanking metal centers are further coordinated by a terminal  $\text{N}_2$  ligand. Increasing the steric bulk in the phosphorus substituents (cyclohexyl) leads to dinuclear complexes, where both chromium atoms are linked by a bridging  $\text{N}_2$  ligand and each metal center is bound by a terminal  $\text{N}_2$  ligand (**XXXIX**). The different nature of the  $\text{N}_2$  ligands in both examples is reflected in distinct bond lengths and IR shifts: While the terminal  $\text{N}_2$  ligands exhibit N-N bond length near to free dinitrogen ( $d_{\text{N-N}} < 1.1$  Å,  $\nu > 1950 \text{ cm}^{-1}$ ) the bridging dinitrogen ligands express reduced character ( $d_{\text{N-N}} = \sim 1.2$  Å,  $\nu = \sim 1740 \text{ cm}^{-1}$ ).<sup>132</sup>

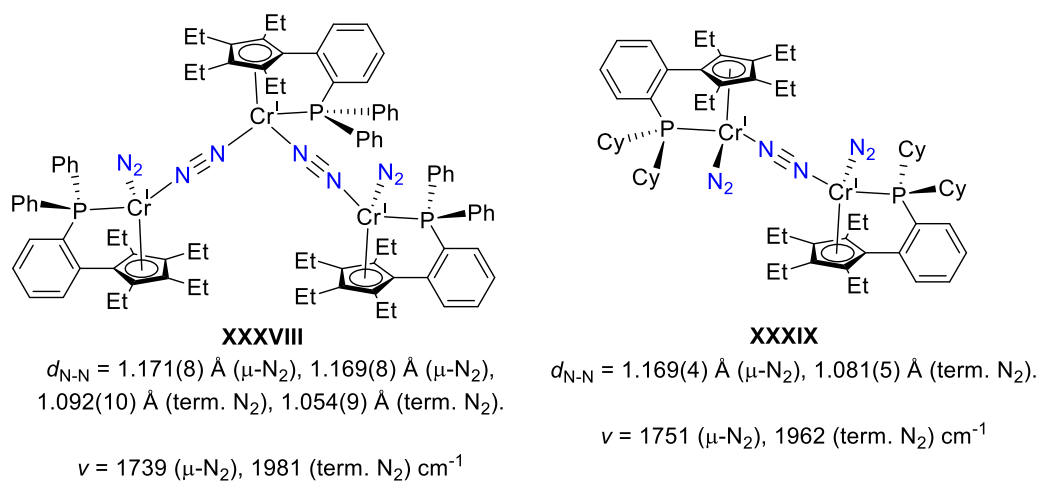
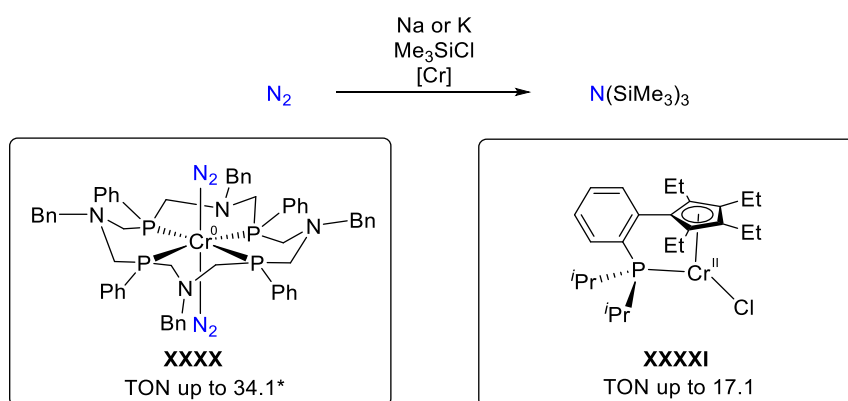


**Figure 1.9** Polynuclear  $\text{Cr}(\text{I})$  dinitrogen complexes.<sup>132</sup>



### 1.3.2 Reactivity of chromium N<sub>2</sub> complexes

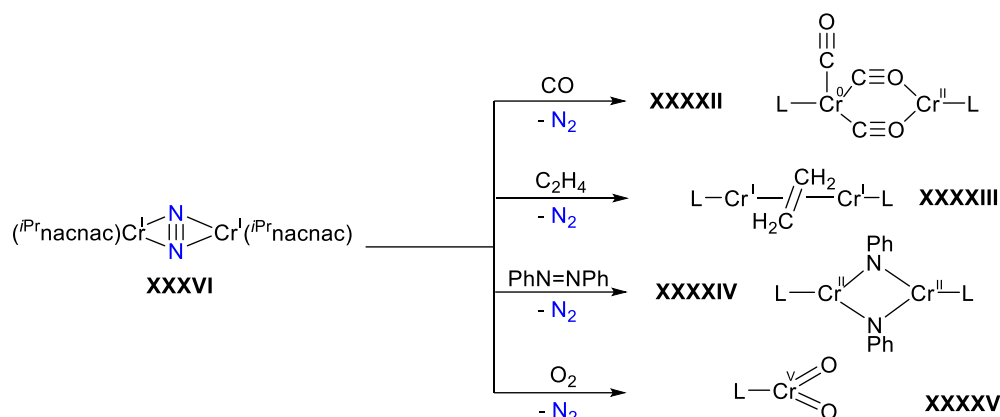
The reactivity of chromium dinitrogen complex is quite versatile and this subchapter aims at presenting the most meaningful examples. Whereas chromium mediated dinitrogen cleavage is limited to very few examples, the field of *N*-functionalization of nitride species is unexplored. Alternatively, the functionalization of a terminal N<sub>2</sub> ligand and the reactivity of low-valent chromium N<sub>2</sub> complexes attracted a lot of attention. In the field of N-H bond formation, early studies of Mock and Bullock focussed on the synthesis of octahedral, Chatt-type Cr<sup>0</sup> complexes bearing multidentate P-N macrocycles with terminal N<sub>2</sub> ligands.<sup>133</sup> Protonation studies of [Cr<sup>0</sup>(N<sub>2</sub>)<sub>2</sub>(P<sup>Ph</sup><sub>4</sub>N<sup>Bn</sup><sub>4</sub>)] **XXXX** revealed the formation of hydrazinium and ammonium salts. The pendant amine function within the ligand backbone plays a crucial role as proton shuttle.<sup>134–138</sup> Finally, a protocol was published for catalytic reduction of dinitrogen to N(SiMe<sub>3</sub>)<sub>3</sub> with TON's up to 34, catalyzed by a chromium complex with a P4 macrocycle (Scheme 1.14, left).<sup>95</sup> Catalytic *N*-silylation with TON's up to 17 was achieved by chromium complex [Cr<sup>II</sup>Cl(P*r*<sub>2</sub>P-Cp<sup>Et</sup>)] **XXXXI** suited with a bidentate ligand that contains donating a phosphine and a donating ethyl substituted Cp moiety.<sup>132</sup>



**Scheme 1.14** Catalytic N<sub>2</sub> reduction to N(SiMe<sub>3</sub>)<sub>3</sub>.<sup>132,138,139</sup> \* yield refers to formation of NH<sub>4</sub>Cl by an aqueous work-up.

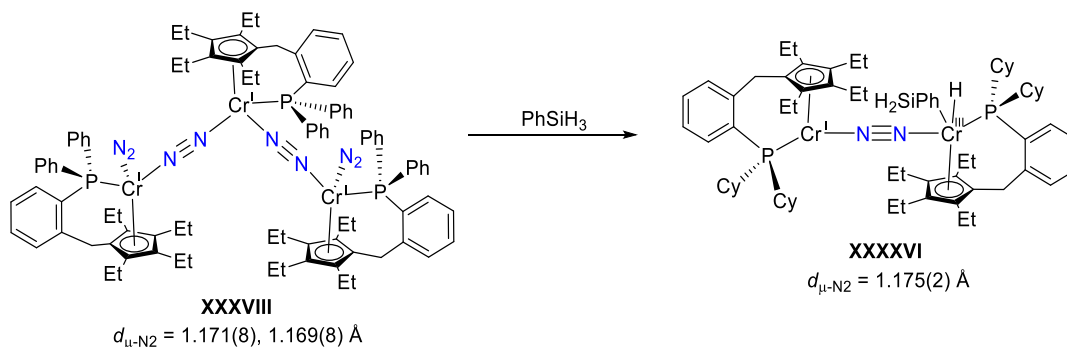
Ligand substitution reactions belong to another attractive branch exploiting the labile nature of dinitrogen ligands.<sup>130,139,140</sup> The reactivity of the highly reduced, formally Cr<sup>I</sup> complex [(μ-N<sub>2</sub>){Cr(<sup>Pr</sup>nacnac)}<sub>2</sub>] **XXXVI** was comprehensively explored by Theopold (Scheme 1.15).<sup>130,140</sup> Exposure to carbon monoxide leads to a dinuclear complex [(μ-CO)<sub>2</sub>{Cr<sup>0</sup>(CO)(<sup>Pr</sup>nacnac)}{Cr<sup>II</sup>(<sup>Pr</sup>nacnac)}] **XXXVII** where the metal centers are connected by two bridging carbonyl ligands, whereas the chromium centers are additionally coordinated by a terminal CO. A mixed-valent situation (low-spin Cr<sup>0</sup>/ high-spin Cr<sup>II</sup>) is assumed. The reaction with ethylene produces [(μ-C<sub>2</sub>H<sub>4</sub>){Cr(<sup>Pr</sup>nacnac)}<sub>2</sub>] **XXXVIII** with retained structural motif where the dinitrogen ligand is replaced by a bridging, side-on coordinated ethylene ligand, with Cr<sup>I</sup> oxidation states. The reaction with azobenzene triggers an oxidative addition by the cleavage of the N-N double bond producing dinuclear complex [(μ-NPh)Cr(<sup>Pr</sup>nacnac)}<sub>2</sub>] **XXXIV** that features two bridging phenyl imido ligands (Scheme 1.15). In presence of dioxygen the mononuclear dioxo species [CrO<sub>2</sub>(<sup>Pr</sup>nacnac)]

**XXXXV** is formed where the metal center possess a  $\text{Cr}^{\text{V}}$  oxidation state.<sup>130</sup> Importantly, the coordination of the substrates in all these complexes leads to complete extrusion of dinitrogen.



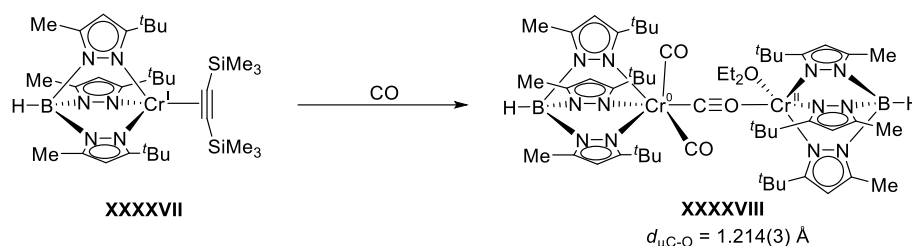
**Scheme 1.15** Reactivity of a the low-valent  $\text{Cr}^{\text{I}}$  complex **XXXXVI**.<sup>130,140</sup>

A multinuclear, asymmetric  $\text{Cr}^{\text{I}}$  complex **XXXXVIII** was utilized for the activation of small molecules. Besides conversions with azobenzene, benzylideneaniline and 2-butyne, a rare example of an oxidative addition of phenylsilane was observed (Scheme 1.16). Importantly, the bridging dinitrogen ligand is still intact in the oxidative addition product **XXXXVI** and the degree of activation is nearly unchanged. A mixed-valent ( $\text{Cr}^{\text{I}}/\text{Cr}^{\text{III}}$ ) situation is suggested.<sup>141</sup>



**Scheme 1.16** Oxidative addition of phenyl silane.<sup>141</sup>

The concept of the using of reduced  $\text{N}_2$  complexes as reductive precursor molecules can be extended from dinitrogen- to low-valent alkyne-complexes. Analogously, the alkyne ligand is also labile and is readily released in presence of stronger  $\pi$ -accepting ligands. Reduced alkyne complexes are not directly associated with this work but the product of the following reaction will be relevant. The reported, low-valent alkyne complex  $[(\text{C}_2(\text{TMS})_2)\text{Cr}^{(\text{tBu},\text{Me}^e\text{Tp})}]$  **XXXXVII** is a highly reactive  $\text{Cr}^{\text{I}}$  synthon and the reactivity was tested, among other substrates, towards carbon monoxide (Scheme 1.17).

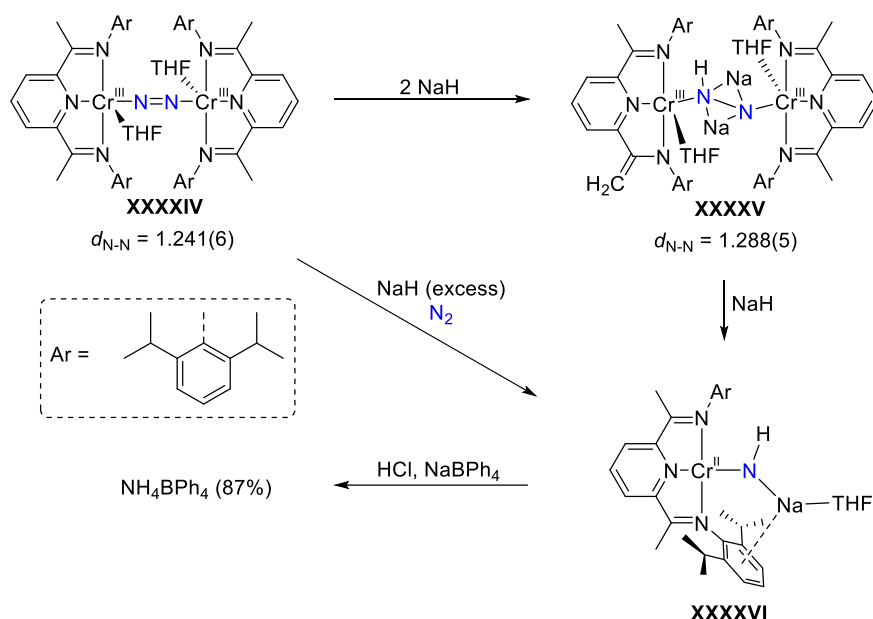


**Scheme 1.17** Carbonylation of Cr<sup>I</sup> precursor **XXXXVII** yielding dinuclear isocarbonyl complex **XXXXVIII**.  
131

The product  $[(\mu\text{-CO})\{\text{Cr}(\text{CO})_2(^{\text{Bu,Me}}\text{Tp})\}\{\text{Cr}(^{\text{Bu,Me}}\text{Tp})\}]$  **XXXXVII** is a dinuclear complex, which consists of a distorted octahedral  $\{\text{Cr}(\text{CO})_2(^{\text{Bu,Me}}\text{Tp})\}$  core, in which the chromium center is facially coordinated by the Tp ligand and two terminal carbonyl ligands. The sixth ligand is a bridging CO ligand that are generally described as isocarbonyl ligands, binding to a five-coordinate  $\{\text{Cr}(^{\text{Bu,Me}}\text{Tp})\}$  unit, where the metal center is additionally coordinated by an diethylether ligand. The isocarbonyl ligand exhibits significant elongation ( $d_{\text{C-O}} = 1.214(3) \text{ \AA}$ ) compared to the free CO molecule ( $d_{\text{C-O}} = 1.151 \text{ \AA}$ )<sup>142</sup>. The electronic situation was suggested as low-spin Cr<sup>0</sup> / high-spin Cr<sup>II</sup>.<sup>131</sup>

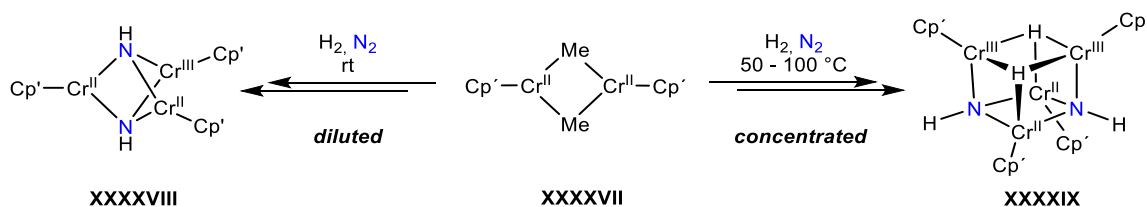
### 1.3.3 Chromium mediated N-N bond cleavage

While there is a relative huge amount of chromium N<sub>2</sub> complexes, examples for chromium mediated N-N bond cleavage are scarce. The first contribution was made by Budzelaar using a chromium complex bearing a redox active PDI ligand (Scheme 1.18).<sup>143,144</sup> The dinuclear N<sub>2</sub> bridged complex  $[(\mu\text{-N}_2)\{\text{Cr}(\text{thf})(^{\text{dipp}}\text{PDI})\}_2]$  **XXXXIV** was isolated, in which both metal centers are coordinated by the PDI ligand, the bridging N<sub>2</sub> ligand ( $d_{\text{N-N}} = 1.241(6) \text{ \AA}$ ) and a coordinating THF ligand. Based on the bond metrics and Evans' measurement the metal centers adapt Cr<sup>III</sup> while both the PDI and the N<sub>2</sub> ligand are doubly reduced. Further reduction of this species using 2 equivalents of sodium hydride leads to further elongation of the N-N bond in  $[(\mu\text{-N}_2\text{Na}_2\text{H})\{\text{Cr}(\text{thf})(^{\text{dipp}}\text{PDI})\}_2]$  **XXXXV** ( $d_{\text{N-N}} = 1.288(5) \text{ \AA}$ ). The authors suspect a PDI centered reduction retaining Cr<sup>III</sup> and N<sub>2</sub><sup>2-</sup>. Importantly, one of the PDI ligands is suggested to be a mono-radical species while the other has to be considered as mono-deprotonated closed shell tri-anion. Further addition of sodium hydride leads to full scission of the N-N bond: Complex  $[\text{CrNHNa}(\text{thf})(^{\text{dipp}}\text{PDI})]$  **XXXXVI** is a mononuclear square planar chromium complex binding an imide  $\{\text{NHNa}(\text{THF})\}$  unit, in which the sodium atom is stabilized by the coordination of a THF molecule and by  $\pi$ -interactions with an adjacent PDI aromatic side arm. The authors anticipate a Cr<sup>II</sup> as judged by characteristic bond metrics. Importantly, subjecting **XXXXVI** to an acidic work-up leads to ammonia formation in high yields (87%).



**Scheme 1.18** Cleavage of the N-N triple bond with a chromium PDI complex.

The other intriguing example of chromium promoted N-N bond cleavage was recently reported by Luo and Hou.<sup>145</sup> Their synthetic fundamnet is represented by the dinuclear complex [ $\{\mu\text{-Me}\}\text{Cr}(\text{Cp}')\}_2$ ] **XXXVII** where each  $\text{Cr}^{\text{II}}$  metal center is coordinated by a  $\text{Cp}'$  ligand and two bridging methylene ligands (Scheme 1.19). Under selected conditions, dinitrogen cleavage gives rise to polynuclear imido complexes. Importantly, the selectivity can be controlled by concentration and temperatures: Under  $\text{N}_2/\text{H}_2$  atmosphere **XXXVII** forms in diluted concentrations at room temperature a trinuclear complex **XXXVIII** containing three chromium atoms spanning a  $\text{Cr}_3$  plane that is capped by two N-H units in the apical position. Elevated temperatures and high concentrations, however, lead to the formation of a tetranuclear, cubane-type structure (complex **XXXIX**) featuring two capping N-H moieties. In both reactions, the initial, methyl bridged complex **XXXVII** initially undergoes hydrogenolysis forming poly hydride intermediates that finally activate  $\text{N}_2$  to the depicted products.<sup>145</sup>

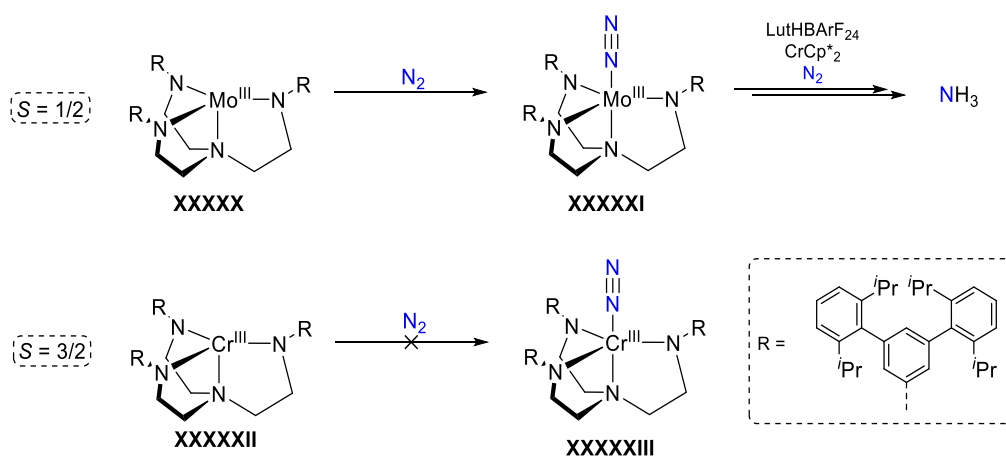


**Scheme 1.19** Chromium mediated  $\text{N}_2$  activation and bond cleavage into multinuclear, mixed-valent chromium imido complexes.<sup>145</sup>

### 1.3.4 Cr vs. Mo in N<sub>2</sub> activation

With the background to examine the metal influence on N<sub>2</sub> reactivity and electronic structure, Schrock published a comparative study where a Mo<sup>III</sup> triamidoamine complex was substituted by chromium (Scheme 1.20).<sup>146</sup> Molybdenum complex [Mo<sup>III</sup>((<sup>R</sup>NCH<sub>2</sub>CH<sub>2</sub>)<sub>3</sub>N)] **XXXXX** readily binds N<sub>2</sub> forming the terminal dinitrogen complex [Mo<sup>III</sup>(N<sub>2</sub>)((<sup>R</sup>NCH<sub>2</sub>CH<sub>2</sub>)<sub>3</sub>N)] **XXXXXI** which has shown to be a potent catalyst for ammonia formation.<sup>93,147</sup> By contrast, N<sub>2</sub> binding of [Cr<sup>III</sup>((<sup>R</sup>NCH<sub>2</sub>CH<sub>2</sub>)<sub>3</sub>N)] **XXXXXII** to the putative complex [Cr<sup>III</sup>(N<sub>2</sub>)((<sup>R</sup>NCH<sub>2</sub>CH<sub>2</sub>)<sub>3</sub>N)] **XXXXXIII** was not observed.<sup>146</sup>

The lack of reactivity of the 3d metal congener was suggested to be a consequence of the general preference of high-spin states, induced by lower ligand field splitting.<sup>148</sup> Consequently, 2e<sup>-</sup> ligands such as dinitrogen, cannot interact with a half-filled orbital unless the approaching ligand promotes spin conversion to create vacant orbitals. From this point of view, it seems plausible, that the Mo<sup>III</sup> complex **XXXXX** (*S* = 1/2) is capable of N<sub>2</sub> binding and the corresponding Cr<sup>III</sup> **XXXXXII** (*S* = 3/2) is not. The electron doublet is suggested to be energetically inaccessible for Cr<sup>III</sup> complex **XXXXXII**. Furthermore, the Mo<sup>III</sup> complex **XXXXX** is proposed to be more reducing compared to the corresponding chromium complex **XXXXXII**, which does not bind dinitrogen even in presence of potassium graphite.



**Scheme 1.20** The lack of reactivity of a Cr<sup>III</sup> triamidoamine complex towards N<sub>2</sub>.<sup>146</sup>

Another physical parameter that might account for a fundamentally different reactivity between 3d and 4d/5d metal are the reduced covalence radii based on contracted 3d-orbitals.<sup>139,149</sup> Stranger published a DFT study that evaluated the thermochemistry of N<sub>2</sub> cleavage of group 6 metals within the Cummins' system [M<sup>III</sup>(NR'<sup>t</sup>Bu)<sub>3</sub>] (Ar = 3,5-dimethylphenyl). Interestingly N<sub>2</sub> cleavage into terminal nitrides is only exergonic for molybdenum and tungsten. The authors stated that the covalence radii play a critical role for the thermodynamics of N<sub>2</sub> cleavage.<sup>150</sup>

## 1.4 Scope of this Work

### 1.4.1 Results and Discussion I

Chromium N<sub>2</sub> chemistry is an underdeveloped research field compared to its heavier homologue molybdenum. For example, the synthetic milestones of N-N bond homolysis<sup>8</sup> and catalytic N<sub>2</sub> reduction<sup>93</sup> to ammonia rely on the heavier homologue molybdenum, reported more than 20 years ago. The broad versatility of molybdenum-based systems in N-functionalization addressed the question whether chromium-based systems behave similar. There are several examples of N<sub>2</sub> bridged dichromium complexes, which is generally a structural motif that is associated with N<sub>2</sub> cleavage. However, there are to date only two examples that report N-N bond scission of atmospheric dinitrogen.<sup>145,151</sup>

The focus of low-valent N<sub>2</sub> bridged dichromium complexes in recent publications was predominantly put on their reactivity, particularly on ligand exchange reaction, to exploit the highly reduced character for the activation of other small molecules. By contrast, surprisingly less is known about the electronic structure of this type of complexes stimulating for investigations in this direction which settles the basis for this work.

A synthetic inspiration is provided by the group 6 dinitrogen complexes [(μ-N<sub>2</sub>){MoCl(<sup>t</sup>BuPNP)}<sub>2</sub>] **III** and [(μ-N<sub>2</sub>){WCl(<sup>t</sup>BuPNP)}<sub>2</sub>] **V** that are both associated with N<sub>2</sub> fixation and N-N bond cleavage. This ligand seems ideal due its steric protection and by its potential chemical and redox non-innocent character, which has shown to be supportive in 3d metal mediated small molecule activation.<sup>143,144</sup>

The scope of the first Chapter is the extension of this series by the lighter homologue chromium. The synthetic accessibility to corresponding dinitrogen complexes will be discussed including an examination of the electronic structure.

### 1.4.2 Results and Discussion II

The first example of N<sub>2</sub> fixation including nitride transfer into organic molecules was achieved by a molybdenum based system within a five-step synthetic cycle as presented in the introduction (Scheme 1.8).<sup>71,72</sup> The reluctant nucleophilic nature of molybdenum nitride species raised the demand for strategies to facilitate nitride transfer. One approach was to go to more electron rich metals with the intention to enforce M≡N bond weakening by population of antibonding π\*-orbitals. Indeed, rhenium nitride species [ReClN(<sup>t</sup>BuPNP)] **XV** can be derived from atmospheric N<sub>2</sub> in high spectroscopic yields and acetonitrile formation is feasible within a three-step synthetic cycle, emphasizing the key role of rhenium in association with N<sub>2</sub> chemistry.<sup>41,84</sup>

Reducing the steric bulk on the phosphorous atoms within this platform to isopropyl, an octahedral nitride species [ReCl<sub>2</sub>N(<sup>i</sup>PrPN<sup>H</sup>P)] (**13<sup>Cl</sup>**) can be accessed by photolysis of the

parent dinitrogen complex  $[(\mu\text{-N}_2)\{\text{ReCl}_2(\text{PrPN}^{\text{H}}\text{P})\}_2]$  (**11<sup>Cl</sup>**). This platform is capable of *N*-functionalization using the mild electrophile benzoyl chloride to form benzonitrile.<sup>43</sup>

The utilization of mild electrophiles opens space for compatibility that is relevant for multicomponent reactions. Therefore, subject of this chapter will be to optimize synthetic accessibility to  $[\text{ReCl}_2\text{N}(\text{PrPN}^{\text{H}}\text{P})]$  (**13<sup>Cl</sup>**) and to improve reaction conditions for nitride transfer.

For this purpose, halide exchange is targeted within the platform  $[\text{ReX}_3(\text{PrPN}^{\text{H}}\text{P})]$  **10** ( $X = \text{Cl, Br, I}$ ), which is advantageous in several directions: Information can be collected to what extent the redox properties change, especially the  $\text{Re}^{\text{III/II}}$  couple, that is associated with  $\text{N}_2$  fixation. Furthermore, there is to date no study which examines halide effects on photolytic  $\text{N}_2$  cleavage. Finally, it will be discussed how nitride transfer benefits from the usage of the better leaving group bromide. Another branch within this project is the examination of the electronic structure of the bromide substituted dinitrogen complex  $[(\mu\text{-N}_2)\{\text{ReBr}_2(\text{PrPN}^{\text{H}}\text{P})\}_2]$  (**11<sup>Br</sup>**) within a redox series. It is targeted to investigate the redox isomers by magnetic and spectroscopic methods.

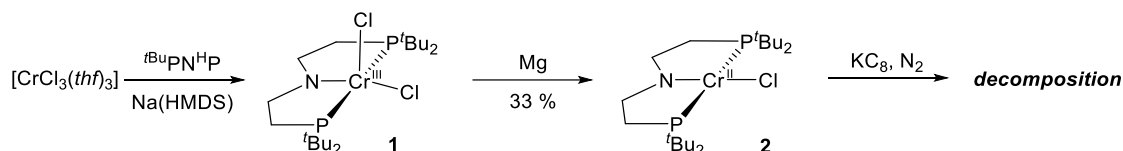
## 2 Results and Discussion I

Subchapter 2.1 describes the synthesis and the electronic structure of the N<sub>2</sub> bridged dichromium complex [(μ-N<sub>2</sub>){Cr(<sup>t</sup>BuPNP<sup>'''</sup>)}]<sub>2</sub> (**3**) which was investigated by SQUID magnetometry and DFT calculations. Subchapter 2.2 focusses on the reactivity towards π-accepting reactants including carbon monoxide and *t*Bu-NC. In both cases, temperature-sensitive intermediates were isolated providing insight into the reaction mechanism. Subchapter 2.3 summarizes the attempts to further activate or split the N-N triple bond of **3**.

### 2.1 An N<sub>2</sub> bridged dichromium complex

#### 2.1.1 Synthetic access of dinitrogen complex [(μ-N<sub>2</sub>){Cr(<sup>t</sup>BuPNP<sup>'''</sup>)}]<sub>2</sub> (**3**)

Stirring the precursor complex [CrCl<sub>3</sub>(thf)<sub>3</sub>] with a slight excess (1.05 eq.) of ligand <sup>t</sup>Bu-PN<sup>H</sup>P and Na(HMDS) (1.05 eq.) forms a brown solution and the five-coordinate complex [CrCl<sub>2</sub>(<sup>t</sup>BuPNP)] (**1**) can be isolated with a yield of 65% by removal of the solvent and washing with pentane (Scheme 2.1). **1** is paramagnetic and shows strongly broadened signals ( $m_{1/2} \sim 700$  Hz) in the <sup>1</sup>H NMR spectrum (Figure 2.1, left) caused by fast proton relaxation.<sup>152</sup> Nevertheless, the low number of chemically inequivalent protons in the ligand scaffold simplifies the assignment of the signals. The dominant signal at 5.51 ppm represents the <sup>t</sup>Bu groups whereas the small signal at -21.87 ppm belongs to the ligand backbone. An effective magnetic moment of  $\mu_{\text{eff}} = 3.8 \pm 0.1 \mu_{\text{B}}$  was determined by Evans' method indicating high-spin Cr<sup>III</sup>.<sup>153</sup>



**Scheme 2.1** Synthesis of square planar complex [CrCl(<sup>t</sup>BuPNP)] (**2**).

In the solid state, **1** forms a square pyramidal complex ( $\tau_5 = 0.05$ ) with one chloride ligand in the apical position (Figure 2.1, right). Exposing a degassed solution of **1** to an atmosphere of dinitrogen neither leads to a color change nor any spectroscopic changes are observed which indicate reactivity towards N<sub>2</sub>. This is not unexpected as N<sub>2</sub> binding with chromium complexes commonly occurs in oxidation states +II or lower.<sup>125,129,151,130,131,133–136,140,146</sup> Cyclic voltammetry reveals an irreversible reduction wave at  $E_{\text{p,c}} = -1.79$  V which is assigned to the Cr<sup>III/II</sup> couple (Appendix, Figure 6.2).



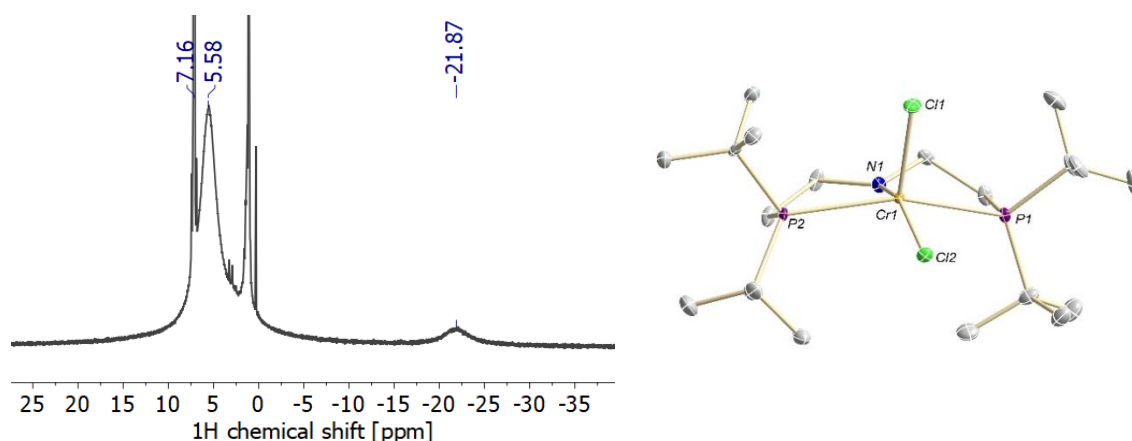


**Figure 2.1** Characterization of **1**. **Left:**  $^1\text{H}$  NMR spectrum ( $\text{C}_6\text{D}_6$ , RT). **Right:** Molecular structure in the solid state. Hydrogen atoms and solvent molecules are omitted for clarity. Anisotropic displacement parameters are set to 50% probability. Selected bond lengths [ $\text{\AA}$ ] and angles [ $^\circ$ ]: N1-Cr1 1.879(5), Cr1-Cl1 2.3036(16), Cr1-Cl2 2.3521(16); P1-Cr1-P2 153.46(6), N1-Cr1-Cl2 156.40(17).

Chemical reduction of **1** with magnesium powder or sodium amalgam leads to a color change from brown into deep blue and the square planar complex  $[\text{CrCl}(\text{}^t\text{BuPNP})]$  (**2**) (Scheme 2.1) can be isolated by pentane extraction and recrystallization with a modest yield of 33%. The  $^1\text{H}$  NMR spectrum shows shifted, very broadened signals suggesting that **2** is paramagnetic (Figure 2.2, left). **2** is highly air sensitive and thermally unstable precluding characterization by elemental analysis or Evans' method.

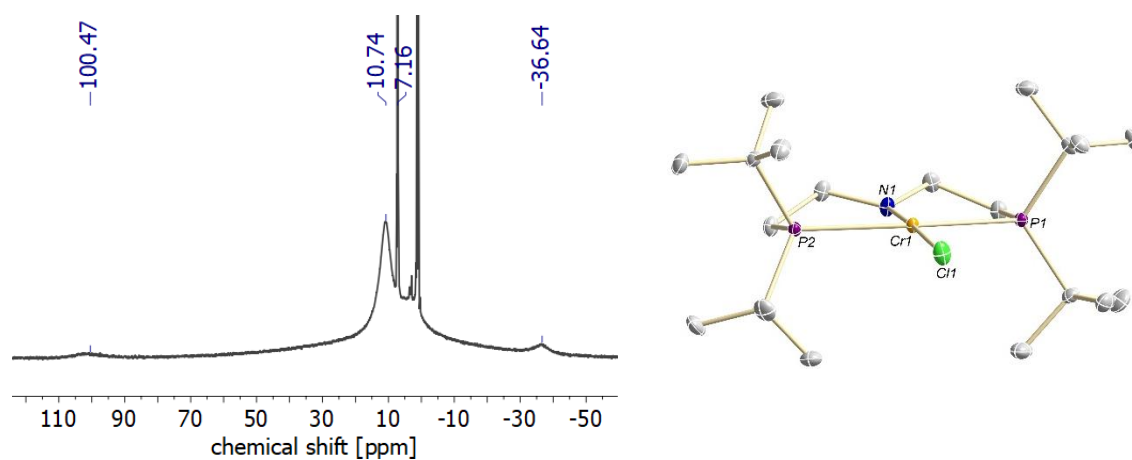
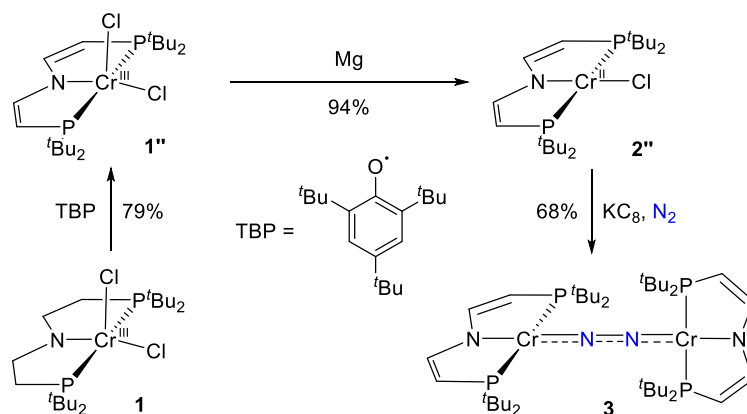


**Figure 2.2** Characterization of **2**. **Left:**  $^1\text{H}$  NMR spectrum ( $\text{C}_6\text{D}_6$ , RT). **Right:** Molecular structure in the solid state. Hydrogen atoms and solvent molecules are omitted for clarity. Anisotropic displacement parameters are set to 50% probability. Selected bond lengths [ $\text{\AA}$ ] and angles [ $^\circ$ ]: N1-Cr1 1.9931(13), Cr1-Cl1 2.3439(4); P1-Cr1-P2 163.471(16), N1-Cr1-Cl1 176.80(4).

Suitable crystals for X-Ray diffraction were obtained from a saturated pentane solution at  $-40$   $^\circ\text{C}$ . The structure in the solid state is shown in Figure 2.2 (right). The N-Cr bond length is significantly elongated ( $d_{\text{N-Cr}} = 1.9931(13)$   $\text{\AA}$ ) in comparison to the five-coordinate parent **1** ( $d_{\text{N-Cr}} = 1.879(5)$   $\text{\AA}$ ) which can be explained by increased repulsive interactions between the more electron rich  $\text{Cr}^{\text{II}}$  center and the strong  $\pi$ -donating amido ligand. A structural related square planar  $\text{Cr}^{\text{II}}$  complex was described as high-spin  $d^4$  and a similar electron configuration

is assumed here.<sup>154</sup> There is no spectroscopic evidence for N<sub>2</sub> binding. Cyclic voltammetry did not show any reductive features until the edge of the solvent window ( $E_{p,c} = -3.5$  V, Appendix, Figure 6.4). Reduction with potassium graphite under N<sub>2</sub> atmosphere led to decomposition into an intractable mixture of unidentified compounds.

An explanation for the inherent instability and unselective reactivity upon reduction under N<sub>2</sub> might be the strong  $\pi$ -donating character of the amide moiety of the pincer ligand. Therefore, the divinylamide ligand {N(CHCHP<sup>t</sup>Bu<sub>2</sub>)}<sup>-</sup> platform was employed in which  $\pi$ -donation is reduced by charge delocalization across the conjugated  $\pi$ -system. In fact, this ligand platform was established to stabilize low oxidation states.<sup>155–158</sup> Synthetic access is provided by a metal templated reaction of [CrCl<sub>2</sub>(<sup>t</sup>BuPNP)] (**1**) with an excess of TBP (TBP = 2,4,6-tri-*tert*-butyl-phenoxy radical) to obtain the corresponding divinylamide species [CrCl<sub>2</sub>(<sup>t</sup>BuPNP<sup>•-</sup>)] (**1''**) in good yields of 79% (Scheme 2.2).



**Scheme 2.2** Synthesis of dinitrogen complex [( $\mu$ -N<sub>2</sub>){Cr(<sup>t</sup>BuPNP<sup>•-</sup>)}<sub>2</sub>] (**3**).

The <sup>1</sup>H NMR exhibits one signal for the <sup>t</sup>Bu groups at  $\delta = 1.14$  ppm and two signals for the CH-groups in the backbone at  $\delta = -115.68$  and  $-142.43$  ppm (Figure 2.3, left). The magnetic moment of **1''** was measured in solution via Evans' method ( $\mu_{\text{eff}} = 3.65 \pm 0.1 \mu_{\text{B}}$ ) suggesting high-spin Cr<sup>III</sup>. Complete ligand oxidation is corroborated by IR spectroscopy which shows an intense, diagnostic band at 1524 cm<sup>-1</sup> (C=C, Figure 2.3, right). All attempts to obtain single crystals suitable for X-Ray diffraction were unsuccessful preventing structural characterization, however, combustion analysis and mass spectrometry confirmed the atomic composition. **1''** was investigated by cyclic voltammetry. A fully reversible, oxidative event is found at a potential of  $E_{1/2} = +0.45$  V which might be a ligand centered oxidation step (Appendix, Figure 6.6).<sup>158</sup> In the reductive regime, an irreversible wave occurs at  $E_{p,c} = -1.14$  V that is ascribed to the Cr<sup>III/II</sup> couple. The potential is anodically shifted ( $\Delta E(\text{Cr}^{\text{III/II}}) = +0.65$  V) compared to the **1** reflecting the less electron rich nature of the chromium center caused by decreased  $\pi$ -donation.

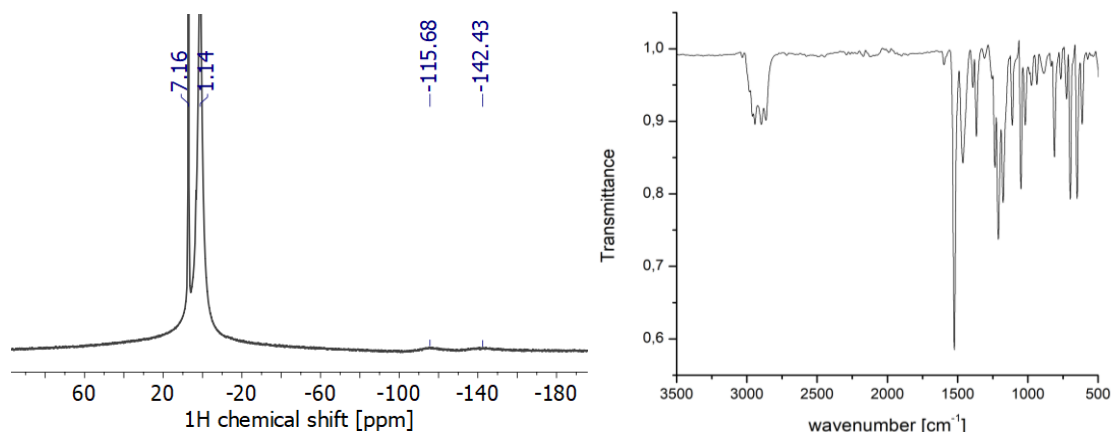


**Figure 2.3** Characterization of **1''**. **Left:**  $^1\text{H}$  NMR spectrum ( $\text{C}_6\text{D}_6$ , RT). **Right:** IR spectrum.

Using magnesium powder as a chemical reductant in THF leads to a color change from vine red into deep blue within 30 minutes. Removal of the solvent and extraction with pentane affords  $[\text{CrCl}(\text{tBuPNP})]$  (**2''**) in high yield (94%, Scheme 2.2) and analytical purity. The  $^1\text{H}$  NMR shows broadened signals and a spin-only value of  $\mu_{\text{eff}} = 4.51 \pm 0.1 \mu_{\text{B}}$  was determined by Evans' method (Figure 2.4, left). This is in good agreement with the spin-only value of an electron quintet, suggesting a  $d^4$  high-spin configuration.<sup>154</sup> X-ray diffraction confirms square planar geometry (Figure 2.4, right). The slight increased N-Cr bond length compared to the saturated complex **2** ( $d_{\text{N-Cr}} = 2.0431(18) \text{ \AA}$  (**2''**) vs.  $d_{\text{N-Cr}} = 1.9931(13) \text{ \AA}$  (**2**)) confirms reduced  $\pi$ -donation.<sup>159</sup>

This complex does not react with  $\text{N}_2$ , phosphines ( $\text{PPh}_3$ ,  $\text{PMe}_3$ ), or carbon monoxide. The inherent lack of reactivity of high-spin complexes towards two-electron ligands is suggested to be a consequence of half-filled metal d-orbitals which do not allow for  $\pi$ - or  $\sigma$ -interactions as discussed in the introduction (subchapter 1.3.4).<sup>146</sup> In the CV, the complex shows a broadened, irreversible reduction feature close to the solvent window ( $E_{\text{p,c}} = -3.31 \text{ V}$ , Appendix, Figure 6.8).

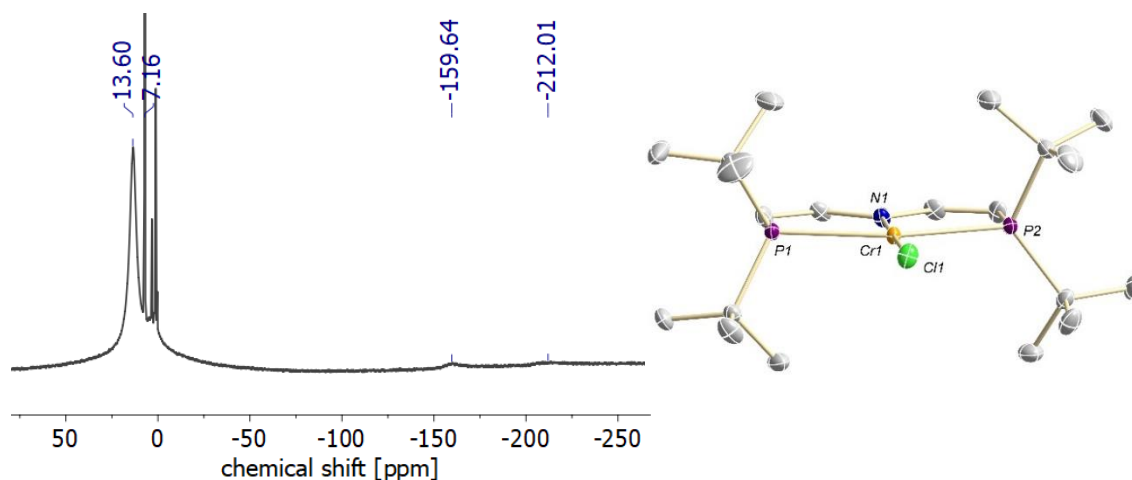


**Figure 2.4** Characterization of **2''**. **Left:**  $^1\text{H}$  NMR spectrum ( $\text{C}_6\text{D}_6$ ). **Right:** Molecular structure in the solid state. Hydrogen atoms and solvent molecules are omitted for clarity. Anisotropic displacement parameters are set to 50% probability. Selected bond lengths [ $\text{\AA}$ ] and angles [ $^\circ$ ]: N1-Cr1 2.0431(18), Cr1-Cl1 2.2998(6), Cr1-P1 2.4760(7), Cr1-P2 2.4723(7). P1-Cr1-P2 160.98(2), N1-Cr1-Cl1 179.15(6).

Chemical reduction of **2''** with potassium graphite under N<sub>2</sub> atmosphere leads to an immediate color change into deep red brown. Extraction with pentane and crystallization obtains dinitrogen complex  $[(\mu\text{-N}_2)\{\text{Cr}(\text{BuPNP}'')\}_2]$  (**3**) in a good yield of 68% (Scheme 2.2). The only resonance found in the <sup>1</sup>H NMR spectrum ( $\delta = -500$  to 300 ppm) is at a chemical shift of  $\delta = 16.33$  ppm (Figure 2.5, left). Mass spectrometry and elemental analysis confirm the identity of dinitrogen complex **3**. The absence of a distinct IR band hints towards a centrosymmetric, bridging dinitrogen ligand which was therefore identified by rRaman spectroscopy. An intense band is observed at 1651 cm<sup>-1</sup> (<sup>15</sup>N-**3** 1594 cm<sup>-1</sup>) being diagnostic for a formally doubly reduced dinitrogen ligand ( $\nu_{\text{N-N}} = 1529$  cm<sup>-1</sup> in *trans*-diazene)<sup>160</sup> (Figure 2.5, middle). The molecular structure in the solid state is shown in Figure 2.5 (right). The bridging dinitrogen ligand binds in a terminal mode to two square planar chromium fragments that are arranged perpendicularly with respect to each other. The square planar geometries around both metal centers are slightly distorted, as shown by the N-Cr-N angles (N1-Cr1-N3 = 166.93(5)°, N2-Cr2-N4 = 172.66(5)°). The N<sub>amide</sub>-Cr bond has become longer ( $d_{\text{N-Cr}} = 2.0748(11)$  Å (**3**) vs. 2.0431(18) Å in (**2''**)) as a consequence of increased repulsion to the unpaired electrons. The N-N bond is considerably elongated ( $d_{\text{N-N}} = 1.208(14)$  Å) in comparison to free dinitrogen which indicates a high degree of backbonding into the N-N  $\pi^*$ -orbital, consistent with related N<sub>2</sub> bridged dichromium complexes.<sup>129,131,132,151</sup>

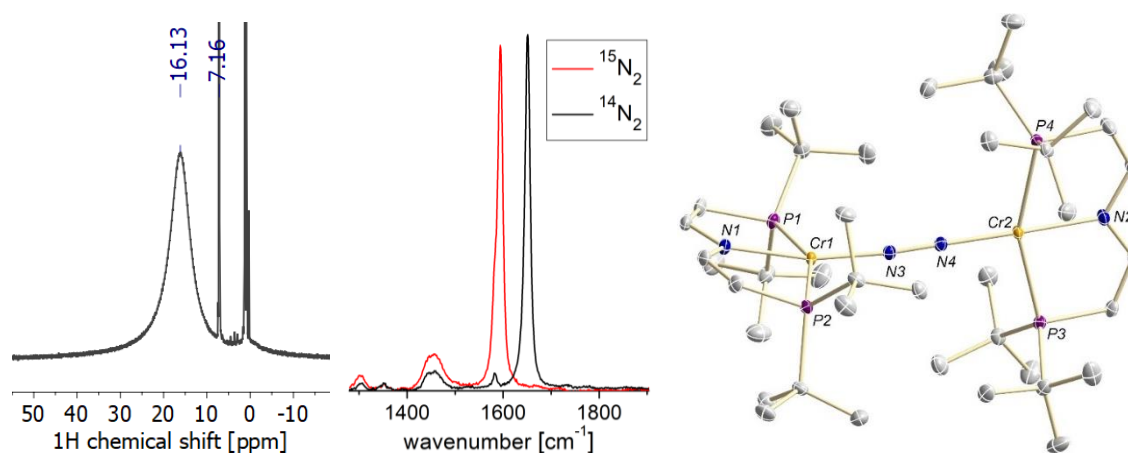


**Figure 2.5** Characterization of **3**. **Left:** <sup>1</sup>H NMR spectrum (C<sub>6</sub>D<sub>6</sub>, RT). **Middle:** rRaman spectrum ( $\lambda_{\text{ex}} = 633$  nm, pentane). **Right:** Molecular structure in the solid state. Hydrogen atoms and solvent molecules are omitted for clarity. Anisotropic displacement parameters are set to 50% probability. Selected bond lengths [Å] and angles [°]: N1-Cr1 2.0784(11), N3-N4 1.208(14), N2-Cr2 2.0854(11), Cr1-N3 1.8335(11); P1-Cr1-P2 156.342(14), N1-Cr1-N3 166.93(5), N2-Cr2-N4 172.66(5).

### 2.1.2 The electronic structure of $[(\mu\text{-N}_2)\{\text{Cr}(\text{BuPNP}'')\}_2]$ (**3**)

After isolation of dinitrogen complex  $[(\mu\text{-N}_2)\{\text{Cr}(\text{BuPNP}'')\}_2]$  (**3**), the electronic structure and magnetism was investigated. A magnetic moment of  $\mu_{\text{eff}} = 6.31 \pm 0.1 \mu_{\text{B}}$  was determined by Evans' method for **3** which corresponds to an  $S = 3$  high-spin ground state. This result can be rationalized by two scenarios: either by two ferromagnetically coupled Cr<sup>I</sup> centers with an intermediate spin configuration ( $S = 3/2$ , d<sup>5</sup>) and a neutral N<sub>2</sub> ligand ( $S = 0$ ) (Figure 2.7,

bottom left) or by two antiferromagnetically coupled Cr<sup>II</sup> centers with a doubly reduced N<sub>2</sub> ligand possessing a triplet ground state ( $S = 1$ ) being isoelectronic to O<sub>2</sub> (Figure 2.7, top left). The latter case refers to the “three-spin model”,<sup>161</sup> which is frequently used to describe the electronic structure of dinuclear, N<sub>2</sub> bridged, 3d transition metal complexes.

The magnetic susceptibility of **3** was investigated by SQUID magnetometry (Figure 2.6, left). Above 12 K, a nearly constant susceptibility of  $\chi_m T \sim 6.0 \text{ cm}^3 \text{ mol}^{-1} \text{ K}$  was found. The data were modelled with an  $S = 3$  ground state where the chromium atoms ( $S_1 = S_2 = 2$ ) are engaged in antiferromagnetic coupling ( $J_{\text{Cr-N}} \geq -450 \text{ cm}^{-1}$ ) with the diazenide ligand ( $S_3 = 1$ ) which is consistent with the “three-spin-model” (Figure 2.7) and also agrees with the N-N stretching vibration. It is important to emphasize that the interpretation of this interaction has to be taken with care. A classical antiferromagnetic coupling shows a temperature dependence in the susceptibility curve consisting of two regimes in which the electrons are (un)paired. The situation here is different because the “coupling” is so strong that the electrons are paired over the entire temperature range, which therefore has to be interpreted as a significant covalent Cr-N  $\pi$ -bonding interaction.

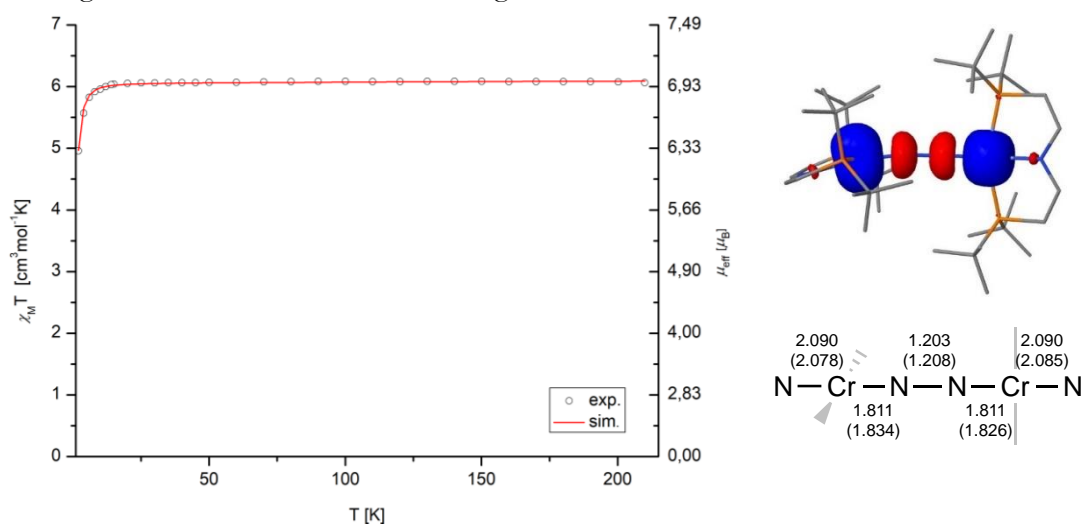


**Figure 2.6 Left:** Temperature dependence of the experimental  $\chi_m T$  product of **3** (Fitting parameter:  $g_1 = g_3 = 2.007$ ,  $g_2 = 2.000$ ,  $S_1 = S_2 = 2$  (Cr),  $S_3 = 1$  (N<sub>2</sub>),  $J_{\text{Cr-N}} \geq 450 \text{ cm}^{-1}$ ,  $D = 1.511 \text{ cm}^{-1}$ ). Applied spin-Hamiltonian is given in the Appendix (Figure 6.10). **Top right:** Spin density plot. **Bottom right:** Bond metrics derived by geometry optimization and XRD analysis (in parentheses). DFT calculations were performed by Dr. Markus Finger (AK Schneider, Georg-August-Universität Göttingen).

DFT calculations<sup>a</sup> were performed in order to gain insight into the electronic structure of **3** (Figure 2.6). On a PBE0/def2-TZVPP (COSMO(THF)) level of theory, an  $S = 3$  electronic ground state could be reproduced (Table 6.27). The bond lengths derived from geometry optimization are in good agreement with the experimental data (Figure 2.6, bottom right). There is negative spin density located on the bridging N<sub>2</sub> ligand ( $\rho_s = -0.86$ ) and a significant amount of spin contamination was found ( $\langle S^2 \rangle = 12.798$ ). An  $S = 5$  ground state is strongly disfavored ( $+135.4 \text{ kJ mol}^{-1}$ ) (Table 6.27). The antiferromagnetic coupling between the

<sup>a</sup> All DFT calculations within chapter “Results and Discussion I” were carried out by Dr. Markus Finger (AK Schneider, Georg-August-Universität Göttingen).

chromium atoms and the diazenide bridge can be estimated by the equation  $J_{AF} = [E_{S=5} - E_{S=3}]/8$  which gives  $J_{Cr-N} \approx -1400 \text{ cm}^{-1}$ .<sup>162</sup> To compare, a related  $N_2$  bridged diiron complex with a similar electronic structure features a stronger coupling constant ( $J_{Fe-N} = -3500 \text{ cm}^{-1}$ ).<sup>162</sup> The “three-spin-model” might be in line with the magnetic data and the experimental derived  $N_2$  stretching vibration, however, it is a very static model of separated charges that neglects covalent interactions.

The electronic structure can also be rationalized by a molecular orbital scheme within a restricted open shell approach (Figure 2.7, right).<sup>1</sup> There are four molecular orbitals with  $\pi$ -symmetry including 0 – 3 nodal planes along the Cr-N-N-Cr core (Figure 2.7, right). The  $\delta/\delta^*$  and  $d_{z^2}$ -orbitals are metal-centered and have non-bonding character. The molecular orbitals are occupied by 14 electrons derived from two formally  $Cr^I$  ( $d^5$ ) atoms and four electrons from the  $\pi$ -orbitals of the  $N_2$  ligand. The energetically lowest  $\pi$ - $\pi$ - $\pi$  and  $\pi$ - $\pi^*$ - $\pi$  molecular orbitals are both fully occupied. The  $\delta/\delta^*$ ,  $d_{z^2}$  and  $\pi^*$ - $\pi$ - $\pi^*$ -orbitals are half-filled, giving rise to a high-spin electron septet with a  $\pi^{10}\delta^2d^2$  configuration. This molecular orbital picture anticipates positive spin density across the Cr-N-N-Cr core which is not consistent with the observed, negative spin density on the  $N_2$  ligand.

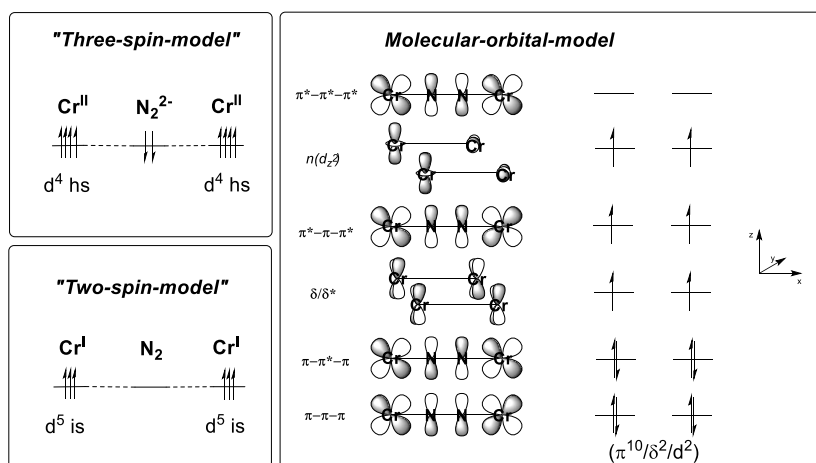


**Figure 2.7** Spin models for **3**. **Top left:** “three-spin model”;<sup>161</sup> **Bottom left:** “two-spin model”. **Right:** Molecular orbital scheme.<sup>12</sup>

The negative spin density on the  $N_2$  ligand can be explained as a result of exchange correlations of the unpaired electrons, as previously discussed by Münck and Bominaar<sup>162</sup>: Spin-polarization shifts the energies of the  $d^{\alpha}$ -orbitals into the range of the  $N_2$   $\pi$ -orbitals and the  $d^{\beta}$ -orbitals into the range of unoccupied  $N_2$   $\pi^*$ -orbitals. Hence, the observed negative spin density can be explained by the fact that the former orbitals predominantly have metal character (Figure 2.8, left), whereas the latter are mostly centered on the  $N_2$  bridge (Figure 2.8, right).

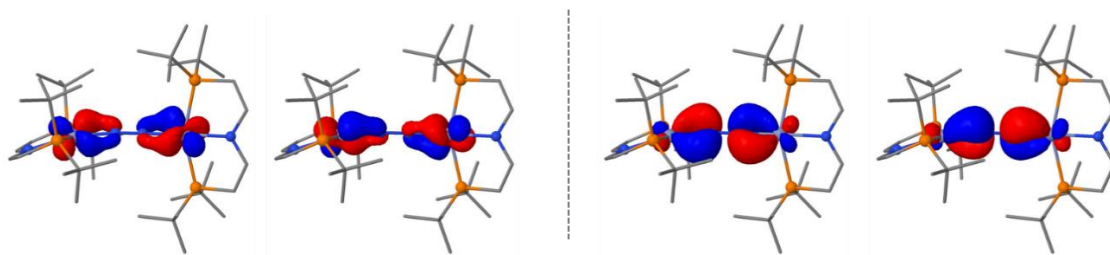


**Figure 2.8**  $\alpha$  (left) and  $\beta$  (right) orbitals of the  $\pi$ - $\pi^*$ - $\pi$  interactions of **3** taken from D3BJ-PBE0/def2-TZVPP (Cosmo(THF))/D3BJ-RJ-PBE/def2-TZVP, def2-SVP) calculations, performed by Dr. Markus Finger (Georg-August-Universität Göttingen).

Importantly, the covalent, molecular orbital approach can be critical for transition metal complexes based on first row metals, which, due to their contracted d-orbitals, exhibit significant smaller covalence radii compared to the heavier homologues (Cr: 1.39 Å, Mo: 1.54 Å, W: 1.62 Å).<sup>139</sup> To conclude, the “three-spin model” might be better suited to describe the bonding situation in **3**.

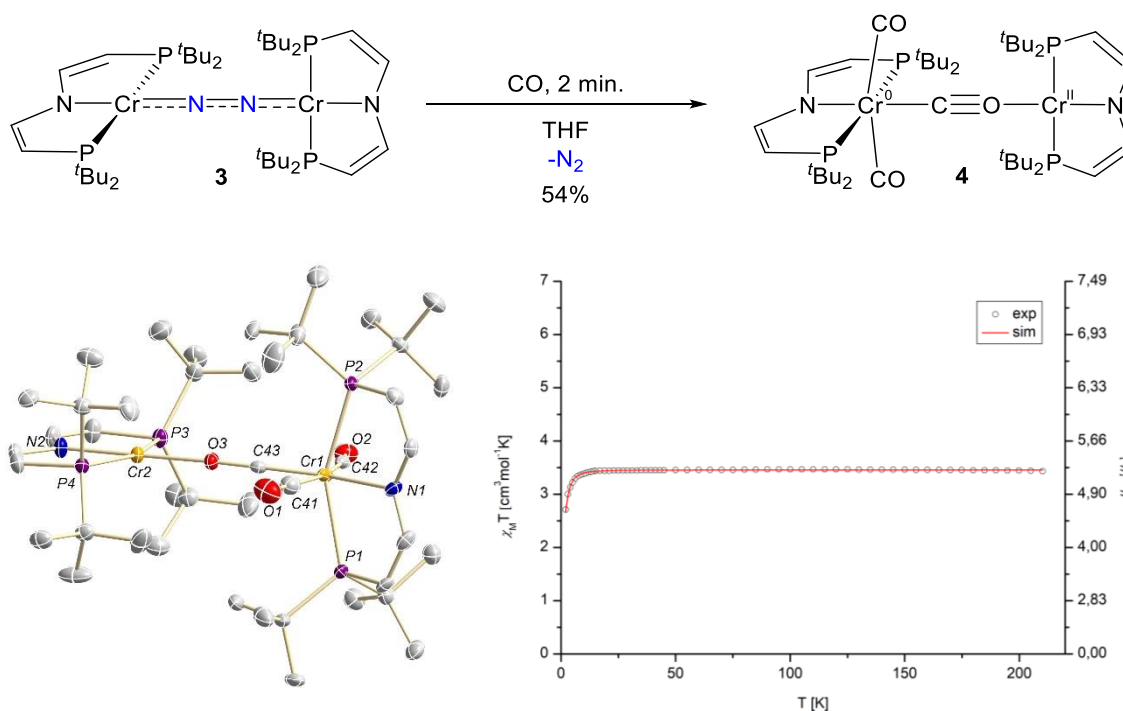
The correlation between the electron configuration of dinuclear  $N_2$  complexes and cleavage into terminal nitrides was recently discussed, where a  $\pi^{10}$  electron configuration is favored (introduction, subchapter 1.1.5).<sup>1,2</sup> Despite  $\pi^{10}\delta^2d^2$  electron configuration in  $[(\mu-N_2)\{Cr(^{Bu}PNP^*)\}_2]$  (**3**) there is no sign of  $N_2$  cleavage neither under thermal (refluxing toluene) nor under photochemical conditions ( $h\nu \geq 305$  nm). This lack of reactivity can have several reasons as introduced in subchapter 1.3.4. One reason might be the strong  $\pi$ -donating amide ligands in *trans*-position to the  $N_2$  bridge that lift the barrier for  $N_2$  cleavage as discussed in subchapter 1.1.5. High kinetic barriers for  $N_2$  cleavage can be potentially accessed under photolytic conditions, exemplified by thermally stable  $N_2$  bridged dirhenium complexes,<sup>2,43,44,49</sup> however, as mentioned before, exposure to light of different wavelengths did not lead to any reaction. Another explanation could be the high-spin configuration. The introduction of strong-field ligands could induce spin pairing leading to a  $\pi^{10}\delta^4$  electron configuration which has shown to undergo  $N_2$  cleavage into terminal nitrides.<sup>41,43,44</sup> As mentioned earlier (subchapter 1.1.5),  $N_2$  splitting proceeds via a zig-zag transition state, in which the occupied M-N-N-M  $\pi$ -orbitals are mixing with a N-N  $\sigma^*$ -orbital where its occupation leads to bond N-N cleavage. Mixing of these orbitals is presumably facilitated in a covalent bonding situation with diffuse d-orbitals, and hence disfavored for contracted d-orbitals as it is the case in first row metals. Indeed,  $N_2$  cleavage into terminal metal nitride complexes is indeed not a typical reactivity pattern of 3d transition metal dinitrogen complexes that tend to form multinuclear nitride complexes.<sup>1,2,145,163</sup>

## 2.2 $[(\mu\text{-N}_2)\{\text{Cr}(\text{tBuPNP}'')\}]$ (**3**) as a reductive precursor complex

The reactivity of dinitrogen complex  $[(\mu\text{-N}_2)\{\text{Cr}(\text{tBuPNP}'')\}]$  **3** towards carbon monoxide and *tert*-butyl isonitrile is discussed in the next two subchapters. The intention behind these reactions is the introduction of strong field ligands which might promote a low-spin electron configuration being associated with thermodynamically favored  $\text{N}_2$  cleavage into terminal nitride complexes.

### 2.2.1 The reactivity of $[(\mu\text{-N}_2)\{\text{Cr}(\text{tBuPNP}'')\}]$ (**3**) towards CO

Exposing a THF solution of  $[(\mu\text{-N}_2)\{\text{Cr}(\text{tBuPNP}'')\}]_2$  (**3**) for two minutes to an atmosphere of carbon monoxide leads to a color change into deep green. Removal of the solvent and recrystallization from pentane at  $-40\text{ }^\circ\text{C}$  establishes isocarbonyl complex  $[(\mu\text{-CO})\{\text{Cr}(\text{CO})_2(\text{tBuPNP}'')\}]\{\text{Cr}(\text{tBuPNP}'')\}$  (**4**) with an isolated yield of 54% as dark green, crystalline solid (Scheme 2.3).



**Scheme 2.3 Top:** Carbonylation of **3** forming isocarbonyl complex **4**. **Bottom left:** Molecular structure in the solid state. Hydrogen atoms, solvent molecules and disordered moieties are omitted for clarity. Selected bond lengths [ $\text{\AA}$ ] and angles [ $^\circ$ ]:  $\text{N1-Cr1}$  2.161(3),  $\text{N2-Cr2}$  2.040(3),  $\text{Cr1-C43}$  1.759(3),  $\text{C43-O3}$  1.222(3),  $\text{C41-O1}$  1.167(4),  $\text{C42-O2}$  1.162(4);  $\text{P1-Cr1-P2}$  153.32(3),  $\text{P3-Cr2-P4}$  160.03(3),  $\text{N1-Cr1-C43}$  162.61,  $\text{N2-Cr2-O3}$  178.04. **Bottom right:** Temperature dependence of the experimental  $\chi_{\text{M}}T$  product (Fitting parameter:  $g = 2.146$ ,  $S = 2$ ,  $D = -1.733\text{ cm}^{-1}$ ). Applied spin-Hamiltonian is given in the Appendix (Figure 6.13).

X-Ray diffraction identified a dinuclear chromium complex consisting of an octahedral and a square planar fragment being connected by a bridging, carbonyl ligand, which are generally denoted as isocarbonyl ligands.<sup>164–167</sup> The square planar unit resembles the bond lengths of the square planar, monomeric species  $[\text{CrCl}(\text{tBuPNP}'')]$  (**2''**) ( $d_{\text{N-Cr}} = 2.040(3)\text{ \AA}$  (**4**) vs.  $2.0431(18)\text{ \AA}$  (**2''**)) (Scheme 2.3, left). The corresponding bond length of the octahedral unit is longer ( $d_{\text{Cr-N}} = 2.161(3)\text{ \AA}$  (**4**)) and the pincer bite angle is smaller



(P1-Cr1-P2 = 153.32(3) $^\circ$  vs P3-Cr2-P4 = 160.03(3) $^\circ$ ). Furthermore, the pincer ligand of the octahedral unit is bent (N1-Cr1-C43 = 162.61 $^\circ$ ) with respect to the Cr-CO-Cr axis. By contrast, the square planar fragment is nearly linearly coordinated (N2-Cr2-O3 = 178.04 $^\circ$ ). **4** features three diagnostic, IR active bands at 1895 cm $^{-1}$  (low intensity), 1792 cm $^{-1}$  and 1542 cm $^{-1}$ . According to DFT calculations (PBE0/def2-TZVPP (COSMO(THF))), the former two bands can be assigned to the symmetric and asymmetric stretching modes of the terminal CO ligands and the latter band corresponds to the asymmetric stretching mode of the bridging isocarbonyl ligand (Appendix, Figure 6.113). The significantly shifted IR band of the isocarbonyl is consistent with increased  $\pi$ -backbonding from two metal centers which coincides with the different C-O bond lengths of the carbonyl ligands ( $d_{\text{C-O}} = 1.222(3)$  Å ( $\mu$ -CO) vs. 1.167(4) Å (CO $_{\text{term}}$ )). In cases of strong  $\pi$ -backbonding, the C-O bond is considered as a reduced double bond.<sup>164,166,168,169</sup> Based on the structural similarity between **2''** and the square planar {(PNP)Cr} unit in **4**, a local high-spin Cr<sup>II</sup> configuration is suggested. The octahedrally coordinated chromium atom presumably exhibits a low-spin d<sup>6</sup> configuration as a consequence of the coordination of three strong-field ligands. For instance, the octahedral complex [(<sup>P</sup>PN<sup>H</sup>P)Cr(CO)<sub>3</sub>] is diamagnetic.<sup>170</sup> To conclude, high-spin Cr<sup>II</sup>/ low-spin Cr<sup>0</sup> is assumed, in agreement with a related dinuclear compound reported from Theopold (introduction, Scheme 1.17).<sup>131</sup> This hypothesis was validated by SQUID magnetometry (Scheme 2.3, bottom right). The magnetic susceptibility is constant at  $\chi_{\text{M}}T \sim 3.40$  cm<sup>3</sup> mol<sup>-1</sup> K above 10 K matching the spin-only value of an electron quintet ( $\chi_{\text{M}}T = 3.0$  cm<sup>3</sup> mol<sup>-1</sup> K;  $\mu_{\text{eff}} = 4.90$   $\mu_{\text{B}}$ ). Accordingly, the obtained data could be decently fitted with an  $S = 2$  spin state that is in line with the proposed electron configuration.

In order to clarify the electronic structure of the isocarbonyl complex **4**, DFT calculations on a PBE0/def2-TZVPP (COSMO(THF)) level of theory were performed (Figure 2.9). A quintet ground state is thermodynamically favored where the major amount of spin density is located on the square planar coordinated chromium atom ( $\rho_{\text{s}} = 3.91/0.14$ ), consistent with a high-spin configuration. The electron triplet is about  $\Delta E = +125.8$  kJ mol<sup>-1</sup> above the ground state (Appendix, Table 6.28). The calculated bond lengths and angles are in good agreement with the metrical parameters derived from XRD analysis (Figure 2.9, middle).

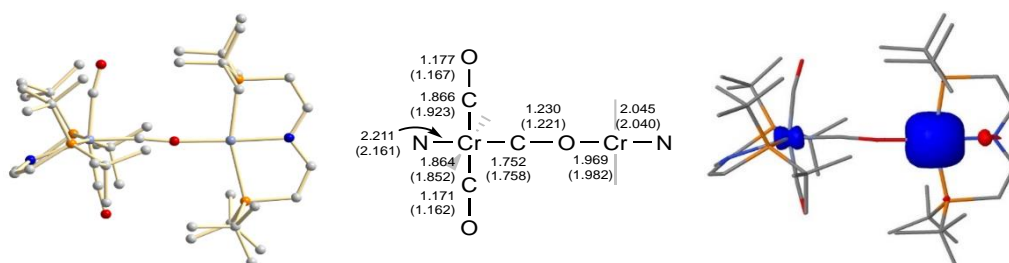
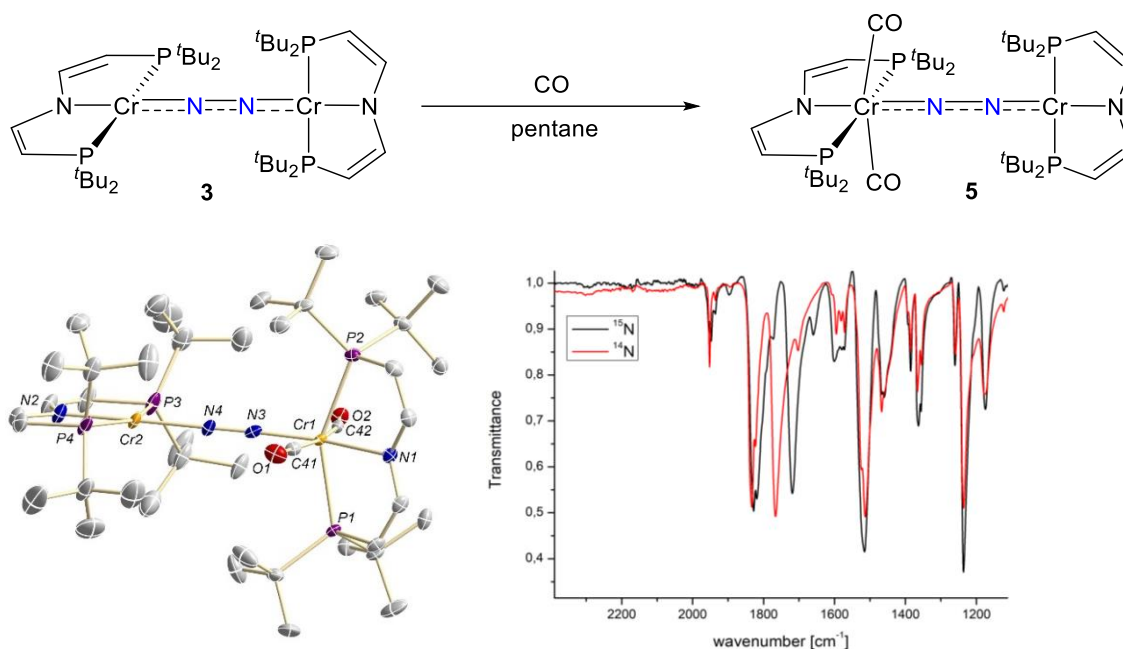


**Figure 2.9** Left: Geometry optimized structure of **4**. Middle: Comparison of theoretical and (experimental) data. Right: Spin density plot. DFT calculations were performed by Dr. Markus Finger (AK Schneider, Georg-August-Universität Göttingen).

To conclude, in presence of carbon monoxide the bridging dinitrogen ligand is released and the isocarbonyl complex is formed. The coordination of these ligands induces a spin change from an  $S = 3$  to an  $S = 2$  ground state. The unequal distribution of the carbonyl ligands over the metal centers raises the question about the origin of the selectivity of this transformation.

When the carbonylation of  $[(\mu\text{-N}_2)\{\text{Cr}(\text{}^t\text{BuPNP}^{\text{''}})\}_2]$  (**3**) is performed in pentane instead of THF, an immediate precipitation of a green, microcrystalline solid can be observed (Scheme 2.4). The CO atmosphere was removed and the solid was collected. The IR spectrum reveals three intense bands at 1952, 1834 and 1766  $\text{cm}^{-1}$  which are significantly different compared to isocarbonyl complex  $[(\mu\text{-CO})\{\text{Cr}(\text{CO})_2(\text{}^t\text{BuPNP}^{\text{''}})\}\{\text{Cr}(\text{}^t\text{BuPNP}^{\text{''}})\}]$  (**4**) (1895  $\text{cm}^{-1}$ , 1792  $\text{cm}^{-1}$  and 1542  $\text{cm}^{-1}$ ). More importantly, the band at 1766  $\text{cm}^{-1}$  is isotope-sensitive and shifts to 1717  $\text{cm}^{-1}$  upon  $^{15}\text{N}$ -labelling, while all other bands stay unaffected (Scheme 2.4, bottom right).



**Scheme 2.4 Top:** Carbonylation of **3** giving rise to dinitrogen complex **5**. **Bottom left:** Molecular structure in the solid state. Hydrogen atoms, solvent molecules and disordered molecules are omitted for clarity. Selected bond lengths [ $\text{\AA}$ ] and angles [ $^\circ$ ]: N1-Cr1 2.176(7), N2-Cr2 2.043(2), Cr1-N3 1.7951(19), N3-N4 1.173(3); P1-Cr1-P2 151.92(2), P3-Cr2-P4 159.58(3) N(3)-Cr(1)-N(1) 162.20(8). **Bottom right:** IR spectrum ( $^{14}\text{N}$ : red;  $^{15}\text{N}$ : black).

This observation can be interpreted as a spectroscopic evidence for a (bridging) dinitrogen ligand.<sup>132,134</sup> Moreover, the presence of an IR active  $\text{N}_2$  ligand anticipates an asymmetric chemical environment, as the N-N stretching vibration in parent **3** is IR silent. Crystallization from pentane at  $-80^\circ\text{C}$  yielded single crystals suitable for X-ray analysis. The solid-state structure shows a dinuclear complex  $[(\mu\text{-N}_2)\{\text{Cr}(\text{CO})_2(\text{}^t\text{BuPNP}^{\text{''}})\}\{\text{Cr}(\text{}^t\text{BuPNP}^{\text{''}})\}]$  (**5**) which is structurally nearly identical to isocarbonyl complex **4** with the exception of a bridging dinitrogen ligand ( $d_{\text{N-N}} = 1.173(3)$   $\text{\AA}$ ). There are only minor differences in the bond metrics, as depicted in (Figure 2.10).

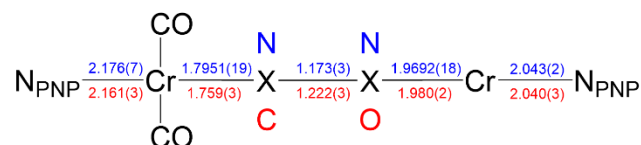


**Figure 2.10** Comparison of relevant bond lengths [Å] between isocarbonyl complex **4** (red) and dinitrogen complex **5** (blue).

There might be space for misinterpretation concerning the nature of the bridging ligand solely by X-Ray diffraction because unlike spectroscopy, this technique cannot appropriately distinguish between CO and N<sub>2</sub>. Nevertheless, the different band pattern in the IR spectrum including the presence of an isotope-sensitive band unambiguously identifies a bridging N<sub>2</sub> ligand, which is further supported by mass spectrometry of both isotopologues.

Compared to parent [(μ-N<sub>2</sub>){Cr(<sup>t</sup>BuPNP<sup>''</sup>)}<sub>2</sub>] (**3**), the N-N bond length of the dinitrogen bridge is shorter in **5** ( $d_{\text{N-N}} = 1.173(3)$  Å (**5**) vs.  $d_{\text{N-N}} = 1.208(14)$  Å (**3**)) which coincides with a shift of the N-N stretching vibration to higher energy ( $\Delta\nu = +115$  cm<sup>-1</sup>). That can be explained by decreased backbonding into the N<sub>2</sub> π\*-orbital as a result of two competing π-accepting CO ligands that withdraw electron density from the Cr-N-N-Cr π-manifold. Due to the labile nature of N<sub>2</sub> ligands, there are only few examples in the literature of chromium complexes in which the N<sub>2</sub> ligand coexists to strong π-accepting ligands.<sup>125,126</sup>

Dinitrogen complex **5** is not stable in solution and decomposes into **4** and unknown products. Therefore, NMR characterization including measurement of the magnetic moment by Evans' method could not be accomplished. There are no indications for N-N bond cleavage. Since **5** could not be obtained in analytical quality, as judged by elemental analysis, SQUID magnetometry could not be performed to examine the magnetism. Hence, **5** was investigated by DFT calculations to explore the electronic structure (Figure 2.11).

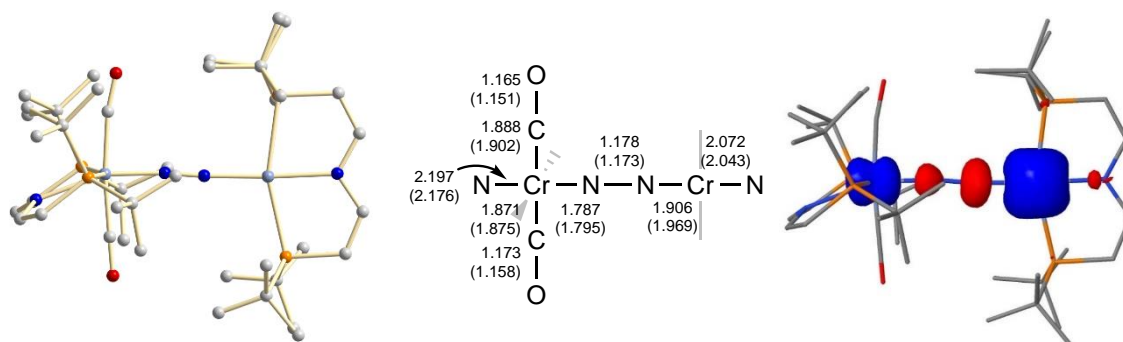
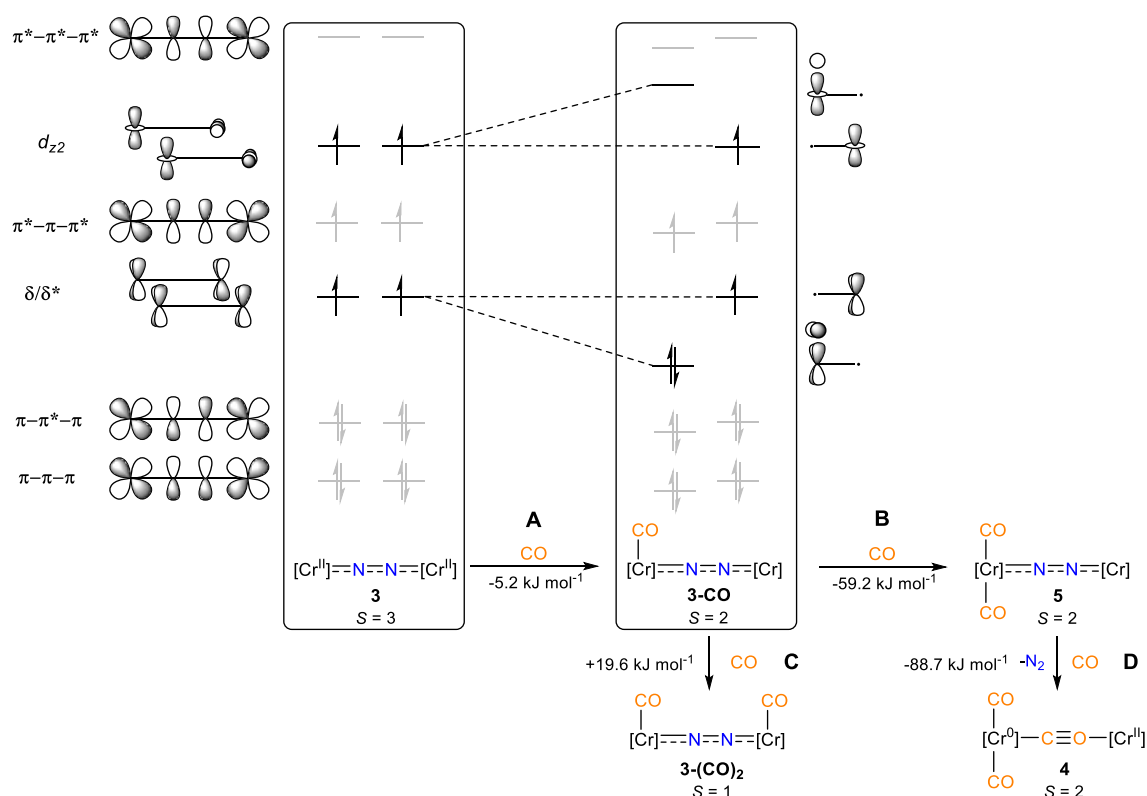


**Figure 2.11 Left:** Geometry optimized structure of **5**. **Middle:** Comparison of theoretical and (experimental) data. **Right:** Spin density plot. DFT calculations were performed by Dr. Markus Finger (AK Schneider, Georg-August-Universität Göttingen).

Different spin states ( $S = 0, 1, 2, 3$ ) were computed whereby the electron quintet is thermodynamically favored, and the septet is +95.1 kJ mol<sup>-1</sup> higher in energy (Appendix, Table 6.29). The comparison between the bond lengths derived from X-Ray diffraction and DFT shows only minor deviations (Figure 2.11, middle). In analogy to isocarbonyl complex

**4**, the major part of the spin density is located on one metal center ( $\rho_s = 3.72$  (Cr)/0.88 (Cr)). The negative spin density on the N<sub>2</sub> bridge ( $\rho_s = -0.45$  (N<sub>2</sub>)) can be explained by spin polarization, similar to dinitrogen complex **3**. Importantly, a clear assignment of the oxidation states is difficult, as the N-N stretching vibration (1766 cm<sup>-1</sup>) is indicative for both, electronically neutral and doubly charged N<sub>2</sub> (introduction, subchapter 1.1.2). Hence, the electronic ground state presumably can be described as an intermediate of high-spin Cr<sup>II</sup> / low-spin Cr<sup>0</sup> / N<sub>2</sub><sup>0</sup> and high-spin Cr<sup>II</sup> / intermediate-spin Cr<sup>II</sup> that is antiferromagnetically coupled to the N<sub>2</sub><sup>2-</sup> ligand. The ambiguity of the oxidation states represents a classical example of redox non-innocence.<sup>171</sup> In the following, the thermochemistry of this carbonylation reaction will be discussed. For this purpose, the free energies of all relevant species were computed.

Starting from dinitrogen complex **3** the first carbonylation step is almost thermoneutral by -5.2 kJ mol<sup>-1</sup> (Step A) and introduces an  $S = 2$  spin state ( $\Delta E_{S=3} = +39.0$  kJ mol<sup>-1</sup>, computational details in Table 6.30, Appendix), as illustrated in a simplified, qualitative molecular orbital picture in the boxes in Scheme 2.5.



**Scheme 2.5** Calculated free energies of the reaction sequence from **3** to **4**. DFT calculations were performed by Dr. Markus Finger (AK Schneider, Georg-August-Universität Göttingen).

The coordination of CO from **3** to **3-CO** predominantly affects the metal-centered orbitals: while CO binding raises the energy of the respective  $d_{z^2}$ -orbital, the  $\delta$ -orbital is stabilized which triggers electron transfer (**3-CO**:  $\rho_s = 3.67$  (Cr), 0.93 (Cr)). Since spin-pairing exclusively includes non-bonding, metal-centered orbitals, the bonding situation in **3-CO** is

not drastically changed. Consequently, analogous to parent dinitrogen complex **3** ( $\rho_s = -0.86$  ( $\text{N}_2$ ), Figure 2.6), there is retained, significant, negative spin density on the  $\text{N}_2$  bridge ( $\rho_s = -0.61$  ( $\text{N}_2$ )), expressed by similar computed N-N stretching vibrations ( $\nu_{\text{N-N}} = 1689 \text{ cm}^{-1}$  (**3**),  $1735 \text{ cm}^{-1}$  (**3-CO**)). Again, the assignment of oxidation states is blurred and the electronic ground state is presumably best described as an intermediate between high-spin  $\text{Cr}^{\text{II}}$  / low-spin  $\text{Cr}^0$  and high-spin  $\text{Cr}^{\text{II}}$  / intermediate-spin  $\text{Cr}^{\text{II}}$  that is antiferromagnetically coupled to  $\text{N}_2^{2-}$ .

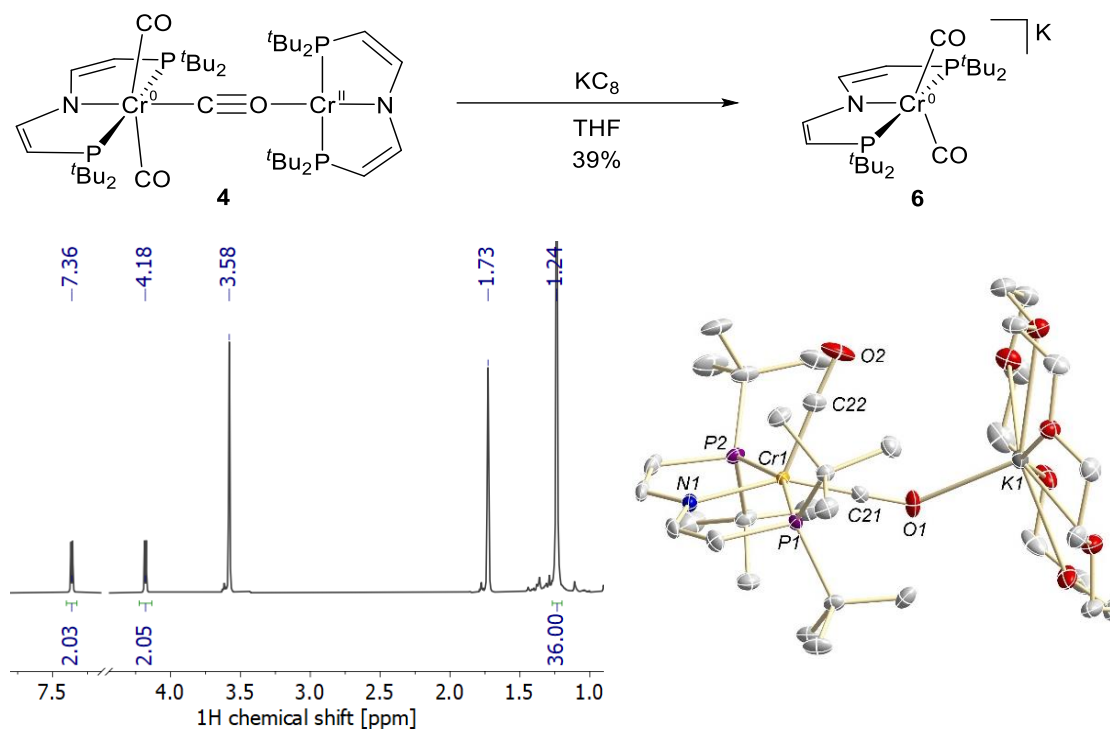
The coordination of a second CO ligand on the same metal center is exergonic by  $\Delta G = -59.2 \text{ kJ mol}^{-1}$  (Step B) while CO binding on the second, square planar unit to the putative complex “[ $(\mu\text{-N}_2)\{\text{Cr}(\text{CO})(^{\text{tBu}}\text{PNP})\}_2$ ]” **3-(CO)**<sub>2</sub> is disfavored ( $\Delta G = 19.6 \text{ kJ}\cdot\text{mol}^{-1}$ , Step C). Hence, initial CO coordination controls the selectivity of this reaction. Dinitrogen complex **5** is formed (Step D) where an  $S = 2$  ground state is suggested. As the final step, the exchange of the bridging dinitrogen ligand by the isocarbonyl to **4** has a huge driving force of  $\Delta G = -88.7 \text{ kJ mol}^{-1}$  (Path D). The computed  $S = 2$  ground state of isocarbonyl complex **4** is in agreement with the experimental SQUID data. The detailed mechanism of the final ligand exchange step (step D) was not investigated.

With the intention to functionalize the activated carbon monoxide ligand, isocarbonyl complex **4** was reacted with silanes such as trimethyl silyl chloride, triethyl silyl hydride and trimethylsilyl azide, to exploit the high oxophilicity for Si-O bond formation.<sup>172–176</sup> Color changes were observed in these reactions, however, the isolation of reaction products remained unsuccessful. Therefore, the reactivity was tested under reductive conditions to further activate the bridging CO ligand.

Reacting [ $(\mu\text{-CO})\{\text{Cr}(\text{CO})_2(^{\text{tBu}}\text{PNP})\}\{\text{Cr}(^{\text{tBu}}\text{PNP})\}$ ] (**4**) with two equivalents of potassium graphite at  $-78 \text{ }^\circ\text{C}$  leads to an immediate color change towards brown. Washing with pentane and extraction with THF establishes the anionic complex  $\text{K}[\text{Cr}(\text{CO})_2(^{\text{tBu}}\text{PNP})]$  (**6**) as a blue solid with a yield of 39% (Scheme 2.6).

In the  $^1\text{H}\{^{31}\text{P}\}$  spectrum one aliphatic ( $\delta = 1.24 \text{ ppm}$ ) and two signals in the downfield region are found which can be assigned to the *tert*-butyl groups and the ligand backbone, respectively, indicating  $C_{2v}$ -symmetry in solution (Scheme 2.6, bottom left). A singlet is observed in the  $^{31}\text{P}\{^1\text{H}\}$  NMR spectrum at a chemical shift of  $\delta = 101.2 \text{ ppm}$  (Appendix, 6.1.8). Characterization by elemental analysis and X-Ray diffraction was accomplished by sequestering the potassium atom with an equimolar amount of 18-crown-6. In the solid state, the chromium atom is surrounded by the tridentate pincer ligand and two carbonyl ligands (Scheme 2.6, bottom right). A  $\tau = 0.09$  parameter determines square pyramidal geometry. The potassium atom is encapsulated by the crown ether binding one carbonyl ligand ( $d_{\text{K-OC}} = 2.6665(13) \text{ \AA}$ ). The IR spectrum shows two pairs of bands ( $1747, 1738 \text{ cm}^{-1}$ ;  $1642, 1633 \text{ cm}^{-1}$ ) both differing by  $9 \text{ cm}^{-1}$ . These “band pairs” presumably belong to the symmetric and asymmetric stretching vibration mode and the splitting into two sets might be explained

by the contact with the potassium atom. Considering the relatively low yield of 39%, the fate of the residual 61% chromium compounds stays unclear.

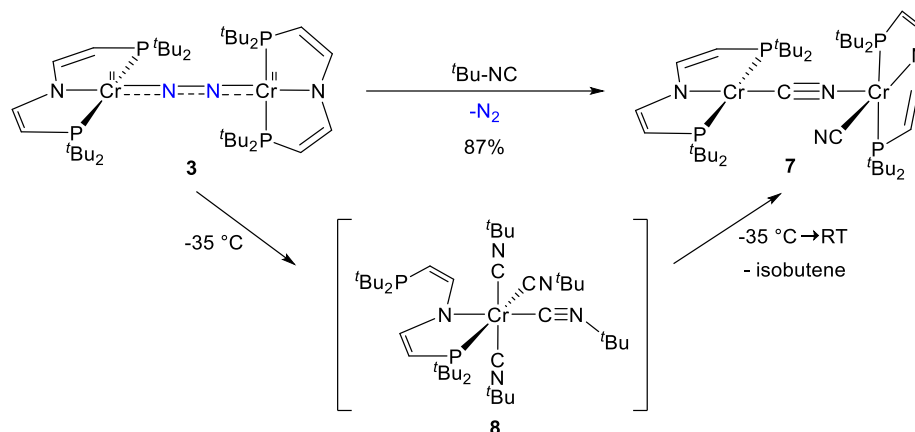


**Scheme 2.6 Top:** Synthesis of **6**. **Bottom left:**  $^1\text{H}\{^{31}\text{P}\}$  NMR spectrum (THF-*d*<sub>8</sub>, RT). **Bottom right:** Single crystals were only obtained by the addition of 18c6. Molecular structure of  $[\text{K}@18\text{c}6]\text{-6}$  in the solid state. Hydrogen atoms, disordered moieties and solvent molecules are omitted for clarity. Anisotropic displacement parameters are set to 50% probability. Selected bond lengths [Å] and angles [°]: N1-Cr1 2.0751(14), C21-O1 1.207(2), C22-O2 1.199(2), O1-K1 2.6665(13); P1-Cr1-P2 158.929(19), N1-Cr1-C21 153.66(7), N1-Cr1-C22 122.83(7).

### 2.2.2 The reactivity of $[(\mu\text{-N}_2)\{\text{Cr}(\text{tBuPNP})\}_2]$ (**3**) towards $\text{tBu-NC}$

Beside the carbonylation of  $[(\mu\text{-N}_2)\{\text{Cr}(\text{tBuPNP})\}_2]$  (**3**), the reactivity was targeted towards isoelectronic *tert*-butyl isocyanide. The addition of an excess *tert*-butyl isocyanide to a solution of dinitrogen complex **3** results in an immediate color change into deep green. Within minutes the color changes into orange. Removal of the solvent and recrystallization establishes cyanide complex  $[(\mu\text{-CN})\{\text{Cr}(\text{CN})(\text{tBuPNP})\}\{\text{Cr}(\text{tBuPNP})\}]$  (**7**) as orange crystals with a yield of 87% (Scheme 2.7). The structure in the solid state is shown in (Figure 2.12, left). X-Ray diffraction reveals a dinuclear complex consisting of two “[CrCN(tBuPNP)]” units and one of these binds the other in apical position resulting in a square pyramidal and a square planar coordination geometry around the metal centers. The bond metrics in these two square planar units are only slightly deviating. The bond lengths of the chromium atoms to the amide group in the ligand backbone are almost similar ( $d_{\text{N1-Cr1}} = 2.0294(14)$  Å vs.  $d_{\text{N2-Cr2}} = 2.0619(14)$  Å). The C-N bond lengths of the cyanide ligands are nearly the same ( $d_{\text{C43-N4}} = 1.159(2)$  Å vs.  $d_{\text{C41-N3}} = 1.149(2)$  Å) in accordance with the stretching vibrations observed in the IR spectrum ( $\nu = 2160\text{ cm}^{-1}$ ,  $2102\text{ cm}^{-1}$ ). The formation of a bridging cyanide complex seems unexpected, however, the transformation of

isonitrile into cyanides has been reported.<sup>177–179</sup> The formation of isobutene was confirmed by <sup>1</sup>H NMR spectroscopy.



**Scheme 2.7** Reactivity of dinitrogen complex  $[(\mu\text{-N}_2)\{\text{Cr}(\text{P}^t\text{Bu}_2\text{PNP}^t\text{Bu}_2)\}_2]$  (**3**) towards *tert*-butyl isocyanide.

Magnetic characterization of **7** was performed by SQUID magnetometry (Figure 2.12, right). The obtained data can be fitted with a model that consists of two  $S = 2$  chromium atoms ( $g = 2.062$ ) which are engaged in antiferromagnetic coupling  $J_{\text{Cr-Cr}} = -19.8 \text{ cm}^{-1}$  (a paramagnetic impurity with  $S = 2$  is present by 2.9%), consistent with exchange coupling of related examples.<sup>180,181</sup> Below 10 K, the susceptibility product is nearly  $\chi_M T = 0$  indicating a non-magnetic ground state. The measurement of the magnetic moment at room temperature by Evans' method is consistent with the SQUID data ( $\mu_{\text{eff}} = 6.11 \pm 0.1 \mu_B$ ,  $\chi_M T = 4.66 \text{ cm}^3 \text{ mol}^{-1} \text{ K}$ ).

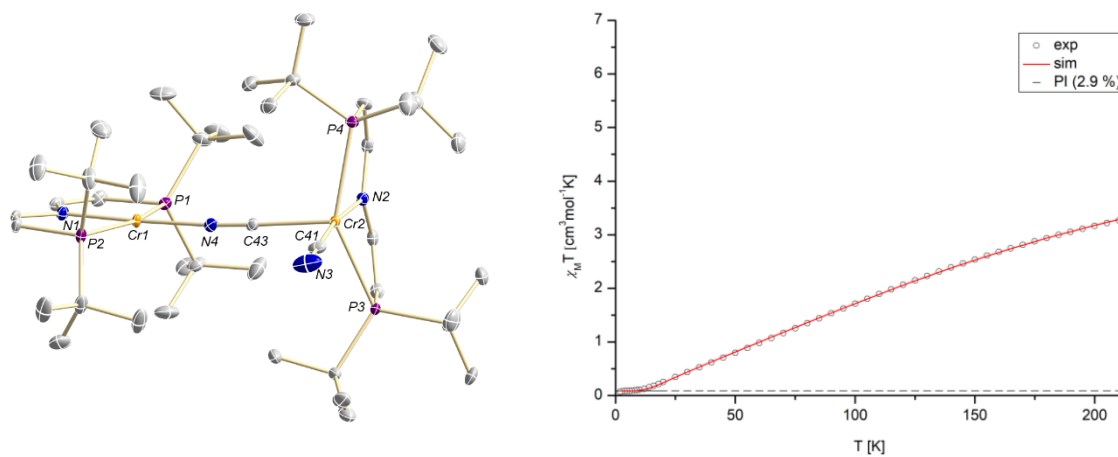


**Figure 2.12 Left:** Molecular structure of **7** in the solid state. Hydrogen atoms, disordered moieties and solvent molecules are omitted for clarity. Anisotropic displacement parameters are set to 50% probability. Selected bond lengths [Å] and angles [°]: N1-Cr1 2.0294(14), Cr2-N2 2.0619(14), Cr1-C43 2.0401(16), Cr2-C41 2.0997(18), C43-N4 1.159(2), C41-N1 1.149(2), N4-Cr2 2.1800(16), P1-Cr1 2.4623(5), P2-Cr1 2.4527(5), P3-Cr2 2.5083(5), P4-Cr2 2.5264(5); P1-Cr1-P2 162.146(19), P3-Cr2-P4 145.105(18), N1-Cr1-C43 177.52(6), N2-Cr2-C41 172.34(7). **Right:** Temperature dependence of the experimental  $\chi_M T$  product. Fitting parameters  $2 \times S = 2$ ,  $2 \times g = 2.062$ ,  $J_{\text{Cr1-Cr2}} = -19.8 \text{ cm}^{-1}$ , PI = 2.9%. Applied spin-Hamiltonian is given in the Appendix (Figure 6.21).

The exchange coupling within the applied fitting model contrasts the magnetic properties of dinitrogen complex **3** discussed in subchapter 2.1.2, where no magnetic exchange coupling

between the chromium centers was observed. Hence, these magnetic data raise the question if a mixed-valent  $\text{Cr}^{\text{I}}/\text{Cr}^{\text{III}}$  model has to be considered. Significant different bond length between the phosphorous and the chromium atoms ( $d_{\text{Cr1-P1/P2}} = 2.45\text{-}2.46 \text{ \AA}$  vs.  $d_{\text{Cr2-P3/P4}} = 2.51\text{-}2.52 \text{ \AA}$ ) might support this hypothesis. DFT calculations are required to understand the electronic structure of this complex, which is beyond the scope of this work.

The initial green color observed in the formation of **7** gave reason to assume a reactive, temperature labile intermediate. In order to trap that species, **3** was treated with  $t\text{Bu-NC}$  in pentane at  $-35 \text{ }^\circ\text{C}$  and crystallization in a concentrated solution at that temperature established  $[\text{Cr}(\text{CN-}t\text{Bu})(\kappa^2\text{-}t\text{BuPNP})]$  (**8**) as green, crystalline solid. The molecular structure in the solid state (Figure 2.13) consists of a mononuclear octahedral chromium complex with a  $\kappa^2$ -binding mode of the pincer ligand and four coordinating isonitrile ligands. One of these is heavily bent ( $\text{Cr-C21-N2} = 131.96(15)^\circ$ ) and the corresponding C-N bond is elongated ( $d_{\text{C26-N3}} = 1.209(2) \text{ \AA}$ ) as a result of strong  $\pi$ -backbonding. This bond elongation is reflected by IR spectroscopy which shows a typical shouldered band at  $1959 \text{ cm}^{-1}$  and a band that is significantly shifted to lower energy at  $1776 \text{ cm}^{-1}$ .<sup>182</sup> The strong  $\pi$ -backbonding anticipates double bond character, however, C-N double bonds are reported significantly longer ( $\sim 1.29 \text{ \AA}$ ).<sup>183</sup> A low-spin  $\text{Cr}^{\text{I}}$  configuration is suggested and consequently EPR spectroscopy was attempted at low temperatures as crystalline solid and as frozen solution but no signals were detected. Examples of the dissociation of one pincer arm are rare, but not unprecedented.<sup>184</sup>

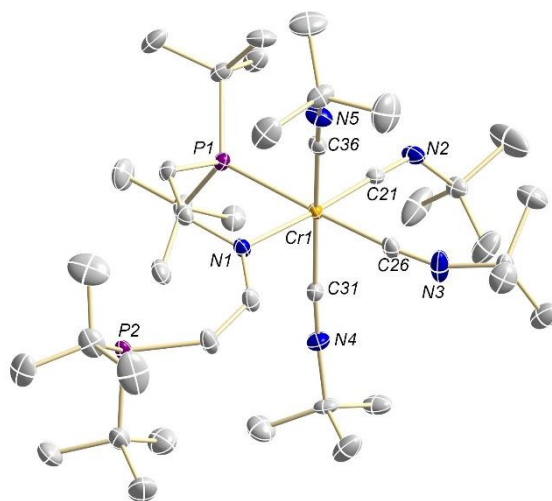


**Figure 2.13** Molecular structure of **8** in the solid state. Hydrogen atoms and solvent molecules are omitted for clarity. Anisotropic displacement parameters are set to 50% probability. Selected bond lengths [ $\text{\AA}$ ] and angles [ $^\circ$ ]: N1-Cr1 2.1105(13), C21-N2 1.209(2), N5-C36 1.166(2)  $\text{\AA}$ , N3-C26 1.170(2)  $\text{\AA}$ , N4-C31 1.163(2)  $\text{\AA}$ , C21-N2-C22 131.96(15).

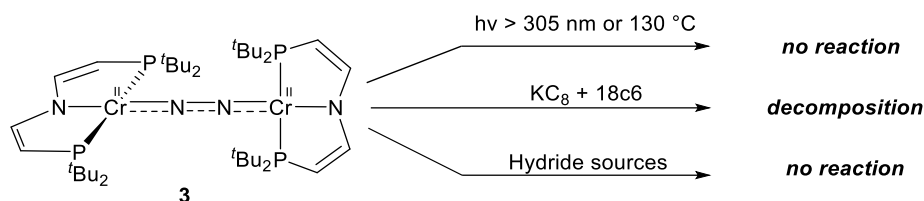
In this reaction sequence, the initial formed species **8** partially converts  $t\text{Bu-NC}$  at room temperature to cyanide under release of isobutene to generate dinuclear cyanide complex **7**. The question if the hypothetical, mononuclear complex “[ $\text{CrCN}(t\text{BuPNP})$ ]” undergoes dimerization was tested by the reaction of [ $\text{CrCl}(t\text{BuPNP})$ ] (**2''**) with potassium cyanide, but



even after heating at 65 °C for days no reaction was observed. To get a deeper insight into the mechanism of this reaction, UVvis kinetics could be performed at varied temperatures, which is not part of this work. It seems unexpected that the dinuclear structure of  $[(\mu\text{-N}_2)\{\text{Cr}(\text{tBuPNP}^{\text{''}})\}_2]$  (**3**) is initially transformed into the mononuclear isocyanide complex **8**, which then dissociates and reacts  $\text{tBu-NC}$  under formation of the dinuclear species **7**. Generally, isonitriles show versatile reactivity that is not restricted to metal coordination including insertion reactions<sup>183,185</sup> and coupling reactions.<sup>186,187</sup>

### 2.3 Attempts of N<sub>2</sub> cleavage

This subchapter briefly summarizes all attempts to further activate or split the N-N bond of  $[(\mu\text{-N}_2)\{\text{Cr}(\text{tBuPNP}^{\text{''}})\}_2]$  (**3**). In these cases, either no reaction took place or the reaction product(s) could not be identified if the reaction did not result in decomposition (Scheme 2.8).

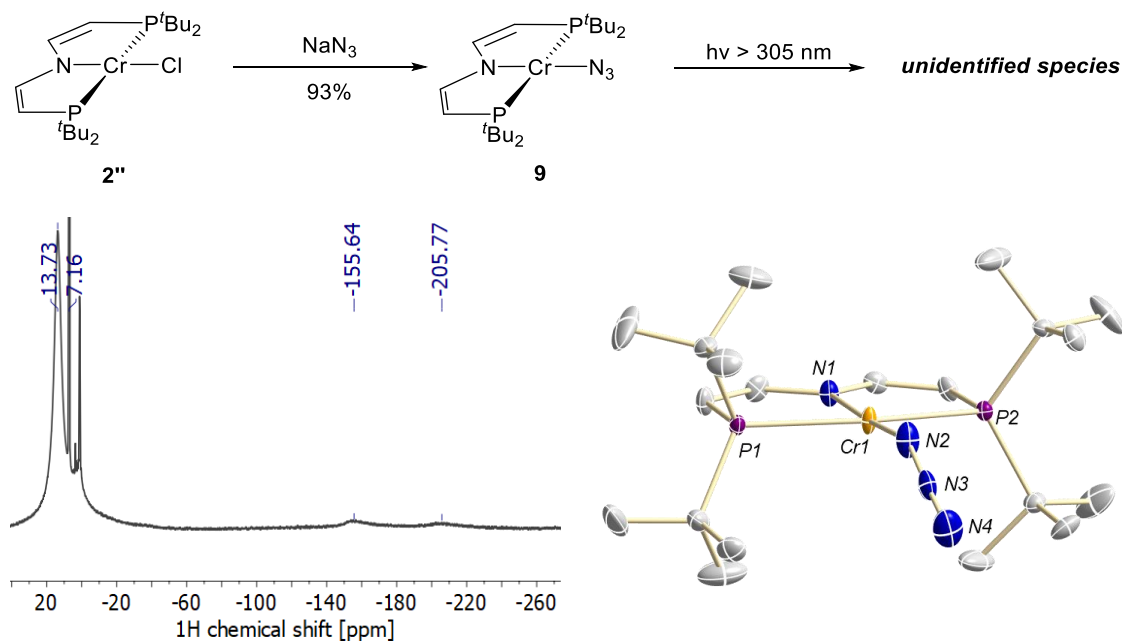


**Scheme 2.8** Attempts of N<sub>2</sub> cleavage starting from dinitrogen complex **3**.

Heating an NMR sample of **3** in refluxing toluene overnight only leads to minor decomposition which demonstrates the striking thermal stability. Therefore, electronic excitation was tested. **3** was exposed to high-energy light sources ( $\lambda \geq 305$  nm (Xe arc), 390 nm (LED)) with different wavelengths, which only gave rise to unreproducible results. Further reduction of **3** using potassium graphite in presence of 18-crown-6 yielded a mixture of unidentified compounds. In analogy to the report of Gambarotta<sup>151</sup>, the reactivity was probed towards different hydride sources such as lithium triethyl borohydride, triethyl silane, sodium borohydride and sodium hydride, but the three former reactants did not lead to any reaction at all and the reaction with sodium hydride ended in decomposition.

The synthetic accessibility of a chromium nitride species within this ligand framework was investigated. In this context, square planar species  $[\text{CrCl}(\text{tBuPNP}^{\text{''}})]$  (**2''**) was reacted with trimethylsilyl azide, without any indication for a reaction which suggests that the Si-Cl bond formation offers a too low driving force. Fortunately, salt metathesis of **2''** with sodium azide in THF overnight at 60 °C was successful and square planar azide complex  $[\text{CrN}_3(\text{tBuPNP}^{\text{''}})]$  (**9**) can be isolated with a decent yield of 93% (Scheme 2.9, top). Note, at this temperature obviously no N<sub>2</sub> release takes place indicated by a near quantitative yield. This complex has a very similar NMR signature in comparison to parent **2''** and shows three broadened signals in the <sup>1</sup>H NMR spectrum at  $\delta = 13.7$ ,  $-155.6$  and  $-205.8$  ppm assigned to the <sup>t</sup>Bu-groups and the ligand backbone, respectively (Scheme 2.9, bottom left).

Single crystals suitable for X-Ray diffraction were grown from a saturated benzene solution (Scheme 2.9, bottom right). In the solid state, the chromium atom is coordinated in a square planar mode by the PNP pincer ligand and azide group in *trans*-position to the amide. The N1-Cr bond is nearly identical to parent **2''** ( $d_{\text{N1-Cr}} = 2.042(3) \text{ \AA}$  vs.  $2.0431(18) \text{ \AA}$  in **2''**). Chromium azide complexes are not unusual in the oxidation state  $\text{Cr}^{\text{III}}$ ,<sup>188–190</sup> whereas only one  $\text{Cr}^{\text{II}}$  azide complex is reported.<sup>191</sup> An intensive, diagnostic group of bands were found in the IR spectrum at 2119, 2102, 2086 and  $2069 \text{ cm}^{-1}$  representing different vibrational modes of the azide moiety. Based on the structural and spectroscopic data, high-spin  $d^4$  electron configuration is suggested being confirmed by an Evans' measurement which revealed a magnetic moment of  $\mu_{\text{eff}} = 4.42 \pm 0.1 \mu_{\text{B}}$ . Upon exposing an NMR sample of **9** to light with the wavelength of  $\lambda > 305 \text{ nm}$  a color change into dark green is observed.  $^1\text{H}$  NMR spectroscopy shows the appearance of paramagnetic signals which neither belong to the starting material nor to dinitrogen complex **3**. Mass spectrometry (LIDFI) detected signal which belongs to two dimerized “[{CrN(<sup>t</sup>BuPNP})<sub>2</sub>]” units, however, this photolysis product could never be isolated or crystallized. Generally, there are several reports of chromium nitride complexes.<sup>190,192–195</sup>



**Scheme 2.9 Top:** Synthesis of azide complex **9** and the reactivity under photolytic conditions. **Bottom left:**  $^1\text{H}$  NMR spectra recorded in  $\text{C}_6\text{D}_6$ . **Bottom Right:** Molecular structure of **9** in the solid state. Hydrogen atoms and solvent molecules are omitted for clarity. Anisotropic displacement parameters are set to 50% probability. Selected bond lengths [ $\text{\AA}$ ] and angles [ $^\circ$ ]: N1-Cr1 2.042(3), Cr(1)-N(2) 1.999(3). N(1)-Cr(1)-N(2) 176.38(15), P(2)-Cr(1)-P(1) 161.45(4), Cr(1)-N(2)-N(3) 146.6(3)  $^\circ$ .

## 2.4 Conclusion

The first part of this chapter explored the reactivity of square planar complex  $[\text{CrCl}(\text{}^{\text{tBu}}\text{PNP})]$  (**2'**) towards dinitrogen. For this purpose, ligand modification was required to the oxidized, divinylamide form to increase stability by reducing  $\pi$ -donation. Reduction under  $\text{N}_2$  atmosphere yielded dinitrogen complex  $[(\mu\text{-N}_2)\{\text{Cr}(\text{}^{\text{tBu}}\text{PNP})\}_2]$  (**3**). Magnetic characterization and vibrational spectroscopy anticipated an  $S = 3$  ground state which was reproduced by DFT calculations. The bonding was rationalized by two  $\text{Cr}^{\text{II}}$  centers that are antiferromagnetically coupled to a doubly reduced  $\text{N}_2^{2-}$  ligand. The M–N–N–M bonding situation is coined by spin polarization justifying the description of separated charges adapting the “three-spin model”. Attempts of  $\text{N}_2$  cleavage remained unsuccessful.

The second part focused on the follow-up reactivity of **3** towards  $\pi$ -accepting ligands. The reaction with carbon monoxide case gave rise to  $[(\mu\text{-CO})\{\text{Cr}(\text{CO})_2(\text{}^{\text{tBu}}\text{PNP})\}\{\text{Cr}(\text{}^{\text{tBu}}\text{PNP})\}]$  (**4**), being a rare example of a mixed-valent isocarbonyl complex. Dinitrogen complex  $[(\mu\text{-N}_2)\{\text{Cr}(\text{CO})_2(\text{}^{\text{tBu}}\text{PNP})\}\{\text{Cr}(\text{}^{\text{tBu}}\text{PNP})\}]$  (**5**) was identified as intermediate, which was characterized by XRD analysis and IR spectroscopy. As derived from DFT calculations, the selectivity in the reaction from **3** to **5** is controlled by the coordination of the first CO ligand that favors binding of the second CO ligand at the same metal center.

The reaction of **3** with  $\text{}^{\text{tBu}}\text{NC}$  has shown to form dinuclear complex  $[(\mu\text{-CN})\{\text{Cr}(\text{CN})(\text{}^{\text{tBu}}\text{PNP})\}\{\text{Cr}(\text{}^{\text{tBu}}\text{PNP})\}]$  (**7**), where both  $\text{Cr}^{\text{II}}$  centers adapt high-spin configuration as determined by SQUID magnetometry. This reaction proceeds via formation of the thermolabile isonitrile complex  $[\text{Cr}(\text{CN-}^{\text{tBu}})(\kappa^2\text{-}^{\text{tBu}}\text{PNP})]$  (**8**).

### 3 Results and Discussion II

This chapter can be divided into three main subsections covering rhenium-mediated dinitrogen activation, rhenium-mediated nitride transfer and evaluation of the electronic structure of N<sub>2</sub> bridged dirhenium complexes.

Within the first topic, the effect of halide variation is investigated on the electrochemical properties of complexes [Re<sup>III</sup>X<sub>3</sub>(<sup>Pr</sup>PN<sup>H</sup>P)] (X = Cl, Br, I) (**10**<sup>Cl/Br/I</sup>) and on the photochemical properties of the respective dinitrogen complexes [(μ-N<sub>2</sub>){ReX<sub>2</sub>(<sup>Pr</sup>PN<sup>H</sup>P)}<sub>2</sub>] (X = Cl, Br, I) **11**<sup>Cl/Br/I</sup> in context of N<sub>2</sub> cleavage.

The second topic investigates the follow-up reactivity of nitride complex [Re<sup>V</sup>Br<sub>2</sub>N(<sup>Pr</sup>PN<sup>H</sup>P)] (**13**<sup>Br</sup>) with the intention to enforce nitride transfer. Particularly *N*-benzoylation is examined and how benzamide production is mediated by the corresponding *N*-benzoyl imido complex [ReBr<sub>2</sub>{N(CO)C<sub>6</sub>H<sub>5</sub>}(<sup>Pr</sup>PN<sup>H</sup>P)]Br (**15**<sup>Br</sup>) via PCET.

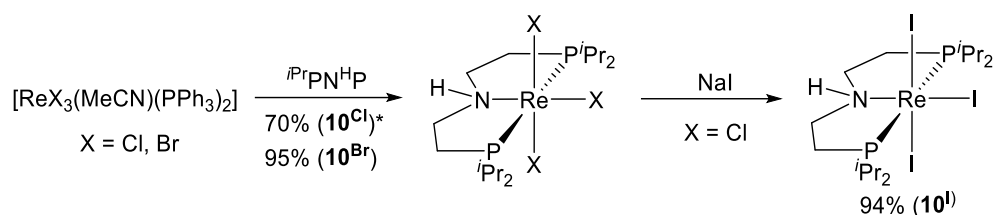
Finally, the oxidation behavior of dinitrogen complex [(μ-N<sub>2</sub>){ReBr<sub>2</sub>(<sup>Pr</sup>PN<sup>H</sup>P)}<sub>2</sub>] is explored to gain insight into the electronic structure. The synthetic access to the redox isomers [(μ-N<sub>2</sub>){ReBr<sub>2</sub>(<sup>Pr</sup>PN<sup>H</sup>P)}<sub>2</sub>]<sup>+ / 2+</sup> is described and their structural, spectroscopic and magnetic properties are comprehensively discussed.

#### 3.1 Electro- and photosynthesis of octahedral Re<sup>V</sup> nitride complexes

##### 3.1.1 Synthesis of [ReX<sub>3</sub>(<sup>Pr</sup>PN<sup>H</sup>P)] (X = Cl, Br, I) and electrochemical evaluation

The complexes [ReX<sub>3</sub>(MeCN)(PPh<sub>3</sub>)<sub>2</sub>] (X = Cl, Br) can be reacted with the pincer ligand HN(CH<sub>2</sub>CH<sub>2</sub>PPr<sub>2</sub>)<sub>2</sub> (<sup>Pr</sup>PN<sup>H</sup>P) and the corresponding rhenium complexes [ReCl<sub>3</sub>(<sup>Pr</sup>PN<sup>H</sup>P)] (**10**<sup>Cl</sup>)<sup>43</sup> and [ReBr<sub>3</sub>(<sup>Pr</sup>PN<sup>H</sup>P)] (**10**<sup>Br</sup>)<sup>b</sup> were isolated in 70% and 95% yield as beige and yellow solids, respectively (Scheme 3.1). Salt metathesis of **10**<sup>Cl</sup> with an excess of sodium iodide obtains [ReI<sub>3</sub>(<sup>Pr</sup>PN<sup>H</sup>P)] (**10**<sup>I</sup>) in excellent yields of 94% as a red solid (Scheme 3.1). These complexes are resistant towards water and oxygen, however, the syntheses must be performed under anhydrous conditions and under exclusion of air.

<sup>b</sup> Characterization of [ReBr<sub>3</sub>(<sup>Pr</sup>PN<sup>H</sup>P)] (**10**<sup>Br</sup>) by NMR and IR spectroscopy and mass spectrometry was carried out by M. Sc. Sessa Kisan (AK Schneider, Georg-August-Universität Göttingen). Characterization by X-Ray diffractometry was performed by Niels Paul (“Abteilungspraktikum” under supervision of Maximilian Fritz). Design of a synthetic route to analytical purity (elemental analysis) was designed by Maximilian Fritz.



**Scheme 3.1** Synthesis of complexes  $\mathbf{10}^{\text{Cl}}$ ,  $\mathbf{10}^{\text{Br}}$  and  $\mathbf{10}^{\text{I}}$ . \*Corresponds to reference<sup>43</sup>

All complexes within this series show strongly shifted resonances in the  $^1\text{H}$  NMR spectrum including  $J$ -coupling in the range of  $-15$  to  $155$  ppm (Figure 3.1). Four isopropyl groups were observed indicating  $C_s$ -symmetry in solution, consistent with the appearance as singlets in the  $^{31}\text{P}\{^1\text{H}\}$  NMR spectrum at large negative shifts ( $\delta = -1525.5$  ( $\mathbf{10}^{\text{Cl}}$ )<sup>43</sup>,  $-1488.0$  ( $\mathbf{10}^{\text{Br}}$ ),  $-1477.3$  ( $\mathbf{10}^{\text{I}}$ ) ppm). These strongly shifted, but well-resolved resonances are indicative for strong contributions of temperature independent paramagnetism (TIP), as recently discussed.<sup>43,155</sup>

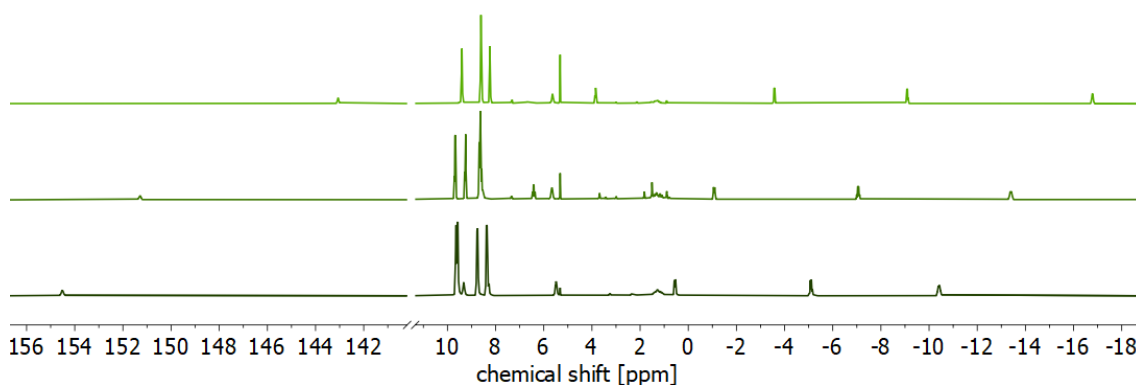


**Figure 3.1**  $^1\text{H}$  NMR spectra of  $\mathbf{10}^{\text{I}}$  (top),  $\mathbf{10}^{\text{Br}}$  (middle) and  $\mathbf{10}^{\text{Cl}}$  (bottom).

The NMR paramagnetic shift is built up by two contributions, the Fermi contact shift (through metal ligand bonds) and the pseudo contact shift (through space magnetic dipolar interaction). These terms are composed of several factors including the electron-nuclear hyperfine coupling constant, the magnetic susceptibility, the  $g$ -value, the Zeeman anisotropy, relaxation and tumbling correlation times.<sup>196,197</sup> Given this complexity, it is not possible to explain the observed trends of the  $^1\text{H}$  and  $^{31}\text{P}$  NMR shifts simply by “deshielding” effects.

Especially octahedral  $\text{Re}^{\text{III}}$  complexes are strongly affected by spin-orbit coupling ( $\zeta$  ( $\text{Mn}^{\text{III}}$ )  $\sim 355$   $\text{cm}^{-1}$ ;  $\zeta$  ( $\text{Tc}^{\text{III}}$ )  $\sim 990$   $\text{cm}^{-1}$ ;  $\zeta$  ( $\text{Re}^{\text{III}}$ )  $\sim 2500$   $\text{cm}^{-1}$ ).<sup>198,199</sup> They formally possess a triplet ground state which is split by spin-orbit coupling. The magnetic susceptibility found in these complexes is exclusively caused by second order Zeeman effect which can be rationalized as mixing of an energetically isolated  $J = 0$  ground state with  $J \neq 0$  excited states.<sup>198,200–206</sup>

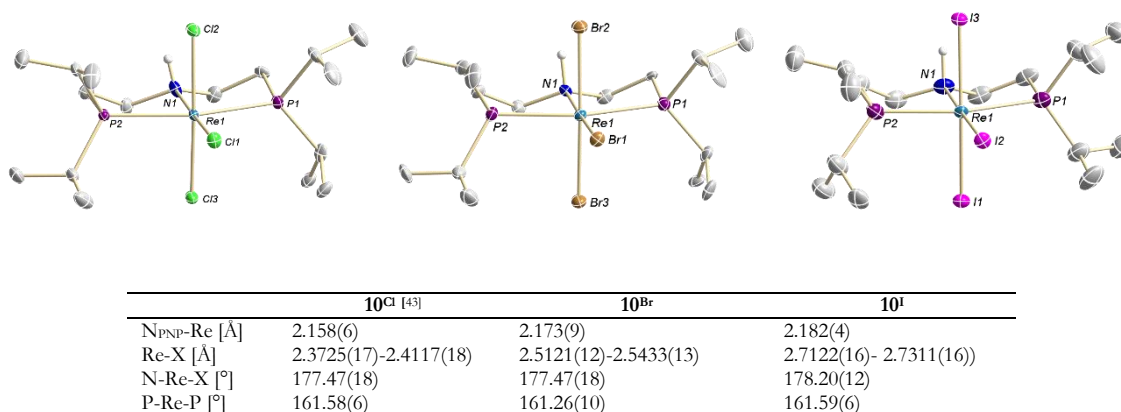


**Figure 3.2** Molecular structures of **10<sup>Cl</sup>** (left), **10<sup>Br</sup>** (middle) and **10<sup>I</sup>** (right), in the solid state. Hydrogen atoms (except N-H), disordered moieties and solvent molecules are omitted for clarity. Anisotropic displacement parameters are set to 50% probability. Selected bond lengths [Å] and angles [°] are summarized in the table (**right**) including the bond metrics of **10<sup>Cl</sup>**.<sup>43</sup>

Complexes **10<sup>Br</sup>** and **10<sup>I</sup>** were obtained as single crystals suitable for X-Ray diffraction and the obtained molecule structures are shown in (Figure 3.2). The structural motif is retained among the [ReX<sub>3</sub>(<sup>dp</sup>PN<sup>HP</sup>)] (**10**) triad. The rhenium atom is nearly ideally octahedrally coordinated by the pincer ligand and the three halide ligands. The pincer bite angle is almost identical about ~161°. The bond distance of the donating amine function to the rhenium center slightly increases going to the heavier halides most likely caused by decreasing Lewis acidity. The rhenium-halide bond lengths significantly rise going from chloride to iodide due to increasing ionic radii.<sup>207,208</sup>

After structural characterization, the electrochemical examination was targeted for **10<sup>Br</sup>** and **10<sup>I</sup>** by cyclic voltammetry at varied scan rate and compared to **10<sup>Cl</sup>**, that was recently published.<sup>43</sup> Qualitatively, the CV signature of these complexes is very similar: All three complexes exhibit in the measured range one oxidative and one reductive redox event, which can be assigned to the Re<sup>IV/III</sup> and to the Re<sup>III/II</sup> couple, respectively.<sup>43</sup>

The oxidative Re<sup>IV/III</sup> couple ( $E_{1/2}$  (**10<sup>Cl</sup>**) = -0.24 V,<sup>43</sup>  $E_{1/2}$  (**10<sup>Br</sup>**) = -0.22 V,  $E_{1/2}$  (**10<sup>I</sup>**) = -0.14 V) is irrespective of the halide ligands reversible at varied scan rate, as judged by peak current ratio analysis which is close to unity (Figure 3.3 and reference<sup>209</sup>). Reversibility in this case speaks against a chemical follow-up step upon oxidation. Indeed, chemical oxidation to the respective cationic Re<sup>IV</sup> complex does not lead to a structural rearrangement.<sup>210</sup> In the reductive regime, the redox events at  $E_{1/2}$  (**10<sup>Cl</sup>**) = -1.84 V,<sup>43</sup>  $E_{1/2}$  (**10<sup>Br</sup>**) = -1.66 V and  $E_{p,c}$  (**10<sup>I</sup>**) = -1.50 V belong to the Re<sup>III/II</sup> couple, that is relevant to N<sub>2</sub> fixation.<sup>1,2,41,42</sup> Comparing these events, there is a loss of reversibility observed going from chloride to iodide ( $i_{p,c}/i_{p,a}$  ( $v = 1000$  mV/s) = 1.20 (**10<sup>Cl</sup>**), 1.46 (**10<sup>Br</sup>**), 2.64 (**10<sup>I</sup>**)). The scan rate dependent peak current ratios of the Re<sup>III/II</sup> couple allowed for the determination of the rate constants for halide loss upon reduction ( $k_{diss} = 0.05$  s<sup>-1</sup> (**10<sup>Cl</sup>**),  $k_{diss} = 0.32$  s<sup>-1</sup> (**10<sup>Br</sup>**) and  $k_{diss} = 2.46$  s<sup>-1</sup> (**10<sup>I</sup>**)) differing in orders of magnitude. This is consistent with an EC type

mechanism where halides are dissociated upon reduction facilitated by heavier halides that are better leaving groups.

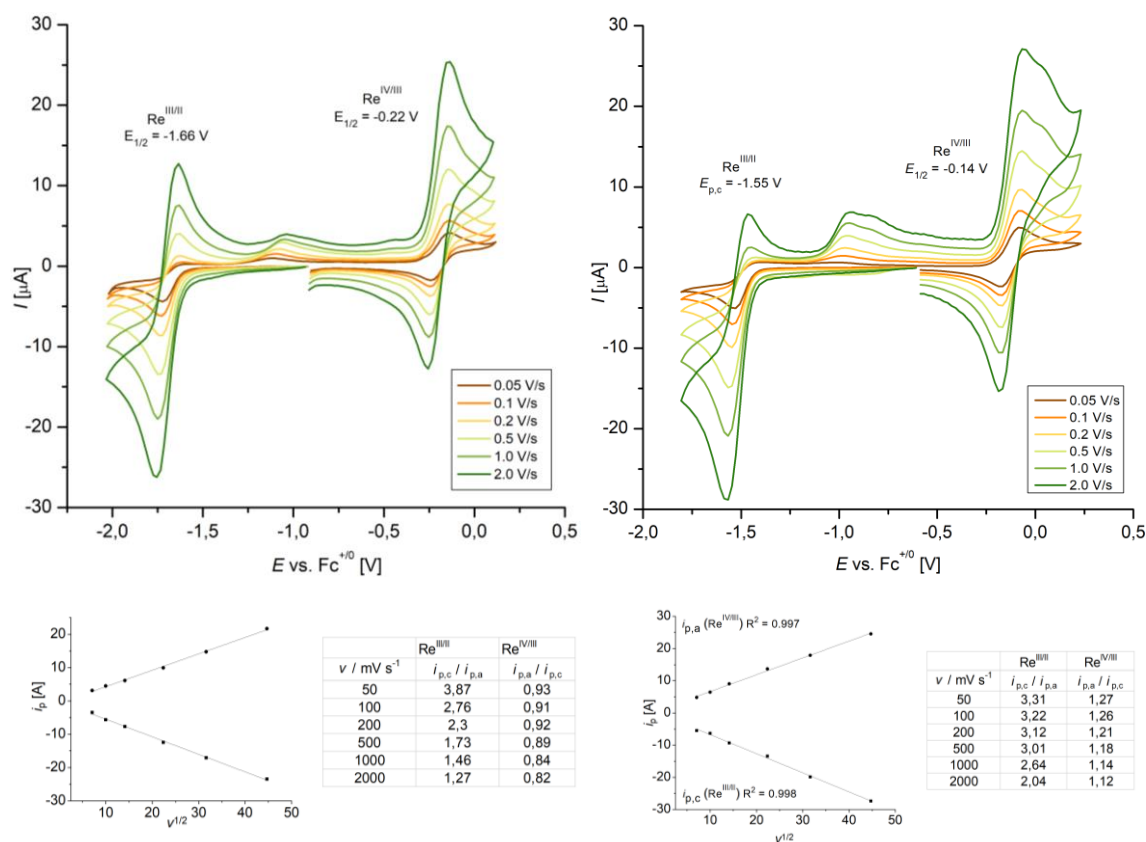


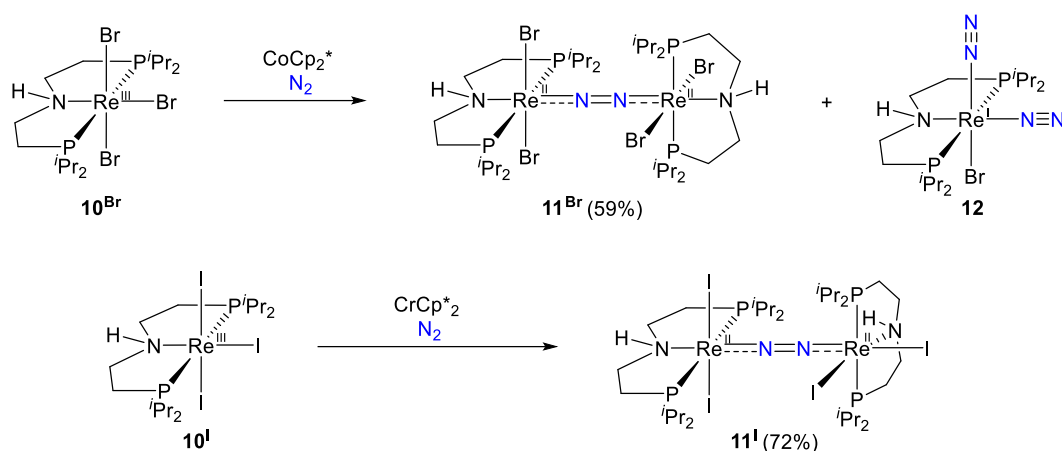
**Figure 3.3** Electrochemical characterization by cyclic voltammetry of  $[\text{ReBr}_3(\text{PrPN}^{\text{H}}\text{P})]$  **10<sup>Br</sup>** (left) and  $[\text{ReI}_3(\text{PrPN}^{\text{H}}\text{P})]$  **10<sup>I</sup>** (right) at different scan rates (1.0 mM; electrolyte: 0.1 M  $\text{N}^{\text{t}}\text{Bu}_4\text{PF}_6$  in THF), including plot of  $i_p$  as a function of  $v^{1/2}$  and peak current ratio analysis ( $i_{\text{pc}}/i_{\text{pa}}$ ).

The Lever parameter is an electrochemical parameter that can be used to explain trends in redox potential, for example of transition metal complexes having different halide ligands.<sup>211,212</sup> Within this model, every halide ligand has its individual parameter ( $E_{\text{L}}(\text{Cl}) = -0.24$  V,  $E_{\text{L}}(\text{Br}) = -0.22$  V,  $E_{\text{L}}(\text{I}) = -0.24$  V) and the ligand contributions are additive within a compound. Applying these values to the trishalide complexes **10<sup>Cl</sup>**, **10<sup>Br</sup>** and **10<sup>I</sup>**, potential shifts are predicted to be  $\Delta E = 66$  mV (Br) and 72 mV (Cl, I) which is much lower than the observed potential shift ( $\Delta E(\text{Re}^{\text{III/II}}) = 340$  mV). Importantly, the applicability requires full reversibility as a chemical follow-up step induces potential shifts. In contrast, the potential shift of the  $\text{Re}^{\text{IV/III}}$  ( $\Delta E(\text{Re}^{\text{IV/III}}) = 100$  mV) lies in that region.

These potential shifts might be explained by different donation capacities of the halide ligands. The fluoride anion is weakly polarizable and thus a hard base, iodide in contrast is easily polarized and as a result a soft base, which coincides with decreasing  $\pi$ -donor strength going from fluoride to iodide.<sup>208,213–219</sup> This trend supports the CV data, because within the series  $[\text{ReX}_3(\text{PrPN}^{\text{H}}\text{P})]$  (**10**), the chloride representative **10<sup>Cl</sup>** has the most negative reduction potential as it is suggested to be most electron-rich.

### 3.1.2 Synthesis and characterization of $[(\mu\text{-N}_2)\{\text{ReX}_2(\text{}^t\text{PrPN}^{\text{H}}\text{P})\}_2]$ ( $\text{X} = \text{Cl}, \text{Br}, \text{I}$ )

According to the CV data discussed in the previous chapter the reduction potentials of  $\mathbf{10}^{\text{Br}}$  and  $\mathbf{10}^{\text{I}}$  are at  $E_{1/2} = -1.66$  V and  $E_{\text{p,c}} = -1.50$  V, allowing for the usage of decamethyl cobaltocene ( $E^0 = -1.94$  V)<sup>220</sup> and decamethyl chromocene ( $E^0 = -1.46$  V)<sup>93,220</sup> as chemical reductant, respectively. The reaction of  $\mathbf{10}^{\text{Br}}$  with decamethyl cobaltocene (1.3 eq.) in THF under  $\text{N}_2$  atmosphere at  $-40$  °C yields dinitrogen complex *trans,trans*- $[(\mu\text{-N}_2)\{\text{ReBr}_2(\text{}^t\text{PrPN}^{\text{H}}\text{P})\}_2]$  ( $\mathbf{11}^{\text{Br}}$ )<sup>c</sup> with a yield of 59% as a dark blue powder (Scheme 3.2, top reaction). Washing with acetonitrile at  $-40$  °C removes all residual salts and  $\mathbf{11}^{\text{Br}}$  can be isolated in analytical purity. From the acetonitrile washing solution the side product  $[\text{ReBr}(\text{N}_2)_2(\text{}^t\text{PrPN}^{\text{H}}\text{P})]$  ( $\mathbf{12}$ ) was crystallized, which will be discussed at a later point in this chapter.



**Scheme 3.2** Dinitrogen activation of  $[\text{ReBr}_3(\text{}^t\text{PrPN}^{\text{H}}\text{P})]$  ( $\mathbf{10}^{\text{Br}}$ ) and  $[\text{ReI}_3(\text{}^t\text{PrPN}^{\text{H}}\text{P})]$  ( $\mathbf{10}^{\text{I}}$ ) under reductive conditions.

The  $\text{N}_2$  reduction step proceeds analogous for the iodide system: reacting  $\mathbf{10}^{\text{I}}$  with decamethyl chromocene (1.3 eq.) in THF at  $-78$  °C leads to a color change into deep green. Removal of the solvent, washing with acetonitrile and subsequent crystallization yields *cis,trans*- $[(\mu\text{-N}_2)\{\text{ReI}_2(\text{}^t\text{PrPN}^{\text{H}}\text{P})\}_2]$  ( $\mathbf{11}^{\text{I}}$ ) as a dark green microcrystalline solid with an isolated yield of 72%. The molecular structures of these dinitrogen complexes in the solid state are shown in Figure 3.4 and compared to the chloride congener.

<sup>c</sup> First attempts of synthesis, characterization and photolysis are documented in the “Abteilungsbericht” from Niels Paul (under supervision of Maximilian Fritz) or in the Bachelor thesis of Paul Julius Weiß (under supervision of Maximilian Fritz).



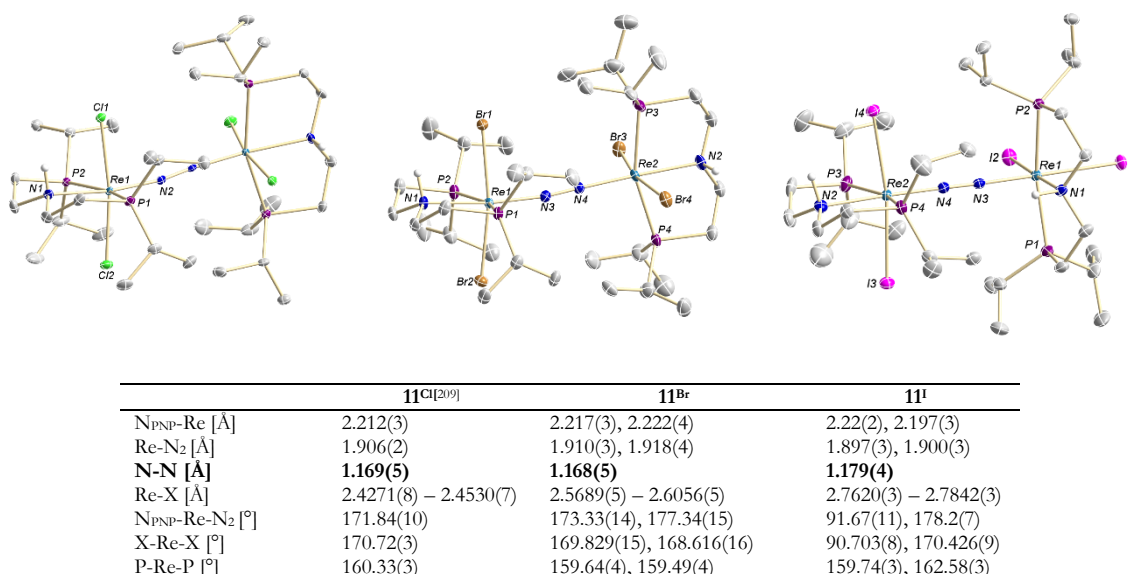


**Figure 3.4** Molecular structures in the solid state and corresponding bond lengths and angles [Å]/[°] of **11<sup>Cl</sup>**<sup>[209]</sup> (left), **11<sup>Br</sup>** (middle), **11<sup>I</sup>** (right). Hydrogen atoms (except N-H), disordered moieties and solvent molecules are omitted for clarity.

The structural motif is retained for the chloride and bromide representatives. The dinitrogen complexes consist of two octahedral coordinated rhenium units, where the pincer ligands are perpendicularly arranged with respect to each other. The bond metrics are all consistent along the N-Re-N≡N-Re-N axis including the N-N bond lengths being nearly identical ( $d_{\text{N-N}} = 1.169(5)$  Å (**11<sup>Cl</sup>**),  $1.168(5)$  Å (**11<sup>Br</sup>**)).

The iodide representative has a varied molecular architecture. As the XRD analysis revealed, it is an asymmetric dirhenium complex with two  $\{\text{ReI}_2(\text{PN}^{\text{H}}\text{P})\}$  cores, binding the N<sub>2</sub> ligand in *trans*- and *cis*-configuration indicated by the N<sub>PNP</sub>-Re-N<sub>2</sub> angles of  $178.2(7)^\circ$  and  $91.67(11)^\circ$ . The asymmetric coordination mode causes minor differences in bond lengths and angles between both metal cores, for example the N<sub>PNP</sub>-Re bond lengths are only slightly divergent ( $d_{\text{N-Re}} = 2.22(2)$  Å vs.  $2.197(3)$  Å). The Re-N<sub>2</sub> bond length and the pincer biting angle are consistent in all three complexes within the halide series. In accordance to the chloride and bromide representative, the N<sub>2</sub> ligand shows a moderate degree of activation ( $d_{\text{N-N}} = 1.179(4)$  Å). The Re-X bond lengths steadily rise from chloride to iodide ( $d_{\text{Re-X}} = \sim 2.43$  Å (**Cl**),  $\sim 2.58$  Å (**Br**),  $\sim 2.77$  Å (**I**)) caused by increasing ionic radii.<sup>207,208</sup>

The  $^1\text{H}\{^{31}\text{P}\}$  NMR spectrum of **11<sup>Br</sup>** shows sharp and well-resolved resonances in a range between  $\delta = -14$  to  $90$  ppm (Figure 3.5, top). The low-field shifted resonance at  $89.48$  ppm is assigned as N-H proton, corroborated by a characteristic band at  $3148$   $\text{cm}^{-1}$  in the IR spectrum. In the  $^{31}\text{P}\{^1\text{H}\}$  NMR spectrum, two doublets are detected exhibiting a roof effect at  $\delta = -381.4, -395.9$  ppm, which in combination with the  $^1\text{H}\{^{31}\text{P}\}$  NMR signature reveal retained C<sub>2</sub>-symmetry in solution (Figure 3.5). The usage of  $^{15}\text{N}_2$  gas during synthesis gives rise to a singlet at  $\delta = -1071.4$  ppm in the  $^{15}\text{N}\{^1\text{H}\}$  NMR spectrum, confirming the uptake of atmospheric N<sub>2</sub> during reduction (Figure 3.5, bottom right). The occurrence of a singlet coincides with a bridging N<sub>2</sub> ligand rather than a terminal N<sub>2</sub> ligand, which would give rise

to two doublets by  $^1J_{N-N}$  coupling.<sup>134</sup> The NMR spectroscopic data are nearly identical to **11**<sup>Cl</sup>.<sup>209</sup> Analogous to the precursor complexes  $[\text{ReX}_3(^{209}\text{PN}^{\text{H}}\text{P})]$  (**10**), significant contributions of temperature independent paramagnetism are suggested. SQUID magnetometry of **11**<sup>Br</sup> revealed a straight, linear increase of the magnetic susceptibility and the data could be indeed fitted with a large TIP-value ( $X_M = 1664.7 \cdot 10^{-6} \text{ cm}^3 \text{ mol}^{-1}$ ). A detailed evaluation of the electronic structure follows in chapter 3.3.

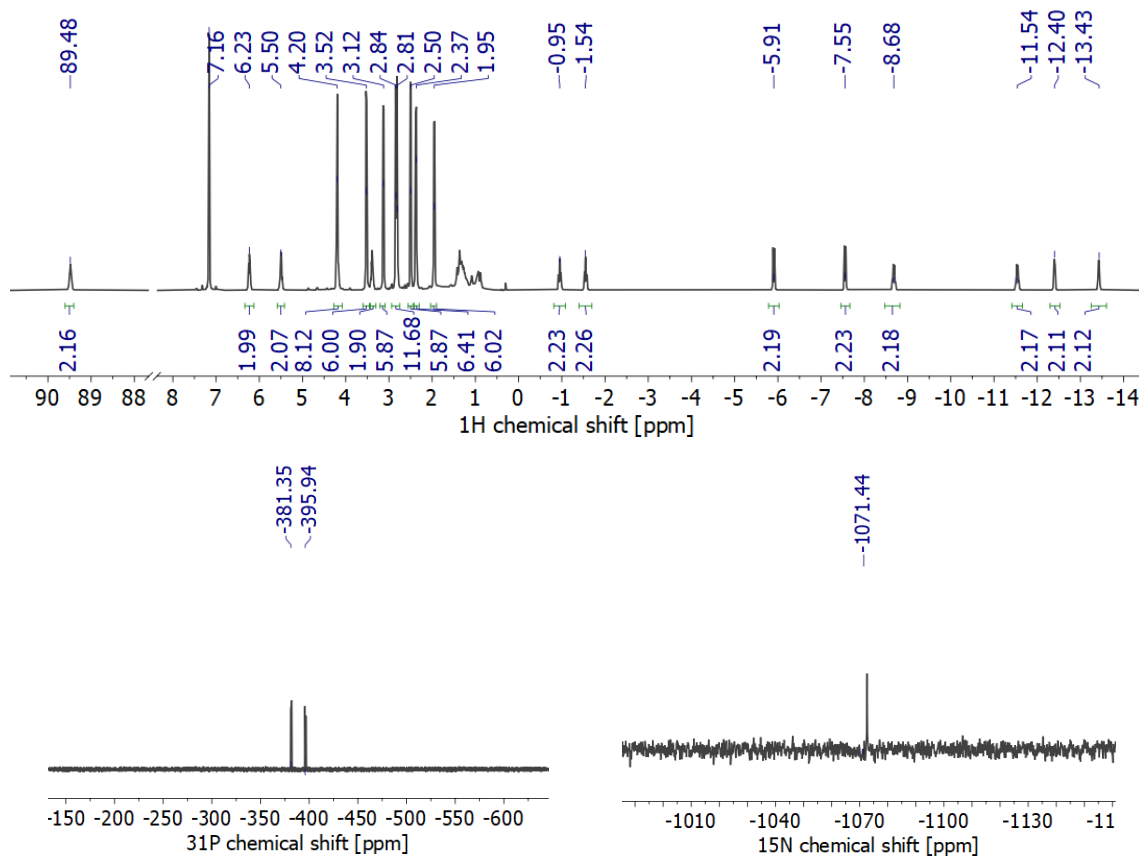


**Figure 3.5** Characterization of **11**<sup>Br</sup> by NMR spectroscopy ( $\text{C}_6\text{D}_6$  at RT). **Top:**  $^1\text{H}\{^{31}\text{P}\}$ ; **Bottom left:**  $^{31}\text{P}\{^1\text{H}\}$ ; **Bottom right:**  $^{15}\text{N}\{^1\text{H}\}$ .

The *cis-trans* coordination in **11**<sup>I</sup> generates  $C_1$ -symmetry giving rise to two sets of doublets with different line widths ( $\delta = -361.3 \text{ ppm}$  ( $w_{1/2} = 22.2 \text{ Hz}$ ),  $-377.5 \text{ ppm}$  ( $w_{1/2} = 17.1 \text{ Hz}$ ),  $-758.4 \text{ ppm}$  ( $w_{1/2} = 44.2 \text{ Hz}$ ),  $-770.3 \text{ ppm}$  ( $w_{1/2} = 53.5 \text{ Hz}$ )) in the  $^{31}\text{P}\{^1\text{H}\}$  NMR spectrum (Figure 3.6, left) including typical *trans*- $^2J_{\text{P-P}}$  coupling (204.5 Hz, 235.5 Hz, respectively). The corresponding  $^{31}\text{P}$  COSY NMR spectrum shows cross peaks for the low-field shifted set of doublets indicating scalar coupling (Figure 3.6, right). The absence of a cross peak for the high-field shifted signal set is attributed to increased broadening of the signals. The asymmetric coordination presumably leads to different electronic structures of both metal centers to account for the huge chemical shift dispersion and the different shaped set of signals which is related to a report of Miller.<sup>44</sup>

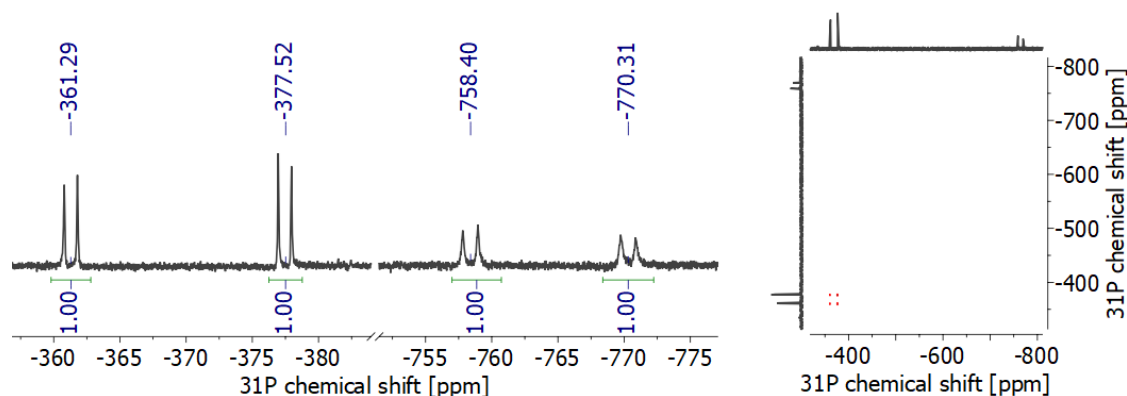


**Figure 3.6**  $^{31}\text{P}\{^1\text{H}\}$  NMR spectroscopy of complex **11I**. **Left:**  $^{31}\text{P}\{^1\text{H}\}$  NMR spectrum. **Right:**  $^{31}\text{P}$  COSY NMR spectrum.

There are 42 resonances in the  $^1\text{H}$  NMR spectrum in the range between  $\delta = -12.15$  to  $143.27$  ppm. The N-H protons are strongly downfield shifted ( $\delta = 143.27$ ,  $88.86$  ppm) supported by a weak band at  $\nu = 3140$   $\text{cm}^{-1}$  in the IR spectrum. Selective  $^1\text{H}\{^{31}\text{P}\}$  decoupling experiments provide insight into the molecular connectivity (Figure 3.7 top: decoupled at  $\delta_{^{31}\text{P}} = -765$  ppm, bottom: decoupled at  $\delta_{^{31}\text{P}} = -377$  ppm). In each spectrum eight methyl groups are affected upon decoupling, splitting into doublets by the  $^3J_{\text{HH}}$  coupling to the adjacent  $\text{P}(\text{CH}(\text{CH}_3)_2)_2$  protons (marked as cycles).

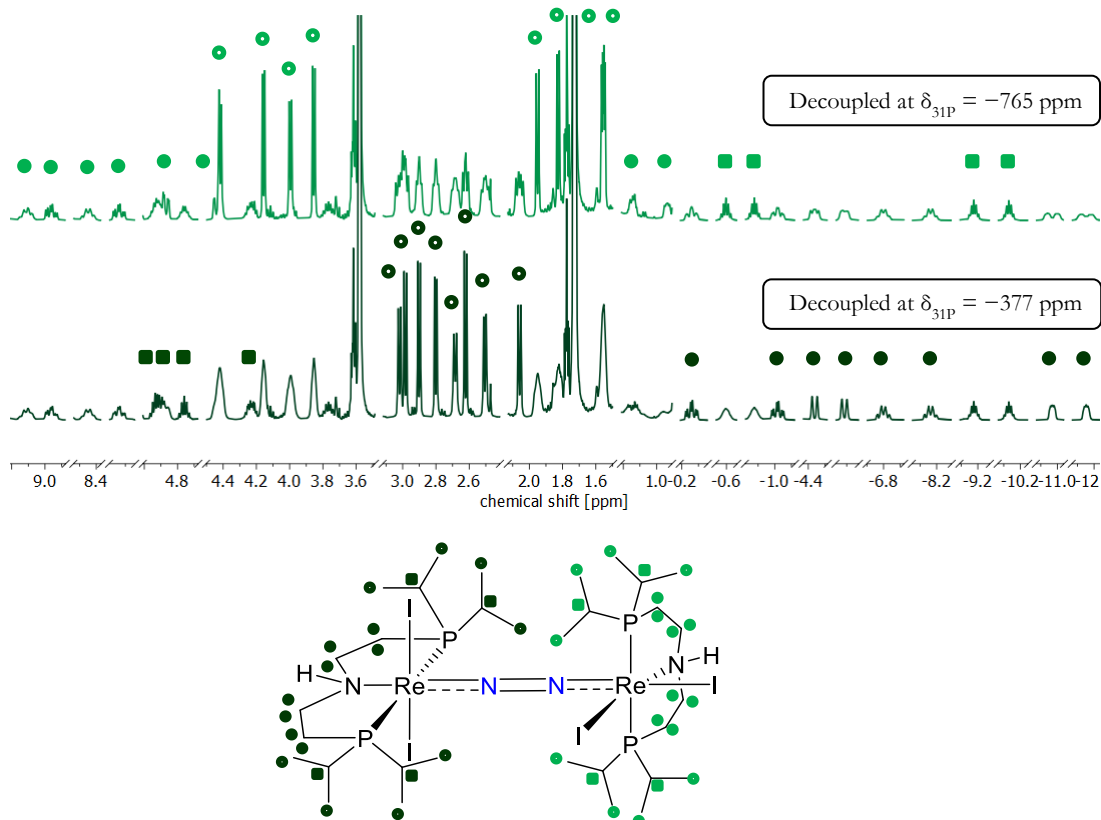


**Figure 3.7**  $^1\text{H}\{^{31}\text{P}\}$  NMR spectra of complex **11I**. **Top spectrum:** decoupled at  $\delta_{^{31}\text{P}} = -765$  ppm; **Bottom spectrum:** decoupled at  $\delta_{^{31}\text{P}} = -377$  ppm; The N-H diagnostic region ( $\delta = 143.27$ ,  $88.86$  ppm) is not displayed for reasons of clarity.

The selective decoupling experiments are consistent with the  $^1\text{H}/^{31}\text{P}$  HSQC NMR spectra (Figure 3.8) where the observed cross peaks coincide with the  $^1\text{H}\{^{31}\text{P}\}$  NMR shift sensitive decoupling pattern. Applying  $^1\text{H}$  COSY,  $^1\text{H}/^{13}\text{C}$  HSQC and  $^1\text{H}/^{13}\text{C}$  HMBC-NMR spectroscopy techniques, the precise assignment of all signals was possible as depicted with corresponding symbols in Figure 3.7. The quality of the  $^{13}\text{C}$  NMR spectrum was hampered by the low solubility of the compound. Several signals remain in the ground noise, however, full assignment was accomplished by  $^1\text{H}/^{13}\text{C}$  HSQC NMR spectroscopy via the respective cross signals. The low solubility is also assumed to be the reason for the absence of signals in the  $^{15}\text{N}\{^1\text{H}\}$  NMR spectrum, where two doublets are expected for the bridging  $\text{N}_2$  ligand due to the given symmetry.

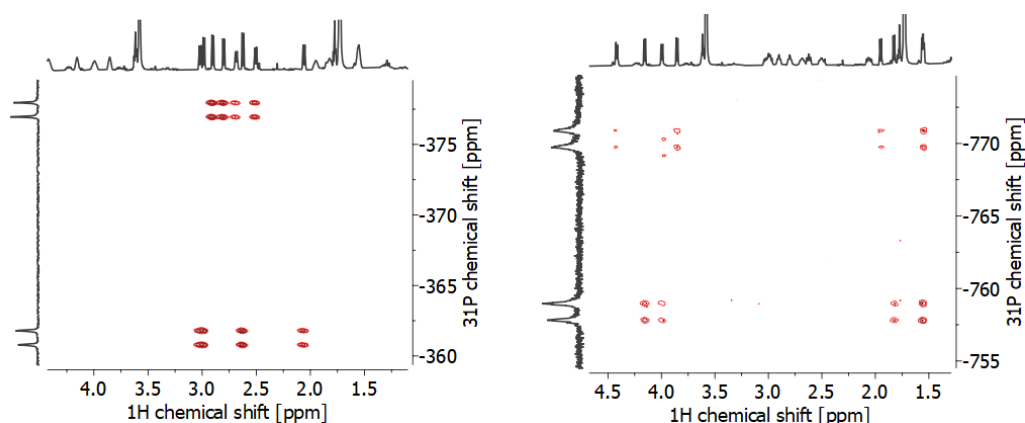


**Figure 3.8**  $^1\text{H}/^{31}\text{P}$  HSQC spectra of  $\mathbf{11}^{\text{I}}$ . **Left:**  $\delta_{\text{offset}(^{31}\text{P})} = -367$  ppm; **Right:**  $\delta_{\text{offset}(^{31}\text{P})} = -765$  ppm.

Reduction of  $\mathbf{10}^{\text{I}}$  under  $\text{N}_2$  atmosphere leads under unclarified condition to the formation of isomers, as illustrated in the  $^{31}\text{P}\{^1\text{H}\}$  NMR spectrum in Figure 3.9 showing the reaction solution. There are seven sets of doublets, estimated by rough integration under consideration of the roof effect. The matching resonances are marked with colored cycles. Based on the integrals, the discussed *cis,trans* isomer  $\mathbf{11}^{\text{I}}$  is the most dominant species (blue dots). There are presumably two additional  $C_1$ -symmetric isomers present (red and orange dots), which are suggested to be diastereomers of  $\mathbf{11}^{\text{I}}$ , as judged from their chemical shift. The different orientation of the N-H proton(s) could be a reasonable explanation.

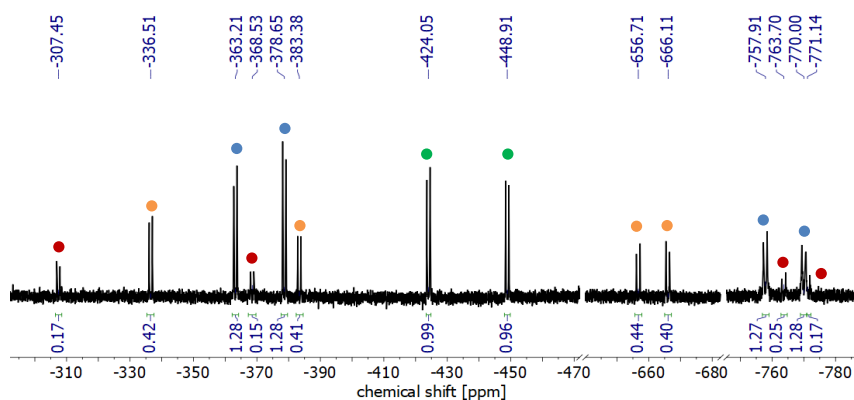


**Figure 3.9**  $^{31}\text{P}\{^1\text{H}\}$  NMR spectrum of the reaction mixture of the reduction of  $\mathbf{10}^{\text{I}}$  under  $\text{N}_2$  atmosphere showing the existence of several species.

The set of doublets with a chemical shift of  $\delta = -424.1, -448.9$  ppm (green dots) presumably belongs to one complex molecule and hint towards a *trans-trans* isomer with a  $C_2$ -symmetry in solution, reminiscent to **11<sup>Cl</sup>** and **11<sup>Br</sup>**. These isomers are very similar in their solubility properties precluding their isolation by polarity. Isomerization and thermal interconversion of N<sub>2</sub> bridged dinitrogen complexes was recently reported by Miller.<sup>44</sup>

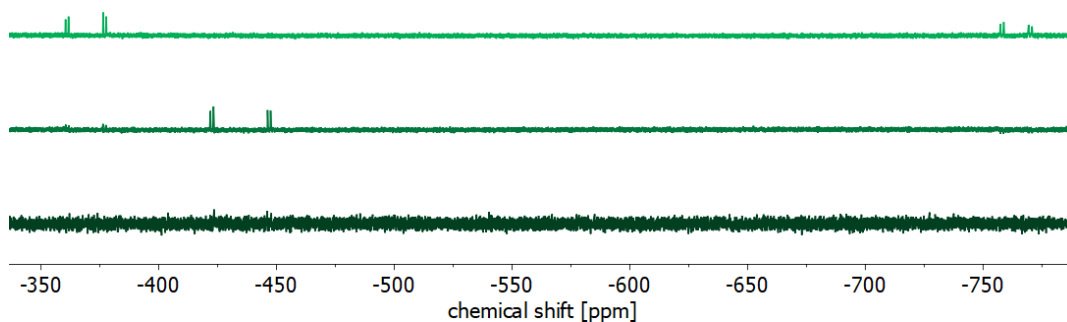


**Figure 3.10** Top:  $^{31}\text{P}\{^1\text{H}\}$  NMR spectrum of isolated **11**; middle: Heating at 70 °C overnight; bottom: Heating two days at 70 °C.

Heating a sample of *cis-trans* **11<sup>I</sup>** at 70 °C overnight in THF leads to an interconversion into the isomer, which has been marked with green dots in Figure 3.9, assigned as *trans-trans* isomer (Figure 3.10). The reaction mixture anticipates a clean conversion, however, further heating for one day obviously leads to decomposition, as all signals in the  $^{31}\text{P}\{^1\text{H}\}$  NMR spectrum vanish.

The series of dinitrogen complexes **11<sup>Cl</sup>**, **11<sup>Br</sup>** and **11<sup>I</sup>** was investigated by rRaman spectroscopy to evaluate the degree of activation of the N<sub>2</sub> ligand. In analogy to the bond lengths derived from XRD analysis ( $d_{\text{N-N}} = 1.169(5)$  Å (**11<sup>Cl</sup>**), 1.168(5) Å (**11<sup>Br</sup>**), 1.179(4) Å (**11<sup>I</sup>**)), the N-N stretching vibration observed in the resonance Raman spectra are all in the same range (Figure 3.11: 1733 cm<sup>-1</sup> (**11<sup>Cl</sup>**), 1734 cm<sup>-1</sup> (**11<sup>Br</sup>**), 1716 cm<sup>-1</sup> (**11<sup>I</sup>**)). All these bands are isotope sensitive and shift upon <sup>15</sup>N<sub>2</sub> labelling about ~60 cm<sup>-1</sup> to lower energy (1675 cm<sup>-1</sup> (**11<sup>Cl</sup>**), 1673 cm<sup>-1</sup> (**11<sup>Br</sup>**), 1658 cm<sup>-1</sup> (**11<sup>I</sup>**)), which is in excellent agreement with the harmonic oscillator approximation. These shifts are matching  $[(\mu\text{-N}_2)\{\text{ReCl}_2(\text{trPONOP})\}_2]$  **XVI** (1766 cm<sup>-1</sup>) reported by Miller (introduction subchapter 1.1.5).<sup>44</sup>

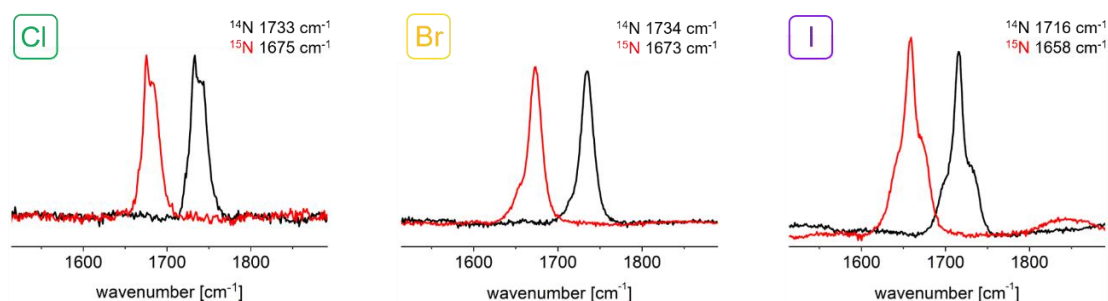


**Figure 3.11** rRaman spectra ( $\lambda = 633$  nm) of **11<sup>Cl</sup>** (left), **11<sup>Br</sup>** (middle) and **11<sup>I</sup>** (right) in THF-*d*<sub>8</sub> solution at room temperature.

<sup>d</sup> Experimental rRaman data adapted from Dr. Florian Wätjen (nee Schendzielorz).

The rRaman shifts of the  $\mathbf{11}^{\text{Cl}}$  and  $\mathbf{11}^{\text{Br}}$  dinitrogen complexes are almost identical, diverging only by 1-2 wavenumbers suggesting that halide exchange has no significant effect on the degree of backbonding into the  $\text{N}_2$   $\pi^*$ -orbital. Thus, the slight shift to lower energy in the iodide case presumably is a consequence of a different coordination geometry. Due to  $C_1$ -symmetry and unlike the chloride and bromide congener, the N-N stretching is IR active. In the solid state, the N-N stretching vibration was located as a weak band at  $1712\text{ cm}^{-1}$  ( $^{15}\text{N}_2$ :  $1657\text{ cm}^{-1}$ ) in the IR spectrum (Appendix, subchapter 6.1.17).

The terminal  $\text{N}_2$  complex  $[\text{ReBr}(\text{N}_2)_2(\text{t}^{\text{Pr}}\text{PN}^{\text{H}}\text{P})]$  ( $\mathbf{12}$ ) was isolated as a side product in the synthesis of  $\mathbf{11}^{\text{Br}}$  (Scheme 3.2, top reaction) by crystallization from the acetonitrile washing solution at  $-40\text{ }^\circ\text{C}$ . The complex is diamagnetic and shows two isopropyl groups in the  $^1\text{H}\{^{31}\text{P}\}$  NMR spectrum which are in the aliphatic region in the range between  $\delta = 1.27$  and  $1.40\text{ ppm}$  accompanied by a singlet in the  $^{31}\text{P}\{^1\text{H}\}$  NMR at  $\delta = 31.1\text{ ppm}$  indicating  $C_s$ -symmetry (Figure 3.12, top). XRD analysis revealed *cis*-coordination of the dinitrogen ligands, which occur in the IR spectrum at  $2040$  and  $1938\text{ cm}^{-1}$  being typical for terminal  $\text{N}_2$  ligands (Figure 3.12, bottom).<sup>221–224</sup> The complex is presumably a product of overreduction.

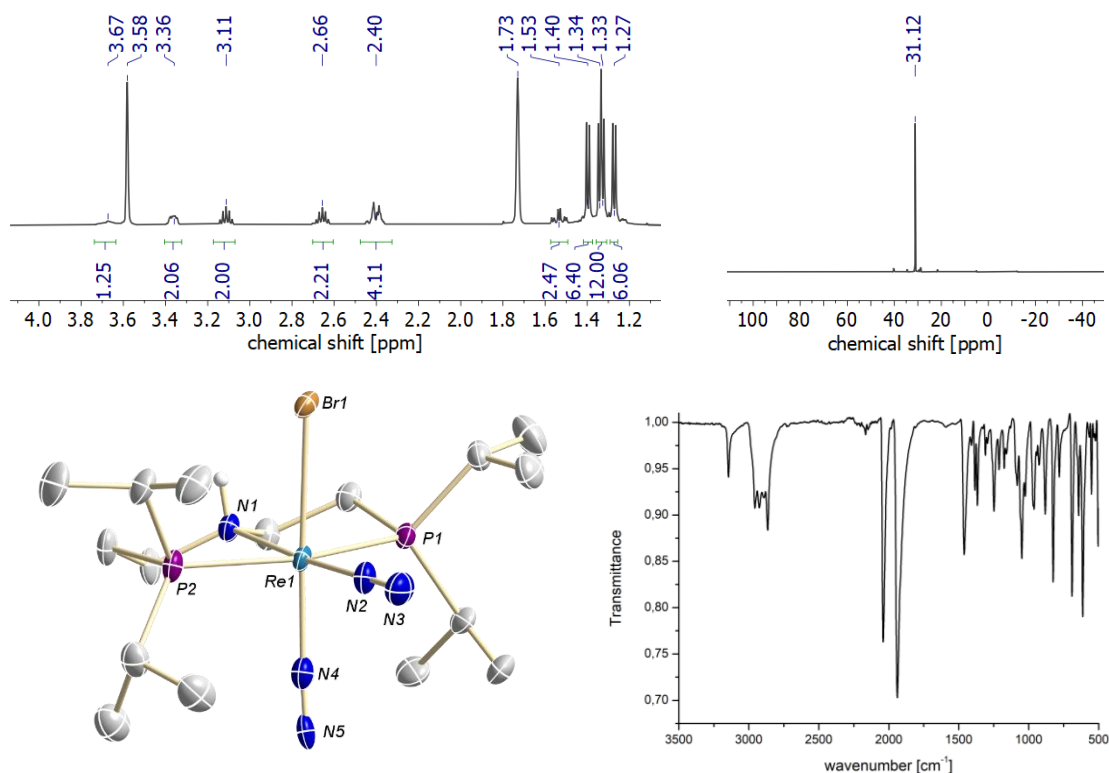
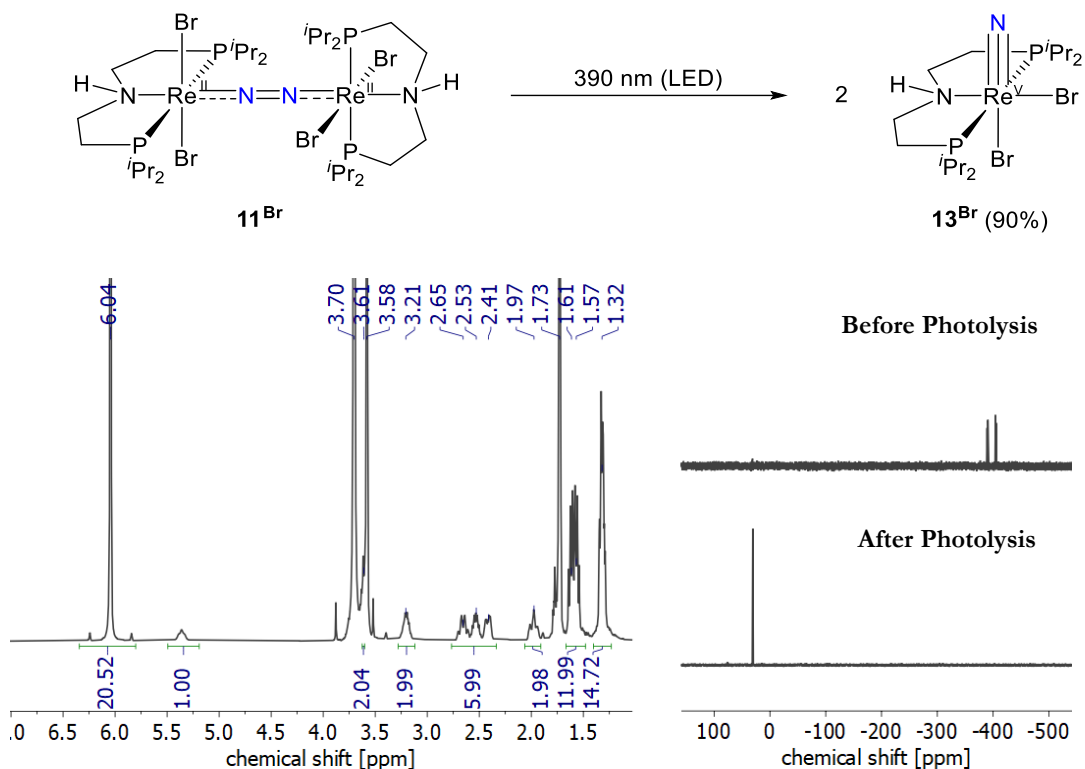


**Figure 3.12** Top: NMR characterization of  $\mathbf{12}$  ( $\text{THF-}d_8$ , RT). **Top left:**  $^1\text{H}\{^{31}\text{P}\}$  NMR spectrum. **Top right:**  $^{31}\text{P}\{^1\text{H}\}$  NMR spectrum. **Bottom left:** The molecular structure in the solid state. Hydrogen atoms (except N-H), disorder and solvent molecules are omitted for clarity. Selected bond lengths [ $\text{\AA}$ ] and angles [ $^\circ$ ]: Re1-N1 2.186(3), Re1-N2 1.967(3), Re1-N4 1.954(4), Re1-Br1 2.6366(4), N2-N3 1.090(4), N4-N5 0.994(4), N1-Re1-N2 175.38(13), P1-Re1-P2 161.19(3), Br1-Re1-N4 177.57(9). **Bottom right:** IR (ATR, solid) spectrum.

### 3.1.3 Photochemical properties of dinitrogen complexes $11^{\text{Cl}}$ , $11^{\text{Br}}$ and $11^{\text{I}}$

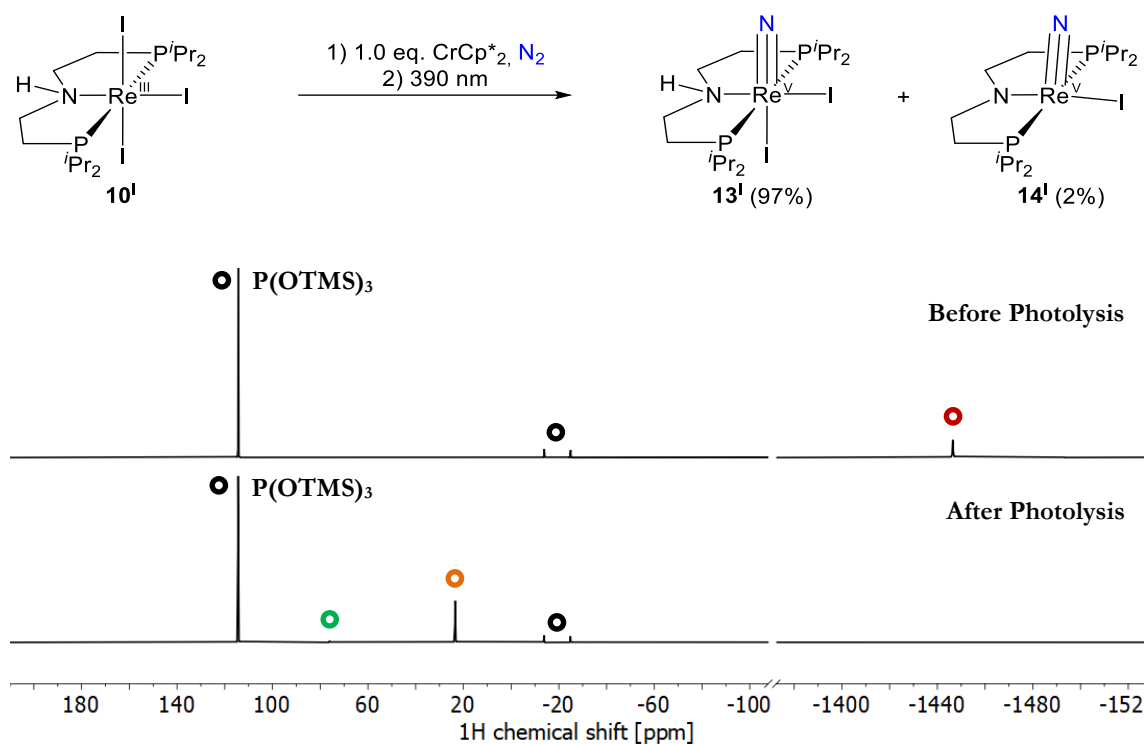
The photolysis of chloride substituted  $[(\mu\text{-N}_2)\{\text{ReCl}_2(\text{P}^{\text{tPr}}\text{PN}^{\text{H}}\text{P})\}_2]$  ( $11^{\text{Cl}}$ ) into the corresponding octahedral rhenium nitride complex  $[\text{ReCl}_2\text{N}(\text{P}^{\text{tPr}}\text{PN}^{\text{H}}\text{P})]$  ( $13^{\text{Cl}}$ ) was recently reported.<sup>43</sup> High-energy wavelengths are required to form the product in high spectroscopic yield of 95% and a quantum yield of 0.36%. These conditions were adapted for initial photolysis experiments of  $11^{\text{Cl}}$ . Exposing an NMR sample of  $[(\mu\text{-N}_2)\{\text{ReBr}_2(\text{P}^{\text{tPr}}\text{PN}^{\text{H}}\text{P})\}_2]$  ( $11^{\text{Br}}$ ) to an LED lamp ( $\lambda = 390$  nm), a color change is observed from dark blue to yellow-orange over the course of 15 minutes (Scheme 3.3).



**Scheme 3.3 Top:** Photolysis of  $11^{\text{Br}}$ . **Bottom left:**  $^1\text{H}$  NMR spectrum of the photolysis product. **Right:** Stacked  $^{31}\text{P}\{^1\text{H}\}$  NMR spectra before (top right) and after photolysis (bottom right).

The comparison of the  $^{31}\text{P}\{^1\text{H}\}$  NMR spectra before and after photolysis suggests a selective transformation into the product  $[\text{ReBr}_2\text{N}(\text{P}^{\text{tPr}}\text{PN}^{\text{H}}\text{P})]$  ( $13^{\text{Br}}$ ), being the only detectable species at  $\delta = 30.8$  ppm in the measured spectrum ( $\delta = -800$  to  $200$  ppm) (Scheme 3.3, right). By using 1,3,5-trimethoxy benzene as internal standard, a spectroscopic yield of 90% was determined by  $^1\text{H}$  NMR spectroscopy (Scheme 3.3, left). The spectroscopic yield could be successfully reproduced when using  $\text{P}(\text{OTMS})_3$  as internal standard by  $^{31}\text{P}\{^1\text{H}\}$  NMR spectroscopy (in a glass capillary). Despite absence of obvious side products formed during photolysis, the fate of the residual 10% rhenium compound stays unclear. Importantly,  $11^{\text{Cl}}$  and  $11^{\text{Br}}$  are thermally stable compounds that persists heating overnight at  $60$  °C. The photolysis product was independently synthesized by the reaction of rhenium tribromide  $10^{\text{Br}}$  with trimethylsilyl azide (Scheme 3.6).

The photoreactivity of iodide complex  $[(\mu\text{-N}_2)\{\text{ReI}_2(\text{}^{\text{tPr}}\text{PN}^{\text{H}}\text{P})\}_2]$  (**11<sup>I</sup>**) was explored (Scheme 3.4). Due to low solubility in its isolated form in THF, it was formed *in situ* by reduction of  $[\text{ReI}_3(\text{}^{\text{tPr}}\text{PN}^{\text{H}}\text{P})]$  (**10<sup>I</sup>**) with decamethyl chromocene under  $\text{N}_2$  atmosphere. The green reaction mixture was exposed to an LED lamp (390 nm), turning into a yellow mixture over the course of an hour. The spectroscopic yield was determined by the comparison of the ratios between starting material and product to the internal standard  $\text{P}(\text{OTMS})_3$  within a glass capillary in the NMR tube (Scheme 3.4). The  ${}^3\text{P}\{^1\text{H}\}$  spectrum before photolysis shows one signal belonging to **10<sup>I</sup>** ( $\delta = -1447.5$  ppm marked as red), the other signals can be assigned to the internal standard ( $\delta = 114.4, -13.8, -24.9$  ppm, the latter two signals are impurities (8%) within the internal standard) (Scheme 3.4). After photolysis, two products are being formed, which can be assigned to rhenium nitride complexes  $[\text{ReI}_2\text{N}(\text{}^{\text{tPr}}\text{PN}^{\text{H}}\text{P})]$  (**13<sup>I</sup>**) (marked as orange) and the corresponding, deprotonated complex  $[\text{ReIN}(\text{}^{\text{tPr}}\text{PNP})]$  (**14<sup>I</sup>**) (marked as green) obtained in spectroscopic yields of 97% and 2%, respectively. The formation of the latter complex can be explained by the presence of minimum overstoichiometric amounts of decamethyl chromocene that might serve as a base.

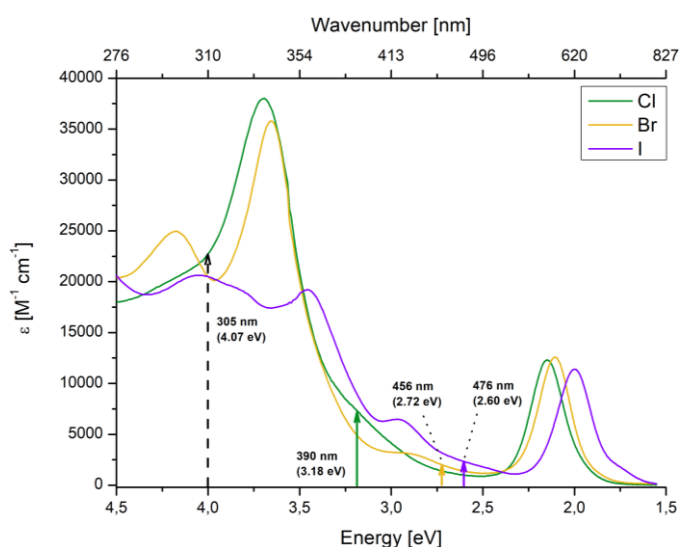


**Scheme 3.4 Top:** Reduction of **10<sup>I</sup>** under  $\text{N}_2$  atmosphere and subsequent photolysis. **Middle:** Before photolysis. **Bottom:** After photolysis.

Wavelength-dependent photolysis experiments were performed to identify the photolytic active regions of **11<sup>Br</sup>** and **11<sup>I</sup>** (Scheme 3.5). Light irradiation at  $\lambda = 305$  nm (Xe-Arc suited with a longwave-pass filter) and  $\lambda = 390$  nm (LED) produces the corresponding nitride complexes **13<sup>Br</sup>** and **13<sup>I</sup>** within minutes. Moving towards wavelengths above 390 nm, photolysis still works but the reaction time required for full conversion is getting significantly longer. The minimum energy required for photolysis within a reasonable time frame are



456 nm (2.72 eV) and 476 nm (2.60 eV) for complex **11**<sup>Br</sup> and **11**<sup>I</sup>, respectively. Exposing an NMR sample of **11**<sup>Br</sup> to  $\lambda = 525$  nm (Xe-Arc, suited with a bandpass filter) provides nitride complex **13**<sup>Br</sup> with a yield of 8% after irradiation for 18 h. Importantly, photolysis of **11**<sup>Cl</sup> requires wavelength of 390 nm or lower. The usage of low-energy wavelength is in regard of multicomponent reactions of fundamental interest to avoid incompatibility with reactants. Benzoyl bromide for instance is reported to form benzoyl radicals upon UV light irradiation, which potentially could lead to undesired side reactions.<sup>88–91</sup>



**Scheme 3.5** UVvis spectra of **11**<sup>Cl</sup>,<sup>e</sup> **11**<sup>Br</sup> and **11**<sup>I</sup>. The minimum energy required for effective N<sub>2</sub> cleavage are marked with solid arrows.

The quantum yield for the photolysis of **11**<sup>Br</sup> was investigated by UVvis spectroscopy. As guided by prior studies,<sup>209</sup> the calculation of the quantum yield implicates three parameters, which are the quantum flow (photons per time), the decay of the photoactive species (derived by the decreasing absorbance of an isolated UV band) and the absorbance of the probe at the emission wavelength (experimental details in subchapter 4.2.12). The quantum yield was determined using a detector probe.

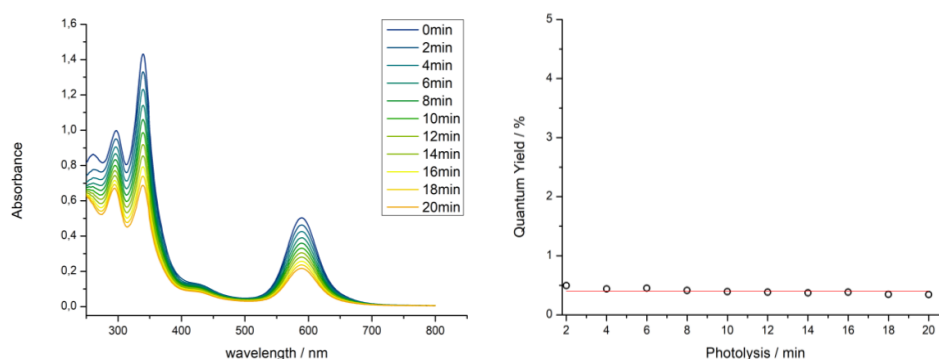
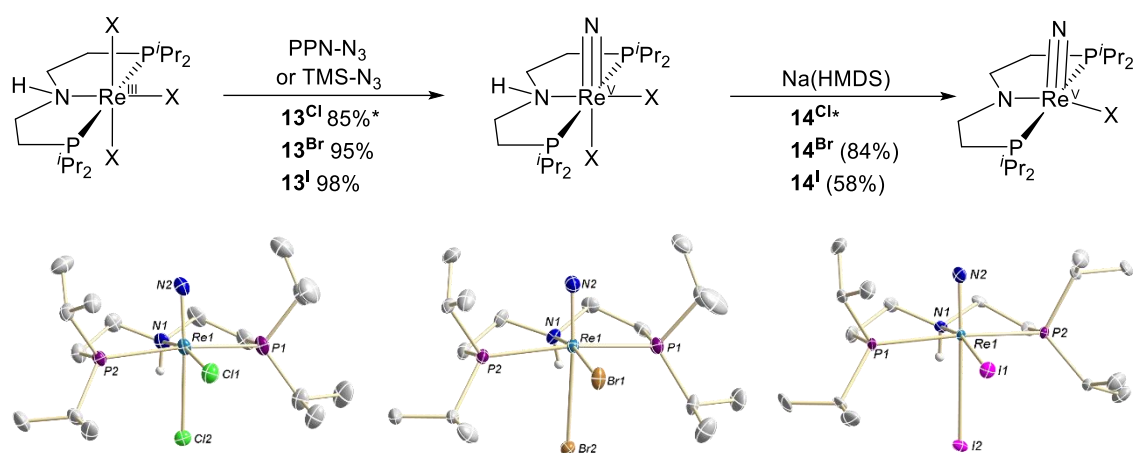


**Figure 3.13** Quantum yield determination of the photolysis of **11**<sup>Br</sup>. **Left:** photolysis tracked by UVvis spectroscopy. **Right:** Averaging the quantum yield.

<sup>e</sup> Experimental UVvis data adapted from Dr. Florian Wätjen (nee Schendzielorz).

It is important that the detector probe and the sample are positioned equally to assure the same distance to the light source. The experiment was performed using  $4 \cdot 10^{-5}$  M solution of  $\mathbf{11}^{\text{Br}}$  in a sealed *J. Young* UVvis cuvette. After recording a start spectrum before photolysis, the sample was exposed for 20 minutes to a 390 nm LED lamp and the progress was tracked every two minutes by recording a UVvis spectrum (Figure 3.13, left). The averaged quantum yield over ten cycles was calculated to be 0.4%, which is almost identical to  $\mathbf{11}^{\text{Cl}}$  (0.36%)<sup>209</sup> (Figure 3.13, right). These quantum yields are significantly lower than in the report of Miller, where a maximum quantum yield of 11% was reported.<sup>44</sup> The rhenium nitride complexes  $[\text{ReX}_2\text{N}(\text{P}^i\text{Pr}_2\text{N}^{\text{H}}\text{P})]$  ( $X = \text{Cl}, \text{Br}, \text{I}$ )  $\mathbf{13}^{\text{Cl}}$ ,<sup>43</sup>  $\mathbf{13}^{\text{Br}}$  and  $\mathbf{13}^{\text{I}}$  can be independently synthesized by the reaction of  $[\text{ReX}_3(\text{P}^i\text{Pr}_2\text{N}^{\text{H}}\text{P})]$  ( $X = \text{Cl}, \text{Br}, \text{I}$ )  $\mathbf{10}$  using different azide sources (Cl: PPN-N<sub>3</sub>; Br/I: TMS-N<sub>3</sub>) to obtain the products in high yields (Scheme 3.6)



**Scheme 3.6 Top:** Synthesis of rhenium nitride complexes  $\mathbf{13}^{\text{Cl}}$ ,  $\mathbf{13}^{\text{Br}}$  and  $\mathbf{13}^{\text{I}}$  and deprotonation. \*Corresponds to reference.<sup>209</sup> **Bottom:** Molecular structures of  $\mathbf{13}^{\text{Cl}}$ ,<sup>209</sup>  $\mathbf{13}^{\text{Br}}$  and  $\mathbf{13}^{\text{I}}$ . Hydrogen atoms (except N-H), disordered moieties and solvent molecules are omitted for clarity. Selected bond lengths [Å] and angles [°]:  $\mathbf{13}^{\text{Cl}}$ : Re1-N1 2.159(2), Re1-N2 1.669(2), Re1-Cl1 2.6712(7), Re1-Cl2 2.4309(7);  $\mathbf{13}^{\text{Br}}$ : Re1-N1 2.161(5), Re1-N2 1.663(5), Re1-Br1 2.8444(6), Re1-Br2 2.5559(6);  $\mathbf{13}^{\text{I}}$ : Re1-N1 2.162(6), Re1-N2 1.659(6), Re1-I1 3.1390(6), Re1-I2 2.7423(6).

The series of rhenium nitride complexes was characterized by XRD analysis (Scheme 3.6). The structural motif is consistent among the series. The rhenium atom is octahedrally coordinated and the nitride ligand is in apical position. The bond lengths of the rhenium atom to the nitrogen in the pincer backbone are invariant about 2.16 Å in all these complexes. The Re-N<sub>nitride</sub> bond lengths are similar about ~1.66 Å. The strong *trans*-influence of the nitride ligand significantly elongates the Re-X bond in the opposite position which is exceptionally large for  $\mathbf{13}^{\text{I}}$  ( $d_{\text{Re-I}} = 3.1390(6)$  Å and 2.7423(6) Å). The reaction with Na(HMDS) yields the corresponding deprotonated species  $[\text{ReXN}(\text{P}^i\text{Pr}_2\text{N}^{\text{P}}\text{P})]$  ( $X = \text{Cl}, \text{Br}, \text{I}$ )  $\mathbf{14}^{\text{Cl/Br/I}}$ .

<sup>†</sup> Characterization of  $\mathbf{13}^{\text{Br}}$  by NMR spectroscopy, IR spectroscopy, mass spectrometry, cyclic voltammetry and XRD analysis was carried out by M. Sc. Sessa Kisan (AK Schneider, Georg-August-Universität Göttingen). Design of a synthetic route to analytical purity (elemental analysis) was designed by Maximilian Fritz.

### 3.1.4 TD-DFT of $\mathbf{11}^{\text{Cl}}$ and $\mathbf{11}^{\text{Br}}$

In analogy to  $[(\mu\text{-N}_2)\{\text{ReCl}_2(\text{P}^{\text{r}}\text{PN}^{\text{H}}\text{P})\}_2]$  ( $\mathbf{11}^{\text{Cl}}$ )<sup>43</sup>, the photolysis of  $[(\mu\text{-N}_2)\{\text{ReBr}_2(\text{P}^{\text{r}}\text{PN}^{\text{H}}\text{P})\}_2]$  ( $\mathbf{11}^{\text{Br}}$ ) was investigated by time-dependent DFT calculations<sup>s</sup> (computational details in subchapter 6.3.2 and 6.3.3). The diagram in Figure 3.14 contains the experimental (solid lines) and the computed UVvis spectra (dashed lines) of  $\mathbf{11}^{\text{Cl}}$  (green) and  $\mathbf{11}^{\text{Br}}$  (yellow). In both cases, the TD-DFT computations could decently reproduce the experimental spectra. The experimental spectra are qualitatively similar: both have a distinctive band in the UV ( $E = 3.70$  eV ( $\mathbf{11}^{\text{Cl}}$ ),  $3.65$  eV ( $\mathbf{11}^{\text{Br}}$ )) and in the visible region ( $E = 2.15$  eV ( $\mathbf{11}^{\text{Cl}}$ ),  $2.10$  eV ( $\mathbf{11}^{\text{Br}}$ )), which, according to the TD-DFT calculations, can be assigned to  $\pi^*\text{-}\pi\text{-}\pi^* \rightarrow \pi^*\text{-}\pi^*\text{-}\pi^*$  and  $\pi\text{-}\pi^*\text{-}\pi \rightarrow \pi^*\text{-}\pi\text{-}\pi^*$  transitions, respectively. Both transitions are suggested to be unproductive with respect of  $\text{N}_2$  cleavage. As indicated by these bands, there is a redshift of  $\Delta E = +0.05$  eV comparing the chloride and the bromide complex.

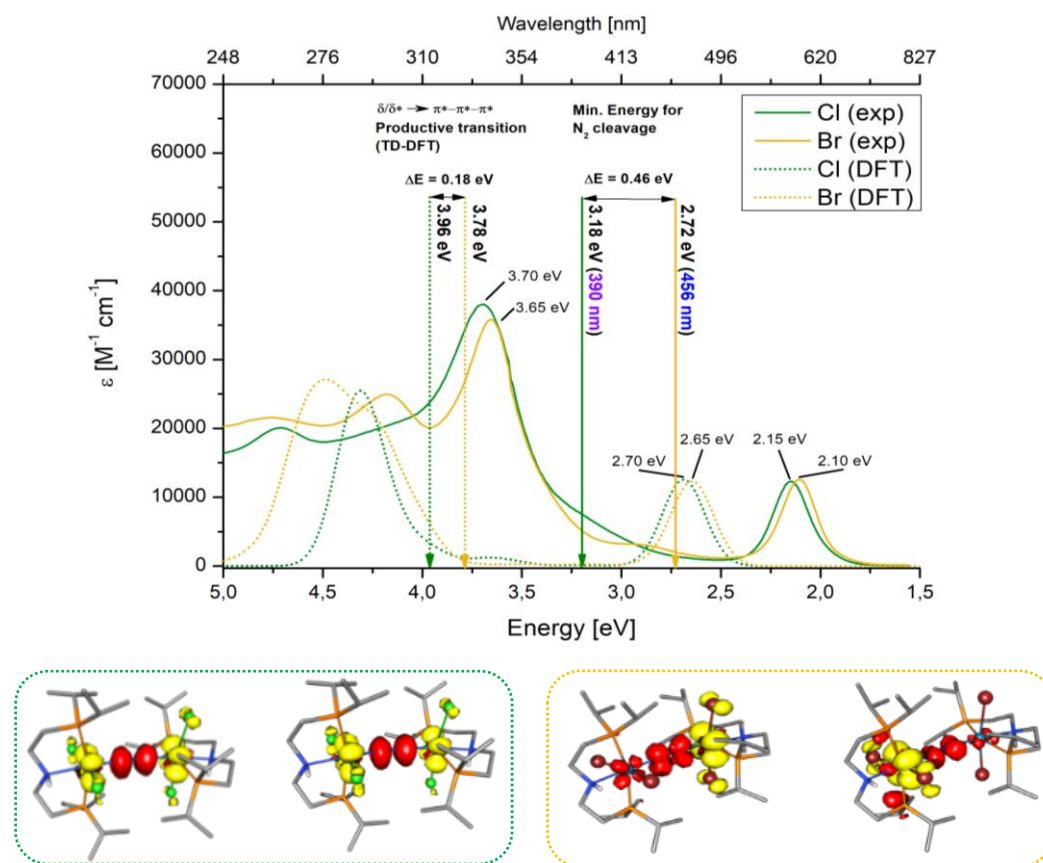


**Figure 3.14** Experimental (solid lines) and calculated (dashed lines) UVvis spectra of  $\mathbf{11}^{\text{Clh}}$  (green) and  $\mathbf{11}^{\text{Br}}$  (yellow) in  $4 \cdot 10^{-5}$  M solution (THF). The solid arrows display the minimum energy for efficient  $\text{N}_2$  cleavage and the corresponding dotted arrows represent the energy of the productive  $\delta/\delta^* \rightarrow \pi^*\text{-}\pi^*\text{-}\pi^*$  transitions, derived by TD-DFT. The difference density plot for the respective transitions are below, Cl in green and Br in orange. Computational details for chloride and bromide complex: ORCA 4.2.1; UKS PBE RI D3BJ Grid7 CPCM(THF); for Re, Cl, N, P, O def2-TZVP def2/J; for C, H def2-SVP def2/J.

<sup>s</sup> TD-DFT calculations were performed by M. Sc. Severine Rupp (AK Krewald, Technische Universität Darmstadt).

<sup>h</sup> Experimental UVvis data adapted from Dr. Florian Wätjen (nee Schendzielorz).

Unlike the chloride complex, the bromide complex **11<sup>Br</sup>** shows an additional, small band at about 3 eV in the UVvis spectrum. The transitions located there are also unproductive  $\pi^*-\pi-\pi^* \rightarrow \pi^*-\pi^*-\pi^*$  transitions within the  $\pi$ -manifold of the Re-N-N-Re core. As derived by the TD-DFT computations, the productive, MLCT type  $\delta/\delta^* \rightarrow \pi^*-\pi^*-\pi^*$  transitions do not have an expressed, characteristic band due to their low oscillator strength. These low-intensity transitions are located in the shoulder of the  $\pi^*-\pi-\pi^* \rightarrow \pi^*-\pi^*-\pi^*$  transitions at 3.7 eV (marked as dashed arrows in Figure 3.14).

Importantly, while the unproductive transitions in **11<sup>Cl</sup>** and **11<sup>Br</sup>** redshift about  $\Delta E = +0.05$  eV, the redshift of the productive region for N<sub>2</sub> cleavage is much more significant (exp:  $\Delta E_{\text{Cl-Br}} = 0.46$  eV, TD-DFT:  $\Delta E_{\text{Cl-Br}} = 0.18$  eV). In other words, the only transitions that are significantly shifted upon halide exchange are the productive  $\delta/\delta^* \rightarrow \pi^*-\pi^*-\pi^*$  transitions. This observation is in line with the model that an MLCT transition facilitates N<sub>2</sub> cleavage (introduction, Scheme 1.10), because it is reasonable that ligands in the first coordination sphere (halide ligands) have a direct effect on the energetics of the metal-centered  $\delta/\delta^*$ -orbitals rather than on the  $\pi/\pi^*$ -orbitals that are delocalized along the Re-N-N-Re core. The corresponding spin density plots of the  $\delta/\delta^* \rightarrow \pi^*-\pi^*-\pi^*$  transitions for the **11<sup>Cl</sup>** (green) and **11<sup>Br</sup>** (yellow) complex are shown in Figure 3.14 (bottom). The yellow parts represent the decrease and the red parts indicate the increase of spin density during excitation.<sup>209</sup>

### 3.1.5 Light-supported electrolysis of **11<sup>Br</sup>** and **11<sup>I</sup>** under N<sub>2</sub> atmosphere

Electrochemical transformations are highly attractive from a synthetic perspective because the fine adjustment of the electrochemical potential provides the possibility to control selectivity by preventing side reactions. Additionally, the replacement of a chemical reactant is a strategy to improve atom economy by producing less chemical waste. Amalgams are still a broadly applied chemical reductant, however, the usage of mercury is highly questionable from an ecological point of view because of its high toxicity.

The establishment of electrochemistry into the field of organic transformations has rapidly evolved in the last decade.<sup>225–230</sup> Nevertheless, electrochemical N<sub>2</sub> fixation and/or functionalization mediated by transition metal complexes is limited to very few examples.<sup>42,231</sup> Inspired by prior work,<sup>42,231</sup> electrochemical N<sub>2</sub> activation was targeted for [ReBr<sub>3</sub>(<sup>4</sup>rPN<sup>1</sup>H<sup>1</sup>P)] (**10<sup>Br</sup>**). According to the cyclic voltammetry data presented in subchapter 3.1.2, the Re<sup>III/II</sup> couple is at  $E_{1/2} = -1.70$  V being relevant for N<sub>2</sub> fixation. Resultantly, controlled potential electrolysis was performed in a THF solution (0.2 M, N<sup>r</sup>Bu<sub>4</sub>PF<sub>6</sub>) at this potential under an atmosphere of dinitrogen. In an initial electrolysis attempt, a color change was observed from yellow into blueish green. The solvent was removed and the crude product was extracted with benzene to separate the product from the electrolyte.

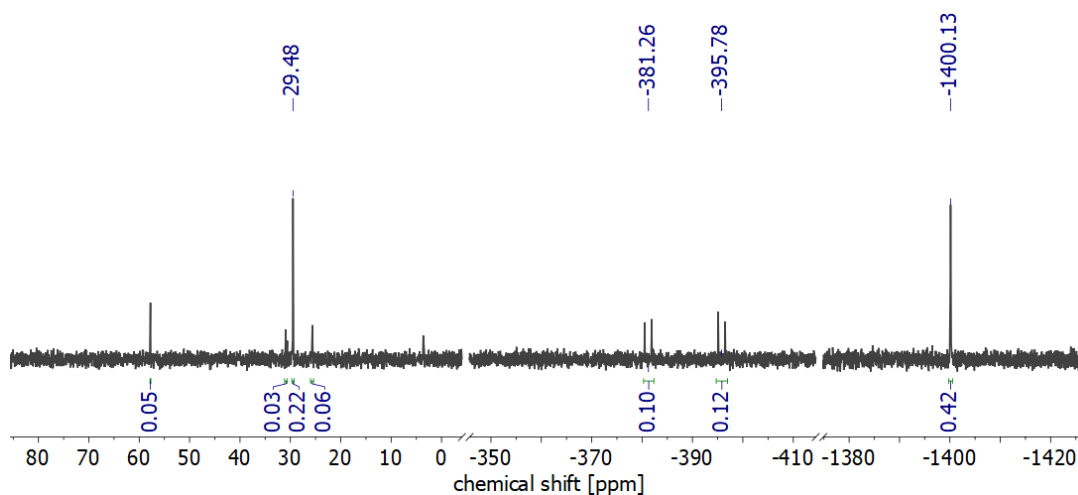


**Figure 3.15**  $^{31}\text{P}\{^1\text{H}\}$  NMR spectroscopy of the crude product of the electrolysis of  $10^{\text{Br}}$  under  $\text{N}_2$  atmosphere. The spectrum was not recorded with extended relaxation time.

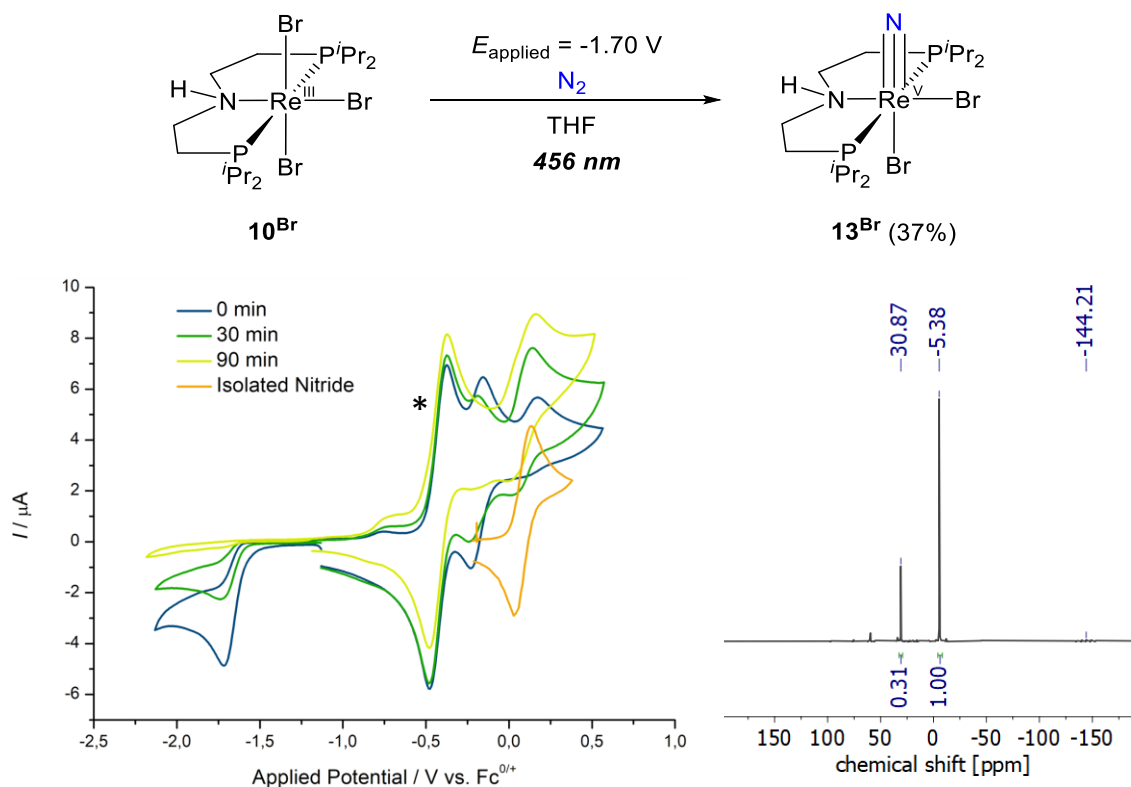
The benzene extract was investigated by  $^{31}\text{P}\{^1\text{H}\}$  NMR spectroscopy and the corresponding spectrum is shown in Figure 3.15. Due to low concentration, the spectrum was not measured with extended delay time so the integrals discussed in this particular spectrum should not be overinterpreted. Dinitrogen complex  $[(\mu\text{-N}_2)\{\text{ReBr}_2(^{\text{Br}}\text{PN}^{\text{H}}\text{P})\}_2]$  ( $11^{\text{Br}}$ ) was formed with a spectroscopic yield of approximately 22% as indicated by two doublets in the negative region at  $\delta = -390$  ppm (yield estimated without internal standard, spectroscopic yield corresponds to the comparison to all  $^{31}\text{P}\{^1\text{H}\}$  NMR active species, Figure 3.15). Another dominant signal arises at 29.5 ppm with the same integral which is close to the NMR chemical shift of rhenium nitride complex  $[\text{ReBr}_2\text{N}(^{\text{Br}}\text{PN}^{\text{H}}\text{P})]$  ( $13^{\text{Br}}$ ) ( $\delta = 30.8$  ppm) but its formation could not be confirmed by mass spectrometry. Furthermore, photolytic splitting into the nitrides under these conditions seems unlikely because  $11^{\text{Br}}$  is a thermally stable compound and the electrolysis experiment was performed in the dark. The high-field shifted resonance at  $\delta = -1400.1$  ppm indicates significant amounts of unreacted starting material despite formal charge transfer of 1.0 eq. electron during electrolysis. By these observations it is assumed that a side reaction is taking place that emerged fine tuning of the reaction conditions.

In a next attempt, controlled potential electrolysis was performed under light irradiation to trap the dinitrogen complex  $11^{\text{Br}}$  by subsequent photolytic cleavage. Once formed, rhenium nitride complex  $13^{\text{Br}}$  is chemically much more robust unlike its low-valent parent  $11^{\text{Br}}$ , which most likely is more prone to undesired side reactions. The CPE experimental setup was placed in front of a 456 nm LED and the reaction progress was tracked by cyclic voltammetry (Scheme 3.7, left)<sup>i</sup>. The  $\text{Re}^{\text{III/II}}$  couple at  $E_{1/2} = -1.70$  V and the  $\text{Re}^{\text{IV/III}}$  wave at  $E_{1/2} = -0.22$  V can be used as indicator for the reaction progress. As electrolysis proceeds, the wave of the  $\text{Re}^{\text{III/II}}$  couple significantly decays confirming substantial conversion of the starting material. After a reaction time of 90 minutes, the integration of the current vs. time

<sup>i</sup> Initial attempts are documented in the Bachelor thesis of Paul Julius Weiß (under supervision of Maximilian Fritz).

plot revealed a charge transfer of 1.7 eq. electrons and a color change was observed from yellow via green into orange.

The  $\text{Re}^{\text{VI/V}}$  couple of the isolated rhenium nitride complex  $\mathbf{13}^{\text{Br}}$  is at a potential of  $E_{1/2} = +0.08 \text{ V}$  (Scheme 3.7, left, orange trace). Unfortunately, this region is in the crude mixture dominated by another wave ( $E_{\text{pa}} = +0.17 \text{ V}$ ) prohibiting direct comparison and thus the formation of the rhenium nitride cannot be unambiguously confirmed by its electrochemical signature. The solvent was removed and the product extracted with benzene. Product quantification was accomplished by  $^{31}\text{P}\{^1\text{H}\}$  NMR spectroscopy using triphenyl phosphine as internal standard ( $\delta = -5.38 \text{ ppm}$ , Scheme 3.7, right). Apart from the internal standard, there is one dominant signal at a chemical shift of  $\delta = 30.87 \text{ ppm}$  which can be assigned to the rhenium nitride complex with a spectroscopic yield of 37%. However, the relatively clean spectrum contrasts the low spectroscopic yields raising the question about the fate of the residual 63% rhenium compound. Notably, full conversion of the starting material requires the transfer of 1.7 eq. electrons although only one equivalent is theoretically needed. Hence, it is possible that the excess of electrons transferred (0.7 eq.) are feeding a side reaction forming a paramagnetic,  $^{31}\text{P}\{^1\text{H}\}$  NMR silent rhenium species to account for the low spectroscopic yield of  $\mathbf{13}^{\text{Br}}$



**Scheme 3.7 Top:** Light supported electrolysis generating  $\mathbf{13}^{\text{Br}}$  under  $\text{N}_2$  atmosphere. **Bottom left:** Controlled potential electrolysis (0.2 M,  $\text{N}^t\text{Bu}_4\text{PF}_6$ ) of  $\mathbf{10}^{\text{Br}}$  tracked by cyclic voltammetry ( $t = 0, 30, 90$  minutes). Decamethyl ferrocene (\*) was used as internal standard ( $E^0 = -0.43 \text{ V}$ ). **Bottom right:**  $^{31}\text{P}\{^1\text{H}\}$  NMR of the crude product with triphenyl phosphine ( $\delta = -5.38 \text{ ppm}$ ) as internal standard.

The analogous electrochemical transformation was performed with  $[\text{ReI}_3(^t\text{PrPN}^i\text{Pr})]$  ( $\mathbf{10}^i$ ). In a similar approach, an initial controlled potential electrolysis experiment was carried out at

$E_{\text{applied}} = -1.5$  V and stopped after transfer of 1.0 eq. electron per rhenium atom and the crude product was investigated by  $^{31}\text{P}\{^1\text{H}\}$  NMR spectroscopy. In the corresponding spectrum in Figure 3.16 are distinctive signals in the negative region reminiscent to **11**<sup>Cl</sup> and **11**<sup>Br</sup> ( $\delta = -300$  to  $-400$  ppm). However, the crude integration anticipates a low yield and a singlet at  $\delta = 25.8$  ppm is much more dominant. The chemical shift is close to the desired rhenium nitride complex  $[\text{ReI}_2\text{N}(\text{PrPN}^{\text{H}}\text{P})]$  (**13**<sup>I</sup>) ( $\delta = 24.0$  ppm), which could not be confirmed by mass spectrometry. The fact that the electrolysis experiment was performed in the dark rather speaks for the formation of a side product.

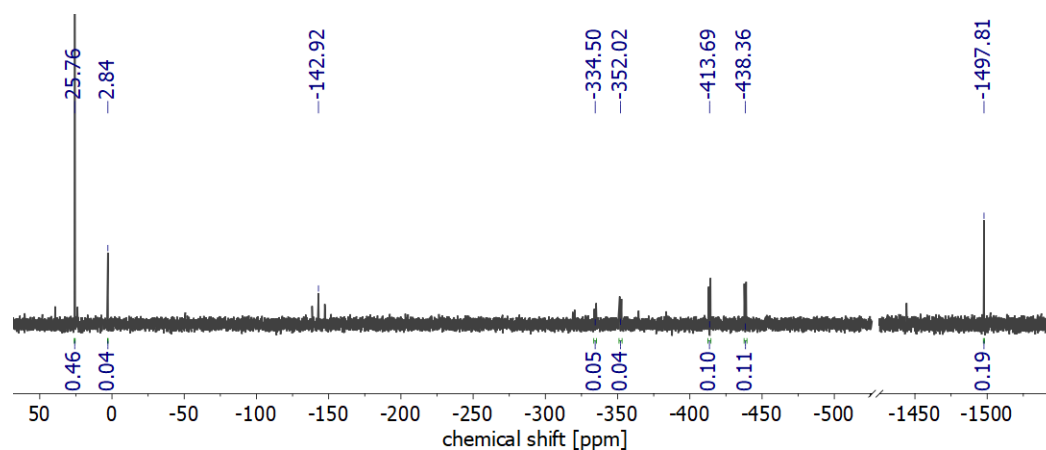
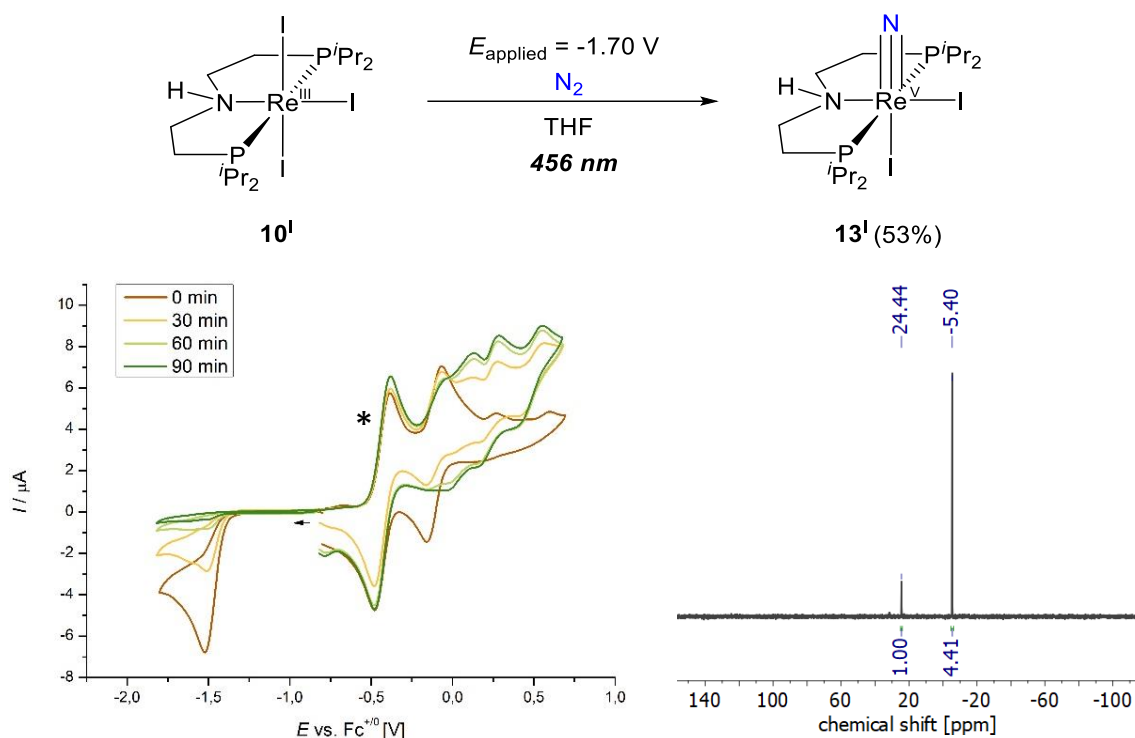


**Figure 3.16**  $^{31}\text{P}\{^1\text{H}\}$  NMR spectroscopy of the crude product of the electrolysis of  $[\text{ReI}_3(\text{PrPN}^{\text{H}}\text{P})]$  (**10**<sup>I</sup>) under  $\text{N}_2$  atmosphere. Spectrum was not recorded with elongated relaxation time.

In accordance to the electrochemical optimization of  $[\text{ReBr}_3(\text{PrPN}^{\text{H}}\text{P})]$  (**10**<sup>Br</sup>), controlled potential electrolysis was performed until complete conversion of the starting complex under constant irradiation of a 456 nm LED (Scheme 3.8) using decamethyl ferrocene as internal standard.

During electrolysis, the color changes from red via green to orange. The consumption of the starting material could be decently tracked by cyclic voltammetry which shows gradual decrease of the  $\text{Re}^{\text{III/II}}$  wave at  $E_{\text{pc}} = -1.50$  V. After a reaction time of 90 minutes, the starting material is consumed equating to 1.2 eq. electrons being transferred (Scheme 3.8, bottom left). The oxidative area is less suited to indicate product formation due to several superimposed electrochemical events in the region between 0 – 0.7 V. The crude product was extracted with toluene and investigated by  $^{31}\text{P}\{^1\text{H}\}$  NMR spectroscopy using triphenylphosphine as internal standard (Scheme 3.8, bottom right,  $\delta = 5.40$  ppm). The only detectable species in the spectrum belongs to the rhenium nitride complex **13**<sup>I</sup> at a chemical shift of  $\delta = 24.4$  ppm with a good spectroscopic yield of 53%. The spectroscopic yield is higher than in the electrolysis to **13**<sup>Br</sup> presented before, however, also in this reaction it stays unclear what happened to the major part of the rhenium compound. Again, most likely  $^{31}\text{P}\{^1\text{H}\}$  NMR silent species are partially formed by the slight excess of transferred electrons lowering the spectroscopic yield.



**Scheme 3.8 Top:** Light supported electrolysis generating **13<sup>I</sup>** under N<sub>2</sub> atmosphere. **Bottom left:** Controlled potential electrolysis (0.2 M, N<sup>n</sup>Bu<sub>4</sub>PF<sub>6</sub>) of **10<sup>I</sup>** tracked by cyclic voltammetry ( $t = 0, 30, 90$  minutes). Decamethyl ferrocene (\*) was used as internal standard ( $E_0 = -0.43$  V). **Bottom right:** <sup>31</sup>P{<sup>1</sup>H} NMR of the crude product with triphenyl phosphine ( $\delta = -5.40$  ppm) as internal standard.

### 3.1.6 Concluding remarks

The exchange of the halide ligands within the platform [ReX<sub>3</sub>(<sup>n</sup>PrPN<sup>H</sup>P)] (**10<sup>Cl</sup>**, **10<sup>Br</sup>**, **10<sup>I</sup>**) has triggered a substantial anodic shift of the Re<sup>III/II</sup> couple by +340 mV which allows for dinitrogen activation at milder potential. Avoiding huge negative reduction potentials is generally of high interest because it prevents incompatibility in multicomponent reactions. A loss of reversibility is observed going from chloride to iodide represented by the corresponding rate constants for halide increasing in orders of magnitude ( $k_{\text{diss}} = 0.05 \text{ s}^{-1}$  (**10<sup>Cl</sup>**),  $0.32 \text{ s}^{-1}$  (**10<sup>Br</sup>**),  $2.46 \text{ s}^{-1}$  (**10<sup>I</sup>**)).

Chemical reduction of the precursor complexes [ReX<sub>3</sub>(<sup>n</sup>PrPN<sup>H</sup>P)] **10** under an N<sub>2</sub> atmosphere yielded the corresponding N<sub>2</sub> bridged, dirhenium complexes [( $\mu$ -N<sub>2</sub>){ReX<sub>2</sub>(<sup>n</sup>PrPN<sup>H</sup>P)}<sub>2</sub>] (X = Cl, Br, I) (**11<sup>Cl/Br/I</sup>**) in good yields. Dinitrogen complexes **11<sup>Cl</sup>** and **11<sup>Br</sup>** exhibit nearly identical bond metrics and spectroscopic signatures. By contrast, **11<sup>I</sup>** shows a varied molecular architecture, as the pincer ligands are in *cis-trans* position to the N<sub>2</sub> bridge generating C<sub>1</sub>-symmetry, which has no influence on the degree of N<sub>2</sub> activation, judged by analogous N-N bond lengths ( $d_{\text{N-N}} = \sim 1.16 \text{ \AA}$ ) and stretching vibrations ( $\nu = \sim 1730 \text{ cm}^{-1}$ ).

The three members of the halide series **11<sup>Cl/Br/I</sup>** are photoactive and facilitate N-N bond cleavage into the corresponding nitride species within minutes in high yields. Distinctively different is the photolytically productive region for N<sub>2</sub> cleavage that is shifted to lower



energy. Photolysis of **11<sup>Cl</sup>** requires high-energy wavelength of 390 nm. Blue light with wavelengths of 456 nm and 467 nm can be used instead for **11<sup>Br</sup>** and **11<sup>I</sup>**, respectively, while the quantum yield stays unaffected ( $\sim 0.4\%$  for **11<sup>Cl</sup>** and **11<sup>Br</sup>**). The striking, bathochromic shift of the productive region ( $\Delta E = \sim 0.46$  eV) in comparison to the unproductive transitions ( $\Delta E = \sim 0.05$  eV) upon halide exchange was interpreted as experimental confirmation for the 'TD-DFT' calculations that suggest an MLCT process ( $\delta/\delta^* \rightarrow \pi^*-\pi^*-\pi^*$ ) being the productive transition that leads to N-N bond cleavage.

With the information in hand about the redox potentials for N<sub>2</sub> binding and electronic absorption behavior for N<sub>2</sub> cleavage, a one-pot synthesis route was designed to generate rhenium nitride complexes **13<sup>Br</sup>** and **13<sup>I</sup>** in moderate yields by light-supported electrolysis (37% and 53%, respectively). The combination of electro- and photochemical techniques in N<sub>2</sub> fixation is unprecedented but more importantly, the nitrides complexes provided this way undergo N-transfer into organic substrates at mild conditions, as discussed in the next chapter.

## 3.2 Rhenium-mediated N-transfer to benzonitrile

### 3.2.1 Acylation of nitride **13<sup>Br</sup>**

In a recent study, nitride complex [ReCl<sub>2</sub>N(<sup>Pr</sup>PN<sup>H</sup>P)] (**13<sup>Cl</sup>**) has shown to produce benzamide and benzonitrile by the reaction with benzoyl chloride. However, elevated temperatures were required.<sup>43</sup> The current work tries to take advantage of the better leaving group bromide to establish milder reaction conditions for nitride transfer.

Reacting nitride complex [ReBr<sub>2</sub>N(<sup>Pr</sup>PN<sup>H</sup>P)] (**13<sup>Br</sup>**) with an excess benzoyl bromide at room temperature leads to a color change from an initial orange solution into yellow within hours. <sup>31</sup>P{<sup>1</sup>H} NMR spectroscopy of the reaction solution revealed the formation of a new product with a chemical shift of  $\delta = 34.5$  ppm, similar to the starting material **13<sup>Br</sup>** ( $\delta = 30.8$  ppm). Layering the reaction solution with pentane leads to crystallization of a species which could be identified as imido complex [ReBr<sub>2</sub>{N(CO)C<sub>6</sub>H<sub>5</sub>}(<sup>Pr</sup>PN<sup>H</sup>P)]Br (**15<sup>Br</sup>**) (Figure 3.17). In the solid state, the imido moiety {N(CO)C<sub>6</sub>H<sub>5</sub>} is rearranged into the *trans*-position (Figure 3.17, left). That results in significant elongation of the N<sub>PNP</sub>-Re bond length due to the strong *trans*-influence of the imido ligand ( $d_{\text{N}(\text{pincer})-\text{Re}} = 2.278(3)$  Å (**15<sup>Br</sup>**) vs. 2.161(5) Å (**13<sup>Br</sup>**). Partial reduction of the bond order is reflected by an increased Re-N bond length ( $d_{\text{Re-imido}} = 1.724(3)$  Å (**15<sup>Br</sup>**) vs.  $d_{\text{Re-nitride}} = 1.663(5)$  Å (**13<sup>Br</sup>**)) suggesting double bond character. The amine N-H forms a hydrogen bridge with the bromide anion.

<sup>i</sup> The synthesis and characterization (NMR and IR spectroscopy, mass spectrometry, elemental analysis and cyclic voltammetry) of complex **15<sup>Br</sup>** was carried out by M. Sc. Sessa Kisan (AK Schneider, Georg-August-Universität Göttingen). XRD analysis and data refinement was performed by Maximilian Fritz.

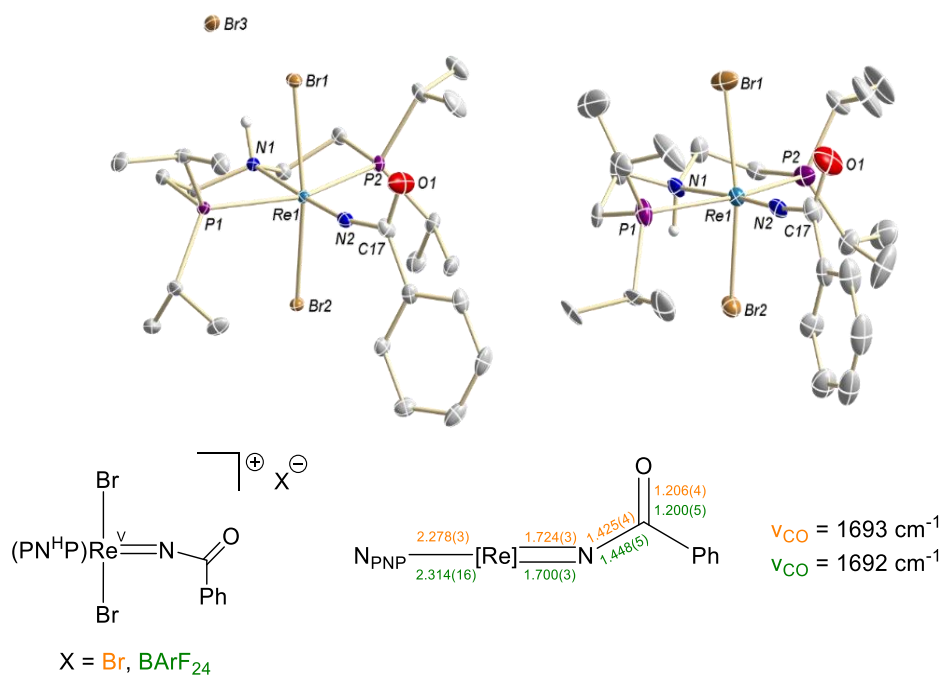
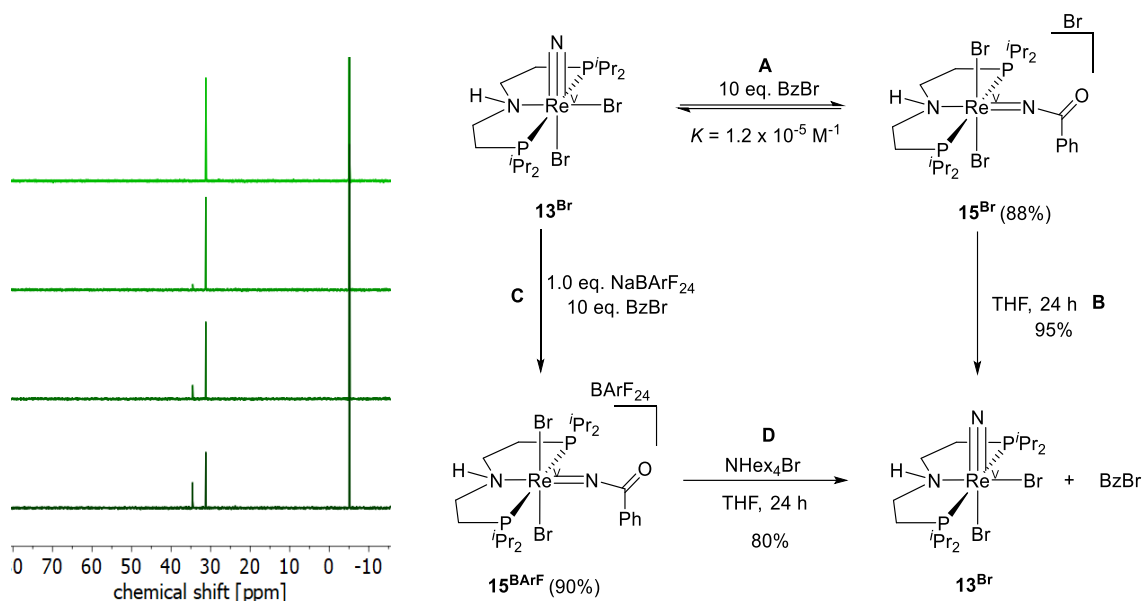


**Figure 3.17** Molecular structures of **15<sup>Br</sup>** (left) and **15<sup>BArF</sup>** (right) in the solid state drawn at the 50% probability level. Hydrogen atoms (except N-H), disordered moieties and solvent molecules are omitted for clarity. Selected bond length [Å] and angles [°]: **15<sup>Br</sup>**: N1-Re1 2.278(3), Re1-N2 1.724(3), N2-C17 1.425(4), C17-O1 1.206(4); Br1-Re1-Br2 165.462(12), N1-Re1-N2 176.37(12). **15<sup>BArF</sup>**: N1-Re1 2.314(16), Re1-N2 1.700(3), N2-C17 1.448(5), C17-O1 1.200(5), H111-Br3 2.42(4); Br1-Re1-Br2 162.621(18), N1-Re1-N2 175.8(3).

It is important to note that the stability of **15<sup>Br</sup>** is strongly solvent dependent. While this compound is stable in dichloromethane for days, rapid dissociation to parent nitride **13<sup>Br</sup>** and benzoyl bromide is observed in THF, suggesting an equilibrium. This hypothesis was validated by an NMR titration experiment, where benzoyl bromide was added stepwise to **13<sup>Br</sup>** resulting in a successive increase of the product peak (Scheme 3.9, left). In presence of 5 eq. benzoyl bromide, the corresponding **15<sup>Br</sup>** is formed by 32%. An equilibrium constant of  $K = 1.1 \cdot 10^{-5} \text{ M}^{-1}$  was extracted indicating that dissociation is strongly favoured (Scheme 3.9, Path A). The hydrogen bridge of the bromide anion to the N-H group found in the solid-state structure is suggested to account for the dissociative behaviour in THF. This observation evoked anion exchange because compatibility towards THF as a solvent was considered as prerequisite for an electrochemical evaluation and follow-up reactivity.



**Scheme 3.9** Left: Titration of benzoyl bromide to  $13^{\text{Br}}$  (top to bottom: 0, 1, 2, 5 eq.), as monitored by  $^{31}\text{P}\{^1\text{H}\}$  NMR spectroscopy. Triphenyl phosphine is used as internal standard ( $\delta = -5.83$  ppm). Right: Path A: Equilibrium between  $13^{\text{Br}}$  and  $15^{\text{Br}}$ . Path B: Dissociation of  $15^{\text{Br}}$  in THF. Path C: Salt metathesis of  $15^{\text{Br}}$  with  $\text{NaBARF}_{24}$  forming  $15^{\text{BARF}}$ . Path D:  $15^{\text{BARF}}$  in presence of a bromide source.

The equilibrium of  $[\text{ReBr}_2\text{N}(\text{P}^{\text{r}}\text{PN}^{\text{H}}\text{P})]$  ( $13^{\text{Br}}$ ) and benzoyl bromide in THF can be shifted by the addition of an equimolar amount of  $\text{NaBARF}_{24}$  forming a green solution accompanied by precipitation of a colorless solid. Removal of the solvent and extraction with diethyl ether obtains  $[\text{ReBr}_2\{\text{N}(\text{CO})\text{C}_6\text{H}_5\}(\text{P}^{\text{r}}\text{PN}^{\text{H}}\text{P})]\text{BARF}_{24}$  ( $15^{\text{BARF}}$ ) in high yields of 90% after crystallization (Scheme 3.9, Path C). As observed in the  $^1\text{H}\{^{31}\text{P}\}$  spectrum, there are four isopropyl groups in the aliphatic region between  $\delta = 1.35 - 1.37$  ppm suggesting  $C_s$ -symmetry in solution. Furthermore, five indicative resonances were observed at  $\delta = 8.06$ , 7.77, 7.59 ppm and  $\delta = 7.79$ , 7.58 ppm in the aromatic region, which can be assigned to the  $\{\text{N}(\text{CO})\text{C}_6\text{H}_5\}$  moiety and the borate anion, respectively (Figure 3.18, left). One singlet is observed in the  $^{31}\text{P}\{^1\text{H}\}$  NMR spectrum at a chemical shift of  $\delta = 32.8$  ppm (Figure 3.18, right). The atomic composition was confirmed by elemental analysis and high-resolution mass spectrometry ( $\text{ESI}^+$ ).

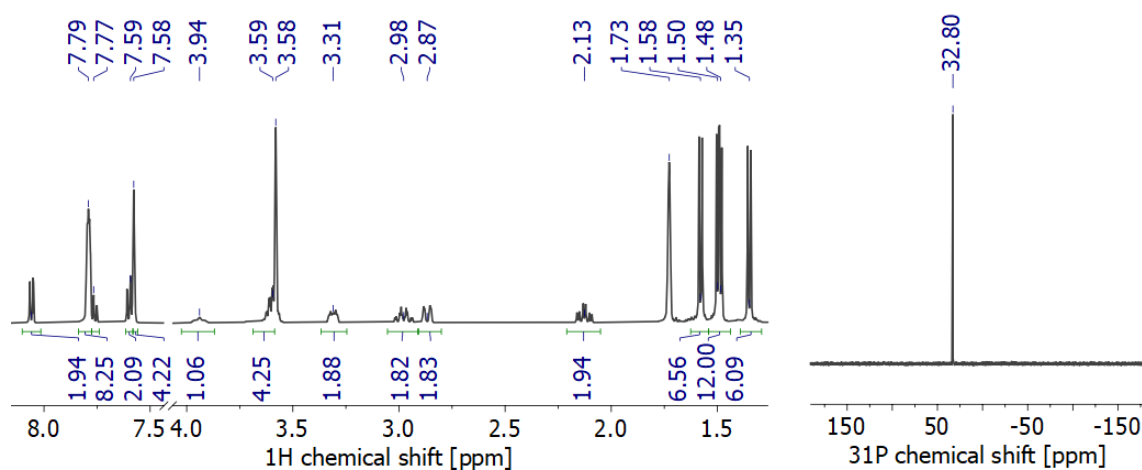


**Figure 3.18**  $^1\text{H}\{^{31}\text{P}\}$  NMR spectrum (left) and  $^{31}\text{P}\{^1\text{H}\}$  NMR (right) spectrum of  $15^{\text{BARF}}$  ( $\text{THF}-d_8$ , RT).

**15<sup>BArF</sup>** is highly soluble in all common commercially available solvents except pentane, but more importantly, there is no evidence for undesired dissociation in any of these solvents. Anion re-exchange with N<sup>n</sup>Hex<sub>4</sub>Br in THF, however, leads to dissociation into nitride complex **13<sup>Br</sup>** and benzoyl bromide (Scheme 3.9, Path D).

The molecular connectivity is analogous to the corresponding cationic bromide complex [ReBr<sub>2</sub>{N(CO)C<sub>6</sub>H<sub>5</sub>}(<sup>n</sup>PN<sup>H</sup>P)]Br (**15<sup>Br</sup>**) (Figure 3.17). Nevertheless, the bond metrics around the metal core are slightly different. The N<sub>pincer</sub>-Re bond length of **15<sup>BArF</sup>** is slightly longer ( $d_{\text{N(pincer)-Re}} = 2.314(16) \text{ \AA}$  (**15<sup>BArF</sup>**) vs.  $2.278(3) \text{ \AA}$  (**15<sup>Br</sup>**)) and the Re-N<sub>imido</sub> bond is shortened ( $d_{\text{Re-N(imido)}} = 1.700(3) \text{ \AA}$  (**15<sup>BArF</sup>**) vs.  $1.724(3) \text{ \AA}$  (**15<sup>Br</sup>**)). This might be caused by less  $\pi$ -donation into the Re-N<sub>imido</sub>  $\pi^*$ -orbital in **15<sup>BArF</sup>** compared to **15<sup>Br</sup>** (Scheme 3.9, Path B). Generally, the observed Re-N<sub>imido</sub> bond lengths are in line with related Re<sup>V</sup> imido complexes where the Re-N bond order is considered intermediate between a double and a triple bond.<sup>57,232–237</sup> The C-O stretching vibration is unaffected upon anion exchange ( $\nu_{\text{CO}} = 1693 \text{ cm}^{-1}$  (**15<sup>Br</sup>**) vs.  $1692 \text{ cm}^{-1}$  (**15<sup>BArF</sup>**)).

The observed, facile *N*-acylation of **13<sup>Br</sup>** at room temperature was not observed in the chloride case emphasizing the benefit of the better leaving group bromide. In this regard, the kinetics of the aminolysis of the benzoyl halides Ph(CO)X (X = F, Cl, Br, I) with morpholine to benzamide strongly depend on the substituted halide expressed by rates that differ by orders of magnitude.<sup>238</sup> The nitride nucleophilicity is suggested to be similar within the series **13<sup>Cl/Br/I</sup>**, as judged by nearly identical Re-N<sub>nitride</sub> bond lengths ( $d_{\text{Re-nitride}} = 1.669(2) \text{ \AA}$  (**13<sup>Cl</sup>**),  $1.663(5) \text{ \AA}$  (**13<sup>Br</sup>**),  $1.659(6) \text{ \AA}$  (**13<sup>I</sup>**)).

Hence, halide variation to bromide has proven to be highly useful, because imido complex **15<sup>BArF</sup>** can be used as a starting point for a comprehensive electrochemical investigation. Information about reduction potentials in absence and presence of protons are of fundamental interest for the application of PCET reactivity, as the transfer of  $2\text{H}^+/2\text{e}^-$  to **15<sup>BArF</sup>** is required for the formation of benzamide.

### 3.2.2 Electrochemical evaluation and reactivity under reductive conditions

This subchapter presents the electrochemical properties of imido complex [ReBr<sub>2</sub>{N(CO)C<sub>6</sub>H<sub>5</sub>}(<sup>n</sup>PN<sup>H</sup>P)]BArF<sub>24</sub> (**15<sup>BArF</sup>**) in absence of a proton source, whereas the following chapter shows how the electrochemical properties are affected by the presence of different acids. The scan rate dependent CV measurement of the Re<sup>V/IV</sup> couple ( $E_{1/2} = -0.71 \text{ V}$ ) of **15<sup>BArF</sup>** is shown in Figure 3.19. This redox event has quasi reversible character as it is irreversible at low scan rates that gradually turns into fully reversible at high scan rates. The shift of 14 mV per decade of the reductive peak potentials anticipates a first order reversible chemical reaction upon electron transfer.<sup>239</sup> Passing the reverse peak leads to the built-up of an additional electrochemical feature at  $E_{\text{p,a}} = -0.42 \text{ V}$ , whose intensity strongly depends on the scan rate. While being very prominent at low scan rates it is fading out with increased scan rates and finally vanishes at 1000 mV/s. Importantly, the ratio

between the sum of the anodic peak currents and the cathodic peak currents is close to unity at least for scan rates between 0.01 – 0.4 V/s (Figure 3.19, right). The peak current ratios for scan rates above 0.4 V/s are not listed as it is difficult to precisely determine the peak current of the small event at  $E_{p,a} = -0.42$  V due to decreasing intensity. Scanning a second cycle shows a reverse peak of this event (Appendix, Figure 6.65), suggesting (quasi)reversibility. However, the low intensity precludes a peak current ratio analysis. In combination with the observed potential peak shift, a chemical follow-up reaction upon reduction of  $\mathbf{15}^{\text{BArF}}$  is suggested, which is resolved on the CV time scale. The nature of this chemical step is discussed below in combination with the CV data of imido complex  $[\text{Re}^{\text{IV}}\text{Br}_2\{\text{N}(\text{CO})\text{C}_6\text{H}_5\}(\text{Pr}^{\text{t}}\text{PN}^{\text{H}}\text{P})]$  ( $\mathbf{16}$ ), being the chemical reduction product of  $\mathbf{15}^{\text{BArF}}$ .

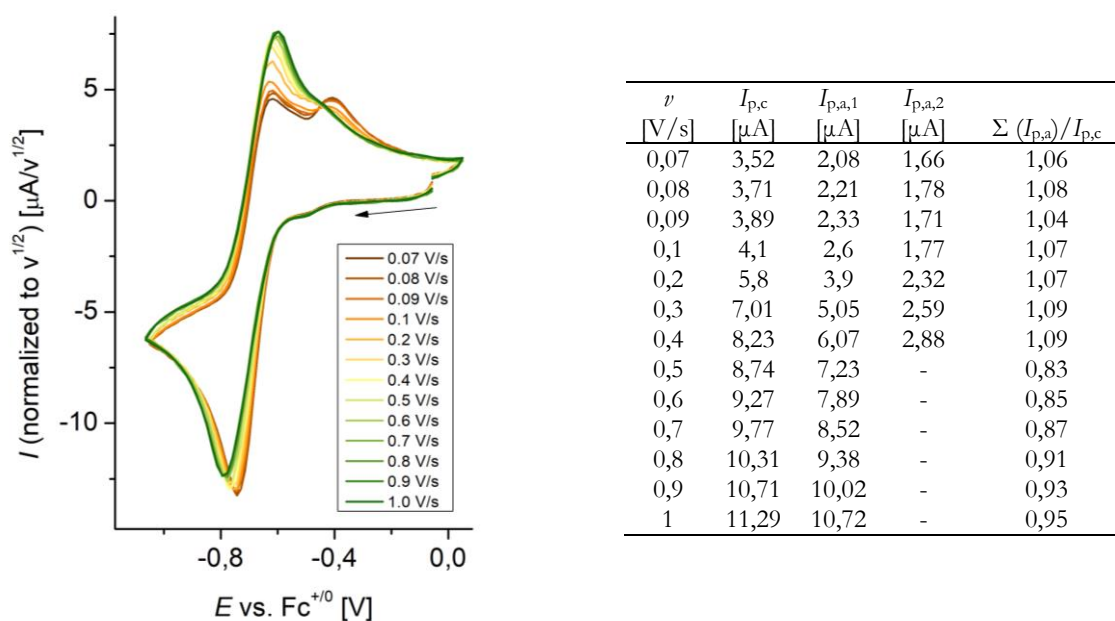


**Figure 3.19 Left:** Selective measurement of the  $\text{Re}^{\text{V/IV}}$  couple of  $\mathbf{15}^{\text{BArF}}$  (1.0 mM; electrolyte: 0.1 M  $\text{N}^{\text{t}}\text{Bu}_4\text{PF}_6$  in THF). **Right:** Table containing cathodic and anodic peak currents including peak current ratio between the sum of the anodic peak currents and the cathodic peak current.

Importantly, nitride benzoylation shifts the  $\text{Re}^{\text{V/IV}}$  wave ( $E_{p,c} = -2.85$  V) about 2 V to milder potentials. Analogously, the  $^t\text{Bu}$  substituted, five-coordinate rhenium nitride complex  $[\text{ReBrN}(\text{Bu}^{\text{t}}\text{PNP})]$   $\mathbf{XV}^{\text{Br}}$  features a reduction potential of  $E_{p,c} = -3.4$  V. By attaching an ethyl group on the nitride ligand, the reduction potential is shifted anodically to  $E_{p,c} = -1.80$  V.<sup>240</sup> Similarly, Schrock reported a  $\text{Mo}^{\text{VI}}$  nitride complex that features a reduction potential of  $E_{1/2} = -2.68$  V<sup>241</sup> shifting to  $E_{1/2} = -1.64$  V<sup>242</sup> upon *N*-alkylation by  $(\text{OEt}_3)\text{BF}_4$ . These potential shifts are larger than the effect of a positive charge, which is about  $\sim 0.5$  V.<sup>243</sup> The huge negative reduction potential of these nitride species represent the strong thermodynamic stabilization of the highly covalent  $\text{M}\equiv\text{N}$  triple bond.<sup>244</sup> Upon N-C bond formation, the bond order and covalency are presumably reduced, resulting in an energetic stabilization of the LUMO ( $\pi^*$ -orbital) (introduction, subchapter 1.2.1).

More negative, an irreversible redox event appears in the CV of  $\mathbf{15}^{\text{BArF}}$ . The shape of this event is also scan rate dependent: While the reduction feature is very broadened and undefined at low scan rates (0 – 1000 mV/s), a sharp irreversible wave is observed at high scan rates (1000 – 5000 mV/s) at  $E_{p,c} = -1.67$  V (Appendix, Figure 6.65). Chemical reduction experiments were conducted with one and two equivalents of chemical reductant to explore the nature of these events.

Reacting  $\text{Re}^{\text{V}}$  imido complex  $\mathbf{15}^{\text{BArF}}$  with one equivalent of cobaltocene ( $E^0 = -1.33$  V in  $\text{CH}_2\text{Cl}_2$ )<sup>220</sup> in toluene at  $-35$  °C leads to an immediate color change into deep red. Extraction with toluene and subsequent crystallization yields  $\text{Re}^{\text{IV}}$  imido complex  $[\text{Re}^{\text{IV}}\text{Br}_2\{\text{N}(\text{CO})\text{C}_6\text{H}_5\}(\text{P}^{\text{H}}\text{PN}^{\text{H}}\text{P})]$  ( $\mathbf{16}$ ) as a red solid with a yield of 85% (Scheme 3.10, top reaction). In accordance to the CV studies (Figure 3.19), decamethyl ferrocene also works as chemical reductant, however, access to elemental pure substance is only achieved by the usage of cobaltocene. The solid-state structure is depicted in Scheme 3.10 and the detailed comparison of the bond metrics to parent  $\mathbf{15}^{\text{BArF}}$  is presented in Figure 3.20.

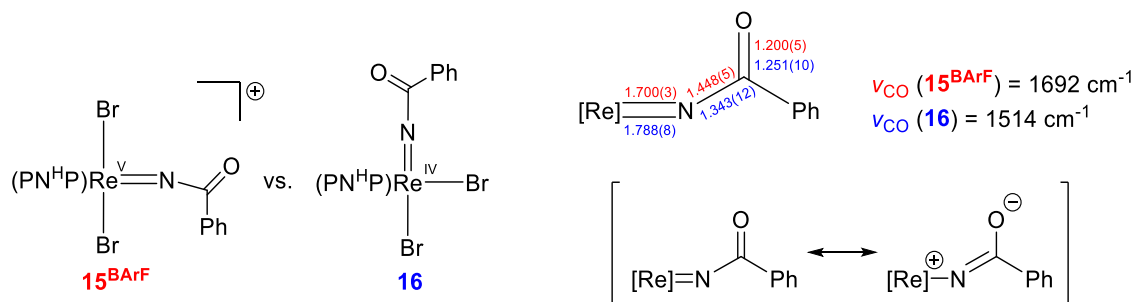
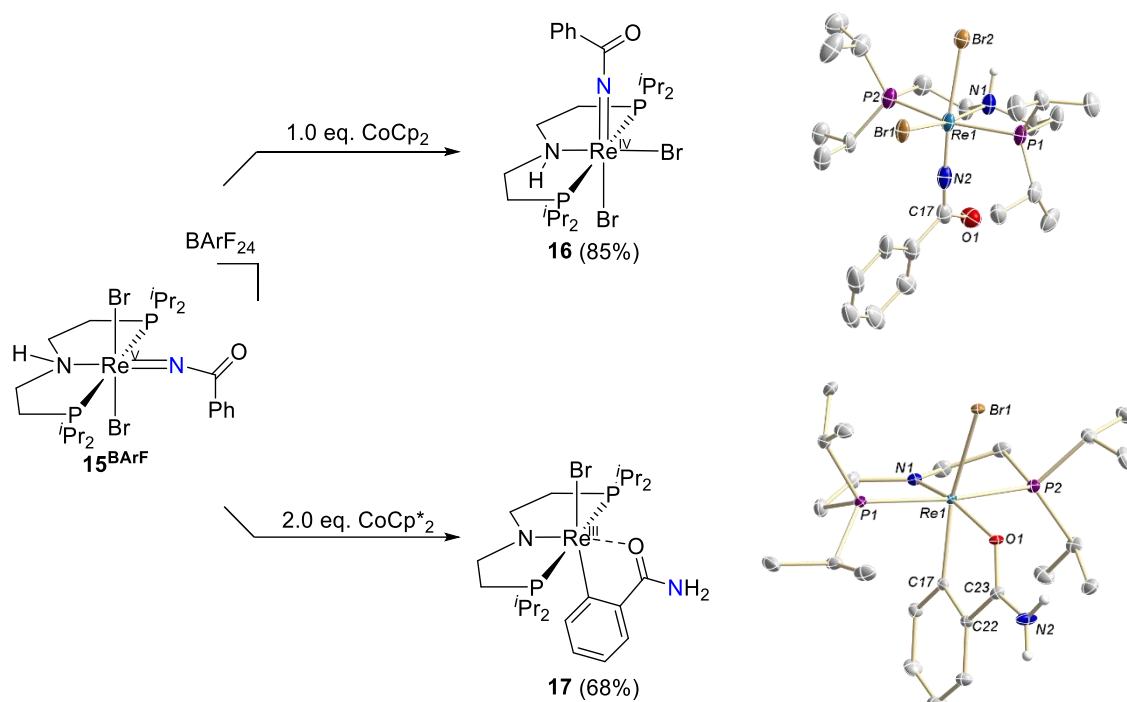


**Figure 3.20** Comparison of the bond metrics between  $\mathbf{15}^{\text{BArF}}$  and  $\mathbf{16}$ .

As XRD analysis revealed, the  $\text{BArF}_{24}$  anion dissociates upon reduction and the imido moiety is rearranged into the apical position. The  $\text{N}_{\text{PNCer}}\text{-Re}$  bond length is therefore less perturbed which is reflected by significant bond shortening ( $d_{\text{N}_{\text{PNCer}}\text{-Re}} = 2.168(7)$  Å ( $\mathbf{16}$ ) vs.  $2.314(16)$  Å ( $\mathbf{15}^{\text{BArF}}$ ). The  $\text{Re-N}_{\text{imido}}$  bond is strongly elongated ( $d_{\text{Re-N}} = 1.788(8)$  Å ( $\mathbf{16}$ ) vs.  $1.700(3)$  Å ( $\mathbf{15}^{\text{BArF}}$ )) indicating further reduction of the  $\text{Re-N}$  bond order by occupation of the corresponding  $\pi^*$ -orbital, as introduced in subchapter 1.2.1.<sup>43,52,156</sup> Furthermore, the bond metrics within the imido moiety are significantly affected upon reduction (Figure 3.20): The  $\text{N-C}_\alpha$  bond within the imido moiety is shortened ( $d_{\text{N-C}} = 1.343(12)$  Å ( $\mathbf{16}$ ) vs.  $1.448(5)$  Å ( $\mathbf{15}^{\text{BArF}}$ )) suggesting double bond character, similar to complexes **XX** and **XXI** discussed in the introduction (Scheme 1.8).<sup>71,72</sup> Moreover, the  $\text{C-O}$  bond is elongated ( $d_{\text{C-O}} = 1.251(10)$  Å ( $\mathbf{16}$ ) vs.  $1.200(5)$  Å ( $\mathbf{15}^{\text{BArF}}$ )) which is corroborated by a shift of the  $\text{C-O}$  stretching vibration in the IR spectrum to lower energy ( $\nu = 1692$   $\text{cm}^{-1}$  ( $\mathbf{15}^{\text{BArF}}$ ) vs.  $1514$   $\text{cm}^{-1}$  ( $\mathbf{16}$ )) (Figure 3.20). Both trends are consistent with partial resonance stabilization of electron density over the  $\{\text{N}(\text{CO})\text{C}_6\text{H}_5\}$  moiety (Figure 3.20) that involves a  $\text{N-C}_\alpha$  double and a  $\text{C-O}$  single bond, typically for amide bonds.<sup>245</sup> This resonance stabilization might also account for the exceptionally low reduction potential of  $\mathbf{15}^{\text{BArF}}$ . In literature, there is only one report of a  $\text{Re}^{\text{IV}}$  imido complex, having a  $\text{Re-N}_{\text{imido}}$  bond length of  $1.75(5)$  Å.<sup>246</sup>



**Scheme 3.10** Chemical one- (top) and two-electron reduction (bottom) of **15**<sup>BARF</sup> to yield **16** and **17**. Molecular structure of **16** and **17** in the solid state drawn at the 50% probability level. Hydrogen atoms (except N-H), disordered moieties and solvent molecules are omitted for clarity. Selected bond length [ $\text{\AA}$ ] and angles [ $^\circ$ ]: **16** N1-Re1 2.168(7), Re1-N2 1.788(8), N2-C17 1.343(12), C17-O1 1.251(10); N1-Re1-Br1 170.9(2), Br2-Re1-N2 170.3, P1-Re1-P2 163.70(8). **17** N1-Re1 1.901(2), N2-C23 1.325(4), C23-O1 1.275(4); N1-Re1-Br1 109.35(8), N1-Re1-O1 166.92(9), Br1-Re1-C17 157.53(8), P1-Re1-P2 166.14(1).

Due to the presence of an unpaired electron, the compound exclusively shows broadened signals in the  $^1\text{H}$  NMR spectrum in the range between  $\delta = -20$  to 25 ppm (Figure 3.21, top). Note, there is a reproducible impurity (2-5%) of complex **18** (the compound will be discussed in detail below) found in the NMR spectrum, judged by the integration versus an internal standard.

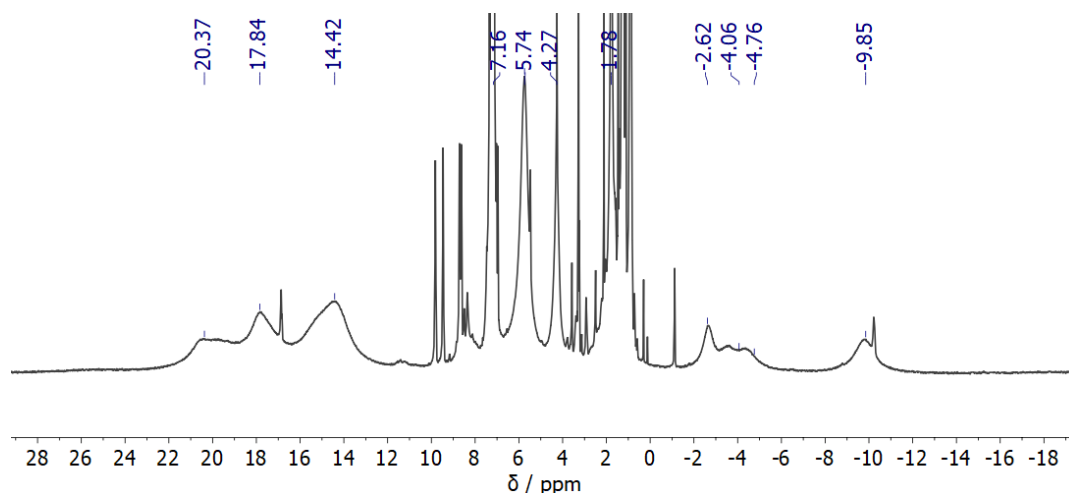


**Figure 3.21**  $^1\text{H}$  NMR spectrum of **16** ( $\text{C}_6\text{D}_6$ , RT).

The  $\text{Re}^{\text{IV}}$  imido complex  $[\text{Re}^{\text{IV}}\text{Br}_2\{\text{N}(\text{CO})\text{C}_6\text{H}_5\}(\text{d}^{\text{Pr}}\text{PN}^{\text{H}}\text{P})]$  (**16**) was investigated by EPR spectroscopy (Figure 3.22). The solution spectrum at room temperature shows a distinctive six-line pattern which arises by hyperfine interaction of the unpaired electron with the  $^{185}\text{Re}$  and  $^{187}\text{Re}$  nuclei, both having a nuclear spin of  $I = 5/2$ . This characteristic signature is in agreement with related, rhenium centered radical species.<sup>247–250</sup> Interestingly, the signal is well-resolved at lower fields and then gradually broadens out towards higher fields. This broadening is suggested to be a tumbling effect in solution.<sup>251</sup> The same sample produces as a more complex spectrum a frozen solution due to  $g$ -anisotropy and hyperfine interaction to other nuclei, for example  $^{31}\text{P}$ ,  $^{14}\text{N}$  and  $^{79}\text{Br}/^{81}\text{Br}$ . In both cases, preliminary simulation attempts were not able to reproduce neither the extreme line broadening in the RT spectrum nor the complex frozen-solution spectrum.

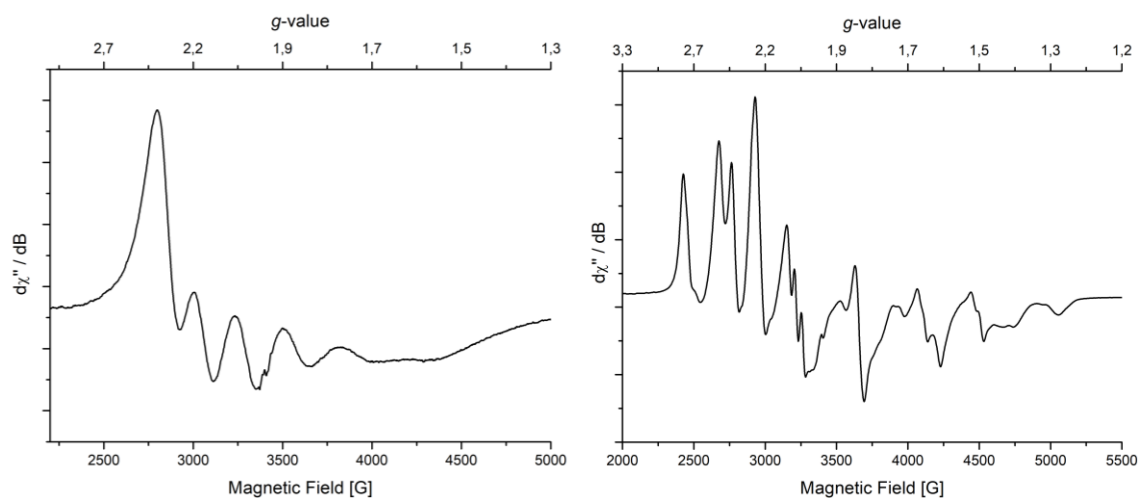


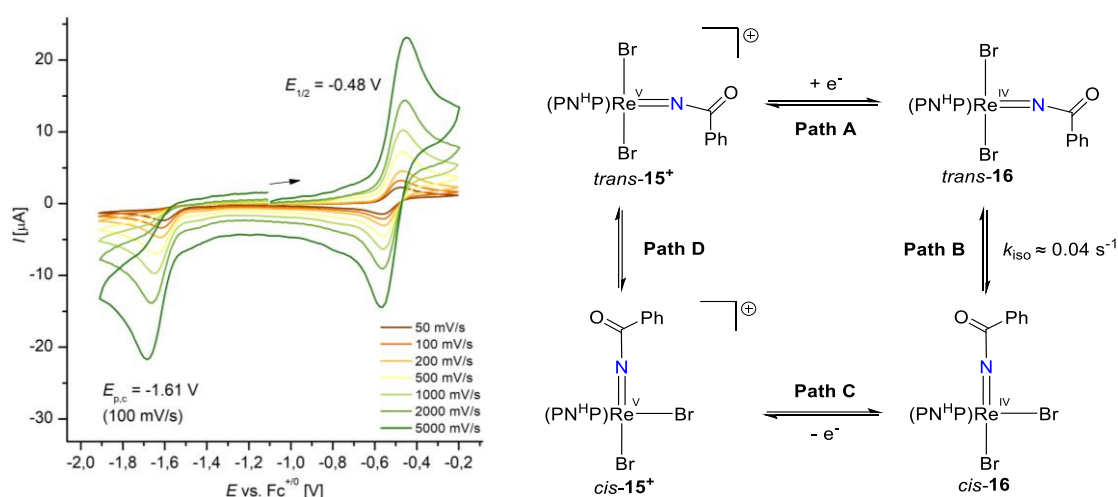
**Figure 3.22** EPR spectroscopy of **16** in toluene at room temperature (**left**) and at 133 K (**right**). EPR-measurements were carried out by Dr. Claudia Stückl (Georg-August-Universität Göttingen).

The cyclic voltammogram of **16** shows a reversible oxidative redox event at a potential of  $E_{1/2} = -0.48$  V ( $\text{Re}^{\text{V/IV}}$ ), which is reversible at all measured scan rates (Scheme 3.11, left). Importantly, this reversible event resembles the minor electrochemical feature of  $\mathbf{15}^{\text{BARF}}$  (Figure 3.19) that was observed after passing the first reductive wave at low scan rates.

A possible explanation for the structural and electrochemical findings of imido complexes  $\mathbf{15}^{\text{BARF}}$  and **16** is provided in Scheme 3.11 (right): Reduction of *trans*- $\mathbf{15}^+$  initially generates a transient species *trans*-**16** (Path A), that rearranges the imido moiety into the apical position, as evidenced by XRD analysis of the isolated substance (Path B). It is assumed, that this isomerization process accounts for the additional oxidative feature discussed in Figure 3.19. Indeed, a first order decay in the scan rate regime between 0.07 and 1 V/s is observed with an estimated rate constant of  $k_{\text{iso}} \sim 0.04$  s<sup>-1</sup>, based on a method from Minteer<sup>252</sup> (Appendix, Figure 6.66). Importantly, the fact that the oxidative  $\text{Re}^{\text{V/IV}}$  couple of *cis*-**16** is fully reversible without any further electrochemical features, might indicate that re-isomerization on the  $\text{Re}^{\text{V}}$  stage (from *cis*- $\mathbf{15}^+$  into *trans*- $\mathbf{15}^+$ , Path D) presumably is not resolved on the CV time scale (Scheme 3.11, left).



However, to validate this hypothesis further experimental work is required which is beyond the scope of this thesis. One suggestion is the chemical oxidation of **16**. If the presumed diamagnetic species *cis*-**15**<sup>+</sup> has a sufficient long lifetime it could be examined by NMR spectroscopy and compared to **15**<sup>BArF</sup> to distinguish *cis*- and *trans*-coordination of the imido group. Moreover, to investigate whether this process proceeds via bromide dissociation, bromide titration to **15**<sup>BArF</sup> in a CV experiment could be conclusive, as the rate for isomerization should correlate with bromide concentration. However, as discussed in Scheme 3.9, **15**<sup>BArF</sup> undergoes salt metathesis in presence of <sup>n</sup>Bu<sub>4</sub>NBr to **15**<sup>Br</sup> that dissociates to rhenium nitride **13**<sup>Br</sup> and benzoyl bromide in THF. Therefore, the CV experiment needs to be performed in a solvent where this dissociation process is suppressed. Finally, the thermochemistry of the isomerization process from *cis*-**15**<sup>+</sup> into *trans*-**15**<sup>+</sup> could be investigated by DFT calculations.



**Scheme 3.11 Left:** Cyclic voltammetry of imido complex **16** (1.0 mM; electrolyte: 0.1 M N<sup>n</sup>Bu<sub>4</sub>PF<sub>6</sub> in THF). **Right:** *Cis/trans*-isomerization of **15**<sup>BArF</sup> upon reduction.

Chemical reduction of **15**<sup>BArF</sup> using two equivalents of decamethyl cobaltocene ( $E^0 = -1.94$  V in CH<sub>2</sub>Cl<sub>2</sub>)<sup>220</sup> in THF leads to a color change from green via deep red into orange brown. Extraction with benzene and filtration over a silica plug (charged with silanized silica) affords complex [Re<sup>III</sup>Br{NH<sub>2</sub>(CO)C<sub>6</sub>H<sub>4</sub>}(<sup>n</sup>PNP)] (**17**) as an orange brown solid with a good yield of 68% (Scheme 3.10, top reaction).

In the solid state, the rhenium center is distorted octahedrally coordinated by the deprotonated PNP ligand and a cyclometalated benzamide ligand in a bidentate fashion, building up a five-membered metallacycle. The N<sub>PNP</sub>-Re bond length is getting significantly shorter ( $d_{\text{Re-N}(\text{pincer})} = 1.901(2)$  Å) compared to parent [ReBr<sub>2</sub>{N(CO)C<sub>6</sub>H<sub>5</sub>}(<sup>n</sup>P<sup>n</sup>H<sup>n</sup>P)]BArF<sub>24</sub> (**15**<sup>BArF</sup>) indicating strong  $\pi$ -donation being in the range for Re<sup>III</sup> complexes with a deprotonated PNP ligand.<sup>41</sup> The bond lengths within the benzamide ligand are nearly identical compared to isolated benzamide ( $d_{\text{C-N}} = 1.343(12)$  Å and  $d_{\text{C-O}} = 1.251(10)$  Å in [Re<sup>III</sup>Br{NH<sub>2</sub>(CO)C<sub>6</sub>H<sub>4</sub>}(<sup>n</sup>P<sup>n</sup>P)] (**17**) vs.  $d_{\text{C-N}} = 1.342(3)$  Å and  $d_{\text{C-O}} = 1.249(3)$  Å in benzamide).<sup>253</sup> The cyclometallation seems unexpected, however,

reduction of  $[\text{Re}^{\text{IV}}\text{Br}_2\{\text{N}(\text{CO})\text{C}_6\text{H}_5\}(\text{P}^{\text{r}}\text{PN}^{\text{H}}\text{P})]$  (**16**) most likely induces halide loss and C-H activation is therefore a consequence of steric unsaturation concomitant to proton transfer onto the imido unit.

Cyclometalated complex **17** shows a singlet in the  $^{31}\text{P}\{^1\text{H}\}$  NMR spectrum at  $\delta = 9.59$  ppm (Figure 3.23, top right). In the  $^1\text{H}\{^{31}\text{P}\}$  NMR spectrum, *J*-resolved signals are observed in the range between  $\delta = 0.75 - 6.87$  ppm (Figure 3.23, top left). The occurrence of four isopropyl groups indicates  $C_s$ -symmetry in solution in agreement with the XRD analysis. The cyclometallation found in the solid-state structure is retained in solution judged by the presence of four, adjacent, chemically inequivalent aromatic protons in the  $^1\text{H}\{^{31}\text{P}\}$  NMR spectrum. Furthermore, the rhenium donating carbon atom splits into a triplet by coupling with the  $^{31}\text{P}$  nuclei ( $^2J_{\text{CP}} = 6.2$  Hz, Figure 3.23, bottom right, purple box) and shows no cross peak in the  $^1\text{H}/^{13}\text{C}$  HSQC. The picture is further supported by NOE contacts between the aromatic protons and the pincer backbone protons ( $\delta = 2.98, 1.62$  ppm) (Figure 3.23, bottom middle, green and orange box). The  $\text{NH}_2$  group appears as a very broadened signal at a chemical shift of  $\delta = 8.58$  ppm presumably caused by fast rotation. The IR spectrum shows the indicative binding modes of the  $\text{NH}_2$  moiety ( $\nu = 3488, 3276, 3205$   $\text{cm}^{-1}$ ) as well as an indicative band that can be assigned to the carbonyl group ( $\nu = 1624$   $\text{cm}^{-1}$ ). The band pattern is close to isolated benzamide.<sup>254</sup> Generally, *ortho*-cyclometalated benzamide ligands are not unprecedented in transition metal complexes.<sup>255,256</sup> Compared to several octahedral  $\text{Re}^{\text{III}}$  species discussed in this work (**10<sup>Cl/Br/I</sup>**) and examples from literature,<sup>200–202,204,209</sup> the NMR signature of this complex is less unusually shifted which indicates an energetically well-separated, closed shell ground state. Generally, arene C-H oxidative addition is known for some  $\text{Re}^{\text{III}}$  complexes utilized in catalytic H/D exchange.<sup>257–259</sup>

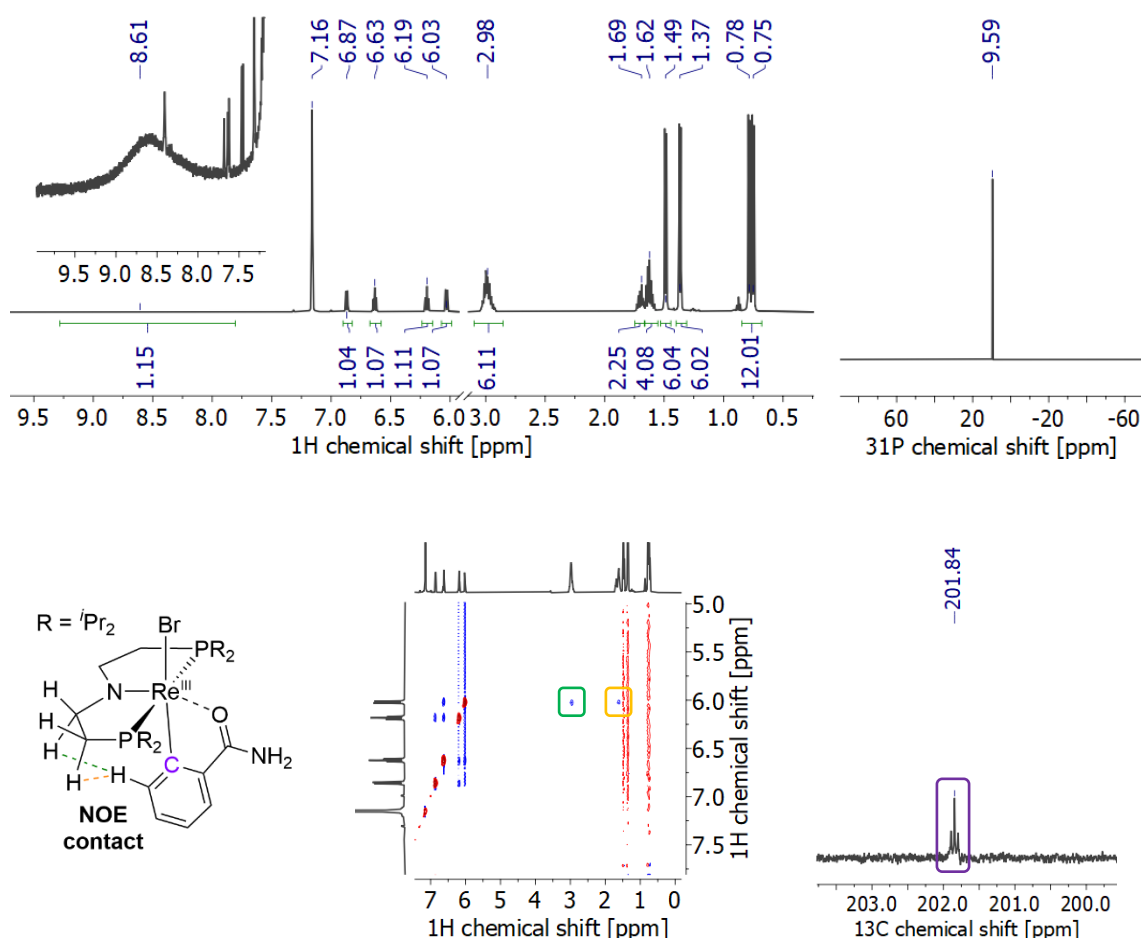
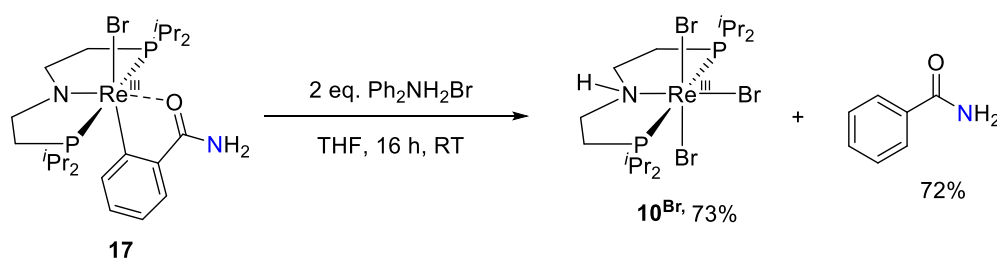


**Figure 3.23** NMR spectroscopy of **17** ( $C_6D_6$ , RT). **Top left:**  $^1H\{^{31}P\}$  NMR spectrum. **Top right:**  $^{31}P\{^1H\}$  NMR spectrum. **Bottom left:** Scheme presenting NOE contacts. **Bottom middle:** NOESY NMR spectrum. **Bottom right:** Presentation of the  $^{13}C$  resonance of the rhenium binding carbon atom in the  $^{13}C\{^1H\}$  NMR spectrum.

The relevance of cyclometalated species  $[Re^{III}Br\{NH_2(CO)C_6H_4\}(\textit{t}PrPNP)]$  (**17**) was tested towards benzamide production. Therefore, it was reacted with two equivalents of diphenylammonium bromide (Scheme 3.12). The reaction was stirred for 16 hours at room temperature and the solvent was removed. The reaction products were quantified by  $^1H$  NMR spectroscopy using 1,3,5-trimethoxy benzene as internal standard: rhenium tribromide complex  $[Re^{III}Br_3(\textit{t}PrPNH^+P)]$  (**10<sup>Br</sup>**) (73%) and benzamide (72%) were identified with good spectroscopic yields closing a synthetic cycle.

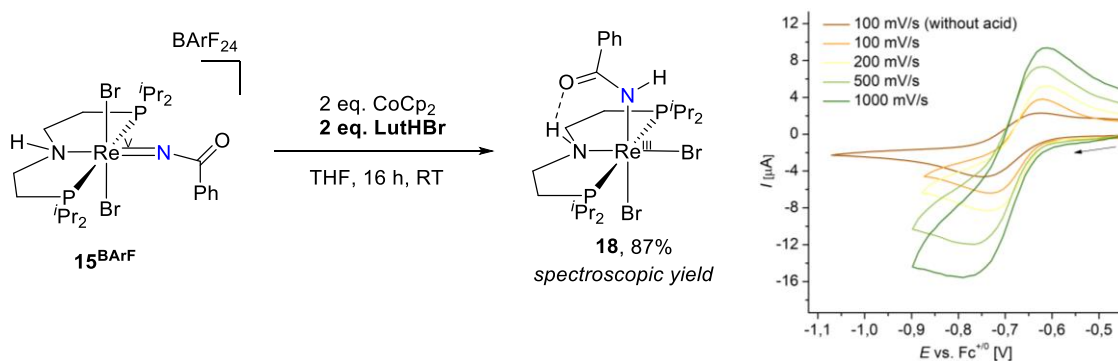


**Scheme 3.12** Benzamide production of **17** upon protonolysis using diphenylammonium bromide.

### 3.2.3 Benzamide production mediated by a rhenium imido complex via PCET

This subchapter focusses on the electrochemical examination of  $[\text{ReBr}_2\{\text{N}(\text{CO})\text{C}_6\text{H}_5\}(\text{}^{\text{Pr}}\text{PN}^{\text{H}}\text{P})]\text{BArF}_{24}$  (**15**<sup>BArF</sup>) in presence of a proton source and on PCET reactivity that forms benzamide and benzonitrile. Compared to the CV trace of the starting material (Scheme 3.13, right, red-brown trace), the addition of 10 eq. of a lutidinium triflate ( $\text{p}K_{\text{a}} = 7.2$  in THF)<sup>260</sup> to a buffered solution of **15**<sup>BArF</sup> induces an anodic peak shift of the  $\text{Re}^{\text{V/IV}}$  couple to  $E_{1/2} = -0.66$  V ( $\Delta E = 50$  mV) (Scheme 3.13, right, orange trace). Moreover, a current increase is observed, indicative for a multielectron process. A pronounced reverse peak indicates reversibility, which was confirmed by scan rate dependent measurement. The qualitative different CV signature in presence of acid anticipates that this reductive wave is coupled to protonation.

Thus, chemical reduction of complex **15**<sup>BArF</sup> was performed using 2 eq. cobaltocene in presence of 2 eq. lutidinium bromide in THF (Scheme 3.13). The main product of this reaction is the octahedral  $\text{Re}^{\text{III}}$  carboxamide  $[\text{Re}^{\text{III}}\text{Br}_2\{\text{NH}(\text{CO})\text{C}_6\text{H}_5\}(\text{}^{\text{Pr}}\text{PN}^{\text{H}}\text{P})]$  (**18**) complex being formed with a spectroscopic yield of 87% (54% isolated yield). In the solid state structure, the rhenium center is coordinated by the pincer ligand and in apical position by a negatively charged carboxamide  $\{\text{NH}(\text{CO})\text{C}_6\text{H}_5\}^-$  ligand (Figure 3.24). There is a close structural relationship to the aforementioned  $\text{Re}^{\text{IV}}$  imido complex  $[\text{Re}^{\text{IV}}\text{Br}_2\{\text{N}(\text{CO})\text{C}_6\text{H}_5\}(\text{}^{\text{Pr}}\text{PN}^{\text{H}}\text{P})]$  (**16**) except the N-H in the imido moiety. This has a significant effect on the  $\text{Re-NH}(\text{CO})\text{Ph}$  bond length which is in **18** tremendously elongated indicating single bond character ( $d_{\text{Re-N}} = 2.113(4)$  Å (**18**) vs.  $1.788(8)$  Å (**16**)).<sup>261</sup>



**Scheme 3.13 Left:** Chemical reduction of **15**<sup>BArF</sup> with cobaltocene in presence of lutidinium bromide. **Right:** Cyclic voltammetry of imido complex **15**<sup>BArF</sup> (1.0 mM; electrolyte: 0.1 M  $\text{N}^{\text{Bu}}_4\text{PF}_6$  in THF) in presence of 10 eq. LutHOTf / Lutidine, at different scan rates. The first CV trace (brown) was recorded in absence of acid with a scan rate of 100 mV/s.

In the  $^1\text{H}\{^{31}\text{P}\}$  NMR spectrum the signals range from  $\delta = -10$  to 225.48 ppm and the  $^{31}\text{P}\{^1\text{H}\}$  NMR spectrum shows a singlet at  $\delta = -1812.0$  ppm, being indicative for strong contributions of temperature independent paramagnetism (TIP), as typical for octahedral  $\text{Re}^{\text{III}}$  complexes with a  $d^4$  electron configuration (Figure 3.24).<sup>200–202,204,209</sup> The  $^1\text{H}/^{15}\text{N}$  HSQC

experiment shows two cross signals at  $\delta = -1165.6$  and  $-1121.0$  ppm identifying the N-H protons ( $^1\text{H}\{^{31}\text{P}\}$  NMR:  $\delta = 225.48$  and  $185.5$  ppm). The CO carbon atom could not be observed in the  $^{13}\text{C}\{^1\text{H}\}$  NMR spectrum which was recorded in the range between  $-50$  to  $450$  ppm. The IR spectrum is in the N-H diagnostic region dominated by a strong band which is suggested to be an electronic transition at  $3422\text{ cm}^{-1}$ . Within this electronic transition, one low-intensity peak appears at  $3348\text{ cm}^{-1}$ , which might be assigned to the N-H protons within the carboxamide ligand. The backbone amine N-H band forms intramolecular hydrogen bonds to the carbonyl group as derived by XRD analysis, leading to line broadening to account for the absence of a second N-H band in the IR spectrum.

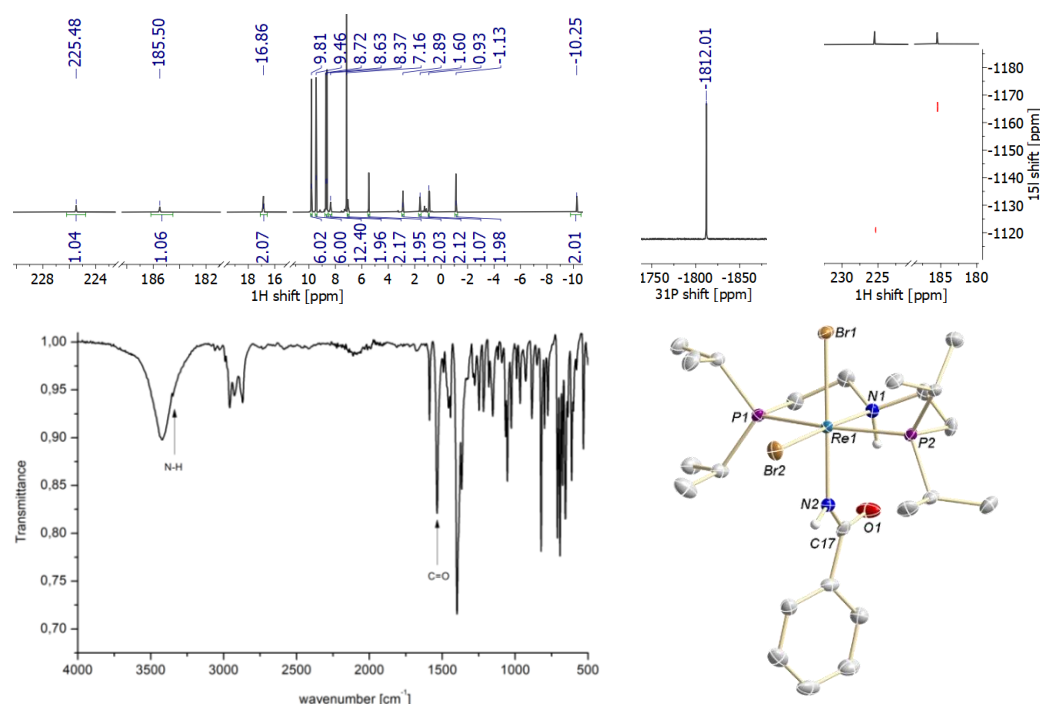
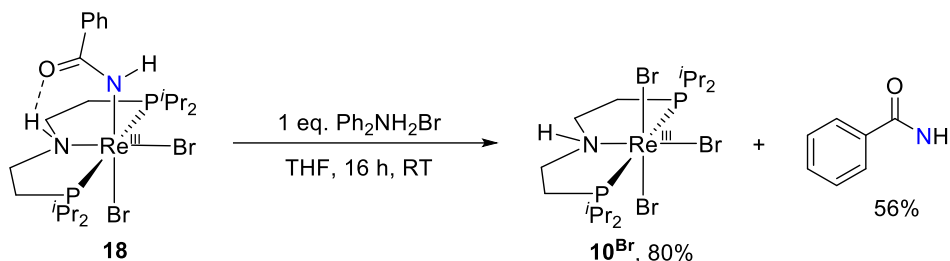


**Figure 3.24** Characterization of  $[\text{Re}^{\text{III}}\text{Br}_2\{\text{NH}(\text{CO})\text{C}_6\text{H}_5\}(\text{P}^r\text{PN}^{\text{H}}\text{P})]$  (**18**).  $^1\text{H}\{^{31}\text{P}\}$  NMR spectrum (**top left**),  $^{31}\text{P}\{^1\text{H}\}$  NMR (**top middle**) and  $^1\text{H}/^{15}\text{N}$  HSQC NMR spectrum (**top right**). NMR spectra recorded in  $\text{C}_6\text{D}_6$  at room temperature. **Bottom left:** IR spectrum. **Bottom Right:** Molecular structure in the solid state. Hydrogen atoms (except N-H) and solvent molecules are omitted for clarity. Selected bond length and angles: [ $\text{\AA}$ ] and angles [ $^\circ$ ]: N1-Re1 2.161(5), Re1-N2 2.113(4), N2-C17 1.289(7), C17-O1 1.259(7); N1-Re1-Br2 177.47(13), Br1-Re1-N2 176.63(12), P1-Re1-P2 163.19(5).

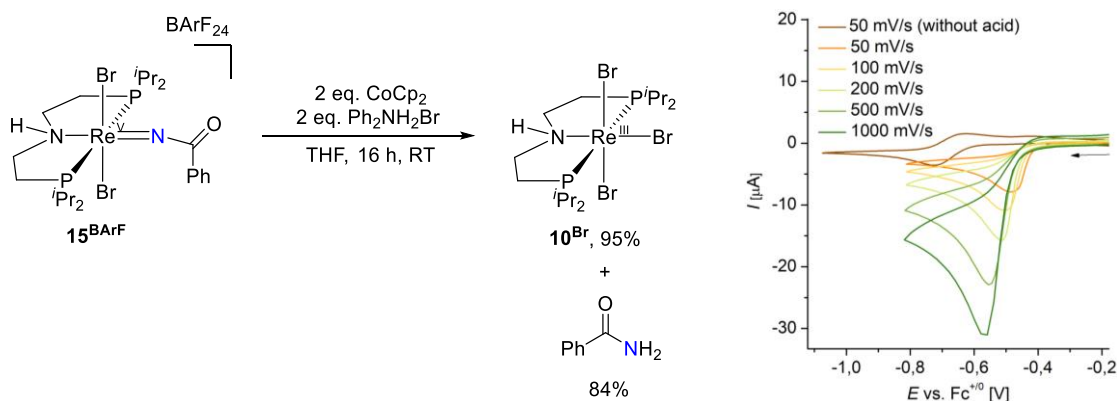
The identification of carboxamide complex **18** can rationalize the CV data of  $\mathbf{15}^{\text{BArF}}$  in presence of lutidinium triflate (Scheme 3.13, right). As **18** is the formal product of hydride transfer to  $\mathbf{15}^{\text{BArF}}$ , the reversible redox event at  $E_{1/2} = -0.66\text{ V}$  has to be regarded as two merged  $\text{e}^-$  transfer steps whereby one of them is coupled to protonation. Since the  $\text{Re}^{\text{IV/III}}$  couple is much more anodically shifted in presence of protons than the  $\text{Re}^{\text{V/IV}}$  couple ( $+1.01\text{ V}$  and  $+50\text{ mV}$ , respectively), the former is assigned as the PCET step. Hence, the formation of carboxamide complex **18** can be seen as incomplete protonation with respect of benzamide production. Nevertheless, the presence of traces tribromide  $\mathbf{10}^{\text{Br}}$  (3% spectroscopic yield, Scheme 3.13 (top)) might suggest a protonation equilibrium of carboxamide complex **18** with lutidinium. Therefore, the reactivity of **18** was tested with the stronger acid diphenylammonium bromide which has a  $\text{p}K_{\text{a}}$  value of 0.6 in THF.<sup>262</sup>

Complex **18** was stirred with an equimolar amount diphenylammonium bromide for 16 hours (Scheme 3.14). The reaction products were quantified by  $^1\text{H}$  NMR spectroscopy using 1,3,5-trimethoxy benzene as internal standard after removal of the solvent. Indeed,  $[\text{Re}^{\text{III}}\text{Br}_3(\text{}^{\text{tPr}}\text{PN}^{\text{H}}\text{P})]$  (**10<sup>Br</sup>**) (80%) and benzamide (56%) were quantified in good yields.



**Scheme 3.14** Benzamide production of  $[\text{Re}^{\text{III}}\text{Br}_2\{\text{N}(\text{CO})\text{C}_6\text{H}_5\}(\text{}^{\text{tPr}}\text{PN}^{\text{H}}\text{P})]$  (**18**) via protonolysis using diphenylammonium bromide.

Based on these observations the electrochemical properties of  $[\text{Re}^{\text{V}}\text{Br}_2\{\text{N}(\text{CO})\text{C}_6\text{H}_5\}(\text{}^{\text{tPr}}\text{PN}^{\text{H}}\text{P})]\text{BARF}_{24}$  (**15<sup>BARF</sup>**) were examined in presence of 10 eq. diphenyl ammonium triflate (Scheme 3.14, right). In contrast to the CV signature of **15<sup>BARF</sup>** in absence of acid (Scheme 3.14, right, brown trace), a significantly anodically shifted, irreversible wave evolves with increased peak current (Scheme 3.15, right, orange trace). Irreversibility is maintained even at high scan rates (1000 mV/s), as no reverse peak appears. The peak potentials are shifting cathodically about 90 mV per decade suggesting follow-up reactivity.



**Scheme 3.15 Left:** Benzamide production by **15<sup>BARF</sup>** via PCET. **Right:** CV measurement (0.1 M in 0.2 M  $\text{N}^{\text{tBu}}\text{PF}_6$  in THF) of **15<sup>BARF</sup>** in presence of 10 eq.  $\text{Ph}_2\text{NH}_2\text{OTf}$  /  $\text{Ph}_2\text{NH}$  at different scan rates (vs.  $\text{Fc}^{+/0}$ ).

Accordingly, imido complex **15<sup>BARF</sup>** was chemically reduced with 2 eq. cobaltocene in presence of 2 eq. diphenyl ammonium bromide in THF (Scheme 3.15, left). The reaction was stirred for 16 hours and the reaction mixture was investigated by  $^1\text{H}$  NMR spectroscopy (Figure 3.25). At lower fields three diagnostic signals are observed at  $\delta = 9.69$ , 9.27 and 8.66 ppm (Figure 3.25, top left spectrum), belonging to the isopropyl groups of rhenium tribromide complex  $[\text{Re}^{\text{III}}\text{Br}_3(\text{}^{\text{tPr}}\text{PN}^{\text{H}}\text{P})]$  (**10<sup>Br</sup>**) being formed with a spectroscopic yield of 95% (Scheme 3.15). This is validated by a dominant signal in the  $^{31}\text{P}\{^1\text{H}\}$  NMR spectrum at  $\delta = -1496.9$  ppm (Figure 3.25, bottom spectrum). The three signals in the aromatic region

in the  $^1\text{H}$  NMR spectrum at  $\delta = 7.81$ , 7.53 and 7.47 ppm identify benzamide (spectroscopic yield: 84%) matching the NMR signature of commercially purchased substance (Figure 3.25, top right spectra). Both products were identified by high-resolution mass spectrometry (ESI<sup>+</sup>).

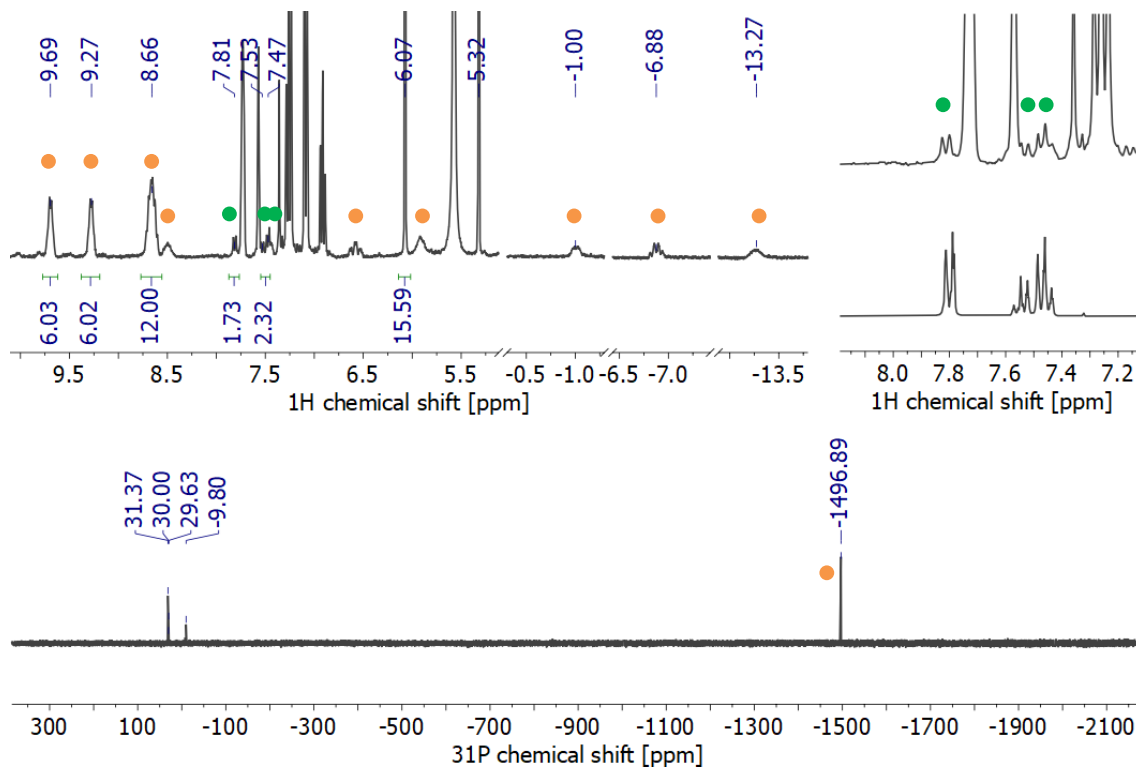


**Figure 3.25**  $^1\text{H}$  NMR Quantification of benzamide (green dots) and  $10^{\text{Br}}$  (orange dots) recovery in  $\text{CD}_2\text{Cl}_2$  using 1,3,5-trimethoxy benzene as internal standard. **Top left:**  $^1\text{H}$  NMR spectrum. **Top right:** Comparison of the  $^1\text{H}$  NMR spectra the reaction mixture (top spectrum) with commercially purchased benzamide (bottom spectrum). **Bottom:**  $^{31}\text{P}\{^1\text{H}\}$  NMR spectrum.

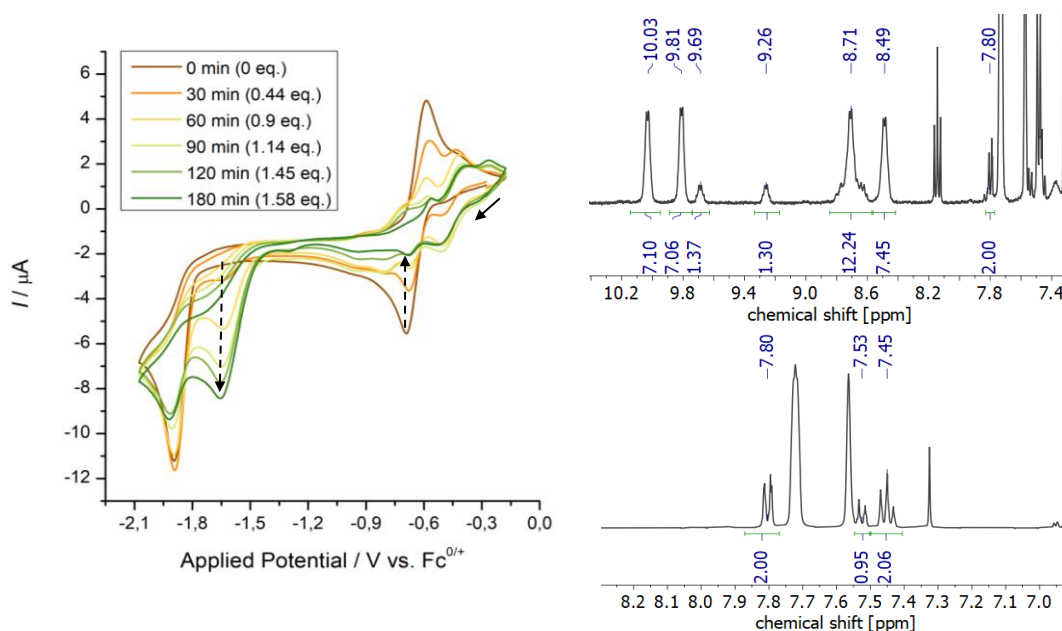
To conclude, a synthetic protocol was established for benzamide formation via PCET. The selectivity can be driven by the  $\text{p}K_{\text{a}}$  value of the acid: While reduction with cobaltocene in presence of lutidinium ( $\text{p}K_{\text{a}} = 7.2$  in THF)<sup>260</sup> facilitates hydride transfer forming carboxamide complex  $[\text{Re}^{\text{III}}\text{Br}_2\{\text{NH}(\text{CO})\text{C}_6\text{H}_5\}(\text{PrPN}^{\text{H}}\text{P})]$  (**18**), benzamide production and reformation of rhenium tribromide complex  $[\text{Re}^{\text{III}}\text{Br}_3(\text{PrPN}^{\text{H}}\text{P})]$  ( $10^{\text{Br}}$ ) in high spectroscopic yields is achieved by using diphenyl ammonium bromide as acid ( $\text{p}K_{\text{a}} = 0.6$  in THF)<sup>262</sup>. The latter result is of fundamental importance because it demonstrates *N*-functionalization of an  $\text{N}_2$ -derived imido species at ambient conditions that closes a synthetic cycle.

### 3.2.4 Electrochemical benzamide formation via PCET

In accordance to the capability of the cationic imido complex  $[\text{Re}^{\text{V}}\text{Br}_2\{\text{N}(\text{CO})\text{C}_6\text{H}_5\}(\text{PrPN}^{\text{H}}\text{P})]\text{BArF}_{24}$  (**15<sup>BArF</sup>**) to produce benzamide via PCET, the analogous electrochemical transformation was intended to surrogate the chemical reductant.

As shown in Scheme 3.16 (left), the CV trace before electrolysis (brown trace) in presence of 2 eq. of lutidinium triflate shows a reversible wave at  $E_{1/2} = -0.66$  V, that was associated

with a  $2e^-/1H^+$  transfer step forming carboxamide complex  $[Re^{III}Br_2\{NH(CO)C_6H_5\}(^{Pr}PN^H P)]$  (**18**) (subchapter 3.2.3). The irreversible wave at a potential of  $E_{p,c} = -1.89$  V is assigned to proton reduction of lutidinium triflate, confirmed in a separate experiment of the isolated acid. The former redox event can be used as an indicator for the reaction progress. After electrolyzing at  $-0.85$  V for 30 minutes in presence of 2 eq. of lutidinium triflate, 0.44 eq. electrons have been transferred and a color change was observed from green to yellow. The control CV experiment after 30 minutes indicates significant decay of the starting material, accompanied by the rise of an irreversible event  $E_{p,c} = -1.65$  V. Further electrolysis gradually decays the former and rises the latter event. Over the course of three hours 1.58 eq. electrons were transferred and the electron transfer rate slows down. The control CV indicates almost full conversion of **15**<sup>BArF</sup> and the reaction products were quantified by  $^1H$  NMR spectroscopy.

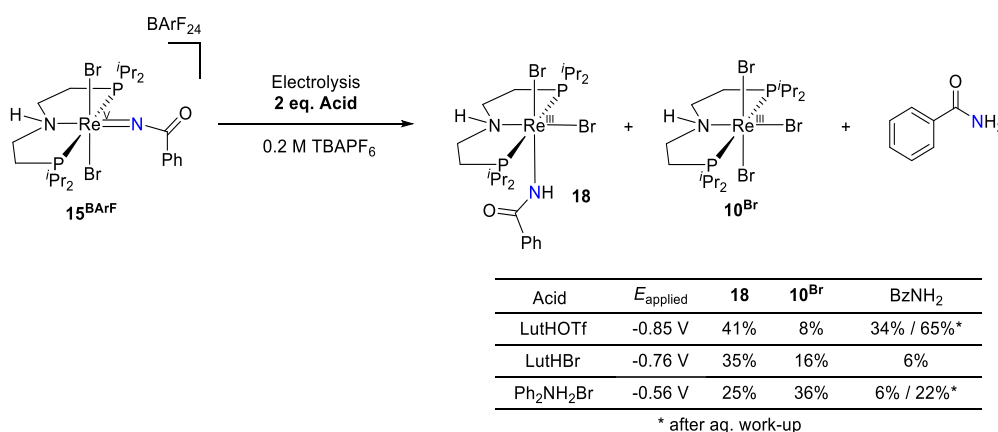


**Scheme 3.16** Analytical data of the electrochemical conversion of imido complex **15**<sup>BArF</sup> into benzamide via PCET. **Left:** Progress of the CPE experiment, monitored by cyclic voltammetry at a scan rate of 50 mV/s. Dotted arrows represent decrease/increase of peak currents and the solid arrow the scan direction. **Right:**  $^1H$  NMR spectroscopy of the crude product before (top spectrum,  $CD_2Cl_2$ ) and after work-up (bottom spectrum,  $CDCl_3$ ).

The crude product was extracted with benzene to remove the majority of the electrolyte. The  $^1H$  NMR spectrum in  $CD_2Cl_2$  is depicted in Scheme 3.16 (top). In the low-field region two sets of signals occur, as judged by integration. One of these ( $\delta = 10.03, 9.81, 8.71, 8.49$  ppm) can be assigned to carboxamide complex **18**, supported by a diagnostic  $^{31}P\{^1H\}$  NMR signal at  $\delta = -1873.3$  ppm. The second, partially superimposed set of signals ( $\delta = 9.69, 9.26, 8.77, 8.63$  ppm) identifies rhenium tribromide complex **10**<sup>Br</sup> which coincides with a singlet at  $\delta = -1493.9$  ppm in the  $^{31}P\{^1H\}$  NMR spectrum. The integration versus 1,3,5-trimethoxy benzene as internal standard determines spectroscopic yields of 41% and 8%, respectively (Scheme 3.17). Importantly, both complexes exhibit a nearly identical CV signature ( $E_{1/2}$  (**10**<sup>Br</sup>) =  $-1.66$  V ( $Re^{III/II}$ ),  $-0.22$  V ( $Re^{IV/V}$ );  $E_{1/2}$  (**18**) =  $-1.69$  V ( $Re^{III/II}$ ),  $-0.19$  V



( $\text{Re}^{\text{IV/V}}$ ) which cannot be distinguished in the control CV measurements in Scheme 3.16. There is no plausible explanation for the presence of  $[\text{Re}^{\text{III}}\text{Br}_3(\text{P}^{\text{Pr}}\text{N}^{\text{H}}\text{P})]$  ( $\mathbf{10}^{\text{Br}}$ ) because its formation requires a bromide source. Nevertheless, the relatively low yield might indicate trace impurities from the electrolyte which is used in huge excess (0.2 M). The spectroscopic yield for rhenium compounds is only 49%, the fate of the residual 51% remains unclear. It is therefore not unlikely that some species are formed which decompose under bromide release. The formation of paramagnetic (NMR silent) species could provide another explanation to account for the moderate yield of rhenium species. The doublet in the  $^1\text{H}$  NMR spectrum at  $\delta = 7.80$  ppm in the crude product corresponds to the *ortho*-protons of benzamide, being formed with a spectroscopic yield of 34%. The product distribution was confirmed by high-resolution mass spectrometry (ESI<sup>+</sup>). Importantly, the spectroscopic yield of benzamide could be increased up to 65% by a basic work-up (Scheme 3.16, bottom right spectrum). The stability of benzamide was evaluated under the conditions of the basic work-up revealing no indication for decomposition. In fact, hydrolysis of benzamide to benzoic acid requires long reaction times and high temperatures (80 °C).<sup>263</sup>



**Scheme 3.17** The formation of benzamide by electrolysis of imido complex  $\mathbf{15}^{\text{BArF}}$  via PCET.

Using lutidinium bromide as acid leads to a slightly different product distribution. Carboxamide complex **18** (35%) and rhenium tribromide complex  $\mathbf{10}^{\text{Br}}$  (16%) were identified while the spectroscopic yield of benzamide is much lower (6%) (experimental details in subchapter 4.4.4). The occurrence of rhenium nitride complex  $\mathbf{13}^{\text{Br}}$  (17%) and benzoyl bromide (13%) can be explained by partial dissociation, introduced by salt metathesis of  $\mathbf{15}^{\text{BArF}}$  with lutidinium bromide, as  $\mathbf{15}^{\text{Br}}$  dissociates in THF (Scheme 3.9). Electrolysis with diphenyl ammonium bromide as proton source produced carboxamide complex **18** (25%), and rhenium tribromide  $\mathbf{10}^{\text{Br}}$  (36%) and low amounts of benzamide (6%).

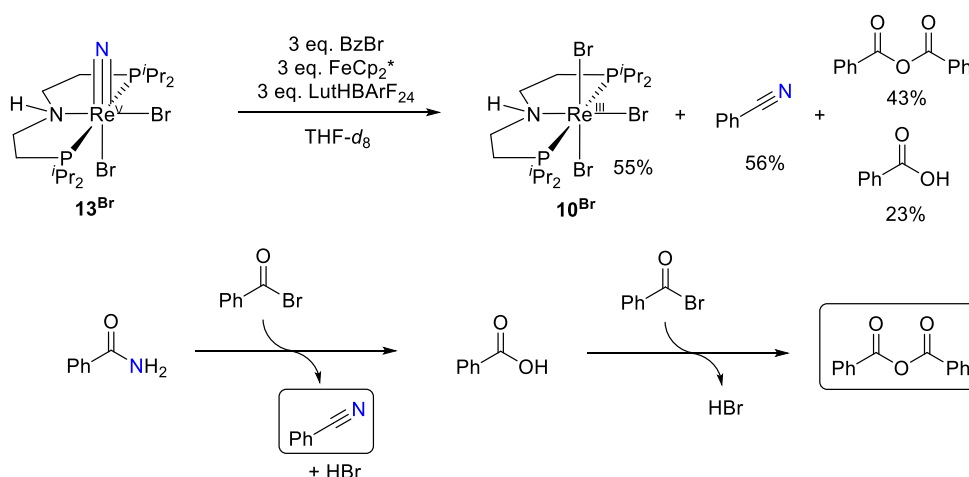
To conclude, controlled potential electrolysis obtained **18**,  $\mathbf{10}^{\text{Br}}$  and benzamide in moderate spectroscopic yields. An additional aqueous work-up of the crude product increased the spectroscopic yield for benzamide production up to 65%, considering that all rhenium compounds are decomposed under these conditions.

### 3.2.5 Nitride transfer forming benzonitrile via PCET

The transfer of atmospheric dinitrogen into an organic molecule includes the fundamental steps such as N<sub>2</sub> fixation, N-N bond cleavage, N-C bond formation and product release. The combination of all these single steps is prerequisite if catalytic N-functionalization is envisioned, which is challenging, because these steps often require very individual conditions that do not allow for compatibility.

In subchapter 3.1.5, a unique protocol was presented combining those first two elemental steps generating nitride species by light-supported electrolysis that undergo promising reactivity with benzoyl bromide. But still, benzoyl bromide and lutidinium triflate exhibit onset reduction potentials of around  $-1.70$  V, being accessible for decamethyl cobaltocene ( $E^0 = -1.94$  V)<sup>220</sup> and close to cobaltocene ( $E^0 = -1.33$  V),<sup>220</sup> which are both common reductants for N<sub>2</sub> fixation and functionalization. For this reason, it is of interest to find an alternative reductant with a sufficient mild reduction potential that substrate reduction can be circumvented. In this regard, this subchapter focusses on the combination of the N-acylation step of nitride **13<sup>Br</sup>** with subsequent PCET steps. The unusual low reduction potential of the cationic imido complex **15<sup>BARF</sup>** is exploited ( $E_{1/2} = -0.71$  V), accessed by the mild reductant decamethyl ferrocene being chemically inert towards lutidinium BARF<sub>24</sub>, lutidine and benzoyl bromide.

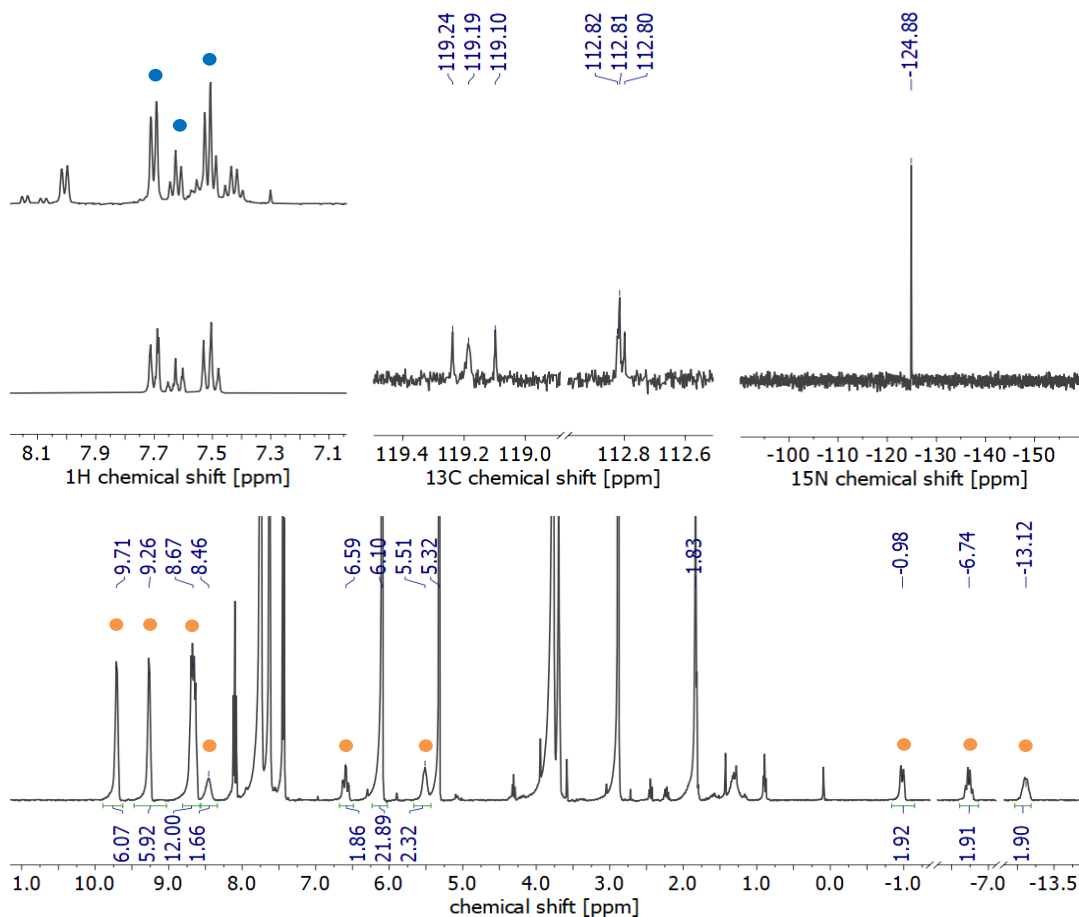
The reaction of rhenium nitride **13<sup>Br</sup>** with 3 eq. benzoyl bromide, 3 eq. decamethyl ferrocene and 3 eq. lutidinium BARF<sub>24</sub> was investigated in THF-*d*<sub>8</sub> (Scheme 3.18. top reaction). Starting from an orange solution, the color changes within minutes via orange-red to yellow over the course of hours. The reaction progress was controlled by <sup>31</sup>P{<sup>1</sup>H} NMR spectroscopy of the reaction solution after 16 hours reaction showing one dominant signal at  $\delta = -1514.1$  ppm characteristic for [Re<sup>III</sup>Br<sub>3</sub>(<sup>i</sup>PrPN<sup>H</sup>P)] (**10<sup>Br</sup>**).



**Scheme 3.18 Top:** Nitride transfer under one-pot-conditions generating benzonitrile and benzoic anhydride. **Bottom:** Reaction pathway of benzamide in presence of benzoyl bromide.

The volatiles were removed via trap to trap condensation and benzonitrile was identified by <sup>1</sup>H NMR spectroscopy with a spectroscopic yield of 57%, matching the NMR signature of

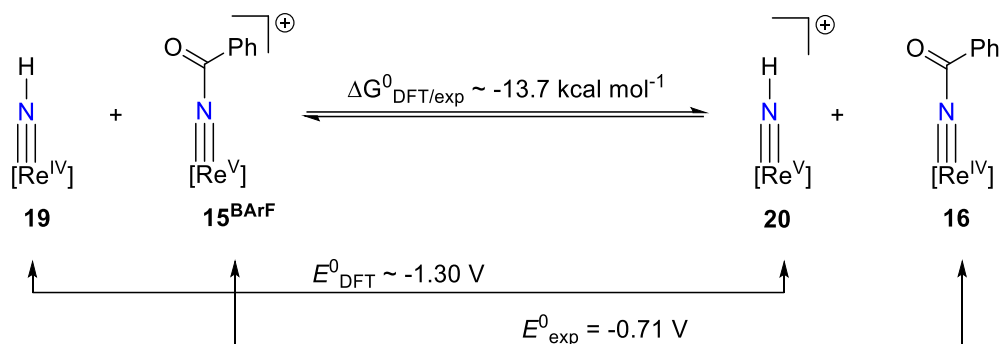
commercially purchased substance (Scheme 3.19, top left, marked with blue dots). The usage of isotopic labelled  $^{15}\text{N}$ - $\mathbf{13}^{\text{Br}}$  gave rise to  $\text{Ph-C}^{15}\text{N}$  which occurs as a singlet in the  $^{15}\text{N}\{^1\text{H}\}$  NMR spectrum at  $\delta = -124.9$  ppm evidencing that transferred nitrogen originates from the rhenium nitride complex (Scheme 3.19).<sup>72,73,264</sup> The presence of the  $^{15}\text{N}$  isotopologue (nuclear spin  $I = 1/2$ ) splits the  $\text{Ph-C}^{15}\text{N}$  carbon atom into a doublet ( $\delta = 119.2$  ppm,  $^1J_{\text{C-}^{15}\text{N}} = 17.8$  Hz) as well as the  $\text{C}_{\text{ipso}}$  atom at ( $\delta = 112.8$  ppm,  $^2J_{\text{C-}^{15}\text{N}} = 3.0$  Hz) (Scheme 3.19, top middle) in agreement with literature.<sup>264</sup> Finally, GC-MS analysis confirmed benzonitrile formation for both isotopologues (Appendix, 4.4.1).



**Scheme 3.19** Benzonitrile formation via *N*-transfer. **Top left:**  $^1\text{H}$  NMR spectrum of the volatiles (top spectrum) and of commercially purchased benzonitrile (bottom spectrum), both recorded in  $\text{THF } d_8$ . **Top middle:** Zoomed aromatic region of the  $^{13}\text{C}\{^1\text{H}\}$  NMR spectrum of  $^{15}\text{N}$ -labelled, volatile crude product (measured in  $\text{CD}_2\text{Cl}_2$ ). **Top right:**  $^{15}\text{N}\{^1\text{H}\}$  NMR of the volatiles (measured in  $\text{CD}_2\text{Cl}_2$ ). **Bottom:**  $^1\text{H}$  NMR spectrum ( $\text{THF}$  extract, measured in  $\text{CD}_2\text{Cl}_2$ ).

Beside the identification of benzonitrile, the product composition on the organic side is at that point not explored in detail. Among the organic product mixture, benzoic anhydride and (43%) benzoic acid (23%) could be identified. These products could potentially be formed by the reaction of benzamide with benzoyl bromide forming benzonitrile and benzoic acid which react with benzoyl bromide to benzoic anhydride (Scheme 3.18, bottom reaction).<sup>265,266</sup> Importantly, rhenium tribromide complex  $\mathbf{10}^{\text{Br}}$  is reformed with a spectroscopic yield of 55% (Scheme 3.19, bottom).

Despite the fact that ammonia production is also a potential reaction path, the main product on the organic side is benzonitrile. The origin of the selectivity of this reaction was examined by DFT<sup>k</sup> calculations. Therefore, the electron cross equilibrium of **15**<sup>BArF</sup>/**16** and [Re<sup>IV</sup>Br<sub>2</sub>{NH}(<sup>Ar</sup>PN<sup>H</sup>P)] (**19**) / [Re<sup>V</sup>Br<sub>2</sub>{NH}(<sup>Ar</sup>PN<sup>H</sup>P)]<sup>+</sup> (**20**) (Complex **19** and **20** are computed compounds) was determined within the isodesmic reaction shown in Scheme 3.20 being thermodynamically downhill by  $\Delta G_{\text{DFT/exp}}^0 \sim -13.7 \text{ kcal mol}^{-1}$ . This equates to a potential difference of  $\Delta E_{\text{DFT/exp}}^0 = -0.59 \text{ V}$  between both redox couples which reasonably explains the preference of benzoyl- over proton-coupled electron transfer. Hence, the reduction potential of cationic imido complex **20** can be estimated as  $E^0 \sim -1.30 \text{ V}$ .



**Scheme 3.20** Electron cross equilibrium of **15**<sup>BArF</sup>/**16** (exp.) and **19**/**20** (DFT).

Furthermore, the thermodynamics for ammonia production of [Re<sup>V</sup>Br<sub>2</sub>N(<sup>Ar</sup>PN<sup>H</sup>P)] **13**<sup>Br</sup> were computed which revealed a very low BDFE for the first N-H bond (36.8 kcal mol<sup>-1</sup>) and significant higher N-H bond strengths for the corresponding amide and ammine complex (72.1 and 57.9 kcal mol<sup>-1</sup>, respectively). This trend resembles the computed bond strengths of 43 and 78 kcal mol<sup>-1</sup> for the first two N-H bonds in the closely related complex [Re<sup>V</sup>Cl<sub>2</sub>N(<sup>Ar</sup>PONOP)] **XVII** reported by Miller (among other examples, see introduction: subchapter 1.2.3).<sup>44</sup> Thus, ammonia production might be unsuitable for this platform because it requires very strong PCET reagents and the low N-H bond strength might favor hydrogen evolution (BDFE (H<sub>2</sub>) = 97.2 kcal mol<sup>-1</sup>).<sup>2,9,44,101,267</sup> This thermodynamic challenge is circumvented by an initial Bz<sup>+</sup>/e<sup>-</sup> step that forms a stable N-C instead of an unstable N-H bond.

### 3.2.6 Concluding remarks

The introduction of bromide ligands provided access to a nucleophilic, N<sub>2</sub> derived rhenium nitride species [Re<sup>V</sup>Br<sub>2</sub>N(<sup>Ar</sup>PN<sup>H</sup>P)] (**13**<sup>Br</sup>) that reacts with benzoyl bromide at room temperature within an equilibrium ( $K = 1.1 \cdot 10^{-5} \text{ M}^{-1}$ ) to form the corresponding imido complex [Re<sup>V</sup>Br<sub>2</sub>{N(CO)C<sub>6</sub>H<sub>5</sub>}(<sup>Ar</sup>PN<sup>H</sup>P)]Br (**15**<sup>Br</sup>). As dissociation is favored in THF, the bromide anion was replaced by BArF<sub>24</sub>. By contrast, **15**<sup>BArF</sup> was found to be stable and does

<sup>k</sup> DFT calculations were performed by M. Sc. Severine Rupp (AK Krewald, Technische Universität Darmstadt). Computational details: ORCA 4.2.1; UKS PBE RI D3BJ Grid7 CPCM(THF); for Re, Br, N, P, O, H def2-TZVP def2/J; for C def2-SVP def2/J; Charge: 0

not undergo undesired dissociation allowing for an electrochemical examination in THF. A tremendously shifted reduction potential of about 2 V was observed compared to the parent nitride species ( $E_{1/2}(\text{Re}^{\text{V/IV}}) = -0.71 \text{ V} (\mathbf{15}^{\text{Br}}), -2.92 \text{ V} (\mathbf{13}^{\text{Br}})$ ), which was explained by charge stabilization over the benzoyl moiety as judged by significant changes of the bond metrics of the reduced species  $[\text{Re}^{\text{IV}}\text{Br}_2\{\text{N}(\text{CO})\text{C}_6\text{H}_5\}(\text{PrPN}^{\text{H}}\text{P})]$  (**16**). Interestingly, the reduction of **15**<sup>BArF</sup> to **16** shifts the imido moiety into the apical position with a rate that is resolved on the CV time scale ( $k_{\text{iso}} \sim 0.04 \text{ s}^{-1}$ ). A distinctive 6-line pattern was observed in the room temperature EPR spectrum by rhenium hyperfine interactions (<sup>185</sup>Re and <sup>187</sup>Re) identifying a metal-centered radical. Further chemical reduction led to unexpected C-H activation of the benzoyl moiety as found in complex  $[\text{Re}^{\text{III}}\text{Br}\{\text{NH}_2(\text{CO})\text{C}_6\text{H}_4\}(\text{PrPNP})]$  (**17**) where the benzamide ligand binds in a bidentate  $\kappa^2$  mode. Importantly, protonolysis using diphenylammonium bromide has shown to release benzamide under reformation of  $[\text{Re}^{\text{III}}\text{Br}_3(\text{PrPN}^{\text{H}}\text{P})]$  (**10**<sup>Br</sup>).

The CV data signature of **15**<sup>BArF</sup> has shown to be strongly affected in presence of acids. In presence of lutidinium triflate, a potential shift of  $\Delta E = +50 \text{ mV}$  was observed concomitant to a significant current increase. Chemical reduction of **15**<sup>BArF</sup> in presence of lutidinium formed  $[\text{Re}^{\text{III}}\text{Br}_2\{\text{NH}(\text{CO})\text{C}_6\text{H}_5\}(\text{PrPN}^{\text{H}}\text{P})]$  (**18**) as a product of  $\text{H}^+/2\text{e}^-$  transfer. Note, protonation with the stronger acid diphenylammonium bromide leads to the formation of benzamide and **10**<sup>Br</sup>. Resultantly, the CV of **15**<sup>BArF</sup> significantly changes in presence of diphenylammonium: an irreversible event appeared with significant current increase, that is anodally shifted by  $\Delta E = \sim +300 \text{ mV}$ . The reduction of **15**<sup>BArF</sup> in presence of diphenyl ammonium provided benzamide and **10**<sup>Br</sup> in high yield. The analogous transformation was examined electrochemically. The most promising results were achieved by electrolyzing **15**<sup>BArF</sup> in presence of lutidinium triflate, obtaining carboxamide complex **18** and benzamide in modest yields (41%/34%). Importantly, an aqueous work-up increased the yield for benzamide up to 65%.

The drastically lowered reduction potential of **15**<sup>BArF</sup> created space for compatibility between benzoyl bromide as acylation reagent, decamethyl ferrocene as chemical reductant and lutidinium BArF<sub>24</sub> as proton source. Hence, a protocol was established that enables nitride transfer into benzonitrile in one pot at ambient conditions. Interestingly, despite the presence of two different electrophiles, initial  $\text{Bz}^+/\text{e}^-$  transfer to **13**<sup>Br</sup> is favored, as  $[\text{Re}^{\text{IV}}\text{Br}_2\{\text{N}(\text{CO})\text{C}_6\text{H}_5\}(\text{PrPN}^{\text{H}}\text{P})]$  (**16**) is an isolated species. Initial  $\text{H}^+/\text{e}^-$  transfer is disfavored judged by the computed, low N-H bond strengths (36.8 kcal mol<sup>-1</sup>).

### 3.3 The electronic structure of the redox series (**11<sup>Br</sup>**, **11<sup>Br+</sup>**, **11<sup>Br2+</sup>**)

This chapter presents the redox triad  $[(\mu\text{-N}_2)\{\text{ReBr}_2(\text{}^{\text{Pr}}\text{PN}^{\text{H}}\text{P})\}_2]^{0/+ / 2+}$  (**11<sup>Br</sup>**, **11<sup>Br+</sup>**, **11<sup>Br2+</sup>**), that has been established to gain insight into the electronic structure of  $\text{N}_2$  bridged dirhenium complexes. There is a fundamental interest in understanding these compounds because they are key species in dinitrogen activation and functionalization. Group 6 dinitrogen complexes have been intensively explored in this regard.<sup>6,7,10,34,46</sup> Dirhenium  $\text{N}_2$  complexes indeed occur in different oxidation states including  $\text{Re}^{\text{I}}/\text{Re}^{\text{I}}$ ,<sup>268</sup>  $\text{Re}^{\text{II}}/\text{Re}^{\text{II}}$ <sup>42–44</sup> and  $\text{Re}^{\text{III}}/\text{Re}^{\text{III}}$ ,<sup>269</sup> however, these are individual examples and are not part of a redox series.

The first three subchapters present and discuss the analytical data of each redox isomer individually, and subchapter 3.3.4 provides a comparison and discusses the observed trends. Finally, all experimental data are rationalized by a qualitative molecular orbital scheme.

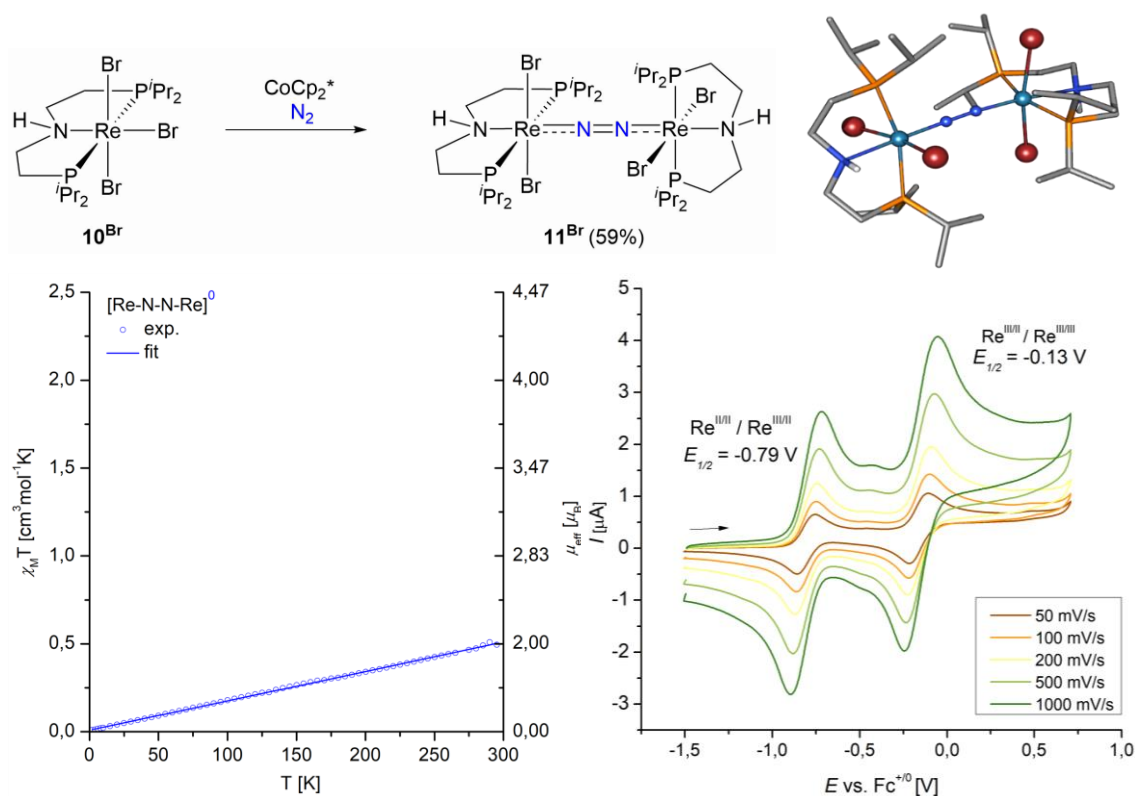
The (photo)reactivity of the complexes  $[(\mu\text{-N}_2)\{\text{ReBr}_2(\text{}^{\text{Pr}}\text{PN}^{\text{H}}\text{P})\}_2]^{+/2+}$  is beyond the scope of this work and is currently investigated by Katharina Wenderoth (AK Schneider, Georg-August-Universität Göttingen).

#### 3.3.1 Synthesis and characterization of **11<sup>Br</sup>**

As introduced earlier, dinitrogen complex  $[(\mu\text{-N}_2)\{\text{ReBr}_2(\text{}^{\text{Pr}}\text{PN}^{\text{H}}\text{P})\}_2]$  (**11<sup>Br</sup>**) can be synthesized upon reduction of rhenium tribromide complex  $[\text{Re}^{\text{III}}\text{Br}_3(\text{}^{\text{Pr}}\text{PN}^{\text{H}}\text{P})]$  (**10<sup>Br</sup>**) with decamethyl cobaltocene under an  $\text{N}_2$  atmosphere (Scheme 3.21, top). The  $^1\text{H}\{^{31}\text{P}\}$  spectrum shows strongly shifted, yet  $J$ -resolved resonances in a range of  $\delta = -13$  to 90 ppm. The  $^{31}\text{P}\{^1\text{H}\}$  NMR spectrum reveals two doublets at  $\delta = -381.4$  and  $-395.9$  ppm (Figure 3.5), in analogy to the previously published chloride representative.<sup>43</sup> These strongly shifted signals were assigned to admixtures of temperature independent paramagnetism.<sup>200</sup>

SQUID magnetometry of **11<sup>Br</sup>** was conducted to evaluate this hypothesis (Scheme 3.21, bottom left). At 2 K, the magnetic susceptibility is nearly 0. From that temperature, the susceptibility constantly increases over the entire temperature range. These data can be modelled with a closed shell singlet ( $S = 0$ ) and significant TIP contributions ( $\chi_{\text{M}} = 1670.5 \cdot 10^{-6} \text{ cm}^3 \text{ mol}^{-1}$ ) (Scheme 3.21, bottom right). Importantly, this fitting model has to be considered as an approximation because a description purely by spin can be problematic in case of huge spin-orbital coupling, as in the case for  $\text{Re}^{\text{III}}$  ( $\zeta = \sim 2500 \text{ cm}^{-1}$ )<sup>198, 270</sup>. However, the straight, linear increase of the magnetic susceptibility is consistent with a thermally well-separated ( $\Delta E \gg k_{\text{B}}T$ ), non-magnetic ground state ( $J = 0$ ). Hence, the magnetic susceptibility arises only by second order paramagnetism by mixing with excited spin-orbit states ( $J \neq 0$ ) by spin-orbit coupling, which is typical for octahedral  $\text{Re}^{\text{III}}$  complexes with a  $d^4$  electron configuration.<sup>200–202, 204, 209</sup> Despite the fact that DFT is a single reference method, the geometry of **11<sup>Br</sup>** is appropriately reproduced (Scheme 3.21, top right). The electron triplet ( $S = 1$ ) is the favored electron configuration close to an  $S = 0$

(+2.8 kcal·mol<sup>-1</sup>) which is in agreement with related systems (subchapter 6.3.3).<sup>42–44</sup> The close energetic gap between both spin states suggests multireference character.



**Scheme 3.21** **Top left:** Synthesis of **11<sup>Br</sup>**. **Top right:** Geometry optimization (ORCA 4.1.2; UKS PBE RI D3BJ Grid7 CPCM(THF); for Re, Br, N, P, O def2-TZVP def2/J; for C, H def2-SVP def2/J). DFT calculations were carried out by M. Sc. Severine Rupp (AK Krewald, Tu Darmstadt). **Bottom left:** CV measurement of **11<sup>Br</sup>** at different scan rates (1.0 mM; electrolyte: 0.1 M N<sup>n</sup>Bu<sub>4</sub>PF<sub>6</sub> in THF). **Bottom right:** Temperature dependence of the experimental  $\chi_M T$  product (cycles) including fitting (line) of **11<sup>Br</sup>** ( $S = 0$  and  $\chi_M = 1670.5 \cdot 10^{-6} \text{ cm}^3 \text{ mol}^{-1}$ ). The equation used for data fitting is given in the Appendix (subchapter 6.1.21).

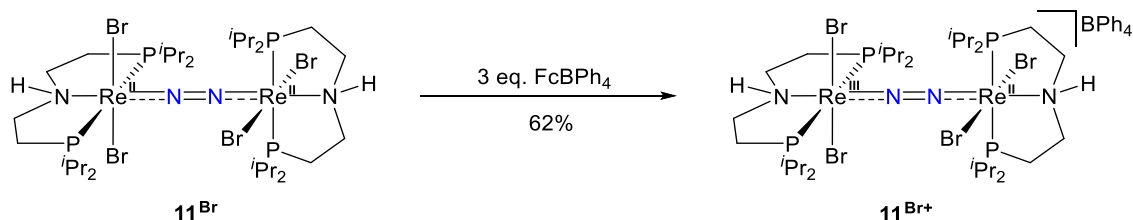
The redox behavior of dinitrogen complex **11<sup>Br</sup>** was assessed by cyclic voltammetry<sup>1</sup> (Scheme 3.21, bottom right). In the presented region are two oxidative events at  $E_{1/2} = -0.79 \text{ V}$  and  $-0.13 \text{ V}$  which are reversible at different scan rates (50 – 1000 mV/s), as judged by the peak current ratios. Both oxidative redox events are negative with regard to the Fc<sup>+0</sup> couple suggesting that ferrocenium based oxidants are a good starting point for chemical oxidation.

### 3.3.2 Synthesis and characterization of **11<sup>Br+</sup>**

The mono cationic complex  $[(\mu\text{-N}_2)\{\text{ReBr}_2(\text{P}^i\text{r}_2\text{PN}^i\text{P})\}_2]$  (**11<sup>Br+</sup>**) can be synthesized by oxidation of **11<sup>Br</sup>** with an excess of ferrocenium tetrphenylborate in 2-MeTHF. The excess of the oxidant is required to maximize the yield because it readily decomposes in solvents such as THF or 2-MeTHF. The reaction mixture turns rapidly black and after stirring overnight a black precipitate has formed, which can be collected to isolate the product with a good yield of 62% (Scheme 3.22).

<sup>1</sup> Measurement and interpretation of the CV data are part of the Bachelor thesis of Paul Julius Weiß (under supervision of Maximilian Fritz).

As XRD analysis reveals, the structural motif is retained upon oxidation and the N-N bond length is nearly unchanged ( $d_{\text{N-N}} = 1.179(8)$  Å, Figure 3.26, (bottom left)). Importantly, the bond lengths and angles around each metal core are nearly identical suggesting valence delocalization in the solid state, similar to examples of Cummins<sup>6</sup> and Nishibayashi.<sup>46</sup> A detailed discussion about the bond lengths including the comparison to the other representatives of the redox series follows in subchapter 3.3.4.



**Scheme 3.22** Synthesis of  $[(\mu\text{-N}_2)\{\text{ReBr}_2(\text{P}^i\text{Pr}_2\text{PN}^{\text{H}}\text{P})\}_2]\text{BPh}_4$  (**11Br<sup>+</sup>**).

In the  $^1\text{H}$  NMR spectrum (THF- $d_8$ ) the signals range between  $\delta = -20$  and  $+133$  ppm. All signals appear as singlets with a low signal width ( $w_{1/2} = 9 - 82$  Hz, Figure 3.26, (top)). There are eight resonances with an integral of six that represent the  $\text{CH}(\text{CH}_3)_2$  groups indicating a  $C_2$ -symmetry and charge delocalization in solution on the NMR timescale. One broadened resonance is strongly downfield shifted at  $\delta = 132.78$  ppm which is proposed as the N-H protons. There were no signals observed in the  $^{31}\text{P}\{^1\text{H}\}$  NMR spectrum.

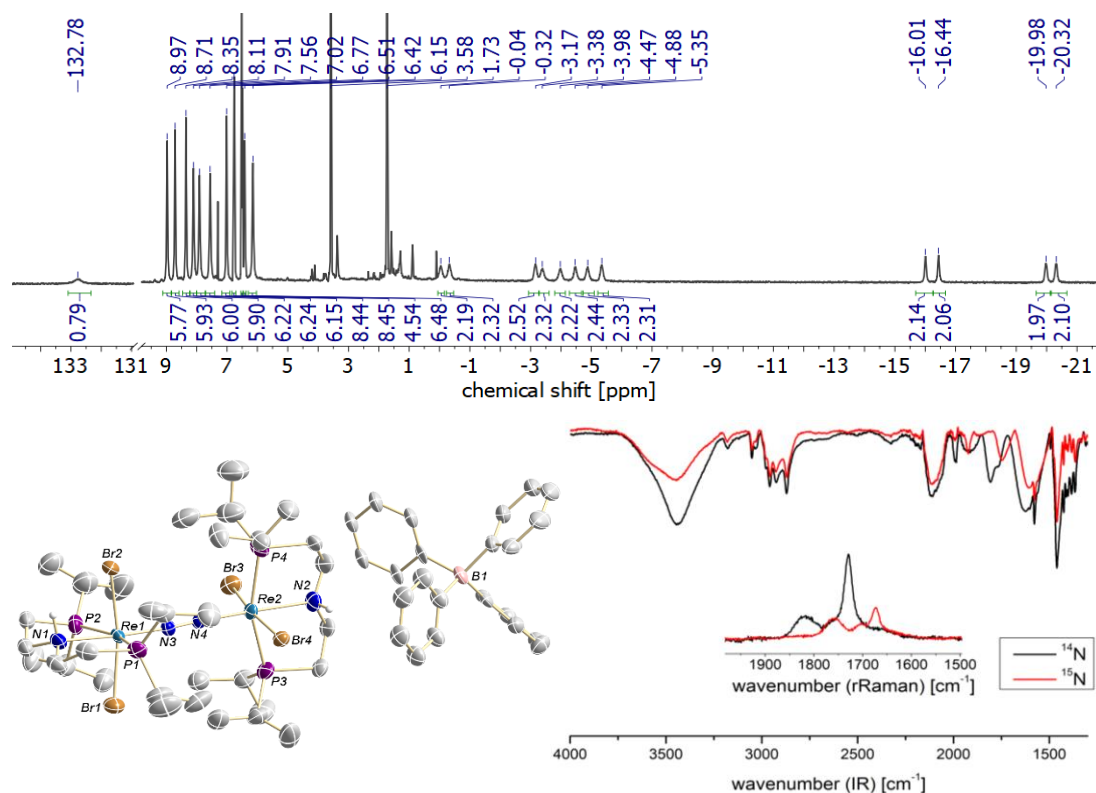


**Figure 3.26 Top:**  $^1\text{H}$  NMR spectrum (THF- $d_8$ , RT). **Bottom left:** The molecular structure in the solid state: Hydrogen atoms (except N-H), disordered moieties and solvent molecules are omitted for clarity. Selected bond lengths [Å] and angles [°]: Re1-N1 2.208(6), Re2-N2 2.207(6), Re1-N3 1.918(5), Re2-Re4 1.910(3), N3-N3 1.179(8), N1-Re1-N3 176.5(3), N2-Re2-N4 175.3(3). **Bottom right:** IR (solid, ATR) and rRaman ( $\lambda = 633$  nm, THF- $d_8$ ) spectroscopy.



The rRaman spectrum shows a sharp and a broadened band in the region between 1600 – 1900  $\text{cm}^{-1}$  (Figure 3.26, bottom right). Both are isotope-sensitive and shift upon  $^{15}\text{N}_2$ -labelling to lower wavenumbers (sharp band: 1728  $\text{cm}^{-1}$   $\rightarrow$  1672  $\text{cm}^{-1}$ ; broad band: 1819  $\text{cm}^{-1}$   $\rightarrow$  1795  $\text{cm}^{-1}$ ) anticipating more than one diatomic stretching mode of the  $\text{N}_2$  ligand.<sup>269</sup> The IR spectrum reveals a weak isotope-sensitive band at 1807  $\text{cm}^{-1}$  shifting to 1745  $\text{cm}^{-1}$  in the  $^{15}\text{N}_2$ -labelled case, speaking for valence localization on the (fast) IR time scale (Figure 3.26, bottom right). However, a quantitative comparison of the N-N stretching to parent  $\mathbf{11}^{\text{Br}}$  is difficult in case of coupled stretching modes or superimposition to other bands. Interestingly, the IR spectrum shows some bands, which in their shape are distinctively different ( $\nu = 3438, 2107, 1625 \text{ cm}^{-1}$ ) assuming low-energy electronic transitions, as previously documented for rhenium trichloride complex  $[\text{ReCl}_3(\text{P}^{\text{r}}\text{PN}^{\text{H}}\text{P})]$  ( $\mathbf{10}^{\text{Cl}}$ ).<sup>209</sup>

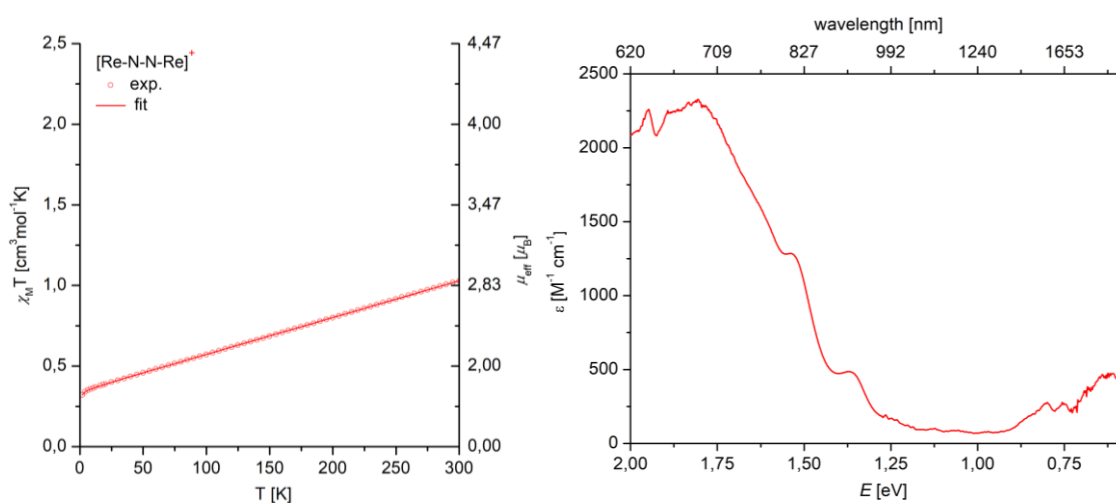


**Figure 3.27** Characterization of  $\mathbf{11}^{\text{Br}+}$ . **Left:** Temperature dependence of the experimental  $\chi_{\text{M}}T$  product (cycles) including fitting (line). The data have been fitted with an  $S = 1/2$  and TIP  $\chi_{\text{M}} = 2282.9 \cdot 10^{-6} \text{ cm}^3 \text{ mol}^{-1}$ . Applied spin-Hamiltonian is given in the Appendix (Figure 6.56). **Right:** Electronic absorption spectrum of the NIR region.

The SQUID magnetometry measurement of mono cationic  $\mathbf{11}^{\text{Br}+}$  is depicted in Figure 3.27 (left). A straight, linear increase of the molar susceptibility is observed, which is diagnostic for temperature independent paramagnetism (TIP). The data can be fitted with a spin Hamiltonian based on an  $S = 1/2$  model with huge contribution of TIP ( $X_{\text{M}} = 1664.7 \cdot 10^{-6} \text{ cm}^3 \text{ mol}^{-1}$ ). The susceptibility adapts at 2 K a value of  $X_{\text{M}}T = 0.32 \text{ cm}^3 \text{ mol}^{-1} \text{ K}$  being consistent with an electron doublet ( $X_{\text{M}}T = 0.37 \text{ cm}^3 \text{ mol}^{-1} \text{ K}$ ,  $\mu_{\text{eff}} = 1.73 \mu_{\text{B}}$ ). The linear increase of the magnetic susceptibility indicates an energetically separated ground state similar to  $\mathbf{11}^{\text{Br}}$ . These data are qualitatively similar to other and mixed-valent dirhenium complexes.<sup>203,206</sup>

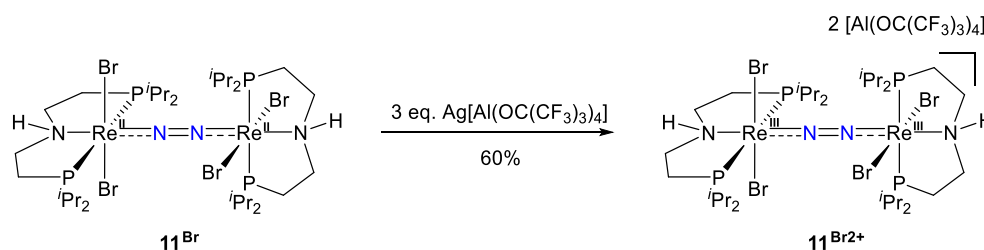
Due to the odd electron count, EPR spectroscopy was performed to identify the chemical environment of the unpaired electron by hyperfine interaction (HFI). Measurements as a frozen THF solution (20 K) obtained no signal and the measurements in the solid state (20 K) only gave a very broadened, featureless signal without any indication of HFI. There are no qualitative differences in the EPR spectra between both isotopologues ( $^{14/15}\text{N}-\mathbf{11}^{\text{Br}+}$ )

(Appendix, Figure 6.57). It is assumed that fast relaxation is the reason for the broadened signals even at low temperature (20 K).<sup>271</sup> Indeed, it is commonly observed that well-resolved, narrow lines in the EPR and NMR spectra of one compound at the same temperature are mutually exclusive.<sup>152</sup>

NIR spectroscopy was performed to examine the presence of characteristic intervalence-charge-transfer (ICVT) bands (ICVT) (Figure 3.27, right), being a strong criterion for the Robin-Day classification (subchapter 1.1.4). Broad, solvent dependent IVCT bands are commonly associated with valance localization (class II), whereas sharp, narrow, solvent independent bands are typical for valance delocalization (class III).<sup>15,22,23,30,31</sup> In fact, there are two weak transitions observed at 0.62 and 0.8 eV with very low extinction coefficients ( $\epsilon = 266, 478 \text{ M}^{-1}\text{cm}^{-1}$ , respectively). However, the low signal to noise ratio does not allow for a detailed examination. To conclude, as judged by the charge delocalization in the solid-state structure and the presence of an IR active  $\text{N}_2$  band, complex  $\mathbf{11}^{\text{Br}^+}$  most likely belongs to the intermediate class II-III.

### 3.3.3 Synthesis and characterization of $\mathbf{11}^{\text{Br}^{2+}}$

Dicationic complex  $[(\mu\text{-N}_2)\{\text{ReBr}_2(\text{P}^{\text{tPr}}\text{PN}^{\text{tPr}})\}_2]^{2+}$  ( $\mathbf{11}^{\text{Br}^{2+}}$ ) can be synthesized by the reaction of neutral parent  $\mathbf{11}^{\text{Br}}$  with a slight excess of  $\text{Ag}[\text{Al}(\text{OC}(\text{CF}_3)_3)_4]_2$ . Filtration and washing with diethyl ether yields  $[(\mu\text{-N}_2)\{\text{ReBr}_2(\text{P}^{\text{tPr}}\text{PN}^{\text{tPr}})\}_2][\text{Al}(\text{OC}(\text{CF}_3)_3)_4]_2$  ( $\mathbf{11}^{\text{Br}^{2+}}$ ) (60%) as a blue solid in analytical purity (Scheme 3.23).



**Scheme 3.23** Synthesis of  $[(\mu\text{-N}_2)\{\text{ReBr}_2(\text{P}^{\text{tPr}}\text{PN}^{\text{tPr}})\}_2][\text{Al}(\text{OC}(\text{CF}_3)_3)_4]_2$  ( $\mathbf{11}^{\text{Br}^{2+}}$ ).

The  $^1\text{H}$  NMR signature of compound  $\mathbf{11}^{\text{Br}^{2+}}$  shows resonances in the range between  $\delta = -42$  to 37 ppm (Figure 3.28, top). Eight signals in the region between  $\delta = 17 - 27$  ppm are representing the  $\text{CH}(\text{CH}_3)_2$  groups which suggests  $C_2$ -symmetry in solution. The signal at a chemical shift of  $\delta = 36.7$  ppm is assigned to the N-*H* protons. Similar to mono cationic  $\mathbf{11}^{\text{Br}^+}$ , the signals appear as sharp singlet without *J*-coupling ( $w_{1/2} = 20 - 60$  Hz). There were no signals observed in the  $^{31}\text{P}\{^1\text{H}\}$  NMR in the range between  $\delta = -2600$  to 200 ppm.

As several initial attempts failed to obtain single crystals suitable for X-Ray diffraction, the anion was consequently changed. Using  $\text{Ag}(\text{OTf})$  as the chemical oxidant in analogous procedure, well-diffracting single crystals were obtained suitable for X-Ray diffraction. Spectroscopic measurements, magnetic measurements and characterization by elemental analysis were performed using the aluminate  $[\text{Al}(\text{OC}(\text{CF}_3)_3)_4]^-$  anions. In analogy to  $\mathbf{11}^{\text{Br}}$  and

$\mathbf{11}^{\text{Br}^+}$ , the structural motif is maintained (Figure 3.28, bottom right). The metric parameters around both metal centers are nearly identical. The degree of activation of dinitrogen ligand is not significantly impacted by further oxidation ( $d_{\text{N-N}} = 1.159(8)$  Å).

The magnetic properties were assessed by SQUID magnetometry (Figure 3.28, bottom left). A linear increase of the susceptibility is observed in the temperature region between 2 – 150 K which then flattens going to higher temperatures. The experimental data were modelled with an electron quintet ( $S = 2$ ), temperature independent paramagnetism (TIP)  $\chi_{\text{M}} = 2282.9 \cdot 10^{-6} \text{ cm}^3 \text{ mol}^{-1}$ , and zero-field splitting (ZFS) ( $D = 374.7 \text{ cm}^{-1}$ ). These data can be rationalized by two isolated  $\text{Re}^{\text{III}}$  centers with both having a strong, energetically separated  $J = 0$  ground state to account for the linear regime increase below 150 K. The slight bending might be attributed to partial thermal population of  $J \neq 0$  spin-orbit states.<sup>202</sup> Recently, a closely related, dinuclear  $\text{Re}^{\text{III}}/\text{Re}^{\text{III}} \text{ N}_2$  complex was reported, which resembles the magnetic data found for ( $\mathbf{11}^{\text{Br}^{2+}}$ ). The authors used a model of two  $S = 1$  rhenium centers engaged in antiferromagnetic coupling ( $J_{\text{Re-Re}} = 22 \text{ cm}^{-1}$ ).<sup>269</sup>

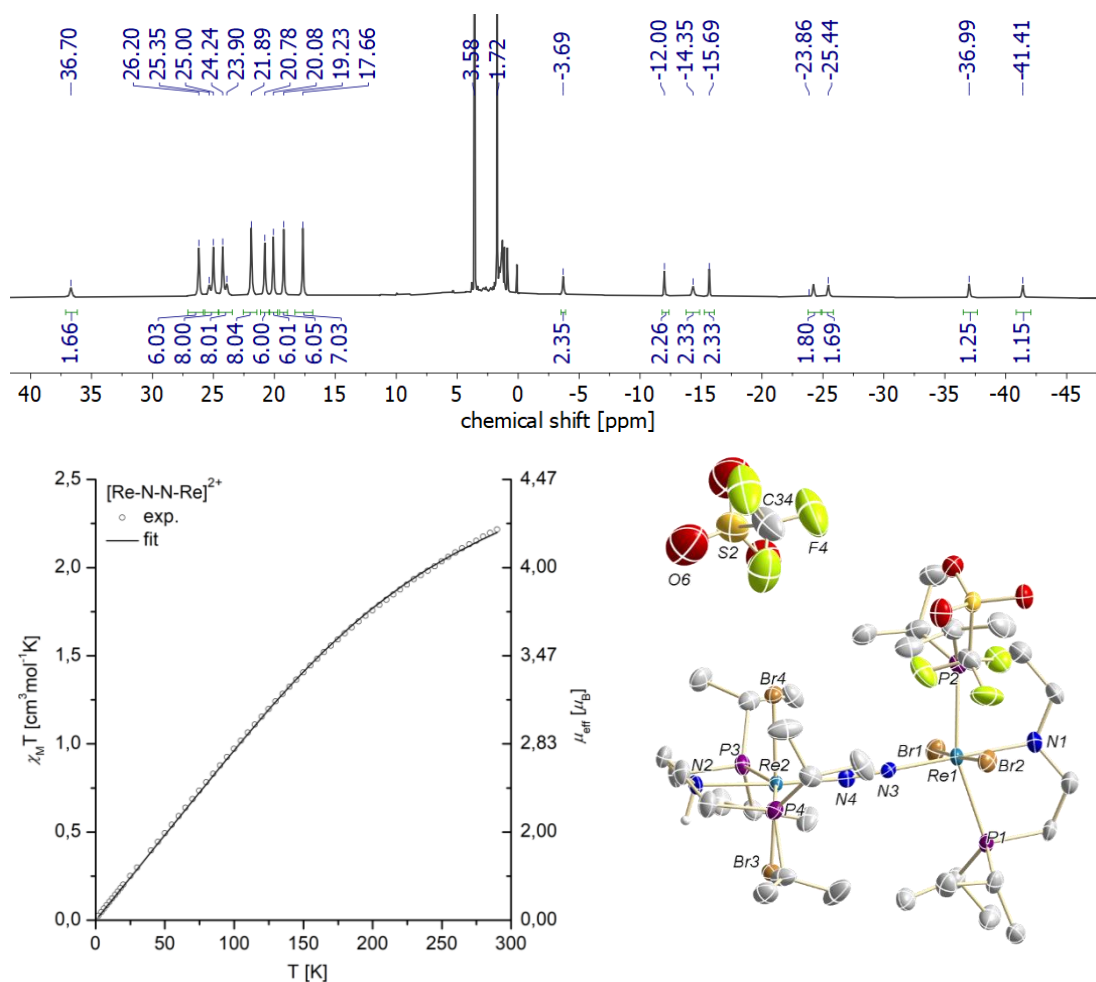


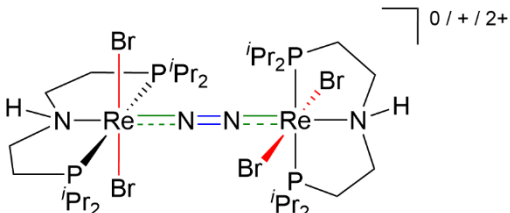
**Figure 3.28 Top:**  $^1\text{H}$  NMR spectrum ( $\text{THF-}d_8$ , RT). **Bottom left:** Temperature dependence of the experimental  $\chi_{\text{M}}T$  product (cycles) including fitting (line) ( $S = 2$ ,  $\chi_{\text{M}}(\text{TIP}) = 2501.0 \cdot 10^{-6} \text{ cm}^3 \text{ mol}^{-1}$ ,  $D = 374.7 \text{ cm}^{-1}$ ). Applied spin-Hamiltonian is given in the Appendix (Figure 6.59). **Bottom right:** Molecular structure in the solid state. Hydrogen atoms (except N-H), disordered moieties and solvent molecules are omitted for clarity. Intermolecular hydrogen bridges between the N-H groups and the triflate anions are not depicted. Selected bond lengths [Å] and angles [°]: Re1-N1 2.205(7), Re2-N2 1.198(7), Re1-N3 1.925(7), Re2-Re4 1.930(7), N3- N3 1.156(9). N1-Re1-N3 177.0(3), N2-Re2-N4 176.0(3).

Vibrational spectroscopy is inconclusive so far. The resonance Raman spectrum ( $\lambda = 427, 633 \text{ nm}$ ) exhibits in the diagnostic region only a very broadened feature at  $1814 \text{ cm}^{-1}$  (Appendix, Figure 6.60). Labelling studies are yet to be done for the assignment of the N-N stretching vibration. The IR spectrum is featureless and shows neither diagnostic bands for  $\text{N}_2$  coordination nor electronic transitions in the measured region ( $500 - 4000 \text{ cm}^{-1}$ ), which might be caused by the dominant C-F stretching vibrations (Appendix, Figure 6.61). The absence of N-H bands can be explained by hydrogen bonds (N-H-OTf), as revealed by XRD analysis.

### 3.3.4 The redox series $[(\mu\text{-N}_2)\{\text{ReBr}_2(\text{PrPN}^{\text{H}}\text{P})\}_2]^{0/+ / 2+}$ : Discussion of trends

The molecular architecture is analogous among the redox series. Two octahedrally coordinated rhenium atoms are connected via a bridging  $\text{N}_2$  ligand and the pincer ligands are perpendicularly arranged. This is consistent with the CV data of the redox neutral  $\mathbf{11}^{\text{Br}}$ , which shows two fully reversible redox events at different scan rates suggesting no chemical follow-up reaction upon oxidation. The oxidation of  $\mathbf{11}^{\text{Br}}$  to  $\mathbf{11}^{\text{Br}+}$  and  $\mathbf{11}^{\text{Br}2+}$  has only a minor effect on the geometry (Table 3.1). The changes in the bond lengths are minimal and should not be overinterpreted.

**Table 3.1:** Summary of selected bond lengths [Å] and angles [°] derived from X-Ray diffraction of  $[(\mu\text{-N}_2)\{\text{ReBr}_2(\text{PrPN}^{\text{H}}\text{P})\}_2]^{0/+ / 2+}$ .



	$\mathbf{11}^{\text{Br}}$	$\mathbf{11}^{\text{Br}+}$	$\mathbf{11}^{\text{Br}2+}$
$\text{N}_{\text{PNP}}\text{-Re}$ [Å]	2.217(3) / 2.222(4)	2.208(6) / 2.207(6)	2.205(7) / 2.198(7)
$\text{Re-N}_{\text{N}_2}$ [Å]	<b>1.918(5) / 1.910(3)</b>	<b>1.889(6) / 1.891(6)</b>	<b>1.925(7) / 1.930(7)</b>
N-N [Å]	<b>1.168(5)</b>	<b>1.179(8)</b>	<b>1.156(9)</b>
Re-Br [Å]	<b>2.5689(5) - 2.6056(5)</b>	<b>2.5316(10) - 2.5320(9)</b>	<b>2.4638(10) - 2.4822(10)</b>
$\text{N}_{\text{PNP}}\text{-Re-N}_2$ [°]	173.33(14) / 177.45(15)	176.5(3) / 175.3(3)	177.0(3) / 176.0(3)
P-Re-P [°]	159.64(4) / 159.49(4)	160.16(7) / 159.86(8)	159.32(8) / 157.72(8)
Br-Re-Br [°]	169.829(15) / 168.616(16)	169.27(4) / 171.43(12)	175.70(3) / 173.76(4)

Comparing the Re- $\text{N}_{\text{N}_2}$  and the N-N bond lengths among the redox isomers  $\mathbf{11}^{\text{Br}}$ ,  $\mathbf{11}^{\text{Br}+}$ , and  $\mathbf{11}^{\text{Br}2+}$ , there are two trends (Table 3.1): The Re- $\text{N}_{\text{N}_2}$  bond slightly contracts upon oxidation of  $\mathbf{11}^{\text{Br}}$  to  $\mathbf{11}^{\text{Br}+}$  and further oxidation to  $\mathbf{11}^{\text{Br}2+}$  leads to slight bond elongation. The reversed trend is observed for the N-N bond, which is minimally elongated going from  $\mathbf{11}^{\text{Br}}$  to  $\mathbf{11}^{\text{Br}+}$  and then contracts in  $\mathbf{11}^{\text{Br}2+}$ .

The SQUID data of all three redox isomers are depicted in Figure 3.30.  $\mathbf{11}^{\text{Br}}$  exhibits a straight line, indicating a non-magnetic, thermally well-stabilized ground state.  $\mathbf{11}^{\text{Br}+}$  is formally an electron doublet, being consistent with an observed susceptibility value of nearly  $\chi_{\text{M}}T = 0.4 \text{ cm}^3 \text{ mol}^{-1} \text{ K}$ . Similar to  $\mathbf{11}^{\text{Br}}$  it is rendered by significant TIP contributions,

indicated by a linear increase of the magnetic susceptibility. In the case of  $\mathbf{11}^{\text{Br}2+}$  the situation seems to be slightly different. Below  $\sim 100$  K, the susceptibility increase is linear, comparable to the former cases. At higher temperature, however, a slight bending is observed which might indicate thermal population of excited states. A comparatively high susceptibility above  $X_M T = \sim 2.2 \text{ cm}^3 \text{ mol}^{-1} \text{ K}$  is diagnostic for four unpaired electrons.

The trends observed in the metric parameters as well as the magnetic data among the redox series  $\mathbf{11}^{\text{Br}}$ ,  $\mathbf{11}^{\text{Br}+}$  and  $\mathbf{11}^{\text{Br}2+}$  can be rationalized within a molecular orbital model, depicted in Figure 3.29. As mentioned earlier (subchapter 1.1.3), the molecular orbital scheme for a complex  $\text{L}_4\text{Re}^{\text{II}}(\text{N}_2)\text{Re}^{\text{II}}\text{L}_4$  with  $D_{4h}$ -symmetry consists of four degenerate molecular orbitals with  $\pi$ -symmetry having 0 ( $\pi$ - $\pi$ - $\pi$ ), 1 ( $\pi$ - $\pi^*$ - $\pi$ ), 2 ( $\pi^*$ - $\pi$ - $\pi^*$ ) and 3 ( $\pi^*$ - $\pi^*$ - $\pi^*$ ) nodal planes. The exclusively metal-centered, non-bonding  $\delta/\delta^*$ -orbitals are energetically located between the latter two  $\pi$ -based MO's. The molecular orbitals are filled with 14 electrons (metal d electrons ( $2 \times 5 e^-$ ) + dinitrogen  $\pi$  electrons ( $2 \times 2 e^-$ )). The HOMO is the  $\pi^*$ - $\pi$ - $\pi^*$ -orbital which is occupied by two unpaired electrons giving rise to a  $\pi^{10}\delta^4$  electron configuration<sup>1,2,42</sup>

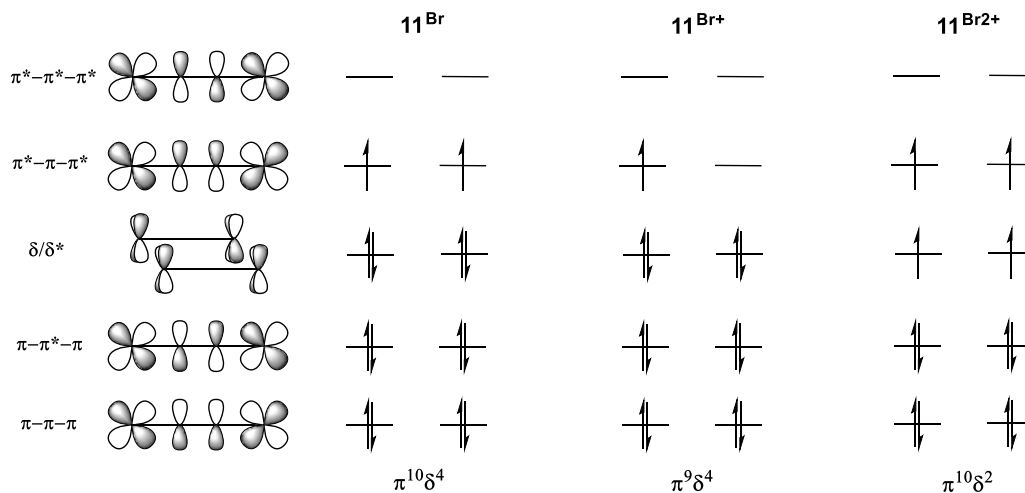


**Figure 3.29** Qualitative molecular orbital scheme of the redox series  $[(\mu\text{-N}_2)\{\text{ReBr}_2(\text{IPrPN}^{\text{H}}\text{P})\}_2]^{0/+ / 2+}$  ( $\mathbf{11}^{\text{Br}}$ ,  $\mathbf{11}^{\text{Br}+}$ ,  $\mathbf{11}^{\text{Br}2+}$ ).<sup>1,2,42</sup>

Consequently, it is reasonable that oxidation of  $\mathbf{11}^{\text{Br}}$  stabilizes the Re- $\text{N}_{\text{N}2}$  and destabilizes the N-N bond. A  $\pi^9\delta^4$  configuration is anticipated for  $\mathbf{11}^{\text{Br}+}$ , which is consistent with the SQUID data (Figure 3.30). As the  $\pi^*-\pi-\pi^*$ -orbitals are degenerate, a doublet ground state ( ${}^2E$ ) is assumed for  $\mathbf{11}^{\text{Br}+}$ . It is tempting to assume that further oxidation leads to a closed-shell system, however, as the SQUID data reveal,  $\mathbf{11}^{\text{Br}2+}$  is paramagnetic and can be formally considered as an overall  $S = 2$  or  $2 \times S = 1$  species suggesting half filled  $\delta/\delta^*$  and half-filled  $\pi^*-\pi-\pi^*$ -orbitals within a  $\pi^{10}\delta^2$  electron configuration. Importantly, this assumption is consistent with the observed Re- $\text{N}_{\text{N}2}$  bond elongation and N-N bond shortening going from  $\mathbf{11}^{\text{Br}+}$  to  $\mathbf{11}^{\text{Br}2+}$ .

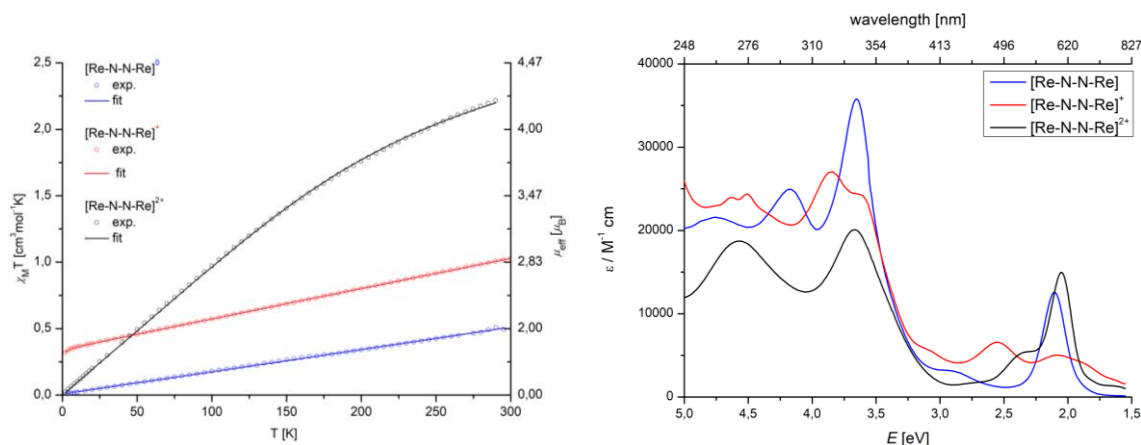


**Figure 3.30** Left: Temperature dependence of the experimental  $\chi_M T$  product (cycles) including fitting (line) of  $\mathbf{11}^{\text{Br}}$  (blue),  $\mathbf{11}^{\text{Br}+}$  (red) and  $\mathbf{11}^{\text{Br}2+}$  (black). Right: Electronic absorption spectra of  $\mathbf{11}^{\text{Br}}$  (blue),  $\mathbf{11}^{\text{Br}+}$  (red) and  $\mathbf{11}^{\text{Br}2+}$  (black) ( $4.0 \cdot 10^{-5}$  M in THF).

The interpretation is supported by UVvis spectroscopy. As discussed earlier, the electronic absorption spectrum of  $\mathbf{11}^{\text{Br}}$  features in the visible range one intense band at 2.11 eV (blue trace, 589 nm Figure 3.30), which was assigned to a  $\pi\text{-}\pi^*\text{-}\pi \rightarrow \pi^*\text{-}\pi\text{-}\pi^*$  transition by TD-DFT calculations (subchapter 3.1.3, blue trace). This band is assumed to account for the intense blue color of  $\mathbf{11}^{\text{Br}}$  in solution. As the  $\pi^*\text{-}\pi\text{-}\pi^*$ -orbitals are partially depopulated upon oxidation, the depletion of the band at 2.11 eV in  $\mathbf{11}^{\text{Br}+}$  is not surprising (red trace, 589 nm Figure 3.30). The presence of multiple bands in the visible region explains the black color of  $\mathbf{11}^{\text{Br}+}$  in solution. Interestingly, the UVvis spectrum of dicationic  $\mathbf{11}^{\text{Br}2+}$  is dominated by an intense absorption at 2.05 eV (black trace, 605 nm Figure 3.30), which is reminiscent to neutral  $\mathbf{11}^{\text{Br}}$ . In fact, both  $\mathbf{11}^{\text{Br}}$  and  $\mathbf{11}^{\text{Br}2+}$  form intense blue colored solutions. The striking similarity of the bands of  $\mathbf{11}^{\text{Br}}$  and  $\mathbf{11}^{\text{Br}2+}$  at around 2 eV might be indicative for half-filled  $\pi^*\text{-}\pi\text{-}\pi^*$ -orbitals in both compounds, assuming that effectively the  $\delta/\delta^*$  are depopulated upon twofold oxidation of  $\mathbf{11}^{\text{Br}}$ .

### 3.3.5 Concluding remarks

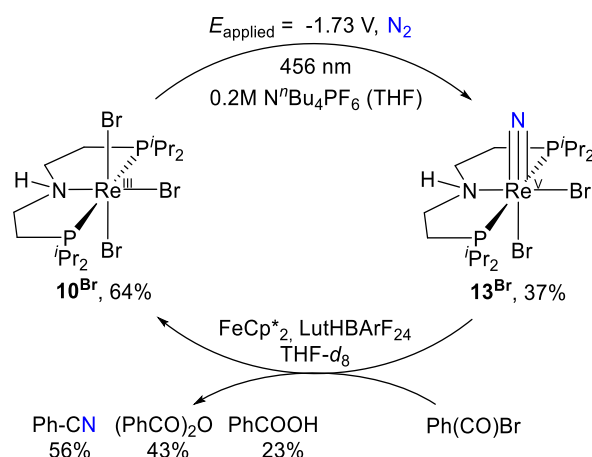
The redox isomers  $\mathbf{11}^{\text{Br}+}$  and  $\mathbf{11}^{\text{Br}2+}$  were successfully synthesized and isolated in good yield by oxidation of the redox neutral parent  $\mathbf{11}^{\text{Br}}$ . These complexes were investigated by XRD analysis, SQUID magnetometry, EPR and UVvis spectroscopy. The observed trends were rationalized within a qualitative molecular orbital model.

The neutral dinitrogen complex  $\mathbf{11}^{\text{Br}}$  with the formal oxidation states  $\text{Re}^{\text{II/II}}$  can be considered as an electron triplet with a  $\pi^{10}\delta^4$  configuration. Upon oxidation  $\mathbf{11}^{\text{Br}+}$  ( $\text{Re}^{\text{III/II}}$ ) it can be described as an electron doublet as examined by SQUID magnetometry, with a suggested  $\pi^9\delta^4$  configuration. Complex  $\mathbf{11}^{\text{Br}+}$  is the first reported mixed-valent dirhenium  $\text{N}_2$  complex. Based on the absence of structural differences between both metal centers and the presence of an IR active  $\text{N}_2$  band, this species was ascribed to the Robin-Day class II-III. EPR spectroscopy was targeted to distinguish between metal vs.  $\text{N}_2$  centered oxidation, however, initial attempts did not produce a decent EPR signal. Further oxidation produced the

paramagnetic complex  $\mathbf{11}^{\text{Br}2+}$  ( $\text{Re}^{\text{III/III}}$ ) where SQUID magnetometry determined an overall intermediate-spin configuration ( $S = 2$ ). Based on these results, a  $\pi^{10}\delta^2$  configuration was suggested.

### 3.4 Conclusion and Outlook

Within the last three subchapters valuable information were collected how halide variation affects  $\text{N}_2$  fixation and functionalization. On the electrochemical side, the reduction potential for  $\text{N}_2$  reduction can be lowered by suiting the platform with better leaving groups, such as bromide and iodide. Furthermore, a redshift of the productive region for photolytic  $\text{N}_2$  cleavage was observed going to the heavier halides. The electronic structure of the key intermediate  $[(\mu\text{-N}_2)\{\text{ReBr}_2(\text{P}^{\text{tPr}}\text{PN}^{\text{H}}\text{P})\}_2]$  ( $\mathbf{11}^{\text{Br}+}$ ) was explored within a redox series. Resultantly, a strategy was found to combine electro- and photochemistry to generate nitride species  $[\text{ReX}_2\text{N}(\text{P}^{\text{tPr}}\text{PN}^{\text{H}}\text{P})]$   $\mathbf{13}^{\text{Br}}$ . Nitride benzoylation was examined and based on an extensive electrochemical analysis of  $[\text{ReBr}_2\{\text{N}(\text{CO})\text{C}_6\text{H}_5\}(\text{P}^{\text{tPr}}\text{PN}^{\text{H}}\text{P})]\text{BArF}_{24}$  ( $\mathbf{15}^{\text{BArF}}$ ) a strategy was found, how to facilitate selective nitride transfer from  $\mathbf{13}^{\text{Br}}$  to form benzonitrile via PCET. The obtained results demonstrate functionalization of atmospheric dinitrogen in two steps (Scheme 3.24).



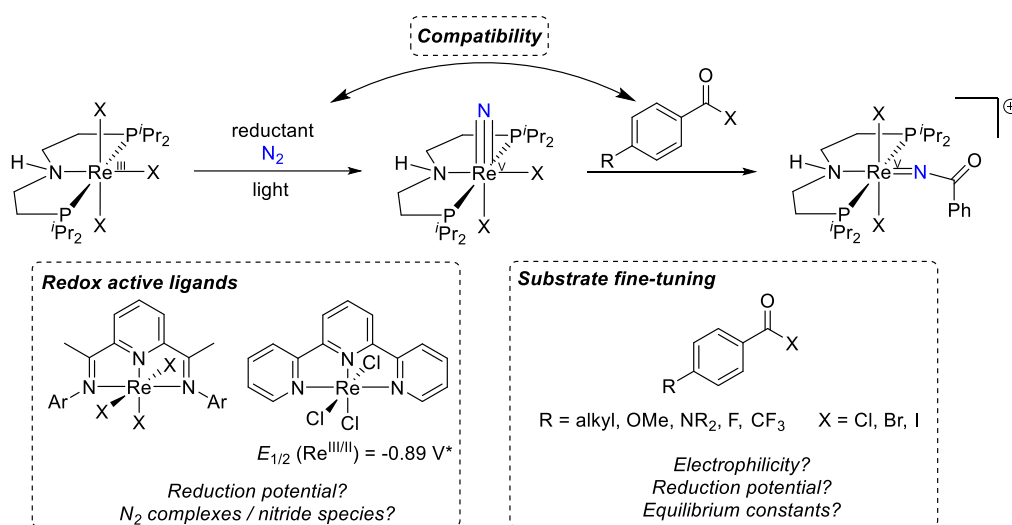
**Scheme 3.24** Functionalization of atmospheric  $\text{N}_2$  in two steps.

The main reason why catalytic N-C bond formation is challenging is an incompatibility issue, as introduced in subchapter 1.2.2. On the one hand, this work successfully established a strategy for simultaneous use of an acylation reagent and PCET reagents to facilitate nitride transfer within a two-step synthetic cycle (Scheme 3.24), on the other hand the compatibility issue between the chemical reductant, required for  $\text{N}_2$  reduction and the acylation reagents, used for N-C bond formation, remains unsolved.

The incompatibility issue is based on overlapping reduction potentials between the chemical reductant and the acylation reagent<sup>83</sup> and thus, a conceivable solution could be to separate these potentials to avoid chemical reduction of the electrophile. Therefore, strategies are needed to shift the  $\text{N}_2$  reduction to milder potentials and to move the reduction potential of

the substrate into the even more negative region. This might reduce electrophilicity, however, this work demonstrated that an equilibrium with a small equilibrium constant is sufficient for follow-up reactivity.

One option is halide variation, that has been shown by this work to shift the reduction potential about 300 mV to milder potentials. Another idea could be the usage of redox-active *N,N,N*-type ligands featuring an energetically low-lying  $\pi^*$ -orbital. Classical representatives of this ligand classes are 2,6-bis(imino)pyridine (PDI) and 2,2':6',2''-terpyridine (tpy) ligands, which both have been broadly applied to catalysis, as recently reviewed (Scheme 3.25).<sup>143</sup> Interestingly, the literature known complex  $[\text{Re}^{\text{III}}\text{Cl}_3(\text{tpy})]$  could be a promising starting point, as the  $\text{Re}^{\text{III/II}}$  couple is at a mild potential of  $\Delta E_{1/2} = -0.89 \text{ V}$ <sup>272,273</sup> that is anodically shifted by almost 1 V compared to  $[\text{ReX}_3(\text{ArPN}^{\text{H}}\text{P})]$  **10** ( $\text{X} = \text{Cl}, \text{Br}, \text{I}$ ). The general popularity of these ligands is due to their facile, synthetic accessibility and manifold molecular modularity (PDI,<sup>274–277</sup> tpy<sup>278–282</sup>). This broad variety of derivatives offers the possibility to adjust redox potentials. For instance, the *para*-position of the PDI ligand is particularly sensitive towards the reduction potential that ranges up to  $\Delta E^0 = 0.5 \text{ V}$  depending on the substituent.<sup>143</sup>  $\text{N}_2$  fixation and functionalization using the PDI and the tpy ligand indeed has been approached by group 6 metals including chromium and molybdenum,<sup>7,51,143,144,283–286</sup> and also by main group elements like aluminium,<sup>287</sup> however, application to rhenium has not been reported yet.



**Scheme 3.25** Optimization approaches in order to increase compatibility.<sup>272</sup> \*estimated reduction potential assuming  $E_{1/2}(\text{Fc}^{+/0}) = 0.4 \text{ V}$  vs. NHE.<sup>273</sup>

Another strategy that pursues the improvement of compatibility is varying the halides and the substitution pattern within the benzoyl moiety (Scheme 3.25). While chloride and bromide substitution was investigated in former studies<sup>43</sup> and this work, respectively, iodide substitution is yet to be explored. Collecting cyclic voltammetry data of benzoyl chloride, bromide and iodide could quantify the effect of halide variation on the reduction potentials.



Relatively little is known about the influence of the phenyl derivatization on the reduction potential of benzoyl halides. As an approximation, the substitution pattern has a huge impact in related compounds, for example acetophenones are ranging in more than 1 V:  $E_{p,c}$  (4<sup>2</sup>-(methyl)acetophenone) ( $\text{Fc}^{+/0}$ ) = -2.58 V,  $E_{p,c}$  (4<sup>2</sup>-(trifluoromethyl)acetophenone) ( $\text{Fc}^{+/0}$ ) = -2.16 V,  $E_{p,c}$  (4<sup>2</sup>-(nitro)acetophenone) ( $\text{Fc}^{+/0}$ ) = -1.35 V. Similar potentials are reported for the corresponding aldehydes.<sup>83</sup> If these trends are applicable to benzoyl halides, there is a lot of space for optimization.

The redox series  $[(\mu\text{-N}_2)\{\text{ReBr}_2(\text{P}^{\text{tr}}\text{N}^{\text{H}}\text{P})\}_2]$  ( $\mathbf{11}^{\text{Br } 0/+ / 2+}$ ) can be further examined. As all three redox isomers obviously show strong spin-orbit coupling effects multireference computations are required to understand the electronic structures of these complexes.

Especially the mixed-valent isomer  $\mathbf{11}^{\text{Br}+}$  could be further experimentally investigated. Magnetic circular dichroism (MCD) spectroscopy would be a suitable technique providing insight into ground and excited state splitting being ideal for complexes with a degenerate ground state. At low temperature, the degeneracy of the ground state is cancelled out and transitions excited states can be observed. Furthermore, the intensity of these transitions is amplified by spin-orbit coupling.<sup>288-290</sup> As the examination of near-IR region bands is a key characteristic for the Robin-Day classification, recording a decent data set with an improved spectral quality and extended range into the IR region could give a lot of valuable information.

## 4 Experimental

### 4.1 General synthesis and materials

All synthetic procedures were performed under an inert atmosphere of Ar or N<sub>2</sub> (both 5.0, Linde Gas) using standard Schlenk and glovebox techniques, unless otherwise noted. Purification of CO gas (Air Liquide, 99.997%) was obtained by passing the gas through a steel coil cooled to -78 °C. <sup>15</sup>N<sub>2</sub> (Sigma Aldrich, 98% <sup>15</sup>N) was used as purchased without further purification.

The used glassware was cleaned in KOH/iso-propanol baths and HCl baths, washed with deionized water and dried at 130 °C. The hot glassware was evacuated either on a Schlenk line with periodically applied heat or in a glove box ante chamber. Small scale reactions (< 10 mg) were typically performed in J-Young NMR tubes.

All solvents were purchased in HPLC or P. A. quality (MERCK, CARL ROTH) and used as obtained from an MBRAUN SOLVENT PURIFICATION SYSTEM (SPS). THF and toluene were further purified by stirring over Na/K alloy for several days. Deuterated solvents were obtained from EURISOTOP GmbH and dried over Na/K (C<sub>6</sub>D<sub>6</sub>, toluene-*d*<sub>8</sub>, THF-*d*<sub>8</sub>) or CaH<sub>2</sub> (CD<sub>2</sub>Cl<sub>2</sub>). CNtBu and PhCOBr were distilled before usage. NaHMDS and PPh<sub>3</sub> were sublimed. All other chemicals were used as purchased without further purification.

ReCl<sub>3</sub>(MeCN)(PPh<sub>3</sub>)<sub>3</sub>,<sup>291,292</sup> ReBr<sub>3</sub>(MeCN)(PPh<sub>3</sub>)<sub>3</sub>,<sup>291,292</sup> KC<sub>8</sub>,<sup>293</sup> 2,3,6-tris-tert-butylphenoxy radical<sup>294</sup> have been synthesized to according procedures.

### 4.2 Analytical methods

#### 4.2.1 Crystallographic details

Suitable single crystals for X-ray structure determination were selected from the mother liquor under an inert gas atmosphere and transferred in protective perfluoro polyether oil on a microscope slide. The selected and mounted crystals were transferred to the cold gas stream on the diffractometer. The diffraction data were obtained at 100 K on a Bruker D8 three-circle diffractometer, equipped with a PHOTON 100 CMOS detector and an INCOATEC microfocus source with Quazar mirror optics (Mo-K $\alpha$  radiation,  $\lambda = 0.71073$  Å).

The data obtained were integrated with SAINT and a semi-empirical absorption correction from equivalents with SADABS was applied. The structures were solved and refined using the Bruker SHELX 2014 software package.<sup>295-298</sup> All non-hydrogen atoms were refined with anisotropic displacement parameters. All C-H hydrogen atoms were refined isotropically on

calculated positions by using a riding model with their  $U_{\text{iso}}$  values constrained to 1.5  $U_{\text{eq}}$  of their pivot atoms for terminal  $\text{sp}^3$  carbon atoms and 1.2 times for all other carbon atoms.

#### 4.2.2 Cyclic voltammetry

All electrochemical experiments were measured under an inert gas atmosphere with a GAMRY 600 reference potentiostat or a METROHM Autolab PGSTAT101 potentiostat using GAMRY or NOVA software, respectively. A 0.1 M solution of  $[\text{Bu}_4\text{N}][\text{PF}_6]$  in THF was used as electrolyte and an appropriate  $iR$  compensation was applied. Cyclic voltammetry (CV) was measured with a Glassy Carbon disk electrode ( $\varnothing = 3$  mm) as working electrode, a Pt wire as counter electrode and an Ag wire as pseudo-reference electrode. Referencing was performed by addition of  $\text{FeCp}_2$  as internal standard ( $E_{1/2}(\text{FeCp}_2^{+/0}) = 0.0$  V). Scan rate dependence of peak currents  $i_p$  were analyzed according to the Randles-Sevcik equation:

$$i_p = 0.446nFAC^0 \left( \frac{nFvD_0}{RT} \right)^{1/2}$$

where  $n$  is the number of transferred electrons,  $F$  is the Faraday's constant,  $A$  is the electrode surface in  $\text{cm}^2$ ,  $C^0$  is the bulk concentration of the analyte in  $\text{mol}\cdot\text{cm}^{-3}$ ,  $v$  is the scan rate in  $\text{V}\cdot\text{s}^{-1}$  and  $D_0$  is the diffusion coefficient of the oxidized species in  $\text{cm}^2\cdot\text{s}^{-2}$ .<sup>299</sup> This equation is valid for freely diffusion, non-absorbed analyte in solution which undergoes vast, electrochemical reversible electron transfer. Thus, deviations from linearity of a plot of  $i_p$  vs.  $v^{1/2}$  can indicate quasi-reversible electron transfer (accompanied by a scan rate dependent peak-to-peak separation) or absorption of the analyte on the electrode surface (which should have a constant peak-to-peak separation). Controlled potential electrolysis (CPE) was carried out with a glass carbon rod as working electrode in a 0.2 M  $[\text{Bu}_4\text{N}][\text{PF}_6]$  solution in THF. The pseudo-reference electrode and the counter electrode were placed in a fritted sample holder separate compartment.  $\text{FeCp}_2$  was used as sacrificial reductant.

#### 4.2.3 Electron paramagnetic resonance

Experimental X-band EPR spectra were recorded on a Bruker ELEXSYS-II E500 CW-EPR.

#### 4.2.4 Elemental analysis

Elemental analysis were obtained from the Analytical Laboratories at the Georg-August-University Göttingen using an Elementar Vario EL 3 analyzer.

#### 4.2.5 Irradiation

All photolysis experiments were performed using a Kessil PR160L LED of with different emission wave lengths (370 nm, 390 nm, 456 nm or 476 nm) or a 150 W Hg(Xe) arc lamp with lamp housing and arc lamp power supply from LOT-Quantum Design GmbH. For the

latter, IR radiation was eliminated by use of a water filter and photolyzed samples were kept at room temperature by a water bath.

#### 4.2.6 Nuclear magnetic resonance

NMR data were recorded on machines from BRUKER (Avance III 300, Avance III 400 and Avance 500 with a Prodigy broadband cryoprobe). Spectra were referenced to the residual solvent signals (THF-*d*<sub>6</sub>:  $\delta$  <sup>1</sup>H = 3.58 ppm,  $\delta$  <sup>13</sup>C = 67.2 ppm; C<sub>6</sub>D<sub>6</sub>:  $\delta$  <sup>1</sup>H = 7.16 ppm,  $\delta$  <sup>13</sup>C = 128.06 ppm; toluene-*d*<sub>8</sub>:  $\delta$  <sup>1</sup>H = 2.08 ppm,  $\delta$  <sup>13</sup>C = 20.4 ppm; CD<sub>2</sub>Cl<sub>2</sub>:  $\delta$  <sup>1</sup>H = 5.32 ppm,  $\delta$  <sup>13</sup>C = 53.8 ppm). <sup>31</sup>P and <sup>15</sup>N NMR spectra are reported relative to external standards (phosphoric acid and nitromethane respectively, both defined as  $\delta$  = 0.0 ppm). Signal multiplicities are abbreviated as: s (singlet), d (doublet), t (triplet), q (quartet), qui (quintet), m (multiplet), br (broad). In all quantitative NMR experiments, the relaxation delay was set to 15 s to allow for full relaxation of all compounds.

#### 4.2.7 Mass spectrometry

LIFDI (LINDEN CMS) mass spectra were measured by the Zentrale Massenabteilung, Fakultät für Chemie, Georg-August-Universität Göttingen.

#### 4.2.8 UVvis spectroscopy

UV/Vis spectra were recorded on an AGILENT Cary 300 spectrometer.

#### 4.2.9 IR spectroscopy

IR spectra were measured in the solid state using a BRUKER ALPHA FT-IR spectrometer with Platinum ATR module.

#### 4.2.10 Resonance Raman spectroscopy

Resonance Raman (rR) spectra were measured using a Horiba Scientific LabRAM HR 800 spectrometer with open-electrode CCD detector in combination with a free space optical microscope and a He:Ne-laser (632.8 nm).

#### 4.2.11 Magnetic measurements

Magnetic moments were determined by Evans' method as modified by Sur and corrected for diamagnetic contribution.<sup>300</sup> Temperature-dependent magnetic susceptibility measurements were carried out with a Quantum-Design MPMS-XL-5 SQUID magnetometer equipped with a 5 T magnet in the range from 210 to 2 K at 0.5 T applied magnetic field. Each raw data file for the measured magnetic moment was corrected for the diamagnetic contribution

of the gel bucket and of the inert oil according to  $M^{\text{dia}} = \chi_g mH$ , with the experimentally obtained gram susceptibility of the gel bucket ( $\chi_g = -5.70 \times 10^{-7} \text{ emu}/(\text{g}\cdot\text{Oe})$ ) and of the oil ( $\chi_g = -3.82 \times 10^{-7} \text{ emu}/(\text{g}\cdot\text{Oe})$ ). The molar susceptibility data were corrected for the diamagnetic contribution according to  $\chi_M^{\text{dia}}(\text{sample}) = -0.5M \times 10^{-6} \text{ cm}^3 \text{ mol}^{-1}$ .<sup>301</sup> Paramagnetic impurities (PI) were included according to  $\chi_{\text{calc}} = (1 - \text{PI})\chi + \text{PI}\chi_{\text{mono}} + \text{TIP}$ . Simultaneous calculation of the experimental temperature-dependent and VTVH data was performed with the julX\_2S program: E. Bill, Max-Planck Institute for Chemical Energy Conversion, Mülheim/Ruhr, Germany. Before simulation, the experimental data were corrected for TIP.

#### 4.2.12 Quantum yield determination of $\mathbf{11}^{\text{Br}}$

The quantum yield of the photolytic process from  $\mathbf{11}^{\text{Br}}$  to  $\mathbf{13}^{\text{Br}}$  was determined at a wavelength of 390 nm LED lamp. The quantum flux of the LED lamp (25% power output) was quantified using a photodiode (Thorlabs S120VC, 200 – 1100 nm) ( $I = 9.032 \cdot 10^{-7} \text{ mol min}^{-1} \text{ cm}^{-1}$ ) which was positioned 20 cm in front of the LED lamp. The photodiode was exchanged by a sealed Young UVvis cuvette equipped with a stirring bar containing a  $4 \cdot 10^{-5} \text{ M}$  solution of  $\mathbf{11}^{\text{Br}}$ . A UVvis spectrum at  $t = 0 \text{ min}$  was recorded and the sample is exposed to the light source under stirring for 20 minutes. The photolysis progress was monitored by recording a UVvis spectrum every 2 minutes (Figure 4.1). The absorbance of the transition at  $\lambda = 589 \text{ nm}$  was chosen for the quantum yield calculation following equation (1):

$$\Phi = \frac{\Delta n_{t_x - t_{(x-1)}}}{n_{\text{Photons}, 2 \text{ min}} \cdot (1 - 10^{-A_{390}})} \quad (1)$$

$$n_{\text{Photons}, 2 \text{ min}} = I \cdot t \cdot a = 3.613 \cdot 10^{-6} \text{ mol} \quad (3)$$

The term  $\Delta n_{t_x - t_{(x-1)}}$  in equation (1) represents the photolytic decay of ( $\mathbf{11}^{\text{Br}}$ ), i.e. the difference of the amount of ( $\mathbf{11}^{\text{Br}}$ ) before and after each photolysis step. The term  $n_{\text{Photons}, 2 \text{ min}}$  defines the number of photons the cuvette is subjected to within 2 minutes as defined in equation (2).  $A_{390}$  is the absorption at  $\lambda = 390 \text{ nm}$ .

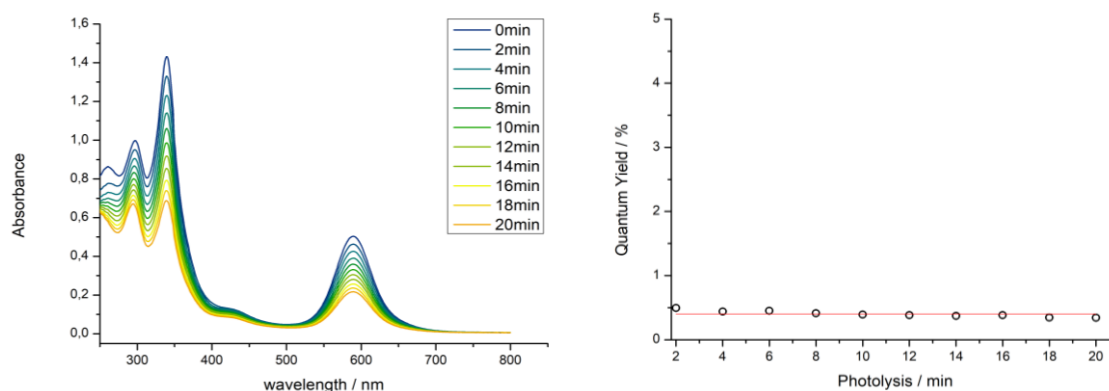


**Figure 4.1** Left: Photolysis of  $\mathbf{11}^{\text{Br}}$  tracked by UVvis spectroscopy. Right: Averaged quantum yield.

The quantum yield is determined for every photolysis step and the plotted data are linearly fitted to converge to a value of  $\Phi = 0.40 \pm 0.02\%$  (Figure S32, right).

#### 4.2.13 Rate constant determination for halide loss of $10^{\text{Cl/Br/I}}$ upon reduction and isomerization of $15^{\text{BArF}}$ upon reduction

The method for the determination of the rate constant of for halide loss of complexes  $10^{\text{Cl}}$ ,  $10^{\text{Br}}$ ,  $10^{\text{I}}$  and for isomerization of  $15^{\text{BArF}}$  was adapted from the group of Minter.<sup>302,303</sup>

The rate constant is determined by plotting  $[\text{Re}^{\text{II}}]$  as a function of the reaction time. The time is derived from the potential window and can be calculated by equation (3):

$$t = \frac{|E_R - E_{ipc}| + |E_R - E_{ipa}|}{\nu} \quad (3)$$

where  $E_R$  is the reverse potential,  $E_{ipc}$  and  $E_{ipa}$  are potentials of the peak currents of the forward and reversed peak, respectively, and  $\nu$  is the scan rate. The concentration of  $[\text{Re}^{\text{II}}]$  at the time  $t$  can be derived from the peak current ratio  $I_{pa}$  and  $I_{pc}$  (Randles Sevcik equation), equation (4):

$$\frac{I_{pa}}{I_{pc}} = \frac{[\text{Re}^{\text{II}}]_t D^{1/2}_{\text{Re}^{\text{II}}}}{[\text{Re}^{\text{II}}]_0 D^{1/2}_{\text{Re}^{\text{III}}}} \quad (4)$$

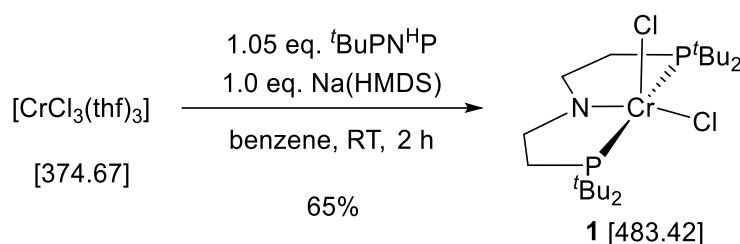
Assuming, that the diffusion coefficients  $D^{1/2}$  are the similar for the  $\text{Re}^{\text{II}}$  and  $\text{Re}^{\text{III}}$  complex gives equation (5):

$$\frac{I_{pa}}{I_{pc}} = \frac{[\text{Re}^{\text{II}}]_t}{[\text{Re}^{\text{II}}]_0} \quad (5)$$

$[\text{Re}^{\text{II}}]_t$  is derived by multiplying  $I_{pa}/I_{pc}$  with the bulk concentration of the  $\text{Re}^{\text{III}}$  complex. The obtained values are then plotted versus the corresponding calculated reaction times. Therefore, cyclic voltammograms of complexes  $10^{\text{Cl}}$  (Figure 6.25),  $10^{\text{Br}}$  (Figure 6.26),  $10^{\text{I}}$  (Figure 6.31) were recorded with the focus on the  $\text{Re}^{\text{III/II}}$  couple at different scan rates over different orders of magnitude. For this analysis, only peak current ratios above  $i_{pa}/i_{pc} = 0.6$  were included.<sup>239</sup>

## 4.3 Synthesis

### 4.3.1 Synthesis of $[\text{CrCl}_2(\text{}^t\text{BuPNP})]$ (**1**)



A solution of  $\text{HN}(\text{CH}_2\text{CH}_2\text{P}^t\text{Bu}_2)_2$  (991 mg, 2.74 mmol, 1.0 eq.) in benzene (50 ml) was added dropwise to a solution of  $\text{CrCl}_3(\text{thf})_3$  (978 mg, 2.61 mmol, 0.95 eq.) in benzene (200 ml) forming a dark blue suspension. A solution of  $\text{Na(HMDS)}$  (479 mg, 2.61 mmol, 1.05 eq.) in benzene (50 ml) was added under rigorously stirring to give a dark brown reaction mixture which was stirred for 2 h and filtrated. The solvent was removed *in vacuo* and the remaining darkish brown solid was washed with pentane (4 x 50 ml) to yield **1** as a brown, crystalline solid (820 mg, 1.7 mmol, 65%).

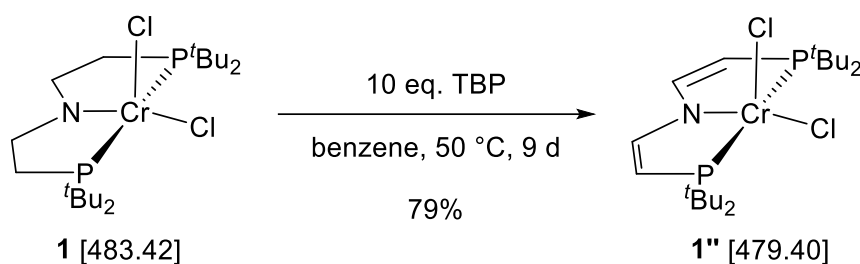
Crystals suitable for X-ray diffraction were obtained from gas diffusion layering of a benzene solution with pentane at room temperature.

**Elem. Anal.** found (calcd) for  $\text{C}_{20}\text{H}_{44}\text{Cl}_2\text{CrNP}_2$ : C, 49.85 (49.69); H, 9.43 (9.17); N, 2.73 (2.90).

**Magnetic Moment** (Evans',  $\text{C}_6\text{D}_6$ )  $\mu_{\text{eff}} = 3.83 \pm 0.1 \mu_{\text{B}}$ .

$^1\text{H NMR}$  ( $\text{C}_6\text{D}_6$ , 300 MHz, ppm): 5.51 ( $^t\text{Bu}$ ,  $w_{1/2} = 743$  Hz), -21.94 ( $\text{CH}_2$ ,  $w_{1/2} = 790$  Hz).

**MS** (LIFDI, THF):  $m/z$  482.2 (100%,  $[\text{M}^+]$ ).

4.3.2 Synthesis of  $[\text{CrCl}_2(\text{tBuPNP})]$  (**1''**)

A solution of **1** (780 mg, 1.62 mmol, 1.0 eq.) and freshly synthesized 2,4,6-*tert*-butylphenoxy radical (3.38 g, 13.0 mmol, 8 eq.) in benzene (250 ml) was stirred for 7 days at 50 °C. A second portion of 2,4,6-*tert*-butylphenoxy radical (0.42 g, 1.62 mmol, 1.0 eq.) in benzene (10 ml) was added and the reaction mixture was stirred for additional 24 h. A third portion of 2,4,6-*tert*-butylphenoxy radical (0.42 g, 1.62 mmol, 1.0 eq.) in benzene (10 ml) was added and stirred for another 24 h. The solvent was evaporated and the dark brown residual solid washed with pentane (5 x 50 ml) to obtain a reddish-brown crude product. The product was extracted with benzene and filtered. Removing the solvent from the vine red benzene solution gives **1''** as red brown solid (1.28 mmol, 613 mg, 79%).

**Elem. Anal.** found (calcd) for  $\text{C}_{20}\text{H}_{40}\text{Cl}_2\text{CrNP}_2$ : C, 50.14 (50.11); H, 8.38 (8.41); N, 2.96 (2.92).

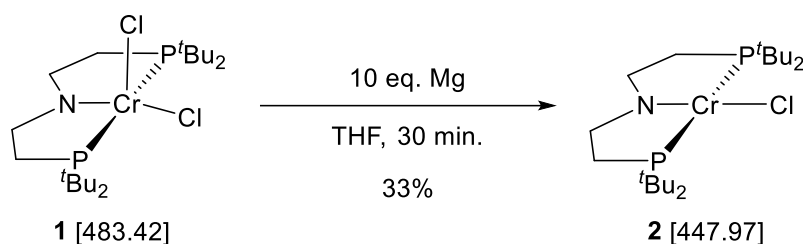
**Magnetic moment** (Evans',  $\text{C}_6\text{D}_6$ )  $\mu_{\text{eff}} = 3.65 \pm 0.1 \mu_{\text{B}}$ .

**$^1\text{H}$  NMR** ( $\text{C}_6\text{D}_6$ , 300 MHz, ppm): 1.14 (tBu,  $m_{1/2} = 723$  Hz), -115.68 (CH,  $m_{1/2} = 3560$  Hz), -142.43 (CH,  $m_{1/2} = 4620$  Hz).

**MS** (LIFDI, toluene):  $m/z$  478.1 (100%,  $[\text{M}^+]$ ).

**IR** (ATR,  $\text{cm}^{-1}$ ): 1524 (C=C).



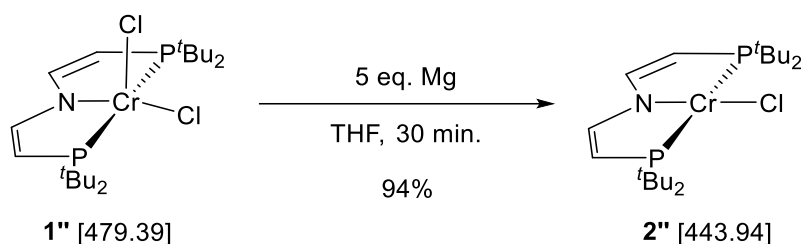
4.3.3 Synthesis of  $[\text{CrCl}(\text{tBuPNP})]$  (**2**)

To a solution of **1** (70 mg, 144  $\mu\text{mol}$ , 1.0 eq.) in THF (6 ml) an excess of magnesium powder was added (35 mg, 1.44 mmol, 100 eq.) and the resulting suspension was stirred for 30 minutes. Within this time, the color turned into purple and the solvent was removed *in vacuo*. The product was extracted with pentane until the filtrate is colourless and filtered through a filter pipette and concentrated until the compound started to crystallize. After storage for three days at  $-80\text{ }^\circ\text{C}$  the supernatant solution was decanted and the crystals washed with pentane to obtain **2** as a crystalline solid (21 mg, 47  $\mu\text{mol}$ , 33%).

Crystals suitable for X-ray diffraction were obtained from a saturated pentane solution stored at  $-40\text{ }^\circ\text{C}$ .

$^1\text{H NMR}$  ( $\text{C}_6\text{D}_6$ , 300 MHz, ppm): 100.46 ( $\text{CH}_2$ ,  $\nu_{1/2} = 2770\text{ Hz}$ ), 10.73 ( $\text{tBu}$ ,  $\nu_{1/2} = 2513\text{ Hz}$ ),  $-39.65$  ( $\text{CH}_2$ ,  $\nu_{1/2} = 1360\text{ Hz}$ ).

**MS** (LIFDI, toluene):  $m/z$  447.2 (100%,  $[\text{M}^+]$ ).

4.3.4 Synthesis of  $[\text{CrCl}(\text{}^t\text{BuPNP})] \mathbf{2''}$ 

To a vine red solution of  $\mathbf{1''}$  (300 mg, 626  $\mu\text{mol}$ , 1.0 eq) in THF (20 ml) an excess of magnesium powder (76 mg, 3.13 mmol, 5 eq.) was added. The reaction mixture was rigorously stirred for 30 minutes forming a deep blue solution. The solvent was evaporated and the purple blue solid extracted with pentane (4 x 3 ml). The deep blue extract was filtered through a filter cannula and the solvent was removed to obtain the product  $\mathbf{2''}$  as a purple crystalline solid (262 mg, 591  $\mu\text{mol}$ , 94%).

Crystals suitable for X-ray diffraction were obtained from a saturated pentane solution stored at  $-40\text{ }^\circ\text{C}$ .

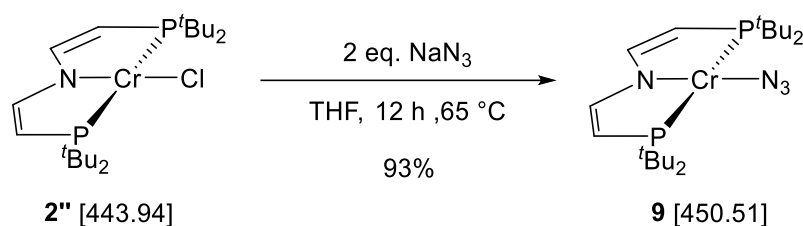
**Elem. Anal.** found (calcd) for  $\text{C}_{20}\text{H}_{40}\text{ClCrNP}_2$ : C, 54.17 (54.11); H, 9.20 (9.08); N, 3.17 (3.16).

**Magnetic moment**  $\mu_{\text{eff}} = 4.51 \pm 0.1 \mu_{\text{B}}$ .

**$^1\text{H}$  NMR** ( $\text{C}_6\text{D}_6$ , 300 MHz, ppm): 13.61 ( $^t\text{Bu}$ ,  $m_{1/2} = 3380$  Hz),  $-161.85$  ( $\text{CH}$ ,  $m_{1/2} = 3140$  Hz),  $-217.13$  ( $\text{CH}$ ,  $m_{1/2} = 5100$  Hz).

**MS** (LIFDI, THF):  $m/z$  443.2 (100%,  $[\text{M}^+]$ ).

**IR** (ATR,  $\text{cm}^{-1}$ ): 1518 (C=C).

4.3.5 Synthesis of  $[\text{CrN}_3(\text{tBuPNP})]$  (**9**)

A Schlenk tube was charged with **2''** (50 mg, 112  $\mu\text{mol}$ , 1.0 eq.) and sodium azide (14.5 mg, 224  $\mu\text{mol}$ , 2.0 eq.). THF (5 ml) was added and the suspension was stirred for 12 h at 65  $^\circ\text{C}$ . The solvent was removed *in vacuo* and the greenish blue residues extracted with benzene (3 x 2 ml). The extract was filtered through a filter pipette. The solvent was removed by lyophilization to obtain **9** as a purple solid (47 mg, 112  $\mu\text{mol}$ , 93%).

Crystals suitable for X-ray diffraction were obtained from a saturated benzene solution.

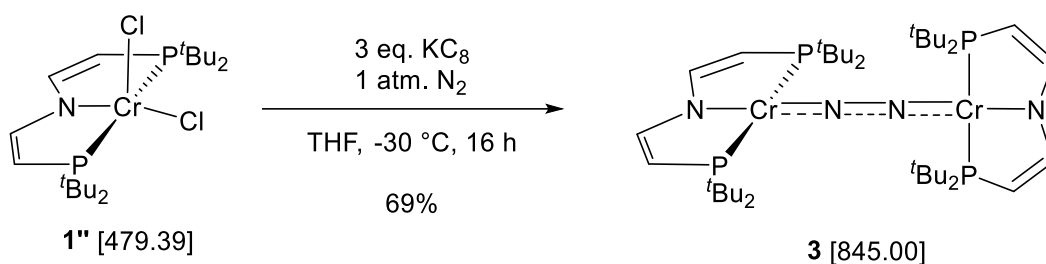
**Elem. Anal.** found (calcd) for  $\text{C}_{20}\text{H}_{40}\text{CrN}_4\text{P}_2$ : C, 53.08 (53.32); H, 8.40 (8.95); N, 11.99 (12.44).

**Magnetic moment**  $\mu_{\text{eff}} = 4.42 \pm 0.1 \mu_{\text{B}}$ .

**$^1\text{H}$  NMR** ( $\text{C}_6\text{D}_6$ , 300 MHz, ppm): 13.73 ( $^t\text{Bu}$ ,  $m_{1/2} = 1457$  Hz), -155.64 ( $\text{CH}$ ,  $m_{1/2} = 3550$  Hz), -155.64 ( $\text{CH}$ ,  $m_{1/2} = 3890$  Hz).

**MS** (LIFDI, toluene):  $m/z$  450.1 (100%,  $[\text{M}^+]$ ).

**IR** (ATR,  $\text{cm}^{-1}$ ): 2119 ( $\text{N}_3$ ), 2102 ( $\text{N}_3$ ), 2086 ( $\text{N}_3$ ), 2069 ( $\text{N}_3$ ), 1522 ( $\text{C}=\text{C}$ ).

4.3.6 Synthesis of  $[(\mu\text{-N}_2)\{\text{Cr}(\text{}^t\text{BuPNP''})\}_2]$  (**3**)

A 100 ml YOUNG flask suited with stirring bar was charged with **1''** (500 mg, 1.04 mmol, 1.0 eq.) and potassium graphite (424 mg, 3.12 mmol, 3.0 eq.). 15 ml of THF were degassed by 3 freeze-pump-thaw cycles and transferred by trap-to-trap condensation. After condensation, the YOUNG tube was backfilled with dinitrogen, sealed, and stirred for 15 hours at  $-30\text{ }^\circ\text{C}$ . A color change was observed from vine red via deep blue to deep red brown. The solvent was removed *in vacuo* and the residue was extracted with pentane (50 ml) until the extract is pale orange. The extract was filtered and concentrated to a volume of 10 ml. The concentrated solution was poured into a vial filled with 10 ml of HMDSO. The solvent was removed until the product starts to crystallize. The saturated solution was stored at  $-40\text{ }^\circ\text{C}$  for 2 days. The mother liquor was decanted to yield **3** as black needles (226 mg, 267  $\mu\text{mol}$ , 51%). Further concentration of the mother liquor and storing at  $-40\text{ }^\circ\text{C}$  gave a second batch of crystals (75 mg, 88.7  $\mu\text{mol}$ , 17%).

Crystals suitable for X-ray diffraction were obtained from a saturated HMDSO solution stored at  $-40\text{ }^\circ\text{C}$ .

**Elem. Anal.** found (calcd) for  $\text{C}_{40}\text{H}_{80}\text{Cr}_2\text{N}_4\text{P}_4$ : C, 56.65 (56.86); H, 9.50 (9.54); N, 5.74 (6.63).

**Magnetic susceptibility** (SQUID)  $\chi_m = 6.08\text{ emu}\cdot\text{mol}^{-1}$  (210 K);  $\mu_{\text{eff}} = 6.95\ \mu_{\text{B}}$ .

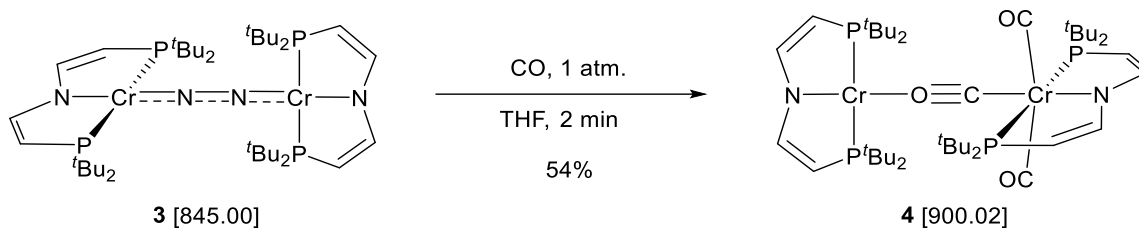
**Magnetic Moment** (Evans',  $\text{C}_6\text{D}_6$ )  $\mu_{\text{eff}} = 6.31 \pm 0.1\ \mu_{\text{B}}$ .

**$^1\text{H}$  NMR** ( $\text{C}_6\text{D}_6$ , 300 MHz, ppm): 16.33 ( $\text{}^t\text{Bu}$ ,  $m_{1/2} = 4071\text{ Hz}$ ), backbone signals were not observed over a spectral width between  $\delta = -500 - 300\text{ ppm}$ .

**MS** (LIFDI, toluene):  $m/z$  844.5 (100%, [ $^{14}\text{N}\text{-M}^+$ ]); 846.4 (100%, [ $^{15}\text{N}\text{-M}^+$ ]).

**rRaman** ( $\lambda_{\text{ex}} = 633\text{ nm}$ , pentane, RT,  $\text{cm}^{-1}$ ),  $^{14}\text{N}$ : 1651 ( $\nu_{\text{NN}}$ );  $^{15}\text{N}$ : 1594 ( $\nu_{\text{NN}}$ ).

**IR** (Nujol,  $\text{cm}^{-1}$ ): 1519 (C=C), 1503 (C=C).

4.3.7 Synthesis of  $[\{\text{Cr}(\text{CO})_2(\text{}^t\text{BuPNP}^{\text{''}})\}(\mu\text{-CO})\{\text{Cr}(\text{}^t\text{BuPNP}^{\text{''}})\}]$  (**4**)

A deep red brown solution of **3** (40 mg, 47.3  $\mu\text{mol}$ , 1.0 eq.) in THF (2 ml) was degassed by three freeze-pump-thaw cycles and sealed under vacuum in a Young tube. The solution was exposed to carbon monoxide for 2 min whereby the color of the solution changes into dark green. The CO gas was stored over a cooling coil at  $-80\text{ }^\circ\text{C}$  for 30 minutes prior to usage. The solvent was removed, and the residual substance was extracted with pentane. The solvent was removed *in vacuo* until the product starts to crystallize. Storing at  $-80\text{ }^\circ\text{C}$  for 18 h formed a dark green crystalline solid. The mother liquor was decanted, and the crystals washed with pentane at  $-80\text{ }^\circ\text{C}$  to obtain **4** (25 mg, 25.7  $\mu\text{mol}$ , 54%).

Crystals suitable for X-ray diffraction were obtained from a saturated pentane solution stored at  $-40\text{ }^\circ\text{C}$ .

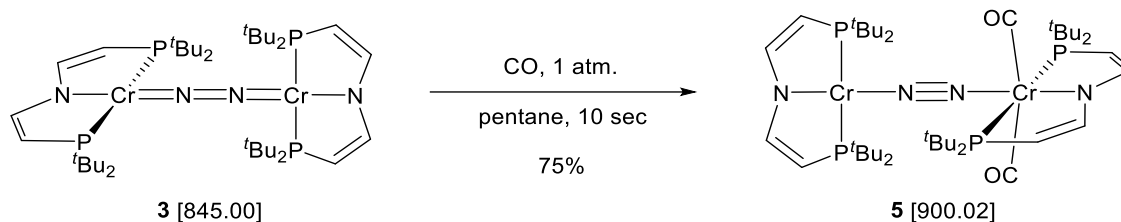
**Elem. Anal.** found (calcd) for  $\text{C}_{43}\text{H}_{80}\text{Cr}_2\text{N}_2\text{O}_3\text{P}_2$ : C, 57.83 (57.32); H, 9.10 (8.95); N, 3.00 (3.11).

**Magnetic susceptibility** (SQUID)  $\chi_{\text{m}} = 3.46\text{ cm}^3 \cdot \text{mol}^{-1}$  (210 K).

**$^1\text{H NMR}$**  ( $\text{C}_6\text{D}_6$ , 300 MHz, ppm): 13.28 ( $^t\text{Bu}$ ,  $w_{1/2}$  not determinable due to superimposed signals), 7.79 ( $\text{CH}$ ,  $w_{1/2} = 133.5\text{ Hz}$ ), 2.79 ( $\text{CH}$ ,  $w_{1/2}$  not determinable due to superimposed signals), 1.57 ( $^t\text{Bu}$ ,  $w_{1/2}$  not determinable due to superimposed signals), 0.38 ( $\text{CH}$ ,  $w_{1/2}$  not determinable due to superimposed signals),  $-1.57$  ( $\text{CH}$ ,  $w_{1/2} = 56.3\text{ Hz}$ ) ppm.

**MS** (LIFDI):  $m/z$  (%) 901.4 (100%).

**IR** (ATR,  $\text{cm}^{-1}$ ): 1792 (term. CO), 1542 ( $\mu\text{-CO}$ ), 1527 ( $\text{C}=\text{C}$ ), 1506 ( $\text{C}=\text{C}$ ).

4.3.8 Synthesis of  $[\{\text{Cr}(\text{CO})_2(\text{}^t\text{BuPNP''})\}(\mu\text{-N}_2)\{\text{Cr}(\text{}^t\text{BuPNP''})\}]$  (**5**)

A dark reddish-brown solution of **3** (130 mg, 154  $\mu\text{mol}$ , 1.0 eq.) in pentane (2 ml) was degassed by three freeze-pump-thaw cycles and sealed under vacuum in a young tube. The solution was exposed to carbon monoxide for 10 seconds resulting in an immediate colour change into deep green followed by precipitation of a black solid. The CO gas was stored over a cooling coil at  $-80\text{ }^\circ\text{C}$  for 30 minutes prior to usage. The CO atmosphere was removed and the tube was transferred into a glove box. The mother liquor was decanted and the crystalline black solid was washed with pentane at  $-80\text{ }^\circ\text{C}$  until the washing solution is almost colourless. Complex **5** was isolated as a black crystalline solid (63 mg, 72.2  $\mu\text{mol}$ , 47%).

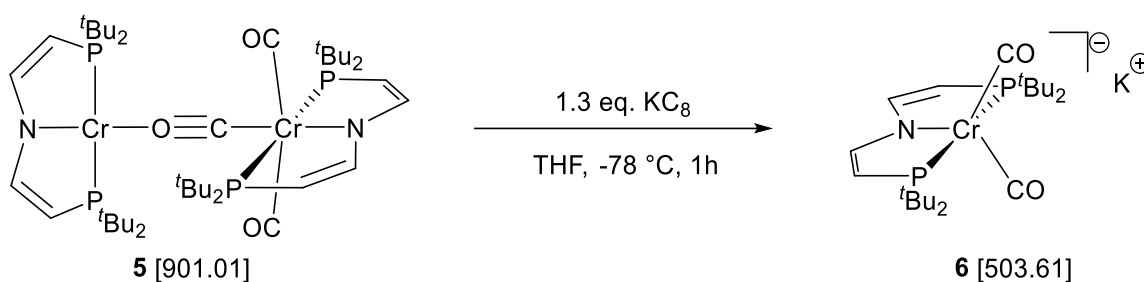
Crystals suitable for X-ray diffraction were obtained from a saturated pentane solution stored at  $-40\text{ }^\circ\text{C}$ .

**Elem. Anal.** found (calcd) for  $\text{C}_{42}\text{H}_{80}\text{Cr}_2\text{N}_4\text{O}_2\text{P}_4$ : C, 55.68 (55.99); H, 9.03 (8.95); N, 4.38 (6.22).

$^1\text{H-NMR}$  complex undergoes decomposition in solution.

**MS** (LIFDI):  $m/z$  (%)  $^{14}\text{N}$ : 844.4 (70,  $[\text{}^{14}\text{N-Cr}_2] - 2\text{CO}$ ), 872.3 (30,  $[\text{}^{14}\text{N-Cr}_2]\text{-N}_2$ );  $^{15}\text{N}$ : 846.6 (75,  $[\text{}^{15}\text{N-Cr}_2] - 2\text{CO}$ ), 872.7 (25,  $[\text{Cr}_2]\text{-N}_2$ ).

**IR** (ATR,  $\text{cm}^{-1}$ ): 1834 (CO) ( $^{15}\text{N}$ : 1828), 1822 (CO) ( $^{15}\text{N}$ : 1817), 1766 ( $^{15}\text{N}$ : 1717).

4.3.9 Synthesis of  $\text{K}[\text{Cr}(\text{CO})_2(\text{tBuPNP}^{\text{''}})]$  (**6**)

A schlenk tube was charged with **5** (23 mg, 25.6  $\mu\text{mol}$ , 1.0 eq.) and potassium graphite (4.5 mg, 30.7  $\mu\text{mol}$ , 1.2 eq.). THF (2 ml) was added at  $-78\text{ }^\circ\text{C}$  to form a deep red reaction mixture. The reaction was stirred for 2 h and the solvent was removed. The dark residual solid was washed with pentane (4 x 3 ml) and extracted with THF (3 x 1 ml). The deep blue extract was filtered through a filter pipette and concentrated to a volume of approximately 0.5 ml. The product was precipitated by the addition of 3 ml pentane. The almost colorless mother liquor was decanted and the blue solid washed with pentane (3 x 2 ml). The product **6** was obtained as a purple solid (10 mg, 9.9  $\mu\text{mol}$ , 39%).

Crystals suitable for X-ray diffraction were only obtained by sequestering the potassium atom with an equimolar amount 18-crown-6. The complex was crystallized by gas diffusion layering of a THF solution of **6** with pentane. The obtained crystalline material was used for elemental analysis.

**Elem. Anal.** (calcd) for  $\text{C}_{34}\text{H}_{64}\text{CrNO}_8\text{P}_2$ : C, 53.24 (53.18); H, 8.57 (8.40); N, 1.68 (1.82).

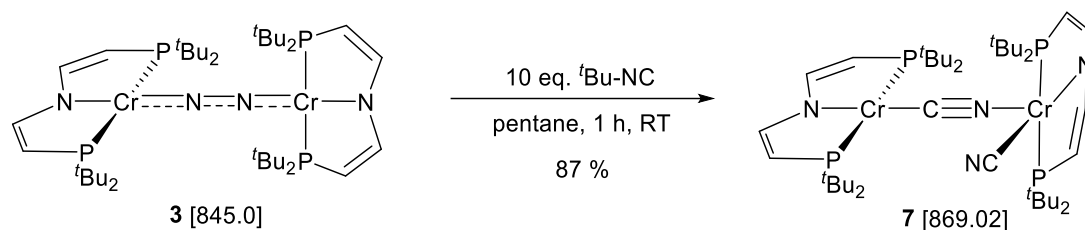
$^1\text{H}\{^{31}\text{P}\}$  NMR (THF- $d_8$ , 500.3 MHz, ppm): 7.36 (d,  $^3J_{\text{HH}} = 5.9\text{ Hz}$ , 2H, NCH), 4.18 (d,  $^3J_{\text{HH}} = 5.9\text{ Hz}$ , 2H, 2H, PCH), 1.24 (s, 36 H, tBu).

$^{13}\text{C}\{^1\text{H}\}$  NMR (THF- $d_8$ , 125.8 MHz, ppm): 253.5 (t,  $^2J_{\text{CP}} = 13.2\text{ Hz}$ , CO), 162.6, (AXY,  $N = |^2J_{\text{AX}} + ^3J_{\text{AY}}| = 30.3\text{ Hz}$ , 2H, N-CH-CH-P), 86.2, (AXY,  $N = |^1J_{\text{AX}} + ^3J_{\text{AY}}| = 18.8\text{ Hz}$ , 2H, N-CH-CH-P), 36.0 (AXY,  $N = |^1J_{\text{AX}} + ^3J_{\text{AY}}| = 4.9\text{ Hz}$ ,  $\text{C}(\text{CH}_3)_3$ ), 30.07 (AXY,  $N = |^2J_{\text{AX}} + ^4J_{\text{AY}}| = 6.2\text{ Hz}$ ,  $\text{C}(\text{CH}_3)_3$ ).

$^{31}\text{P}\{^1\text{H}\}$  NMR (THF- $d_8$ , 202.5 MHz, ppm): 101.2 (s,  $\text{P}^t\text{Bu}_2$ ).

**IR** (ATR-IR,  $\text{cm}^{-1}$ ): 1746 (CO), 1738 (CO), 1634 (C=C), 1510 (C=C).

**MS** (LIFDI, THF):  $m/z$  436.2 (100%,  $[\text{M}^+] - \text{CO}$ ).

4.3.10 Synthesis of  $[\{\text{Cr}(\text{CN})(^t\text{BuPNP}^{\text{''}})\}_2(\mu\text{-CN})\{\text{Cr}(^t\text{BuPNP}^{\text{''}})\}]$  (**7**)

In an argon filled glovebox, a vial suited with stirring bar was charged with **3** (40 mg, 47.3  $\mu\text{mol}$ , 1.0 eq.) and dissolved in 4 ml of pentane. A solution of *tert*-butyl isocyanide (39 mg, 473  $\mu\text{mol}$ , 10 eq.) in 1 ml pentane was added. The reaction solution turned immediately deep green and then orange over the course of one hour. The solvent was removed *in vacuo* and the residue was extracted with pentane. The extract was filtered and concentrated until the substance starts to crystallize. Storing at  $-40\text{ }^\circ\text{C}$  for two days formed a crystalline solid. The supernatant was decanted and the obtained crystalline solid was washed with pentane at  $-40\text{ }^\circ\text{C}$ . Drying *in vacuo* obtained the product **7** as dark orange crystals (24 mg, 27.6  $\mu\text{mol}$ , 58%). Further concentration of the mother liquor provides a second batch of crystals (12 mg, 13.8  $\mu\text{mol}$ , 29%).

Crystals suitable for X-ray diffraction were obtained by slow evaporation of a pentane/HMDSO mixture.

**Elem. Anal.** found (calcd) for  $\text{C}_{42}\text{H}_{80}\text{Cr}_2\text{N}_4\text{P}_4$ : C, 57.72 (58.05); H, 9.14 (9.28); N, 6.69 (6.45).

**Magnetic Moment** (Evans',  $\text{C}_6\text{D}_6$ ):  $\mu_{\text{eff}} = 6.11 \pm 0.1 \mu_{\text{B}}$ .

**$^1\text{H NMR}$**  ( $\text{C}_6\text{D}_6$ , 300 MHz, ppm): 12.37 ( $^t\text{Bu}$ ,  $m_{1/2} = 1887\text{ Hz}$ ), 3.20 ( $^t\text{Bu}$ ,  $m_{1/2} = 80.31\text{ Hz}$ ),  $-75.12$  ( $\text{CH}$ ,  $m_{1/2}$  not determinable due to low signal to noise ratio)  $-114.50$  ( $\text{CH}$ ,  $m_{1/2} = 3821\text{ Hz}$ ),  $-178.45$  ( $\text{CH}$ ,  $m_{1/2}$  not determinable due to low signal to noise ratio).

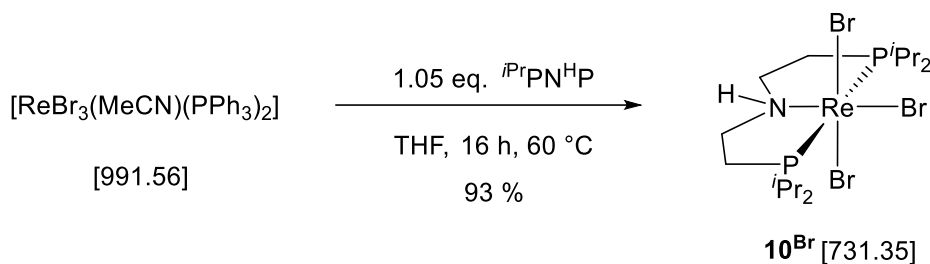
**IR** (ATR,  $\text{cm}^{-1}$ ): 2160 (term. CN), 2102 ( $\mu\text{-CN}$ ), 1509 ( $\text{C}=\text{C}$ ).

**MS** (LIFDI):  $m/z$  (%) 486.4 (100).



#### 4.3.11 Synthesis of [ReBr<sub>3</sub>(<sup>*i*</sup>PrPN<sup>H</sup>P)] (10<sup>Br</sup>)

Characterization of [ReBr<sub>3</sub>(<sup>*i*</sup>PrPN<sup>H</sup>P)] 10<sup>Br</sup> by NMR / IR spectroscopy and mass spectrometry was carried out by M. Sc. Sessa Kisan (AK Schneider, Georg-August-Universität Göttingen). Characterization by X-Ray diffractometry was performed by Niels Paul (“Abteilungspraktikum” under supervision of Maximilian Fritz). The synthetic route to analytical purity (elemental analysis) was designed by Maximilian Fritz.



A 250 ml Schlenk tube was charged with precursor [ReBr<sub>3</sub>(MeCN)(PPh<sub>3</sub>)<sub>3</sub>] (1.49 g, 1.50 mmol, 1.0 eq.). A solution of <sup>*i*</sup>PrPN<sup>H</sup>P (482 mg, 1.58 mmol, 1.05 eq.) in THF (50 ml) was added and the reaction mixture was heated for 16 h at 60 °C to give a yellow solution. The solvent was removed *in vacuo* and the yellow solid was intensively washed with pentane (4 x 30 ml) and diethyl ether (4 x 30 ml) to obtain 10<sup>Br</sup> (1.04 g, 1.43 mmol, 95%) as a yellow solid.

Crystals suitable for X-ray diffraction were obtained from gas diffusion layering of a THF solution with pentane at room temperature.

**Elem. Anal.** found (calcd) for C<sub>16</sub>H<sub>37</sub>Br<sub>3</sub>ReNP<sub>2</sub>: C, 26.25 (26.28); H, 5.09 (5.10); N, 1.97 (1.92).

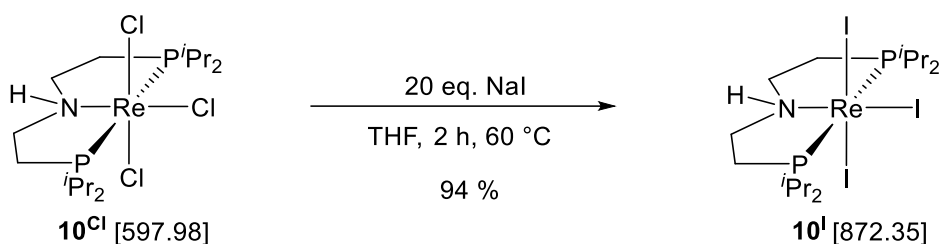
**<sup>1</sup>H NMR** (THF-*d*<sub>8</sub>, 300.2 MHz, ppm): 147.19 (s, 1H, NH), 9.42 (q, <sup>3</sup>J<sub>HH</sub> = 6.2 Hz, 6H, CHMe<sub>2</sub>), 9.2 (q, <sup>3</sup>J<sub>HH</sub> = 6.2 Hz, 6H, CHMe<sub>2</sub>), 8.57 (m, 12H, 2 CHMe<sub>2</sub> (signals superimposed)), 6.67 (m, 2H, 2 CHMe<sub>2</sub>), 6.29 (dt, <sup>3</sup>J<sub>HH</sub> = 5.2 Hz, <sup>3</sup>J<sub>HH</sub> = 14.6 Hz, 2H, CHMe<sub>2</sub>), 1.45 (q, <sup>3</sup>J<sub>HH</sub> = 7.2 Hz, 2H, CH<sub>2</sub>), -0.6 (d, <sup>3</sup>J<sub>HH</sub> = 14.5 Hz, 2H, CH<sub>2</sub>), -7.87 (q, <sup>3</sup>J<sub>HH</sub> = 12.3 Hz, 2H, CH<sub>2</sub>), -14.69 (m, 2H, CH<sub>2</sub>).

**<sup>1</sup>H NMR** (CD<sub>2</sub>Cl<sub>2</sub>, 300.2 MHz, ppm): 141.26 (s, 1H, NH), 9.68 (q, <sup>3</sup>J<sub>HH</sub> = 6.2 Hz, 6H, CHMe<sub>2</sub>), 9.25 (q, <sup>3</sup>J<sub>HH</sub> = 6.2 Hz, 6H, CHMe<sub>2</sub>), 8.64 (m, 12H, 2 CHMe<sub>2</sub> (signals are superimposed)), 8.55 (m, 2H, 2 CH<sub>2</sub> signal is superimposed), 6.42 (dt, <sup>3</sup>J<sub>HH</sub> = 5.2 Hz, <sup>3</sup>J<sub>HH</sub> = 14.6 Hz, 2H, CHMe<sub>2</sub>), 5.66 (m, 2H, CHMe<sub>2</sub>), -1.08 (d, <sup>3</sup>J<sub>HH</sub> = 14.5 Hz, 2H, CH<sub>2</sub>), -7.06 (q, <sup>3</sup>J<sub>HH</sub> = 12.3 Hz, 2H, CH<sub>2</sub>), -13.39 (m, 2H, CH<sub>2</sub>).

**<sup>31</sup>P{<sup>1</sup>H} NMR** (THF-*d*<sub>8</sub>, 121.4 MHz, ppm): -1426.2 (s, 2P, PPr<sub>2</sub>).

**<sup>31</sup>P{<sup>1</sup>H} NMR** (CD<sub>2</sub>Cl<sub>2</sub>, 121.4 MHz, ppm): -1488.0 (s, 2P, PPr<sub>2</sub>).

**CV** (0.1 M, N<sup>*n*</sup>Bu<sub>4</sub>PF<sub>6</sub> in THF): E<sub>1/2</sub> = -1.66 V (Re<sup>III/II</sup>), -0.22 V (Re<sup>IV/III</sup>).

4.3.12 Synthesis of  $[\text{ReI}_3(\text{P}^i\text{Pr}_2\text{NH}^i\text{P})]$  ( $\mathbf{10}^{\text{I}}$ )

A Schlenk tube was charged with  $\mathbf{10}^{\text{Cl}}$ <sup>43</sup> (321 mg, 537  $\mu\text{mol}$ , 1.0 eq.) and sodium iodide (10.7 mmol, 1.61 g, 20 eq.). The solids were suspended in THF (30 ml) and heated for 2 h at 60  $^\circ\text{C}$ . The initial yellow beige suspension turned into a deep red solution within this time. The solvent was removed *in vacuo* and the remaining solid was washed with diethyl ether (3 x 15 ml). The product was extracted with dichloromethane until the extract is nearly colourless. The solvent is evaporated and the solid was washed with demineralized water (3 x 2 ml) to obtain  $\mathbf{10}^{\text{I}}$  as a red solid (442 mg, 507  $\mu\text{mol}$ , 94%) after drying *in vacuo*.

Crystals suitable for X-ray diffraction were obtained from a saturated benzene solution.

**Elem. Anal.** found (calcd) for  $\text{C}_{16}\text{H}_{37}\text{I}_3\text{NP}_2\text{Re}$ : C, 22.07 (22.03); H, 4.32 (4.28); N, 1.61 (1.61).

$^1\text{H}\{^{31}\text{P}\}$  NMR ( $\text{CD}_2\text{Cl}_2$ , 500.3 MHz, ppm): 143.06 (s, 1H, NH), 9.40 (s, 6H,  $\text{CHMe}_2$ ), 8.61 (m, 12H,  $\text{CHMe}_2$ ), 8.23 (m, 6H,  $\text{CHMe}_2$ ), 6.62 (s, br, 2H,  $\text{CHMe}_2$ ), 5.63 (s, 2H,  $\text{CHMe}_2$ ), 3.84 (dt,  $^3J_{\text{HH}} = 5.0$  Hz,  $^3J_{\text{HH}} = 14.9$  Hz, 2H, N- $\text{CH}_2$ -CHH-P), -3.58 (d,  $^3J_{\text{HH}} = 14.7$  Hz, 2H, N- $\text{CH}_2$ -CHH-P), -9.09 (q,  $^3J_{\text{HH}} = 12.0$  Hz, 2H, N-CHH- $\text{CH}_2$ -P), -16.79 (m, 2H, N-CHH- $\text{CH}_2$ -P).

$^{13}\text{C}\{^1\text{H}\}$  NMR ( $\text{CD}_2\text{Cl}_2$ , 125.8 MHz, ppm): 189.2 (AXY,  $N = |^2J_{\text{AX}} + ^3J_{\text{AY}}| = 149.31$  Hz, N- $\text{CH}_2$ - $\text{CH}_2$ -P), 148.0 (s, br,  $\text{CHMe}_2$ ), 116.3 (AXY,  $N = |^1J_{\text{AX}} + ^3J_{\text{AY}}| = 21.8$  Hz, N- $\text{CH}_2$ - $\text{CH}_2$ -P), 110.8 (s, br,  $\text{CHMe}_2$ ), 28.13 (s,  $\text{CHMe}_2$ ), 19.02 (s,  $\text{CHMe}_2$ ), 18.56 (s,  $\text{CHMe}_2$ ), 17.46 (s, br,  $\text{CHMe}_2$ ).

$^{31}\text{P}\{^1\text{H}\}$  NMR ( $\text{CD}_2\text{Cl}_2$ , 202.2 MHz, ppm): -1480.7 (s,  $\text{P}^i\text{Pr}_2$ ).

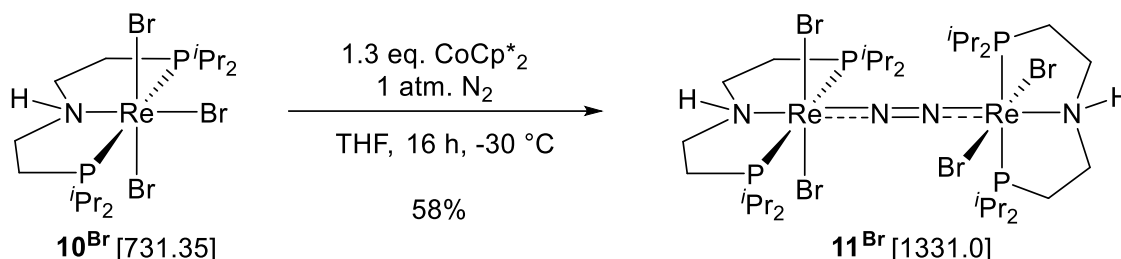
**MS** (LIFDI, THF):  $m/z$  873.0 (100%,  $[\text{M}^+]$ ).

**IR** (ATR,  $\text{cm}^{-1}$ ): 3124 (N-H).

**CV** (0.1 M,  $\text{N}^t\text{Bu}_4\text{PF}_6$  in THF):  $E_{\text{pc}} = -1.55$  V ( $\text{Re}^{\text{III/II}}$ ),  $E_{1/2} = -0.14$  V ( $\text{Re}^{\text{IV/III}}$ ).

### 4.3.13 Synthesis of $[(\mu\text{-N}_2)\{\text{ReBr}_2(\text{P}^i\text{Pr}_2\text{NH}^i\text{P})\}_2]$ ( $\mathbf{11}^{\text{Br}}$ )

The synthesis of  $\mathbf{11}^{\text{Br}}$  must be performed under exclusion of light.



A 250 ml round neck flask was charged with  $\mathbf{10}^{\text{Br}}$  (300 mg, 410  $\mu\text{mol}$ , 1.0 eq.) and dissolved in dinitrogen saturated THF (70 ml). A solution of decamethyl cobaltocene (134 mg, 410  $\mu\text{mol}$ , 1.0 eq.) in THF (45 ml) was added dropwise at  $-30\text{ }^\circ\text{C}$  over the course of 30 minutes via dropping funnel. The dark blue reaction mixture was stirred for one hour at  $-30\text{ }^\circ\text{C}$  and an additional solution of decamethyl cobaltocene (41 mg, 123  $\mu\text{mol}$ , 0.3 eq.) in THF (15 ml) was added. The reaction mixture was warmed to room temperature und stirred for 16 h. The solvent was removed *in vacuo* and the crude product was washed with pentane (4 x 30 ml). The dark blue solid was extracted with toluene until the extract was nearly colorless. The toluene extract was filtered and the solvent was removed. The dark blue substance was washed with acetonitrile (5 x 1.5 ml) at  $-40\text{ }^\circ\text{C}$  until the wash solution was nearly colorless. The crude product was finally washed with diethyl ether (5 x 2 ml) at  $-40\text{ }^\circ\text{C}$  and with pentane (3 x 5 ml) and dried *in vacuo*. The product  $\mathbf{11}^{\text{Br}}$  (158 mg, 119  $\mu\text{mol}$ , 58%) was isolated as a dark blue solid.

Crystals suitable for X-ray diffraction were obtained from a saturated benzene solution.

Procedure for the  $^{15}\text{N}$  isotopologue: A 10 ml young tube was charged with  $\mathbf{10}^{\text{Br}}$  (20 mg, 27.3  $\mu\text{mol}$ , 1.0 eq.) and decamethyl cobaltocene (10.5 mg, 32.4  $\mu\text{mol}$ , 1.2 eq.). THF (3 ml) was degassed and transferred by trap-to-trap condensation. After complete solvent transfer, the reaction flask was backfilled with  $^{15}\text{N}_2$  gas. Stirring 4 h at  $-40\text{ }^\circ\text{C}$  gave a dark blue solution. The solvent is removed *in vacuo* and the crude product was washed with pentane (4 x 2 ml) and with acetonitrile (5 x 1 ml) at  $-40\text{ }^\circ\text{C}$ . The blue reaction product was washed with diethyl ether (4 x 2 ml) to obtain  $^{15}\text{N}\text{-}\mathbf{11}^{\text{Br}}$  (7 mg, 5.3  $\mu\text{mol}$ , 39%).

**Elem. Anal.** found (calcd) for  $\text{C}_{32}\text{H}_{74}\text{Br}_4\text{Re}_2\text{N}_4\text{P}_4$ : C, 29.05 (28.88); H, 5.61 (5.60); N, 4.17 (4.21).

$^1\text{H}\{^{31}\text{P}\}$  NMR ( $\text{C}_6\text{D}_6$ , 500.3 MHz, ppm): 89.48 (t,  $^1J_{\text{NH}} = 11.0$  Hz, 2H, NH), 6.23 (h,  $^3J_{\text{HH}} = 7.4$  Hz, 2H, CHMe<sub>2</sub>), 5.50 (h,  $^3J_{\text{HH}} = 7.4$  Hz, 2H, CHMe<sub>2</sub>), 4.21 – 4.16 (m, 8H, CHMe<sub>2</sub> + CHMe<sub>2</sub> (signals superimposed)), 3.53 (d,  $^3J_{\text{HH}} = 7.2$  Hz, 6H, CHMe<sub>2</sub>), 3.39 (h,  $^3J_{\text{HH}} = 7.4$  Hz, 2H, CHMe<sub>2</sub>), 3.13 (d,  $^3J_{\text{HH}} = 7.6$  Hz, 6H, CHMe<sub>2</sub>), 2.84 (d,  $^3J_{\text{HH}} = 7.4$  Hz, 6H, CHMe<sub>2</sub>), 2.81 (d,  $^3J_{\text{HH}} = 7.1$  Hz, 6H, CHMe<sub>2</sub>), 2.50 (d,  $^3J_{\text{HH}} = 7.4$  Hz, 6H, CHMe<sub>2</sub>), 2.38 (d,  $^3J_{\text{HH}} = 7.6$  Hz, 6H, CHMe<sub>2</sub>), 1.96 (d,  $^3J_{\text{HH}} = 7.6$  Hz, 6H, CHMe<sub>2</sub>), 0.95 (dt,  $^3J_{\text{HH}} = 14.9$  Hz,  $^3J_{\text{HH}} = 5.2$  Hz, 2H, 2H, N-CH<sub>2</sub>-HH-P), -1.55 (dt, 2H,  $^3J_{\text{HH}} = 14.9$  Hz,  $^3J_{\text{HH}} = 5.2$  Hz, 2H,

N-CH<sub>2</sub>-HH-P), -5.90 (d, 2H, <sup>3</sup>J<sub>HH</sub> = 15.5 Hz, 2H, N-CH<sub>2</sub>-CHH-P), -7.55 (d, 2H, <sup>3</sup>J<sub>HH</sub> = 14.9 Hz, 2H, N-CH<sub>2</sub>-CHH-P), -8.68 (q, <sup>3</sup>J<sub>HH</sub> = 11.5 Hz, 2H, N-CHH-CH<sub>2</sub>-P), -11.54 (q, <sup>3</sup>J<sub>HH</sub> = 11.8 Hz, 2H, N-CHH-CH<sub>2</sub>-P), -12.4 (m, 2H, N-CHH-CH<sub>2</sub>-P), -13.4 (m, 2H, N-CHH-CH<sub>2</sub>-P) ppm.

<sup>13</sup>C{<sup>1</sup>H} NMR (C<sub>6</sub>D<sub>6</sub>, 125.8 MHz, ppm): 154.1 (s, N-CH<sub>2</sub>-CH<sub>2</sub>-P), 152.4 (s, N-CH<sub>2</sub>-CH<sub>2</sub>-P), 147.2 (d, <sup>1</sup>J<sub>CP</sub> = 19.2 Hz, CHMe<sub>2</sub>), 133.3 (d, <sup>1</sup>J<sub>CP</sub> = 19.8 Hz, CHMe<sub>2</sub>), 82.9 (d, <sup>1</sup>J<sub>CP</sub> = 20.4 Hz, N-CH<sub>2</sub>-CH<sub>2</sub>-P), 82.6 (d, <sup>1</sup>J<sub>CP</sub> = 20.4 Hz, N-CH<sub>2</sub>-CH<sub>2</sub>-P), 67.7 (d, <sup>1</sup>J<sub>CP</sub> = 17.2 Hz, CHMe<sub>2</sub>), 55.1 (d, <sup>1</sup>J<sub>CP</sub> = 17.5 Hz, CHMe<sub>2</sub>), 36.7 (s, CH<sub>3</sub>), 35.8 (s, CH<sub>3</sub>), 22.3 (s, CH<sub>3</sub>), 21.5 (s, CH<sub>3</sub>), 21.1 (s, CH<sub>3</sub>), 19.9 (s, CH<sub>3</sub>), 19.3 (s, CH<sub>3</sub>), 19.2 (s, CH<sub>3</sub>) ppm.

<sup>31</sup>P{<sup>1</sup>H} NMR (C<sub>6</sub>D<sub>6</sub>, 202.4 MHz, ppm): -381.4 (d, <sup>2</sup>J<sub>PP</sub> = 223.3 Hz, PPr<sub>2</sub>), -396.2 (d, <sup>2</sup>J<sub>PP</sub> = 224.5 Hz, PPr<sub>2</sub>).

<sup>15</sup>N{<sup>1</sup>H} NMR (C<sub>6</sub>D<sub>6</sub>, 50.7 MHz, ppm): -1071.4 (s, 2N, μ-N<sub>2</sub>).

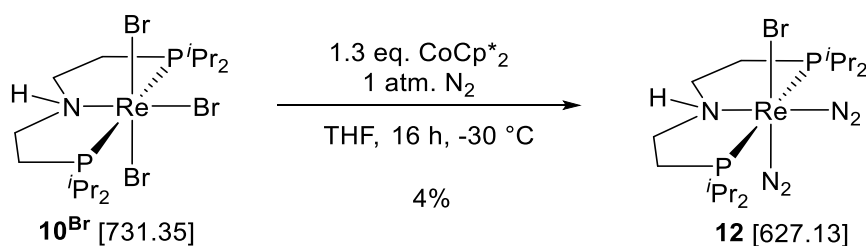
MS (LIFDI, THF): m/z 1330.1 (100%, [M<sup>+</sup>]),

IR (ATR, cm<sup>-1</sup>): 3150 (NH).

rRaman (λ<sub>ex</sub> = 633 nm, THF-d<sub>8</sub>, RT, cm<sup>-1</sup>): 1735 (μ-<sup>14</sup>N<sub>2</sub>); 1673 (μ-<sup>15</sup>N<sub>2</sub>).

CV (0.1 M <sup>n</sup>Bu<sub>4</sub>NPF<sub>6</sub> (THF)): E<sub>1/2</sub> = -0.81 V (Re<sup>II</sup>Re<sup>II</sup>/Re<sup>II</sup>Re<sup>III</sup>), -0.15 V (Re<sup>II</sup>Re<sup>III</sup>/Re<sup>III</sup>Re<sup>III</sup>).

UVvis (THF, RT): λ (ε / M<sup>-1</sup> cm<sup>-1</sup>) = 589 (12573), 341 (36162).

4.3.14 Synthesis of  $[\text{ReBr}(\text{N}_2)_2(\text{P}^i\text{Pr}^{\text{H}}\text{P})]$  (**12**)

This complex is a side product in the synthesis of  $\text{11}^{\text{Br}}$  and was isolated by crystallization of the saturated acetonitrile washing solution at  $-35$  °C for 3 days. The mother liquor was removed and the crystalline solid was washed with acetonitrile and diethyl ether at  $-40$  °C to obtain **12** as a green, crystalline solid (10 mg, 15.9  $\mu\text{mol}$ , 4%).

Crystals suitable for X-ray diffraction were obtained from a saturated acetonitrile solution stored at  $-40$  °C.

**Elem. Anal.** found (calcd) for  $\text{C}_{16}\text{H}_{37}\text{BrRe}_1\text{N}_5\text{P}_2$ : C, 30.81 (30.62); H, 5.83 (5.94); N, 10.01 (11.16).

$^1\text{H}\{^{31}\text{P}\}$  NMR (THF- $d_8$ , 500.3 MHz, ppm): 3.67 (m, 1H, NH), 3.36 (m, 2H, N-CHH- $\text{CH}_2\text{P}$ ), 3.11 (h,  $^3J_{\text{HH}} = 7.3$  Hz, 2H, CH( $\text{CH}_3$ ) $_2$ ), 2.66 (h,  $^3J_{\text{HH}} = 7.3$  Hz, 2H, CH( $\text{CH}_3$ ) $_2$ ), 2.40 (m, 4H, N-CHH- $\text{CH}_2\text{P}$  + N- $\text{CH}_2$ -CHHP), 1.53 (dt,  $^3J_{\text{HH}} = 5.9$  Hz,  $^3J_{\text{HH}} = 14.9$  Hz, 2H, N- $\text{CH}_2$ -CHHP), 1.40 (d,  $^3J_{\text{HH}} = 7.1$  Hz, 6H, CH( $\text{CH}_3$ ) $_2$ ), 1.34 (d,  $^3J_{\text{HH}} = 6.6$  Hz, 6H, CH( $\text{CH}_3$ ) $_2$ ), 1.33 (d,  $^3J_{\text{HH}} = 6.6$  Hz, 6H, CH( $\text{CH}_3$ ) $_2$ ), 1.27 (d,  $^3J_{\text{HH}} = 7.1$  Hz, 6H, CH( $\text{CH}_3$ ) $_2$ ).

$^{13}\text{C}\{^1\text{H}\}$  NMR (THF- $d_8$ , 125.8 MHz, ppm): 55.7 (AXY,  $N = |^2J_{\text{AX}} + ^3J_{\text{AY}}| = 8.3$  Hz, N- $\text{CH}_2$ - $\text{CH}_2$ -P), 29.3 (AXY,  $N = |^1J_{\text{AX}} + ^3J_{\text{AY}}| = 20.2$  Hz, N- $\text{CH}_2$ - $\text{CH}_2$ -P), 25.3 (AXY,  $N = |^1J_{\text{AX}} + ^3J_{\text{AY}}| = 24.4$  Hz, CH( $\text{CH}_3$ ) $_2$ ), 23.7 (AXY,  $N = |^1J_{\text{AX}} + ^3J_{\text{AY}}| = 21.2$  Hz, CH( $\text{CH}_3$ ) $_2$ ), 20.2 (AXY,  $N = |^2J_{\text{AX}} + ^4J_{\text{AY}}| = 4.1$  Hz, CH( $\text{CH}_3$ ) $_2$ ), 19.9 (m, 2 x CH( $\text{CH}_3$ ) $_2$ , signals superimposed), 18.4 (AXY,  $N = |^2J_{\text{AX}} + ^4J_{\text{AY}}| = 2.0$  Hz, CH( $\text{CH}_3$ ) $_2$ ).

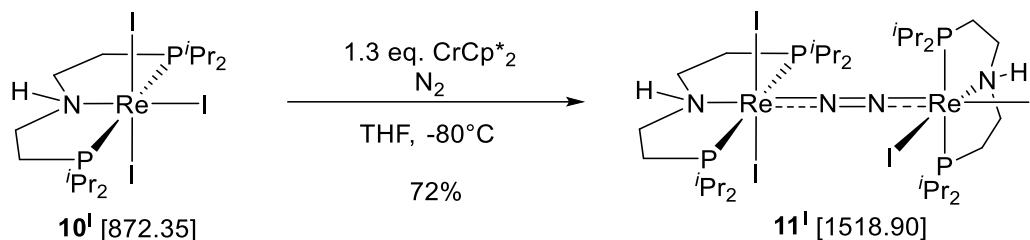
$^{31}\text{P}\{^1\text{H}\}$  NMR (THF- $d_8$ , 202.4 MHz, ppm): 31.1 (s,  $\text{P}^i\text{Pr}_2$ )

$^{15}\text{N}\{^1\text{H}\}$  NMR (THF- $d_8$ , 50.7 MHz, ppm):  $-340.1$  (s NH).

**IR** (ATR,  $\text{cm}^{-1}$ ): 3145 (NH), 2040 (term.  $\text{N}\equiv\text{N}$ ), 1938 (term.  $\text{N}\equiv\text{N}$ ).

### 4.3.15 Synthesis of $[(\mu\text{-N}_2)\{\text{ReI}_2(\text{P}^i\text{Pr}_2\text{N}^i\text{H})\}_2]$ (**11**<sup>I</sup>)

The synthesis of **11**<sup>I</sup> has to be performed under exclusion of light.



A schlenk tube was charged with **10**<sup>I</sup> (50 mg, 57  $\mu\text{mol}$ , 1.0 eq.) and decamethyl chromocene (24 mg, 74.5  $\mu\text{mol}$ , 1.3 eq.).  $\text{N}_2$  saturated THF (6 ml) was added at  $-80^\circ\text{C}$ . The reaction mixture was stirred 2 h at  $-80^\circ\text{C}$  and then 2 h at RT and the solvent is evaporated. The dark solid was washed with acetonitrile at  $-40^\circ\text{C}$  until the washing solution is almost colourless and then washed with ether (3 x 2 ml) to obtain the product **11**<sup>I</sup> as a dark green solid (32 mg, 42  $\mu\text{mol}$ , 74%).

Crystals suitable for X-ray diffraction were obtained from a saturated acetonitrile solution stored at  $-40^\circ\text{C}$ .

**Elem. Anal.** found (calcd) for  $\text{C}_{32}\text{H}_{74}\text{N}_4\text{P}_4\text{Re}_2$ : C, 25.88 (25.30); H, 4.94 (4.91); N, 3.51 (3.69).

**$^1\text{H}\{^3\text{P}\}$  NMR** (THF- $d_8$ , 500.3 MHz, ppm): 143.27 (s, 1H, NH), 88.86 (t,  $^3J_{\text{HH}} = 10.6$  Hz, 1H, NH), 9.11 (q,  $^3J_{\text{HH}} = 12.5$  Hz, 1H, NCHH), 8.96 (dt,  $^3J_{\text{HH}} = 5.8$  Hz,  $^3J_{\text{HH}} = 14.1$  Hz, 1H, CHH-P), 8.45 (q,  $^3J_{\text{HH}} = 12.0$  Hz, 1H, NCHH), 8.14 (dt,  $^3J_{\text{HH}} = 5.6$  Hz,  $^3J_{\text{HH}} = 14.4$  Hz, 1H, CHH-P), 4.92 (m, 2H,  $\text{CH}(\text{CH}_3)_2 + \text{CH}(\text{CH}_3)_2$ , signals superimposed), 4.87 (m, 1H, CHH-P), 4.76 (h,  $^3J_{\text{HH}} = 7.5$  Hz, 1H,  $\text{CH}(\text{CH}_3)_2$ ), 4.45 (m, 1H, CHH-P, signal superimposed), 4.42 (d,  $^3J_{\text{HH}} = 7.3$  Hz, 3H,  $\text{CH}_3$ ), 4.22 (m, 1H,  $\text{CH}(\text{CH}_3)_2$ , signal superimposed), 4.16 (d,  $^3J_{\text{HH}} = 6.8$  Hz, 3H,  $\text{CH}_3$ ), 3.99 (d,  $^3J_{\text{HH}} = 7.5$  Hz, 3H,  $\text{CH}_3$ ), 3.85 (d,  $^3J_{\text{HH}} = 7.2$  Hz, 3H,  $\text{CH}_3$ ), 3.02 (d,  $^3J_{\text{HH}} = 8.2$  Hz, 3H,  $\text{CH}_3$ ), 2.98 (d,  $^3J_{\text{HH}} = 7.4$  Hz, 3H,  $\text{CH}_3$ ), 2.90 (d,  $^3J_{\text{HH}} = 7.0$  Hz, 3H,  $\text{CH}_3$ ), 2.80 (d,  $^3J_{\text{HH}} = 6.6$  Hz, 3H,  $\text{CH}_3$ ), 2.68 (d,  $^3J_{\text{HH}} = 7.8$  Hz, 3H,  $\text{CH}_3$ ), 2.62 (d,  $^3J_{\text{HH}} = 7.0$  Hz, 3H,  $\text{CH}_3$ ), 2.50 (d,  $^3J_{\text{HH}} = 7.9$  Hz, 3H,  $\text{CH}_3$ ), 2.06 (d,  $^3J_{\text{HH}} = 7.8$  Hz, 3H,  $\text{CH}_3$ ), 1.95 (d,  $^3J_{\text{HH}} = 7.2$  Hz, 3H,  $\text{CH}_3$ ), 1.82 (d,  $^3J_{\text{HH}} = 7.5$  Hz, 3H,  $\text{CH}_3$ ), 1.56 (d,  $^3J_{\text{HH}} = 7.1$  Hz, 3H,  $\text{CH}_3$ ), 1.55 (d,  $^3J_{\text{HH}} = 7.2$  Hz, 3H,  $\text{CH}_3$ ), 1.14 (m, 1H, NCHH), 0.94 (q,  $^3J_{\text{HH}} = 5.0$  Hz, 1H, NCHH),  $-0.26$  (dt,  $^3J_{\text{HH}} = 5.4$  Hz,  $^3J_{\text{HH}} = 15.0$  Hz, 1H, CHH-P),  $-0.60$  (h,  $^3J_{\text{HH}} = 7.2$  Hz, 1H,  $\text{CH}(\text{CH}_3)_2$ ),  $-0.88$  (h,  $^3J_{\text{HH}} = 6.8$  Hz, 1H,  $\text{CH}(\text{CH}_3)_2$ ),  $-1.02$  (dt,  $^3J_{\text{HH}} = 5.4$  Hz,  $^3J_{\text{HH}} = 14.2$  Hz, 1H, CHH-P),  $-4.44$  (d,  $^3J_{\text{HH}} = 15.2$  Hz, 1H, CHH-P),  $-5.09$  (d,  $^3J_{\text{HH}} = 15.2$  Hz, 1H, CHH-P),  $-6.80$  (q,  $^3J_{\text{HH}} = 11.2$  Hz, 1H, NCHH),  $-8.16$  (q,  $^3J_{\text{HH}} = 11.3$  Hz, 1H, NCHH),  $-9.18$  (h,  $^3J_{\text{HH}} = 7.0$  Hz, 1H,  $\text{CH}(\text{CH}_3)_2$ ),  $-10.13$  (h,  $^3J_{\text{HH}} = 7.0$  Hz, 1H,  $\text{CH}(\text{CH}_3)_2$ ),  $-10.97$  (m, 1H, NCHH),  $-12.15$  (m, 1H, NCHH).

**$^{31}\text{P}\{^1\text{H}\}$  NMR** (THF- $d_8$ , 202.4 MHz, ppm): -361.3 (d,  $^2J_{\text{PP}} = 204.5$  Hz, 1P,  $P\text{Pr}_2$ ), -377.5 (d,  $^2J_{\text{PP}} = 204.5$  Hz, 1P,  $P\text{Pr}_2$ ), -758.4 (d,  $^2J_{\text{PP}} = 235.5$  Hz, 1P,  $P\text{Pr}_2$ ), -770.3 (d,  $^2J_{\text{PP}} = 235.5$  Hz, 1P,  $P\text{Pr}_2$ ).

**$^{13}\text{C}\{^1\text{H}\}$  NMR** (THF- $d_8$ , 125.8 MHz, ppm): 140.0 (s, NCHH), 136.7 (s, NCHH), 117.7 (d,  $^2J_{\text{CP}} = 23.0$  Hz,  $\text{CH}(\text{CH}_3)_2$ ), 117.1 ( $\text{CH}(\text{CH}_3)_2^*$ ), 93.2 ( $\text{CH}(\text{CH}_3)_2^*$ ), 84.7 (s, NCHH), 83.3 (s, NCHH), 79.2 (s,  $\text{CH}_3$ ), 78.5 (d,  $^2J_{\text{CP}} = 19.3$  Hz,  $\text{CH}(\text{CH}_3)_2$ ), 77.0 ( $\text{CH}(\text{CH}_3)_2^*$ ), 76.7 (d,  $^2J_{\text{CP}} = 23.0$  Hz, CHHP), 75.4 (d,  $^2J_{\text{CP}} = 23.0$  Hz, CHHP), 74.0 (s,  $\text{CH}_3$ ), 73.6 (d,  $^2J_{\text{CP}} = 19.4$  Hz,  $\text{CH}(\text{CH}_3)_2$ ), 33.6 (s,  $\text{CH}_3$ ), 27.6 (s,  $\text{CH}_3$ ), 23.1 (s,  $\text{CH}_3$ ), 22.8 (s,  $\text{CH}_3$ ), 22.7 (s,  $\text{CH}_3$ ), 22.5 ( $\text{CH}_3^*$ ), 22.2 (s,  $\text{CH}_3$ ), 18.8 (s,  $\text{CH}_3$ ), 17.9 (s,  $\text{CH}_3$ ), 16.9 (s,  $\text{CH}_3$ ), 16.9 (s,  $\text{CH}_3$ ), 15.0 (s,  $\text{CH}_3$ ), 10.1 ( $\text{CH}(\text{CH}_3)_2^*$ ), 6.3 (d,  $^2J_{\text{CP}} = 16.1$  Hz,  $\text{CH}(\text{CH}_3)_2$ ), 5.8 (s,  $\text{CH}_3$ ), 5.3 (s,  $\text{CH}_3$ ), 2.73 (d,  $^2J_{\text{CP}} = 23.3$  Hz, CHHP), 1.60 (d,  $^2J_{\text{CP}} = 23.4$  Hz, CHHP). \*signals identified by  $^1\text{H}/^{13}\text{C}$  HSQC.

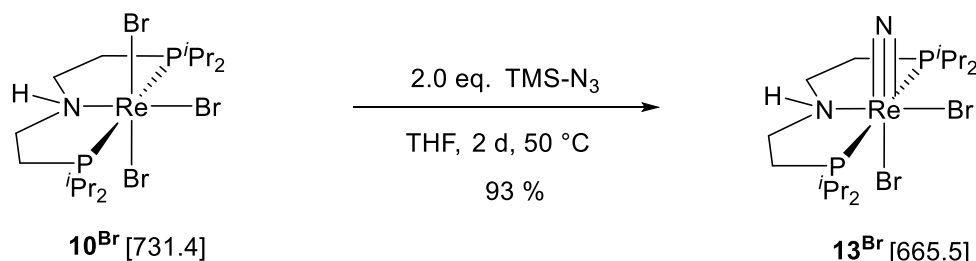
**MS** (LIFDI, THF):  $m/z$   $^{14}\text{N}$ : 1518.1 (100%,  $[\text{M}^+]$ );  $^{15}\text{N}$ : 1519.7 (100%,  $[\text{M}^+]$ ).

**IR** (ATR,  $\text{cm}^{-1}$ ): 3139 (N-H), 1712 ( $^{14}\text{N}_2$ ), 1657 ( $^{15}\text{N}_2$ ).

**rRaman** ( $\lambda_{\text{ex}} = 633$  nm, THF- $d_8$ , RT,  $\text{cm}^{-1}$ ): 1716 ( $^{14}\text{N}_2$ ), 1658 ( $^{15}\text{N}_2$ ).

#### 4.3.16 Synthesis of [ReBr<sub>2</sub>N(<sup>*i*</sup>PrPN<sup>H</sup>P)] (13<sup>Br</sup>)

Characterization of 13<sup>Br</sup> by NMR spectroscopy, IR spectroscopy, mass spectrometry, cyclic voltammetry and XRD analysis was carried out by M. Sc. Sessa Kisan (AK Schneider, Georg-August-Universität Göttingen). Design of a synthetic route to analytical purity (elemental analysis) was designed by Maximilian Fritz.



##### Azide-route

A 50 ml Schlenk tube was charged with 10<sup>Br</sup> (300 mg, 410 μmol, 1.0 eq.) and the solid was dissolved in THF (10 ml). Trimethylsilyl azide (94 mg, 820 μmol, 2.0 eq.) was added and the reaction was heated for 2 d at 50 °C. During that time, the colour changes from initially red to orange. The solvent was removed *in vacuo* and the orange crude product was washed with pentane (4 x 3 ml) and diethyl ether (4 x 3 ml) to give 13<sup>Br</sup> (253 mg, 381 μmol, 93%) as an orange solid.

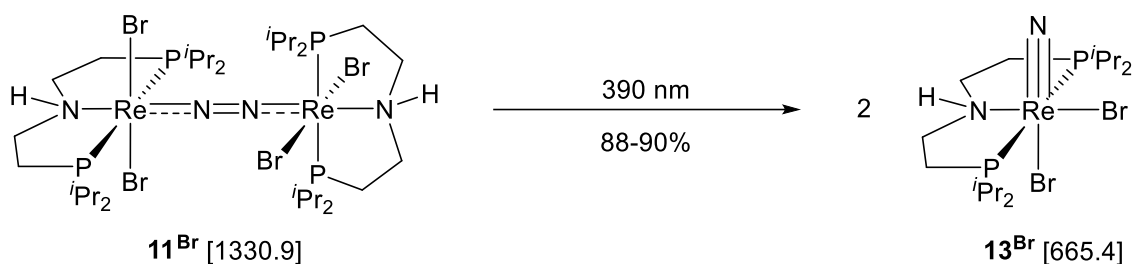
**Elem. Anal.** found (calcd) for C<sub>16</sub>H<sub>37</sub>Br<sub>2</sub>ReN<sub>2</sub>P<sub>2</sub>: C, 29.18 (28.88); H, 5.39 (5.60); N, 3.95 (4.21).

**<sup>1</sup>H NMR** (C<sub>6</sub>D<sub>6</sub>, 300.1 MHz, ppm): 5.07 (t, <sup>1</sup>J<sub>NH</sub> = 10.8 Hz, 1H, NH), 3.36 (m, 2H, CH<sub>2</sub>), 2.59 (m, 2H, CH<sub>2</sub>), 2.07 (m, 2H, CH<sub>2</sub>), 1.78 (m, <sup>3</sup>J<sub>HH</sub> = 7.6 Hz, 6H, CHMe<sub>2</sub>), 1.57 (m, <sup>3</sup>J<sub>HH</sub> = 7.0 Hz, 10H, CHMe<sub>2</sub> and CHMe<sub>2</sub>, signals superimposed), 1.12 (m, <sup>3</sup>J<sub>HH</sub> = 7.1 Hz, 6H, CHMe<sub>2</sub>), 0.97 (m, <sup>3</sup>J<sub>HH</sub> = 7.0 Hz, 6H, CHMe<sub>2</sub>).

**<sup>31</sup>P{<sup>1</sup>H} NMR** (C<sub>6</sub>D<sub>6</sub>, 121.5 MHz, ppm): 31.7 (s, 2P, PPr<sub>2</sub>).

**IR** (ATR, cm<sup>-1</sup>): 3140 (NH).



**Photolysis-route****Quantification via  $^{31}\text{P}\{^1\text{H}\}$  NMR spectroscopy:**

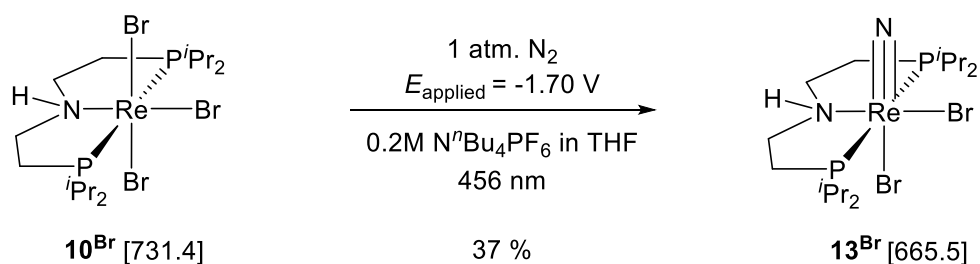
A J. YOUNG NMR tube was suited with a glass capillary containing  $\text{P}(\text{OTMS})_3$  and filled with a solution of  $11^{\text{Br}}$  (3 mg, 2.2  $\mu\text{mol}$ , 1.0 eq.) in  $\text{THF}-d_8$  (0.5 ml). A  $^{31}\text{P}\{^1\text{H}\}$  NMR spectrum was recorded to determine the ratio between the starting material and the internal standard. The dark blue solution was exposed for 2 h to an LED lamp (390 nm). A color change was observed from dark blue to yellow orange. A  $^{31}\text{P}\{^1\text{H}\}$  NMR spectrum was recorded to determine the ratio between the photolysis product and the internal standard. Rhenium nitride complex  $13^{\text{Br}}$  was formed with a spectroscopic yield of 90%.

**Quantification via  $^1\text{H}$  NMR spectroscopy:**

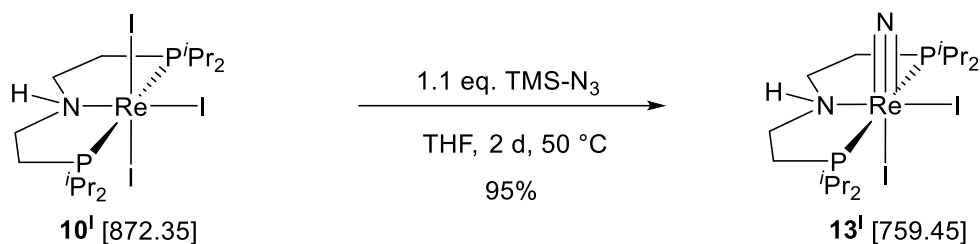
A J. YOUNG NMR tube was filled with a solution of  $11^{\text{Br}}$  (2.2 mg, 1.7  $\mu\text{mol}$ , 1.0 eq.) and 1,3,5-trimethoxy benzene (3.5 mg, 20.7  $\mu\text{mol}$ , 12.2 eq.) and the solids were dissolved in  $\text{THF } d_8$  (0.5 ml). The dark blue solution was exposed for 2 h to an LED lamp (390 nm). A color change was observed from dark blue to yellow orange. The photolysis product was investigated by  $^1\text{H}$  NMR spectroscopy. Rhenium nitride complex  $13^{\text{Br}}$  was formed with a spectroscopic yield of 88%.

$^{15}\text{N}\{^1\text{H}\}$  NMR ( $\text{C}_6\text{D}_6$ , 50.7 MHz, ppm): 387.1 (s, 1N,  $\text{Re}\equiv\text{N}$ ).

MS (LIFDI, THF):  $m/z$   $^{15}\text{N}$ : 666.9 (100%,  $[\text{M}^+]$ ).

*Electro-photochemical route*

In a dinitrogen filled glove box, a 10 ml three neck flask equipped with working-, counter-, and reference electrode (glassy carbon, Pt-wire, Ag-wire, respectively). The flask was charged with  $\mathbf{10}^{\text{Br}}$  (3.7 mg, 5.1  $\mu\text{mol}$ , 1.0 eq.) and dissolved in electrolyte solution (4 ml, 0.2 M  $\text{N}^t\text{Bu}_4\text{PF}_6$  in THF). The solution was electrolyzed for 1.5 h at the peak potential of the first reduction wave ( $E_{\text{applied}} = -1.70 \text{ V}$ ). The electrolysis progress was monitored by cyclic voltammetry and the integration of the current vs. time plot revealed a charge transfer of  $1.7 e^-$  per mol rhenium within that time. The electrolysis cell was constantly irradiated with a 456 nm LED. A color change was observed from yellow via green to orange. The reaction solution was concentrated and transferred into an NMR tube. Triphenylphosphine (3.7 mg, 14.1  $\mu\text{mol}$ , 2.8 eq.) was added as an internal standard and  $^{31}\text{P}\{^1\text{H}\}$  NMR spectroscopy determined a spectroscopic yield of 37% for nitride complex  $\mathbf{13}^{\text{Br}}$ .

4.3.17 Synthesis of  $[\text{ReI}_2\text{N}(\text{P}^i\text{Pr}_2\text{NH}^i\text{P})]$  ( $\mathbf{13}^{\text{I}}$ )*Azide-route*

A 50 ml Schlenk tube was charged with  $\mathbf{10}^{\text{I}}$  (40 mg, 45.9  $\mu\text{mol}$ , 1.0 eq.) and the solid was dissolved in THF (10 ml). Trimethylsilyl azide (5.8 mg, 50.5  $\mu\text{mol}$ , 1.1 eq.) was added via Hamilton syringe and the reaction was heated for 2 d at 50  $^\circ\text{C}$ . During that time, the colour changes from initially red to orange. The solvent was removed *in vacuo* and the orange crude product was washed with pentane (4 x 3 ml) and diethyl ether (4 x 3 ml) to give  $\mathbf{13}^{\text{I}}$  (33 mg, 43.3  $\mu\text{mol}$ , 95%) as an orange solid.

Crystals suitable for X-ray diffraction were obtained from gas diffusion layering of a THF solution of  $\mathbf{13}^{\text{I}}$  with pentane at room temperature.

**Elem. Anal.** found (calcd) for  $\text{C}_{16}\text{H}_{37}\text{I}_2\text{ReN}_2\text{P}_2$ : C, 25.78 (25.30); H, 4.96 (4.91); N, 3.81 (3.69).

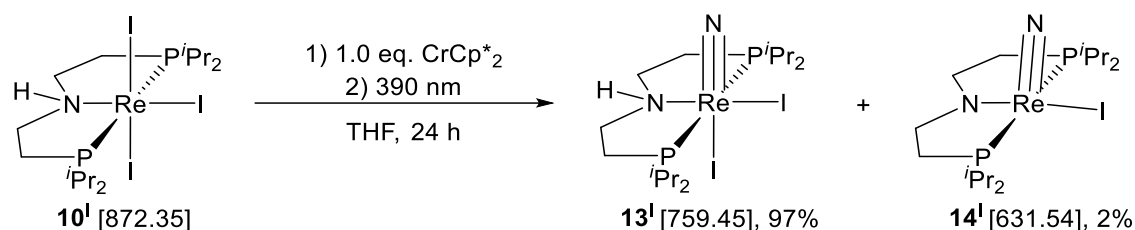
$^1\text{H}\{^{31}\text{P}\}$  NMR ( $\text{C}_6\text{D}_6$ , 500.3 MHz, ppm): 5.41 (t,  $^1J_{\text{NH}} = 11.4$  Hz, 1H, NH), 3.61 (m, 2H, P-CHMe<sub>2</sub>), 2.59 (m, 2H, N-CHH-CH<sub>2</sub>-P), 2.05 (m, 4H, N-CHH-CH<sub>2</sub>-P and P-CHMe<sub>2</sub>, signals superimposed), 1.83 (m,  $^3J_{\text{HH}} = 7.2$  Hz, 8H, P-CHMe<sub>2</sub> and N-CH<sub>2</sub>-CHHP, signals superimposed), 1.59 (m,  $^3J_{\text{HH}} = 6.9$  Hz, 8H, P-CHMe<sub>2</sub> and N-CH<sub>2</sub>-CHHP, signals superimposed), 1.05 (m,  $^3J_{\text{HH}} = 6.7$  Hz, 6H, P-CHMe<sub>2</sub>), 0.96 (m,  $^3J_{\text{HH}} = 6.5$  Hz, 6H, P-CHMe<sub>2</sub>).

$^{13}\text{C}\{^1\text{H}\}$  NMR ( $\text{C}_6\text{D}_6$ , 125.8 MHz, ppm): 61.8 (s, N-CH<sub>2</sub>-CH<sub>2</sub>-P), 31.4 (AXY,  $N = |^1J_{\text{AX}} + ^3J_{\text{AY}}| = 24.5$  Hz, N-CH<sub>2</sub>-CH<sub>2</sub>-P), 30.9 (AXY,  $N = |^1J_{\text{AX}} + ^3J_{\text{AY}}| = 29.4$  Hz, CH(CH<sub>3</sub>)<sub>2</sub>), 24.9 (AXY,  $N = |^1J_{\text{AX}} + ^3J_{\text{AY}}| = 20.3$  Hz, CH(CH<sub>3</sub>)<sub>2</sub>), 22.4 (AXY,  $N = |^2J_{\text{AX}} + ^4J_{\text{AY}}| = 4.0$  Hz, CH(CH<sub>3</sub>)<sub>2</sub>), 20.6 (s, CH<sub>3</sub>), 18.3 (AXY,  $N = |^2J_{\text{AX}} + ^4J_{\text{AY}}| = 4.0$  Hz, CH(CH<sub>3</sub>)<sub>2</sub>), 17.9 (s, CH<sub>3</sub>).

$^{31}\text{P}\{^1\text{H}\}$  NMR ( $\text{C}_6\text{D}_6$ , 121.5 MHz, ppm): 24.0 (s, P<sup>*i*</sup>Pr<sub>2</sub>).

**MS** (LIFDI, THF):  $m/z$  760.0 (100%, [M<sup>+</sup>]).

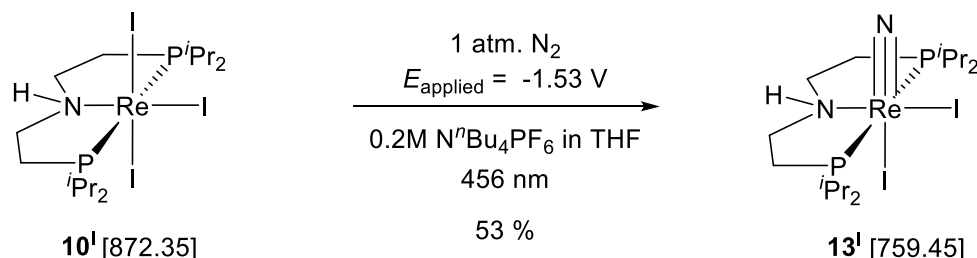
**IR** (ATR,  $\text{cm}^{-1}$ ): 3108 (NH).

**Photolysis-route**

In an N<sub>2</sub> filled glove box, a J. YOUNG NMR tube was suited with a glass capillary containing P(OTMS)<sub>3</sub> and filled with a solution of **10<sup>I</sup>** (15 mg, 17.2 μmol, 1.0 eq.) in THF-*d*<sub>8</sub> (0.7 ml). A <sup>31</sup>P{<sup>1</sup>H} NMR spectrum was recorded to determine the ratio between the starting material and the internal standard. Decamethyl chromocene (5.6 mg, 17.2 μmol, 1.0 eq.) was added and to the solution and the NMR tube was sealed and shaken carefully. A color change was observed from red to deep green. The reaction mixture was exposed for 2 h to an LED lamp (390 nm). During photolysis, the NMR tube was shaken every 15 minutes. A <sup>31</sup>P{<sup>1</sup>H} NMR spectrum was recorded to determine the ratio between the photolysis product and the internal standard. Rhenium nitride complexes **13<sup>I</sup>** (97%) and **14<sup>I</sup>** (2%) were identified as reaction products.

<sup>15</sup>N{<sup>1</sup>H} NMR (C<sub>6</sub>D<sub>6</sub>, 50.7 MHz, ppm): 386.2 (s, 1N, Re≡N).

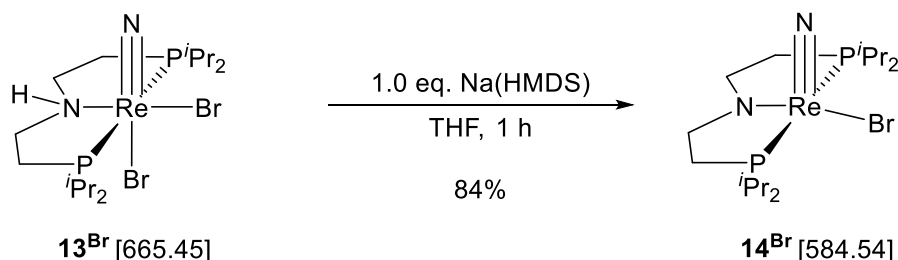
MS (ESI<sup>+</sup>, THF) found (calcd) for C<sub>16</sub>H<sub>37</sub>Br<sup>15</sup>N<sup>14</sup>NP<sub>2</sub>Re: m/z 586.1113 (100%, [M<sup>+</sup>]), 586.1120.

**Electro-photochemical route**

A 10 ml three neck flask equipped with working-, counter-, and reference electrode (glassy carbon, Pt-wire, Ag-wire, respectively) was charged with **10<sup>I</sup>** (3.9 mg, 4.5 μmol, 1.0 eq.) and dissolved in electrolyte solution (4 ml, 0.2 M N<sup>t</sup>Bu<sub>4</sub>PF<sub>6</sub> in THF). The solution was electrolyzed for 45 min at the peak potential of the first reduction wave ( $E_{\text{applied}} = -1.53$  V). The electrolysis progress was monitored by cyclic voltammetry and the integration of the current vs time plot revealed a charge transfer of 1.0 e<sup>-</sup> per mol rhenium. The electrolysis cell was constantly irradiated by a 456 nm LED lamp. A color change was observed from red via green to orange. The reaction solution was concentrated and transferred into an NMR tube. Triphenylphosphine (1.8 mg, 6.9 μmol, 1.5 eq.) was added as an internal standard and <sup>31</sup>P{<sup>1</sup>H} NMR spectroscopy determined a spectroscopic yield of 53% for nitride complex **13<sup>I</sup>**.

#### 4.3.18 Synthesis of [ReBrN(<sup>i</sup>PrPNP)] (14<sup>Br</sup>)

Compound 14<sup>Br</sup> was synthesized by Paul Julius Weiß during his Bachelor thesis under supervision of Maximilian Fritz.



In a glove box, a vial was charged with 13<sup>Br</sup> (27 mg, 40.7  $\mu\text{mol}$ , 1.0 eq.) and dissolved in THF (5 ml). A solution of Na(HMDS) (7.8 mg, 42.5  $\mu\text{mol}$ , 1.06 eq.) in THF (1 ml) was added and the reaction stirred for one hour. The volatiles were removed *in vacuo* and the residual substance is extracted with pentane (3 x 2 ml) and filtered. Removal of the solvent obtained 14<sup>Br</sup> (20 mg, 34.2  $\mu\text{mol}$ , 84%) as an orange solid.

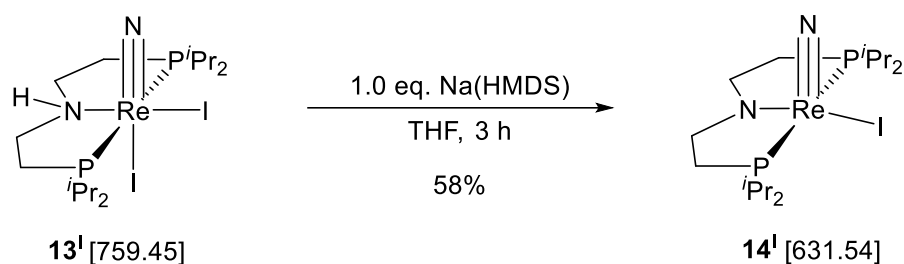
Crystals suitable for X-ray diffraction were obtained from a saturated with pentane solution stored at  $-40\text{ }^{\circ}\text{C}$ .

**<sup>1</sup>H{<sup>31</sup>P} NMR** ( $\text{C}_6\text{D}_6$ , 500.3 MHz, ppm): 3.43 (ddd,  $^3J_{\text{HH}} = 2.9\text{ Hz}$ ,  $^3J_{\text{HH}} = 7.8\text{ Hz}$ ,  $^3J_{\text{HH}} = 11.1\text{ Hz}$ , 2H, N-CHH-CH<sub>2</sub>-P), 3.13 (ddd,  $^3J_{\text{HH}} = 1.9\text{ Hz}$ ,  $^3J_{\text{HH}} = 6.5\text{ Hz}$ ,  $^3J_{\text{HH}} = 9.3\text{ Hz}$ ,  $^3J_{\text{HH}} = 10.1\text{ Hz}$ , 2H, N-CHH-CH<sub>2</sub>-P), 2.82 (h,  $^3J_{\text{HH}} = 7.1\text{ Hz}$ , 2H, P-CHMe<sub>2</sub>), 1.85 (h,  $^3J_{\text{HH}} = 6.0\text{ Hz}$ , 2H, CH(CH<sub>3</sub>)<sub>2</sub>), 1.60 (ddd,  $^3J_{\text{HH}} = 7.9\text{ Hz}$ ,  $^3J_{\text{HH}} = 9.2\text{ Hz}$ ,  $^3J_{\text{HH}} = 14.4\text{ Hz}$ , 2H, N-CH<sub>2</sub>-CHH-P), 1.37 (d,  $^3J_{\text{HH}} = 6.9\text{ Hz}$ , 6H, P-CHMe<sub>2</sub>), 1.21 (ddd,  $^3J_{\text{HH}} = 3.0\text{ Hz}$ ,  $^3J_{\text{HH}} = 6.5\text{ Hz}$ ,  $^3J_{\text{HH}} = 14.4\text{ Hz}$ , 2H, N-CH<sub>2</sub>-CHH-P), 1.16 ( $^3J_{\text{HH}} = 6.9\text{ Hz}$ , 6H, P-CHMe<sub>2</sub>), 0.94 ( $^3J_{\text{HH}} = 7.1\text{ Hz}$ , 6H, P-CHMe<sub>2</sub>), 0.84 ( $^3J_{\text{HH}} = 7.1\text{ Hz}$ , 6H, P-CHMe<sub>2</sub>).

**<sup>13</sup>C{<sup>1</sup>H} NMR** ( $\text{C}_6\text{D}_6$ , 125.8 MHz, ppm): **<sup>13</sup>C{<sup>1</sup>H} NMR** ( $\text{C}_6\text{D}_6$ , 125.8 MHz, ppm): 70.4 (AXY,  $N = |^2J_{\text{AX}} + ^3J_{\text{AY}}| = 9.2\text{ Hz}$ , N-CH<sub>2</sub>-CH<sub>2</sub>-P), 25.1 (AXY,  $N = |^1J_{\text{AX}} + ^3J_{\text{AY}}| = 24.7\text{ Hz}$ , CH(CH<sub>3</sub>)<sub>2</sub>), 23.5 (AXY,  $N = |^1J_{\text{AX}} + ^3J_{\text{AY}}| = 24.7\text{ Hz}$ , N-CH<sub>2</sub>-CH<sub>2</sub>-P), 21.8 (AXY,  $N = |^1J_{\text{AX}} + ^3J_{\text{AY}}| = 28.3\text{ Hz}$ , CH(CH<sub>3</sub>)<sub>2</sub>), 18.9 (AXY,  $N = |^1J_{\text{AX}} + ^3J_{\text{AY}}| = 2.1\text{ Hz}$ , CH(CH<sub>3</sub>)<sub>2</sub>), 18.5 (AXY,  $N = |^2J_{\text{AX}} + ^4J_{\text{AY}}| = 4.6\text{ Hz}$ , CH(CH<sub>3</sub>)<sub>2</sub>), 17.9 (AXY,  $N = |^2J_{\text{AX}} + ^4J_{\text{AY}}| = 3.5\text{ Hz}$ , CH(CH<sub>3</sub>)<sub>2</sub>), 16.5 (AXY,  $N = |^2J_{\text{AX}} + ^4J_{\text{AY}}| = 3.5\text{ Hz}$ , CH(CH<sub>3</sub>)<sub>2</sub>).

**<sup>31</sup>P{<sup>1</sup>H} NMR** ( $\text{C}_6\text{D}_6$ , 121.5 MHz, ppm): 75.4 (s, P-CHMe<sub>2</sub>).

**MS** (LIFDI, THF):  $m/z$  632.1 (100%, [M<sup>+</sup>]).

4.3.19 Synthesis of [ReIN(<sup>*i*</sup>PrPNP)] (14<sup>I</sup>)

In a glove box, a vial was charged with **13<sup>I</sup>** (33 mg, 43.4  $\mu\text{mol}$ , 1.0 eq.) and Na(HMDS) (8.8 mg, 47.8  $\mu\text{mol}$ , 1.1 eq.). THF (4 ml) was added, and the reaction was stirred for 3 h. The reaction mixture was filtrated, and the volatiles are removed *in vacuo*. The yellow orange solid was washed with pentane (3 x 1 ml) and recrystallized from a saturated diethyl ether solution at  $-40$  °C. The mother liquor is decanted, and the crystals were washed with diethyl ether at  $-40$  °C (3 x 1 ml) to obtain **14<sup>I</sup>** (16 mg, 25  $\mu\text{mol}$ , 58%) as a yellow orange crystalline solid.

Crystals suitable for X-ray diffraction were obtained from a saturated with pentane solution stored at  $-40$  °C.

**Elem. Anal.** found (calcd) for  $\text{C}_{16}\text{H}_{36}\text{IReN}_2\text{P}_2$ : C, 30.64 (30.43); H, 5.74 (5.75); N, 4.40 (4.44).

**<sup>1</sup>H{<sup>31</sup>P} NMR** ( $\text{C}_6\text{D}_6$ , 500.3 MHz, ppm): 3.41 (ddd,  $^3J_{\text{HH}} = 3.0$  Hz,  $^3J_{\text{HH}} = 7.9$  Hz,  $^3J_{\text{HH}} = 11.2$  Hz, 2H, N-CHH-CH<sub>2</sub>-P), 3.12 (ddd,  $^3J_{\text{HH}} = 6.6$  Hz,  $^3J_{\text{HH}} = 9.2$  Hz,  $^3J_{\text{HH}} = 10.3$  Hz, 2H, N-CHH-CH<sub>2</sub>-P), 3.04 (h,  $^3J_{\text{HH}} = 7.05$  Hz, 2H, CH(CH<sub>3</sub>)<sub>2</sub>), 1.86 (h,  $^3J_{\text{HH}} = 6.80$  Hz, 2H, CH(CH<sub>3</sub>)<sub>2</sub>), 1.59 (ddd,  $^3J_{\text{HH}} = 7.9$  Hz,  $^3J_{\text{HH}} = 9.3$  Hz,  $^3J_{\text{HH}} = 14.4$  Hz, 2H, N-CH<sub>2</sub>-CHH-P), 1.4 (d,  $^3J_{\text{HH}} = 6.8$  Hz, 6H, P-CH(CH<sub>3</sub>)<sub>2</sub>), 1.22 (ddd,  $^3J_{\text{HH}} = 2.9$  Hz,  $^3J_{\text{HH}} = 6.6$  Hz,  $^3J_{\text{HH}} = 14.3$  Hz, 2H, N-CH<sub>2</sub>-CHH-P), 1.15 ( $^3J_{\text{HH}} = 6.8$  Hz, 6H, CH(CH<sub>3</sub>)<sub>2</sub>), 0.83 ( $^3J_{\text{HH}} = 7.1$  Hz, 6H, CH(CH<sub>3</sub>)<sub>2</sub>), 0.81 ( $^3J_{\text{HH}} = 7.1$  Hz, 6H, P-CH(CH<sub>3</sub>)<sub>2</sub>).

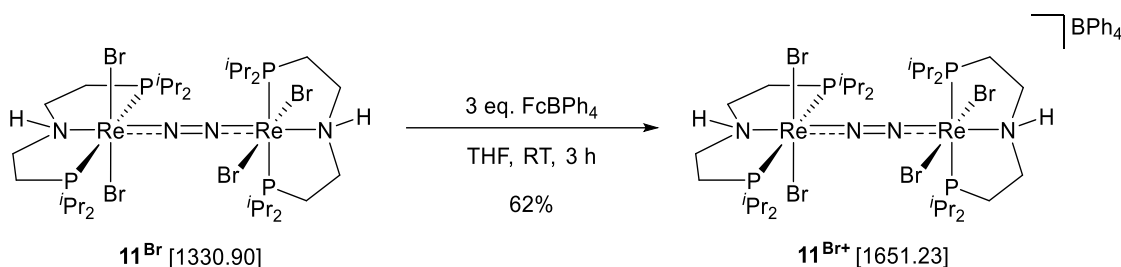
**<sup>13</sup>C{<sup>1</sup>H} NMR** ( $\text{C}_6\text{D}_6$ , 125.8 MHz, ppm): 70.3 (AXY,  $N = |^2J_{\text{AX}} + ^3J_{\text{AY}}| = 9.3$  Hz, N-CH<sub>2</sub>-CH<sub>2</sub>-P), 25.4 (AXY,  $N = |^1J_{\text{AX}} + ^3J_{\text{AY}}| = 24.9$  Hz, CH(CH<sub>3</sub>)<sub>2</sub>), 23.1 (AXY,  $N = |^1J_{\text{AX}} + ^3J_{\text{AY}}| = 24.4$  Hz, N-CH<sub>2</sub>-CH<sub>2</sub>-P), 22.8 (AXY,  $N = |^1J_{\text{AX}} + ^3J_{\text{AY}}| = 29.6$  Hz, CH(CH<sub>3</sub>)<sub>2</sub>), 19.1 (AXY,  $N = |^2J_{\text{AX}} + ^4J_{\text{AY}}| = 2.4$  Hz, CH(CH<sub>3</sub>)<sub>2</sub>), 19.0 (AXY,  $N = |^2J_{\text{AX}} + ^4J_{\text{AY}}| = 4.3$  Hz, CH(CH<sub>3</sub>)<sub>2</sub>), 17.9 (AXY,  $N = |^2J_{\text{AX}} + ^4J_{\text{AY}}| = 4.1$  Hz, CH(CH<sub>3</sub>)<sub>2</sub>), 16.4 (AXY,  $N = |^2J_{\text{AX}} + ^4J_{\text{AY}}| = 3.9$  Hz, CH(CH<sub>3</sub>)<sub>2</sub>).

**<sup>31</sup>P{<sup>1</sup>H} NMR** ( $\text{C}_6\text{D}_6$ , 121.5 MHz, ppm): 75.9 (s, P-CHMe<sub>2</sub>).

**MS** (LIFDI, THF):  $m/z$  632.1 (100%, [M<sup>+</sup>]).

#### 4.3.20 Synthesis of $[(\mu\text{-N}_2)\{\text{ReBr}_2(\text{}^i\text{PrPN}^{\text{H}}\text{P})\}_2][\text{BPh}_4]$ ( $\mathbf{11}^{\text{Br}^+}$ )

The synthesis of  $\mathbf{11}^{\text{Br}^+}$  has to be performed under exclusion of light.



A schlenk tube was charged with  $\mathbf{11}^{\text{Br}}$  (30 mg, 22.5  $\mu\text{mol}$ , 1.0 eq.) and ferrocenium tetraphenyl borate (34 mg, 67  $\mu\text{mol}$ , 3.0 eq). Me-THF (10 ml) was added and the reaction was stirred for overnight. The initial blue solution turned into a black suspension. The solvent was reduced to a volume of approximately 3 ml and the supernatant solution was decanted. The black precipitate was washed with benzene (3 x 2 ml) and 2-Me-THF (3 x 1 ml). The remaining black solid was dissolved in THF, filtrated and the solvent removed *in vacuo*. The product  $\mathbf{11}^{\text{Br}^+}$  (23 mg, 13.9  $\mu\text{mol}$ , 62%) was obtained as a black solid.

Crystals suitable for X-ray diffraction were obtained from a saturated 2-Me-THF / pentane solution.

**Elem. Anal.** found (calcd) for  $\text{C}_{56}\text{H}_{94}\text{BBr}_4\text{Re}_2\text{N}_4\text{P}_4$ : C, 41.26 (40.76); H, 5.85 (5.74); N, 3.53 (3.40).

**$^1\text{H}$  NMR** (THF- $d_8$ , 400.2 MHz, ppm): 132.8 (s,  $m_{1/2}$  = 81.8 Hz, 2 H, NH), 8.97 (s,  $m_{1/2}$  = 10.3 Hz, 6H, PCHMe<sub>2</sub>), 8.71 (s,  $m_{1/2}$  = 9.1 Hz, 6H, PCHMe<sub>2</sub>), 8.35 (s,  $m_{1/2}$  = 8.9 Hz, 6H, PCHMe<sub>2</sub>), 8.11 (s,  $m_{1/2}$  = 12.8 Hz, 6H, PCHMe<sub>2</sub>), 7.91 (s,  $m_{1/2}$  = 13.2 Hz, 6H, PCHMe<sub>2</sub>), 7.56 (s,  $m_{1/2}$  = 14.2 Hz, 6H, PCHMe<sub>2</sub>), 7.02 (s,  $m_{1/2}$  = 9.6 Hz, 6H, PCHMe<sub>2</sub>), 6.77 (s, 8 H, H<sub>A</sub>), 6.51 (t,  $^3J_{\text{HH}}$  = 7.1 Hz, 8H, H<sub>A</sub>), 6.42 (t,  $^3J_{\text{HH}}$  = 6.6 Hz, 8H, H<sub>A</sub>), 6.15 (s,  $m_{1/2}$  = 13.3 Hz, 6 H, PCHMe<sub>2</sub>), 0.0 (s,  $m_{1/2}$  = 37.9 Hz, 2H), -0.32 (s,  $m_{1/2}$  = 32.6 Hz, 2H), -3.17 (s,  $m_{1/2}$  = 35.9 Hz, 2H), -3.38 (s,  $m_{1/2}$  = 41.0 Hz, 2H), -3.98 (s,  $m_{1/2}$  = 41.0 + Hz, 2H), -4.47 (s,  $m_{1/2}$  = 32.7 Hz, 2H), -4.88 (s,  $m_{1/2}$  = 35.0 Hz, 2H), -5.35 (s,  $m_{1/2}$  = 32.7 Hz, 2H), -16.01 (s,  $m_{1/2}$  = 19.5 Hz, 2H), -16.44 (s,  $m_{1/2}$  = 19.3 Hz, 2H), -19.99 (s,  $m_{1/2}$  = 26.1 Hz, 2H), -20.32 (s,  $m_{1/2}$  = 26.2 Hz, 2H).

**MS** (ESI+, THF) found (calcd) for  $\text{C}_{23}\text{H}_{74}\text{Br}_4\text{N}_4\text{P}_4\text{Re}_2$ :  $m/z$  1330.06 ( $[\text{M}^+]$ , 1330.0644).

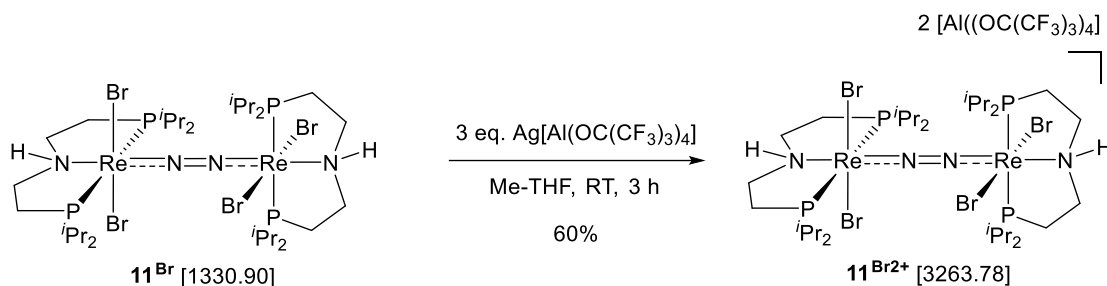
**Magnetic susceptibility** (SQUID)  $\chi_m = 1.03 \text{ emu}\cdot\text{mol}^{-1}$  (300 K).

**Magnetic Moment** (Evans', C<sub>6</sub>D<sub>6</sub>)  $\mu_{\text{eff}} = 2.05 \pm 0.1 \mu_{\text{B}}$ ; (SQUID)  $\mu_{\text{eff}} = 1.64\mu_{\text{B}}$ .

**IR** (ATR, cm<sup>-1</sup>): 3181 (NH)

### 4.3.21 Synthesis of $[(\mu\text{-N}_2)\{\text{ReBr}_2(\text{P}^i\text{Pr}_2\text{N}^{\text{H}}\text{P})\}_2][\text{Al}(\text{OC}(\text{CF}_3)_3)_4]_2$ ( $\mathbf{11}^{\text{Br}2+}$ )

The synthesis of  $\mathbf{11}^{\text{Br}2+}$  has to be performed under exclusion of light.



A Schlenk-tube was charged with  $\mathbf{11}^{\text{Br}}$  (30 mg, 22.5  $\mu\text{mol}$ , 1.0 eq.) and dissolved in Me-THF (15 ml). A solution of  $\text{Ag}[\text{Al}(\text{OC}(\text{CF}_3)_3)_4]$  (67 mg, 67.5  $\mu\text{mol}$ , 3.0 eq.) in Me-THF (2 ml) was added and a colour was observed from blue via black to blue. The reaction solution was stirred overnight, filtrated and the solvent was removed *in vacuo*. The blue solid was washed with diethyl ether (3 x 2 ml) to obtain the product  $\mathbf{11}^{\text{Br}2+}$  (44 mg, 13.5  $\mu\text{mol}$ , 60%) as a purple solid.

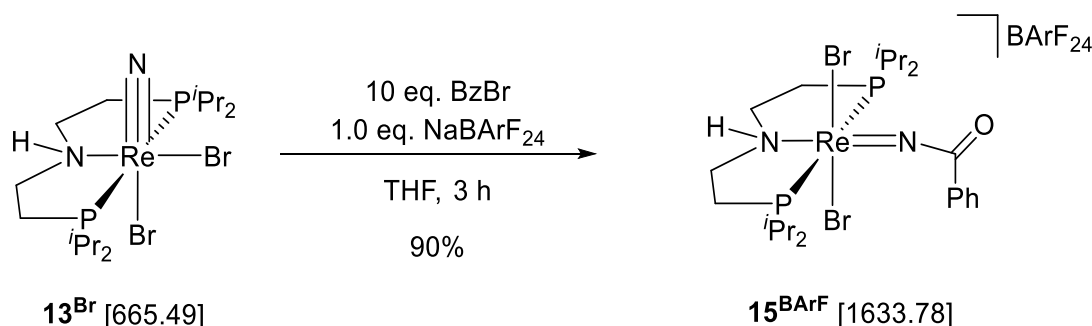
Suitable single crystals for X-ray diffraction were only obtained with triflate anions. For that, the analogous synthesis was performed using  $\text{Ag}(\text{OTf})$  as oxidant. The single crystals suitable for X-Ray diffraction were obtained from gas phase diffusion of a DCM solution with pentane.

**Elem. Anal.** found (calcd) for  $\text{C}_{64}\text{H}_{74}\text{Al}_2\text{Br}_4\text{F}_{72}\text{N}_4\text{O}_8\text{P}_4\text{Re}_2$ : C, 23.57 (23.54); H, 2.28 (2.18); N, 1.58 (1.72).

**$^1\text{H}$  NMR** (THF-*d*<sub>8</sub>, 400.2 MHz, ppm): 36.70 (s,  $m_{1/2}$  = 54.2 Hz, 2H), 26.2 (s,  $m_{1/2}$  = 34.6 Hz, 6H), 25.35 (s,  $m_{1/2}$  not determinable due to superimposed signals, 2H), 25.00 (s,  $m_{1/2}$  = 36.0 Hz, 6H), 23.90 (s,  $m_{1/2}$  not determinable due to superimposed signals, 2H), 21.89 (s,  $m_{1/2}$  = 33.2 Hz, 6H), 20.78 (s,  $m_{1/2}$  = 31.8 Hz, 6H), 20.08 (s,  $m_{1/2}$  = 27.6 Hz, 6H), 19.23 (s,  $m_{1/2}$  = 26.2 Hz, 6H), 17.66 (s,  $m_{1/2}$  = 23.4 Hz, 6H), -3.69 (s,  $m_{1/2}$  = 35.6 Hz, 2H), -12.00 (s,  $m_{1/2}$  = 26.0 Hz, 2H), -14.35 (s,  $m_{1/2}$  = 60.6 Hz, 2H), -15.69 (s,  $m_{1/2}$  = 29.2 Hz, 2H), -23.86 (s,  $m_{1/2}$  = 44.9 Hz, 2H), -25.44 (s,  $m_{1/2}$  = 49.2 Hz, 2H), -36.99 (s,  $m_{1/2}$  = 40.0 Hz, 2H), -41.41 (s,  $m_{1/2}$  = 43.3 Hz, 2H).

**MS** (ESI+, THF) found (calcd) for  $\text{C}_{23}\text{H}_{42}\text{Br}_2\text{N}_2\text{OP}_2\text{Re}$ :  $m/z$  652.0275 ( $[\text{M}^{2+}]\text{-N}_2$ , 652.0290), 665.0312 ( $[\text{M}^{2+}]$ , 665.0312), 1330.0644 ( $[\text{M}^+]\text{-N}_2$ , 1330.0651),



4.3.22 Synthesis of  $[\text{ReBr}_2\{\text{N}(\text{CO})\text{C}_6\text{H}_5\}(\text{}^{\text{tPr}}\text{PN}^{\text{tPr}}\text{P})][\text{BArF}_{24}]$  ( $15^{\text{BArF}}$ )

A vial was charged with  $13^{\text{Br}}$  (200 mg, 301  $\mu\text{mol}$ , 1.0 eq.) and suspended in THF (4 ml). Benzoyl bromide (279 mg, 1.50 mmol, 5.0 eq.) was added and the mixture was stirred for 3 hours. During this time, a yellow suspension has formed. A solution of  $\text{NaBArF}_{24}$  (266 mg, 301  $\mu\text{mol}$ , 1.0 eq.) in THF (2 ml) was added dropwise forming a green solution with a colourless solid. The reaction mixture is stirred for another 10 minutes and the solvent was removed *in vacuo* to give a green oil. Pentane was added (4 ml) and the oily crude product was scratched until it becomes a green solid. The washing solution was decanted and washing was repeated (3 x 2 ml). The residual solid was extracted with diethyl ether (5 x 2 ml) and filtered through a filter pipette. The extract was concentrated and layered with pentane to isolate the product  $15^{\text{BArF}}$  as a green crystalline solid (420 mg, 262  $\mu\text{mol}$ , 87%).

Crystals suitable for X-ray diffraction were obtained from a saturated diethyl ether solution at room temperature.

**Elem. Anal.** found (calcd) for  $\text{C}_{55}\text{H}_{54}\text{BBr}_2\text{F}_{24}\text{N}_2\text{P}_2\text{Re}$ : C, 40.66 (40.43); H, 3.57 (3.33); N, 1.71 (1.71).

$^1\text{H}\{^{31}\text{P}\}$  NMR (THF- $d_8$ , 500.3 MHz, ppm): 8.06 (m, 2H,  $\text{H}_{\text{ortho}}(\text{NCOPh})$ ), 7.78 (m, 8H,  $\text{H}_{\text{ortho}}(\text{BArF})$ ), 7.77 (m, 1H,  $\text{H}_{\text{para}}(\text{NCOPh})$ , signal partially superimposed), 7.59 (m, 2H,  $\text{H}_{\text{meta}}(\text{NCOPh})$ , signal partially superimposed), 7.58 (s, 4H,  $\text{H}_{\text{para}}(\text{BArF})$ ), 3.94 (m, 1H, NH), 3.59 (m, 4H,  $\text{CH}(\text{CH}_3)_2$ , signal superimposed by THF), 3.31 (m, 2H, N-CHH- $\text{CH}_2$ -P), 2.98 (ddd,  $^3J_{\text{HH}} = 3.5$  Hz,  $^3J_{\text{HH}} = 11.9$  Hz,  $^3J_{\text{HH}} = 23.7$  Hz, N-CHH- $\text{CH}_2$ -P), 2.87 (dd,  $^3J_{\text{HH}} = 2.6$  Hz,  $^3J_{\text{HH}} = 15.2$  Hz, N- $\text{CH}_2$ -CHH-P), 2.13 (dt,  $^3J_{\text{HH}} = 5.4$  Hz,  $^3J_{\text{HH}} = 14.8$  Hz, N- $\text{CH}_2$ -CHH-P), 1.58 (d,  $^3J_{\text{HH}} = 7.3$  Hz,  $\text{CH}(\text{CH}_3)_2$ ), 1.50 (d,  $^3J_{\text{HH}} = 7.4$  Hz,  $\text{CH}(\text{CH}_3)_2$ ), 1.48 (d,  $^3J_{\text{HH}} = 7.4$  Hz,  $\text{CH}(\text{CH}_3)_2$ ), 1.35 (d,  $^3J_{\text{HH}} = 7.3$  Hz,  $\text{CH}(\text{CH}_3)_2$ ).

$^{13}\text{C}\{^1\text{H}\}$  NMR (THF- $d_8$ , 125.8 MHz, ppm): 176.3 (s, NCOPh), 162.6 (q,  $^1J_{\text{C-11B}} = 49.9$  Hz,  $\text{C}_{\text{ipso}}(\text{BArF}_{24})$ ) + (h,  $^1J_{\text{C-10B}} = 16.8$  Hz,  $\text{C}_{\text{ipso}}(\text{BArF}_{24})$ ), 137.4 (s,  $\text{C}_{\text{para}}(\text{NCOPh})$ ), 135.4 (s,  $\text{C}_{\text{ortho}}(\text{BArF}_{24})$ ), 131.5 (s,  $\text{C}_{\text{ortho}}(\text{NCOPh})$ ), 130.3 (s,  $\text{C}_{\text{meta}}(\text{NCOPh})$ ), 129.8 (dq,  $^4J_{\text{CF}} = 3.0$  Hz,  $^2J_{\text{CF}} = 31.5$  Hz,  $\text{C}_{\text{meta}}(\text{BArF}_{24})$ ), 129.3 (s,  $\text{C}_{\text{ipso}}(\text{NCOPh})$ ), 125.30 (q,  $^1J_{\text{CF}} = 272.9$  Hz,  $\text{CF}_3$ ), 118.0 (h,  $^3J_{\text{CF}} = 4.0$  Hz,  $\text{C}_{\text{para}}(\text{BArF}_{24})$ ), 51.9 (AXY,  $N = |^2J_{\text{AX}} + ^3J_{\text{AY}}| = 3.8$  Hz, N- $\text{CH}_2$ - $\text{CH}_2$ -P), 27.7 (AXY,  $N = |^1J_{\text{AX}} + ^3J_{\text{AY}}| = 27.1$  Hz,  $\text{CH}(\text{CH}_3)_2$ ), 27.3 (AXY,  $N = |^1J_{\text{AX}} + ^3J_{\text{AY}}| = 30.3$  Hz, N- $\text{CH}_2$ - $\text{CH}_2$ -P), 19.7 (s,  $\text{CH}(\text{CH}_3)_2$ ), 19.5 (s,  $\text{CH}(\text{CH}_3)_2$ ), 19.0

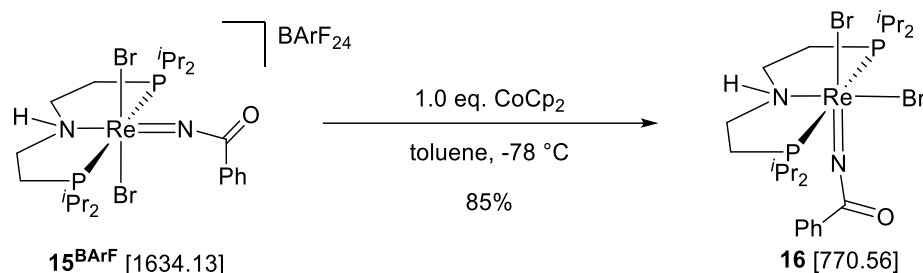
(AXY,  $N = |^2J_{AX} + ^4J_{AY}| = 3.0$  Hz, CH(CH<sub>3</sub>)<sub>2</sub>), 18.5 (AXY,  $N = |^2J_{AX} + ^4J_{AY}| = 3.0$  Hz, CH(CH<sub>3</sub>)<sub>2</sub>).

**<sup>31</sup>P{<sup>1</sup>H} NMR** (THF-*d*<sub>8</sub>, 202.4 MHz, ppm): 32.8 (s, *PiPr*<sub>2</sub>).

**<sup>15</sup>N{<sup>1</sup>H} NMR** (THF-*d*<sub>8</sub>, 50.7 MHz, ppm): -321.1 (s, 1N, NH).

**MS** (ESI+, THF) found (calcd) for C<sub>23</sub>H<sub>42</sub>Br<sub>2</sub>N<sub>2</sub>OP<sub>2</sub>Re: *m/z* 771.0663 (100%, [M<sup>+</sup>]), 771.0662.

**IR** (ATR, cm<sup>-1</sup>): 3224 (NH), 1692 (C=O).

4.3.23 Synthesis of  $[\text{ReBr}_2\{\text{N}(\text{CO})\text{C}_6\text{H}_5\}\{\text{P}^{\text{iPr}}_2\text{N}^{\text{H}}\text{P}\}]$  (**16**)

A vial is charged with **15**<sup>BArF</sup> (40.0 mg, 24.4  $\mu\text{mol}$ , 1.0 eq.) and dissolved in toluene (2 ml) and cooled down to  $-35\text{ }^\circ\text{C}$ . A solution of cobaltocene (4.6 mg, 24.4  $\mu\text{mol}$ , 1.0 eq.) in toluene (2 ml) is added dropwise and the color turns immediately into deep red. The reaction solution is stirred for 10 minutes, concentrated to 1 ml and filtered through a filter pipette. The solvent is removed *in vacuo* and the residual solid is washed with diethyl ether (3 x 2 ml). The product is recrystallized by layering a toluene solution with pentane to obtain **16** as a red, crystalline solid (16 mg, 20.8  $\mu\text{mol}$ , 85%).

Crystals suitable for X-ray diffraction are obtained by layering a toluene solution of **16** with pentane at  $-80\text{ }^\circ\text{C}$ .

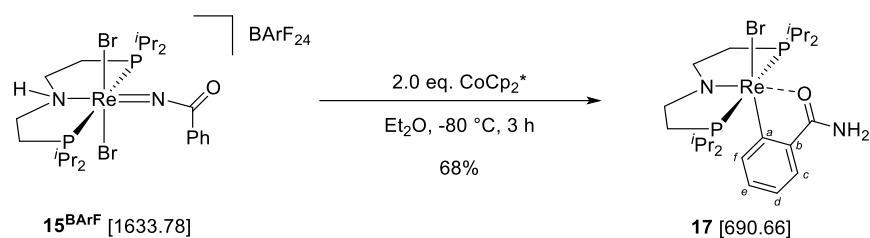
**Elem. Anal.** found (calcd) for  $\text{C}_{23}\text{H}_{42}\text{Br}_2\text{N}_2\text{OP}_2\text{Re}$ : C, 35.95 (35.85); H, 5.49 (5.43); N, 3.37 (3.64).

**$^1\text{H NMR}$**  ( $\text{C}_6\text{D}_6$ , MHz):  $\delta$  (ppm) = 20.37 (s, br,  $m_{1/2} = 448\text{ Hz}$ ), 17.54 (s, br,  $m_{1/2} = 509\text{ Hz}$ ), 14.44 (s, br,  $m_{1/2} = 600\text{ Hz}$ ), 14.42 (s, br,  $m_{1/2} = 143\text{ Hz}$ ), 5.74 (s, br,  $m_{1/2} = 833\text{ Hz}$ ), 4.27 (s, br,  $m_{1/2} = 46\text{ Hz}$ ), 1.78 (s, br,  $m_{1/2} = 98\text{ Hz}$ ),  $-2.62$  (s, br,  $m_{1/2} = 252\text{ Hz}$ ),  $-4.06$  (s, br, signal superimposed),  $-4.76$  (s, br, signal superimposed),  $-9.85$  (s, br,  $m_{1/2} = 456\text{ Hz}$ ).

**MS** (ESI+, THF) found (calcd) for  $\text{C}_{23}\text{H}_{42}\text{Br}_2\text{N}_2\text{OP}_2\text{Re}$ :  $m/z$  771.0667 ( $[\text{M}^+]$ , 771.0662), 689.1416 ( $[\text{M}^+]\text{-HBr}$ , 689.1412).

**IR** (ATR,  $\text{cm}^{-1}$ ): 3170 (N-H), 1515 (C=O).

**CV** (0.1 M  $\text{N}^t\text{Bu}_4\text{PF}_6$  in THF):  $E_{\text{p,c}} = -1.61\text{ V}$  ( $\text{Re}^{\text{III/II}}$ );  $E_{1/2} = +0.48\text{ V}$  ( $\text{Re}^{\text{IV/III}}$ ).

4.3.24 Synthesis of  $[\text{ReBr}\{\text{NH}_2(\text{CO})\text{C}_6\text{H}_4\}\{\text{P}^{\text{t}}\text{PNP}}]$  (**17**)

A schlenk tube was charged with a solution of  $\text{15}^{\text{BArF}}$  (76.0 mg, 46.7  $\mu\text{mol}$ , 1.0 eq.) in diethyl ether (6 ml) and cooled down to  $-80\text{ }^\circ\text{C}$ . A solution of decamethyl cobaltocene (30.7 mg, 93.4  $\mu\text{mol}$ , 2.0 eq.) in diethyl ether (6 ml) was added and a color change was observed via deep red to orange-brown. The reaction mixture was stirred for 3 h and allowed to warm to room temperature. The solvent was removed and the Schlenk tube was transferred into a glove box. The crude product was extracted with benzene (5 x 2 ml), filtrated and concentrated to a volume of approximately 2 ml. The extract was flushed through a filter pipette charged with silanized silica. The solvent was removed *in vacuo* and the residual substance was washed with pentane (5 x 2 ml) to obtain **17** as a reddish brown solid (22 mg, 31.9  $\mu\text{mol}$ , 68%).

Crystals suitable for X-ray diffraction were obtained from a saturated pentane solution.

**Elem. Anal.** found (calcd) for  $\text{C}_{23}\text{H}_{42}\text{BrN}_2\text{ONP}_2\text{Re}$ : C, 40.30 (40.00); H, 6.20 (6.13); N, 4.02 (4.06).

$^1\text{H}\{^{31}\text{P}\}$  NMR ( $\text{C}_6\text{D}_6$ , 500.3 MHz, ppm): 8.61 (s, br,  $\text{NH}_2$ ), 6.87 (dd,  $^4J_{\text{HH}} = 1.2\text{ Hz}$ ,  $^3J_{\text{HH}} = 8.0\text{ Hz}$ , 1H,  $\text{H}_c$ ), 6.63 (dt,  $^4J_{\text{HH}} = 1.2\text{ Hz}$ ,  $^3J_{\text{HH}} = 7.3\text{ Hz}$ , 1H,  $\text{H}_d$ ), 6.19 (dt,  $^4J_{\text{HH}} = 1.2\text{ Hz}$ ,  $^3J_{\text{HH}} = 7.3\text{ Hz}$ , 1H,  $\text{H}_d$ ), 6.03 (dd,  $^4J_{\text{HH}} = 0.6\text{ Hz}$ ,  $^3J_{\text{HH}} = 8.0\text{ Hz}$ , 1H,  $\text{H}_b$ ), 2.98 (m, 2H + 4H,  $\text{CH}(\text{CH}_3)_2 + \text{N-CH}_2\text{-CH}_2\text{-P}$ ), 1.69 (m, 2H,  $\text{N-CH}_2\text{-CHH-P}$ ), 1.62 (h, 2H + 2H,  $\text{CH}(\text{CH}_3)_2 + \text{N-CH}_2\text{-CHH-P}$ ), 1.49 (d,  $^3J_{\text{HH}} = 7.4\text{ Hz}$ , 6H,  $\text{CH}(\text{CH}_3)_2$ ), 1.37 (d,  $^3J_{\text{HH}} = 7.1\text{ Hz}$ , 6H,  $\text{CH}(\text{CH}_3)_2$ ), 0.78 (d,  $^3J_{\text{HH}} = 7.1\text{ Hz}$ , 6H,  $\text{CH}(\text{CH}_3)_2$ ), 0.75 (d,  $^3J_{\text{HH}} = 7.4\text{ Hz}$ , 6H,  $\text{CH}(\text{CH}_3)_2$ ), ( $\text{NH}_2$  signals were not observed).

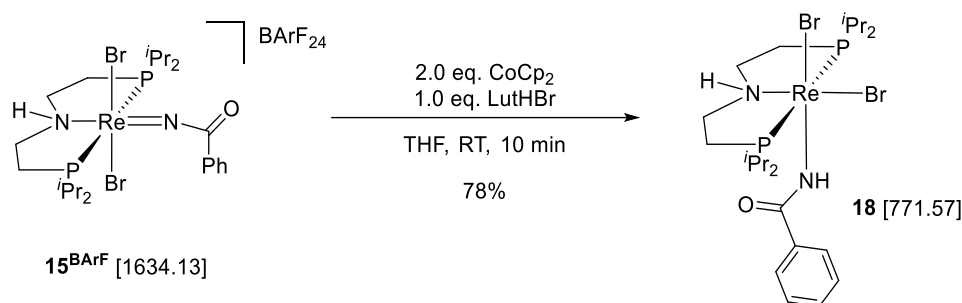
$^{13}\text{C}\{^1\text{H}\}$  NMR ( $\text{C}_6\text{D}_6$ , 125.8 MHz, ppm): 201.8 (t,  $^2J_{\text{CP}} = 6.2\text{ Hz}$ ,  $\text{C}_a$ ), 173.4 (s, CO), 133.3 (s,  $\text{C}_f$ ), 128.6 (s,  $\text{C}_b$ ), 128.5 (s,  $\text{C}_e$ ), 126.1 (s,  $\text{C}_d$ ), 119.8 (s,  $\text{C}_d$ ), 85.8 (AXY,  $N = |^2J_{\text{AX}} + ^3J_{\text{AY}}| = 10.6\text{ Hz}$ ,  $\text{N-CH}_2\text{-CH}_2\text{-P}$ ), 33.6 (AXY,  $N = |^1J_{\text{AX}} + ^3J_{\text{AY}}| = 18.0\text{ Hz}$ ,  $\text{N-CH}_2\text{-CH}_2\text{-P}$ ), 29.0 (AXY,  $N = |^1J_{\text{AX}} + ^3J_{\text{AY}}| = 20.9\text{ Hz}$ ,  $\text{CH}(\text{CH}_3)_2$ ), 28.0 (AXY,  $N = |^1J_{\text{AX}} + ^3J_{\text{AY}}| = 22.0\text{ Hz}$ ,  $\text{CH}(\text{CH}_3)_2$ ), 20.3 (s,  $\text{CH}(\text{CH}_3)_2$ ), 19.5 (s,  $\text{CH}(\text{CH}_3)_2$ ), 19.1 (AXY,  $N = |^2J_{\text{AX}} + ^4J_{\text{AY}}| = 2.6\text{ Hz}$ ,  $\text{CH}(\text{CH}_3)_2$ ), 18.7 (s,  $\text{CH}(\text{CH}_3)_2$ ).

$^{31}\text{P}\{^1\text{H}\}$  NMR ( $\text{C}_6\text{D}_6$ , 202.5 MHz, ppm): 9.59 (s,  $\text{PPr}_2$ ),

**MS** (ESI+, THF) found (calcd) for  $\text{C}_{23}\text{H}_{42}\text{BrN}_2\text{ONP}_2\text{Re}$ :  $m/z$  690.1493 (100%,  $[\text{M}^+]$ , 690.1491).

**IR** (ATR,  $\text{cm}^{-1}$ ): 3488 (N-H), 3276 (N-H), 3205 (N-H), 1624 (C=O).

**CV** (0.1 M  $\text{N}^t\text{Bu}_4\text{PF}_6$  in THF):  $E_{1/2}$  (vs  $\text{Fc}^{+/0}$ ) =  $-0.68\text{ V}$  ( $\text{Re}^{\text{IV/III}}$ ),  $+0.42\text{ V}$  ( $\text{Re}^{\text{V/IV}}$ ).

4.3.25 Synthesis [ReBr<sub>2</sub>{NH(CO)C<sub>6</sub>H<sub>5</sub>}(<sup>i</sup>PrPN<sup>H</sup>P)] (18)

In an argon filled glove box, a vial was charged with **15**<sup>BArF</sup> (27.0 mg, 16.6  $\mu\text{mol}$ , 1.0 eq.) and lutidinium bromide (3.1 mg, 16.6  $\mu\text{mol}$ , 1.0 eq.). The solids were suspended in THF (2 ml). A solution of cobaltocene (6.3 mg, 33.2  $\mu\text{mol}$ , 2.0 eq.) in THF (2 ml) is added dropwise under stirring and a color change from pale green via red to orange was observed. The reaction solution is stirred for 30 minutes and the solvent was removed *in vacuo*. The crude product was extracted with benzene and filtrated. The solvent was removed *in vacuo*. The residual substance was dissolved in diethyl ether and flushed through a filter pipette loaded with silanized silica. The solvent is removed *in vacuo* and the step is repeated. The filtrate is concentrated and stored at  $-40\text{ }^\circ\text{C}$  to obtain **18** as dark orange crystals (10 mg, 13.0  $\mu\text{mol}$ , 78%).

Crystals suitable for X-ray diffraction were obtained from gas diffusion layering of a benzene solution with pentane at room temperature.

**Elem. Anal.** found (calcd) for C<sub>23</sub>H<sub>43</sub>Br<sub>2</sub>N<sub>2</sub>OP<sub>2</sub>Re: C, 35.69 (35.80); H, 5.61 (5.62); N, 3.50 (3.62).

**<sup>1</sup>H{<sup>31</sup>P} NMR** (C<sub>6</sub>D<sub>6</sub>, 500.3 MHz, ppm): 225.48 (s, 1H, NH), 185.50 (s, 1H, NH), 16.86 (dt, <sup>3</sup>J<sub>HH</sub> = 5.7 Hz, <sup>3</sup>J<sub>HH</sub> = 14.4 Hz, 2H, N-CH<sub>2</sub>-CHH-P), 9.81 (d, <sup>3</sup>J<sub>HH</sub> = 6.9 Hz, 6H, CH(CH<sub>3</sub>)<sub>2</sub>), 9.64 (d, <sup>3</sup>J<sub>HH</sub> = 6.3 Hz, 6H, CH(CH<sub>3</sub>)<sub>2</sub>), 8.72 (d, <sup>3</sup>J<sub>HH</sub> = 7.8 Hz, 6H, CH(CH<sub>3</sub>)<sub>2</sub>), 8.63 (d, <sup>3</sup>J<sub>HH</sub> = 6.8 Hz, 6H, CH(CH<sub>3</sub>)<sub>2</sub>), 8.36 (m, 2H, CH(CH<sub>3</sub>)<sub>2</sub>), 7.04 (m, 2H, N-CHH-CH<sub>2</sub>-P), 5.47 (m, 2H, H<sub>meta</sub>), 2.89 (dd, <sup>3</sup>J<sub>HH</sub> = 2.2 Hz, <sup>3</sup>J<sub>HH</sub> = 13.9 Hz, 2H, N-CH<sub>2</sub>-CHH-P), 1.60 (h, <sup>3</sup>J<sub>HH</sub> = 6.9 Hz, 2H, CH(CH<sub>3</sub>)<sub>2</sub>), 0.93 (t, 1H, <sup>3</sup>J<sub>HH</sub> = 7.5 Hz, H<sub>para</sub>), -1.13 (dd, <sup>3</sup>J<sub>HH</sub> = 1.1 Hz, <sup>3</sup>J<sub>HH</sub> = 8.6 Hz, 2H, H<sub>ortho</sub>), -10.27 (dd, <sup>3</sup>J<sub>HH</sub> = 5.8 Hz, <sup>3</sup>J<sub>HH</sub> = 8.9 Hz, 2H, N-CHH-CH<sub>2</sub>-P).

**<sup>13</sup>C{<sup>1</sup>H} NMR** (C<sub>6</sub>D<sub>6</sub>, 125.8 MHz, ppm): 191.4 (s, N-CH<sub>2</sub>-CH<sub>2</sub>-P), 172.98 (s, C<sub>ortho</sub>), 170.8 (s, br, CH(CH<sub>3</sub>)<sub>2</sub>), 156.0 (s, C<sub>para</sub>), 126.1 (s, br, CH(CH<sub>3</sub>)<sub>2</sub>), 109.0 (s, C<sub>meta</sub>), 26.2 (s, N-CH<sub>2</sub>-CH<sub>2</sub>-P), 23.1 (s, CH(CH<sub>3</sub>)<sub>2</sub>), 18.2 (s, CH(CH<sub>3</sub>)<sub>2</sub>), 17.4 (s, C<sub>ipso</sub>), 14.8 (s, CH(CH<sub>3</sub>)<sub>2</sub>), 11.3 (s, CH(CH<sub>3</sub>)<sub>2</sub>). The CO was not observed.

**<sup>31</sup>P{<sup>1</sup>H} NMR** (C<sub>6</sub>D<sub>6</sub>, 202.1 MHz, ppm): -1812.0 (s, PPr<sub>2</sub>),

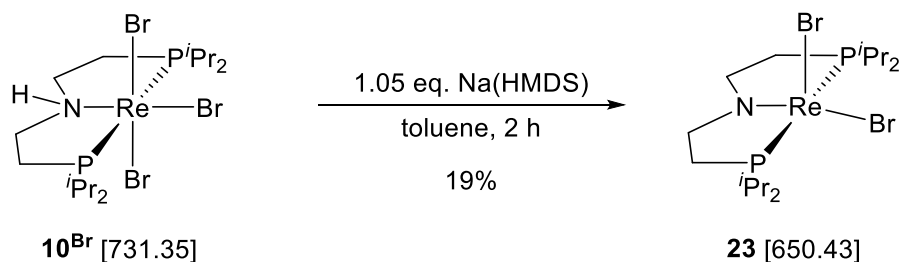
**MS** (LIFDI, THF): m/z 771.9 (100%, [M<sup>+</sup>]).

**IR** (ATR, cm<sup>-1</sup>): 3345 (N-H), 1536 (C=O).

**CV** (0.1 M N<sup>n</sup>Bu<sub>4</sub>PF<sub>6</sub> in THF): E<sub>1/2</sub> = -1.69 V (Re<sup>III/II</sup>), -0.19 V (Re<sup>IV/V</sup>).

#### 4.3.26 Synthesis of $[\text{ReBr}_2(\text{P}^i\text{Pr}_2\text{PNP})]$ (**23**)

Compound **23** was synthesized by Paul Julius Weiß (Bachelor thesis) under supervision of Maximilian Fritz.



In a glove box, a vial was charged with  $\text{10}^{\text{Br}}$  (30 mg, 41.2  $\mu\text{mol}$ , 1.0 eq.) and suspended in toluene (5 ml). A solution of sodium hexamethyl disilazide (8 mg, 43  $\mu\text{mol}$ , 1.05 eq.) in toluene (2 ml) was added to give a brown solution. The reaction mixture was stirred for 2 h and all the volatiles were removed *in vacuo*. The residual substance was extracted with pentane until the extract was pale brown. The extract was filtered and concentrated. The saturated pentane solution was stored 3 d at  $-80\text{ }^\circ\text{C}$ . The obtained crystalline solid was washed with pentane at  $-80\text{ }^\circ\text{C}$  to give complex **23** (5 mg, 7.7  $\mu\text{mol}$ , 19%) as a black crystalline solid.

Crystals suitable for X-ray diffraction were obtained from a saturated with pentane solution stored at  $-40\text{ }^\circ\text{C}$ .

**Elem. Anal.** found (calcd) for  $\text{C}_{16}\text{H}_{36}\text{Br}_2\text{ReNP}_2$ : C, 30.25 (29.55); H, 5.63 (5.58); N, 2.19 (2.15).

$^1\text{H NMR}$  ( $\text{C}_6\text{D}_6$ , 500.3 MHz, ppm): 2.87 (m, 4H, P-CHMe<sub>2</sub>), 2.40 (m, 4H, N-CH<sub>2</sub>-CH<sub>2</sub>-P), 1.63 (m, 4H, N-CH<sub>2</sub>-CH<sub>2</sub>-P), 1.39 (m,  $^3J_{\text{HH}} = 7.0\text{ Hz}$ , 12H, P-CHMe<sub>2</sub>), 1.28 (m,  $^3J_{\text{HH}} = 6.7\text{ Hz}$ , 12H, P-CHMe<sub>2</sub>).

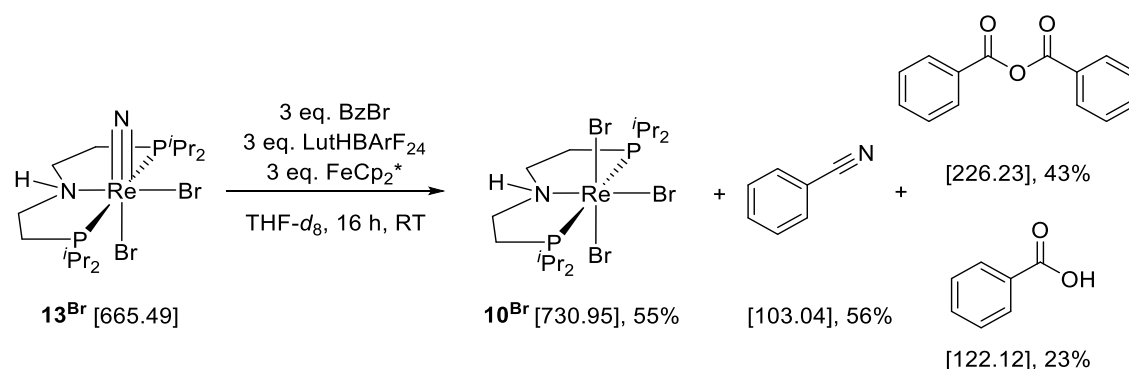
$^{13}\text{C}\{^1\text{H}\}$  NMR ( $\text{C}_6\text{D}_6$ , 125.8 MHz, ppm): 88.3 (AXY,  $N = |^2J_{\text{AX}} + ^3J_{\text{AY}}| = 9.8\text{ Hz}$ , N-CH<sub>2</sub>-CH<sub>2</sub>-P), 35.3 (AXY,  $N = |^1J_{\text{AX}} + ^3J_{\text{AY}}| = 16.6\text{ Hz}$ , N-CH<sub>2</sub>-CH<sub>2</sub>-P), 31.7 (AXY,  $N = |^1J_{\text{AX}} + ^3J_{\text{AY}}| = 22.9\text{ Hz}$ , CH(CH<sub>3</sub>)<sub>2</sub>), 19.7 (s, CH(CH<sub>3</sub>)<sub>2</sub>), 19.2 (s, CH(CH<sub>3</sub>)<sub>2</sub>).

$^{31}\text{P}\{^1\text{H}\}$  NMR ( $\text{C}_6\text{D}_6$ , 121.5 MHz, ppm): 1.79 (s, P-CHMe<sub>2</sub>).

**MS** (LIFDI, THF):  $m/z$  651.9 (100%,  $[\text{M}^+]$ ).

## 4.4 Nitride transfer reactions via PCET and protonation

### 4.4.1 Benzonitrile formation via PCET starting from nitride complex $13^{\text{Br}}$



A Young NMR tube was charged with  $13^{\text{Br}}$  (3.0 mg, 4.5  $\mu\text{mol}$ , 1.0 eq.), decamethyl ferrocene (4.4 mg, 13.5  $\mu\text{mol}$ , 3.0 eq.), lutidinium BArF<sub>24</sub> (13.0 mg, 13.5  $\mu\text{mol}$ , 3.0 eq.) and benzoyl bromide (2.5 mg, 13.5  $\mu\text{mol}$ , 3.0 eq.). The reactants were dissolved in THF-*d*<sub>8</sub> (0.7 ml) and the reaction solution was stirred for 16 h. The color changed from orange into green.  $^{31}\text{P}\{^1\text{H}\}$  NMR spectroscopy of the reaction solution confirmed complete consumption of the starting material and identified  $10^{\text{Br}}$  as the only  $^{31}\text{P}\{^1\text{H}\}$  NMR active product (Figure 4.2,  $\delta = -1500.98$  ppm).

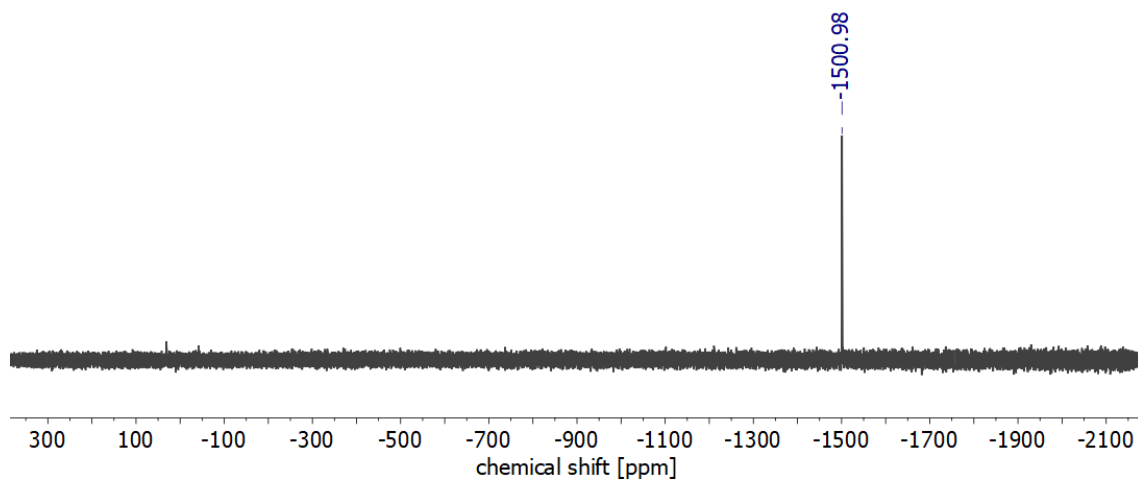
The reaction solution was degassed by 3 freeze-pump-thaw cycles and the volatiles were collected via condensation (static vacuum, RT, 2 h). Benzonitrile (Figure 4.3,  $\delta = 7.70, 7.63, 7.51$  ppm) and benzoic acid (Figure 4.3,  $\delta = 8.01$  ppm) were quantified by  $^1\text{H}$  NMR spectroscopy with a spectroscopic yield of 56% and 23%, respectively, using 1,3,5-trimethoxy benzene (2.8 mg, 16.6  $\mu\text{mol}$ , 3.69 eq.) as internal standard. The chemical shifts are identical compared to the commercially purchased substances (Figure 4.3, right).

The residual substance was extracted with pentane (5 x 2 ml), the solvent was removed *in vacuo* and 1,3,5-trimethoxy benzene was added as an internal standard (4.0 mg, 23.7  $\mu\text{mol}$ , 5.23 eq.). The solids were dissolved in C<sub>6</sub>D<sub>6</sub> and  $^1\text{H}$  NMR spectroscopy quantified benzoic anhydride (Figure 4.4,  $\delta = 7.95, 6.94$  ppm) with a spectroscopic yield of 43%.

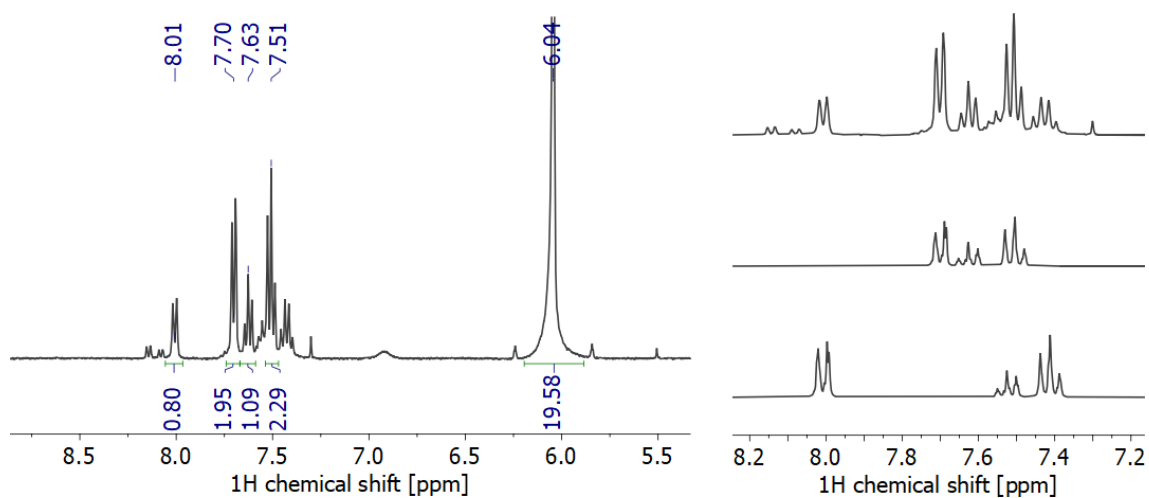
The residual substance was extracted with THF and filtrated. The solvent was removed *in vacuo* and 1,3,5-trimethoxy benzene was added as an internal standard (3.1 mg, 18.3  $\mu\text{mol}$ , 4.02 eq.). Quantification by  $^1\text{H}$  NMR spectroscopy in CD<sub>2</sub>Cl<sub>2</sub> revealed a spectroscopic yield of 64% for rhenium tribromide complex for  $10^{\text{Br}}$  (Figure 4.5,  $\delta = 9.71, 9.26, 8.07$  ppm).

The corresponding  $^{15}\text{N}$  labelled condensation product was further analyzed by  $^{13}\text{C}\{^1\text{H}\}$  and  $^{15}\text{N}\{^1\text{H}\}$  NMR spectroscopy. By 2D NMR spectroscopy, following  $^{13}\text{C}\{^1\text{H}\}$  signals were assigned to benzonitrile:  $\delta = 133.2$  (*C*<sub>para</sub>), 132.5 (*C*<sub>ortho</sub>), 129.5 (*C*<sub>meta</sub>), 119.2 (CN,  $^{14}\text{N}$ : s;  $^{15}\text{N}$ : d,  $^1J_{\text{C}15\text{N}} = 17.6$  Hz), 112.8 (*C*<sub>ipso</sub>) ( $^{14}\text{N}$ : s;  $^{15}\text{N}$ : d,  $^2J_{\text{C}15\text{N}} = 3.0$  Hz) ppm (Figure 4.6).<sup>264</sup> In the  $^{15}\text{N}\{^1\text{H}\}$  NMR spectrum one resonance was observed at  $\delta = -124.9$  ppm, which, according to literature, can be assigned to Ph- $^{15}\text{N}$  (Figure 4.6).<sup>72,73,264</sup>

The reaction products were identified by mass spectrometry (GC-MS, ED):  $m/z = 103.0417$  ( $C_7H_5^{14}N$ , calc: 103.0417, [M]), 104.0387 ( $C_7H_5^{15}N$ , calc: 104.0387, [M]). (ESI+, THF):  $m/z = 227.0700$  ( $C_{14}H_{11}O_3$ , calc. 227.0703, [M]+H), 249.0524 ( $C_{14}H_{11}O_3$ , calc. 249.0522, [M]+Na), 730.9436 ( $C_{16}H_{37}Br_3NP_2Re$ , calc. 730.9466, [M]), 651.0213 ( $C_{16}H_{36}Br_2NP_2Re$ , calc. 651.0211, [M]-HBr).

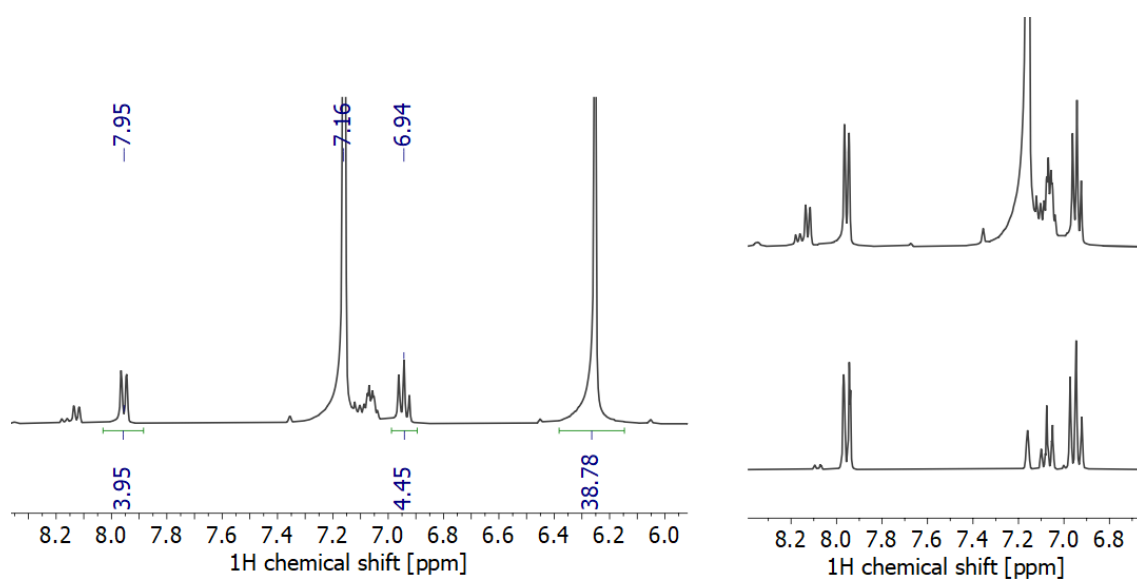


**Figure 4.2**  $^{31}P\{^1H\}$  NMR spectrum of the reaction solution (THF- $d_8$ ).

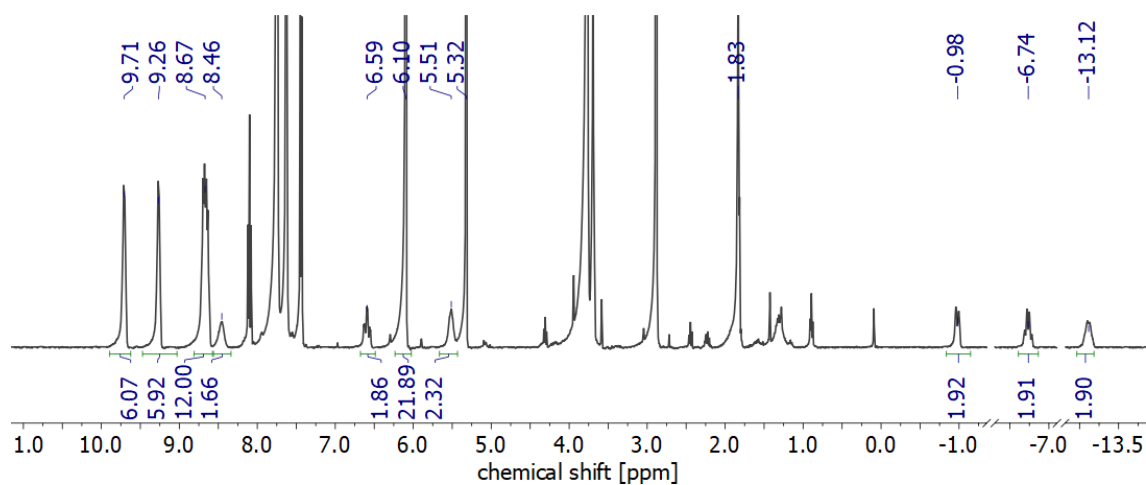


**Figure 4.3 Left:**  $^1H$  NMR spectrum of the condensation product in THF- $d_8$ . **Right:** Comparison of the volatiles (top spectrum) with commercially purchased benzonitrile (middle spectrum) and benzoic acid (bottom spectrum).

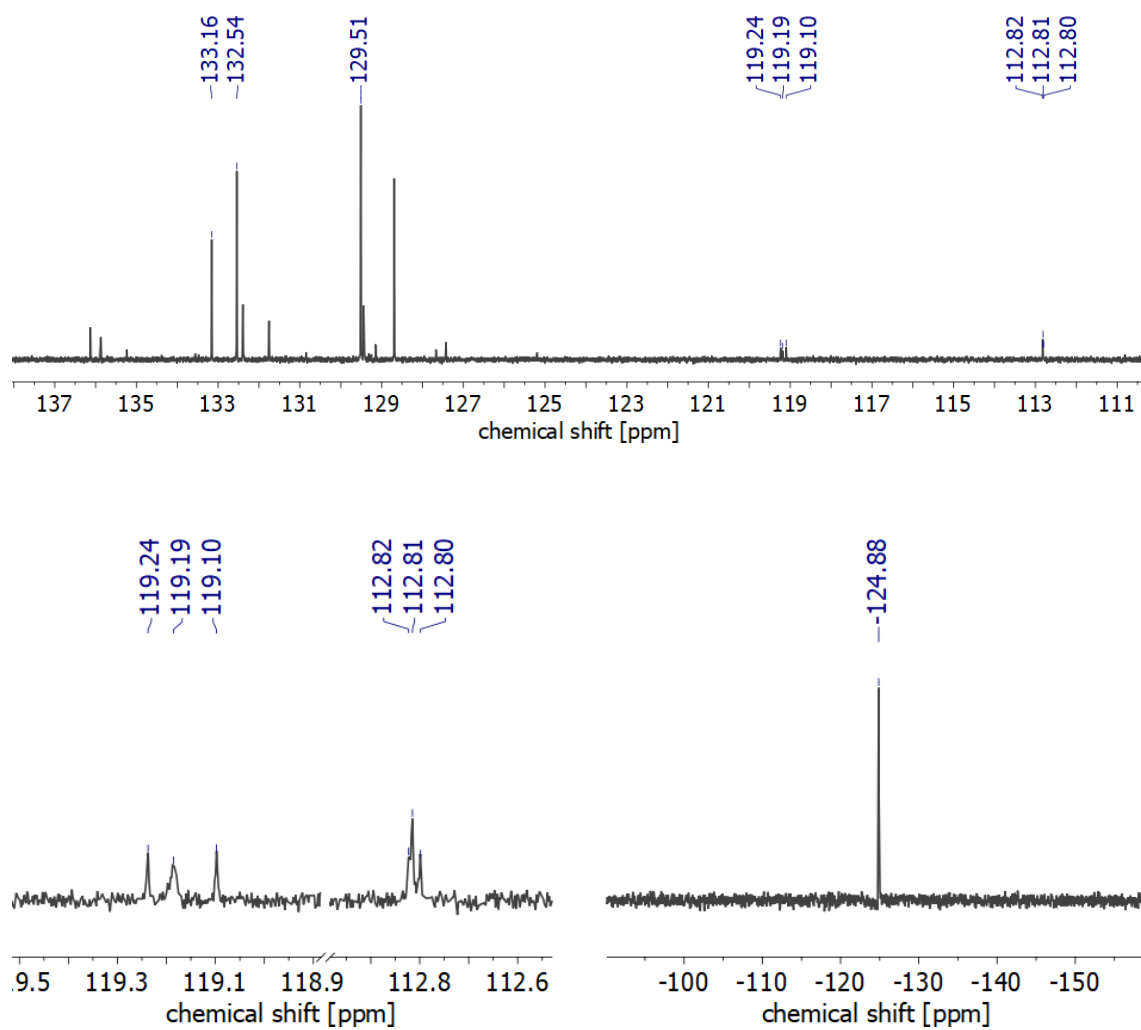




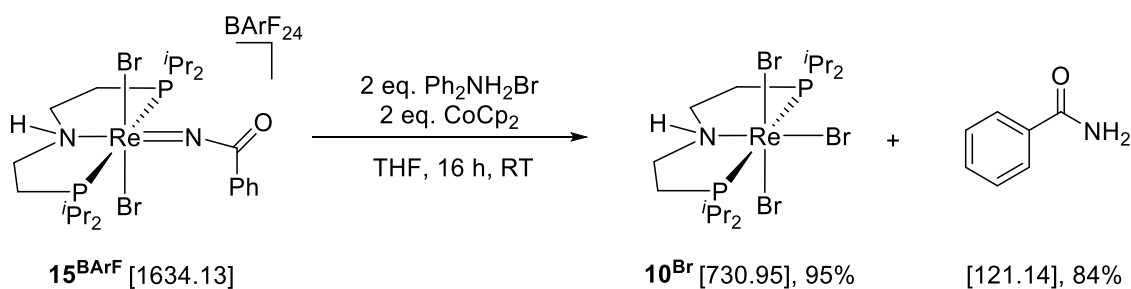
**Figure 4.4 Left:**  $^1\text{H}$  NMR spectrum of the pentane extract in  $\text{C}_6\text{D}_6$ . **Right:** Comparison of the pentane extract (top spectrum) with commercially purchased benzoic anhydride (bottom spectrum).



**Figure 4.5**  $^1\text{H}$  NMR spectrum of the THF extract in  $\text{CD}_2\text{Cl}_2$ .



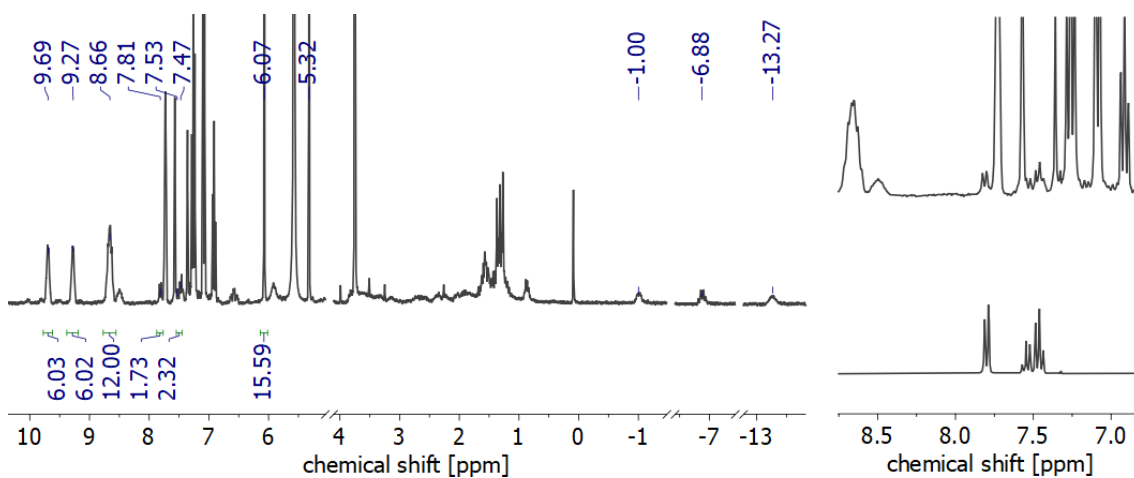
**Figure 4.6** Heteronuclear NMR characterization of the  $^{15}\text{N}$  labelled condensation product. **Top:**  $^{13}\text{C}\{^1\text{H}\}$  NMR. **Bottom left:**  $^{13}\text{C}\{^1\text{H}\}$  NMR spectrum with focus on the aromatic *ipso* and CN resonances. **Bottom right:**  $^{15}\text{N}\{^1\text{H}\}$  NMR spectrum.

4.4.2 Benzamide formation via PCET starting from imido complex  $15^{\text{BArF}}$ 

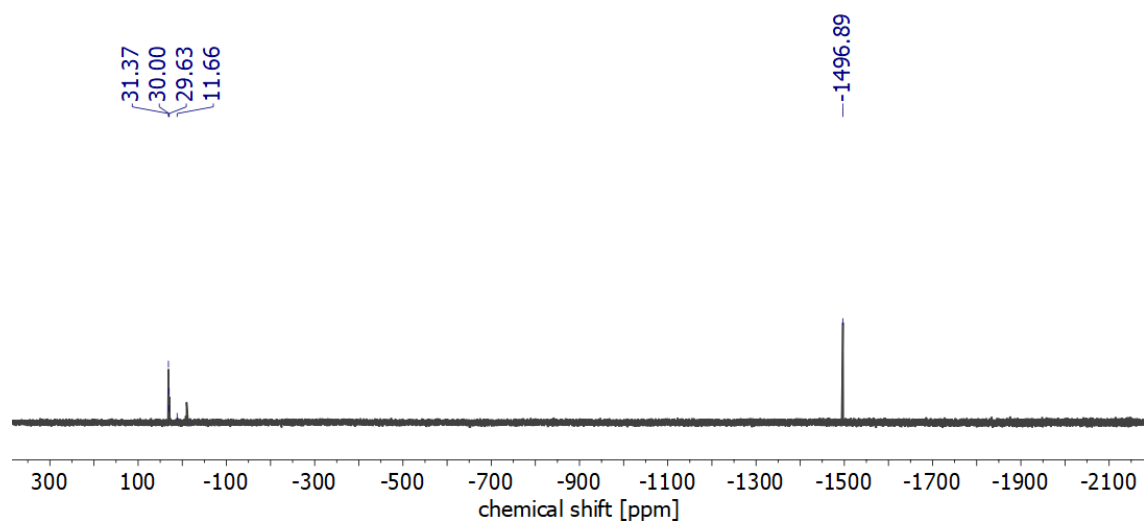
In a glove box, a vial was charged with  $15^{\text{BArF}}$  (5.5 mg, 3.8  $\mu\text{mol}$ , 1.0 eq.), diphenylammonium bromide (1.7 mg, 6.7  $\mu\text{mol}$ , 2.0 eq.) and cobaltocene (1.2 mg, 6.7  $\mu\text{mol}$ , 2.0 eq.) and THF was added (2 ml). The reaction mixture turned immediately red and then to orange. The reaction was stirred for 18 h and the solvent is removed *in vacuo*. 1,3,5-trimethoxy benzene (3.2 mg, 18.9  $\mu\text{mol}$ , 5.0 eq.) was added as an internal standard and the solids were dissolved in  $\text{CD}_2\text{Cl}_2$ .

According to  $^1\text{H}$  NMR spectroscopy,  $10^{\text{Br}}$  (Figure 4.7,  $\delta = 9.67, 9.27, 8.66$  ppm) and benzamide (Figure 4.7,  $\delta = 7.81$  ppm) were formed with spectroscopic yields of 95% and 84%, respectively. The chemical shift of the latter product is identical compared to commercially purchased benzamide (Figure 4.7, right). Further confirmation for the formation of  $10^{\text{Br}}$  was obtained by  $^{31}\text{P}\{^1\text{H}\}$  NMR spectroscopy ( $\delta = -1496.9$  ppm, Figure 4.8).

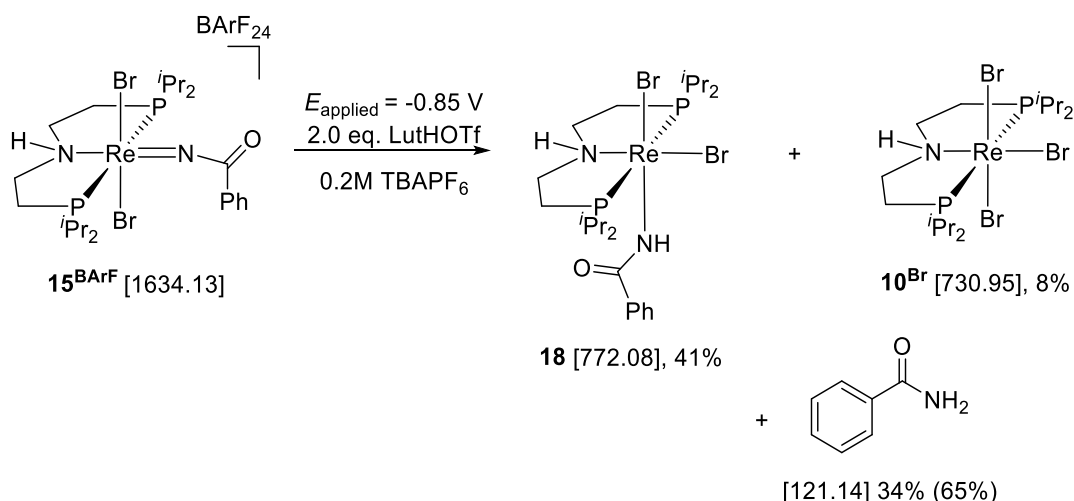
The reaction products were identified by mass spectrometry (ESI+, THF):  $m/z = 122.0599$  ( $\text{C}_7\text{H}_7\text{NO}$ , calc: 122.0600,  $[\text{M}]+\text{H}^+$ ), 144.0417 ( $\text{C}_7\text{H}_7\text{NONa}$ , calc: 144.0420,  $[\text{M}]+\text{Na}^+$ ), 730.9439 ( $\text{C}_{16}\text{H}_{37}\text{Br}_3\text{NP}_2\text{Re}$ , calc. 730.9466,  $[\text{M}]$ ), 753.9358 ( $\text{C}_{16}\text{H}_{37}\text{Br}_3\text{NP}_2\text{ReNa}$ , calc. 753.9363,  $[\text{M}]+\text{Na}^+$ ).



**Figure 4.7 Left:**  $^1\text{H}$  NMR spectrum of the crude product (RT,  $\text{CD}_2\text{Cl}_2$ ). **Right:** Comparison of the crude product (top spectrum) to commercially purchased benzamide (bottom spectrum).



**Figure 4.8**  $^{31}\text{P}\{^1\text{H}\}$  NMR spectrum of the crude product (RT,  $\text{CD}_2\text{Cl}_2$ ).

4.4.3 Electrochemical benzamide formation mediated by  $15^{\text{BArF}}$  using LutHOTf

A 10 ml three neck flask equipped with working-, counter-, and reference electrode (glassy carbon, Pt-wire, Ag-wire, respectively) was charged with  $15^{\text{BArF}}$  (30 mg, 18.4  $\mu\text{mol}$ , 1.0 eq.) and dissolved in electrolyte solution (4 ml, 0.2 M  $\text{N}^t\text{Bu}_4\text{PF}_6$  in THF). The solution was electrolyzed for 3 h at the peak potential of the first reduction wave ( $E_{\text{applied}} = -0.85 \text{ V}$ ) with ferrocene as sacrificial oxidant. The electrolysis progress was monitored by cyclic voltammetry and the integration of the current vs. time plot revealed a charge transfer of 1.59  $e^-$  per mol rhenium after electrolysis (Figure 4.9). A color change was observed from pale green via red orange to yellow orange. After electrolysis, the reaction solution was divided into two aliquots.

The solvent was evaporated from the first aliquot and the reaction products are extracted with benzene until the extract was colorless. The extract was filtrated and the solvent was removed. 1,3,5-trimethoxy benzene (9.2 mg, 54.4  $\mu\text{mol}$ , 3.0 eq.) was added as internal standard and the reaction products were quantified by  $^1\text{H}$  NMR spectroscopy. According to the obtained spectrum, carboxamide complex  $18$  (Figure 4.10,  $\delta = 10.03, 9.81, 8.71, 8.49 \text{ ppm}$ ), rhenium tribromide  $10^{\text{Br}}$  (Figure 4.10,  $\delta = 9.69, 9.22, 8.71$  (partially superimposed), 8.49 ppm) and benzamide (Figure 4.10,  $\delta$  ( $H_{\text{ortho}}$ ) = 7.80 ppm) were formed with spectroscopic yields of 41%, 8% and 35%, respectively.

The product distribution could be confirmed by  $^{31}\text{P}\{^1\text{H}\}$  NMR spectroscopy (Figure 4.11,  $\delta = -1495.2$  ( $10^{\text{Br}}$ ),  $-1874.9$  ( $18$ ) ppm). Mass spectrometry (ESI+, THF) identified following species:  $m/z = 122.0597$  ( $\text{C}_7\text{H}_7\text{NO}$ , calc: 122.0600,  $[\text{M}]+\text{H}^+$ ), 585.1138 ( $\text{C}_{16}\text{H}_{37}\text{BrN}_2\text{P}_2\text{Re}$ , calc. 585.1150,  $[\text{M}]-\text{Br}$ ), 652.0266 ( $\text{C}_{16}\text{H}_{37}\text{Br}_2\text{NP}_2\text{Re}$ , calc. 652.0290,  $[\text{M}]-\text{Br}$ ), 773.0795 ( $\text{C}_{23}\text{H}_{43}\text{Br}_2\text{N}_2\text{OP}_2\text{Re}$ , calc. 773.0818,  $[\text{M}]+\text{H}^+$ ).

The second aliquot was subjected to an aqueous work-up. The crude product was dissolved in dichloromethane (0.5 ml) and diethyl ether (2 ml) which led to precipitation of the electrolyte. An aqueous sodium hydroxide solution (2 M, 1 ml) was added and the vial was intensively shaken. The organic phase was decanted and the aqueous phase was extracted with diethyl ether (4 x 2 ml). The solvent was removed *in vacuo* and 1,3,5-trimethoxy benzene

(8.9 mg, 52.7  $\mu\text{mol}$ , 2.86 eq.) was added as internal standard. The solids were dissolved in  $\text{CD}_2\text{Cl}_2$  and  $^1\text{H}$  NMR spectroscopy was quantified benzamide (Figure 4.12 (left),  $\delta = 7.8, 7.53, 7.45$  ppm) with a spectroscopic yield of 65%. The signal shifts are identical compared to commercially purchased benzamide (Figure 4.12, right).

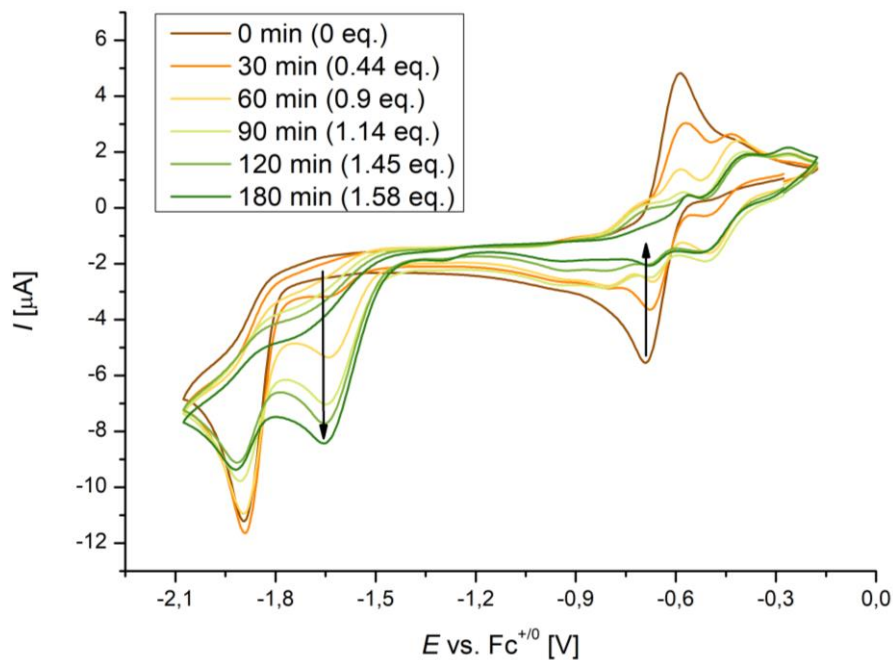


**Figure 4.9** Controlled potential electrolysis ( $E_{\text{applied}} = -0.85$  V) monitored by cyclic voltammetry at a scan rate of 50 mV/s.

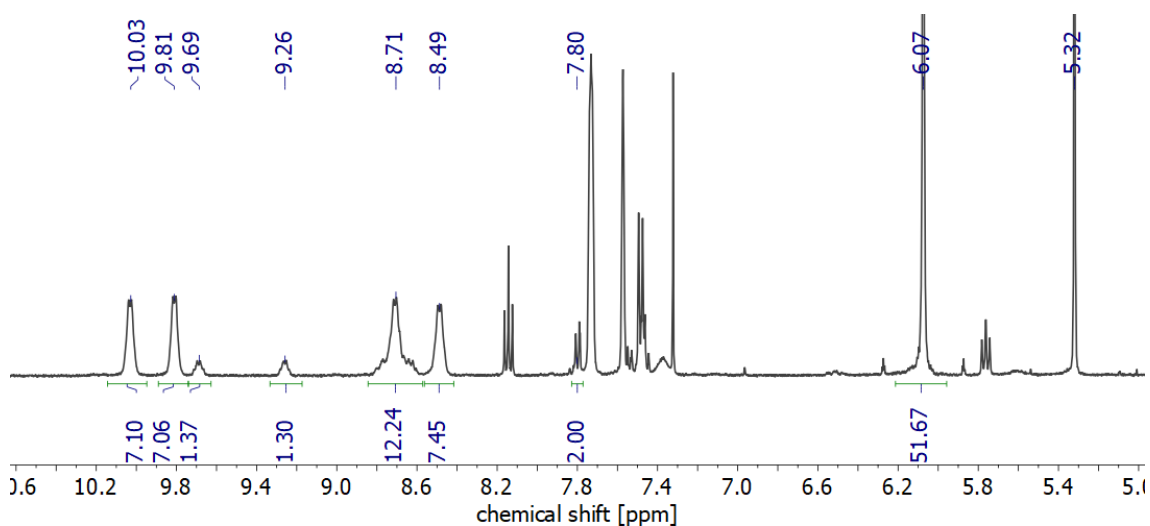


**Figure 4.10**  $^1\text{H}$  NMR spectrum of the crude product (RT,  $\text{CD}_2\text{Cl}_2$ ).

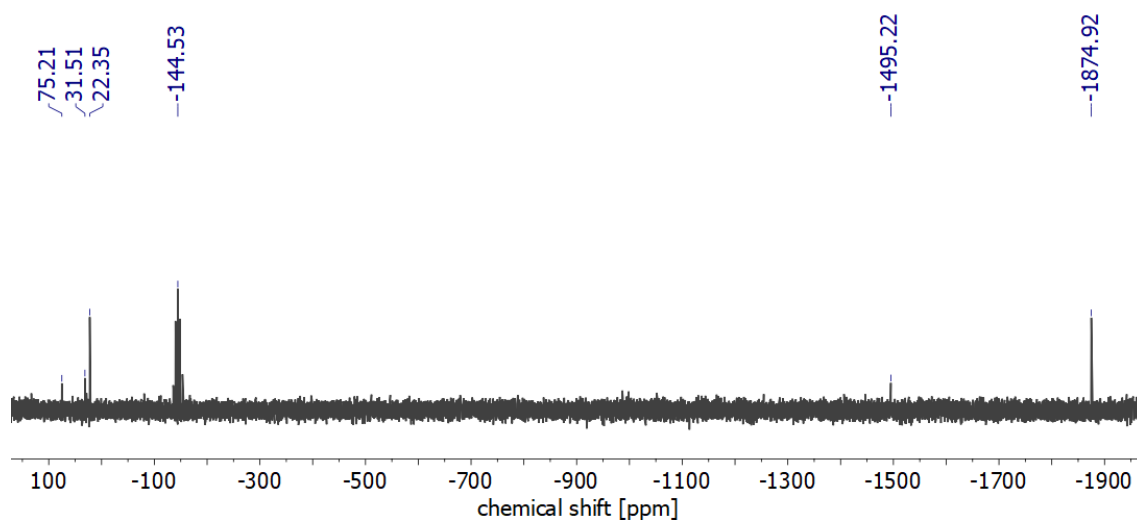


Figure 4.11  $^{31}\text{P}\{^1\text{H}\}$  NMR spectrum of the crude product (RT,  $\text{CD}_2\text{Cl}_2$ ).

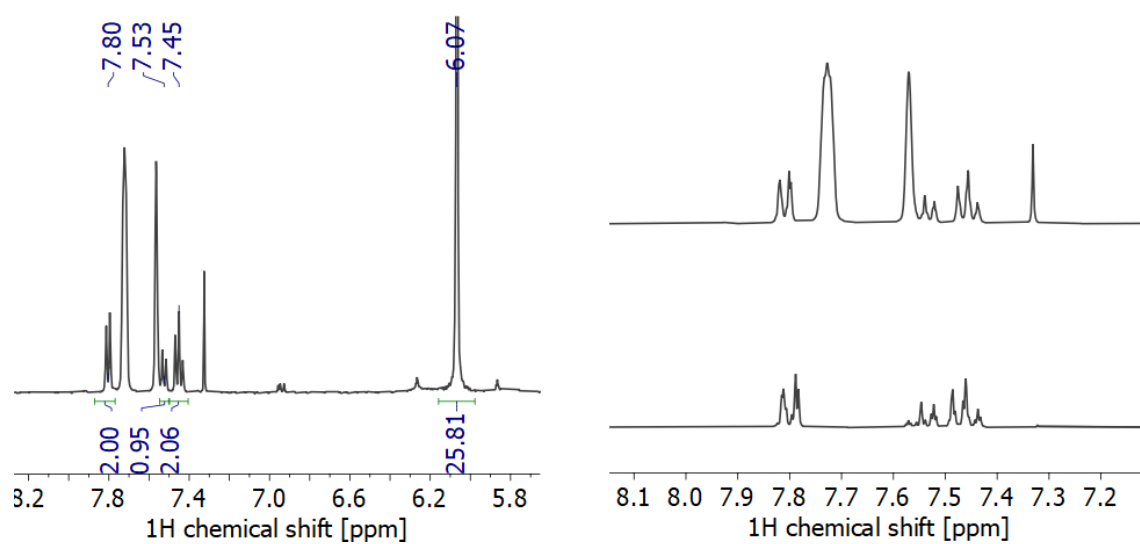
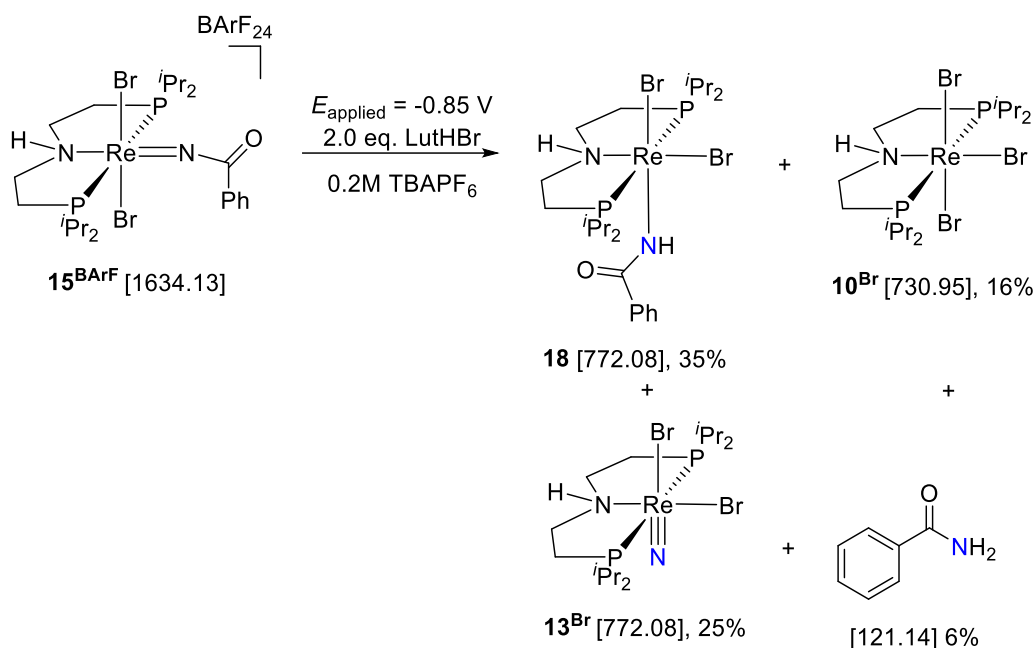


Figure 4.12 **Left:**  $^1\text{H}$  NMR spectrum of the crude product after aqueous work up (RT,  $\text{CD}_2\text{Cl}_2$ ). **Right:** Comparison of the crude product (**top spectrum**) with commercially purchased substance (**bottom spectrum**).

4.4.4 Electrochemical benzamide formation mediated by  $15^{\text{BArF}}$  using LutHBr

A 10 ml three neck flask equipped with working-, counter-, and reference electrode (glassy carbon, Pt-wire, Ag-wire, respectively) was charged with  $15^{\text{BArF}}$  (10.0 mg, 6.1  $\mu\text{mol}$ , 1.0 eq.) and dissolved in electrolyte solution (4 ml, 0.2 M  $\text{N}^{\text{t}}\text{Bu}_4\text{PF}_6$  in THF). The solution was electrolyzed for 15 h at the peak potential of the first reduction wave ( $E_{\text{applied}} = -0.75$  V) with ferrocene as sacrificial oxidant. The electrolysis progress was monitored by cyclic voltammetry and the integration of the current vs. time plot revealed a charge transfer of 1.46  $e^-$  per mol rhenium after 15 h (Figure 4.14). A color change was observed from pale green via red orange to yellow.

After electrolysis, the solvent was removed and the reaction products extracted with benzene. The extract was filtrated and the solvent was removed. 1,3,5-trimethoxy benzene (4.7 mg, 27.8  $\mu\text{mol}$ , 4.56 eq.) was added as internal standard. The solids were dissolved in  $\text{CD}_2\text{Cl}_2$  and the spectroscopic yields of the reaction products were determined by  $^1\text{H}$  NMR spectroscopy (Figure 4.13, left). The signals at  $\delta = 10.03, 9.80, 8.68$  and 8.49 (superimposed) ppm can be assigned to carboxamide complex  $18$  (spec. yield: 35%), and the set of signals of  $\delta = 9.68, 9.27, 8.68$  (partially superimposed), 8.63 (partially superimposed) ppm to rhenium tribromide  $10^{\text{Br}}$  (spec. yield: 16%). Benzamide ( $\delta$  ( $H_{\text{ortho}}$ ) = 7.81 ppm) was formed with a spectroscopic yield of 6% and rhenium nitride complex  $13^{\text{Br}}$  ( $\delta = 2.71, 2.55, 2.36$ ) by 25%. The product distribution could be confirmed by  $^{31}\text{P}\{^1\text{H}\}$  NMR spectroscopy:  $\delta = 31.4$  ( $13^{\text{Br}}$ ),  $-1498.2$  ( $10^{\text{Br}}$ ),  $-1872.03$  ( $18$ ) (Figure 4.13, right) and mass spectrometry (ESI+, THF) identified following species:  $m/z = 122.0599$  ( $\text{C}_7\text{H}_7\text{NO}$ , calc: 122.0600,  $[\text{M}]+\text{H}^+$ ), 585.1138 ( $\text{C}_{16}\text{H}_{37}\text{BrN}_2\text{P}_2\text{Re}$ , calc. 585.1150,  $[\text{M}]-\text{Br}$ ), 651.0208 ( $\text{C}_{16}\text{H}_{36}\text{Br}_2\text{N}_2\text{P}_2\text{Re}$ , calc. 651.0211,  $[\text{M}]^+-\text{HBr}$ ), 773.0798 ( $\text{C}_{23}\text{H}_{43}\text{Br}_2\text{N}_2\text{OP}_2\text{Re}$ , calc. 773.0818,  $[\text{M}]+\text{H}^+$ ).



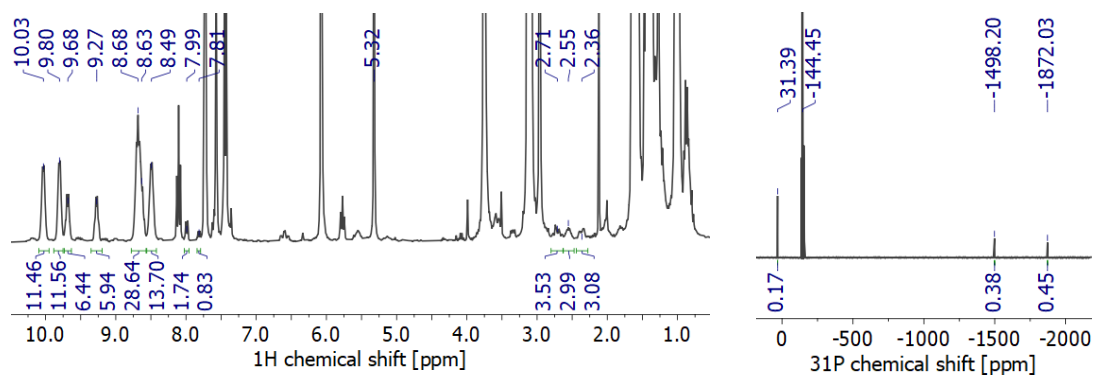


Figure 4.13  $^1\text{H}$  NMR (left) and  $^{31}\text{P}\{^1\text{H}\}$  spectrum (right) of the benzene extract (RT,  $\text{CD}_2\text{Cl}_2$ ).

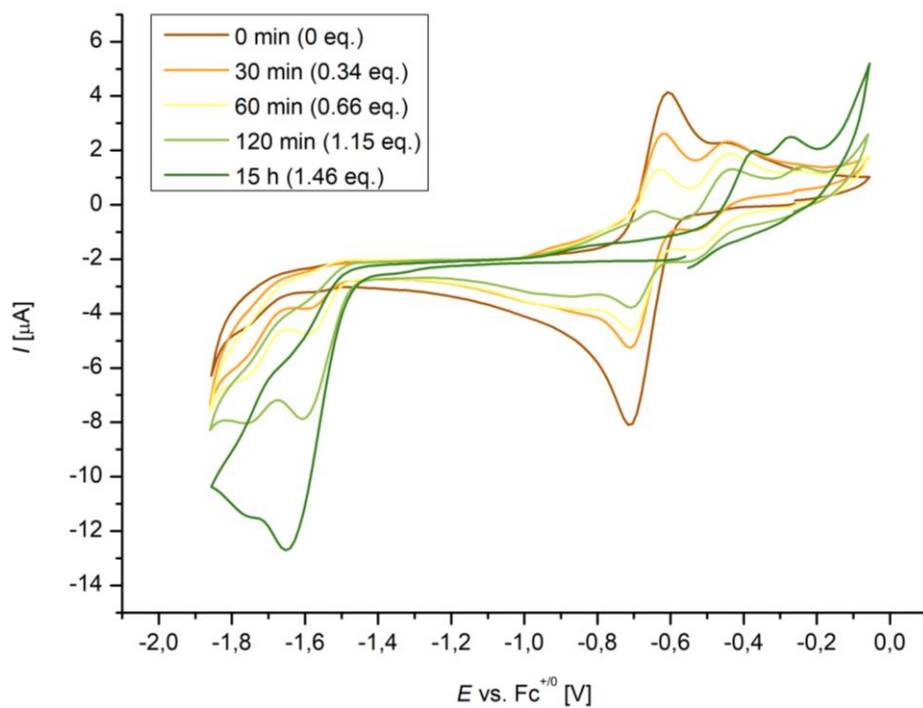
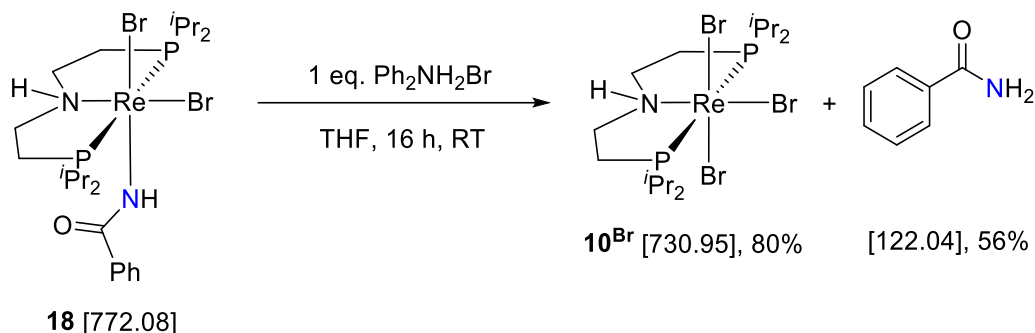
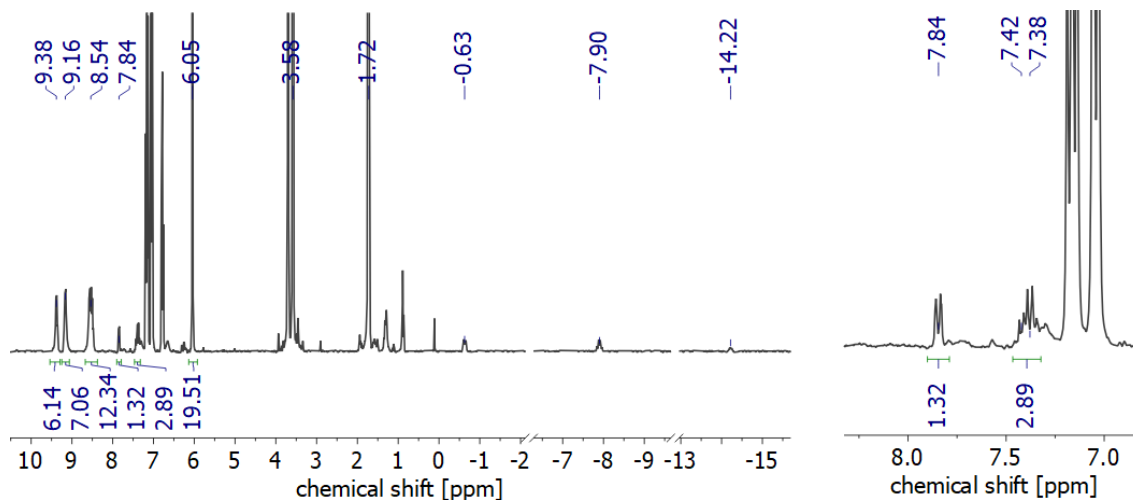


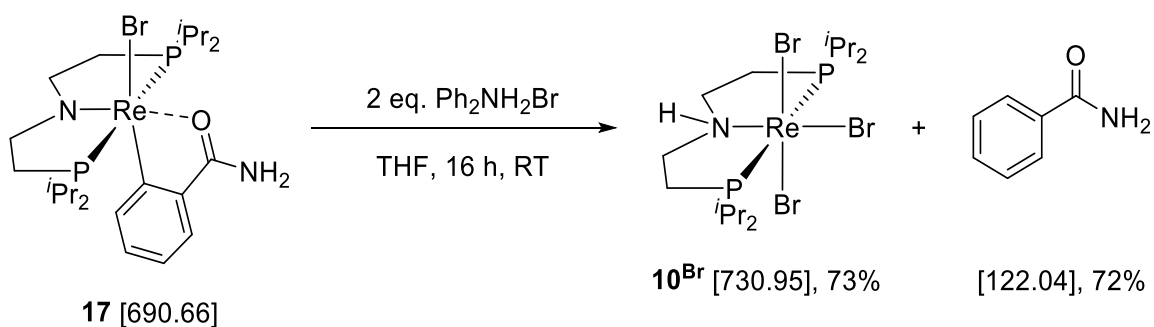
Figure 4.14 Controlled potential electrolysis ( $E_{\text{applied}} = -0.75$  V) monitored by cyclic voltammetry at a scan rate of 50 mV/s.

4.4.5 Benzonitrile formation by protonolysis of **18**

In a glove box, a vial was charged with **18** (3.0 mg, 3.9  $\mu\text{mol}$ , 1.0 eq.) and diphenylammonium bromide (1.0 mg, 3.9  $\mu\text{mol}$ , 1.0 eq.) and THF was added (2 ml). The reaction was stirred for 20 h and the solvent is removed *in vacuo*. 1,3,5-trimethoxy benzene (3.5 mg, 20.7  $\mu\text{mol}$ , 5.33 eq.) was added as an internal standard. The solids were dissolved in THF- $d_8$ , filtrated and the reaction products were quantified by  $^1\text{H}$  NMR spectroscopy. Rhenium tribromide **10**<sup>Br</sup> (Figure 4.15(left),  $\delta = 9.38, 9.16, 8.54$  ppm) and benzonitrile (Figure 4.15 (right),  $\delta = 7.84$  ppm) were formed with spectroscopic yields of 80% and 56%, respectively.



**Figure 4.15 Left:**  $^1\text{H}$  NMR spectrum of the crude product (RT, THF- $d_8$ ). **Right:** Zoom-in of the aromatic region.

4.4.6 Benzonitrile formation by protonolysis of **17**

In a glove box, a vial was charged with **17** (3.0 mg, 4.3  $\mu\text{mol}$ , 1.0 eq.) and diphenylammonium bromide (2.2 mg, 8.6  $\mu\text{mol}$ , 2.0 eq.) and THF was added (2 ml). The reaction was stirred for 18 h and the solvent is removed *in vacuo*. 1,3,5-trimethoxy benzene (5.0 mg, 29.6  $\mu\text{mol}$ , 6.88 eq.) was added as an internal standard. The residual solid was dissolved in THF- $d_6$ , filtrated and the reaction products were quantified by  $^1\text{H}$  NMR spectroscopy. Rhenium tribromide **10<sup>Br</sup>** (Figure 4.16 (left),  $\delta = 9.38, 9.15, 9.00$  ppm) and benzamide (Figure 4.16 (right),  $\delta = 7.84$  ppm) were identified as reaction products with spectroscopic yields of 73% and 72%, respectively. **10<sup>Br</sup>** formation is further confirmed by  $^{31}\text{P}\{^1\text{H}\}$  NMR spectroscopy (Figure 4.17,  $\delta = -1425.0$  ppm).

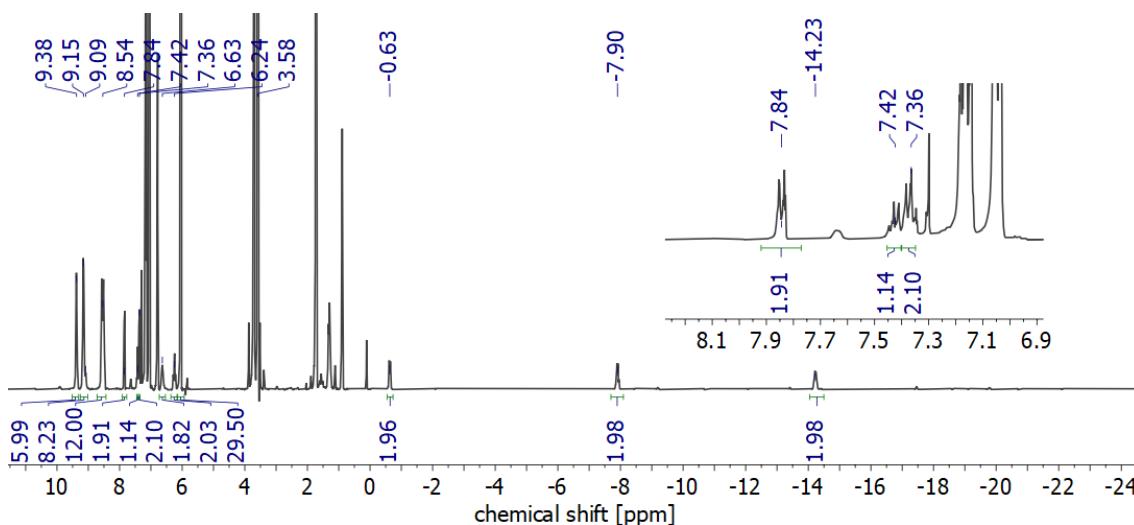


**Figure 4.16**  $^1\text{H}$  NMR spectrum of the crude product (RT, THF- $d_6$ ).

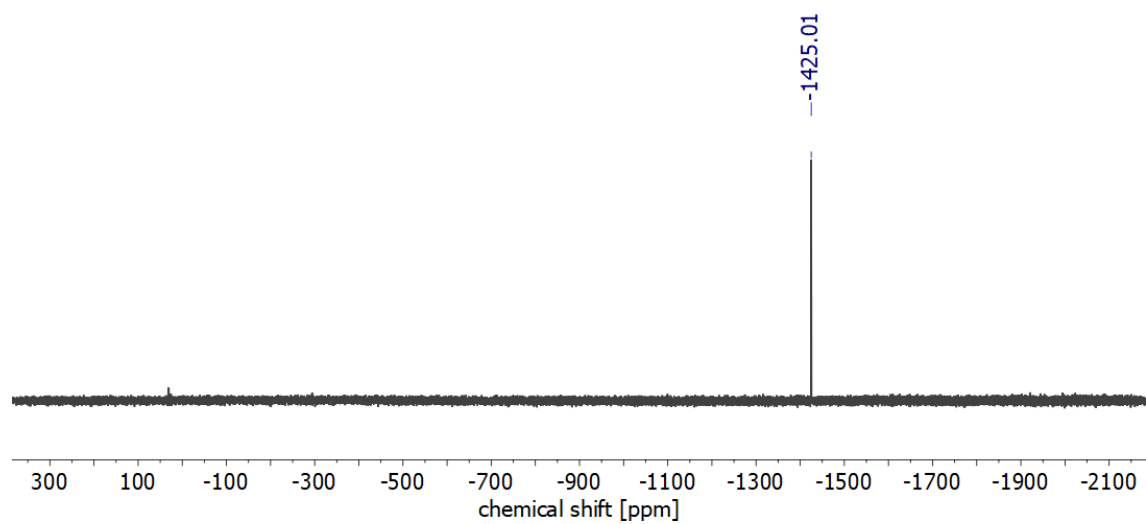


**Figure 4.17**  $^{31}\text{P}\{^1\text{H}\}$  NMR spectrum of the crude product (RT,  $\text{THF-}d_8$ ).

## 5 References

- (1) Klopsch, I.; Yuzik-Klimova, E. Y.; Schneider, S. Functionalization of N<sub>2</sub> by Mid to Late Transition Metals via N–N Bond Cleavage. In *Top Organomet Chem (2013) 43: 1–20*; 2017; Vol. 48, pp 71–112.
- (2) Forrest, S. J. K.; Schluschaß, B.; Yuzik-Klimova, E. Y.; Schneider, S. Nitrogen Fixation via Splitting into Nitrido Complexes. *Chem. Rev.* **2021**, *121*, 6522–6587.
- (3) Bezdek, M. J.; Chirik, P. J. Expanding Boundaries: N<sub>2</sub> Cleavage and Functionalization beyond Early Transition Metals. *Angew. Chemie Int. Ed.* **2016**, *55*, 7892–7896.
- (4) Humphreys, J.; Lan, R.; Tao, S. Development and Recent Progress on Ammonia Synthesis Catalysts for Haber–Bosch Process. *Adv. Energy Sustain. Res.* **2021**, *2*, 2000043.
- (5) Appl, M. *Ullmann's Encyclopedia of Industrial Chemistry*; Wiley, 2000; Vol. 3.
- (6) Curley, J. J.; Cook, T. R.; Reece, S. Y.; Müller, P.; Cummins, C. C. Shining Light on Dinitrogen Cleavage: Structural Features, Redox Chemistry, and Photochemistry of the Key Intermediate Bridging Dinitrogen Complex. *J. Am. Chem. Soc.* **2008**, *130*, 9394–9405.
- (7) Bezdek, M. J.; Guo, S.; Chirik, P. J. Terpyridine Molybdenum Dinitrogen Chemistry: Synthesis of Dinitrogen Complexes That Vary by Five Oxidation States. *Inorg. Chem.* **2016**, *55*, 3117–3127.
- (8) Laplaza, C. E.; Cummins, C. C. Dinitrogen Cleavage by a Three-Coordinate Molybdenum(III) Complex. *Science (80-. )*. **1995**, *268*, 861–863.
- (9) Schluschaß, B.; Abbenseth, J.; Demeshko, S.; Finger, M.; Franke, A.; Herwig, C.; Würtele, C.; Ivanovic-Burmazovic, I.; Limberg, C.; Telser, J.; et al. Selectivity of Tungsten Mediated Dinitrogen Splitting vs. Proton Reduction. *Chem. Sci.* **2019**, *10*, 10275–10282.
- (10) Abbenseth, J.; Oudsen, J.-P. H.; Venderbosch, B.; Demeshko, S.; Finger, M.; Herwig, C.; Würtele, C.; Holthausen, M. C.; Limberg, C.; Tromp, M.; et al. Examination of Protonation-Induced Dinitrogen Splitting by in Situ EXAFS Spectroscopy. *Inorg. Chem.* **2020**, *59*, 14367–14375.
- (11) Tshuva, E. Y.; Lippard, S. J. Synthetic Models for Non-Heme Carboxylate-Bridged Diiron Metalloproteins: Strategies and Tactics. *Chem. Rev.* **2004**, *104*, 987–1012.
- (12) Solomon, E. I.; Randall, D. W.; Glaser, T. Electronic Structures of Active Sites in Electron Transfer Metalloproteins: Contributions to Reactivity. *Coord. Chem. Rev.* **2000**, *200–202*, 595–632.
- (13) Creutz, C.; Taube, H. Direct Approach to Measuring the Franck-Condon Barrier to Electron Transfer between Metal Ions. *J. Am. Chem. Soc.* **1969**, *91*, 3988–3989.
- (14) Creutz, C.; Taube, H. Binuclear Complexes of Ruthenium Ammines. *J. Am. Chem. Soc.* **1973**, *95*, 1086–1094.
- (15) Richardson, D. E.; Sen, J. P.; Buhr, J. D.; Taube, H. Preparation and Properties of Mixed-Valence ( $\mu$ -Dinitrogen)Bis(Pentaammine) Complexes of Osmium and Ruthenium. *Inorg. Chem.* **1982**, *21*, 3136–3140.
- (16) Dubicki, L.; Ferguson, J.; Krausz, E. R.; Lay, P. A.; Maeder, M.; Taube, H. Electronic

- Absorption and MCD Spectra of Mononuclear and Binuclear Complexes of Osmium(III) Ammines with  $\pi$ -Bonding Aromatic Ligands: Complexes with  $C_{2v}$  and  $D_{2h}$  Symmetry. *J. Phys. Chem.* **1984**, *88*, 3940–3941.
- (17) Aguirre-Etcheverry, P.; O'Hare, D. Electronic Communication through Unsaturated Hydrocarbon Bridges in Homobimetallic Organometallic Complexes. *Chem. Rev.* **2010**, *110*, 4839–4864.
- (18) Launay, J.-P. Mixed-Valent Compounds and Their Properties - Recent Developments. *Eur. J. Inorg. Chem.* **2020**, *2020*, 329–341.
- (19) Launay, J. P. Long-Distance Intervalence Electron Transfer. *Chem. Soc. Rev.* **2001**, *30*, 386–397.
- (20) Hildebrandt, A.; Lang, H. (Multi)Ferrocenyl Five-Membered Heterocycles: Excellent Connecting Units for Electron Transfer Studies. *Organometallics* **2013**, *32*, 5640–5653.
- (21) Kaim, W.; Sarkar, B. Mixed Valency in Ruthenium Complexes-Coordinative Aspects. *Coord. Chem. Rev.* **2007**, *251*, 584–594.
- (22) Parthey, M.; Kaupp, M. Quantum-Chemical Insights into Mixed-Valence Systems: Within and beyond the Robin-Day Scheme. *Chem. Soc. Rev.* **2014**, *43*, 5067–5088.
- (23) Demadis, K. D.; Hartshorn, C. M.; Meyer, T. J. The Localized-to-Delocalized Transition in Mixed-Valence Chemistry. *Chem. Rev.* **2001**, *101*, 2655–2686.
- (24) D'Alessandro, D. M.; Keene, F. R. Current Trends and Future Challenges in the Experimental, Theoretical and Computational Analysis of Intervalence Charge Transfer (IVCT) Transitions. *Chem. Soc. Rev.* **2006**, *35*, 424–440.
- (25) Hankache, J.; Wenger, O. S. Organic Mixed Valence. *Chem. Rev.* **2011**, *111*, 5138–5178.
- (26) Robin, M. B.; Day, P. Mixed Valence Chemistry-A Survey and Classification. In *Advances in Inorganic Chemistry and Radiochemistry*; 1968; Vol. 10, pp 247–422.
- (27) Parthey, M.; Gluyas, J. B. G.; Fox, M. A.; Low, P. J.; Kaupp, M. Mixed-Valence Ruthenium Complexes Rotating through a Conformational Robin-Day Continuum. *Chem. - A Eur. J.* **2014**, *20*, 6895–6908.
- (28) Field, L. D.; Guest, R. W.; Turner, P. Mixed-Valence Dinitrogen-Bridged Fe(0)/Fe(II) Complex. *Inorg. Chem.* **2010**, *49*, 9086–9093.
- (29) McWilliams, S. F.; Bunting, P. C.; Kathiresan, V.; Mercado, B. Q.; Hoffman, B. M.; Long, J. R.; Holland, P. L. Isolation and Characterization of a High-Spin Mixed-Valent Iron Dinitrogen Complex. *Chem. Commun.* **2018**, *54*, 13339–13342.
- (30) Demadis, K. D.; El-Samanody, E. S.; Coia, G. M.; Meyer, T. J. Os(III)(N<sub>2</sub>)Os(II) Complexes at the Localized-to-Delocalized, Mixed-Valence Transition. *J. Am. Chem. Soc.* **1999**, *121*, 535–544.
- (31) Demadis, K. D.; Meyer, T. J.; White, P. S. Localization in Trans,Trans - [(Tpy)(Cl)<sub>2</sub>Os(III)(N<sub>2</sub>)Os(II)(Cl)<sub>2</sub>(Tpy)] + (Tpy = 2,2':6',2''-Terpyridine). *Inorg. Chem.* **1997**, *36*, 5678–5679.
- (32) Cui, Q.; Musaev, D. G.; Svensson, M.; Sieber, S.; Morokuma, K. N<sub>2</sub> Cleavage by Three-Coordinate Group 6 Complexes. W(III) Complexes Would Be Better Than Mo(III) Complexes. *J. Am. Chem. Soc.* **1995**, *117*, 12366–12367.
- (33) Shih, K.; Schrock, R. R.; Kempe, R. Synthesis of Molybdenum Complexes That Contain Silylated Triamidoamine Ligands. A  $\mu$ -Dinitrogen Complex, Methyl and Acetylide Complexes, and Coupling of Acetylides. *J. Am. Chem. Soc.* **1994**, *116*, 8804–8805.

- (34) Silantyev, G. A.; Förster, M.; Schluschaß, B.; Abbenseth, J.; Würtele, C.; Volkmann, C.; Holthausen, M. C.; Schneider, S. Dinitrogen Splitting Coupled to Protonation. *Angew. Chemie - Int. Ed.* **2017**, *56*, 5872–5876.
- (35) Tanabe, Y.; Sekiguchi, Y.; Tanaka, H.; Konomi, A.; Yoshizawa, K.; Kuriyama, S.; Nishibayashi, Y. Preparation and Reactivity of Molybdenum Complexes Bearing Pyrrole-Based PNP-Type Pincer Ligand. *Chem. Commun.* **2020**, *56*, 6933–6936.
- (36) Liao, Q.; Cavaillé, A.; Saffon-Merceron, N.; Mézailles, N. Direct Synthesis of Silylamine from N<sub>2</sub> and a Silane: Mediated by a Tridentate Phosphine Molybdenum Fragment. *Angew. Chemie Int. Ed.* **2016**, *55*, 11212–11216.
- (37) Arashiba, K.; Eizawa, A.; Tanaka, H.; Nakajima, K.; Yoshizawa, K.; Nishibayashi, Y. Catalytic Nitrogen Fixation via Direct Cleavage of Nitrogen–Nitrogen Triple Bond of Molecular Dinitrogen under Ambient Reaction Conditions. *Bull. Chem. Soc. Jpn.* **2017**, *90*, 1111–1118.
- (38) Pucino, M.; Allouche, F.; Gordon, C. P.; Wörle, M.; Mougél, V.; Copéret, C. A Reactive Coordinatively Saturated Mo(III) Complex: Exploiting the Hemi-Lability of Tris(*Tert*-Butoxy)Silanolate Ligands. *Chem. Sci.* **2019**, *10*, 6362–6367.
- (39) Song, J.; Liao, Q.; Hong, X.; Jin, L.; Mézailles, N. Conversion of Dinitrogen into Nitrile: Cross-Metathesis of N<sub>2</sub>-Derived Molybdenum Nitride with Alkynes. *Angew. Chemie Int. Ed.* **2021**, *60*, 12242–12247.
- (40) Tanabe, Y.; Nishibayashi, Y. Comprehensive Insights into Synthetic Nitrogen Fixation Assisted by Molecular Catalysts under Ambient or Mild Conditions. *Chem. Soc. Rev.* **2021**, *50*, 5201–5242.
- (41) Klopsch, I.; Finger, M.; Würtele, C.; Milde, B.; Werz, D. B.; Schneider, S. Dinitrogen Splitting and Functionalization in the Coordination Sphere of Rhenium. *J. Am. Chem. Soc.* **2014**, *136*, 6881–6883.
- (42) Lindley, B. M.; van Alten, R. S.; Finger, M.; Schendzielorz, F.; Würtele, C.; Miller, A. J. M.; Siewert, I.; Schneider, S. Mechanism of Chemical and Electrochemical N<sub>2</sub> Splitting by a Rhenium Pincer Complex. *J. Am. Chem. Soc.* **2018**, *140*, 7922–7935.
- (43) Schendzielorz, F.; Finger, M.; Abbenseth, J.; Würtele, C.; Krewald, V.; Schneider, S. Metal-Ligand Cooperative Synthesis of Benzonitrile by Electrochemical Reduction and Photolytic Splitting of Dinitrogen. *Angew. Chemie Int. Ed.* **2019**, *58*, 830–834.
- (44) Bruch, Q. J.; Connor, G. P.; Chen, C.-H.; Holland, P. L.; Mayer, J. M.; Hasanayn, F.; Miller, A. J. M. Dinitrogen Reduction to Ammonium at Rhenium Utilizing Light and Proton-Coupled Electron Transfer. *J. Am. Chem. Soc.* **2019**, jacs.9b10031.
- (45) Schluschaß, B.; Borter, J.-H.; Rupp, S.; Demeshko, S.; Herwig, C.; Limberg, C.; Maciulis, N. A.; Schneider, J.; Würtele, C.; Krewald, V.; et al. Cyanate Formation via Photolytic Splitting of Dinitrogen. *JACS Au* **2021**, *1*, 879–894.
- (46) Miyazaki, T.; Tanaka, H.; Tanabe, Y.; Yuki, M.; Nakajima, K.; Yoshizawa, K.; Nishibayashi, Y. Cleavage and Formation of Molecular Dinitrogen in a Single System Assisted by Molybdenum Complexes Bearing Ferrocenyldiphosphine. *Angew. Chemie - Int. Ed.* **2014**, *53*, 11488–11492.
- (47) Huss, A. S.; Curley, J. J.; Cummins, C. C.; Blank, D. A. Relaxation and Dissociation Following Photoexcitation of the (μ-N<sub>2</sub>)[Mo(N[t-Bu]Ar)<sub>3</sub>]<sub>2</sub> Dinitrogen Cleavage Intermediate. *J. Phys. Chem. B* **2013**, *117*, 1429–1436.
- (48) Solari, E.; Silva, C. Da; Iacono, B.; Hesschenbrouck, J.; Rizzoli, C.; Scopelliti, R.; Floriani, C. Photochemical Activation of the N≡N Bond in a Dimolybdenum-

- Dinitrogen Complex: Formation of a Molybdenum Nitride. *Angew. Chemie - Int. Ed.* **2001**, *40*, 3907–3909.
- (49) Krewald, V. Dinitrogen Photoactivation: Status Quo and Future Perspectives. *Dalt. Trans.* **2018**, *47*, 10320–10329.
- (50) Krewald, V.; González, L. A Valence-Delocalised Osmium Dimer Capable of Dinitrogen Photocleavage: Ab Initio Insights into Its Electronic Structure. *Chem. - A Eur. J.* **2018**, *24*, 5112–5123.
- (51) Rafiq, S.; Bezdek, M. J.; Koch, M.; Chirik, P. J.; Scholes, G. D. Ultrafast Photophysics of a Dinitrogen-Bridged Molybdenum Complex. *J. Am. Chem. Soc.* **2018**, *140*, 6298–6307.
- (52) Eikey, R. A.; Abu-Omar, M. M. Nitrido and Imido Transition Metal Complexes of Groups 6-8. *Coord. Chem. Rev.* **2003**, *243*, 83–124.
- (53) Dehnicke, K.; Strähle, J. Nitrido Complexes of Transition Metals. *Angew. Chemie Int. Ed. English* **1992**, *31*, 955–978.
- (54) Dehnicke, K.; Strähle, J. The Transition Metal-Nitrogen Multiple Bond. *Angew. Chemie Int. Ed. English* **1981**, *20*, 413–426.
- (55) Berry, J. F. TERMINAL NITRIDO AND IMIDO COMPLEXES OF THE LATE TRANSITION METALS. *Comments Inorg. Chem.* **2009**, *30*, 28–66.
- (56) Nugent, W. A.; Haymore, B. L. Transition Metal Complexes Containing Organoimido (Nr) and Related Ligands. *Coord. Chem. Rev.* **1980**, *31*, 123–175.
- (57) Cundari, T. R. Transition Metal Imido Complexes. *J. Am. Chem. Soc.* **1992**, *114*, 7879–7888.
- (58) Ray, K.; Heims, F.; Pfaff, F. F. Terminal Oxo and Imido Transition-Metal Complexes of Groups 9-11. *Eur. J. Inorg. Chem.* **2013**, *2013*, 3784–3807.
- (59) Smith, J. M. Reactive Transition Metal Nitride Complexes. In *Progress in Inorganic Chemistry*; 2014; Vol. 58, pp 417–470.
- (60) Yi, X. Y.; Liang, Y.; Li, C. Recent Developments in Ruthenium Nitrido Complexes. *RSC Adv.* **2013**, *3*, 3477–3486.
- (61) Henderickx, H.; Kwakkenbos, G.; Peters, A.; Spoel, J. van der; de Vries, K. Direct Formation of an Organonitrogen Compound from a Molybdenum Nitrido Species. *Chem. Commun.* **2003**, *16*, 2050.
- (62) Scepaniak, J. J.; Young, J. A.; Bontchev, R. P.; Smith, J. M. Formation of Ammonia from an Iron Nitrido Complex. *Angew. Chemie* **2009**, *121*, 3204–3206.
- (63) Crevier, T. J.; Bennett, B. K.; Soper, J. D.; Bowman, J. A.; Dehestani, A.; Hrovat, D. A.; Lovell, S.; Kaminsky, W.; Mayer, J. M. C–N Bond Formation on Addition of Aryl Carbanions to the Electrophilic Nitrido Ligand in TpOs(N)Cl<sub>2</sub>. *J. Am. Chem. Soc.* **2001**, *123*, 1059–1071.
- (64) Scepaniak, J. J.; Bontchev, R. P.; Johnson, D. L.; Smith, J. M. Snapshots of Complete Nitrogen Atom Transfer from an Iron(IV) Nitrido Complex. *Angew. Chemie* **2011**, *123*, 6760–6763.
- (65) Leung, S. K.; Huang, J.; Liang, J.-L.; Che, C.; Zhou, Z. Nitrido Ruthenium Porphyrins: Synthesis, Characterization, and Amination Reactions with Hydrocarbon or Silyl Enol Ethers. *Angew. Chemie Int. Ed.* **2003**, *42*, 340–343.
- (66) Man, W.-L.; Lam, W. W. Y.; Kwong, H.-K.; Yiu, S.-M.; Lau, T.-C. Ligand-Accelerated



- Activation of Strong C–H Bonds of Alkanes by a (Salen)Ruthenium(VI)-Nitrido Complex. *Angew. Chemie Int. Ed.* **2012**, *51*, 9101–9104.
- (67) Henning, H.; Hofbauer, K.; Handke, K.; Stich, R. Unusual Reaction Pathways in the Photolysis of Diazido(Phosphane)Nickel(II) Complexes: Nitrenes As Intermediates in the Formation of Nickel(0) Complexes. *Angew. Chemie Int. Ed. English* **1997**, *36*, 408–410.
- (68) Tran, B. L.; Pink, M.; Gao, X.; Park, H.; Mindiola, D. J. Low-Coordinate and Neutral Nitrido Complexes of Vanadium. *J. Am. Chem. Soc.* **2010**, *132*, 1458–1459.
- (69) Du Bois, J.; Tomooka, C. S.; Hong, J.; Carreira, E. M. Nitridomanganese(V) Complexes: Design, Preparation, and Use as Nitrogen Atom-Transfer Reagents. *Acc. Chem. Res.* **1997**, *30*, 364–372.
- (70) Sieh, D.; Schöffel, J.; Burger, P. Synthesis of a Chloro Protected Iridium Nitrido Complex. *Dalt. Trans.* **2011**, *40*, 9512–9524.
- (71) Sceats, E. L.; Figueroa, J. S.; Cummins, C. C.; Loening, N. M.; Van der Wel, P.; Griffin, R. G. Complexes Obtained by Electrophilic Attack on a Dinitrogen-Derived Terminal Molybdenum Nitride: Electronic Structure Analysis by Solid State CP/MAS <sup>16</sup>N NMR in Combination with DFT Calculations. *Polyhedron* **2004**, *23*, 2751–2768.
- (72) Curley, J. J.; Sceats, E. L.; Cummins, C. C. A Cycle for Organic Nitrile Synthesis via Dinitrogen Cleavage. *J. Am. Chem. Soc.* **2006**, *128*, 14036–14037.
- (73) Figueroa, J. S.; Piro, N. A.; Clough, C. R.; Cummins, C. C. A Nitridoniobium(V) Reagent That Effects Acid Chloride to Organic Nitrile Conversion: Synthesis via Heterodinuclear (Nb/Mo) Dinitrogen Cleavage, Mechanistic Insights, and Recycling. *J. Am. Chem. Soc.* **2006**, *128*, 940–950.
- (74) Curley, J. J.; Cozzolino, A. F.; Cummins, C. C. Nitrogen Fixation to Cyanide at a Molybdenum Center. *Dalt. Trans.* **2011**, *40*, 2429.
- (75) Sabatini, M. T.; Boulton, L. T.; Sneddon, H. F.; Sheppard, T. D. A Green Chemistry Perspective on Catalytic Amide Bond Formation. *Nat. Catal.* **2019**, *2*, 10–17.
- (76) Brown, D. G.; Boström, J. Analysis of Past and Present Synthetic Methodologies on Medicinal Chemistry: Where Have All the New Reactions Gone? *J. Med. Chem.* **2016**, *59*, 4443–4458.
- (77) Bryan, M. C.; Dunn, P. J.; Entwistle, D.; Gallou, F.; Koenig, S. G.; Hayler, J. D.; Hickey, M. R.; Hughes, S.; Kopach, M. E.; Moine, G.; et al. Key Green Chemistry Research Areas from a Pharmaceutical Manufacturers' Perspective Revisited. *Green Chem.* **2018**, *20*, 5082–5103.
- (78) Jagadeesh, R. V.; Junge, H.; Beller, M. Green Synthesis of Nitriles Using Non-Noble Metal Oxides-Based Nanocatalysts. *Nat. Commun.* **2014**, *5*, 4123.
- (79) Anbarasan, P.; Schareina, T.; Beller, M. Recent Developments and Perspectives in Palladium-Catalyzed Cyanation of Aryl Halides: Synthesis of Benzonitriles. *Chem. Soc. Rev.* **2011**, *40*, 5049.
- (80) Fleming, F. F.; Yao, L.; Ravikumar, P. C.; Funk, L.; Shook, B. C. Nitrile-Containing Pharmaceuticals: Efficacious Roles of the Nitrile Pharmacophore. *J. Med. Chem.* **2010**, *53*, 7902–7917.
- (81) Kim, S.; Loose, F.; Chirik, P. J. Beyond Ammonia: Nitrogen–Element Bond Forming Reactions with Coordinated Dinitrogen. *Chem. Rev.* **2020**, *120*, 5637–5681.
- (82) Bennaamane, S.; Espada, M.; Mulas, A.; Personeni, T.; Saffon-Merceron, N.; Fustier-

- Boutignon, M.; Bucher, C.; Mézailles, N. Catalytic Reduction of N<sub>2</sub> to Borylamine at a Molybdenum Complex. *Angew. Chemie* **2021**, ange.202106025.
- (83) Roth, H. G.; Romero, N. A.; Nicewicz, D. A. Experimental and Calculated Electrochemical Potentials of Common Organic Molecules for Applications to Single-Electron Redox Chemistry. *Synlett* **2016**, 27, 714–723.
- (84) Klopsch, I.; Kinauer, M.; Finger, M.; Würtele, C.; Schneider, S. Conversion of Dinitrogen into Acetonitrile under Ambient Conditions. *Angew. Chemie - Int. Ed.* **2016**, 55, 4786–4789.
- (85) Klopsch, I.; Schendzielorz, F.; Volkmann, C.; Würtele, C.; Schneider, S. Synthesis of Benzotrile from Dinitrogen. *Zeitschrift für Anorg. und Allg. Chemie* **2018**, 644, 916–919.
- (86) Cheek, G. T.; Horine, P. A. Electrochemical Reduction of Benzoyl Chloride and Benzoyl Fluoride. *J. Electrochem. Soc.* **1984**, 131, 1796–1801.
- (87) Matthaei, C. T.; Mukhopadhyay, D. P.; Fischer, I. Photodissociation of Benzoyl Chloride: A Velocity Map Imaging Study Using VUV Detection of Chlorine Atoms. *J. Phys. Chem. A* **2021**, 125, 2816–2825.
- (88) Schmidt, U.; Kabitzke, K.; Markau, K. Lichtreaktionen Mit Carbonsäurederivaten, 6. Mitt.: Über Die Isolierung von Aroyl-Radikalen Nach Photolyse von Aroylbromiden Und Benzaldehyd in Der Gasphase. *Monatshefte für Chemie* **1966**, 97, 1000–1009.
- (89) Schmidt, U.; Kabitzke, K. H.; Markau, K. Isolierung von Benzoyl-Radikalen. *Angew. Chemie* **1965**, 77, 378–378.
- (90) Sluggett, G. W.; McGarry, P. F.; Koptuyg, I. V.; Turro, N. J. Laser Flash Photolysis and Time-Resolved ESR Study of Phosphinoyl Radical Structure and Reactivity. *J. Am. Chem. Soc.* **1996**, 118, 7367–7372.
- (91) Schmidt, U. Reduktion von Säurebromiden Zu Aldehyden Durch Bestrahlung in Einem Wasserstoffdonator. *Angew. Chemie* **1965**, 77, 169–169.
- (92) CHATT, J.; PEARMAN, A. J.; RICHARDS, R. L. The Reduction of Mono-Coordinated Molecular Nitrogen to Ammonia in a Protic Environment. *Nature* **1975**, 253, 39–40.
- (93) Yandulov, D. V. Catalytic Reduction of Dinitrogen to Ammonia at a Single Molybdenum Center. *Science (80-. )*. **2003**, 301, 76–78.
- (94) Ashida, Y.; Arashiba, K.; Nakajima, K.; Nishibayashi, Y. Molybdenum-Catalysed Ammonia Production with Samarium Diiodide and Alcohols or Water. *Nature* **2019**, 568, 536–540.
- (95) Stephan, G. C.; Sivasankar, C.; Studt, F.; Tuczek, F. Energetics and Mechanism of Ammonia Synthesis through the Chatt Cycle: Conditions for a Catalytic Mode and Comparison with the Schrock Cycle. *Chem. - A Eur. J.* **2008**, 14, 644–652.
- (96) Bezdek, M. J.; Pappas, I.; Chirik, P. J. Determining and Understanding N-H Bond Strengths in Synthetic Nitrogen Fixation Cycles. In *Topics in Organometallic Chemistry*; 2017; Vol. 60, pp 1–21.
- (97) Chalkley, M. J.; Drover, M. W.; Peters, J. C. Catalytic N<sub>2</sub>-to-NH<sub>3</sub> (or-N<sub>2</sub>H<sub>4</sub>) Conversion by Well-Defined Molecular Coordination Complexes. *Chem. Rev.* **2020**, 120, 5582–5636.
- (98) Johnson, S. I.; Heins, S. P.; Klug, C. M.; Wiedner, E. S.; Bullock, R. M.; Raugei, S. Design and Reactivity of Pentapyridyl Metal Complexes for Ammonia Oxidation. *Chem. Commun.* **2019**, 55, 5083–5086.

- (99) Wang, D.; Loose, F.; Chirik, P. J.; Knowles, R. R. N-H Bond Formation in a Manganese(V) Nitride Yields Ammonia by Light-Driven Proton-Coupled Electron Transfer. *J. Am. Chem. Soc.* **2019**, *141*, 4795–4799.
- (100) Matson, B. D.; Peters, J. C. Fe-Mediated HER vs N<sub>2</sub>RR: Exploring Factors That Contribute to Selectivity in P<sub>3</sub>E Fe(N<sub>2</sub>) (E = B, Si, C) Catalyst Model Systems. *ACS Catal.* **2018**, *8*, 1448–1455.
- (101) Scheibel, M. G.; Abbenseth, J.; Kinauer, M.; Heinemann, F. W.; Würtele, C.; De Bruin, B.; Schneider, S. Homolytic N-H Activation of Ammonia: Hydrogen Transfer of Parent Iridium Ammine, Amide, Imide, and Nitride Species. *Inorg. Chem.* **2015**, *54*, 9290–9302.
- (102) Warren, J. J.; Tronic, T. A.; Mayer, J. M. Thermochemistry of Proton-Coupled Electron Transfer Reagents and Its Implications. *Chem. Rev.* **2010**, *110*, 6961–7001.
- (103) Hoffman, B. M.; Dean, D. R.; Seefeldt, L. C. Climbing Nitrogenase: Toward a Mechanism of Enzymatic Nitrogen Fixation. *Acc. Chem. Res.* **2009**, *42*, 609–619.
- (104) Hickey, A. K.; Wickramasinghe, L. A.; Schrock, R. R.; Tsay, C.; Müller, P. Protonation Studies of Molybdenum(VI) Nitride Complexes That Contain the [2,6-(ArNCH<sub>2</sub>)<sub>2</sub>NC<sub>5</sub>H<sub>3</sub>] 2- Ligand (Ar = 2,6-Diisopropylphenyl). *Inorg. Chem.* **2019**, *58*, 3724–3731.
- (105) Yandulov, D. V.; Schrock, R. R. Studies Relevant to Catalytic Reduction of Dinitrogen to Ammonia by Molybdenum Triamidoamine Complexes. *Inorg. Chem.* **2005**, *44*, 1103–1117.
- (106) Cummins, C. C.; Schrock, R. R.; Davis, W. M. Synthesis of Terminal Vanadium(V) Imido, Oxo, Sulfido, Selenido, and Tellurido Complexes by Imido Group or Chalcogenide Atom Transfer to Trigonal Monopyramidal V[N<sub>3</sub>N] (N<sub>3</sub>N = [(Me<sub>2</sub>SiNCH<sub>2</sub>CH<sub>2</sub>)<sub>3</sub>]). *Inorg. Chem.* **1994**, *33*, 1448–1457.
- (107) Haug, A.; Strähle, J. Synthese Und Struktur von [Re(NH)Cl<sub>2</sub>(PMe<sub>2</sub>Ph)<sub>3</sub>][TaCl<sub>6</sub>] Und [(Me<sub>2</sub>PhP)<sub>3</sub>Cl<sub>2</sub>Re≡N]<sub>2</sub>VOCl<sub>2</sub>. *Zeitschrift für Anorg. und Allg. Chemie* **1998**, *624*, 1746–1750.
- (108) Chatt, J.; Dilworth, J. R. Preparation of Stable Imido(Nitrene)-Complexes of Molybdenum and Their Conversion into Nitrido-Complexes. *J. Chem. Soc. Chem. Commun.* **1975**, No. 24, 983.
- (109) Chatt, J.; Choukroun, R.; Dilworth, J. R.; Hyde, J.; Vella, P.; Zubieta, J. The Preparation, Crystal and Molecular Structure of [MoCl<sub>2</sub>(NH)O(EtPh<sub>2</sub>PO)<sub>2</sub>] the Preparation, Crystal and Molecular Structure of [MoCl<sub>2</sub>(NH)O(EtPh<sub>2</sub>PO)<sub>2</sub>]. An Example of Terminal, Nonlinear-Imid. *Transit. Met. Chem.* **1979**, *4*, 59–63.
- (110) Herrmann, W. A.; Bogdanovic, S.; Poli, R.; Priermeier, T. Nitridotris(Neopentyl)molybdenum(VI). *J. Am. Chem. Soc.* **1994**, *116*, 4989–4990.
- (111) Herrmann, W. A.; Stumpf, A. W.; Priermeier, T.; Bogdanovic, S.; Dufaud, V.; Basset, J.-M. Ein Molekular Definiertes, Oberflächengebundener Katalysator Zur Olefin-Metathese Aus Tris(Neopentyl)Nitridomolybdän(VI). *Angew. Chemie* **1996**, *108*, 2978–2980.
- (112) Tran, B. L.; Washington, M. P.; Henckel, D. A.; Gao, X.; Park, H.; Pink, M.; Mindiola, D. J. A Four Coordinate Parent Imidevia a Titanium Nitridyl. *Chem. Commun.* **2012**, *48*, 1529–1531.
- (113) Thompson, R.; Chen, C.-H.; Pink, M.; Wu, G.; Mindiola, D. J. A Nitrido Salt Reagent of Titanium. *J. Am. Chem. Soc.* **2014**, *136*, 8197–8200.

- (114) Lutz, C. M.; Wilson, S. R.; Shapley, P. A. The First Imido Complex of Osmium(VI), [CpOs(NH)(CH<sub>2</sub>SiMe<sub>3</sub>)<sub>2</sub>][SO<sub>3</sub>CF<sub>3</sub>]. *Organometallics* **2005**, *24*, 3350–3353.
- (115) King, D. M.; McMaster, J.; Tuna, F.; McInnes, E. J. L.; Lewis, W.; Blake, A. J.; Liddle, S. T. Synthesis and Characterization of an F-Block Terminal Parent Imido [U=NH] Complex: A Masked Uranium(IV) Nitride. *J. Am. Chem. Soc.* **2014**, *136*, 5619–5622.
- (116) Dilworth, J. R.; Lewis, J. S.; Miller, J. R.; Zheng, Y. Rhenium Complex of a Triply Deprotonated Chelated Thiosemicarbazide and Its Conversion to a Nitride Complex via a Hydrazide Intermediate. Crystal Structure of [ReCl<sub>2</sub>(NH)(NHNH<sub>2</sub>)(PPh<sub>3</sub>)<sub>2</sub>]. *J. Chem. Soc. Dalt. Trans.* **1995**, No. 8, 1357.
- (117) Zhang, S.; Cui, P.; Liu, T.; Wang, Q.; Longo, T. J.; Thierer, L. M.; Manor, B. C.; Gau, M. R.; Carroll, P. J.; Papaefthymiou, G. C.; et al. N–H Bond Formation at a Diiron Bridging Nitride. *Angew. Chemie* **2020**, *132*, 15327–15331.
- (118) Arashiba, K.; Miyake, Y.; Nishibayashi, Y. A Molybdenum Complex Bearing PNP-Type Pincer Ligands Leads to the Catalytic Reduction of Dinitrogen into Ammonia. *Nat. Chem.* **2011**, *3*, 120–125.
- (119) Arashiba, K.; Kinoshita, E.; Kuriyama, S.; Eizawa, A.; Nakajima, K.; Tanaka, H.; Yoshizawa, K.; Nishibayashi, Y. Catalytic Reduction of Dinitrogen to Ammonia by Use of Molybdenum–Nitride Complexes Bearing a Tridentate Triphosphine as Catalysts. *J. Am. Chem. Soc.* **2015**, *137*, 5666–5669.
- (120) Ashida, Y.; Arashiba, K.; Nakajima, K.; Nishibayashi, Y. Molybdenum-Catalysed Ammonia Production with Samarium Diiodide and Alcohols or Water. *Nature* **2019**, *568*, 536–540.
- (121) Wickramasinghe, L. A.; Ogawa, T.; Schrock, R. R.; Müller, P. Reduction of Dinitrogen to Ammonia Catalyzed by Molybdenum Diamido Complexes. *J. Am. Chem. Soc.* **2017**, *139*, 9132–9135.
- (122) Karsch, H. H. Cis-Bis(Dinitrogen)Tetrakis(Trimethylphosphane)Chromium. *Angew. Chemie Int. Ed. English* **1977**, *16*, 56–57.
- (123) Sobota, P.; Jezowska-Trzebiatowska, B. Fixation of Dinitrogen and Acetylene by the System CrCl<sub>2</sub>–Mg. Isolation and Properties of Chromium Complexes with Fixed N<sub>2</sub> and C<sub>2</sub>H<sub>2</sub>. *J. Organomet. Chem.* **1977**, *131*, 341–345.
- (124) Sellmann, D.; Maisel, G. Notizen: Systematische Synthese von N<sub>2</sub>-Komplexen: Erste N<sub>2</sub>-Komplexe Des Chroms / Systematic Synthesis of N<sub>2</sub> Complexes: First N<sub>2</sub> Complexes of Chromium. *Zeitschrift für Naturforsch. B* **1972**, *27*, 465–466.
- (125) Denholm, S.; Hunter, G.; Weakley, T. J. R. Dinitrogen Complexes Derived from Tricarbonyl(η<sup>6</sup>-Hexaethylbenzene)Chromium(0): Crystal and Molecular Structure of μ-Dinitrogen-Bis[Dicarbonyl(η<sup>6</sup>-Hexaethylbenzene)Chromium(0)]–Toluene (1/1). *J. Chem. Soc., Dalt. Trans.* **1987**, No. 11, 2789–2791.
- (126) Turner, J. J.; Simpson, M. B.; Poliakoff, M.; Maier, W. B.; Graham, M. A. Mixed Carbonyl-Dinitrogen Compounds: Synthesis and Thermal Stability of Cr(CO)<sub>6-x</sub>(N<sub>2</sub>)<sub>x</sub> in Liquid Xenon Solution and Low-Temperature Matrixes. *Inorg. Chem.* **1983**, *22*, 911–920.
- (127) Girolami, G. S.; Salt, J. E.; Wilkinson, G.; Thornton-Pett, M.; Hursthouse, M. B. Alkyl, Hydride, and Dinitrogen 1,2-Bis(Dimethylphosphino)Ethane Complexes of Chromium. Crystal Structures of Me<sub>2</sub>Cr(Dmpe)<sub>2</sub>, CrH<sub>4</sub>(Dmpe)<sub>2</sub>, and Cr(N<sub>2</sub>)<sub>2</sub>(Dmpe)<sub>2</sub>. *J. Am. Chem. Soc.* **1983**, *105*, 5954–5956.
- (128) Berben, L. A.; Kozimor, S. A. Dinitrogen and Acetylide Complexes of Low-Valent

- Chromium. *Inorg. Chem.* **2008**, *47*, 4639–4647.
- (129) Hoffert, W. A.; Rappé, A. K.; Shores, M. P. Unusual Electronic Effects Imparted by Bridging Dinitrogen: An Experimental and Theoretical Investigation. *Inorg. Chem.* **2010**, *49*, 9497–9507.
- (130) Monillas, W. H.; Yap, G. P. A.; MacAdams, L. A.; Theopold, K. H. Binding and Activation of Small Molecules by Three-Coordinate Cr(I). *J. Am. Chem. Soc.* **2007**, *129*, 8090–8091.
- (131) Akturk, E. S.; Yap, G. P. A.; Theopold, K. H. Mechanism-Based Design of Labile Precursors for Chromium(i) Chemistry. *Chem. Commun.* **2015**, *51*, 15402–15405.
- (132) Yin, J.; Li, J.; Wang, G. X.; Yin, Z. B.; Zhang, W. X.; Xi, Z. Dinitrogen Functionalization Affording Chromium Hydrazido Complex. *J. Am. Chem. Soc.* **2019**, *141*, 4241–4247.
- (133) Mock, M. T.; Chen, S.; Rousseau, R.; O'Hagan, M. J.; Dougherty, W. G.; Kassel, W. S.; DuBois, D. L.; Bullock, R. M. A Rare Terminal Dinitrogen Complex of Chromium. *Chem. Commun.* **2011**, *47*, 12212–12214.
- (134) Mock, M. T.; Pierpont, A. W.; Egbert, J. D.; O'Hagan, M.; Chen, S.; Bullock, R. M.; Dougherty, W. G.; Kassel, W. S.; Rousseau, R. Protonation Studies of a Mono-Dinitrogen Complex of Chromium Supported by a 12-Membered Phosphorus Macrocycle Containing Pendant Amines. *Inorg. Chem.* **2015**, *54*, 4827–4839.
- (135) Egbert, J. D.; O'Hagan, M.; Wiedner, E. S.; Bullock, R. M.; Piro, N. A.; Kassel, W. S.; Mock, M. T. Putting Chromium on the Map for N<sub>2</sub> Reduction: Production of Hydrazine and Ammonia. A Study of Cis-M(N<sub>2</sub>)<sub>2</sub> (M = Cr, Mo, W) Bis(Diphosphine) Complexes. *Chem. Commun.* **2016**, *52*, 9343–9346.
- (136) Mock, M. T.; Chen, S.; O'Hagan, M.; Rousseau, R.; Dougherty, W. G.; Scott Kassel, W.; Morris Bullock, R. Dinitrogen Reduction by a Chromium(0) Complex Supported by a 16-Membered Phosphorus Macrocycle. *J. Am. Chem. Soc.* **2013**, *135*, 11493–11496.
- (137) Bhattacharya, P.; Prokopchuk, D. E.; Mock, M. T. Exploring the Role of Pendant Amines in Transition Metal Complexes for the Reduction of N<sub>2</sub> to Hydrazine and Ammonia. *Coord. Chem. Rev.* **2017**, *334*, 67–83.
- (138) Kendall, A. J.; Johnson, S. I.; Bullock, R. M.; Mock, M. T. Catalytic Silylation of N<sub>2</sub> and Synthesis of NH<sub>3</sub> and N<sub>2</sub>H<sub>4</sub> by Net Hydrogen Atom Transfer Reactions Using a Chromium P<sub>4</sub> Macrocycle. *J. Am. Chem. Soc.* **2018**, *140*, 2528–2536.
- (139) Kendall, A. J.; Mock, M. T. Dinitrogen Activation and Functionalization with Chromium. *Eur. J. Inorg. Chem.* **2020**, *2020*, 1358–1375.
- (140) Monillas, W. H.; Yap, G. P. A.; Theopold, K. H. Reactivity of a Low-Valent Chromium Dinitrogen Complex. *Inorganica Chim. Acta* **2011**, *369*, 103–119.
- (141) Li, J.; Yin, J.; Wang, G.-X.; Yin, Z.-B.; Zhang, W.-X.; Xi, Z. Synthesis and Reactivity of Asymmetric Cr(I) Dinitrogen Complexes Supported by Cyclopentadienyl-Phosphine Ligands. *Chem. Commun.* **2019**, *55*, 9641–9644.
- (142) Goldman, A. S.; Krogh-Jespersen, K. Why Do Cationic Carbon Monoxide Complexes Have High C–O Stretching Force Constants and Short C–O Bonds? Electrostatic Effects, Not  $\sigma$ -Bonding. *J. Am. Chem. Soc.* **1996**, *118*, 12159–12166.
- (143) Alig, L.; Fritz, M.; Schneider, S. First-Row Transition Metal (De)Hydrogenation Catalysis Based On Functional Pincer Ligands. *Chem. Rev.* **2019**, *119*, 2681–2751.

- (144) Fritz, M.; Schneider, S. The Renaissance of Base Metal Catalysis Enabled by Functional Ligands; 2019; pp 1–36.
- (145) Shima, T.; Yang, J.; Luo, G.; Luo, Y.; Hou, Z. Dinitrogen Activation and Hydrogenation by  $C_5Me_4SiMe_3$ -Ligated Di- and Trinuclear Chromium Hydride Complexes. *J. Am. Chem. Soc.* **2020**, *142*, 9007–9016.
- (146) Smythe, N. C.; Schrock, R. R.; Müller, P.; Weare, W. W. Synthesis of  $[(HIPTNCH_2CH_2)_3N]Cr$  Compounds (HIPT=3,5-(2,4,6-*i*-Pr $_3$ C $_6$ H $_2$ ) $_2$ C $_6$ H $_3$ ) and an Evaluation of Chromium for the Reduction of Dinitrogen to Ammonia. *Inorg. Chem.* **2006**, *45*, 7111–7118.
- (147) Schrock, R. R. Catalytic Reduction of Dinitrogen to Ammonia at a Single Molybdenum Center. *Acc. Chem. Res.* **2005**, *38*, 955–962.
- (148) Gade, L. H. *Koordinationschemie*; Wiley-VCH Verlag GmbH & Co. KGaA: Weinheim, Germany, 1998.
- (149) Fontaine, P. P.; Yonke, B. L.; Zavalij, P. Y.; Sita, L. R. Dinitrogen Complexation and Extent of  $N\equiv N$  Activation within the Group 6 “End-On-Bridged” Dinuclear Complexes,  $\{(\eta^5-C_5Me_5)M[N(i-Pr)C(Me)N(i-Pr)]\}_2(\mu-\eta^2:\eta^1-N_2)$  (M = Mo and W). *J. Am. Chem. Soc.* **2010**, *132*, 12273–12285.
- (150) Christian, G.; Driver, J.; Stranger, R. Dinitrogen Activation in Sterically-Hindered Three-Coordinate Transition Metal Complexes. *Faraday Discuss.* **2003**, *124*, 331.
- (151) Vidyaratne, I.; Scott, J.; Gambarotta, S.; Budzelaar, P. H. M. Dinitrogen Activation, Partial Reduction, and Formation of Coordinated Imide Promoted by a Chromium Diiminepyridine Complex. *Inorg. Chem.* **2007**, *46*, 7040–7049.
- (152) Satterlee, J. D. Fundamental Concepts of NMR in Paramagnetic Systems. Part II: Relaxation Effects. *Concepts Magn. Reson.* **1990**, *2*, 119–129.
- (153) Fryzuk, M. D.; Leznoff, D. B.; Rettig, S. J.; Young, Jr., V. G. One-Electron Oxidation of Paramagnetic Chromium(II) Alkyl Complexes with Alkyl Halides: Synthesis and Structure of Five-Coordinate Chromium(III) Complexes. *J. Chem. Soc. Dalton Trans.* **1999**, No. 2, 147–154.
- (154) Fryzuk, M. D.; Leznoff, D. B.; Rettig, S. J. Synthesis and Structure of Even-Electron Paramagnetic Chromium(II) Complexes. *Organometallics* **1995**, *14*, 5193–5202.
- (155) Abbenseth, J.; Diefenbach, M.; Bete, S. C.; Würtele, C.; Volkmann, C.; Demeshko, S.; Holthausen, M. C.; Schneider, S. A Square-Planar Osmium(II) Complex. *Chem. Commun.* **2017**, *53*, 5511–5514.
- (156) Kinauer, M.; Diefenbach, M.; Bamberger, H.; Demeshko, S.; Reijerse, E. J.; Volkmann, C.; Würtele, C.; Van Slageren, J.; De Bruin, B.; Holthausen, M. C.; et al. An Iridium(III/IV/V) Redox Series Featuring a Terminal Imido Complex with Triplet Ground State. *Chem. Sci.* **2018**, *9*, 4325–4332.
- (157) Askevold, B.; Khusniyarov, M. M.; Kroener, W.; Gieb, K.; Müller, P.; Herdtweck, E.; Heinemann, F. W.; Diefenbach, M.; Holthausen, M. C.; Vieru, V.; et al. Square-Planar Ruthenium(II) Complexes: Control of Spin State by Pincer Ligand Functionalization. *Chem. - A Eur. J.* **2015**, *21*, 579–589.
- (158) Schneck, F.; Finger, M.; Tromp, M.; Schneider, S. Chemical Non-Innocence of an Aliphatic PNP Pincer Ligand. *Chem. - A Eur. J.* **2017**, *23*, 33–37.
- (159) Lagaditis, P. O.; Schluschaß, B.; Demeshko, S.; Würtele, C.; Schneider, S. Square-Planar Cobalt(III) Pincer Complex. *Inorg. Chem.* **2016**, *55*, 4529–4536.

- (160) *Nitrogen Fixation*; Nishibayashi, Y., Ed.; Topics in Organometallic Chemistry; Springer International Publishing: Cham, 2017; Vol. 60.
- (161) Holland, P. L. Metal-Dioxygen and Metal-Dinitrogen Complexes: Where Are the Electrons? *Dalt. Trans.* **2010**, *39*, 5415–5425.
- (162) Stoian, S. A.; Vela, J.; Smith, J. M.; Sadique, A. R.; Holland, P. L.; Münck, E.; Bominaar, E. L. Mössbauer and Computational Study of an N<sub>2</sub>-Bridged Diiron Diketiminato Complex: Parallel Alignment of the Iron Spins by Direct Antiferromagnetic Exchange with Activated Dinitrogen. *J. Am. Chem. Soc.* **2006**, *128*, 10181–10192.
- (163) Reiners, M.; Baabe, D.; Münster, K.; Zaretske, M.-K.; Freytag, M.; Jones, P. G.; Coppel, Y.; Bontemps, S.; Rosal, I. del; Maron, L.; et al. NH<sub>3</sub> Formation from N<sub>2</sub> and H<sub>2</sub> Mediated by Molecular Tri-Iron Complexes. *Nat. Chem.* **2020**, *12*, 740–746.
- (164) Pappas, I.; Chirik, P. J. Catalytic Proton Coupled Electron Transfer from Metal Hydrides to Titanocene Amides, Hydrazides and Imides: Determination of Thermodynamic Parameters Relevant to Nitrogen Fixation. *J. Am. Chem. Soc.* **2016**, *138*, 13379–13389.
- (165) Ward, A. L.; Lukens, W. W.; Lu, C. C.; Arnold, J. Photochemical Route to Actinide-Transition Metal Bonds: Synthesis, Characterization and Reactivity of a Series of Thorium and Uranium Heterobimetallic Complexes. *J. Am. Chem. Soc.* **2014**, *136*, 3647–3654.
- (166) Hou, H.; Rheingold, A. L.; Kubiak, C. P. An Anionic Zerovalent Nickel Carbonyl Complex Supported by a Triphosphine Borate Ligand: An Ni–C≡O–Li Isocarbonyl. *Organometallics* **2005**, *24*, 231–233.
- (167) Nishibayashi, S.; Mitsui, K.; Matsubara, K.; Nagashima, H. Novel Titanium-Cobalt Complexes Formed by Reductive Cleavage of a Co-Co Bond in Co<sub>2</sub>(CO)<sub>8</sub> by Titanocene Tert-Butoxides: Synthesis, Characterization, and Mechanistic Aspects for Metal-Metal Bond Recombination. *Organometallics* **2003**, *22*, 4885–4892.
- (168) Chen, J.; Chen, T.; Norton, J. R.; Rauch, M. Insertion of Isonitriles into the Zr–CH<sub>3</sub> Bond of Cp\*<sub>2</sub>Zr(CH<sub>3</sub>)<sub>2</sub> and Electrophilic Cleavage of the Remaining Methyl Group. *Organometallics* **2018**, *37*, 4424–4430.
- (169) Meyer, J.; González-Gallardo, S.; Hohnstein, S.; Garnier, D.; Armbruster, M. K.; Fink, K.; Klopfer, W.; Breher, F. Tris(3,5-Dimethylpyrazolyl)Methane-Based Heterobimetallic Complexes That Contain Zn- and Cd-Transition-Metal Bonds: Synthesis, Structures, and Quantum Chemical Calculations. *Chem. - A Eur. J.* **2015**, *21*, 2905–2914.
- (170) Ellermann, J.; Moll, M.; Will, N. Chemie Polyfunktioneller Moleküle CV. Chrom-, Molybdän- Und Wolframtricarbonyl-Komplexe Des Bis(2-Diphenylphosphinoethyl)amins. *J. Organomet. Chem.* **1989**, *378*, 73–79.
- (171) Jørgensen, C. K. Differences between the Four Halide Ligands, and Discussion Remarks on Trigonal-Bipyramidal Complexes, on Oxidation States, and on Diagonal Elements of One-Electron Energy. *Coord. Chem. Rev.* **1966**, *1*, 164–178.
- (172) Lee, Y.; Peters, J. C. Silylation of Iron-Bound Carbon Monoxide Affords a Terminal Fe Carbyne. **2011**, 4438–4446.
- (173) West, N. M.; Miller, A. J. M.; Labinger, J. A.; Bercaw, J. E. Homogeneous Syngas Conversion. *Coord. Chem. Rev.* **2011**, *255*, 881–898.
- (174) Arnold, P. L.; Turner, Z. R.; Bellabarba, R. M.; Tooze, R. P. Carbon Monoxide

- Coupling and Functionalisation at a Simple Uranium Coordination Complex. *Chem. Sci.* **2011**, *2*, 77–79.
- (175) Deegan, M. M.; Peters, J. C. CO Reduction to CH<sub>3</sub>OSiMe<sub>3</sub>: Electrophile-Promoted Hydride Migration at a Single Fe Site. *J. Am. Chem. Soc.* **2017**, *139*, 2561–2564.
- (176) Cutler, A. R.; Hanna, P. K.; Vites, J. C. Carbon Monoxide and Carbon Dioxide Fixation: Relevant C<sub>1</sub> and C<sub>2</sub> Ligand Reactions Emphasizing (η<sup>5</sup>C<sub>5</sub>H<sub>5</sub>) Fe-Containing Complexes. **1988**, 1363–1403.
- (177) Evans, W. J.; Drummond, D. K. Reactivity of Isocyanides with (C<sub>5</sub>Me<sub>5</sub>)<sub>2</sub>Sm(THF)<sub>2</sub>: Synthesis and Structure of Trimeric [(C<sub>5</sub>Me<sub>5</sub>)<sub>2</sub>Sm(CNC<sub>6</sub>H<sub>11</sub>)(μ-CN)]<sub>3</sub>. *Organometallics* **1988**, *7*, 797–802.
- (178) Ma, M.; Stasch, A.; Jones, C. Magnesium(I) Dimers as Reagents for the Reductive Coupling of Isonitriles and Nitriles. *Chem. - A Eur. J.* **2012**, *18*, 10669–10676.
- (179) Weiss, C. J.; Marks, T. J. Organo-f-Element Catalysts for Efficient and Highly Selective Hydroalkoxylation and Hydrothiolation. *Dalt. Trans.* **2010**, *39*, 6576–6588.
- (180) Weihe, H.; Güdel, H. U. Magnetic Exchange Across the Cyanide Bridge. *Comments Inorg. Chem.* **2000**, *22*, 75–103.
- (181) Alborés, P.; Slep, L. D.; Weyhermüller, T.; Rentschler, E.; Baraldo, L. M. Exchange Coupling across the Cyanide Bridge: Structural and DFT Interpretation of the Magnetic Properties of a Binuclear Chromium(III) Complex. *Dalt. Trans.* **2006**, No. 7, 948–954.
- (182) Mialki, W. S.; Wigley, D. E.; Wood, T. E.; Walton, R. A. Homoleptic Seven- and Six-Coordinate Alkyl Isocyanide Complexes of Chromium: Synthesis, Characterization and Redox and Substitution Chemistry. *Inorg. Chem.* **1982**, *21*, 480–485.
- (183) Braunschweig, H.; Ewing, W. C.; Ferkinghoff, K.; Hermann, A.; Kramer, T.; Shang, R.; Siedler, E.; Werner, C. Activation of Boryl-, Borylene and Metalloborylene Complexes by Isonitriles. *Chem. Commun.* **2015**, *51*, 13032–13035.
- (184) Schneck, F.; Ahrens, J.; Finger, M.; Stückl, A. C.; Würtele, C.; Schwarzer, D.; Schneider, S. The Elusive Abnormal CO<sub>2</sub> Insertion Enabled by Metal-Ligand Cooperative Photochemical Selectivity Inversion. *Nat. Commun.* **2018**, *9*, 1–8.
- (185) Luo, M.; Long, L.; Zhang, H.; Yang, Y.; Hua, Y.; Liu, G.; Lin, Z.; Xia, H. Reactions of Isocyanides with Metal Carbyne Complexes: Isolation and Characterization of Metallacyclopropenimine Intermediates. *J. Am. Chem. Soc.* **2017**, *139*, 1822–1825.
- (186) Collazo, C.; Rodewald, D.; Schmidt, H.; Rehder, D. Niobium-Centered C–C Coupling of Isonitriles. *Organometallics* **1996**, *15*, 4884–4887.
- (187) Shen, J.; Yap, G. P. A.; Theopold, K. H. Chromium Mediated Reductive Coupling of Isonitrile Forms Unusual Heterocycles. *J. Am. Chem. Soc.* **2014**, *136*, 3382–3384.
- (188) Tsuchimoto, M.; Yoshioka, N.; Ohba, S. Synthesis and Magnetic Properties of a Polymeric Nitridochromium(V) Complex with a Tetradentate Schiff Base Ligand. *Eur. J. Inorg. Chem.* **2001**, *2001*, 1045–1049.
- (189) Song, Y. F.; Berry, J. F.; Weyhermüller, T.; Bill, E. Bond Distances Are Not Always What They Appear to Be: Discovery and Un-Discovery of the Longest Cr(v)≡N Triple Bond. *Dalt. Trans.* **2008**, No. 14, 1864–1871.
- (190) Meyer, K.; Bendix, J.; Bill, E.; Weyhermüller, T.; Wieghardt, K. Molecular and Electronic Structure of Nitridochromium(V) Complexes with Macrocyclic Amine Ligands. *Inorg. Chem.* **1998**, *37*, 5180–5188.



- (191) Lin, K. M.; Wang, P. Y.; Shieh, Y. J.; Chen, H. Z.; Kuo, T. S.; Tsai, Y. C. Reductive N-N Bond Cleavage and Coupling of Organic Azides Mediated by Chromium(I) and Vanadium(I)  $\beta$ -Diketiminates. *New J. Chem.* **2010**, *34*, 1737–1745.
- (192) Beaumier, E. P.; Billow, B. S.; Singh, A. K.; Biros, S. M.; Odom, A. L. A Complex with Nitrogen Single, Double, and Triple Bonds to the Same Chromium Atom: Synthesis, Structure, and Reactivity. *Chem. Sci.* **2016**, *7*, 2532–2536.
- (193) Odom, A. L.; Cummins, C. C.; Protasiewicz, J. D. Nitric Oxide Cleavage: Synthesis of Terminal Chromium(VI) Nitrido Complexes via Nitrosyl Deoxygenation. *J. Am. Chem. Soc.* **1995**, *117*, 6613–6614.
- (194) Odom, A. L.; Cummins, C. C. A Chromium(VI) Nitrido–Silylmethyl Complex and a Chromium(V)  $\mu$ -Nitrido Dimer: Synthetic and Structural Details. *Organometallics* **1996**, *15*, 898–900.
- (195) Billow, B. S.; Bemowski, R. D.; DiFranco, S. A.; Staples, R. J.; Odom, A. L. Synthesis and Structure of Chromium(VI) Nitrido Cyclopentadienyl Complexes. *Organometallics* **2015**, *34*, 4567–4573.
- (196) Bolvin, H.; Autillo, M.; Islam, M. A.; Héron, J.; Guérin, L.; Acher, E.; Tamain, C.; Illy, M.-C.; Moisy, P.; Colineau, E.; et al. Temperature Dependence of  $^1\text{H}$  Paramagnetic Chemical Shifts in Actinide Complexes, beyond Bleaney's Theory. The AnVIO22+ – DPA Complexes (An = Np, Pu) as an Example. *Chem. – A Eur. J.* **2021**.
- (197) Walker, I. M.; Rosenthal, L.; Quereshi, M. S. Fermi Contact and Dipolar Nuclear Magnetic Resonance Shifts in Paramagnetic Ion-Paired Systems. Anionic Lanthanide Complexes. *Inorg. Chem.* **1971**, *10*, 2463–2471.
- (198) Chatt, J.; Leigh, G. J.; Mingos, D. M. P.; Randall, E. W.; Shaw, D. Nuclear Magnetic Resonance in Complexes Exhibiting Second-Order Paramagnetism. *Chem. Commun.* **1968**, No. 7, 419.
- (199) Dunn, T. M. Spin-Orbit Coupling in the First and Second Transition Series. *Trans. Faraday Soc.* **1961**, *57*, 1441.
- (200) Chatt, J.; Leigh, G. J.; Mingos, D. M. P. Configurations of Some Complexes of Rhenium, Ruthenium, Osmium, Rhodium, Iridium, and Platinum Halides with Mono(Tertiary Phosphines) and Mono(Tertiary Arsines). *J. Chem. Soc. A Inorganic, Phys. Theor.* **1969**, No. 1674, 1674.
- (201) Gunz, H. P.; Leigh, G. J. Magnetic Susceptibilities of Some Rhenium(III) and Osmium(IV) Halide Complexes; Preparation of Some New  $d^4$  Complexes. *J. Chem. Soc. A Inorganic, Phys. Theor.* **1971**, No. iii, 2229.
- (202) Palion-Gazda, J.; Gryca, I.; Machura, B.; Lloret, F.; Julve, M. Synthesis, Crystal Structure and Magnetic Properties of the Complex  $[\text{ReCl}_3(\text{Tppz})]\cdot\text{MeCN}$ . *RSC Adv.* **2015**, *5*, 101616–101622.
- (203) Kalofolias, D. A.; Weselski, M.; Siczek, M.; Lis, T.; Tsipis, A. C.; Tangoulis, V.; Milios, C. J. Dinuclear and Mononuclear Rhenium Coordination Compounds upon Employment of a Schiff-Base Triol Ligand: Structural, Magnetic, and Computational Studies. *Inorg. Chem.* **2019**, *58*, 8596–8606.
- (204) Abramov, P. A.; Gritsan, N. P.; Sutura, E. A.; Bogomyakov, A. S.; Sokolov, M. N. Rhenium Complex with Noninnocent Dioxolene Ligand: Combined Experimental and Ab Initio Study of  $[(3,5\text{-Di-Tert-Bu}_2\text{C}_6\text{H}_2\text{O}_2)\text{ReCl}_3(\text{OPPh}_3)]$ . *Inorg. Chem.* **2015**, *54*, 6727–6735.
- (205) Dunbar, K. R.; Schelter, E. J.; Pali, A. V.; Ostrovsky, S. M.; Mirovitskii, V. Y.;

- Hudson, J. M.; Omary, M. A.; Klokishner, S. I.; Tsukerblat, B. S. Unusual Magnetic Behavior of Six-Coordinate, Mixed-Ligand Re(II) Complexes: Origin of a Strong Temperature-Independent Paramagnetism. *J. Phys. Chem. A* **2003**, *107*, 11102–11111.
- (206) Uzelmeier, C. E.; Bartley, S. L.; Fourmigué, M.; Rogers, R.; Grandinetti, G.; Dunbar, K. R. Reaction of Octachlorodirhenate with a Redox-Active Tetrathiafulvalene Phosphine Ligand: Spectroscopic, Magnetic, and Structural Characterization of the Unusual Paramagnetic Salt  $[\text{ReCl}_2(\text{o-P2})_2][\text{Re}_2\text{Cl}_6(\text{o-P2})]$  (O-. *Inorg. Chem.* **1998**, *37*, 6706–6713.
- (207) Lang, P. F.; Smith, B. C. Ionic Radii for Group 1 and Group 2 Halide, Hydride, Fluoride, Oxide, Sulfide, Selenide and Telluride Crystals. *Dalt. Trans.* **2010**, *39*, 7786.
- (208) Graves, C. R.; Yang, P.; Kozimor, S. A.; Vaughn, A. E.; Clark, D. L.; Conradson, S. D.; Schelter, E. J.; Scott, B. L.; Thompson, J. D.; Hay, P. J.; et al. Organometallic Uranium(V)–Imido Halide Complexes: From Synthesis to Electronic Structure and Bonding. *J. Am. Chem. Soc.* **2008**, *130*, 5272–5285.
- (209) Wätjen, F. Rhenium and Osmium PNP Pincer Complexes for Nitrogen Fixation and Nitride Transfer, Georg-August Universität Göttingen, 2019.
- (210) Delony, D. Proton Coupled Electron Transfer at Heavy Metal Sites, 2020.
- (211) Lever, A. B. P. Electrochemical Parametrization of Metal Complex Redox Potentials, Using the Ruthenium(III)/Ruthenium(II) Couple to Generate a Ligand Electrochemical Series. *Inorg. Chem.* **1990**, *29*, 1271–1285.
- (212) Lever, A. B. P. Electrochemical Parametrization of Rhenium Redox Couples. *Inorg. Chem.* **1991**, *30*, 1980–1985.
- (213) Poulton, J. T.; Sigalas, M. P.; Folting, K.; Streib, W. E.; Eisenstein, O.; Caulton, K. G.  $\text{RuHX}(\text{CO})(\text{PR}_3)_2$ : Can  $\nu_{\text{CO}}$  Be a Probe for the Nature of the Ru-X Bond? *Inorg. Chem.* **1994**, *33*, 1476–1485.
- (214) Doherty, N. M.; Hoffmann, N. W. Transition-Metal Fluoro Compounds Containing Carbonyl, Phosphine, Arsine, and Stibine Ligands. *Chem. Rev.* **1991**, *91*, 553–573.
- (215) Fagnou, K.; Lautens, M. Halide Effects in Transition Metal Catalysis. *Angew. Chemie Int. Ed.* **2002**, *41*, 26–47.
- (216) Rottink, M. K.; Angelici, R. J. Ligand and Metal Effects on the Enthalpies of Protonation of  $\text{Cp}^*\text{M}(\text{PR}_3)(\text{PR}'_3)\text{X}$  Complexes (M = Ruthenium or Osmium). *J. Am. Chem. Soc.* **1993**, *115*, 7267–7274.
- (217) Al-Salih, T. I.; Pickett, C. J. Electron-Transfer Reactions in Nitrogen Fixation. Part 1. The Electrosynthesis of Dinitrogen, Hydride, Isocyanide, and Carbonyl Complexes of Molybdenum: Intermediates, Mechanisms, and Energetics. *J. Chem. Soc. Dalt. Trans.* **1985**, *53*, 1255.
- (218) Bemowski, R. D.; Singh, A. K.; Bajorek, B. J.; DePorre, Y.; Odom, A. L. Effective Donor Abilities of E-t-Bu and EPh (E = O, S, Se, Te) to a High Valent Transition Metal. *Dalt. Trans.* **2014**, *43*, 12299.
- (219) DiFranco, S. A.; Maciulis, N. A.; Staples, R. J.; Batrice, R. J.; Odom, A. L. Evaluation of Donor and Steric Properties of Anionic Ligands on High Valent Transition Metals. *Inorg. Chem.* **2012**, *51*, 1187–1200.
- (220) Connelly, N. G.; Geiger, W. E. Chemical Redox Agents for Organometallic Chemistry. *Chem. Rev.* **1996**, *96*, 877–910.
- (221) Smoleński, P.; Pombeiro, A. J. L. Water-Soluble and Stable Dinitrogen Phosphine

- Complexes Trans-[ReCl(N<sub>2</sub>)(PTA-H)<sub>n</sub>(PTA)<sub>4-n</sub>]<sup>N+</sup> (n = 0–4), the First with 1,3,5-Triaza-7-Phosphaadamantane. *Dalt. Trans.* **2008**, No. 1, 87–91.
- (222) Tully, M. E.; Ginsberg, A. P. Trans-Hydriddinitrogenbis[1,2-Bis(Diphenylphosphino)Ethane]Rhenium(I). *J. Am. Chem. Soc.* **1973**, *95*, 2042–2044.
- (223) Chin, R. M.; Barrera, J.; Dubois, R. H.; Helberg, L. E.; Sabat, M.; Bartucz, T. Y.; Lough, A. J.; Morris, R. H.; Harman, W. D. Preparation of Rhenium(I) and Rhenium(II) Amine Dinitrogen Complexes and the Characterization of an Elongated Dihydrogen Species. *Inorg. Chem.* **1997**, *36*, 3553–3558.
- (224) Wang, Y.; Fraústo Da Silva, J. J. R.; Pombeiro, A. J. L.; Pellinghelli, M. A.; Tiripicchio, A. Synthesis of the Pseudohalide-Dinitrogen Complexes Trans-[ReX(N<sub>2</sub>)(Ph<sub>2</sub>PCH<sub>2</sub>CH<sub>2</sub>PPh<sub>2</sub>)<sub>2</sub>](X = NCS, NCO or N<sub>3</sub>) and Crystal Structures of the Isothiocyanate and Azide Complexes. *J. Organomet. Chem.* **1993**, *454*, 211–216.
- (225) Kärkäs, M. D. Electrochemical Strategies for C–H Functionalization and C–N Bond Formation. *Chem. Soc. Rev.* **2018**, *47*, 5786–5865.
- (226) Frontana-Urbe, B. A.; Little, R. D.; Ibanez, J. G.; Palma, A.; Vasquez-Medrano, R. Organic Electrosynthesis: A Promising Green Methodology in Organic Chemistry. *Green Chem.* **2010**, *12*, 2099–2119.
- (227) Wiebe, A.; Gieshoff, T.; Möhle, S.; Rodrigo, E.; Zirbes, M.; Waldvogel, S. R. Electrifying Organic Synthesis. *Angew. Chemie Int. Ed.* **2018**, *57*, 5594–5619.
- (228) Möhle, S.; Zirbes, M.; Rodrigo, E.; Gieshoff, T.; Wiebe, A.; Waldvogel, S. R. Modern Electrochemical Aspects for the Synthesis of Value-Added Organic Products. *Angew. Chemie - Int. Ed.* **2018**, *57*, 6018–6041.
- (229) Pollok, D.; Waldvogel, S. R. Electro-Organic Synthesis – a 21 St Century Technique. *Chem. Sci.* **2020**, *11*, 12386–12400.
- (230) Yuan, Y.; Lei, A. Is Electrosynthesis Always Green and Advantageous Compared to Traditional Methods? *Nat. Commun.* **2020**, *11*, 802.
- (231) van Alten, R. S.; Wätjen, F.; Demeshko, S.; Miller, A. J. M.; Würtele, C.; Siewert, I.; Schneider, S. (Electro-)Chemical Splitting of Dinitrogen with a Rhenium Pincer Complex. *Eur. J. Inorg. Chem.* **2020**, *2020*, 1402–1410.
- (232) Chatt, J.; Dilworth, J. R.; Leigh, G. J. Some Alkylimido-(or Alkylnitrene) Complexes of Rhenium. *J. Chem. Soc. A Inorganic, Phys. Theor.* **1970**, 2239.
- (233) Archer, C. M.; Dilworth, J. R.; Jobanputra, P.; Harman, M. E.; Hursthouse, M. B.; Karaulov, A. The Preparation and Characterization of Some Imido- and Diazenido-Rhenium Complexes of Maltol. The X-Ray Crystal Structure of [Re(Maltol)<sub>2</sub>(NPh)(PPh<sub>3</sub>)] [BPh<sub>4</sub>]. *Polyhedron* **1991**, *10*, 1539–1543.
- (234) Lohrey, T. D.; Cortes, E. A.; Fostvedt, J. I.; Oanta, A. K.; Jain, A.; Bergman, R. G.; Arnold, J. Diverse Reactivity of a Rhenium(V) Oxo Imido Complex: [2 + 2] Cycloadditions, Chalcogen Metathesis, Oxygen Atom Transfer, and Protic and Hydridic 1,2-Additions. *Inorg. Chem.* **2020**, *59*, 11096–11107.
- (235) Couillens, X.; Gressier, M.; Turpin, R.; Dartiguenave, M.; Coulais, Y.; Beauchamp, A. L. Synthesis and Characterisation of Oxo- and Phenylimido-Rhenium(v) Complexes Containing Bidentate Phosphinoenolato Ligands. *J. Chem. Soc. Dalt. Trans.* **2002**, *6*, 914–924.
- (236) Alemayehu, A. B.; Teat, S. J.; Borisov, S. M.; Ghosh, A. Rhenium-Imido Corroles. *Inorg. Chem.* **2020**, *59*, 6382–6389.

- (237) Clark, G. R.; Nielson, A. J.; Rickard, C. E. F. Organoimido Complexes of Tungsten and Rhenium: Oxo-Imido and Bis-Imido Complexes of Tungsten(VI), and Phenylimido Complexes of Rhenium(VI) and (V). The X-Ray Crystal Structures of [W(NCMe<sub>3</sub>)(NPh)Cl<sub>2</sub>(Bipy)] and [Re(NPh)Cl<sub>3</sub>(N). *Polyhedron* **1988**, *7*, 117–128.
- (238) Bender, M. L.; Jones, J. M. Nucleophilic Reactions of Morpholine with the Benzoyl Halides. The Presence of an Element Effect 1. *J. Org. Chem.* **1962**, *27*, 3771–3774.
- (239) Piero Zanello, Fabrizia Fabrizi de Biani, C. N. Voltammetric Techniques. In *Inorganic Electrochemistry*; Royal Society of Chemistry: Cambridge, 2007; pp 49–136.
- (240) Alten, R. S. van. Electrochemical N<sub>2</sub>-Splitting and Functionalisation in the Coordination Sphere of Rhenium. **2016**.
- (241) Munisamy, T.; Schrock, R. R. An Electrochemical Investigation of Intermediates and Processes Involved in the Catalyticreduction of Dinitrogen by [HIPTN<sub>3</sub>N]Mo (HIPTN<sub>3</sub>N = (3,5-(2,4,6-*i*-Pr<sub>3</sub>C<sub>6</sub>H<sub>2</sub>)<sub>2</sub>C<sub>6</sub>H<sub>3</sub>N). *Dalt. Trans.* **2012**, *41*, 130–137.
- (242) Kupfer, T.; Schrock, R. R. Alkylation of Dinitrogen in [(HIPTNCH<sub>2</sub>CH<sub>2</sub>)<sub>3</sub>N]Mo Complexes (HIPT = 3,5-(2,4,6-*i*-Pr<sub>3</sub>C<sub>6</sub>H<sub>2</sub>)<sub>2</sub>CH<sub>3</sub>). *J. Am. Chem. Soc.* **2009**, *131*, 12829–12837.
- (243) Bennett, B. K.; Crevier, T. J.; Dumez, D. D.; Matano, Y.; McNeil, W. S.; Mayer, J. M. Electrochemical and Reactivity Comparisons among Isoelectronic Oxo, Imido, and Nitrido Complexes of Rhenium and Osmium. *J. Organomet. Chem.* **1999**, *591*, 96–103.
- (244) Bendix, J.; Meyer, K.; Weyhermüller, T.; Bill, E.; Metzler-Nolte, N.; Wieghardt, K. Nitridocyanometalates of Cr V , Mn V , and Mn VI †. *Inorg. Chem.* **1998**, *37*, 1767–1775.
- (245) Mujika, J. I.; Matxain, J. M.; Eriksson, L. A.; Lopez, X. Resonance Structures of the Amide Bond: The Advantages of Planarity. *Chem. - A Eur. J.* **2006**, *12*, 7215–7224.
- (246) Masood, M. A.; Sullivan, B. P.; Hodgson, D. J. Synthesis and Electrochemical and Structural Chemistry of Rhenium in High Oxidation States with Sterically Hindered Polypyridine Ligands. *Inorg. Chem.* **1999**, *38*, 5425–5430.
- (247) Jiang, Y.; Blacque, O.; Fox, T.; Freeh, C. M.; Berke, H. Facile Synthetic Access to Rhenium(II) Complexes: Activation of Carbonbromine Bonds by Single-Electron Transfer. *Chem. - A Eur. J.* **2010**, *16*, 2240–2249.
- (248) DeLearie, L. A.; Haltiwanger, R. C.; Pierpont, C. G. Synthesis, Structures, and Properties of the Tris(Catecholato)Rhenium(VI) Complexes Re(O<sub>2</sub>C<sub>6</sub>H<sub>2</sub>(*t*-Bu)<sub>2</sub>)<sub>3</sub> and Re(O<sub>2</sub>C<sub>6</sub>Cl<sub>4</sub>)<sub>3</sub>. *Inorg. Chem.* **1987**, *26*, 817–821.
- (249) Banerjee, S.; Kumar Dirghangi, B.; Menon, M.; Pramanik, A.; Chakravorty, A. Pyridine-2-Carboxamide Complexes of Arylimidorhenium(VI) Derived from 2-Pyridylmethyleamine Complexes of Arylimidorhenium(V) via Oxygen-Atom Transfer. *J. Chem. Soc. Dalt. Trans.* **1997**, *2153*, 2149–2154.
- (250) Abbenseth, J.; Wätjen, F.; Finger, M.; Schneider, S. The Metaphosphite (PO<sub>2</sub><sup>-</sup>) Anion as a Ligand. *Angew. Chemie - Int. Ed.* **2020**, *59*, 23574–23578.
- (251) Wang, R.; Brugh, A. M.; Rawson, J.; Therien, M. J.; Forbes, M. D. E. Alkyne-Bridged Multi[Copper(II) Porphyrin] Structures: Nuances of Orbital Symmetry in Long-Range, Through-Bond Mediated, Isotropic Spin Exchange Interactions. *J. Am. Chem. Soc.* **2017**, *139*, 9759–9762.
- (252) Hickey, D. P.; Sandford, C.; Rhodes, Z.; Gensch, T.; Fries, L. R.; Sigman, M. S.; Minter, S. D. Investigating the Role of Ligand Electronics on Stabilizing Electrocatalytically Relevant Low-Valent Co(I) Intermediates. *J. Am. Chem. Soc.* **2019**,

- 141, 1382–1392.
- (253) Blake, C. C. F.; Small, R. W. H. The Crystal Structure of Benzamide. *Acta Crystallogr. Sect. B Struct. Crystallogr. Cryst. Chem.* **1972**, *28*, 2201–2206.
- (254) Zhang, L.; Wang, S.; Zhou, S.; Yang, G.; Sheng, E. Cannizzaro-Type Disproportionation of Aromatic Aldehydes to Amides and Alcohols by Using Either a Stoichiometric Amount or a Catalytic Amount of Lanthanide Compounds. *J. Org. Chem.* **2006**, *71*, 3149–3153.
- (255) Martínez de Salinas, S.; Sanjosé-Orduna, J.; Odena, C.; Barranco, S.; Benet-Buchholz, J.; Pérez-Temprano, M. H. Weakly Coordinated Cobaltacycles: Trapping Catalytically Competent Intermediates in Cp\*Co<sup>III</sup> Catalysis. *Angew. Chemie Int. Ed.* **2020**, *59*, 6239–6243.
- (256) Frutos-Pedreño, R.; González-Herrero, P.; Vicente, J.; Jones, P. G. Reactivity of Ortho-Palladated Benzamides toward CO, Isocyanides, and Alkynes. Synthesis of Functionalized Isoindolin-1-Ones and 4,5-Disubstituted Benzo[ c ]Azepine-1,3-Diones. *Organometallics* **2013**, *32*, 4664–4676.
- (257) Jones, W. D.; Maguire, J. A. The Activation of Methane by Rhenium. Catalytic Hydrogen/Deuterium Exchange in Alkanes with CpRe(PPh<sub>3</sub>)<sub>2</sub>H<sub>2</sub>. *Organometallics* **1986**, *5*, 590–591.
- (258) Klahn-Oliva, A. H.; Singer, R. D.; Sutton, D. Rhenium Dinitrogen Complex ( $\eta$ -C<sub>5</sub>Me<sub>5</sub>)Re(CO)(PMe<sub>3</sub>)(N<sub>2</sub>). Facile Photochemical Generation of a Rhenium Intermediate and Oxidative Addition of Hydrocarbon C-H Bonds. *J. Am. Chem. Soc.* **1986**, *108*, 3107–3108.
- (259) Jones, W. D.; Rosini, G. P.; Maguire, J. A. Photochemical C–H Activation and Ligand Exchange Reactions of CpRe(PPh<sub>3</sub>)<sub>2</sub>H<sub>2</sub>. Phosphine Dissociation Is Not Involved. *Organometallics* **1999**, *18*, 1754–1760.
- (260) Kaljurand, I.; Kütt, A.; Sooväli, L.; Rodima, T.; Mäemets, V.; Leito, I.; Koppel, I. A. Extension of the Self-Consistent Spectrophotometric Basicity Scale in Acetonitrile to a Full Span of 28 PKa Units: Unification of Different Basicity Scales. *J. Org. Chem.* **2005**, *70*, 1019–1028.
- (261) Hevia, E.; Pérez, J.; Riera, V.; Miguel, D. Reactivity of the Amido Complex [Re(NHpTol)(CO)<sub>3</sub>(Bipy)] toward Neutral Organic Electrophiles. *Organometallics* **2003**, *22*, 257–263.
- (262) Tshepelevitsh, S.; Kütt, A.; Lõkov, M.; Kaljurand, I.; Saame, J.; Heering, A.; Plieger, P. G.; Vianello, R.; Leito, I. On the Basicity of Organic Bases in Different Media. *European J. Org. Chem.* **2019**, *2019*, 6735–6748.
- (263) Theodorou, V.; Paraskevopoulos, G.; Skobridis, K. A Mild Alkaline Hydrolysis of N- and N,N-Substituted Amides and Nitriles. *Arkivoc* **2015**, *2015*, 101–112.
- (264) Creary, X.; Sky, A. F. Reaction of Arylbromodiazirines with Azide Ion. Evidence for N-Azidodiazirine Intermediates. *J. Am. Chem. Soc.* **1990**, *112*, 368–374.
- (265) Davidson, D.; Skovronek, H. The Acylation of Amides. *J. Am. Chem. Soc.* **1958**, *80*, 376–379.
- (266) Spránitz, P.; Sóregi, P.; Botlik, B.; Berta, M.; Soós, T. Organocatalytic Desymmetrisation of Fittig's Lactones: Deuterium as a Reporter Tag for Hidden Racemisation. *Synthesis (Stuttg.)* **2019**, *51*, 1263–1272.
- (267) Bezdek, M. J.; Guo, S.; Chirik, P. J. Coordination-Induced Weakening of Ammonia,

- Water, and Hydrazine X–H Bonds in a Molybdenum Complex. *Science (80-. )*. **2016**, *354*, 730–733.
- (268) Nishibayashi, Y.; Meng, F.; Kuriyama, S.; Tanaka, H.; Egi, A.; Yoshizawa, K. Ammonia Formation Catalyzed by Dinitrogen-Bridged Dirhenium Complex Bearing PNP-Pincer Ligands under Mild Reaction Conditions. *Angew. Chemie* **2021**, ange.202102175.
- (269) Weber, J. E.; Hasanayn, F.; Fataftah, M.; Mercado, B. Q.; Crabtree, R. H.; Holland, P. L. Electronic and Spin-State Effects on Dinitrogen Splitting to Nitrides in a Rhenium Pincer System. *Inorg. Chem.* **2021**, acs.inorgchem.0c03778.
- (270) Atanasov, M.; Aravena, D.; Suturina, E.; Bill, E.; Maganas, D.; Neese, F. First Principles Approach to the Electronic Structure, Magnetic Anisotropy and Spin Relaxation in Mononuclear 3d-Transition Metal Single Molecule Magnets. *Coord. Chem. Rev.* **2015**, 289–290, 177–214.
- (271) Roessler, M. M.; Salvadori, E. Principles and Applications of EPR Spectroscopy in the Chemical Sciences. *Chem. Soc. Rev.* **2018**, 47, 2534–2553.
- (272) Helberg, L. E.; Orth, S. D.; Sabat, M.; Harman, W. D. Coordination Chemistry of Low-Valent Rhenium Polypyridyl Complexes: Synthesis, Reactivity, and Electrochemistry †. *Inorg. Chem.* **1996**, 35, 5584–5594.
- (273) Pavlishchuk, V. V.; Addison, A. W. Conversion Constants for Redox Potentials Measured versus Different Reference Electrodes in Acetonitrile Solutions at 25°C. *Inorganica Chim. Acta* **2000**, 298, 97–102.
- (274) Flisak, Z.; Sun, W. H. Progression of Diiminopyridines: From Single Application to Catalytic Versatility. *ACS Catal.* **2015**, 5, 4713–4724.
- (275) Gibson, V. C.; Redshaw, C.; Solan, G. A. Bis(Imino)Pyridines: Surprisingly Reactive Ligands and a Gateway to New Families of Catalysts. *Chem. Rev.* **2007**, 107, 1745–1776.
- (276) Bianchini, C.; Giambastiani, G.; Luconi, L.; Meli, A. Olefin Oligomerization, Homopolymerization and Copolymerization by Late Transition Metals Supported by (Imino)Pyridine Ligands. *Coord. Chem. Rev.* **2010**, 254, 431–455.
- (277) Sieh, D.; Schlimm, M.; Andernach, L.; Angersbach, F.; Nüchel, S.; Schöffel, J.; Šušnjar, N.; Burger, P. Metal-Ligand Electron Transfer in 4d and 5d Group 9 Transition Metal Complexes with Pyridine, Diimine Ligands. *Eur. J. Inorg. Chem.* **2012**, No. 3, 444–462.
- (278) Constable, E. C. 2,2':6',2''-Terpyridines: From Chemical Obscurity to Common Supramolecular Motifs. *Chem. Soc. Rev.* **2007**, 36, 246–253.
- (279) Elgrishi, N.; Chambers, M. B.; Wang, X.; Fontecave, M. Molecular Polypyridine-Based Metal Complexes as Catalysts for the Reduction of CO<sub>2</sub>. *Chem. Soc. Rev.* **2017**, 46, 761–796.
- (280) Winter, A.; Newkome, G. R.; Schubert, U. S. Catalytic Applications of Terpyridines and Their Transition Metal Complexes. *ChemCatChem* **2011**, 3, 1384–1406.
- (281) Wei, C.; He, Y.; Shi, X.; Song, Z. Terpyridine-Metal Complexes: Applications in Catalysis and Supramolecular Chemistry. *Coord. Chem. Rev.* **2019**, 385, 1–19.
- (282) Dickenson, J. C.; Haley, M. E.; Hyde, J. T.; Reid, Z. M.; Tarring, T. J.; Iovan, D. A.; Harrison, D. P. Fine-Tuning Metal and Ligand-Centered Redox Potentials of Homoleptic Bis-Terpyridine Complexes with 4'-Aryl Substituents. *Inorg. Chem.* **2021**, 60, 9956–9969.

- (283) Bezdek, M. J.; Chirik, P. J. Interconversion of Molybdenum Imido and Amido Complexes by Proton-Coupled Electron Transfer. *Angew. Chemie* **2018**, *130*, 2246–2250.
- (284) Singh, D.; Buratto, W. R.; Torres, J. F.; Murray, L. J. Activation of Dinitrogen by Polynuclear Metal Complexes. *Chem. Rev.* **2020**, *120*, 5517–5581.
- (285) Margulieux, G. W.; Turner, Z. R.; Chirik, P. J. Synthesis and Ligand Modification Chemistry of a Molybdenum Dinitrogen Complex: Redox and Chemical Activity of a Bis(Imino)Pyridine Ligand. *Angew. Chemie* **2014**, *126*, 14435–14439.
- (286) Rafiq, S.; Bezdek, M. J.; Chirik, P. J.; Scholes, G. D. Dinitrogen Coupling to a Terpyridine-Molybdenum Chromophore Is Switched on by Fermi Resonance. *Chem* **2019**, *5*, 402–416.
- (287) Sherbow, T. J.; Thompson, E. J.; Arnold, A.; Sayler, R. I.; Britt, R. D.; Berben, L. A. Electrochemical Reduction of N<sub>2</sub> to NH<sub>3</sub> at Low Potential by a Molecular Aluminum Complex. *Chem. – A Eur. J.* **2019**, *25*, 454–458.
- (288) Wolford, N. J.; Radovic, A.; Neidig, M. L. C -Term Magnetic Circular Dichroism (MCD) Spectroscopy in Paramagnetic Transition Metal and f-Element Organometallic Chemistry. *Dalt. Trans.* **2021**, *50*, 416–428.
- (289) Neese, F.; Solomon, E. I. MCD C -Term Signs, Saturation Behavior, and Determination of Band Polarizations in Randomly Oriented Systems with Spin  $S \geq 1/2$ . Applications to  $S = 1/2$  and  $S = 5/2$ . *Inorg. Chem.* **1999**, *38*, 1847–1865.
- (290) Dubicki, L.; Ferguson, J.; Krausz, E. R.; Lay, P. A.; Maeder, M.; Magnuson, R. H.; Taube, H. Absorption and MCD Spectral Studies of the Decaammine(μ-Dinitrogen-N,N')Diosmium(5+) Mixed-Valence Ion. *J. Am. Chem. Soc.* **1985**, *107*, 2167–2171.
- (291) Rouschias, G.; Wilkinson, G. The Preparation and Reactions of Trihaolgeno(Alkanonitrile)Bis(Triphenylphosphine)Rhenium(III) Complexes. *J. Chem. Soc. A Inorganic, Phys. Theor.* **1967**, No. iii, 993.
- (292) Parshall, G. W.; Shive, L. W.; Cotton, F. A. Phosphine Complexes of Rhenium; 1977; Vol. XVII, pp 110–112.
- (293) Lalancette, J.-M.; Rollin, G.; Dumas, P. Metals Intercalated in Graphite. I. Reduction and Oxidation. *Can. J. Chem.* **1972**, *50*, 3058–3062.
- (294) Manner, V. W.; Markle, T. F.; Freudenthal, J. H.; Roth, J. P.; Mayer, J. M. The First Crystal Structure of a Monomeric Phenoxyl Radical: 2,4,6-Tri-Tert-Butylphenoxyl Radical. *Chem. Commun.* **2008**, *246*, 256–258.
- (295) APEX2 V2014.9-0 (SAINT/SADABS/SHELXT/SHELXL), Bruker AXS Inc., Madison, WI, USA, 2014.
- (296) Sheldrick, G. M. Crystal Structure Refinement with SHELXL. *Acta Crystallogr. Sect. C Struct. Chem.* **2015**, *71*, 3–8.
- (297) Sheldrick, G. M. SHELXT – Integrated Space-Group and Crystal-Structure Determination. *Acta Crystallogr. Sect. A Found. Adv.* **2015**, *71*, 3–8.
- (298) Sheldrick, G. M. A Short History of SHELX. *Acta Crystallogr. Sect. A Found. Crystallogr.* **2008**, *64*, 112–122.
- (299) Elgrishi, N.; Rountree, K. J.; McCarthy, B. D.; Rountree, E. S.; Eisenhart, T. T.; Dempsey, J. L. A Practical Beginner's Guide to Cyclic Voltammetry. *J. Chem. Educ.* **2018**, *95*, 197–206.

- (300) Sur, S. K. Measurement of Magnetic Susceptibility and Magnetic Moment of Paramagnetic Molecules in Solution by High-Field Fourier Transform NMR Spectroscopy. *J. Magn. Reson.* **1989**, *82*, 169–173.
- (301) Kahn, O. *Molecular Magnetism*. VCH Publ. Inc., New York, **1993**.
- (302) Hickey, D. P.; Sandford, C.; Rhodes, Z.; Gensch, T.; Fries, L. R.; Sigman, M. S.; Minter, S. D. SI Investigating the Role of Ligand Electronics on Stabilizing Electrocatalytically Relevant Low-Valent Co(I) Intermediates. *J. Am. Chem. Soc.* **2019**, *141*, 1382–1392.
- (303) Sandford, C.; Edwards, M. A.; Klunder, K. J.; Hickey, D. P.; Li, M.; Barman, K.; Sigman, M. S.; White, H. S.; Minter, S. D. A Synthetic Chemist's Guide to Electroanalytical Tools for Studying Reaction Mechanisms. *Chem. Sci.* **2019**, *10*, 6404–6422.
- (304) Spek, A. L. PLATON SQUEEZE: A Tool for the Calculation of the Disordered Solvent Contribution to the Calculated Structure Factors. *Acta Crystallogr. Sect. C Struct. Chem.* **2015**, *71*, 9–18.
- (305) *Single Point Energies of the Respective Fully Optimized Structures.*
- (306) *BS(3,3) Broken Symmetry Approach with Two Coupling  $S = 3/2$  Spin Centers (3 Spin up and 3 Spin down Electrons). For 6, 7 and 5CO, BS(2,2) Configurations Were Evaluated, Too, but without Convergence in All Cases.*



## 6 Appendix

### 6.1 Spectroscopic results

#### 6.1.1 $[\text{CrCl}_2(\text{}^t\text{BuPNP})]$ (**1**)

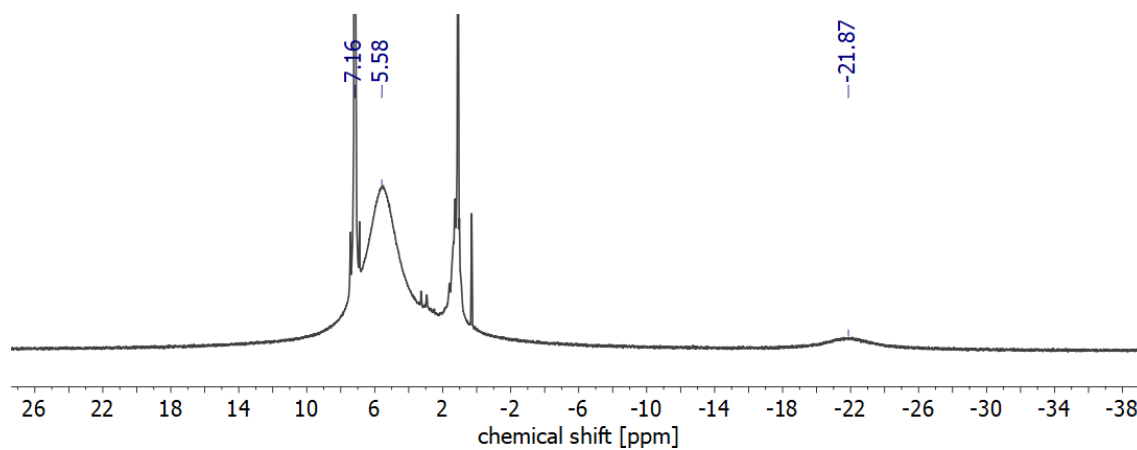


Figure 6.1  $^1\text{H}$  NMR spectrum of **1** ( $\text{C}_6\text{D}_6$ , RT).

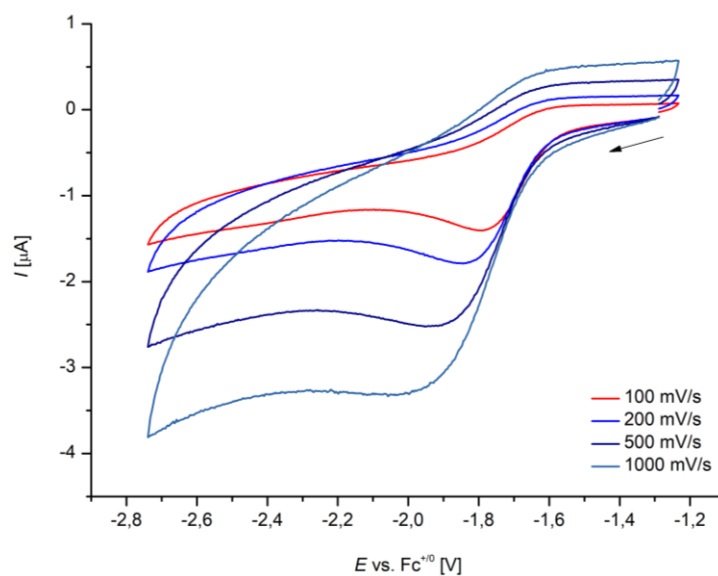


Figure 6.2 Cyclic voltammetry of  $[\text{CrCl}_2(\text{}^t\text{BuPNP})]$  **1** (1.0 mM; electrolyte: 0.1 M  $\text{N}^t\text{Bu}_4\text{PF}_6$  in THF), referenced to ferrocene.

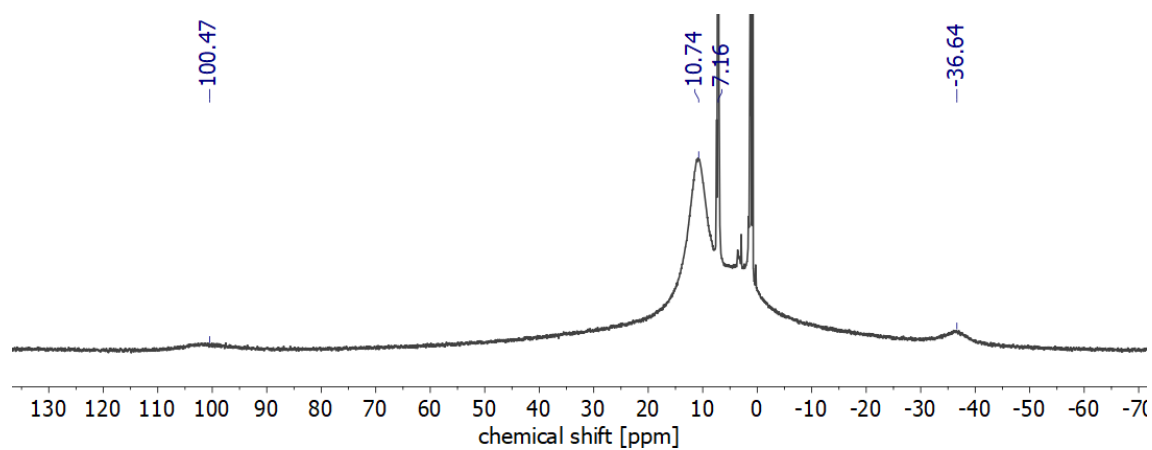
6.1.2 [CrCl(<sup>t</sup>BuPNP)] (2)

Figure 6.3 <sup>1</sup>H NMR spectrum of **2** (C<sub>6</sub>D<sub>6</sub>, RT).

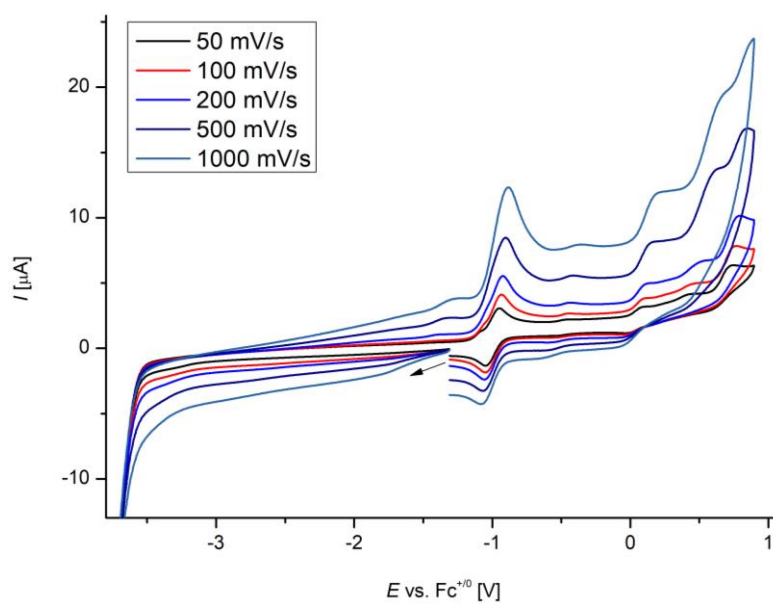


Figure 6.4 Cyclic voltammetry of **2** (1.0 mM; electrolyte: 0.1 M N<sup>n</sup>Bu<sub>4</sub>PF<sub>6</sub> in THF), referenced to ferrocene.

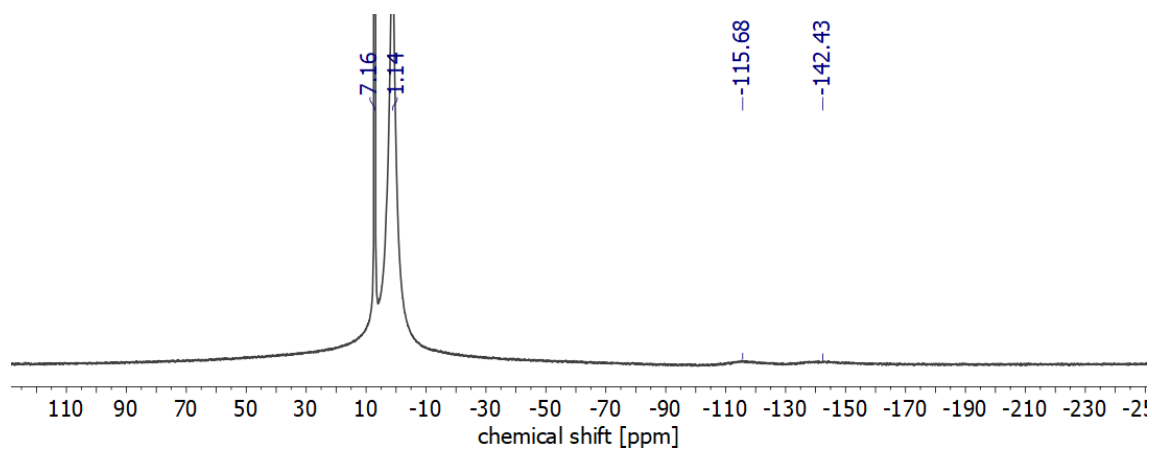
6.1.3  $[\text{CrCl}_2(\text{}^t\text{BuPNP})]$  (**1''**)

Figure 6.5  $^1\text{H}$  NMR spectrum of **1''** ( $\text{C}_6\text{D}_6$ , RT).

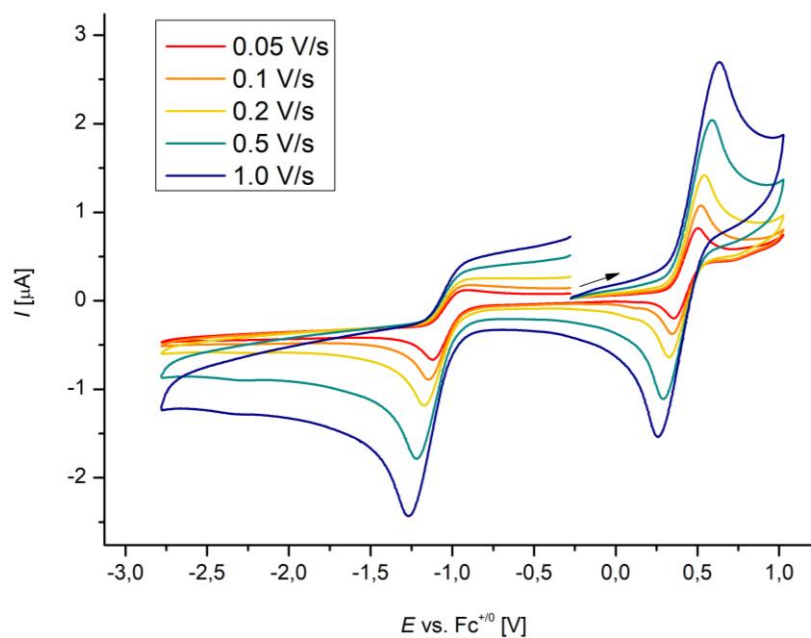
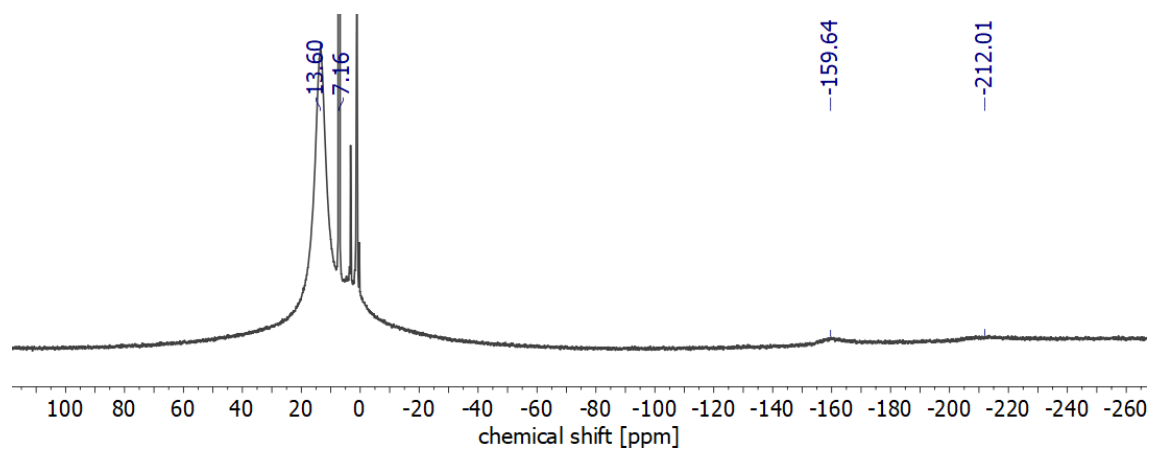
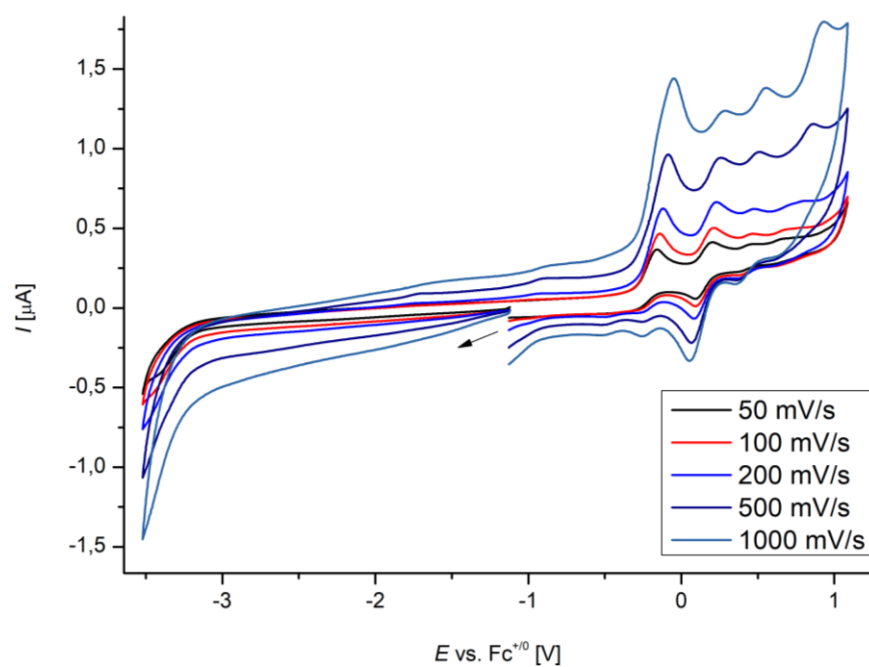
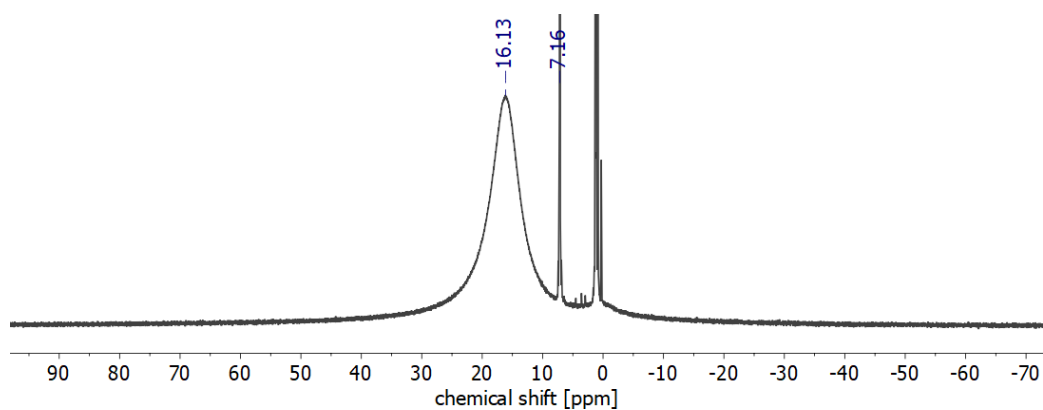
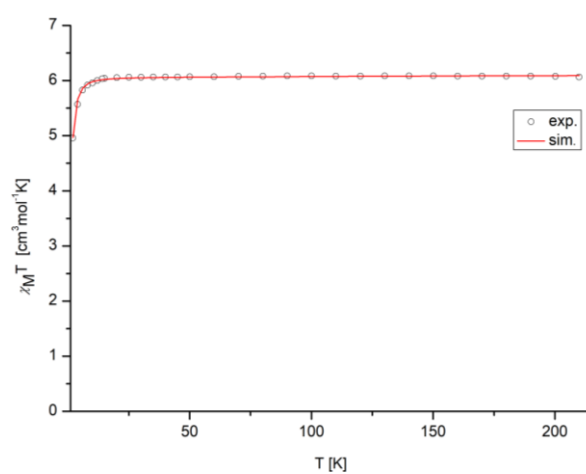


Figure 6.6 Cyclic voltammetry of **2''** (1.0 mM; electrolyte: 0.1 M  $\text{N}^t\text{Bu}_4\text{PF}_6$  in THF), referenced to ferrocene.

6.1.4  $[\text{CrCl}(\text{t}^{\text{Bu}}\text{PNP})]$  (**2''**)Figure 6.7  $^1\text{H}$  NMR spectrum of **2''** ( $\text{C}_6\text{D}_6$ , RT).Figure 6.8 Cyclic voltammetry of **2''** (1.0 mM; electrolyte: 0.1 M  $\text{NBu}_4\text{PF}_6$  in THF), referenced to ferrocene.

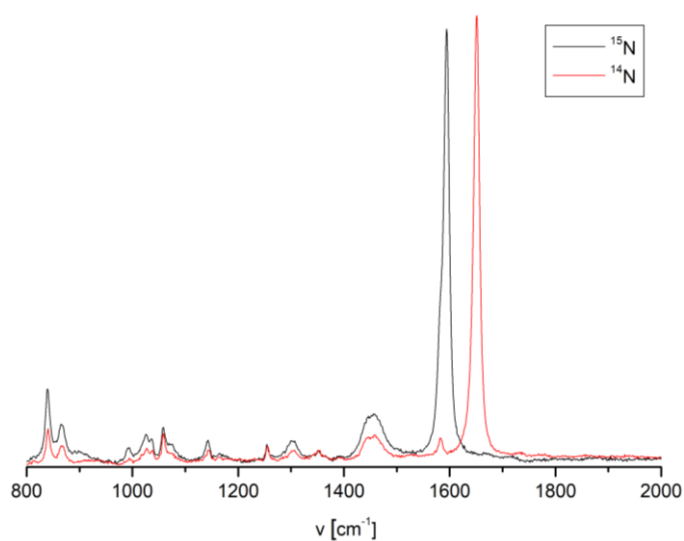
6.1.5  $[(\mu\text{-N}_2)\{\text{Cr}(\text{BuPNP}^{\text{H}})\}_2]$  (**3**)

**Figure 6.9**  $^1\text{H}$  NMR spectrum of **3** ( $\text{C}_6\text{D}_6$ , RT).

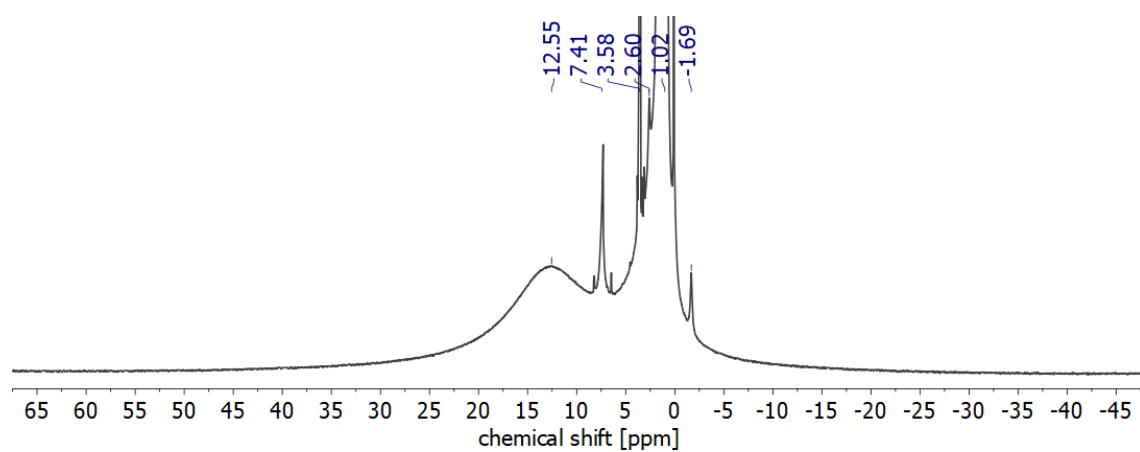
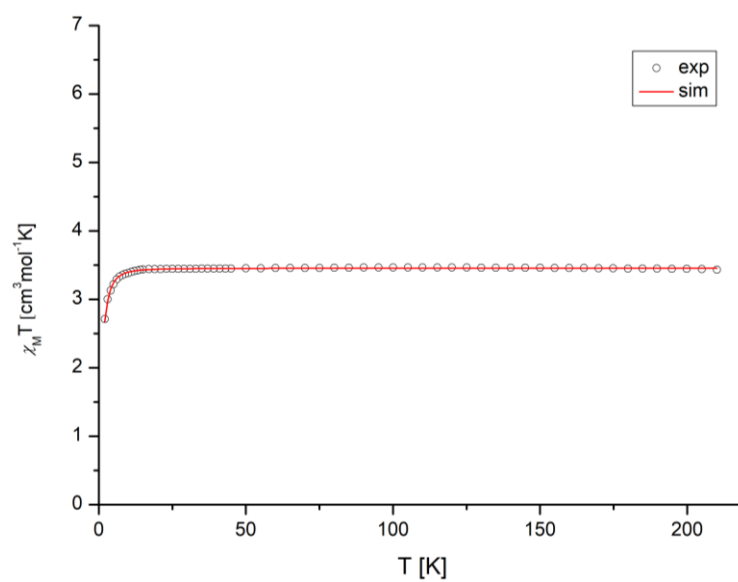


$$\hat{H} = -2J(\hat{S}_1\hat{S}_2 + \hat{S}_2\hat{S}_3) + g\mu_B\vec{B} \sum_{i=1,2,3} \vec{S}_i + D \sum_{i=1,3} \left[ \hat{S}_{z,i}^2 - \frac{1}{3} S(S+1) \right]$$

**Figure 6.10** Temperature dependence of the experimental  $\chi_T$ -product (circles) of complex **3**. (fit parameters:  $S_{\text{total}} = 3$ ;  $g_1 = g_3 = 2.007$ ,  $g_2 = 2.000$ ;  $D_1 = D_3 = 1.511 \text{ cm}^{-1}$ ,  $D_2 = 0 \text{ cm}^{-1}$ ) including spin Hamiltonian.



**Figure 6.11**  $\text{rRaman}$  spectrum ( $\lambda = 633 \text{ nm}$ ) of **3** in pentane solution at room temperature (red line:  $^{14}\text{N}$ ; black line:  $^{15}\text{N}$ ).

6.1.6  $[\{\text{Cr}(\text{CO})_2(\text{tBuPNP}^{\text{r}})\}(\mu\text{-CO})\{\text{Cr}(\text{tBuPNP}^{\text{r}})\}]$  (4)Figure 6.12  $^1\text{H}$  NMR spectrum of 4 ( $\text{C}_6\text{D}_6$ , RT).

$$\hat{H} = g\mu_B \vec{B} \vec{S} + D \left[ \hat{S}_z^2 - \frac{1}{3} S(S+1) \right]$$

Figure 6.13 Temperature dependence of the experimental  $\chi_T$ -product (circles) of complex 4. (fit parameters:  $S=2$ ;  $g_1 = 2.146$ ;  $D_1 = -1.733 \text{ cm}^{-1}$ ) including spin-Hamiltonian.

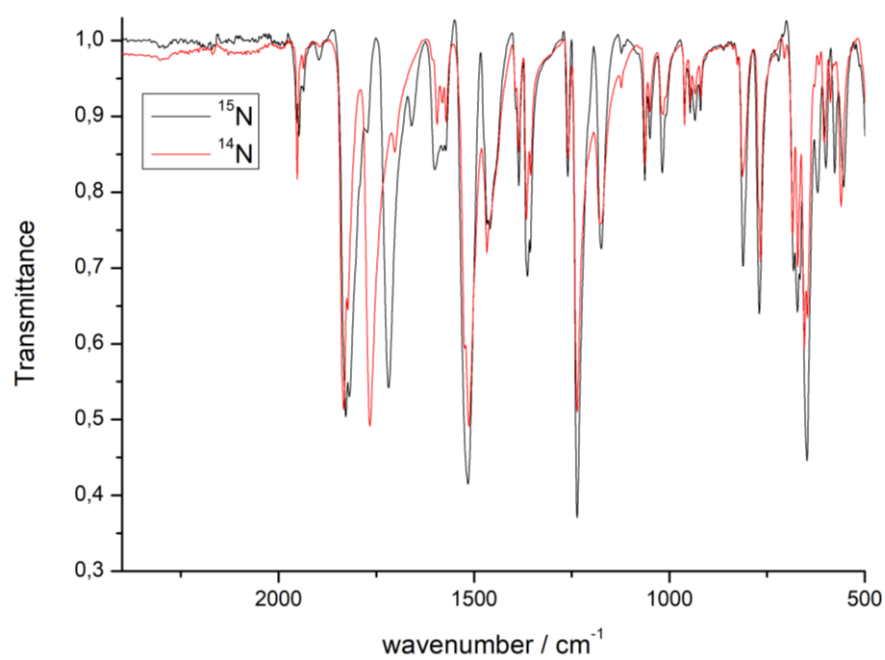
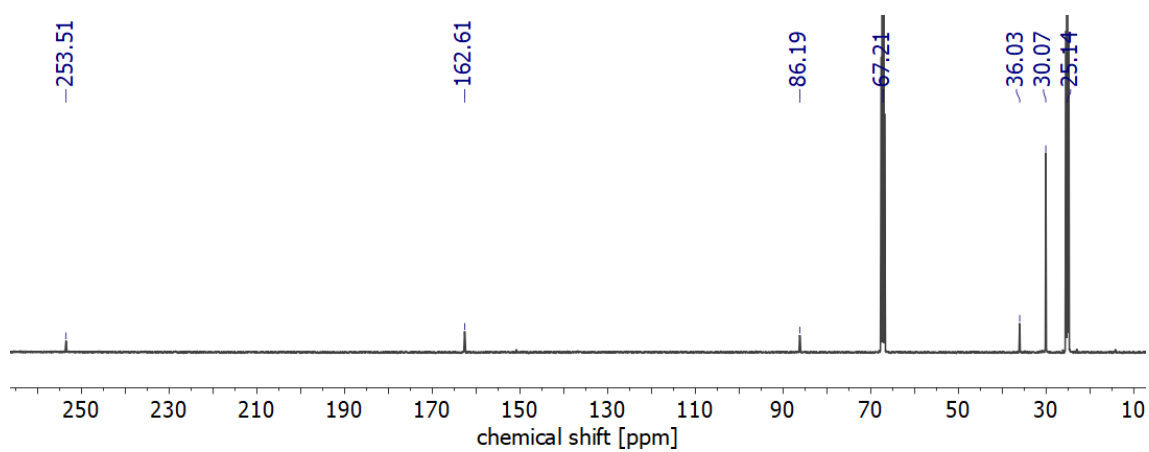
6.1.7  $[\{\text{Cr}(\text{CO})_2(\text{}^t\text{BuPNP''})\}(\mu\text{-N}_2)\{\text{Cr}(\text{}^t\text{BuPNP''})\}]$  (5)

Figure 6.14 IR spectrum (ATR) of 5.

6.1.8  $\text{K}[\text{Cr}(\text{CO})_2(\text{}^t\text{BuPNP''})]$  (6)Figure 6.15 <sup>31</sup>P NMR spectrum of 6 (THF-*d*<sub>8</sub>, RT).

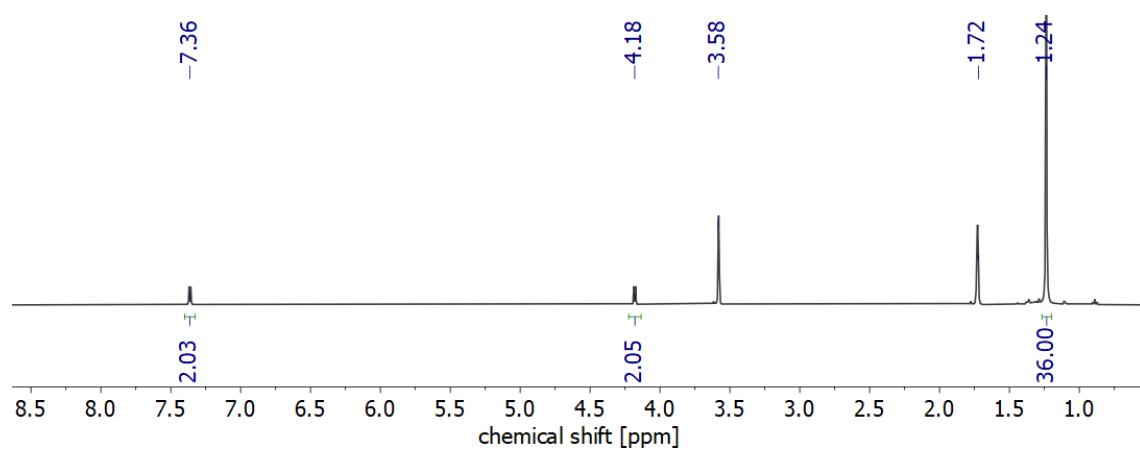


Figure 6.16  $^{13}\text{C}$  NMR spectrum of **6** (THF- $d_8$ , RT).

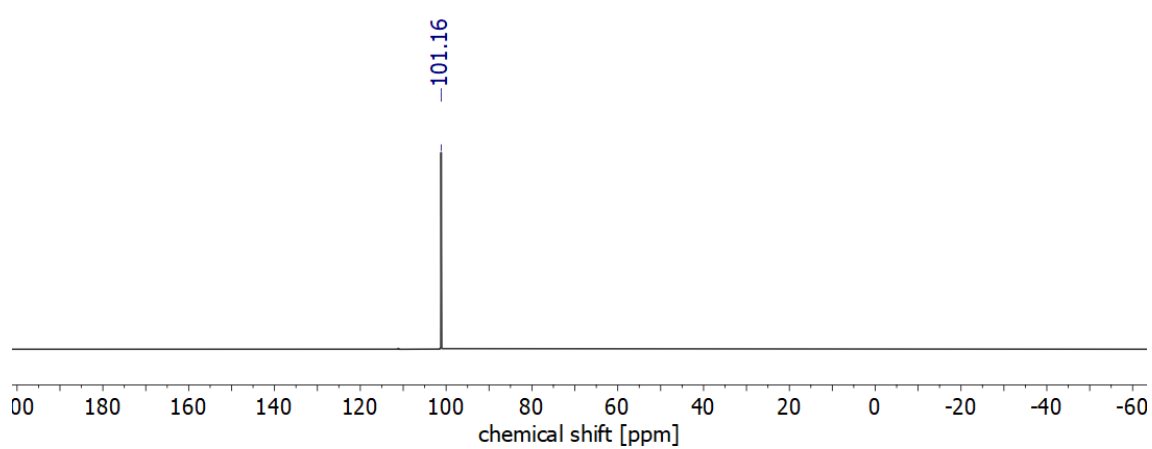


Figure 6.17  $^{31}\text{P}\{^1\text{H}\}$  NMR spectrum of **6** (THF- $d_8$ , RT).

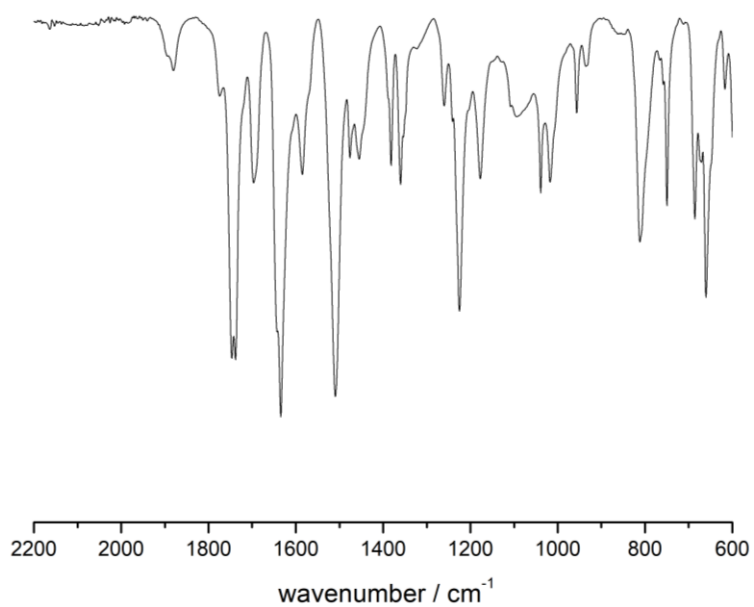


Figure 6.18 IR spectrum (ATR) of **6**.



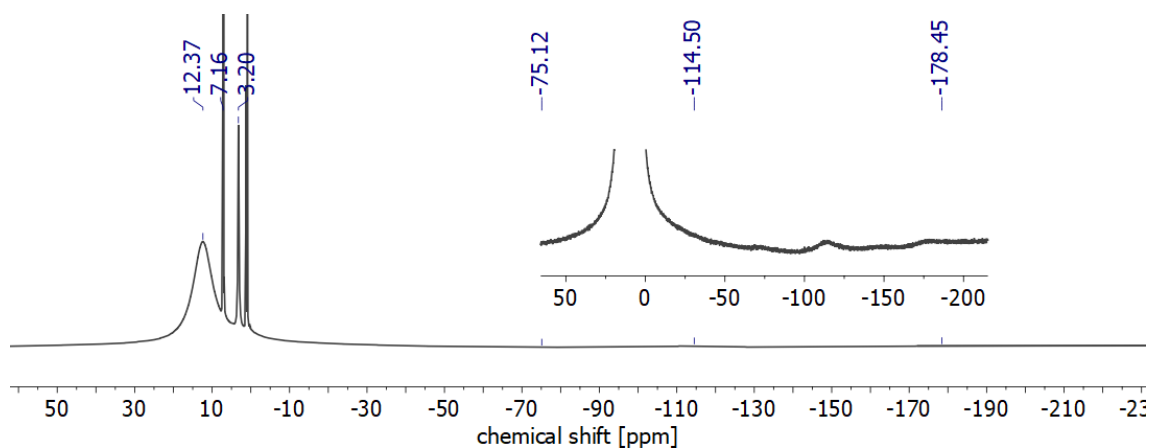
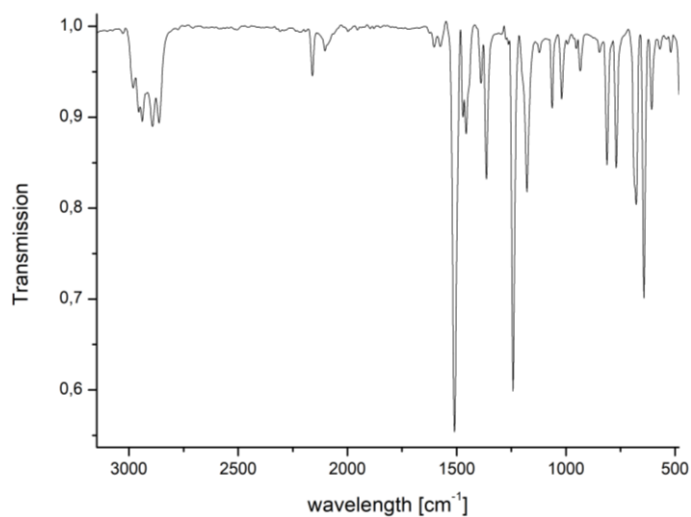
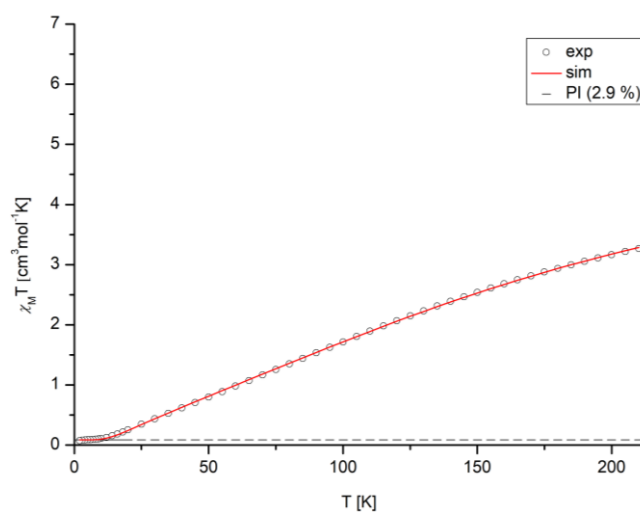
6.1.9  $[\{\text{Cr}(\text{CN})(^t\text{BuPNP}^{\text{H}})\}_2(\mu\text{-CN})\{\text{Cr}(^t\text{BuPNP}^{\text{H}})\}]$  (7)Figure 6.19  $^1\text{H}$  NMR spectrum of 7 ( $\text{C}_6\text{D}_6$ , RT).

Figure 6.20 IR spectrum (ATR) of 7.



$$\hat{H} = -2J\hat{S}_1\hat{S}_2 + g\mu_B\vec{B}(\vec{S}_1 + \vec{S}_2)$$

Figure 6.21 Temperature dependence of the experimental  $\chi_T$ -product (circles) of complex 7 (fit parameters:  $S_1 = 2$ ,  $S_2 = 2$ ;  $g_1 = g_2 = 2.062$ ;  $J = -19.8 \text{ cm}^{-1}$ ; PI = 2.9% ( $S = 2$ )) including spin-Hamiltonian.

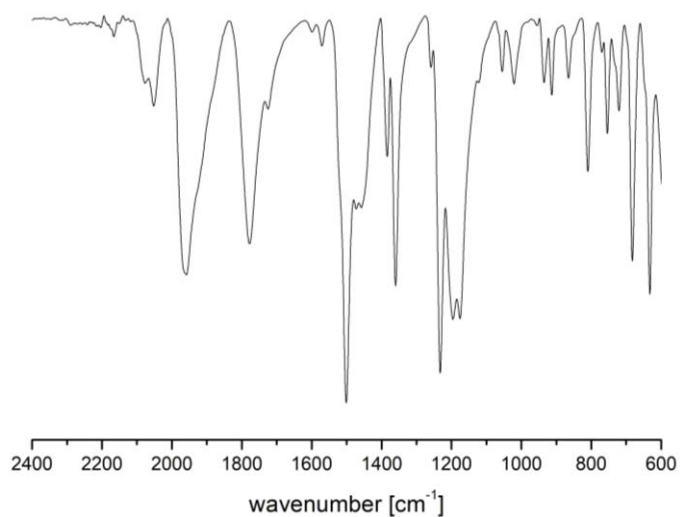
6.1.10  $[\text{Cr}(\text{CN}^t\text{Bu})_4(\chi^2\text{-}^t\text{BuPNP}^{\prime\prime})]$  (8)

Figure 6.22 IR spectrum of 8.

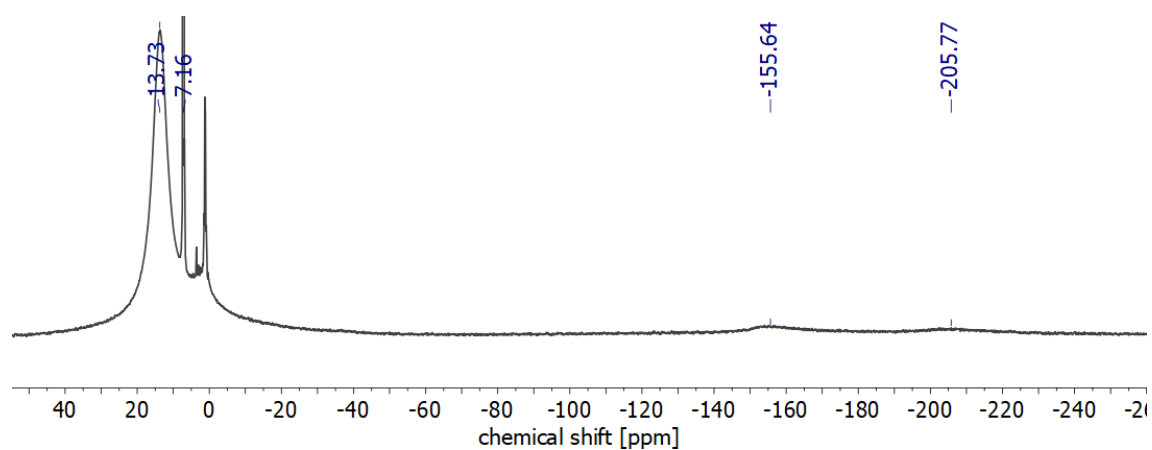
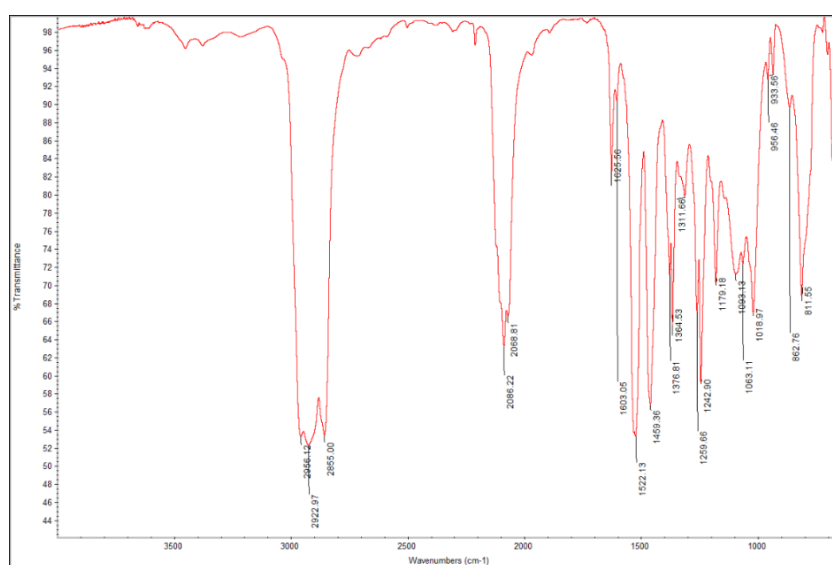
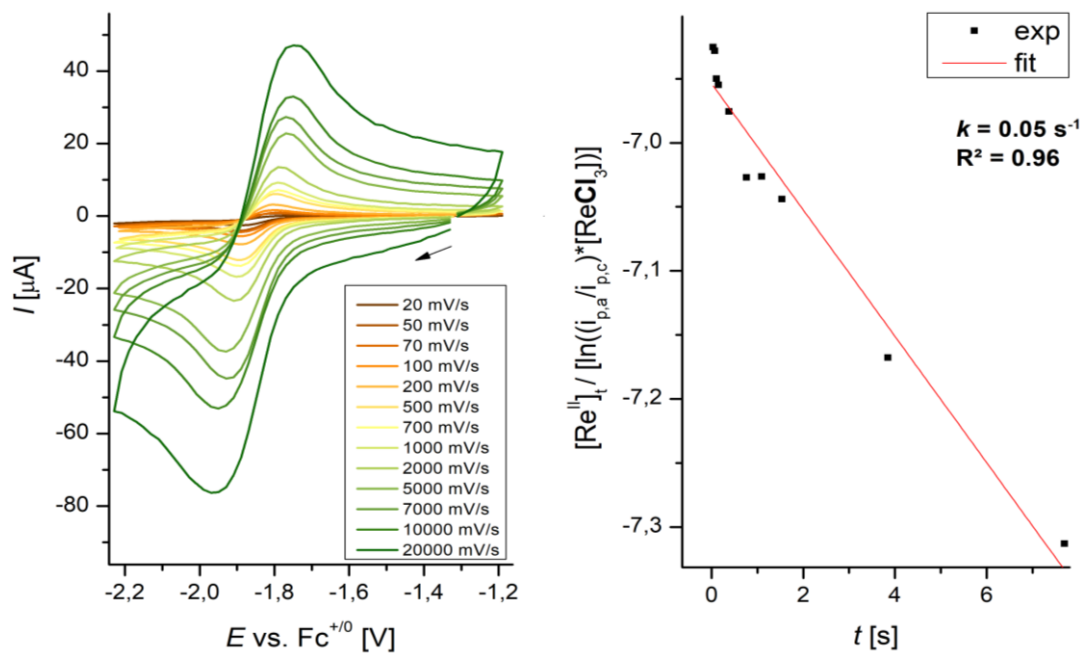
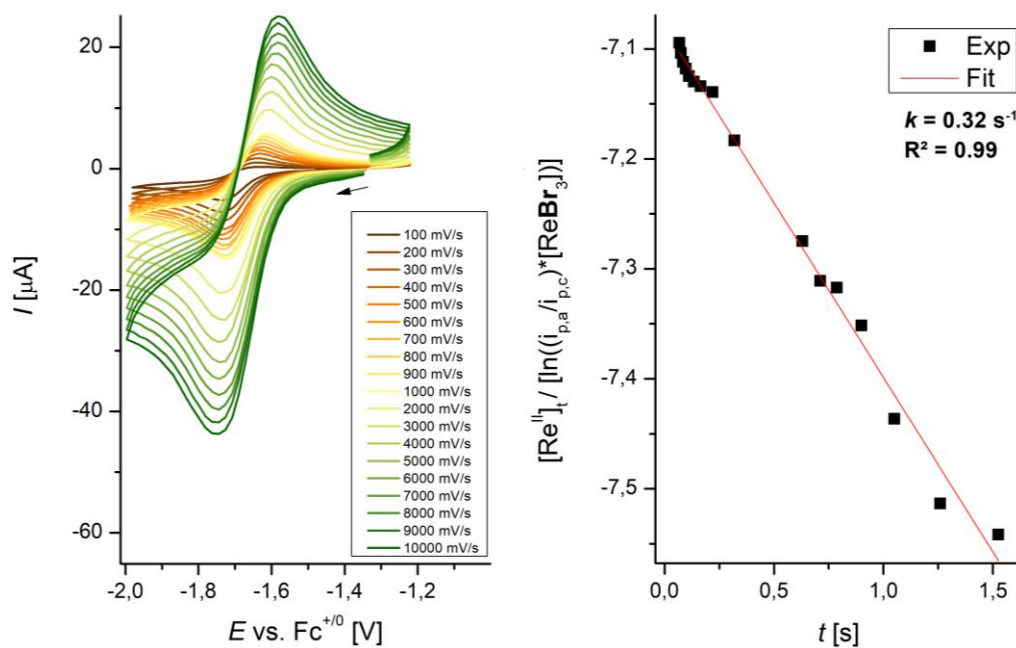
6.1.11  $[\text{CrN}_3(^t\text{BuPNP}^{\prime\prime})]$  (9)Figure 6.23  $^1\text{H}$  NMR spectrum of 9 ( $\text{C}_6\text{D}_6$ , RT).

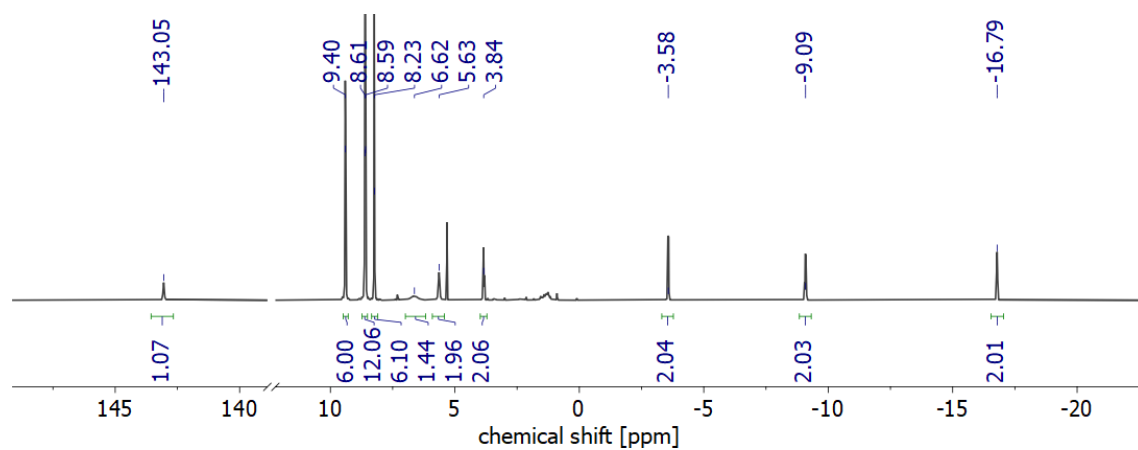
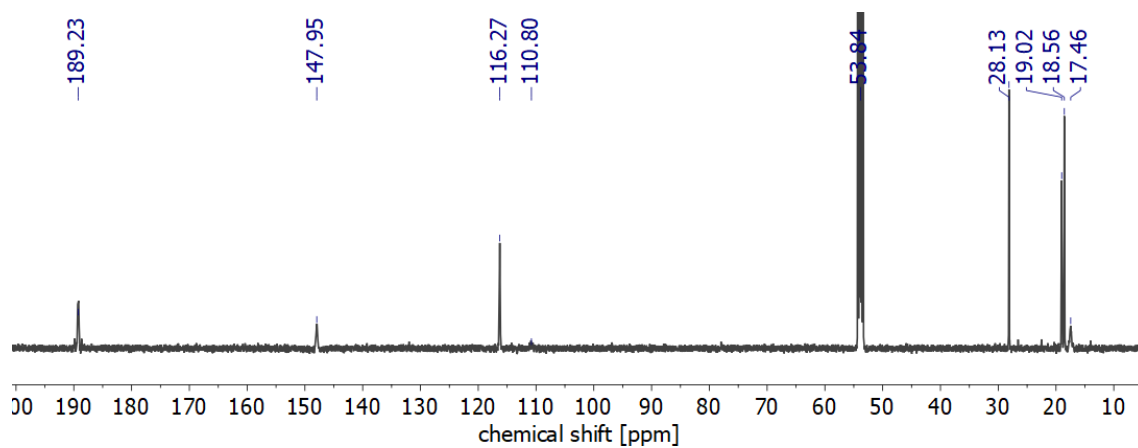
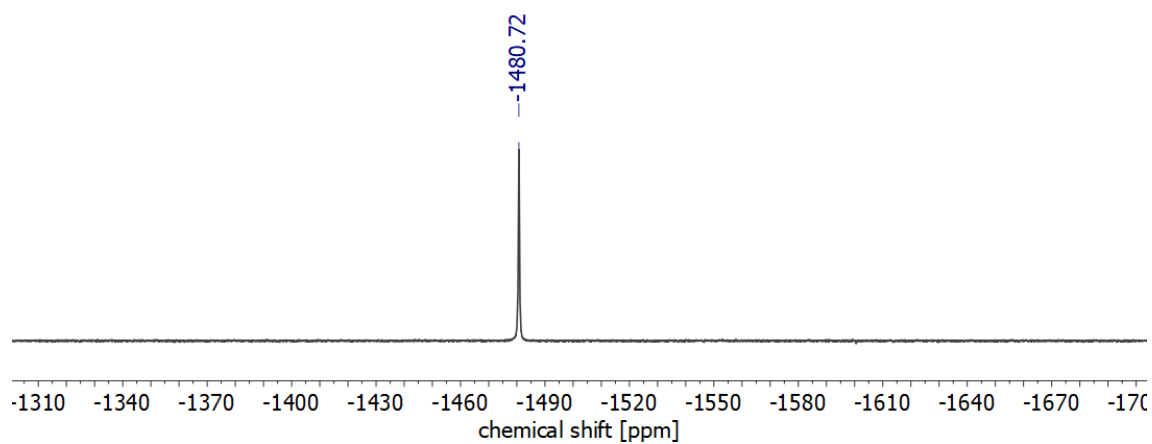
Figure 6.24 IR spectrum of 9.

6.1.12  $[\text{ReCl}_3(^{Pr}\text{PN}^{\text{H}}\text{P})] (10^{\text{Cl}})$ 

**Figure 6.25 Left:** Selective CV measurement of the  $\text{Re}^{\text{III/II}}$  couple of  $10^{\text{Cl}}$  ( $1 \cdot 10^{-3}$  M in  $0.1$  M  $\text{N}^{\text{t}}\text{Bu}_4\text{PF}_6$  (THF)). **Right:** Determination of  $k_{\text{obs}}$ .

6.1.13  $[\text{ReBr}_3(^{Pr}\text{PN}^{\text{H}}\text{P})] (10^{\text{Br}})$ 

**Figure 6.26 Left:** Selective CV measurement of the  $\text{Re}^{\text{III/II}}$  couple of  $10^{\text{Br}}$  ( $1 \cdot 10^{-3}$  M in  $0.1$  M  $\text{N}^{\text{t}}\text{Bu}_4\text{PF}_6$  (THF)). **Right:** Determination of  $k_{\text{obs}}$ .

6.1.14  $[\text{ReI}_3(\text{P}^{\text{r}}\text{PN}^{\text{H}}\text{P})]$  ( $10^{\text{I}}$ )Figure 6.27  $^1\text{H}\{^{31}\text{P}\}$  NMR spectrum of  $10^{\text{I}}$  ( $\text{CD}_2\text{Cl}_2$ , RT).Figure 6.28  $^{13}\text{C}$  NMR spectrum of  $10^{\text{I}}$  ( $\text{CD}_2\text{Cl}_2$ , RT).Figure 6.29  $^{31}\text{P}\{^1\text{H}\}$  NMR spectrum of  $10^{\text{I}}$  ( $\text{CD}_2\text{Cl}_2$ , RT).

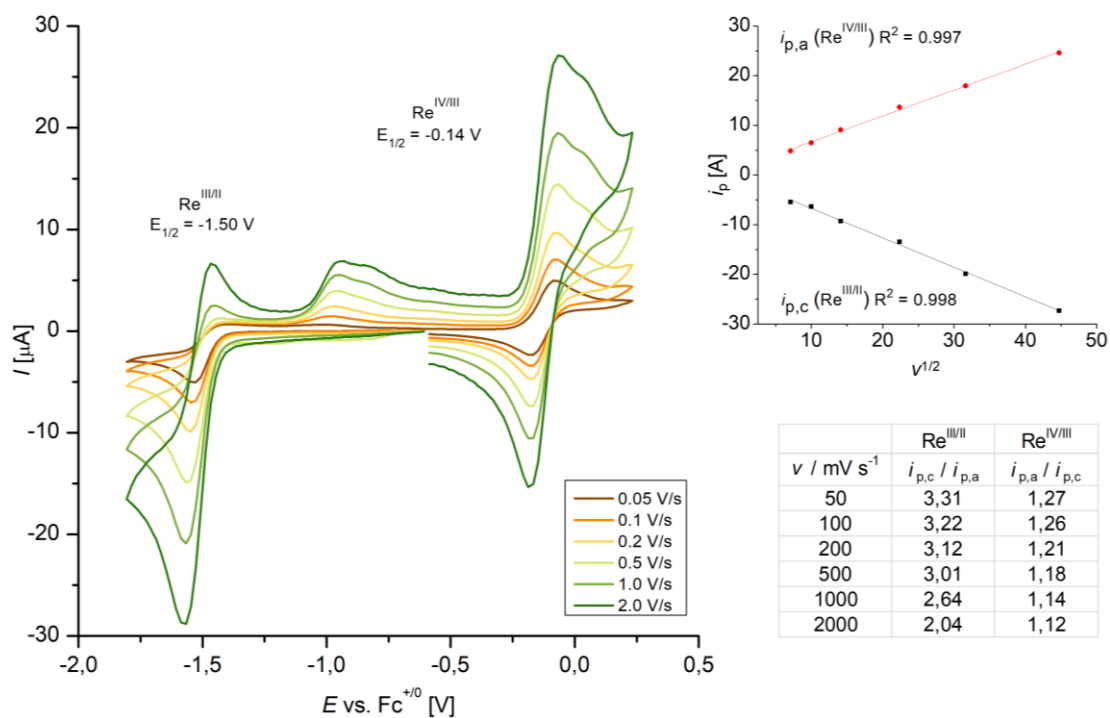


**Figure 6.30** Electrochemical characterization by cyclic voltammetry of  $10^{\text{I}}$  at different scan rates (1.0 mM; electrolyte: 0.1 M  $n\text{Bu}_4\text{NPF}_6$  in THF), including plot of  $i_p$  as a function of  $v^{1/2}$  and peak current ratio analysis ( $i_{p,c}/i_{p,a}$ ).

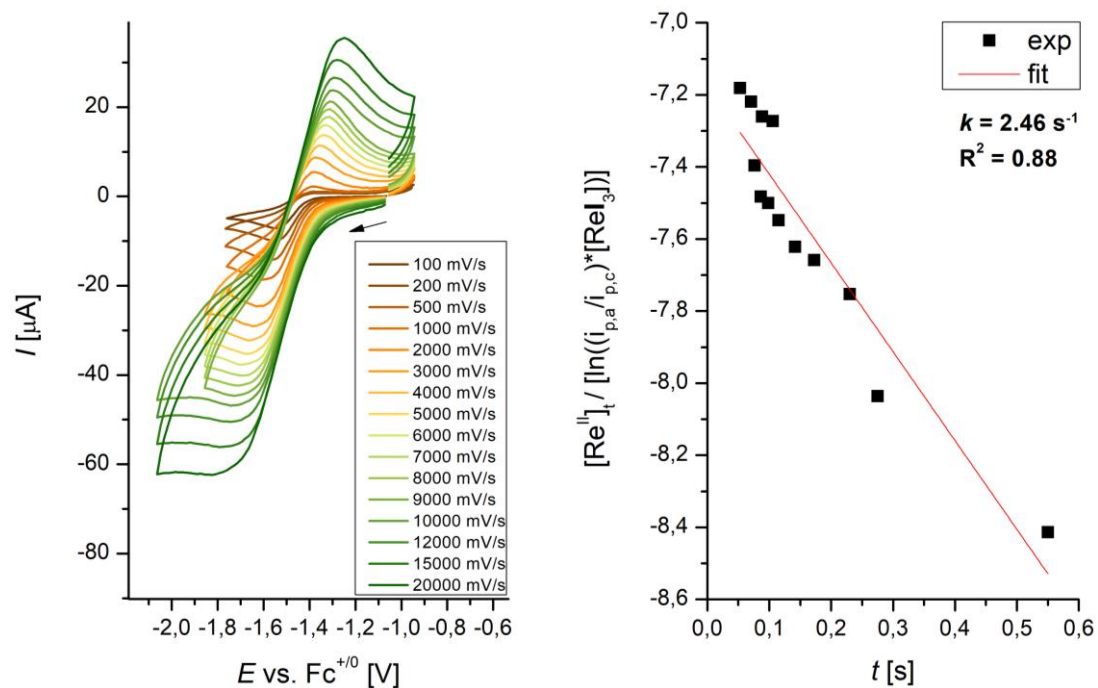


**Figure 6.31** Selective CV measurement of the  $\text{Re}^{\text{III/II}}$  couple of  $10^{\text{I}}$  ( $1 \cdot 10^{-3}$  M in 0.1 M  $n\text{Bu}_4\text{NPF}_6$  (THF)) (left). **Right:** Determination of  $k_{\text{obs}}$ .

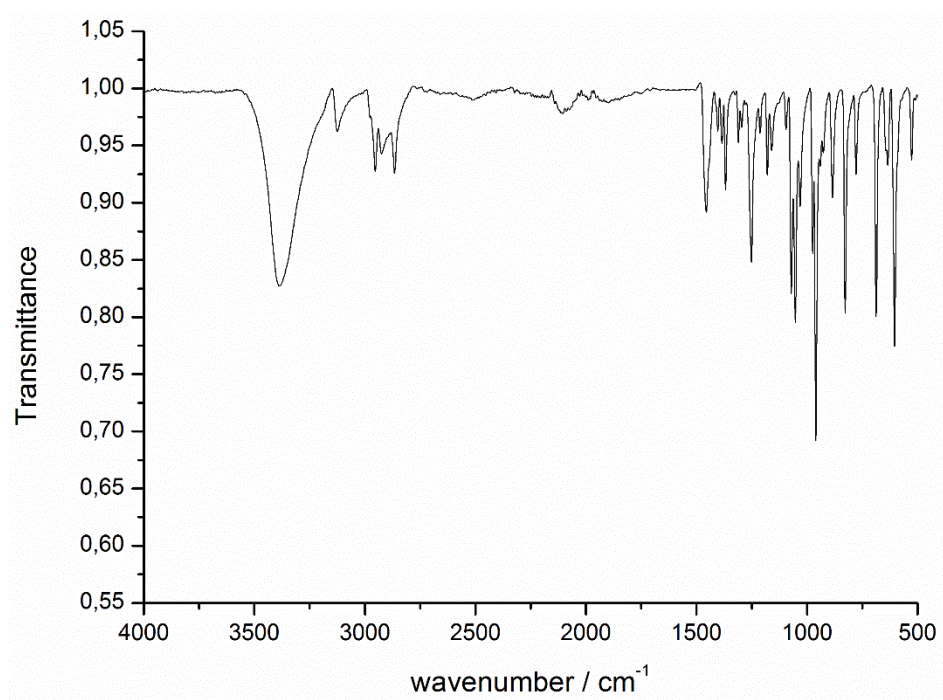
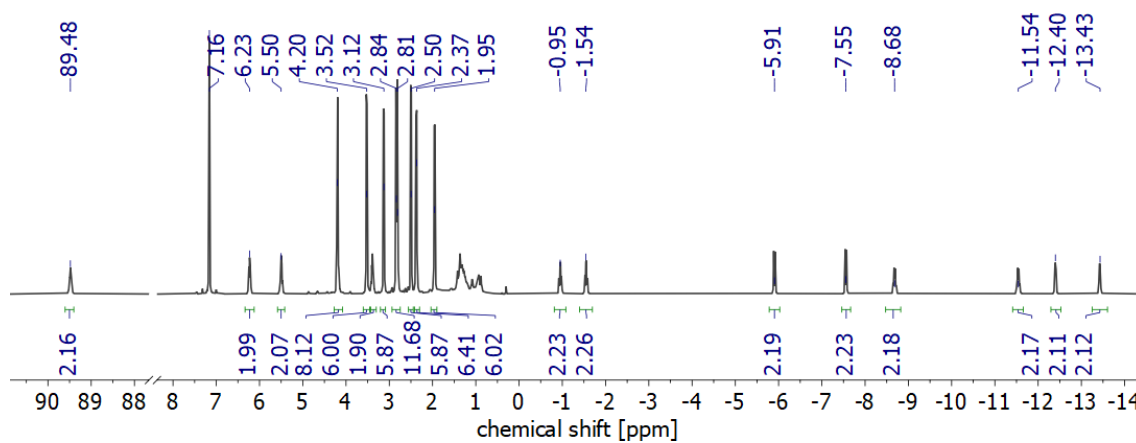
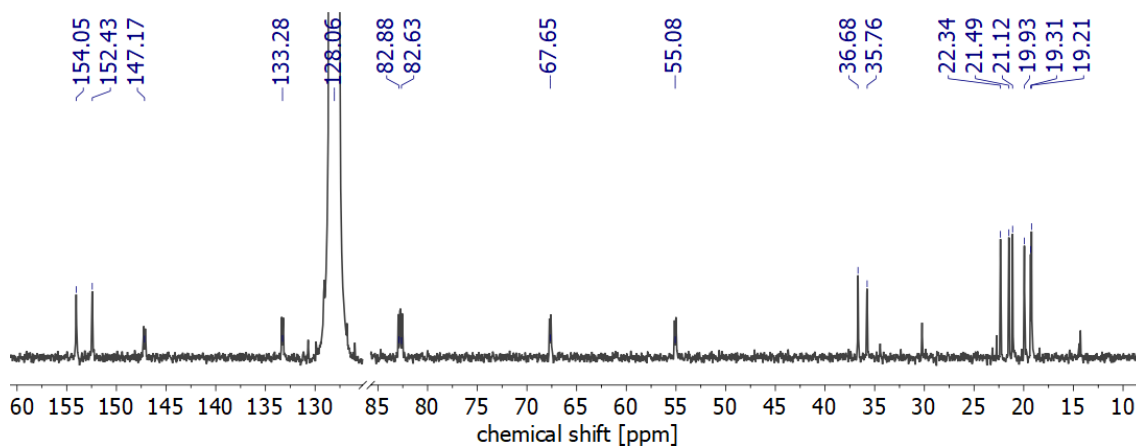
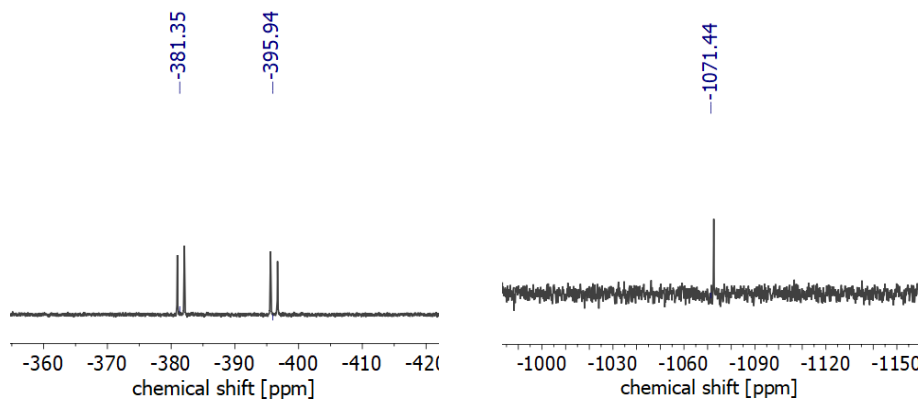
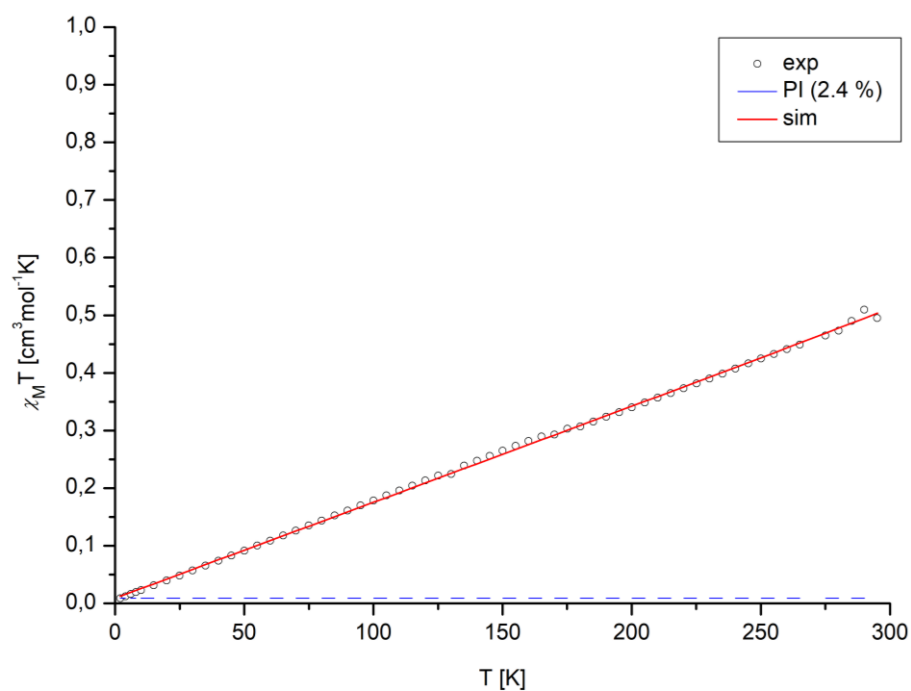


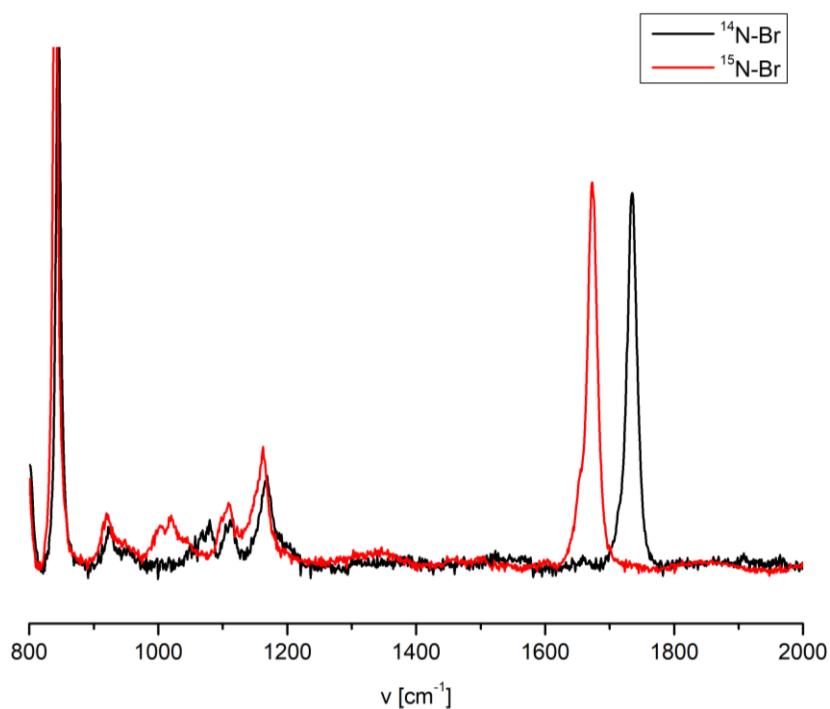
Figure 6.32 IR (ATR) of 10I.

6.1.15  $[(\mu\text{-N}_2)\{\text{ReBr}_2(\text{}^i\text{PrPN}^{\text{H}}\text{P})\}_2]$  (**11**<sup>Br</sup>)Figure 6.33  $^1\text{H}\{^{31}\text{P}\}$  NMR spectrum of **11**<sup>Br</sup> ( $\text{C}_6\text{D}_6$ , RT).Figure 6.34  $^{13}\text{C}\{^1\text{H}\}$  NMR spectrum of **11**<sup>Br</sup> ( $\text{C}_6\text{D}_6$ , RT).Figure 6.35 Left:  $^{31}\text{P}\{^1\text{H}\}$  NMR spectrum of **11**<sup>Br</sup> ( $\text{C}_6\text{D}_6$ , RT); Right:  $^{15}\text{N}\{^1\text{H}\}$  NMR spectrum ( $\text{C}_6\text{D}_6$ , RT).



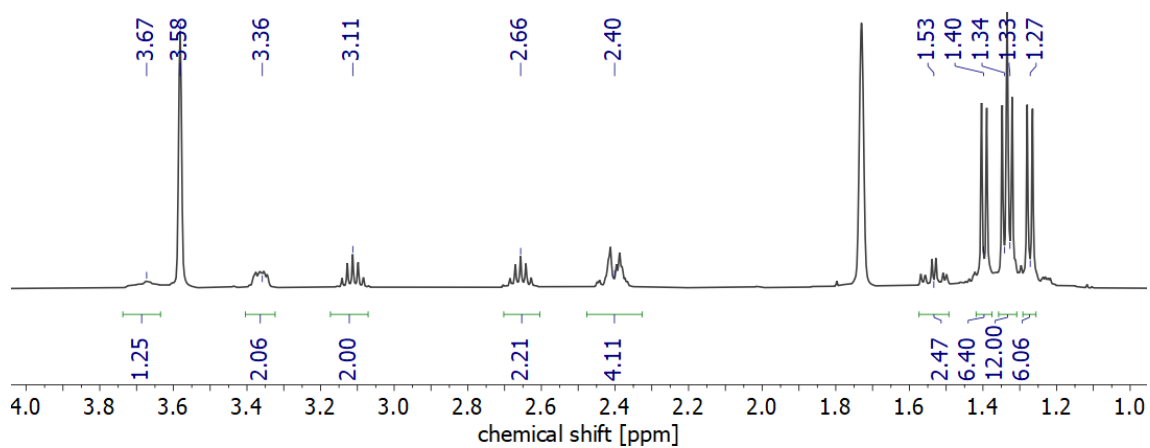
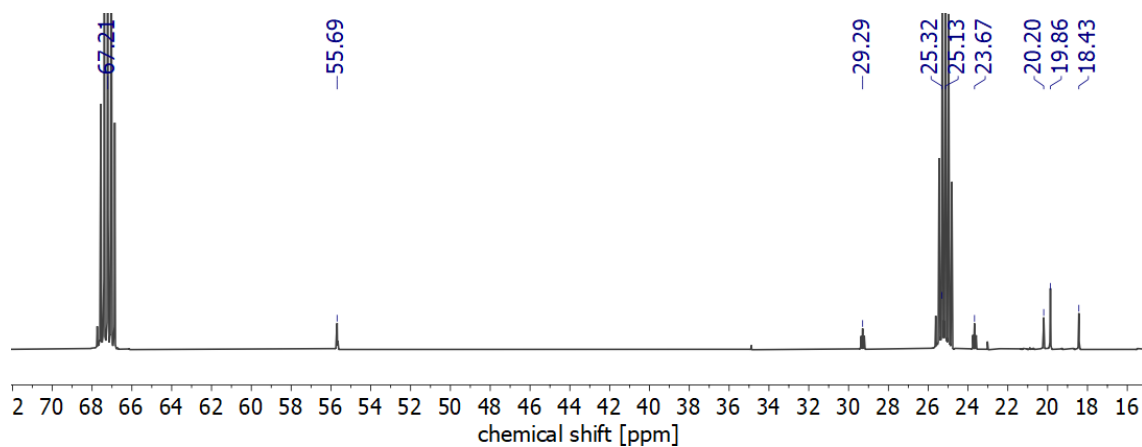
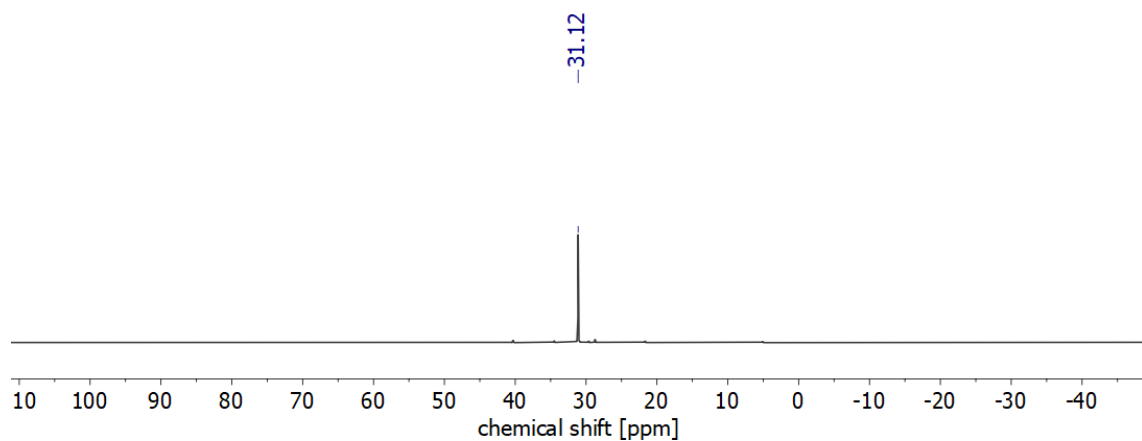
$$\chi_{\text{exp}} = \alpha \cdot \chi_{\text{PI}} \cdot \chi_{\text{TIP}}.$$

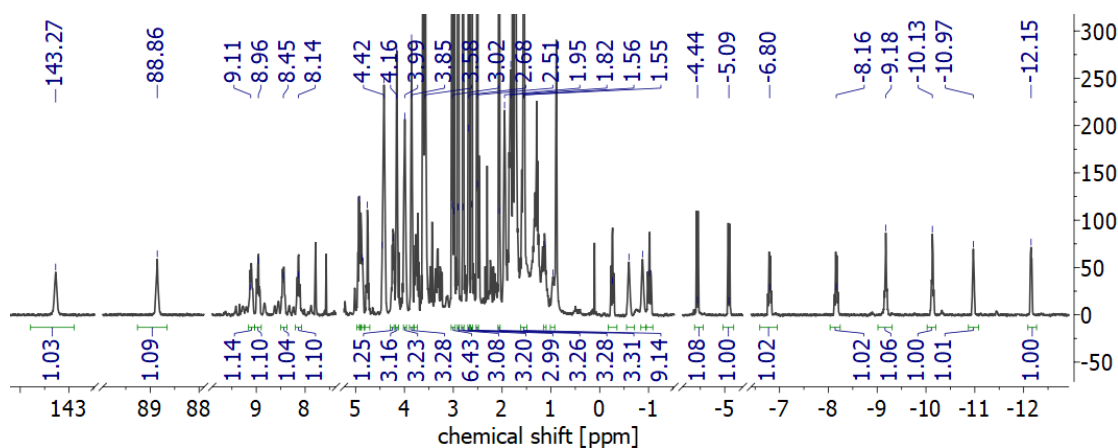
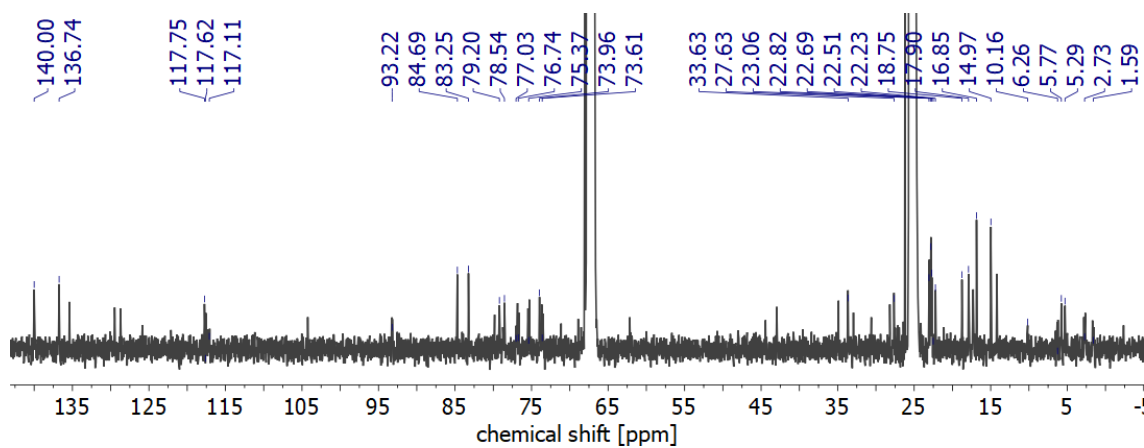
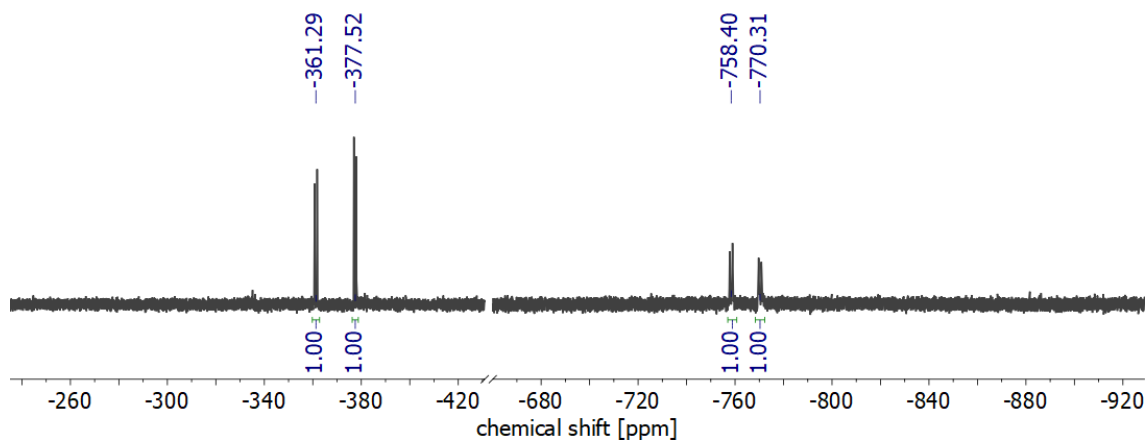
**Figure 6.36** Temperature dependence of the experimental  $\chi_{\text{T}}$ -product (circles) of complex **11<sup>Br</sup>** (fit parameters:  $S_1 = 1/2$ ,  $S_2 = 1/2$ ;  $g_1 = g_2 = 2.000$ ;  $J = -700 \text{ cm}^{-1}$ ; PI = 2.4% ( $S = 1/2$ ); TIP =  $1664.7 \cdot 10^{-6} \text{ cm}^3 \text{ mol}^{-1}$ ).

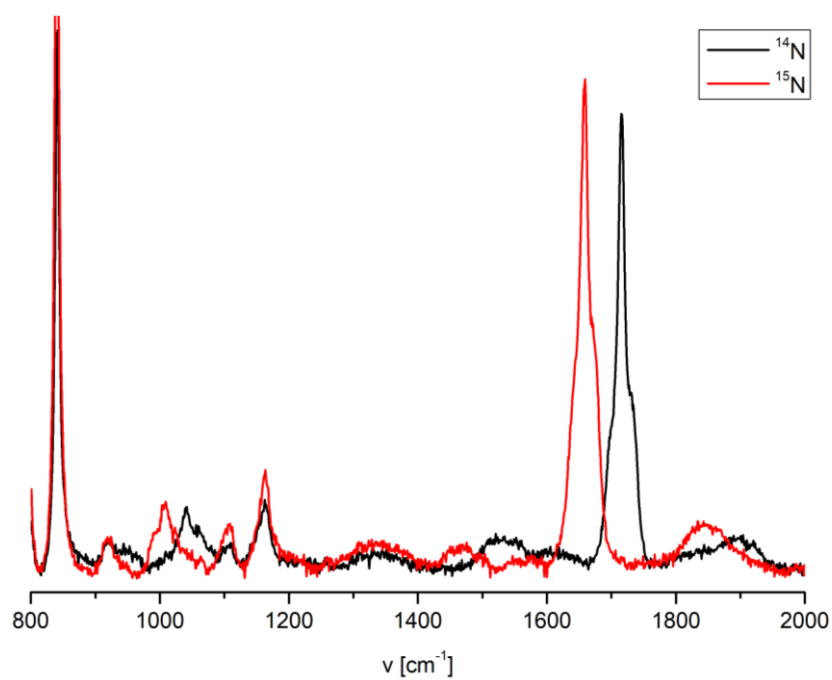


**Figure 6.37** rRaman spectrum ( $\lambda = 633 \text{ nm}$ ) of **11<sup>Br</sup>** in THF- $d_8$  solution at room temperature (red line:  $^{15}\text{N}$ ; black line:  $^{14}\text{N}$ ).

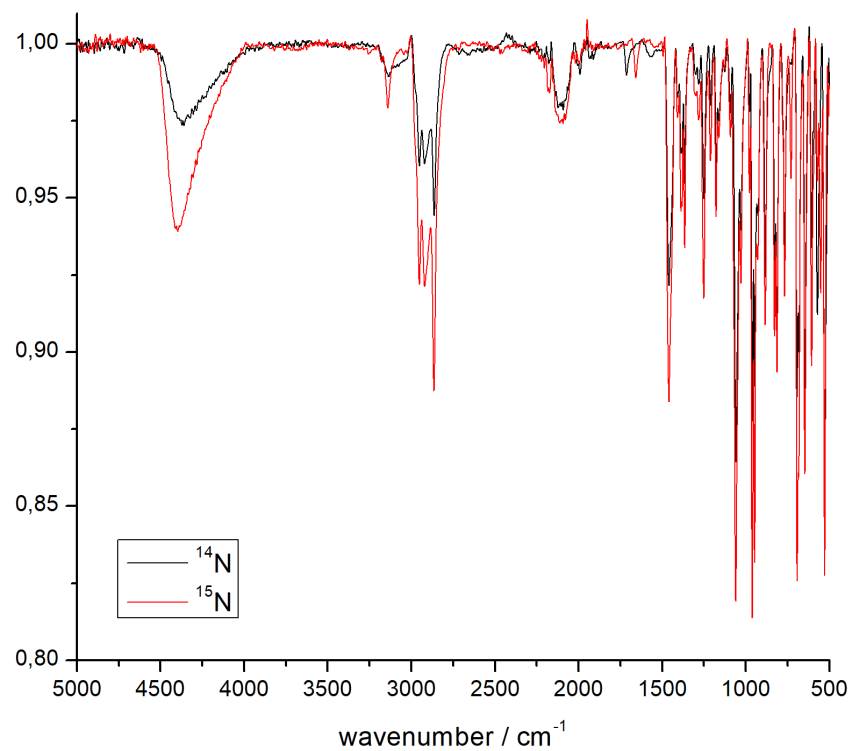


6.1.16  $[\text{ReBr}(\text{N}_2)_2(\text{P}^i\text{PN}^i\text{P})]$  (**12**)Figure 6.38  $^1\text{H}\{^{31}\text{P}\}$  NMR spectrum of **12** ( $\text{THF-}d_8$ , RT).Figure 6.39  $^{13}\text{C}\{^1\text{H}\}$  NMR spectrum of **12** ( $\text{THF-}d_8$ , RT).Figure 6.40  $^{31}\text{P}\{^1\text{H}\}$  NMR spectrum of **12** ( $\text{THF-}d_8$ , RT).

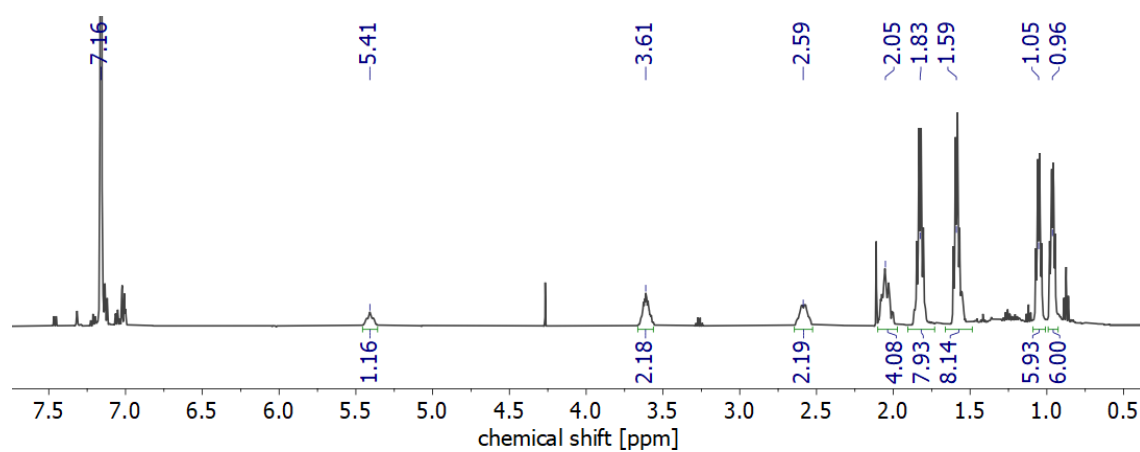
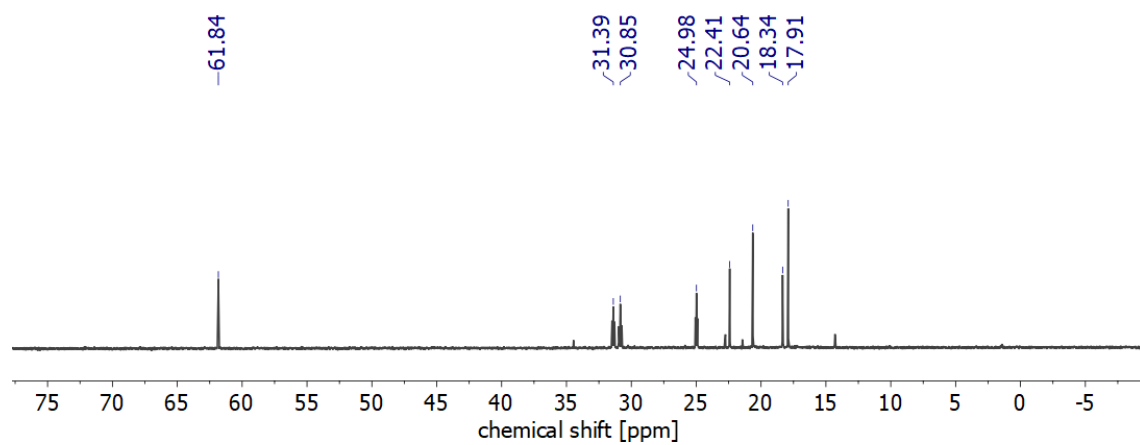
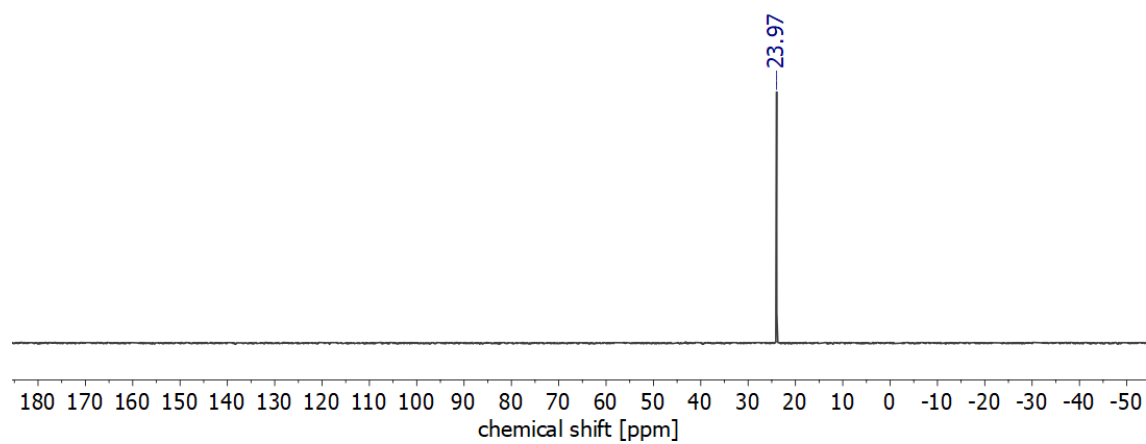
6.1.17  $[(\mu\text{-N}_2)\{\text{ReI}_2(\text{P}^{\text{r}}\text{PN}^{\text{H}}\text{P})\}_2]$  (**11**<sup>I</sup>)Figure 6.41  $^1\text{H}\{^{31}\text{P}\}$  NMR spectrum of **11**<sup>I</sup> (THF-*d*<sub>8</sub>, RT).Figure 6.42  $^{13}\text{C}\{^1\text{H}\}$  NMR spectrum of **11**<sup>I</sup> (THF-*d*<sub>8</sub>, RT).Figure 6.43  $^{31}\text{P}\{^1\text{H}\}$  NMR spectrum of **11**<sup>I</sup> (THF-*d*<sub>8</sub>, RT).

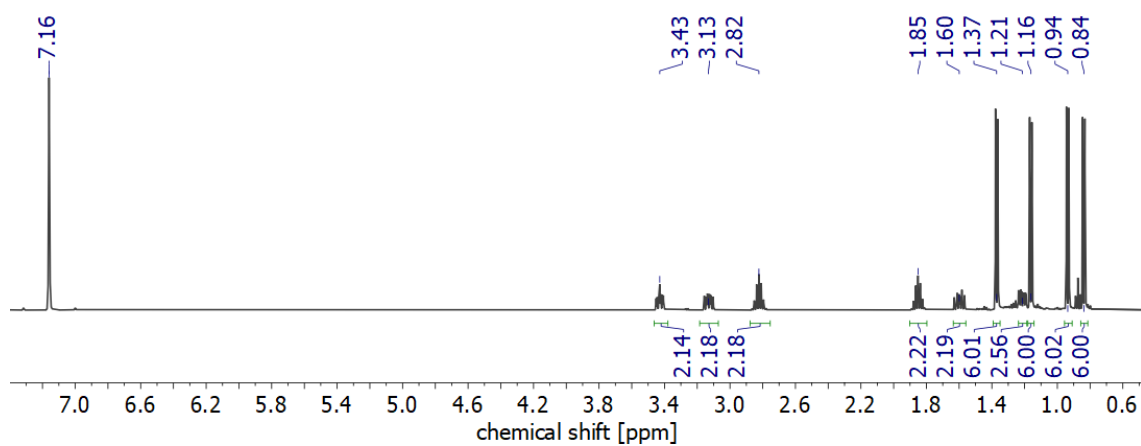
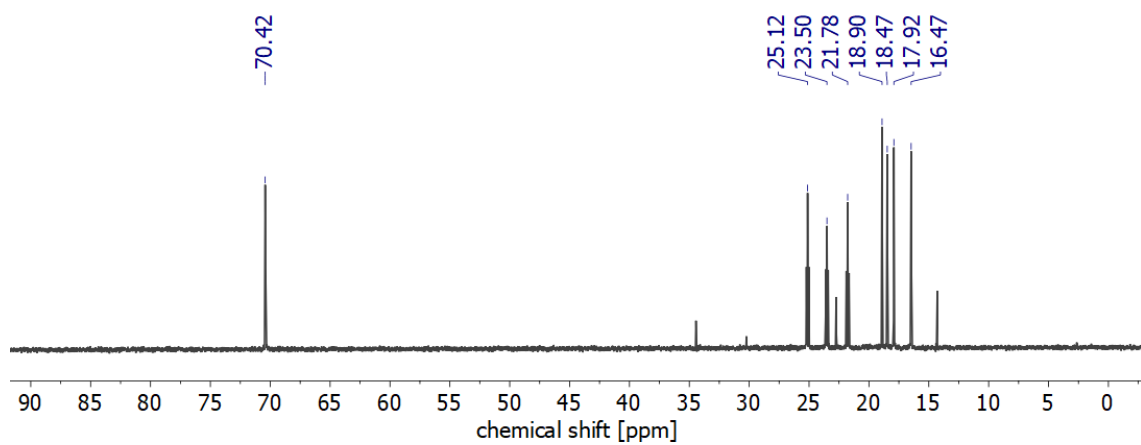
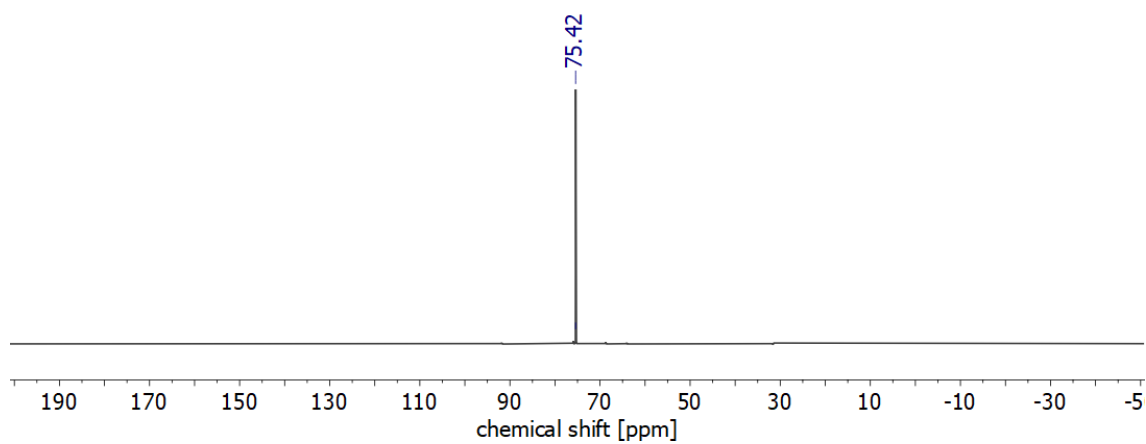


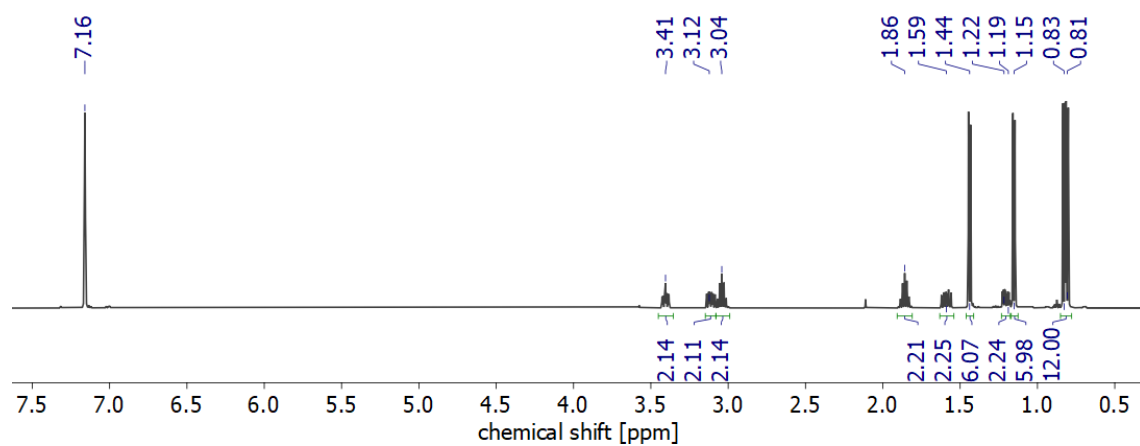
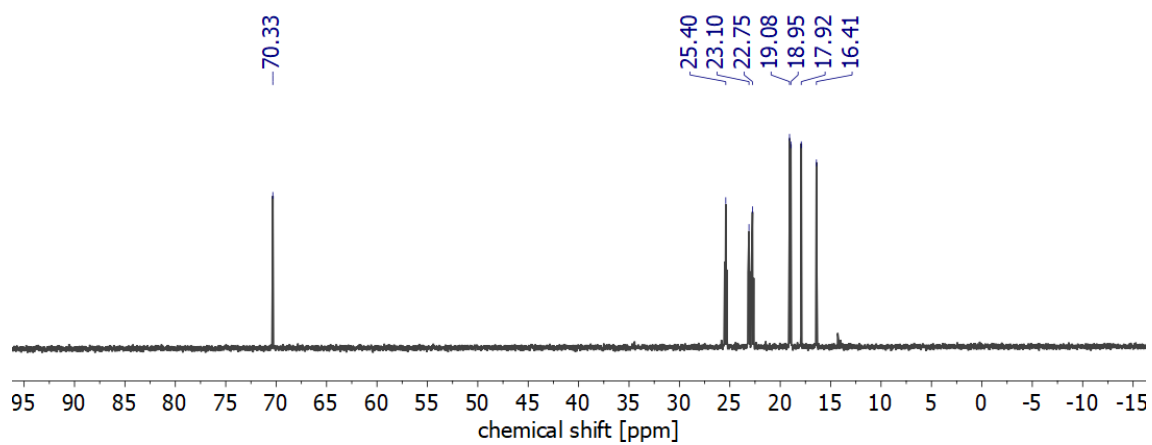
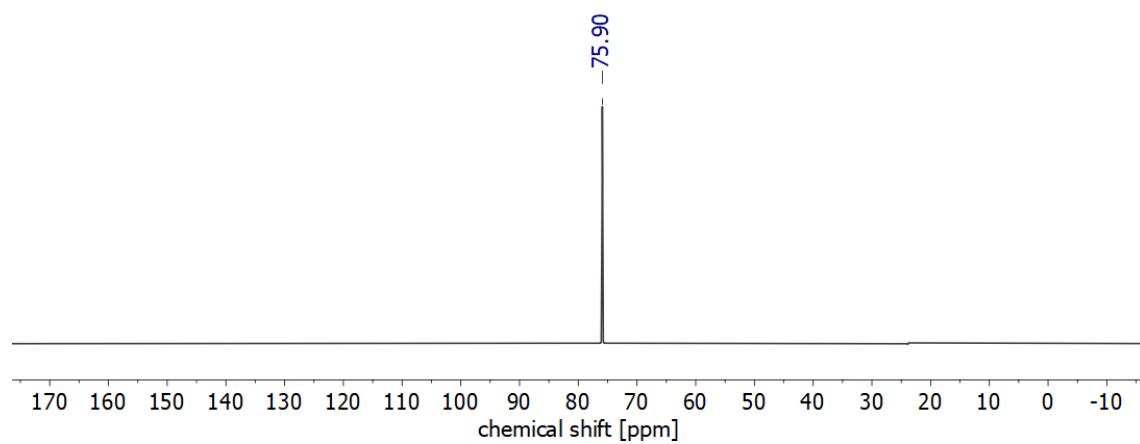
**Figure 6.44** rRaman spectrum ( $\lambda = 633$  nm) of **11<sup>I</sup>** in THF-*d*<sub>8</sub> solution at room temperature (red line: <sup>15</sup>N; black line: <sup>14</sup>N).

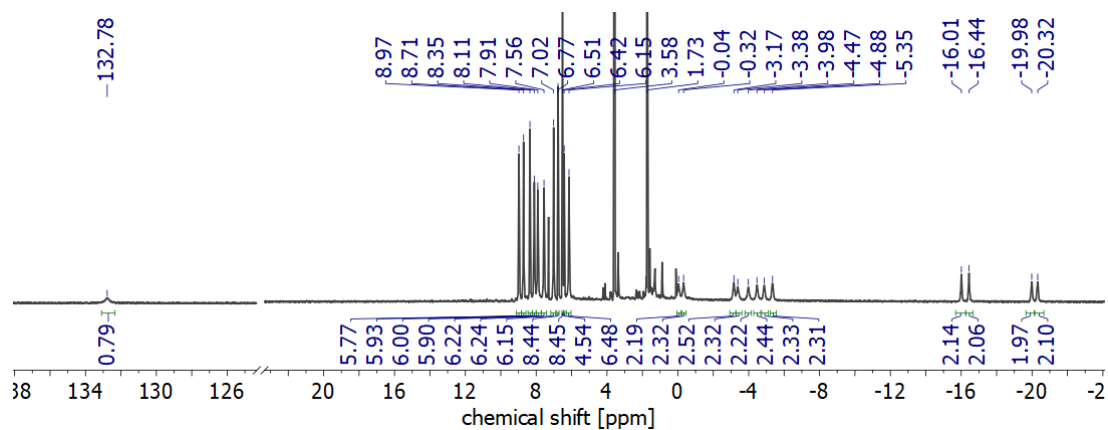
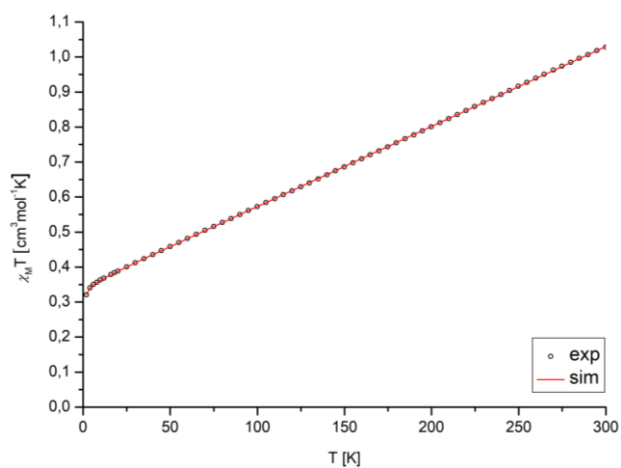


**Figure 6.45** IR (ATR) spectrum of **11<sup>I</sup>** (red line: <sup>15</sup>N; black line: <sup>14</sup>N).

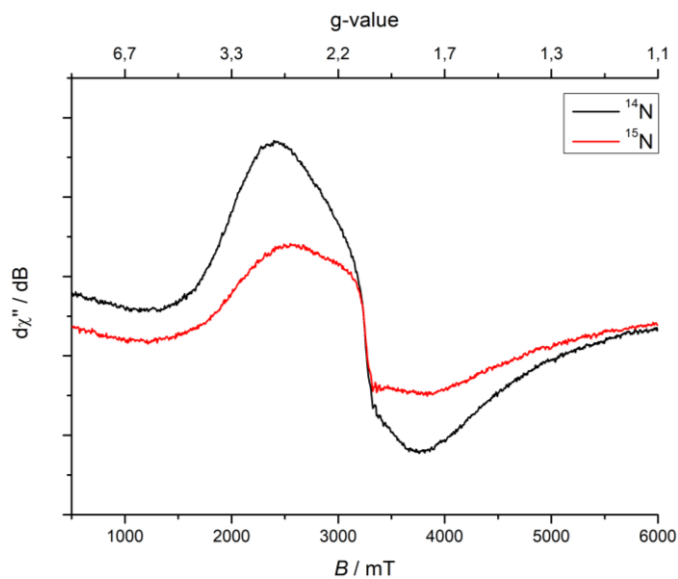
6.1.18  $[\text{ReI}_2\text{N}(\text{Pr}^i\text{PN}^i\text{H}^i\text{P})]$  ( $\mathbf{13}^i$ )Figure 6.46  $^1\text{H}\{^{31}\text{P}\}$  NMR spectrum of  $\mathbf{13}^i$  ( $\text{C}_6\text{D}_6$ , RT).Figure 6.47  $^{13}\text{C}\{^1\text{H}\}$  NMR spectrum of  $\mathbf{13}^i$  ( $\text{C}_6\text{D}_6$ , RT).Figure 6.48  $^{31}\text{P}\{^1\text{H}\}$  NMR spectrum of  $\mathbf{13}^i$  ( $\text{C}_6\text{D}_6$ , RT).

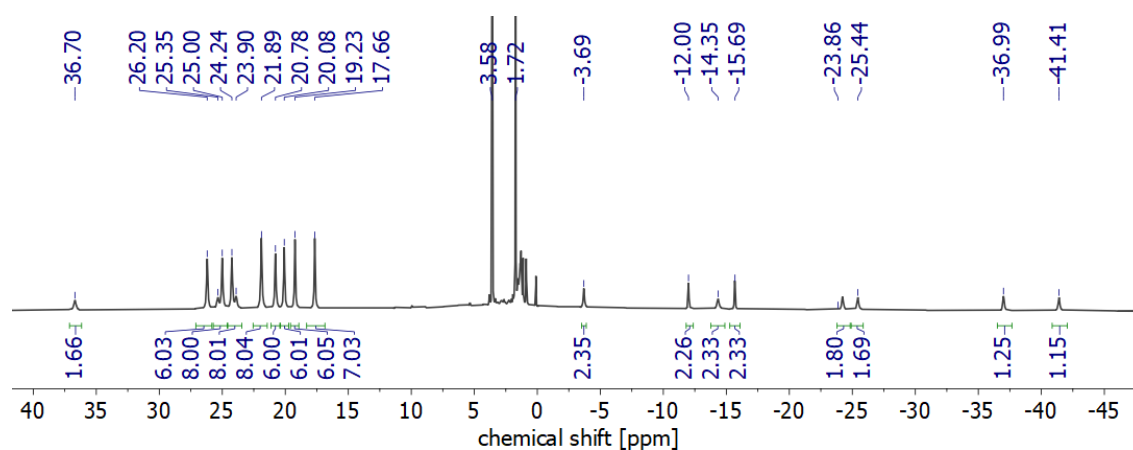
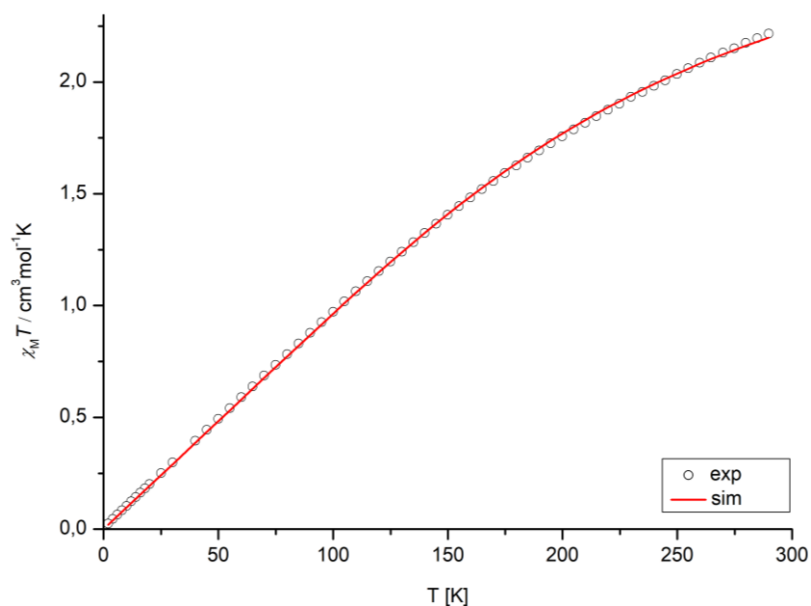
6.1.19 [ReBrN(<sup>i</sup>PrPNP)] (14<sup>Br</sup>)Figure 6.49 <sup>1</sup>H{<sup>31</sup>P} NMR spectrum of 14<sup>Br</sup> (C<sub>6</sub>D<sub>6</sub>, RT).Figure 6.50 <sup>13</sup>C{<sup>1</sup>H} NMR spectrum of 14<sup>Br</sup> (C<sub>6</sub>D<sub>6</sub>, RT).Figure 6.51 <sup>31</sup>P{<sup>1</sup>H} NMR spectrum of 14<sup>Br</sup> (C<sub>6</sub>D<sub>6</sub>, RT).

6.1.20 [ReIN(<sup>r</sup>PNP)] (14<sup>I</sup>)Figure 6.52  $^1\text{H}\{^{31}\text{P}\}$  NMR spectrum of **14<sup>I</sup>** ( $\text{C}_6\text{D}_6$ , RT).Figure 6.53  $^{13}\text{C}\{^1\text{H}\}$  NMR spectrum of **14<sup>I</sup>** ( $\text{C}_6\text{D}_6$ , RT).Figure 6.54  $^{31}\text{P}\{^1\text{H}\}$  NMR spectrum of **14<sup>I</sup>** ( $\text{C}_6\text{D}_6$ , RT).

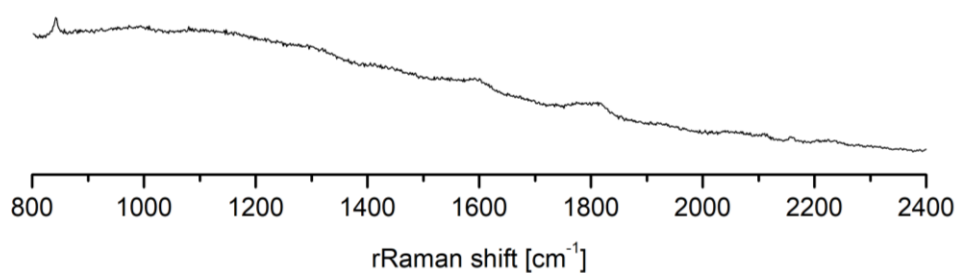
6.1.21  $[(\mu\text{-N}_2)\{\text{ReBr}_2(\text{P}^i\text{PN}^H\text{P})\}_2]\text{BPh}_4$  ( $11^{\text{Br}+}$ )Figure 6.55  $^1\text{H}$  NMR spectrum of  $11^{\text{Br}+}$  ( $\text{THF-}d_8$ , RT).

$$\hat{H} = g\mu_B \vec{B} \hat{S}$$

Figure 6.56 Temperature dependence of the experimental  $\chi T$ -product (circles) of complex  $11^{\text{Br}+}$  (fit parameters:  $S = 1/2$ ;  $g_1 = 1.919$ ;  $\text{TIP} = 2282.9 \cdot 10^{-6} \text{ cm}^3 \text{mol}^{-1}$ ) including applied spin-Hamiltonian.Figure 6.57 EPR spectra (solid,  $T = 20 \text{ K}$ ) of  $^{14}\text{N-}11^{\text{Br}}$  (black) and  $^{15}\text{N-}11^{\text{Br}}$  (red).

6.1.22  $[(\mu\text{-N}_2)\{\text{ReBr}_2(\text{P}^r\text{PN}^{\text{H}}\text{P})\}_2][\text{Al}(\text{OC}(\text{CF}_3)_3)_4]$  ( $11^{\text{Br}2+}$ )Figure 6.58  $^1\text{H}$  NMR spectrum of  $11^{\text{Br}2+}$  ( $\text{THF-}d_8$ , RT).

$$\hat{H} = g\mu_B \vec{B} \vec{S} + D \left[ \hat{S}_z^2 - \frac{1}{3} S(S+1) \right]$$

Figure 6.59 Temperature dependence of the experimental  $\chi_T$ -product (circles) of complex  $11^{\text{Br}2+}$  (fit parameters:  $S = 2$ ;  $g_1 = 1.619$ ;  $D = 374.7 \text{ cm}^{-1}$ ;  $\text{TIP} = 2501.0 \cdot 10^{-6} \text{ cm}^3 \text{ mol}^{-1}$ ) including applied spin-Hamiltonian.Figure 6.60 rRaman spectrum ( $\lambda = 633 \text{ nm}$ ) of  $11^{\text{Br}2+}$  in  $\text{THF-}d_8$  solution at room temperature.



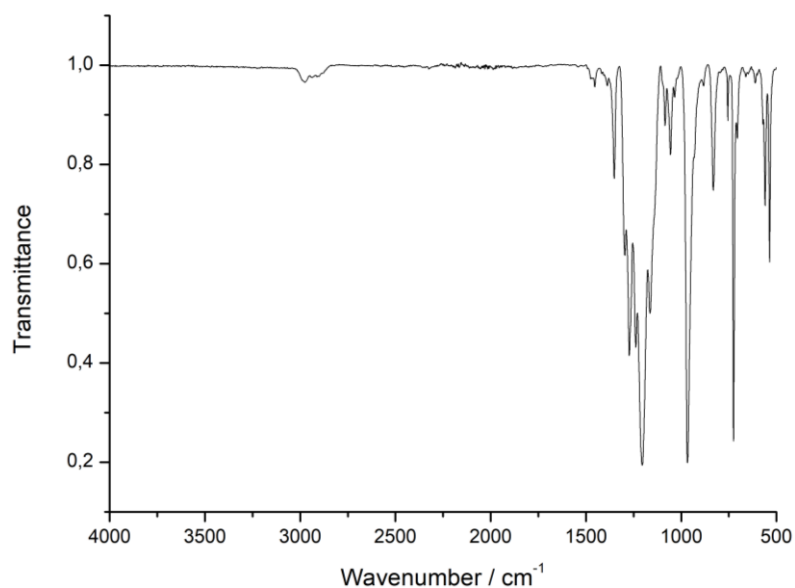


Figure 6.61 IR (ATR) spectrum of  $11\text{Br}_2^+$ .

### 6.1.23 $[\text{ReBr}_2\{\text{N}(\text{CO})\text{C}_6\text{H}_5\}(\text{}^i\text{PrPN}^{\text{H}}\text{P})][\text{BArF}_{24}]$ ( $15^{\text{BArF}}$ )

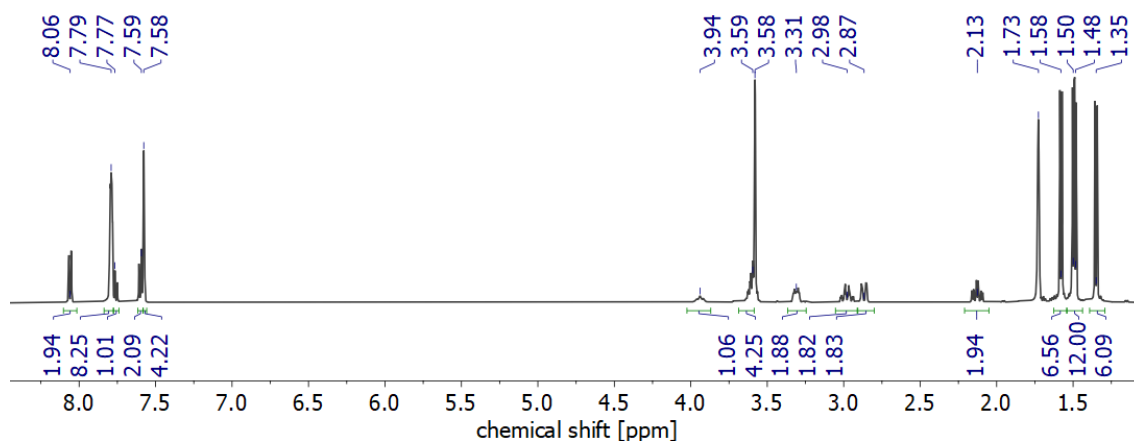


Figure 6.62  $^1\text{H}\{^{31}\text{P}\}$  NMR spectrum of  $15^{\text{BArF}}$  (THF- $d_6$ , RT).

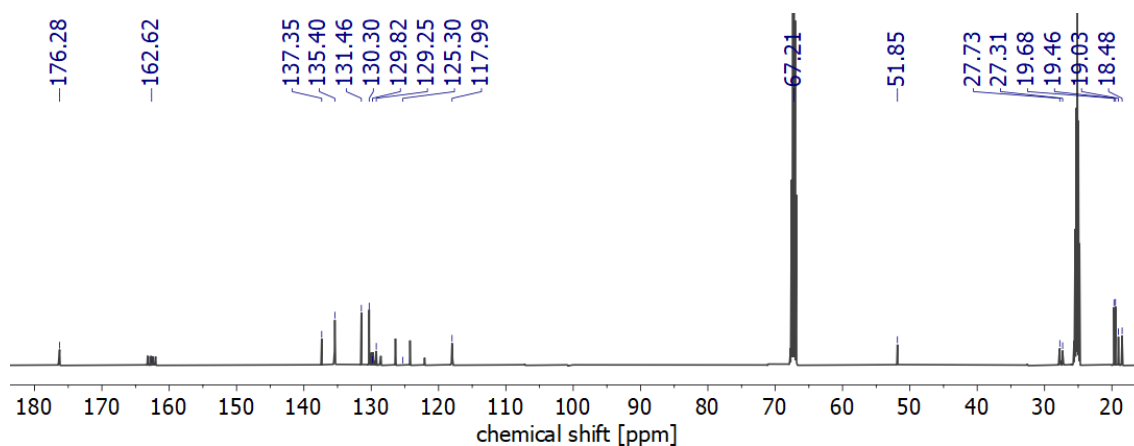
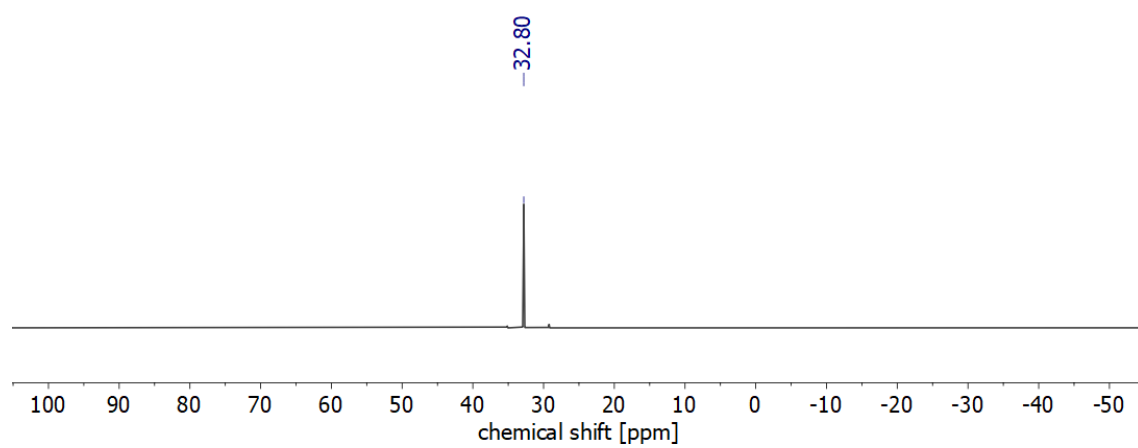
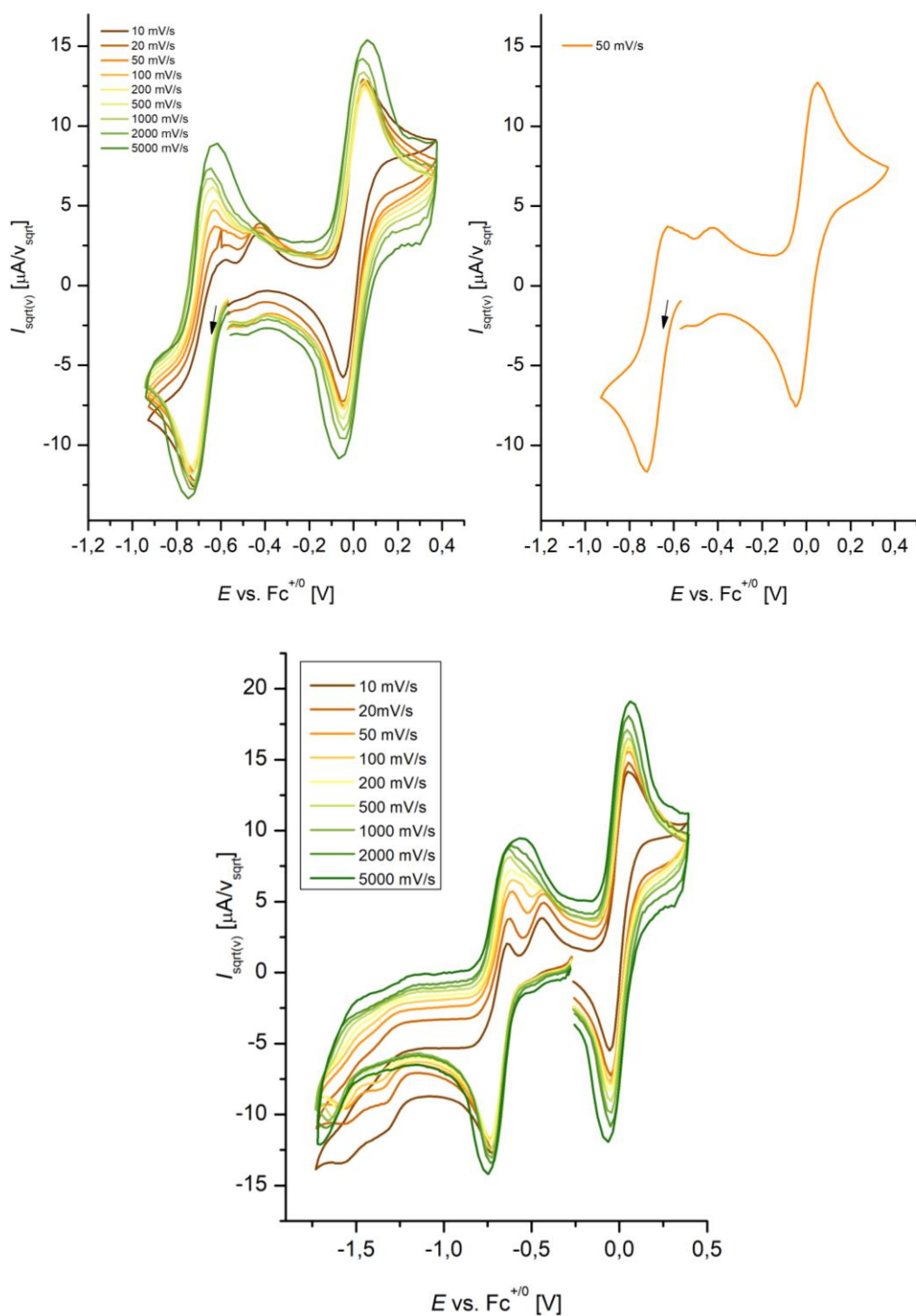


Figure 6.63  $^{13}\text{C}\{^1\text{H}\}$  NMR spectrum of  $15^{\text{BArF}}$  (THF- $d_6$ , RT).



**Figure 6.64**  $^{31}\text{P}$   $\{^1\text{H}\}$  NMR spectrum of **15BArF** (THF- $d_8$ , RT).



**Figure 6.65** Top left: Selected second scan CV data of imido complex  $15^{BArF}$  (1.0 mM; electrolyte: 0.1 M  $n\text{-Bu}_4\text{PF}_6$  in THF) with ferrocene as internal standard, normalized vs  $v^{1/2}$ . Top right: Isolated trace of the 50 mV/s scan. Bottom: Full reductive scan of  $15^{BArF}$  using ferrocene as internal standard.

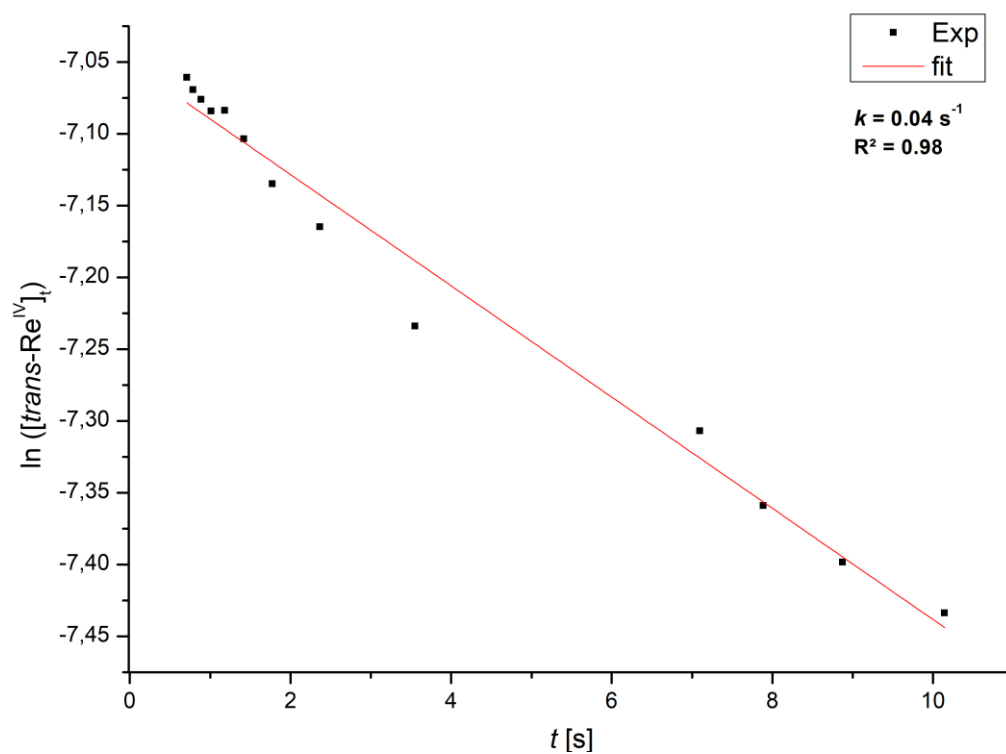


Figure 6.66 Determination of  $k_{\text{iso}}$ .

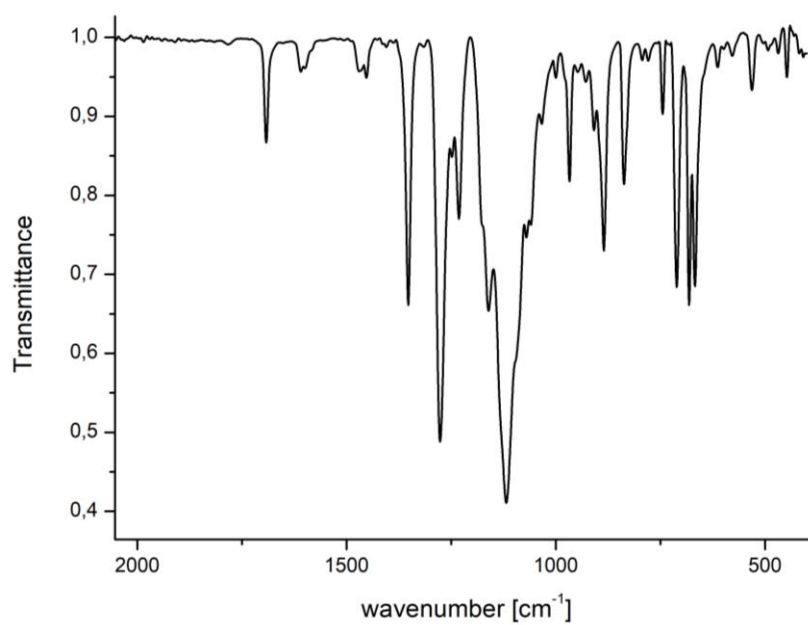
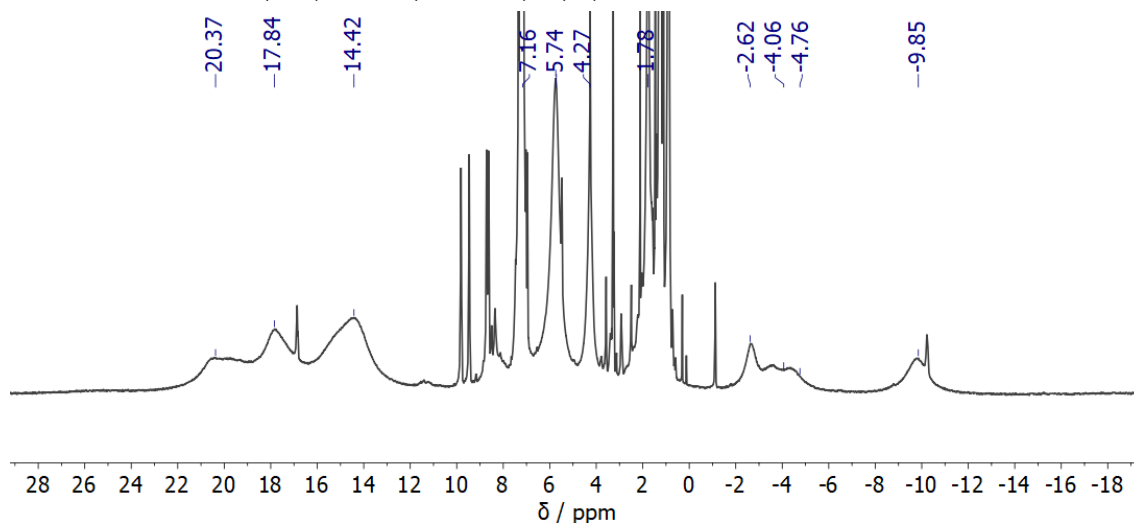
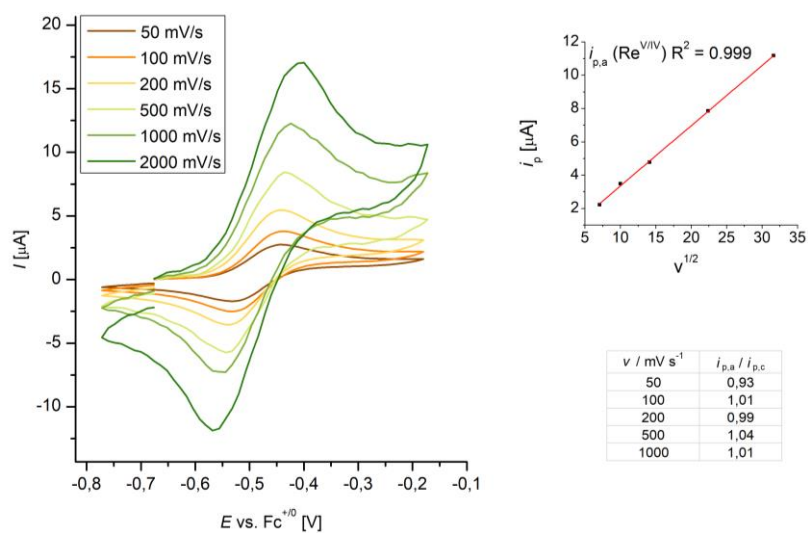
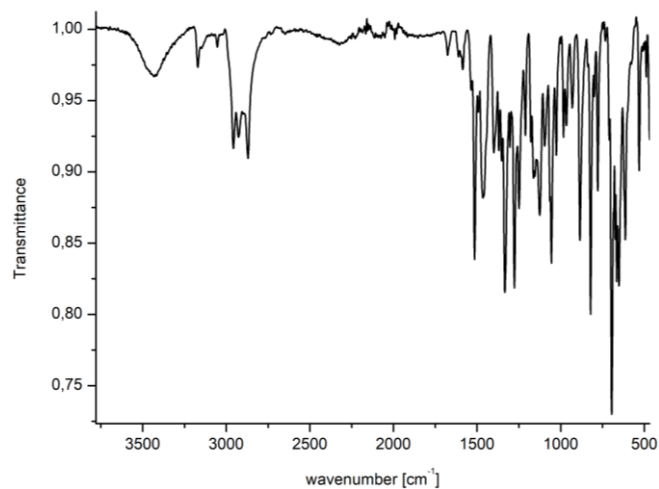
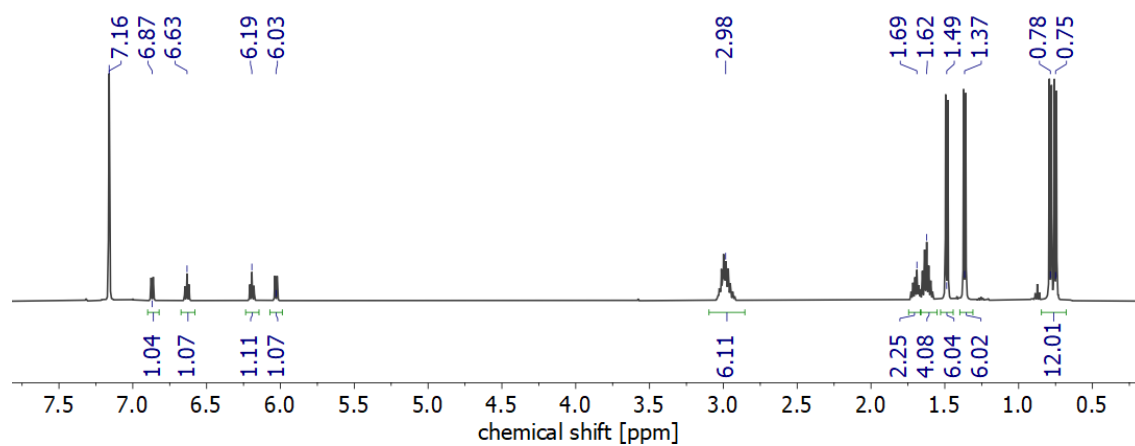
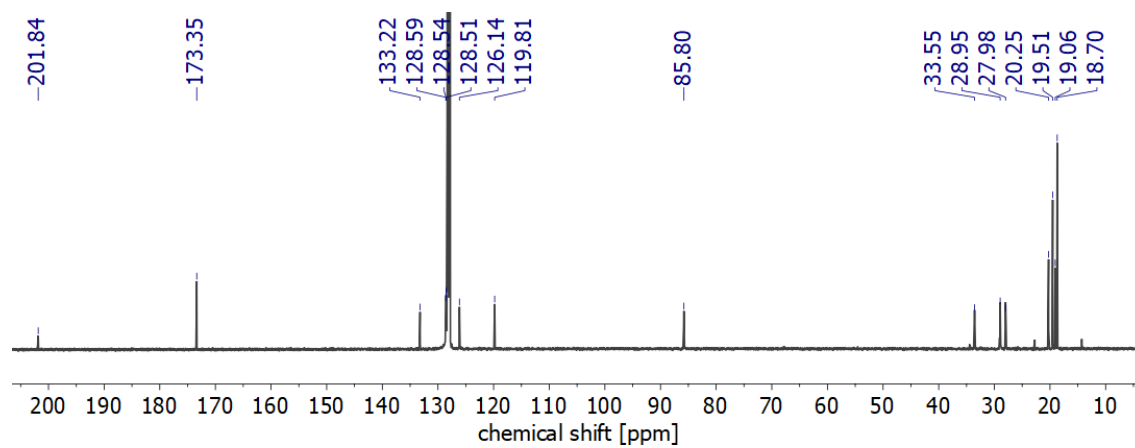
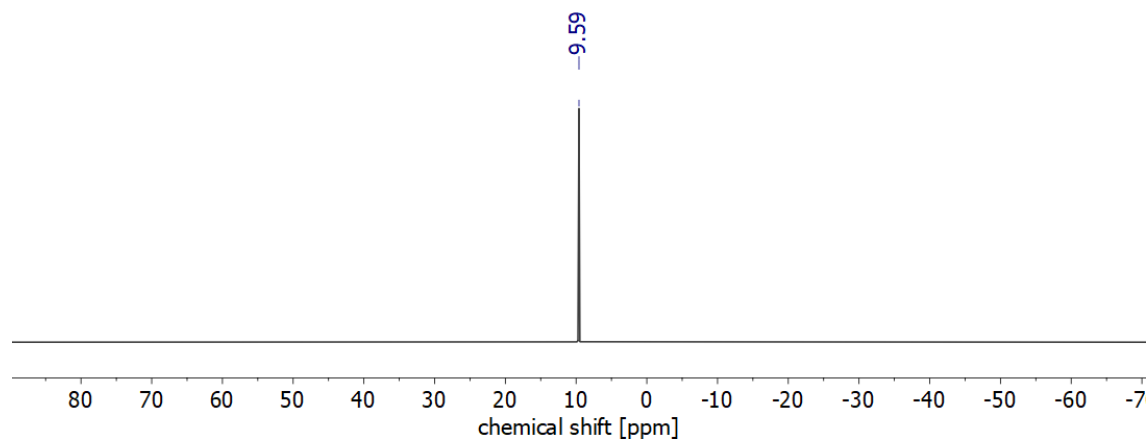


Figure 6.67 IR (ATR) spectrum of  $15^{\text{BArF}}$ .

6.1.24  $[\text{Re}^{\text{IV}}\text{Br}_2\{\text{N}(\text{CO})\text{C}_6\text{H}_5\}(\text{PrPN}^{\text{H}}\text{P})]$  (**16**)Figure 6.68  $^1\text{H}$  NMR spectrum of **16** ( $\text{C}_6\text{D}_6$ , RT).Figure 6.69 Scan rate dependent CV data of imido complex **16** (1.0 mM; electrolyte: 0.1 M  $\text{N}^{\text{t}}\text{Bu}_4\text{PF}_6$  in THF) including plot of  $i_p$  as a function of  $v^{1/2}$  and linear fitting and plot of the scan rate dependent peak ratios ( $i_{p,c}$  and  $i_{p,a}$ ).Figure 6.70 IR (ATR) spectrum of **16**.

6.1.25  $[\text{ReBr}\{\text{NH}_2(\text{CO})\text{C}_6\text{H}_4\}(\text{}^i\text{PrPNP})]$  (**17**)Figure 6.71  $^1\text{H}\{^{31}\text{P}\}$  NMR spectrum of **17** ( $\text{C}_6\text{D}_6$ , RT).Figure 6.72  $^{13}\text{C}\{^1\text{H}\}$  NMR spectrum of **17** ( $\text{C}_6\text{D}_6$ , RT).Figure 6.73  $^{31}\text{P}\{^1\text{H}\}$  NMR spectrum of **17** ( $\text{C}_6\text{D}_6$ , RT).

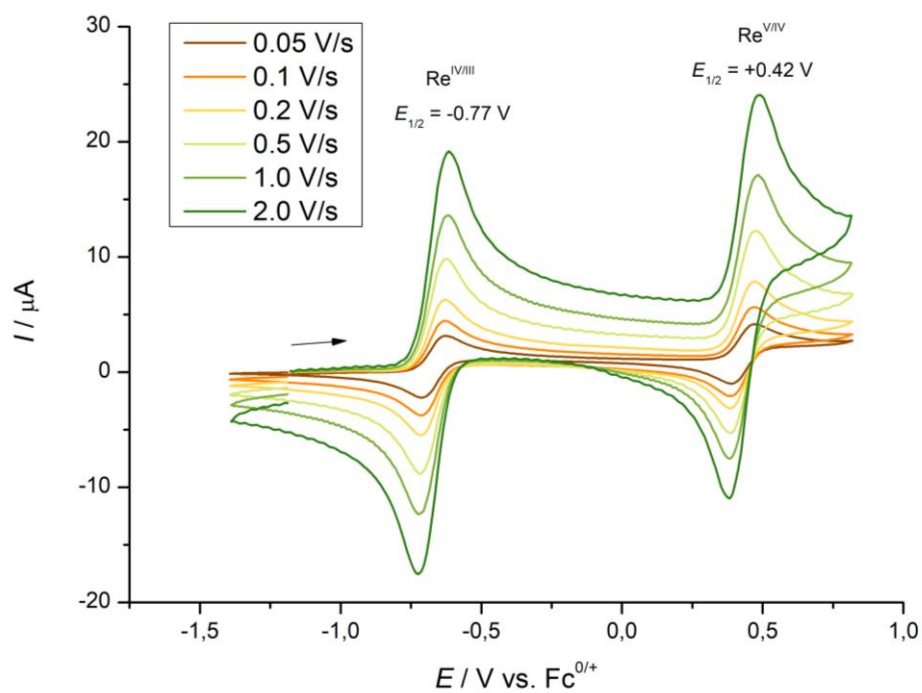


Figure 6.74 Cyclic voltammety of **17** (1.0 mM; electrolyte: 0.1 M  $\text{N}^{\text{t}}\text{Bu}_4\text{PF}_6$  in THF), referenced to ferrocene.

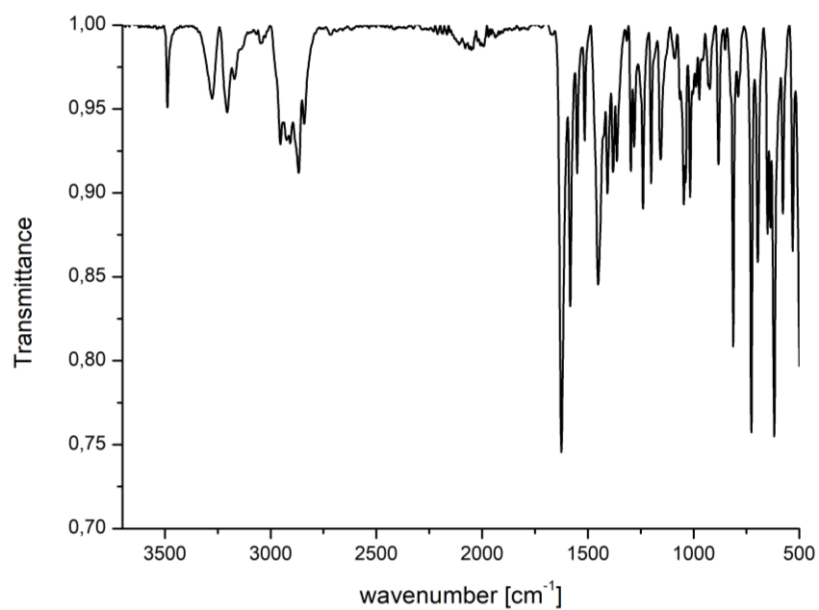
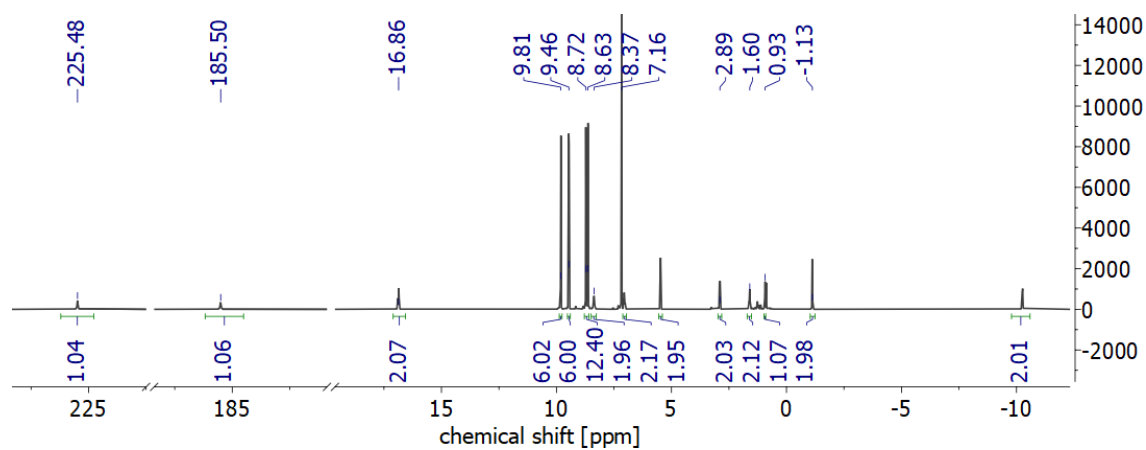
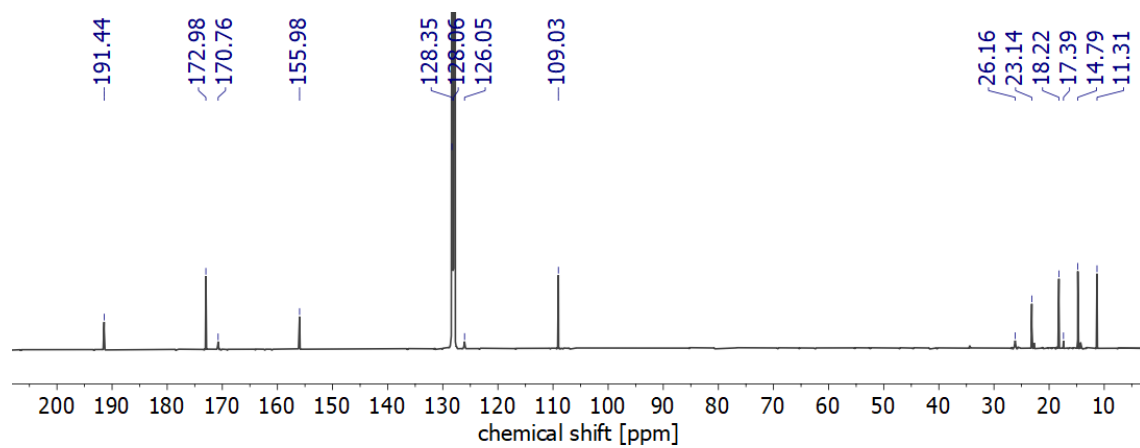
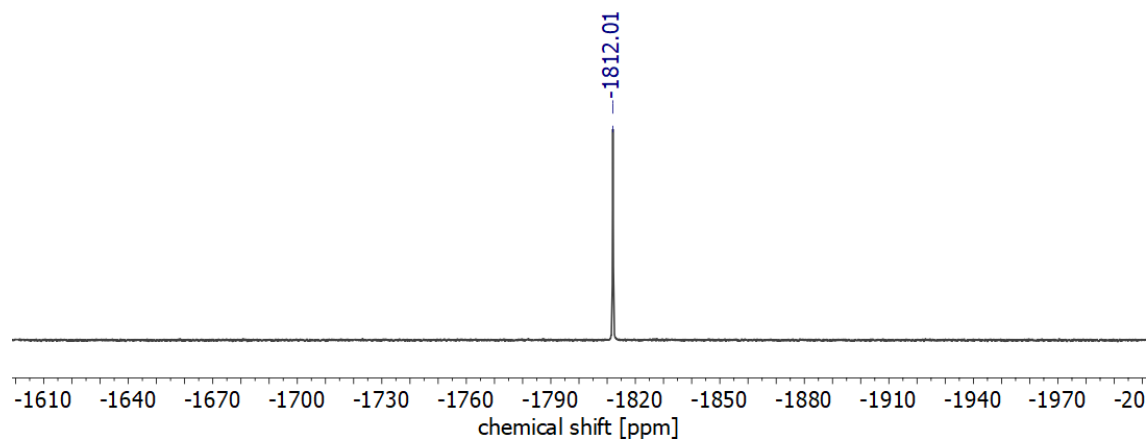
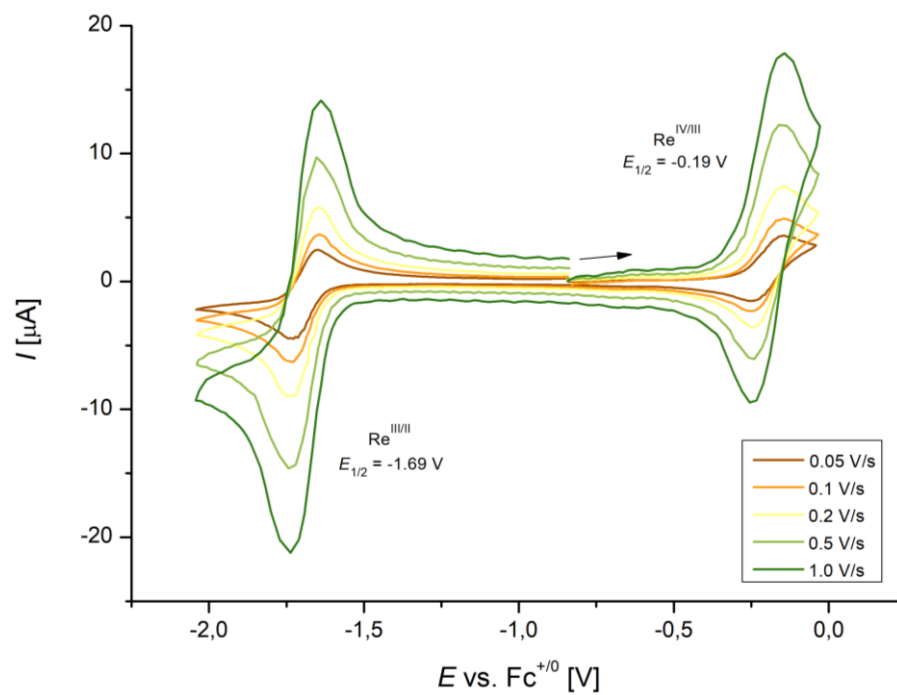


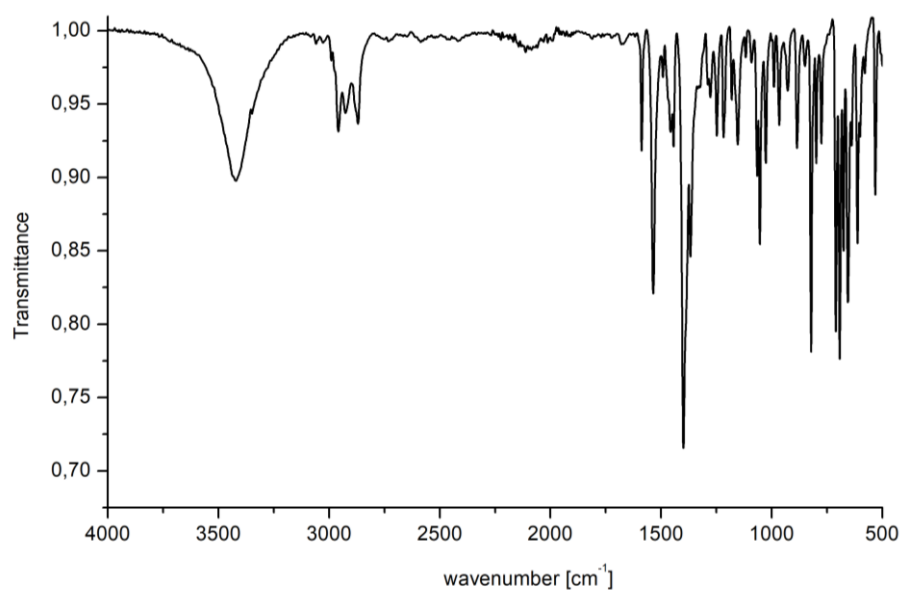
Figure 6.75 IR (ATR) spectrum of **17**.

6.1.26  $[\text{ReBr}_2\{\text{NH}(\text{CO})\text{C}_6\text{H}_5\}(\text{}^i\text{PrPN}^i\text{H}^i\text{P})]$  (**18**)Figure 6.76  $^1\text{H}\{^{31}\text{P}\}$  NMR spectrum of **18** ( $\text{C}_6\text{D}_6$ , RT).Figure 6.77  $^{13}\text{C}\{^1\text{H}\}$  NMR spectrum of **18** ( $\text{C}_6\text{D}_6$ , RT).Figure 6.78  $^{31}\text{P}\{^1\text{H}\}$  NMR spectrum of **18** ( $\text{C}_6\text{D}_6$ , RT).

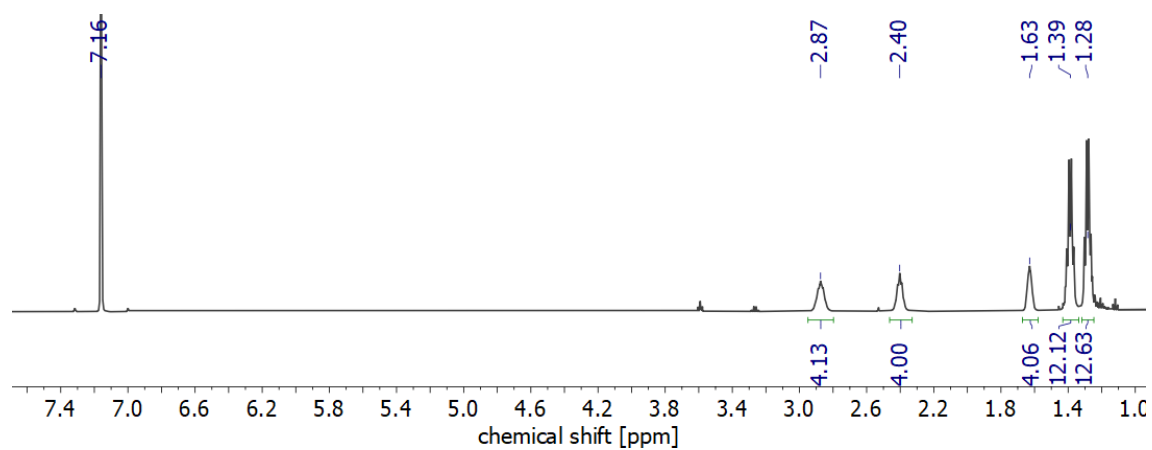
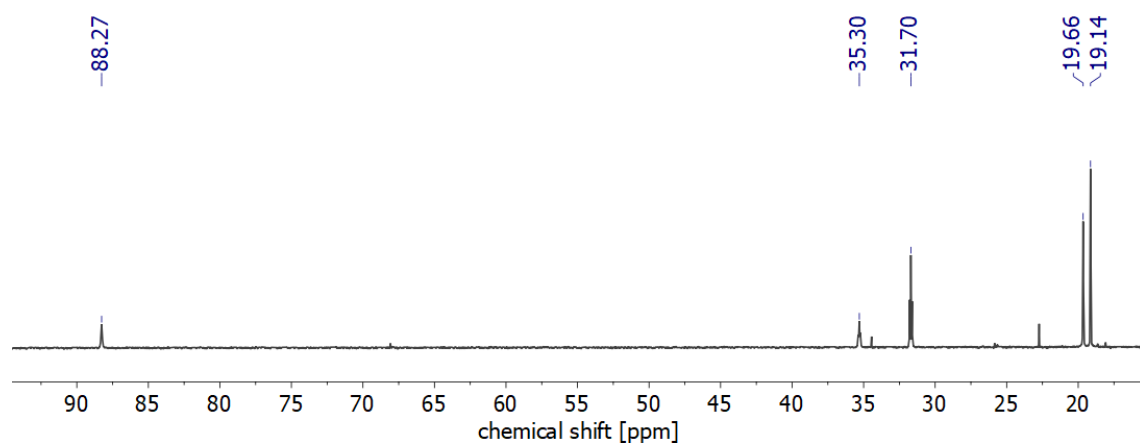
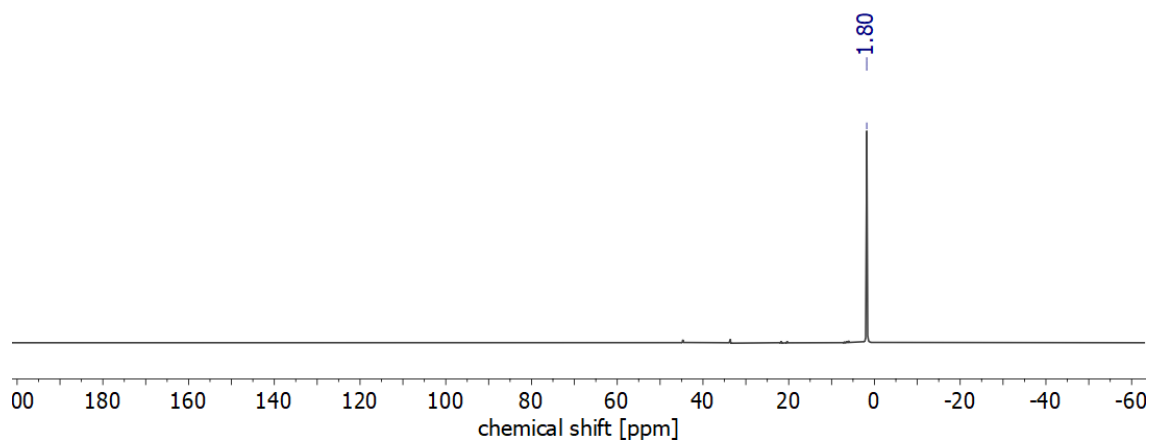




**Figure 6.79** Cyclic voltammetry of **18** (1.0 mM; electrolyte: 0.1 M  $\text{N}^t\text{Bu}_4\text{PF}_6$  in THF), referenced to ferrocene.

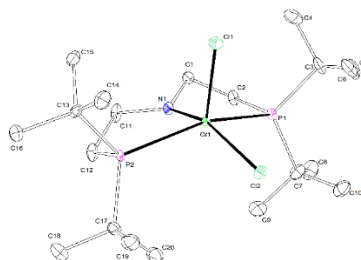


**Figure 6.80** IR (ATR) spectrum of **18**.

6.1.27 [ReBr<sub>2</sub>(<sup>i</sup>PrPNP)] (23)Figure 6.81 <sup>1</sup>H NMR spectrum of **23** (C<sub>6</sub>D<sub>6</sub>, RT).Figure 6.82 <sup>13</sup>C{<sup>1</sup>H} NMR spectrum of **23** (C<sub>6</sub>D<sub>6</sub>, RT).Figure 6.83 <sup>31</sup>P{<sup>1</sup>H} NMR spectrum of **23** (C<sub>6</sub>D<sub>6</sub>, RT).

## 6.2 Crystallographic details

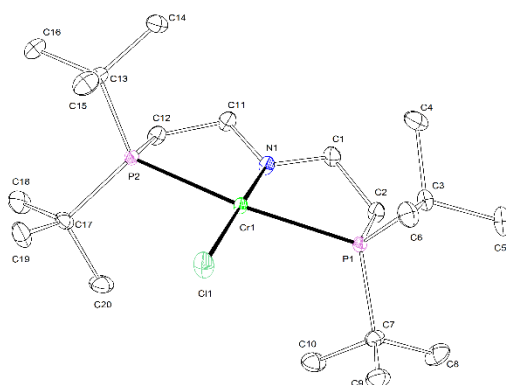
### 6.2.1 $[\text{CrCl}_2(\text{t}^{\text{Bu}}\text{PNP})]$ (1)



**Figure 6.84** Thermal ellipsoid plot of **1** with the anisotropic displacement parameters drawn at the 50% probability level. The asymmetric unit contains one complex molecule. The structure was refined using some restraints (RIGU).

**Table 6.1** Crystal data and structure refinement for **1**.

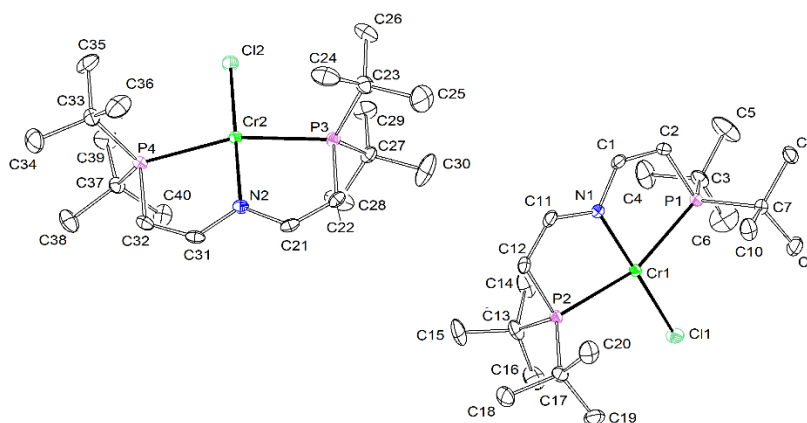
Identification code	mo_CW_FM_230117_0m_a (MF6)	
Empirical formula	$\text{C}_{20}\text{H}_{44}\text{Cl}_2\text{CrNP}_2$	
Formula weight	483.40	
Temperature	100(2) K	
Wavelength	0.71073 Å	
Crystal system	Monoclinic	
Space group	$P2_1$	
Unit cell dimensions	$a = 7.2363(4)$ Å	$\alpha = 90^\circ$
	$b = 14.4976(6)$ Å	$\beta = 92.379(3)^\circ$
	$c = 12.1320(6)$ Å	$\gamma = 90^\circ$
Volume	$1271.66(11)$ Å <sup>3</sup>	
Z	2	
Density (calculated)	$1.262$ Mg/m <sup>3</sup>	
Absorption coefficient	$0.792$ mm <sup>-1</sup>	
F(000)	518	
Crystal size	$0.187 \times 0.084 \times 0.034$ mm <sup>3</sup>	
Crystal shape and color	Plate,	clear light brown
Theta range for data collection	2.190 to 26.450°	
Index ranges	$-9 \leq h \leq 9, -18 \leq k \leq 18, -15 \leq l \leq 15$	
Reflections collected	19928	
Independent reflections	5165 [R(int) = 0.0764]	
Completeness to theta = 25.242°	99.8%	
Max. and min. transmission	0.7454 and 0.5694	
Refinement method	Full-matrix least-squares on F <sup>2</sup>	
Data / restraints / parameters	5165 / 241 / 247	
Goodness-of-fit on F <sup>2</sup>	1.140	
Final R indices [I > 2σ(I)]	R1 = 0.0527,	wR2 = 0.0915
R indices (all data)	R1 = 0.0600,	wR2 = 0.0934
Absolute structure parameter	0.028(18)	
Largest diff. peak and hole	0.659 and -0.571 eÅ <sup>-3</sup>	

6.2.2 [CrCl(<sup>t</sup>BuPNP)] (2)

**Figure 6.85** Thermal ellipsoid plot of **2** with the anisotropic displacement parameters drawn at the 50% probability level. The asymmetric unit contains one complex molecule.

**Table 6.2** Crystal data and structure refinement for **2**.

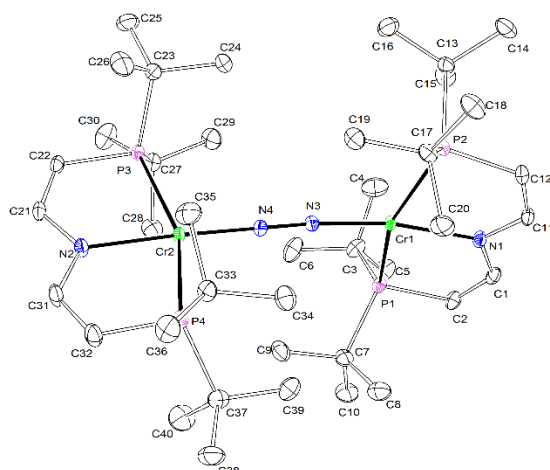
Identification code	CW_FM_100217_a (MF17)	
Empirical formula	C <sub>20</sub> H <sub>44</sub> ClCrNP <sub>2</sub>	
Formula weight	447.95	
Temperature	100(2) K	
Wavelength	0.71073 Å	
Crystal system	Orthorhombic	
Space group	Pbca	
Unit cell dimensions	a = 16.1848(4) Å	α = 90°
	b = 12.4186(3) Å	β = 90°
	c = 24.0438(6) Å	γ = 90°
Volume	4832.6(2) Å <sup>3</sup>	
Z	8	
Density (calculated)	1.231 Mg/m <sup>3</sup>	
Absorption coefficient	0.721 mm <sup>-1</sup>	
F(000)	1936	
Crystal size	0.187 x 0.162 x 0.050 mm <sup>3</sup>	
Crystal shape and color	Plate,	clear light green
Theta range for data collection	2.234 to 30.545°	
Index ranges	-22 ≤ h ≤ 23, -17 ≤ k ≤ 17, -34 ≤ l ≤ 34	
Reflections collected	118674	
Independent reflections	7382 [R(int) = 0.0945]	
Completeness to theta = 25.242°	100.0%	
Max. and min. transmission	0.7461 and 0.6924	
Refinement method	Full-matrix least-squares on F <sup>2</sup>	
Data / restraints / parameters	7382 / 0 / 238	
Goodness-of-fit on F <sup>2</sup>	1.040	
Final R indices [I > 2σ(I)]	R1 = 0.0362,	wR2 = 0.0649
R indices (all data)	R1 = 0.0621,	wR2 = 0.0729
Largest diff. peak and hole	0.422 and -0.486 eÅ <sup>-3</sup>	

6.2.3 [CrCl(<sup>t</sup>BuPNP'')] (2'')

**Figure 6.86** Thermal ellipsoid plot of **2''** with the anisotropic displacement parameters drawn at the 50% probability level. The asymmetric unit contains two complex molecules. The reflections 0 1 3 and 0 2 1 are removed from the refinement using OMIT commands.

**Table 6.3** Crystal data and structure refinement for **2''**.

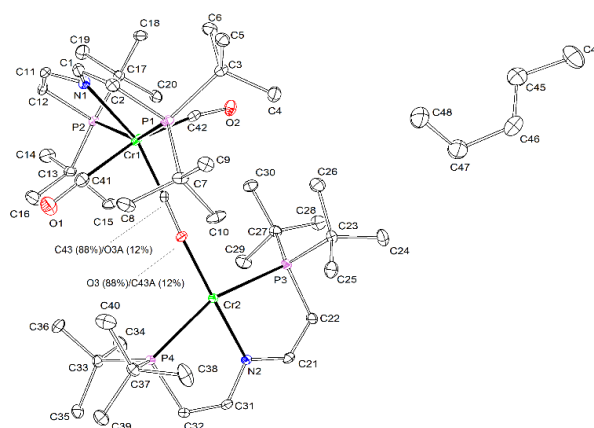
Identification code	mo_FM_FM_270417_0m_a	
Empirical formula	C <sub>20</sub> H <sub>40</sub> ClCrNP <sub>2</sub>	
Formula weight	443.92	
Temperature	100(2) K	
Wavelength	0.71073 Å	
Crystal system	Monoclinic	
Space group	P2 <sub>1</sub> /c	
Unit cell dimensions	a = 12.4430(6) Å	α = 90°
	b = 12.9738(6) Å	β = 91.124(2)°
	c = 30.1512(15) Å	γ = 90°
Volume	4866.5(4) Å <sup>3</sup>	
Z	8	
Density (calculated)	1.212 Mg/m <sup>3</sup>	
Absorption coefficient	0.716 mm <sup>-1</sup>	
F(000)	1904	
Crystal size	0.185 x 0.129 x 0.069 mm <sup>3</sup>	
Crystal shape and color	Block,	clear pale purple
Theta range for data collection	2.268 to 28.349°	
Index ranges	-16 ≤ h ≤ 16, -17 ≤ k ≤ 17, -40 ≤ l ≤ 40	
Reflections collected	139121	
Independent reflections	12132 [R(int) = 0.0948]	
Completeness to theta = 25.242°	99.9%	
Refinement method	Full-matrix least-squares on F <sup>2</sup>	
Data / restraints / parameters	12132 / 0 / 475	
Goodness-of-fit on F <sup>2</sup>	1.068	
Final R indices [I > 2σ(I)]	R1 = 0.0487,	wR2 = 0.0769
R indices (all data)	R1 = 0.0822,	wR2 = 0.0841
Largest diff. peak and hole	0.430 and -0.403 eÅ <sup>-3</sup>	

6.2.4  $[(\mu\text{-N}_2)\{\text{Cr}(\text{tBuPNP}^{\text{H}})\}_2] (3)$ 

**Figure 6.87** Thermal ellipsoid plot of **3** with the anisotropic displacement parameters drawn at the 50% probability level. The asymmetric unit contains one complex molecule.

**Table 6.4** Crystal data and structure refinement for **3**.

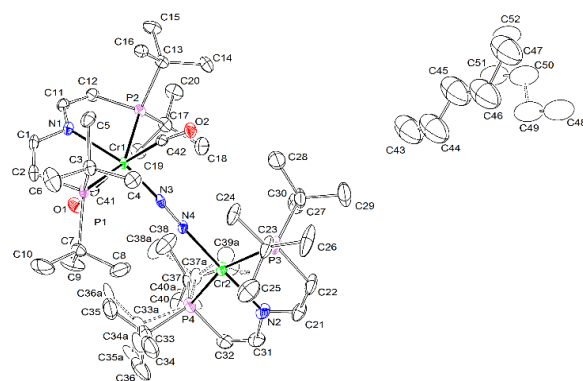
Identification code	mo_FM_FM_210617_0m_a (MF119)	
Empirical formula	$\text{C}_{40}\text{H}_{80}\text{Cr}_2\text{N}_4\text{P}_4$	
Formula weight	844.96	
Temperature	226(2) K	
Wavelength	0.71073 Å	
Crystal system	Triclinic	
Space group	P-1	
Unit cell dimensions	$a = 11.6350(6)$ Å	$\alpha = 79.702(2)^\circ$
	$b = 13.1432(8)$ Å	$\beta = 89.283(2)^\circ$
	$c = 17.0793(10)$ Å	$\gamma = 68.384(2)^\circ$
Volume	$2384.9(2)$ Å <sup>3</sup>	
Z	2	
Density (calculated)	1.177 Mg/m <sup>3</sup>	
Absorption coefficient	0.620 mm <sup>-1</sup>	
F(000)	912	
Crystal size	0.369 x 0.318 x 0.254 mm <sup>3</sup>	
Crystal shape and color	Block,	clear dark orange-red
Theta range for data collection	2.241 to 33.273°	
Index ranges	-17 ≤ h ≤ 17, -20 ≤ k ≤ 20, -26 ≤ l ≤ 26	
Reflections collected	163054	
Independent reflections	18257 [R(int) = 0.0525]	
Completeness to theta = 25.242°	99.9%	
Refinement method	Full-matrix least-squares on F <sup>2</sup>	
Data / restraints / parameters	18257 / 0 / 475	
Goodness-of-fit on F <sup>2</sup>	1.052	
Final R indices [I > 2σ(I)]	R1 = 0.0380,	wR2 = 0.0808
R indices (all data)	R1 = 0.0563,	wR2 = 0.0877
Largest diff. peak and hole	0.656 and -0.697 eÅ <sup>-3</sup>	

6.2.5  $[(\mu\text{-CO})\{\text{Cr}(\text{CO})_2(\text{tBuPNP}^{\text{''}})\}\{\text{Cr}(\text{tBuPNP}^{\text{''}})\}]$  (4)

**Figure 6.88** Thermal ellipsoid plot of **4** with the anisotropic displacement parameters drawn at the 50% probability level. The asymmetric unit contains one complex molecule and one pentane solvent molecule. An oxygen/carbon disorder inside the bridging CO ligand was refined with site occupation factors of 0.88(1) on the main domain using PART, EXYZ and EADP commands.

**Table 6.5** Crystal data and structure refinement for **4**.

Identification code	mo_FM_FM_170717_0m_a (MF151)	
Empirical formula	$\text{C}_{48}\text{H}_{92}\text{Cr}_2\text{N}_2\text{O}_3\text{P}_4$	
Formula weight	973.11	
Temperature	100(2) K	
Wavelength	0.71073 Å	
Crystal system	Triclinic	
Space group	P-1	
Unit cell dimensions	$a = 12.3899(8)$ Å	$\alpha = 71.061(3)^\circ$
	$b = 13.0663(8)$ Å	$\beta = 84.178(4)^\circ$
	$c = 20.0375(13)$ Å	$\gamma = 62.028(3)^\circ$
Volume	$2704.8(3)$ Å <sup>3</sup>	
Z	2	
Density (calculated)	1.195 Mg/m <sup>3</sup>	
Absorption coefficient	0.558 mm <sup>-1</sup>	
F(000)	1052	
Crystal size	0.390 x 0.240 x 0.200 mm <sup>3</sup>	
Crystal shape and color	Block,	dark green
Theta range for data collection	2.360 to 27.552°	
Index ranges	-16 ≤ h ≤ 16, -16 ≤ k ≤ 16, -26 ≤ l ≤ 25	
Reflections collected	96480	
Independent reflections	12401 [R(int) = 0.1325]	
Completeness to theta = 25.242°	99.9%	
Refinement method	Full-matrix least-squares on F <sup>2</sup>	
Data / restraints / parameters	12401 / 0 / 559	
Goodness-of-fit on F <sup>2</sup>	1.055	
Final R indices [I > 2σ(I)]	R1 = 0.0569,	wR2 = 0.1055
R indices (all data)	R1 = 0.1013,	wR2 = 0.1215
Largest diff. peak and hole	0.859 and -1.000 eÅ <sup>-3</sup>	

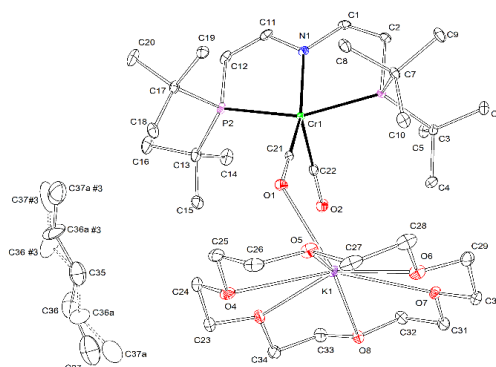
6.2.6  $[\{\text{Cr}(\text{CO})_2(\text{tBuPNP}^{\text{H}})\}(\mu\text{-N}_2)\{\text{Cr}(\text{tBuPNP}^{\text{H}})\}]$  (5)

**Figure 6.89** Thermal ellipsoid plot of **5** with the anisotropic displacement parameters drawn at the 50% probability level. The asymmetric unit contains one disordered complex molecule and a disordered pentane solvent molecule. The disordered complex molecule was refined with population of 0.74(2) on the main domain using some restraints and constraints (SADI, RIGU, EADP). The disordered pentane solvent molecule was refined with population of 0.708(4) on the main domain using some restraints and constraints (SADI, RIGU, EADP).

**Table 6.6** Crystal data and structure refinement for **5**.

Identification code	mo_FM_FM_251018_0m_a (MFb148)	
Empirical formula	$\text{C}_{47}\text{H}_{92}\text{Cr}_2\text{N}_4\text{O}_2\text{P}_4$	
Formula weight	973.12	
Temperature	100(2) K	
Wavelength	0.71073 Å	
Crystal system	Monoclinic	
Space group	$P2_1/c$	
Unit cell dimensions	$a = 12.2508(5)$ Å	$\alpha = 90^\circ$
	$b = 20.0120(8)$ Å	$\beta = 97.773(2)^\circ$
	$c = 23.1799(9)$ Å	$\gamma = 90^\circ$
Volume	$5630.6(4)$ Å <sup>3</sup>	
Z	4	
Density (calculated)	1.148 Mg/m <sup>3</sup>	
Absorption coefficient	0.536 mm <sup>-1</sup>	
F(000)	2104	
Crystal size	0.239 x 0.142 x 0.110 mm <sup>3</sup>	
Crystal shape and color	Plate,	clear dark green
Theta range for data collection	2.220 to 28.355°	
Index ranges	-16 ≤ h ≤ 16, -26 ≤ k ≤ 26, -30 ≤ l ≤ 30	
Reflections collected	152977	
Independent reflections	14052 [R(int) = 0.0823]	
Completeness to theta = 25.242°	99.9%	
Refinement method	Full-matrix least-squares on F <sup>2</sup>	
Data / restraints / parameters	14052 / 126 / 619	
Goodness-of-fit on F <sup>2</sup>	1.064	
Final R indices [I > 2σ(I)]	R1 = 0.0463,	wR2 = 0.1100
R indices (all data)	R1 = 0.0716,	wR2 = 0.1246
Largest diff. peak and hole	1.296 and -1.161 eÅ <sup>-3</sup>	

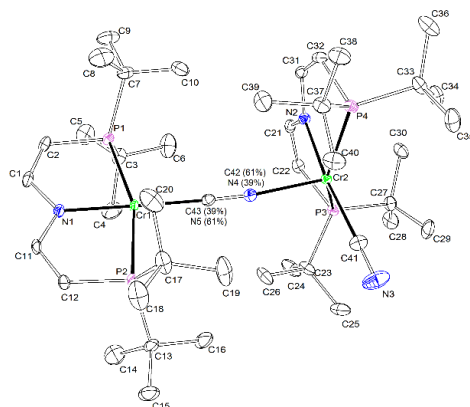


6.2.7  $[\text{Cr}(\text{CO})_2(\text{tBuPNP}^{\text{'''}})]\text{K}(\text{18c6})$  (**6**)

**Figure 6.90** Thermal ellipsoid plot of **6** with the anisotropic displacement parameters drawn at the 50% probability level. The asymmetric unit contains one complex molecule, a crown ether molecule that ligates one potassium ion, and a half-disordered pentane solvent molecule. The disordered solvent molecule was refined with site occupation factors of 0.5 for both sites using some restraints (SADI).

**Table 6.7** Crystal data and structure refinement for **6**.

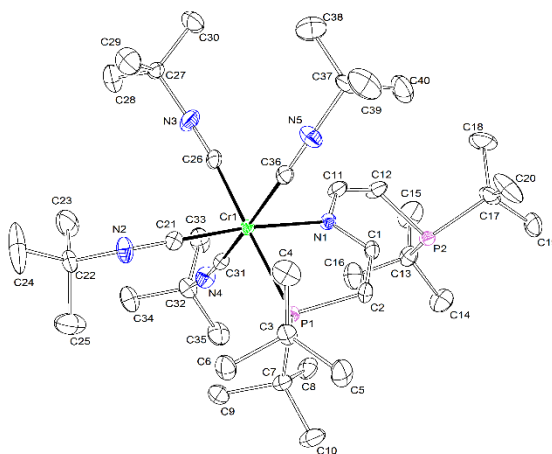
Identification code	FM_FM_080318_a (MFb83)	
Empirical formula	$\text{C}_{34}\text{H}_{64}\text{CrKNO}_8\text{P}_2 * \frac{1}{2} \text{C}_5\text{H}_{12}$	
Formula weight	803.97	
Temperature	100(2) K	
Wavelength	0.71073 Å	
Crystal system	Monoclinic	
Space group	C2/c	
Unit cell dimensions	$a = 27.3015(11)$ Å	$\alpha = 90^\circ$
	$b = 19.3792(8)$ Å	$\beta = 116.8090(10)^\circ$
	$c = 18.4292(7)$ Å	$\gamma = 90^\circ$
Volume	$8702.5(6)$ Å <sup>3</sup>	
Z	8	
Density (calculated)	1.227 Mg/m <sup>3</sup>	
Absorption coefficient	0.477 mm <sup>-1</sup>	
F(000)	3464	
Crystal size	$0.229 \times 0.190 \times 0.131$ mm <sup>3</sup>	
Crystal shape and color	block,	clear pale pink blue
Theta range for data collection	2.279 to 28.337°	
Index ranges	$-36 \leq h \leq 36, -25 \leq k \leq 25, -23 \leq l \leq 24$	
Reflections collected	156218	
Independent reflections	10863 [R(int) = 0.1055]	
Completeness to theta = 25.242°	99.9%	
Refinement method	Full-matrix least-squares on F <sup>2</sup>	
Data / restraints / parameters	10863 / 6 / 480	
Goodness-of-fit on F <sup>2</sup>	1.035	
Final R indices [I > 2sigma(I)]	R1 = 0.0387,	wR2 = 0.0712
R indices (all data)	R1 = 0.0615,	wR2 = 0.0776
Largest diff. peak and hole	0.365 and -0.470 eÅ <sup>-3</sup>	

6.2.8  $\{[\text{Cr}(\text{CN})(\text{t}^{\text{Bu}}\text{PNP}^{\text{'''}})](\mu\text{-CN})[\text{Cr}(\text{t}^{\text{Bu}}\text{PNP}^{\text{'''}})]\}$  (7)

**Figure 6.91** Thermal ellipsoid plot of **7** with the anisotropic displacement parameters drawn at the 50% probability level. The asymmetric unit contains one complex molecule. A nitrogen/carbon disorder inside the complex molecule was refined with population of 0.62(2) on the main domain using constraints (EXYZ, EADP).

**Table 6.8** Crystal data and structure refinement for **7**.

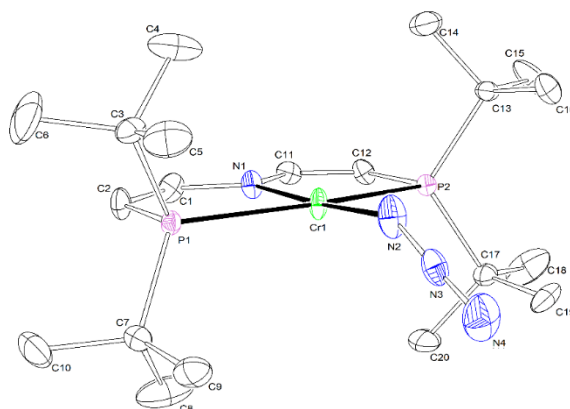
Identification code	mo_FM_FM_140917_0m_a (MFb24)	
Empirical formula	$\text{C}_{42}\text{H}_{80}\text{Cr}_2\text{N}_4\text{P}_4$	
Formula weight	868.98	
Temperature	100(2) K	
Wavelength	0.71073 Å	
Crystal system	Monoclinic	
Space group	$P2_1/c$	
Unit cell dimensions	$a = 15.4600(8)$ Å	$\alpha = 90^\circ$
	$b = 19.6971(8)$ Å	$\beta = 100.177(2)^\circ$
	$c = 16.7519(9)$ Å	$\gamma = 90^\circ$
Volume	$5021.0(4)$ Å <sup>3</sup>	
Z	4	
Density (calculated)	1.150 Mg/m <sup>3</sup>	
Absorption coefficient	$0.590$ mm <sup>-1</sup>	
F(000)	1872	
Crystal size	$0.241 \times 0.123 \times 0.114$ mm <sup>3</sup>	
Crystal shape and color	Block,	clear orange
Theta range for data collection	2.229 to 26.439°	
Index ranges	$-19 \leq h \leq 19$ , $-24 \leq k \leq 24$ , $-20 \leq l \leq 20$	
Reflections collected	78687	
Independent reflections	10294 [R(int) = 0.0642]	
Completeness to theta = 25.242°	99.9%	
Refinement method	Full-matrix least-squares on F <sup>2</sup>	
Data / restraints / parameters	10294 / 0 / 494	
Goodness-of-fit on F <sup>2</sup>	1.059	
Final R indices [I > 2σ(I)]	R1 = 0.0320,	wR2 = 0.0661
R indices (all data)	R1 = 0.0465,	wR2 = 0.0719
Largest diff. peak and hole	0.351 and -0.320 eÅ <sup>-3</sup>	

6.2.9  $[\text{Cr}(\text{CN}^t\text{Bu})_4(\chi^2\text{-}^t\text{BuPNP}^{\prime\prime})]$  (**8**)

**Figure 6.92** Thermal ellipsoid plot of **8** with the anisotropic displacement parameters drawn at the 50% probability level. The asymmetric unit contains one complex molecule.

**Table 6.9** Crystal data and structure refinement for **8**.

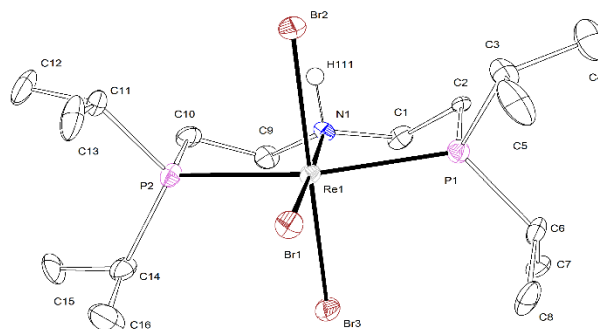
Identification code	FM_FM_040917 (MFb25)	
Empirical formula	$\text{C}_{40}\text{H}_{76}\text{CrN}_5\text{P}_2$	
Formula weight	740.99	
Temperature	100(2) K	
Wavelength	0.71073 Å	
Crystal system	Monoclinic	
Space group	$P2_1/c$	
Unit cell dimensions	$a = 22.0379(10)$ Å	$\alpha = 90^\circ$
	$b = 11.7562(6)$ Å	$\beta = 93.081(2)^\circ$
	$c = 17.7175(9)$ Å	$\gamma = 90^\circ$
Volume	$4583.6(4)$ Å <sup>3</sup>	
Z	4	
Density (calculated)	$1.074$ Mg/m <sup>3</sup>	
Absorption coefficient	$0.350$ mm <sup>-1</sup>	
F(000)	1620	
Crystal size	$0.375 \times 0.257 \times 0.086$ mm <sup>3</sup>	
Crystal shape and color	Block,	clear dark green
Theta range for data collection	$2.251$ to $29.225^\circ$	
Index ranges	$-30 \leq h \leq 30$ , $-16 \leq k \leq 16$ , $-23 \leq l \leq 24$	
Reflections collected	150334	
Independent reflections	12432 [R(int) = 0.1271]	
Completeness to theta = $25.242^\circ$	100.0%	
Refinement method	Full-matrix least-squares on $F^2$	
Data / restraints / parameters	12432 / 0 / 457	
Goodness-of-fit on $F^2$	1.048	
Final R indices [I > 2σ(I)]	R1 = 0.0444,	wR2 = 0.0917
R indices (all data)	R1 = 0.0746,	wR2 = 0.1028
Largest diff. peak and hole	$0.401$ and $-0.595$ Å <sup>-3</sup>	

6.2.10 [CrN<sub>3</sub>(<sup>Bu</sup>PNP<sup>'''</sup>)] (9)

**Figure 6.93** Thermal ellipsoid plot of **9** with the anisotropic displacement parameters drawn at the 50% probability level. The asymmetric unit contains one complex molecule. The reflections -1 1 3, 0 -7 5, 0 -3 5 and 3 -5 9 are removed from the refinement using OMIT commands.

**Table 6.10** Crystal data and structure refinement for **9**.

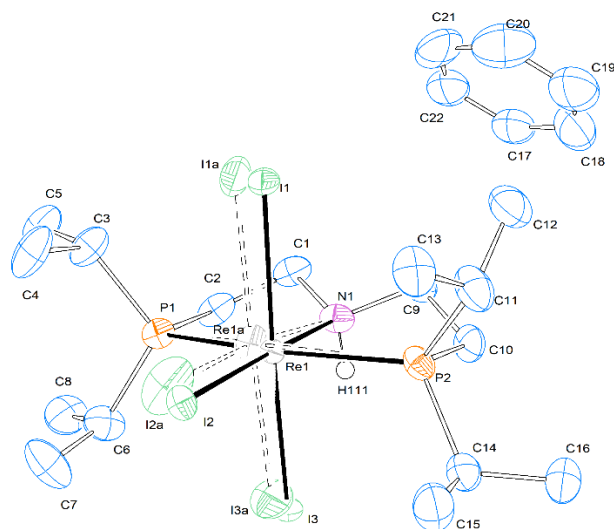
Identification code	mo_FM_FM_110817_0m_a (MFb11)	
Empirical formula	C <sub>20</sub> H <sub>40</sub> CrN <sub>4</sub> P <sub>2</sub>	
Formula weight	450.50	
Temperature	100(2) K	
Wavelength	0.71073 Å	
Crystal system	Triclinic	
Space group	P-1	
Unit cell dimensions	a = 8.3176(5) Å	α = 102.666(2)°
	b = 12.5035(8) Å	β = 96.166(2)°
	c = 12.6672(8) Å	γ = 104.342(2)°
Volume	1226.90(13) Å <sup>3</sup>	
Z	2	
Density (calculated)	1.219 Mg/m <sup>3</sup>	
Absorption coefficient	0.609 mm <sup>-1</sup>	
F(000)	484	
Crystal size	0.303 x 0.297 x 0.276 mm <sup>3</sup>	
Crystal shape and color	Block, clear dark orange-purple	
Theta range for data collection	2.565 to 26.489°	
Index ranges	-10 ≤ h ≤ 10, -15 ≤ k ≤ 15, -15 ≤ l ≤ 15	
Reflections collected	42662	
Independent reflections	5062 [R(int) = 0.0870]	
Completeness to theta = 25.242°	99.8%	
Refinement method	Full-matrix least-squares on F <sup>2</sup>	
Data / restraints / parameters	5062 / 0 / 256	
Goodness-of-fit on F <sup>2</sup>	1.136	
Final R indices [I > 2σ(I)]	R1 = 0.0559,	wR2 = 0.1149
R indices (all data)	R1 = 0.0771,	wR2 = 0.1225
Largest diff. peak and hole	0.672 and -0.452 eÅ <sup>-3</sup>	

6.2.11 [ReBr<sub>3</sub>(<sup>i</sup>PrPN<sup>H</sup>P)] (10<sup>Br</sup>)

**Figure 6.94** Thermal ellipsoid plot of **10<sup>Br</sup>** with the anisotropic displacement parameters drawn at the 50% probability level. The asymmetric unit contains one complex molecule. The N-H hydrogen atom was refined isotropically on calculated position using AFIX 13 command.

**Table 6.11** Crystal data and structure refinement for **10<sup>Br</sup>**.

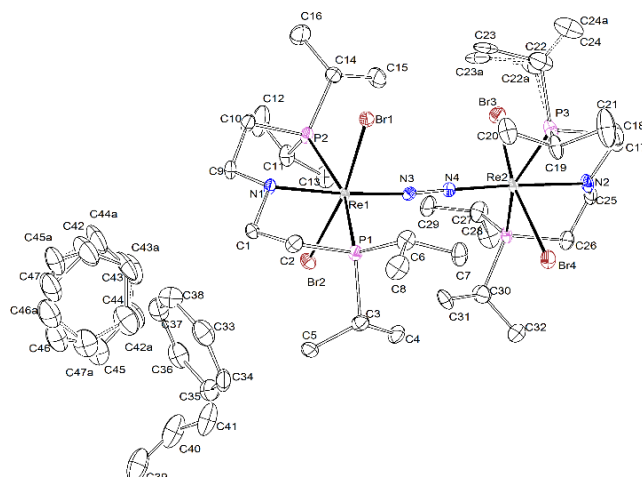
Identification code	mo_FM_FM_070319_0m_b (NP-V80)	
Empirical formula	C <sub>16</sub> H <sub>37</sub> Br <sub>3</sub> NP <sub>2</sub> Re	
Formula weight	731.33	
Temperature	100(2) K	
Wavelength	0.71073 Å	
Crystal system	Orthorhombic	
Space group	P2 <sub>1</sub> 2 <sub>1</sub> 2 <sub>1</sub>	
Unit cell dimensions	a = 7.4411(7) Å	α = 90°
	b = 13.3625(12) Å	β = 90°
	c = 23.954(2) Å	γ = 90°
Volume	2381.8(4) Å <sup>3</sup>	
Z	4	
Density (calculated)	2.040 Mg/m <sup>3</sup>	
Absorption coefficient	10.269 mm <sup>-1</sup>	
F(000)	1400	
Crystal size	0.164 x 0.139 x 0.116 mm <sup>3</sup>	
Crystal shape and color	Block, clear intense red-brown	
Theta range for data collection	2.284 to 30.493°	
Index ranges	-9 ≤ h ≤ 10, -19 ≤ k ≤ 19, -34 ≤ l ≤ 30	
Reflections collected	33704	
Independent reflections	7004 [R(int) = 0.1518]	
Completeness to theta = 25.242°	96.8%	
Refinement method	Full-matrix least-squares on F <sup>2</sup>	
Data / restraints / parameters	7004 / 0 / 216	
Goodness-of-fit on F <sup>2</sup>	0.981	
Final R indices [I > 2σ(I)]	R1 = 0.0461,	wR2 = 0.0700
R indices (all data)	R1 = 0.0883,	wR2 = 0.0808
Absolute structure parameter	0.015(13)	
Largest diff. peak and hole	1.897 and -1.892 eÅ <sup>-3</sup>	

6.2.12 [ReI<sub>3</sub>(<sup>Pr</sup>PN<sup>H</sup>P)] (10<sup>I</sup>)

**Figure 6.95** Thermal ellipsoid plot of **10<sup>I</sup>** with the anisotropic displacement parameters drawn at the 50% probability level. The asymmetric unit contains one disordered complex molecule and one solvent (benzene) molecule. The disordered complex molecule was refined with population of 0.88971 on the main domain using some restraints (RIGU).

**Table 6.12** Crystal data and structure refinement for **10<sup>I</sup>**.

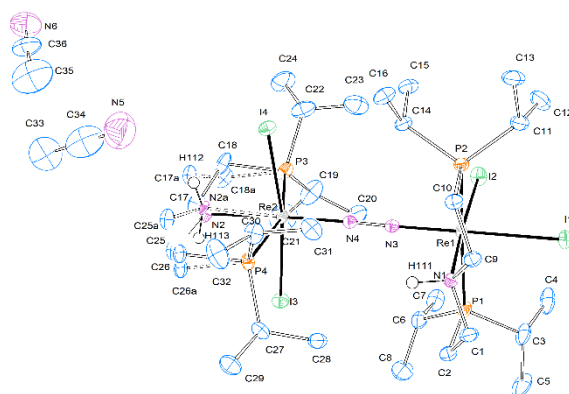
Identification code	mo_FM_220121_FM_0m_a	(MFe205)
Empirical formula	C <sub>22</sub> H <sub>43</sub> I <sub>3</sub> NP <sub>2</sub> Re	
Formula weight	950.41	
Temperature	100(2) K	
Wavelength	0.71073 Å	
Crystal system	Monoclinic	
Space group	P2 <sub>1</sub> /c	
Unit cell dimensions	a = 7.6780(8) Å	α = 90°
	b = 14.6392(15) Å	β = 93.831(4)°
	c = 26.572(3) Å	γ = 90°
Volume	2980.0(5) Å <sup>3</sup>	
Z	4	
Density (calculated)	2.118 Mg/m <sup>3</sup>	
Absorption coefficient	7.303 mm <sup>-1</sup>	
F(000)	1784	
Crystal size	0.308 x 0.209 x 0.060 mm <sup>3</sup>	
Crystal shape and color	Block, red	
Theta range for data collection	2.073 to 25.681°	
Index ranges	-9 ≤ h ≤ 9, -17 ≤ k ≤ 17, -32 ≤ l ≤ 32	
Reflections collected	146950	
Independent reflections	5660 [R(int) = 0.0683]	
Completeness to theta = 25.242°	100.0%	
Refinement method	Full-matrix least-squares on F <sup>2</sup>	
Data / restraints / parameters	5660 / 260 / 307	
Goodness-of-fit on F <sup>2</sup>	1.163	
Final R indices [I > 2σ(I)]	R1 = 0.0252,	wR2 = 0.0449
R indices (all data)	R1 = 0.0287,	wR2 = 0.0457
Largest diff. peak and hole	0.845 and -0.840 e.Å <sup>-3</sup>	

6.2.13  $[(\mu\text{-N}_2)\{\text{ReBr}_2(\text{PrPN}^{\text{H}}\text{P})\}_2] (\mathbf{11}^{\text{Br}})$ 

**Figure 6.96** Thermal ellipsoid plot of  $\mathbf{11}^{\text{Br}}$  with the anisotropic displacement parameters drawn at the 50% probability level. The asymmetric unit contains one disordered complex and two and a half benzene solvent molecules. The disordered complex molecule and one benzene solvent molecule were refined with a population of 0.55(1) on the main domain using some restraints and constraints (RIGU, SADI, SIMU).

**Table 6.13** Crystal data and structure refinement for  $\mathbf{11}^{\text{Br}}$ .

Identification code	FM_FM_091019 (MFC108)	
Empirical formula	$\text{C}_{47}\text{H}_{89}\text{Br}_4\text{N}_4\text{P}_4\text{Re}_2$	
Formula weight	1526.14	
Temperature	100(2) K	
Wavelength	0.71073 Å	
Crystal system	Triclinic	
Space group	P-1	
Unit cell dimensions	$a = 13.2866(6)$ Å	$\alpha = 99.1370(10)^\circ$
	$b = 14.5839(6)$ Å	$\beta = 92.399(2)^\circ$
	$c = 15.2359(6)$ Å	$\gamma = 102.956(2)^\circ$
Volume	$2831.4(2)$ Å <sup>3</sup>	
Z	2	
Density (calculated)	1.790 Mg/m <sup>3</sup>	
Absorption coefficient	7.241 mm <sup>-1</sup>	
F(000)	1498	
Crystal size	0.186 x 0.131 x 0.050 mm <sup>3</sup>	
Crystal shape and color	Plate,	clear blue
Theta range for data collection	2.245 to 28.429°	
Index ranges	-17 ≤ h ≤ 17, -19 ≤ k ≤ 19, -20 ≤ l ≤ 20	
Reflections collected	101618	
Independent reflections	14162 [R(int) = 0.0640]	
Completeness to theta = 25.242°	99.9%	
Refinement method	Full-matrix least-squares on F <sup>2</sup>	
Data / restraints / parameters	14162 / 348 / 627	
Goodness-of-fit on F <sup>2</sup>	1.047	
Final R indices [I > 2σ(I)]	R1 = 0.0299,	wR2 = 0.0566
R indices (all data)	R1 = 0.0502,	wR2 = 0.0655
Largest diff. peak and hole	2.275 and -1.676 eÅ <sup>-3</sup>	

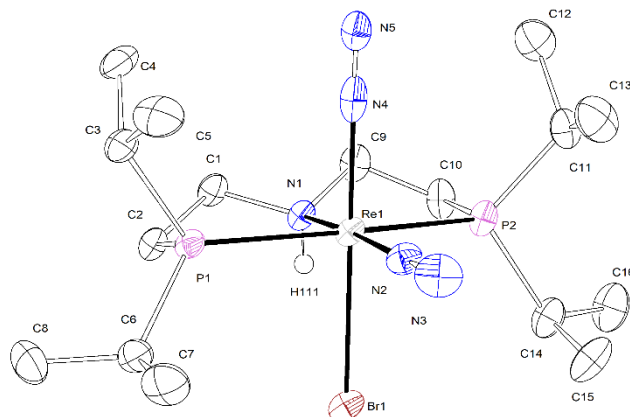
6.2.14  $[(\mu\text{-N}_2)\{\text{ReI}_2(\text{P}^{\text{r}}\text{PN}^{\text{H}}\text{P})\}_2]$  (**11<sup>I</sup>**)

**Figure 1.** Thermal ellipsoid plot of **11<sup>I</sup>** with the anisotropic displacement parameters drawn at the 50% probability level. The asymmetric unit contains one disordered complex molecule. The disordered complex molecule was refined with population of 0.74795 on the main domain using some restraints and constraints (RIGU, EADP).

**Table 6.14** Crystal data and structure refinement for **11<sup>I</sup>**.

Identification code	FM_270121_FM (MFe66)	
Empirical formula	$\text{C}_{35.75}\text{H}_{80}\text{I}_4\text{N}_{5.75}\text{P}_4\text{Re}_2$	
Formula weight	1594.38	
Temperature	100(2) K	
Wavelength	0.71073 Å	
Crystal system	Triclinic	
Space group	P-1	
Unit cell dimensions	$a = 13.1148(6)$ Å	$\alpha = 86.875(2)^\circ$
	$b = 13.5836(7)$ Å	$\beta = 75.809(2)^\circ$
	$c = 17.0260(7)$ Å	$\gamma = 62.360(2)^\circ$
Volume	$2598.8(2)$ Å <sup>3</sup>	
Z	2	
Density (calculated)	2.038 Mg/m <sup>3</sup>	
Absorption coefficient	7.183 mm <sup>-1</sup>	
F(000)	1513	
Crystal size	0.255 x 0.218 x 0.164 mm <sup>3</sup>	
Crystal shape and color	Block, green	
Theta range for data collection	1.81 to 26.37°	
Index ranges	-16 ≤ h ≤ 16, -16 ≤ k ≤ 16, -21 ≤ l ≤ 21	
Reflections collected	187694	
Independent reflections	10616 [R(int) = 0.0462]	
Completeness to theta = 26.37°	99.9%	
Absorption correction	Semi-empirical from equivalents	
Refinement method	Full-matrix least-squares on F <sup>2</sup>	
Data / restraints / parameters	10616 / 423 / 509	
Goodness-of-fit on F <sup>2</sup>	1.102	
Final R indices [I > 2σ(I)]	R1 = 0.0186,	wR2 = 0.0419
R indices (all data)	R1 = 0.0202,	wR2 = 0.0427
Largest diff. peak and hole	1.747 and -1.168 eÅ <sup>-3</sup>	

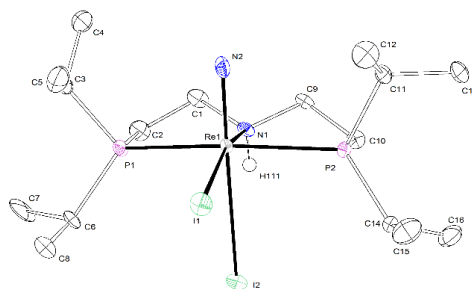


6.2.15  $[\text{ReBr}(\text{N}_2)_2(\text{PrPN}^{\text{H}}\text{P})]$  (12)

**Figure 6.97** Thermal ellipsoid plot of **12** with the anisotropic displacement parameters drawn at the 50% probability level. The asymmetric unit contains one complex molecule which was refined by using some restraints and constraints (SADI, RIGU, EADP). The N-H hydrogen atom was found from the residual density map and isotropically refined.

**Table 6.15** Crystal data and structure refinement for **12**.

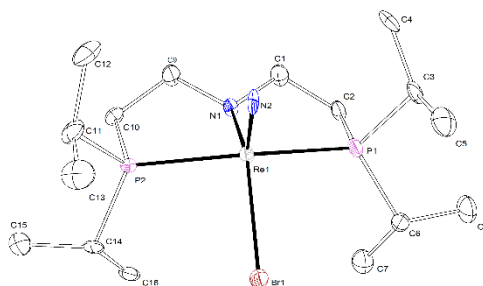
Identification code	FM_FM_160221 (Mfd97)	
Empirical formula	$\text{C}_{16}\text{H}_{37}\text{BrN}_5\text{P}_2\text{Re}$	
Formula weight	627.55	
Temperature	100(2) K	
Wavelength	0.71073 Å	
Crystal system	Monoclinic	
Space group	P 1 21/n 1	
Unit cell dimensions	$a = 8.3268(3)$ Å	$\alpha = 90^\circ$
	$b = 12.9651(5)$ Å	$\beta = 96.2130(10)^\circ$
	$c = 21.5249(8)$ Å	$\gamma = 90^\circ$
Volume	$2310.13(15)$ Å <sup>3</sup>	
Z	4	
Density (calculated)	1.804 Mg/m <sup>3</sup>	
Absorption coefficient	7.138 mm <sup>-1</sup>	
F(000)	1232	
Crystal size	0.116 x 0.111 x 0.102 mm <sup>3</sup>	
Crystal shape and color	Plate, green	
Theta range for data collection	2.47 to 25.68°	
Index ranges	$-10 \leq h \leq 8$ , $-15 \leq k \leq 15$ , $-26 \leq l \leq 26$	
Reflections collected	61471	
Independent reflections	4383 [R(int) = 0.0442]	
Completeness to theta = 25.68°	99.9%	
Max. and min. transmission	0.53 and 0.49	
Refinement method	Full-matrix least-squares on F <sup>2</sup>	
Data / restraints / parameters	4383 / 180 / 233	
Goodness-of-fit on F <sup>2</sup>	1.095	
Final R indices [I > 2σ(I)]	R1 = 0.0209,	wR2 = 0.0422
R indices (all data)	R1 = 0.0266,	wR2 = 0.0445
Largest diff. peak and hole	1.065 and -1.081 e.Å <sup>-3</sup>	

6.2.16 [ReI<sub>2</sub>N(<sup>i</sup>PrPN<sup>H</sup>P)] (13<sup>I</sup>)

**Figure 6.98** Thermal ellipsoid plot of **13<sup>I</sup>** with the anisotropic displacement parameters drawn at the 50% probability level. The asymmetric unit contains one complex molecule and was refined with some restraints (RIGU). The N-H hydrogen atom was found from the residual density map and isotropically refined.

**Table 6.16** Crystal data and structure refinement for **13<sup>I</sup>**.

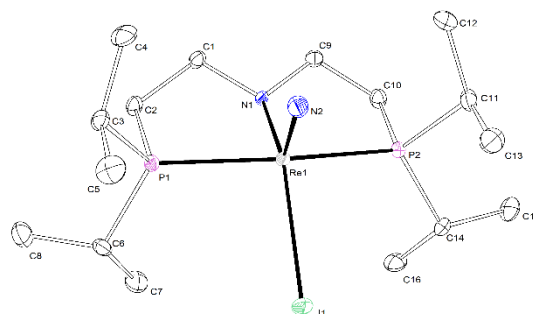
Identification code	mo_FM_FM_260619_0m_a (MFC59)	
Empirical formula	C <sub>16</sub> H <sub>37</sub> I <sub>2</sub> N <sub>2</sub> P <sub>2</sub> Re	
Formula weight	759.41	
Temperature	100(2) K	
Wavelength	0.71073 Å	
Crystal system	Monoclinic	
Space group	P2 <sub>1</sub> /n	
Unit cell dimensions	a = 8.2556(7) Å	α = 90°
	b = 14.1438(11) Å	β = 98.271(3)°
	c = 20.5753(18) Å	γ = 90°
Volume	2377.5(3) Å <sup>3</sup>	
Z	4	
Density (calculated)	2.122 Mg/m <sup>3</sup>	
Absorption coefficient	7.845 mm <sup>-1</sup>	
F(000)	1432	
Crystal size	0.136 x 0.041 x 0.031 mm <sup>3</sup>	
Crystal shape and color	Needle,	clear orange
Theta range for data collection	2.465 to 26.406°	
Index ranges	-10 ≤ h ≤ 10, -17 ≤ k ≤ 17, -25 ≤ l ≤ 25	
Reflections collected	57648	
Independent reflections	4881 [R(int) = 0.1224]	
Completeness to theta = 25.242°	100.0%	
Refinement method	Full-matrix least-squares on F <sup>2</sup>	
Data / restraints / parameters	4881 / 210 / 220	
Goodness-of-fit on F <sup>2</sup>	1.112	
Final R indices [I > 2σ(I)]	R1 = 0.0421	wR2 = 0.0656
R indices (all data)	R1 = 0.0603	wR2 = 0.0694
Extinction coefficient	n/a	
Largest diff. peak and hole	1.228 and -1.767 e.Å <sup>-3</sup>	

6.2.17 [ReBrN(<sup>i</sup>P<sub>r</sub>PNP)] (14<sup>Br</sup>)

**Figure 6.99** Thermal ellipsoid plot of **14<sup>Br</sup>** with the anisotropic displacement parameters drawn at the 50% probability level. The asymmetric unit contains one complex molecule and was refined using some restraints (RIGU, SIMU).

**Table 6.17** Crystal data and structure refinement for **14<sup>Br</sup>**.

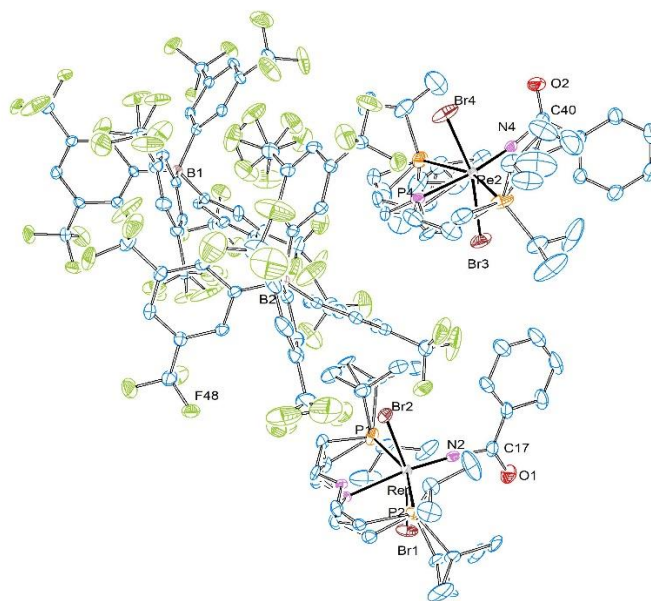
Identification code	mo_FM_FM_170619_0m_e (MF_PW_31)	
Empirical formula	C <sub>16</sub> H <sub>36</sub> BrN <sub>2</sub> P <sub>2</sub> Re	
Formula weight	584.52	
Temperature	131(2) K	
Wavelength	0.71073 Å	
Crystal system	Monoclinic	
Space group	Cc	
Unit cell dimensions	a = 11.0966(11) Å	α = 90°
	b = 13.6383(14) Å	β = 102.007(3)°
	c = 14.5765(13) Å	γ = 90°
Volume	2157.7(4) Å <sup>3</sup>	
Z	4	
Density (calculated)	1.799 Mg/m <sup>3</sup>	
Absorption coefficient	7.631 mm <sup>-1</sup>	
F(000)	1144	
Crystal size	0.083 x 0.064 x 0.052 mm <sup>3</sup>	
Crystal shape and color	Block,	clear pale yellow
Theta range for data collection	2.398 to 26.377°	
Index ranges	-12 ≤ h ≤ 13, -16 ≤ k ≤ 16, -18 ≤ l ≤ 18	
Reflections collected	5905	
Independent reflections	3873 [R(int) = 0.0504]	
Completeness to theta = 25.242°	99.6%	
Refinement method	Full-matrix least-squares on F <sup>2</sup>	
Data / restraints / parameters	3873 / 206 / 207	
Goodness-of-fit on F <sup>2</sup>	0.946	
Final R indices [I > 2σ(I)]	R1 = 0.0396,	wR2 = 0.0688
R indices (all data)	R1 = 0.0592,	wR2 = 0.0744
Absolute structure parameter	0.020(15)	
Largest diff. peak and hole	1.530 and -1.223 eÅ <sup>-3</sup>	

6.2.18 [ReIN(<sup>IP</sup>rPNP)] (14<sup>I</sup>)

**Figure 6.100** Thermal ellipsoid plot of **14<sup>I</sup>** with the anisotropic displacement parameters drawn at the 50% probability level. The asymmetric unit contains one complex molecule.

**Table 6.18** Crystal data and structure refinement for **14<sup>I</sup>**.

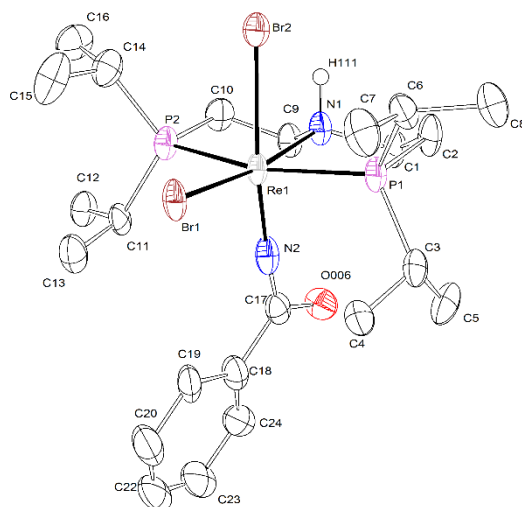
Identification code	mo_FM_FM_230719_0m_a (MFC61)	
Empirical formula	C <sub>16</sub> H <sub>36</sub> IN <sub>2</sub> P <sub>2</sub> Re	
Formula weight	631.51	
Temperature	102(2) K	
Wavelength	0.71073 Å	
Crystal system	Monoclinic	
Space group	P2 <sub>1</sub> /c	
Unit cell dimensions	a = 9.0780(5) Å	α = 90°
	b = 13.1917(7) Å	β = 93.648(3)°
	c = 18.1107(10) Å	γ = 90°
Volume	2164.4(2) Å <sup>3</sup>	
Z	4	
Density (calculated)	1.938 Mg/m <sup>3</sup>	
Absorption coefficient	7.188 mm <sup>-1</sup>	
F(000)	1216	
Crystal size	0.261 x 0.204 x 0.133 mm <sup>3</sup>	
Crystal shape and color	Block,	clear light orange
Theta range for data collection	2.248 to 30.507°	
Index ranges	-12 ≤ h ≤ 12, -18 ≤ k ≤ 18, -25 ≤ l ≤ 25	
Reflections collected	116653	
Independent reflections	6582 [R(int) = 0.0927]	
Completeness to theta = 25.242°	100.0%	
Refinement method	Full-matrix least-squares on F <sup>2</sup>	
Data / restraints / parameters	6582 / 0 / 207	
Goodness-of-fit on F <sup>2</sup>	1.076	
Final R indices [I > 2σ(I)]	R1 = 0.0269,	wR2 = 0.0512
R indices (all data)	R1 = 0.0453,	wR2 = 0.0573
Largest diff. peak and hole	1.828 and -2.000 eÅ <sup>-3</sup>	

6.2.19 [ReBr<sub>2</sub>{N(CO)C<sub>6</sub>H<sub>5</sub>}(<sup>i</sup>PrPN<sup>H</sup>P)][BArF<sub>24</sub>] (15<sup>BArF</sup>)

**Figure 6.101** Thermal ellipsoid plot of **15<sup>BArF</sup>** with the anisotropic displacement parameters drawn at the 50% probability level. The asymmetric unit contains two disordered complex molecules and two disordered anion molecules. The disordered complex molecules were refined with population of 0.55641 and the anion molecules refined with a population of 0.63136 on the main domain, respectively, using some restraints (RIGU).

**Table 6.19** Crystal data and structure refinement for **15<sup>BArF</sup>**.

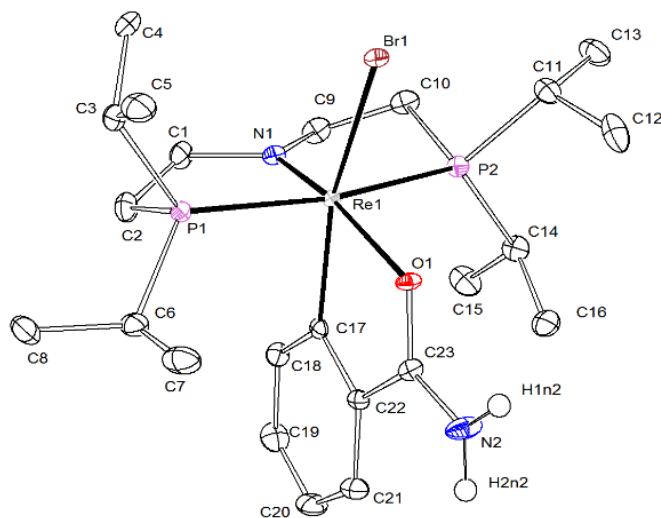
Identification code	mo_FM_180121_0m_a (Mfd174)	
Empirical formula	C <sub>110</sub> H <sub>108</sub> B <sub>2</sub> Br <sub>4</sub> F <sub>48</sub> N <sub>4</sub> O <sub>2</sub> P <sub>4</sub> Re <sub>2</sub>	
Formula weight	1633.77	
Temperature	100(2) K	
Wavelength	0.71073 Å	
Crystal system	Monoclinic	
Space group	P2 <sub>1</sub> /n	
Unit cell dimensions	a = 18.360(3) Å	α = 90°
	b = 25.132(4) Å	β = 94.480(4)°
	c = 26.504(5) Å	γ = 90°
Volume	12193(3) Å <sup>3</sup>	
Z	8	
Density (calculated)	1.780 Mg/m <sup>3</sup>	
Absorption coefficient	3.471 mm <sup>-1</sup>	
F(000)	6416	
Crystal size	0.118 x 0.167 x 0.363 mm <sup>3</sup>	
Crystal shape and color	Block, green	
Theta range for data collection	1.794 to 28.348°.	
Index ranges	-24 ≤ h ≤ 24, -33 ≤ k ≤ 33, -35 ≤ l ≤ 35	
Reflections collected	246993	
Independent reflections	30360 [R(int) = 0.1225]	
Completeness to theta = 25.242°	100.0%	
Refinement method	Full-matrix least-squares on F <sup>2</sup>	
Data / restraints / parameters	30360 / 1744 / 1917	
Goodness-of-fit on F <sup>2</sup>	1.028	
Final R indices [I > 2σ(I)]	R1 = 0.0437,	wR2 = 0.0720
R indices (all data)	R1 = 0.0743,	wR2 = 0.0809
Largest diff. peak and hole	1.282 and -1.955 e.Å <sup>-3</sup>	

6.2.20  $[\text{ReBr}_2\{\text{N}(\text{CO})\text{C}_6\text{H}_5\}(\text{P}^i\text{rPN}^{\text{H}}\text{P})]$  (**16**)

**Figure 6.102** Thermal ellipsoid plot of **16** with the anisotropic displacement parameters drawn at the 50% probability level. The asymmetric unit contains one complex molecule. The disordered complex molecule was refined using some restraints and constraints (RIGU, SADI, EADP).

**Table 6.20** Crystal data and structure refinement for **16**.

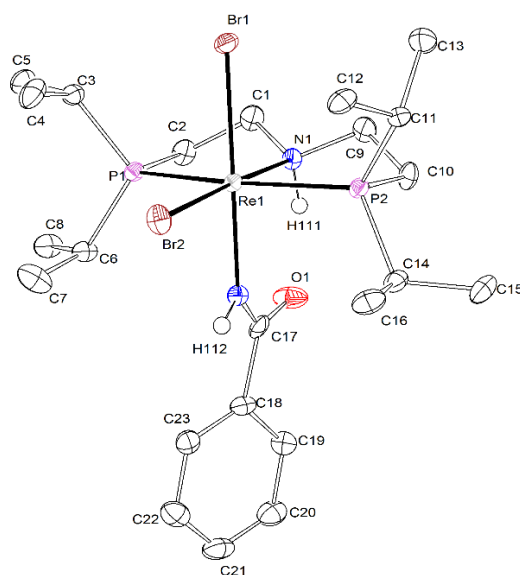
Identification code	FM_FM_141220	
Empirical formula	$\text{C}_{23}\text{H}_4\text{Br}_2\text{N}_2\text{OP}_2\text{Re}$	
Formula weight	770.54	
Temperature	100(2) K	
Wavelength	0.71073 Å	
Crystal system	Monoclinic	
Space group	$P 1 2_1/n 1$	
Unit cell dimensions	$a = 13.0483(9)$ Å	$\alpha = 90^\circ$
	$b = 16.0470(10)$ Å	$\beta = 96.690(2)^\circ$
	$c = 13.5735(8)$ Å	$\gamma = 90^\circ$
Volume	$2822.7(3)$ Å <sup>3</sup>	
Z	4	
Density (calculated)	1.813 Mg/m <sup>3</sup>	
Absorption coefficient	7.267 mm <sup>-1</sup>	
F(000)	1508	
Crystal size	0.137 x 0.132 x 0.050 mm <sup>3</sup>	
Crystal shape and color	Block, clear orange	
Theta range for data collection	1.97 to 25.68°	
Index ranges	$-15 \leq h \leq 15$ , $-19 \leq k \leq 19$ , $-16 \leq l \leq 16$	
Reflections collected	45591	
Independent reflections	5365 [R(int) = 0.1445]	
Completeness to theta = 25.68°	100.0%	
Absorption correction	Semi-empirical from equivalents	
Max. and min. transmission	0.71 and 0.55	
Refinement method	Full-matrix least-squares on F <sup>2</sup>	
Data / restraints / parameters	5365 / 230 / 289	
Goodness-of-fit on F <sup>2</sup>	1.037	
Final R indices [I > 2σ(I)]	R1 = 0.0466,	wR2 = 0.0791
R indices (all data)	R1 = 0.0822,	wR2 = 0.0899
Largest diff. peak and hole	1.621 and -1.735 eÅ <sup>-3</sup>	

6.2.21 [ReBr{NH<sub>2</sub>(CO)C<sub>6</sub>H<sub>4</sub>}(<sup>Pr</sup>PNP)] (17)

**Figure 6.103** Thermal ellipsoid plot of **17** with the anisotropic displacement parameters drawn at the 50% probability level. The asymmetric unit contains one complex molecule.

**Table 6.21** Crystal data and structure refinement for **17**.

Identification code	mo_MO_MO_MF_180520_3_0m_a (Mfd118)	
Empirical formula	C <sub>23</sub> H <sub>42</sub> BrN <sub>2</sub> OP <sub>2</sub> Re	
Formula weight	690.63	
Temperature	100(2) K	
Wavelength	0.71073 Å	
Crystal system	Monoclinic	
Space group	C 1 2/c 1	
Unit cell dimensions	a = 20.0598(9) Å	α = 90°
	b = 10.3716(3) Å	β = 92.840(3)°
	c = 25.6814(8) Å	γ = 90°
Volume	5336.5(3) Å <sup>3</sup>	
Z	8	
Density (calculated)	1.719 Mg/m <sup>3</sup>	
Absorption coefficient	6.189 mm <sup>-1</sup>	
F(000)	2736	
Crystal size	0.290 x 0.120 x 0.110 mm <sup>3</sup>	
Theta range for data collection	2.21 to 26.45°	
Index ranges	-25 ≤ h ≤ 25, -12 ≤ k ≤ 12, -32 ≤ l ≤ 32	
Reflections collected	134289	
Crystal shape and color	Plate,	clear orange
Independent reflections	5480 [R(int) = 0.0972]	
Completeness to theta = 26.45°	99.7%	
Absorption correction	Semi-empirical from equivalents	
Max. and min. transmission	0.75 and 0.64	
Refinement method	Full-matrix least-squares on F <sup>2</sup>	
Data / restraints / parameters	5480 / 0 / 279	
Goodness-of-fit on F <sup>2</sup>	1.124	
Final R indices [I > 2σ(I)]	R1 = 0.0219,	wR2 = 0.0370
R indices (all data)	R1 = 0.0300,	wR2 = 0.0383
Largest diff. peak and hole	0.587 and -1.486 eÅ <sup>-3</sup>	

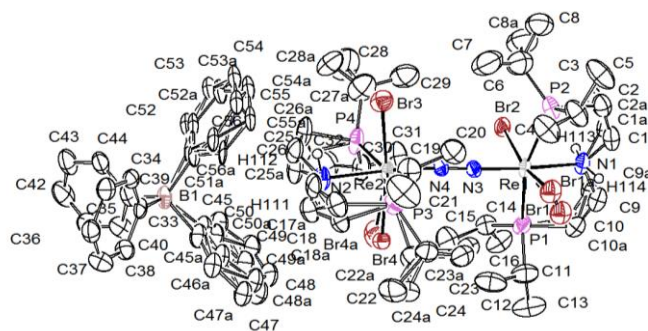
6.2.22  $[\text{ReBr}_2\{\text{NH}(\text{CO})\text{C}_6\text{H}_5\}(\text{P}^i\text{PN}^{\text{H}}\text{P})]$  (**18**)

**Figure 6.104** Thermal ellipsoid plot of **18** with the anisotropic displacement parameters drawn at the 50% probability level. The asymmetric unit contains one complex molecule.

**Table 6.22** Crystal data and structure refinement for **18**.

Identification code	mo_FM_FM_301020_0m (MFe73)	
Empirical formula	$\text{C}_{23}\text{H}_4\text{Br}_2\text{N}_2\text{OP}_2\text{Re}$	
Formula weight	771.55	
Temperature	100(2) K	
Wavelength	0.71073 Å	
Crystal system	Orthorhombic	
Space group	$P2_12_12_1$	
Unit cell dimensions	$a = 9.9879(19)$ Å	$\alpha = 90^\circ$
	$b = 13.276(3)$ Å	$\beta = 90^\circ$
	$c = 20.859(4)$ Å	$\gamma = 90^\circ$
Volume	$2765.9(9)$ Å <sup>3</sup>	
Z	4	
Density (calculated)	1.853 Mg/m <sup>3</sup>	
Absorption coefficient	7.417 mm <sup>-1</sup>	
F(000)	1512	
Crystal size	0.343 x 0.098 x 0.089 mm <sup>3</sup>	
Crystal shape and color	Block,	clear orange
Theta range for data collection	2.26 to 28.79°	
Index ranges	-13 ≤ h ≤ 13, -17 ≤ k ≤ 17, -27 ≤ l ≤ 28	
Reflections collected	86970	
Independent reflections	7183 [R(int) = 0.0781]	
Completeness to theta = 28.79°	99.6%	
Absorption correction	Semi-empirical from equivalents	
Max. and min. transmission	0.75 and 0.54	
Refinement method	Full-matrix least-squares on F <sup>2</sup>	
Data / restraints / parameters	7183 / 0 / 288	
Goodness-of-fit on F <sup>2</sup>	1.059	
Final R indices [I > 2σ(I)]	R1 = 0.0249,	wR2 = 0.0435
R indices (all data)	R1 = 0.0316,	wR2 = 0.0456
Absolute structure parameter	0.001(4)	
Largest diff. peak and hole	1.022 and -0.897 eÅ <sup>-3</sup>	

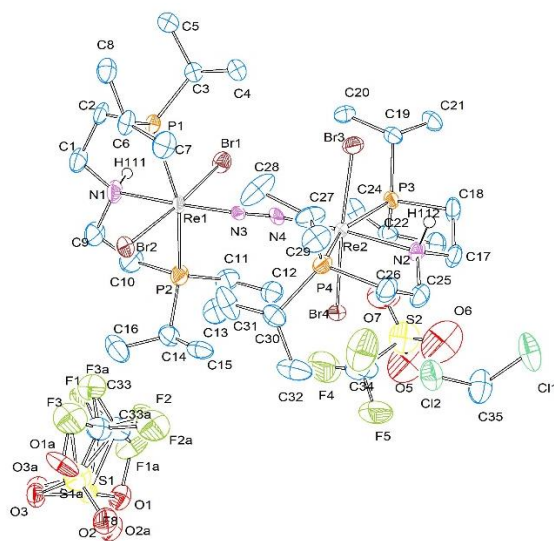


6.2.23  $[(\mu\text{-N}_2)\{\text{ReBr}_2(\text{P}^{\text{r}}\text{PN}^{\text{H}}\text{P})\}_2]\text{BPh}_4$  ( $11^{\text{Br}^+}$ )

**Figure 6.105** Thermal ellipsoid plot of FM\_FM\_101219 with the anisotropic displacement parameters drawn at the 50% probability level. The asymmetric unit contains one disordered complex molecule and one disordered anion. One triflate anion is disordered and was refined with population of 0.55641 and the anion molecules refined with populations of 0.51423, 0.63397, 0.87662, 0.87498, 0.40811 on the main domain using some restraints and constraints (RIGU, SADI, EADP). Residual electron density was removed using the SQUEEZE command. The SQUEEZE algorithm was used to omit a disordered diethyl ether molecule from the refinement.<sup>304</sup>

**Table 6.23** Crystal data and structure refinement for FM\_FM\_101219.

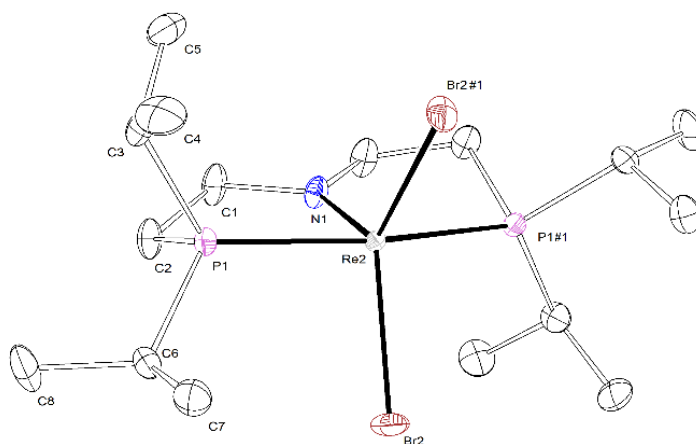
Identification code	FM_FM_101219 (MFd7)
Empirical formula	$\text{C}_{56}\text{H}_{94}\text{BBr}_4\text{N}_4\text{P}_4\text{Re}_2$
Formula weight	1650.08
Temperature	100(2) K
Wavelength	0.71073 Å
Crystal system	Monoclinic
Space group	P 1 21/n 1
Unit cell dimensions	$a = 19.7654(14)$ Å $\alpha = 90^\circ$ $b = 18.6339(16)$ Å $\beta = 112.326(4)^\circ$ $c = 20.0034(16)$ Å $\gamma = 90^\circ$
Volume	$6815.1(10)$ Å <sup>3</sup>
Z	4
Density (calculated)	1.608 Mg/m <sup>3</sup>
Absorption coefficient	6.024 mm <sup>-1</sup>
F(000)	3252
Crystal size	0.200 x 0.149 x 0.045 mm <sup>3</sup>
Crystal shape and color	Plate, yellow
Theta range for data collection	2.20 to 25.35°
Index ranges	-23 ≤ h ≤ 23, -22 ≤ k ≤ 22, -24 ≤ l ≤ 23
Reflections collected	51049
Independent reflections	12461 [R(int) = 0.0752]
Completeness to theta = 25.35°	99.9%
Absorption correction	Semi-empirical from equivalents
Max. and min. transmission	0.77 and 0.51
Refinement method	Full-matrix least-squares on F <sup>2</sup>
Data / restraints / parameters	12461 / 1343 / 850
Goodness-of-fit on F <sup>2</sup>	1.016
Final R indices [I > 2σ(I)]	R1 = 0.0452, wR2 = 0.0994
R indices (all data)	R1 = 0.0741, wR2 = 0.1117
Largest diff. peak and hole	2.112 and -1.290 eÅ <sup>-3</sup>

6.2.24  $[(\mu\text{-N}_2)\{\text{ReBr}_2(\text{P}^{\text{r}}\text{PN}^{\text{H}}\text{P})\}_2]\text{OTf}_2 (\mathbf{11}^{\text{Br}_2^+})$ 

**Figure 6.106** Thermal ellipsoid plot of  $\mathbf{11}^{\text{Br}_2^+}$  with the anisotropic displacement parameters drawn at the 50% probability level. The asymmetric unit contains one complex, two anion (OTf) and one solvent molecule (dichloromethane) molecule. One triflate anion is disordered and was refined with population of 0.55641 and the anion molecules refined with a population of 0.87413 on the main domain using some restraints and constraints (RIGU, SADI, EADP).

**Table 6.24** Crystal data and structure refinement for  $\mathbf{11}^{\text{Br}_2^+}$ .

Identification code	FM_120121_FM (MFe28)	
Empirical formula	$\text{C}_{35}\text{H}_7\text{Br}_4\text{Cl}_2\text{F}_6\text{N}_4\text{O}_6\text{P}_4\text{Re}_2\text{S}_2$	
Formula weight	1713.93	
Temperature	100(2) K	
Wavelength	0.71073 Å	
Crystal system	Monoclinic	
Space group	$P 1 21/c 1$	
Unit cell dimensions	$a = 20.1020(4)$ Å	$\alpha = 90^\circ$
	$b = 14.7621(3)$ Å	$\beta = 93.7630(10)^\circ$
	$c = 19.0681(4)$ Å	$\gamma = 90^\circ$
Volume	$5646.2(2)$ Å <sup>3</sup>	
Z	4	
Density (calculated)	2.016 Mg/m <sup>3</sup>	
Absorption coefficient	7.459 mm <sup>-1</sup>	
F(000)	3328	
Crystal size	0.283 x 0.097 x 0.072 mm <sup>3</sup>	
Crystal shape and color	Plate, red	
Theta range for data collection	1.98 to 25.72°	
Index ranges	$-24 \leq h \leq 24, -18 \leq k \leq 18, -23 \leq l \leq 23$	
Reflections collected	125619	
Independent reflections	10750 [R(int) = 0.0867]	
Completeness to theta = 25.72°	99.8%	
Absorption correction	Semi-empirical from equivalents	
Refinement method	Full-matrix least-squares on F <sup>2</sup>	
Data / restraints / parameters	10750 / 539 / 657	
Goodness-of-fit on F <sup>2</sup>	1.139	
Final R indices [I > 2sigma(I)]	R1 = 0.0478,	wR2 = 0.0967
R indices (all data)	R1 = 0.0614,	wR2 = 0.1023
Largest diff. peak and hole	2.114 and -1.556 eÅ <sup>-3</sup>	

6.2.25 [ReBr<sub>2</sub>(<sup>Pr</sup>PNP)] (23)

**Figure 6.107** Thermal ellipsoid plot of **21** with the anisotropic displacement parameters drawn at the 50% probability level. The asymmetric unit contains one half complex molecule.

**Table 6.25** Crystal data and structure refinement for **21**.

Identification code	mo_FM_FM_200519_0m_a (MF_PW_17)	
Empirical formula	C <sub>16</sub> H <sub>36</sub> Br <sub>2</sub> NP <sub>2</sub> Re	
Formula weight	650.42	
Temperature	111(2) K	
Wavelength	0.71073 Å	
Crystal system	Monoclinic	
Space group	C2/c	
Unit cell dimensions	a = 21.3531(19) Å	α = 90°
	b = 7.6094(8) Å	β = 120.854(3)°
	c = 15.9435(17) Å	γ = 90°
Volume	2223.9(4) Å <sup>3</sup>	
Z	4	
Density (calculated)	1.943 Mg/m <sup>3</sup>	
Absorption coefficient	9.199 mm <sup>-1</sup>	
F(000)	1256	
Crystal size	0.136 x 0.103 x 0.072 mm <sup>3</sup>	
Crystal shape and color	Block,	clear pale brown
Theta range for data collection	2.648 to 25.709°	
Index ranges	-23 ≤ h ≤ 26, -9 ≤ k ≤ 9, -19 ≤ l ≤ 19	
Reflections collected	26000	
Independent reflections	2112 [R(int) = 0.0388]	
Completeness to theta = 25.242°	100.0%	
Refinement method	Full-matrix least-squares on F <sup>2</sup>	
Data / restraints / parameters	2112 / 0 / 105	
Goodness-of-fit on F <sup>2</sup>	1.172	
Final R indices [I > 2σ(I)]	R1 = 0.0156,	wR2 = 0.0353
R indices (all data)	R1 = 0.0175,	wR2 = 0.0358
Largest diff. peak and hole	0.359 and -1.047 eÅ <sup>-3</sup>	

## 6.3 DFT calculations

All DFT calculations within the Chapter Results and Discussion I were carried out by Dr. Markus Finger (Georg-August-Universität Göttingen).

All DFT calculations within the Chapter Results and Discussion II were carried out by M. Sc. Severine Rupp (AK Krewald, Technische Universität Darmstadt).

### 6.3.1 Computational details of **3**, **3-CO**, **3-(CO)<sub>2</sub>**, **4** and **5**

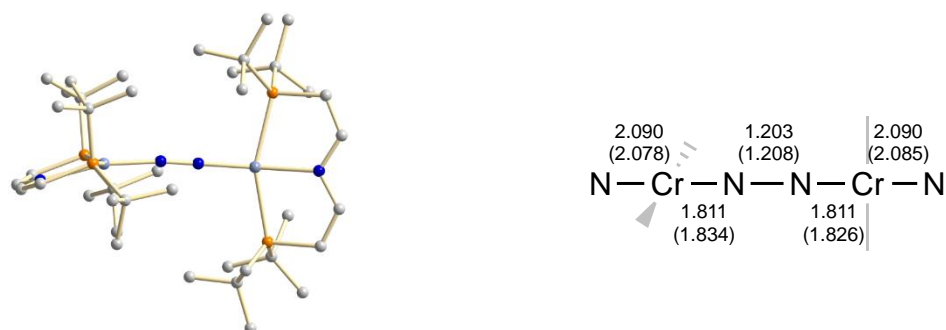


**Figure 6.108** Calculated ground state structure of  $[(\mu\text{-N}_2)\{\text{Cr}(\text{tBuPNP})\}]_2$  **3** (without hydrogen atoms) and calculated bond lengths in comparison to experiment (in parentheses, both in Å, experimental values rounded and without error).

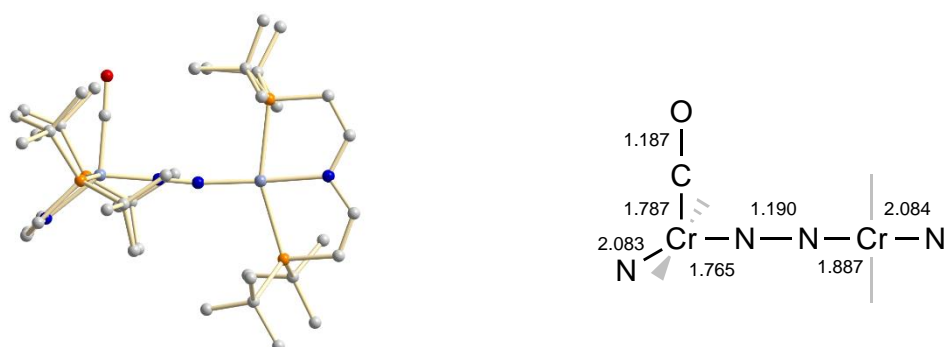


**Figure 6.109** Calculated ground state structure of  $[(\mu\text{-N}_2)\{\text{Cr}(\text{CO})(\text{tBuPNP})\}]\{\text{Cr}(\text{tBuPNP})\}$  **3-CO** (without hydrogen atoms) and calculated bond lengths in Å.

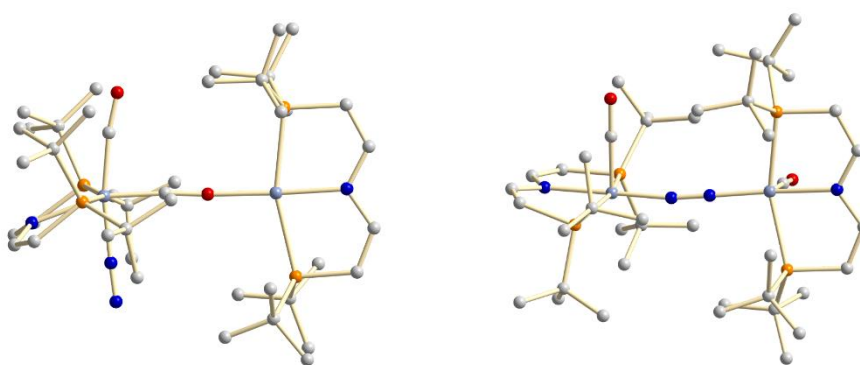


**Figure 6.110** Calculated alternative structures of **3-(CO)<sub>2</sub>**:  $[(\mu\text{-CO})\{\text{Cr}(\text{CO})(\text{N}_2)(\text{tBuPNP})\}]\{\text{Cr}(\text{tBuPNP})\}$  **3-(CO)<sub>2</sub> A** and  $[(\mu\text{-N}_2)\{\text{Cr}(\text{CO})_2(\text{tBuPNP})\}]\{\text{Cr}(\text{tBuPNP})\}$  **3-(CO)<sub>2</sub> B**. **Left: 3-(CO)<sub>2</sub> A** - terminal binding of  $\text{N}_2$  and a bridging carbonyl ligand,  $S=2$  ground state; **Right: 3-(CO)<sub>2</sub> B** - binding of one CO to each Cr,  $S=1$  ground state.

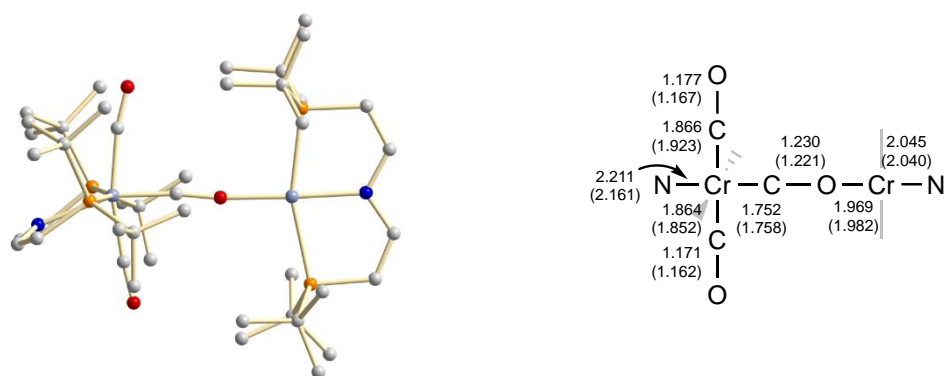


**Figure 6.111** Calculated ground state structure of  $[(\mu\text{-CO})\{\text{Cr}(\text{CO})_2(\text{BuPNP}^{\text{B}})\}\{\text{Cr}(\text{BuPNP}^{\text{B}})\}]$  **4** (without hydrogen atoms) and calculated bond lengths in comparison to experiment (in parentheses, both in Å, experimental values rounded and without error).

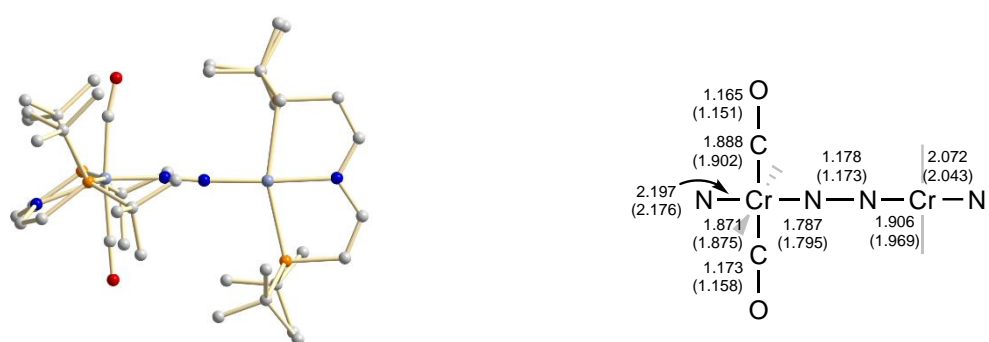


**Figure 6.112** Calculated ground state structure of  $[(\mu\text{-N}_2)\{\text{Cr}(\text{CO})_2(\text{BuPNP}^{\text{B}})\}\{\text{Cr}(\text{BuPNP}^{\text{B}})\}]$  **5** (without hydrogen atoms) and calculated bond lengths in comparison to experiment (in parentheses, both in Å,

**Table 6.26** Calculated stretching vibrations (in  $\text{cm}^{-1}$ ) of the CO and  $\text{N}_2$  ligands in comparison to experiment if known.

		Calculated	Experiment
<b>3</b>	S=3	1689 ( $^{14}\text{N}$ ), 1632 ( $^{15}\text{N}$ )	1651 ( $^{14}\text{N}$ ), 1594 ( $^{15}\text{N}$ )
<b>3-CO</b>	S=2	1735, 1818	
<b>5</b>	S=2	1809, 1856, 1943 ( $^{14}\text{N}$ ) 1755, 1853, 1939 ( $^{15}\text{N}$ )	1766, 1834, 1952 ( $^{14}\text{N}$ ) 1716, 1827, 1947 ( $^{15}\text{N}$ )
<b>3-(CO)<sub>2</sub> A</b>	S=2	1623 ( $\mu\text{-CO}$ ), 1838 ( $\text{CO}_{\text{term}}$ ), 2113 ( $\text{N}_2_{\text{term}}$ )	-
<b>3-(CO)<sub>2</sub> B</b>	S=1	1718, 1840 ( $\nu_{\Lambda}$ ), 1861 ( $\nu_{\text{S}}$ )	-
<b>4</b>	S=2	1630, 1836 ( $\nu_{\Lambda}$ ), 1918 ( $\nu_{\text{S}}$ )	1542, 1792, 1895

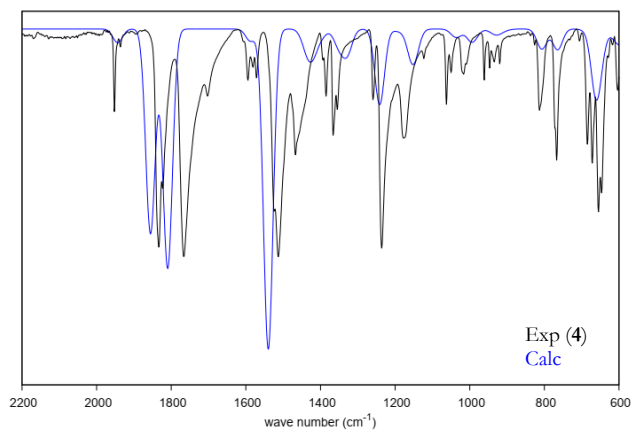


Figure 6.113 Calculated IR-spectrum of **4** in comparison to experiment.

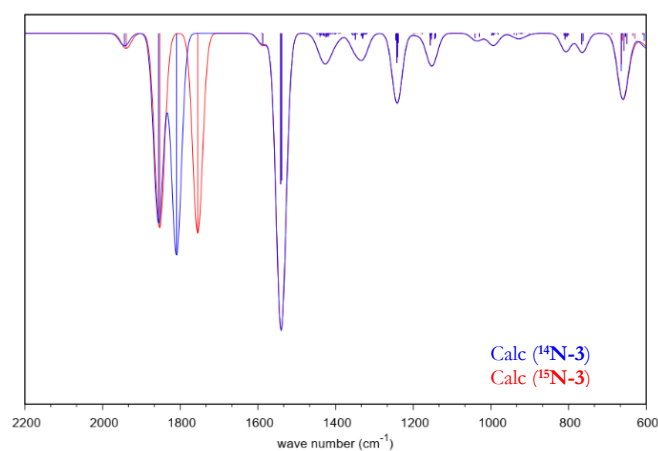


Figure 6.114 Calculated isomer shift of **3** by  $^{15}\text{N}_2$ -substitution.

Table 6.27 Evaluated electronic configurations<sup>305</sup> of **3**, their relative SCF energies and computed (PBE0) Löwdin spin populations of the Cr centers and the bridging  $\text{N}_2$  ligand.

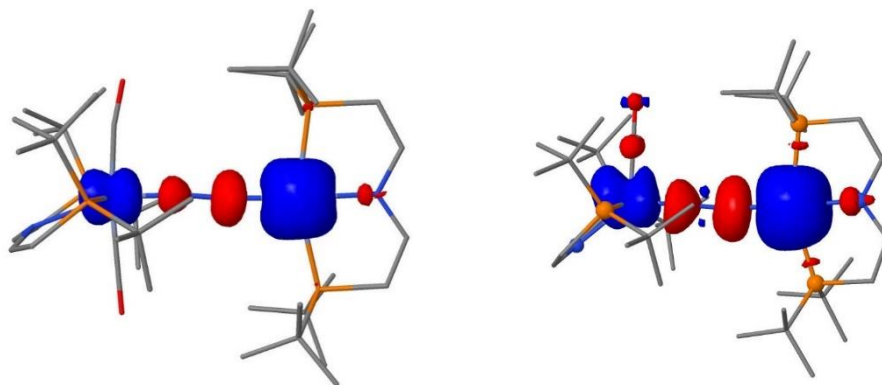
Spin state	PBE(THF)	$\langle S^2 \rangle$	$\Delta E$ (kJ/mol)	PBE0(THF)	$\langle S^2 \rangle$	$\Delta E$ (kJ/mol)	$\rho_s(\text{Cr})$	$\rho_s(\text{N}_2)$
S = 5	-5243.310419	30.051	189.1	-5243.696469	30.066	135.4	4.32	0.92
S = 3	-5243.382444	12.249	0.0	-5243.748041	12.798	0.0	3.38	-0.86
BS(3,3) <sup>306</sup>	-5243.363696	3.207	49.2	-5243.722010	3.879	68.3	3.53 / -3.53	0
S=2	-5243.356519	7.099	68.1	-5243.712169	7.595	94.2	3.48 / 1.20	-0.74
S=1	-5243.326759	3.998	146.2	-5243.673413	4.481	195.8	1.32	-0.67
S = 0	-5243.288903	-	245.6	195.9	195.9	195.9	-	-

**Table 6.28** Evaluated electronic configurations<sup>305</sup> of **4** and their relative energies and computed (PBE0) Löwdin spin populations of the Cr centers and the bridging N<sub>2</sub> ligand.

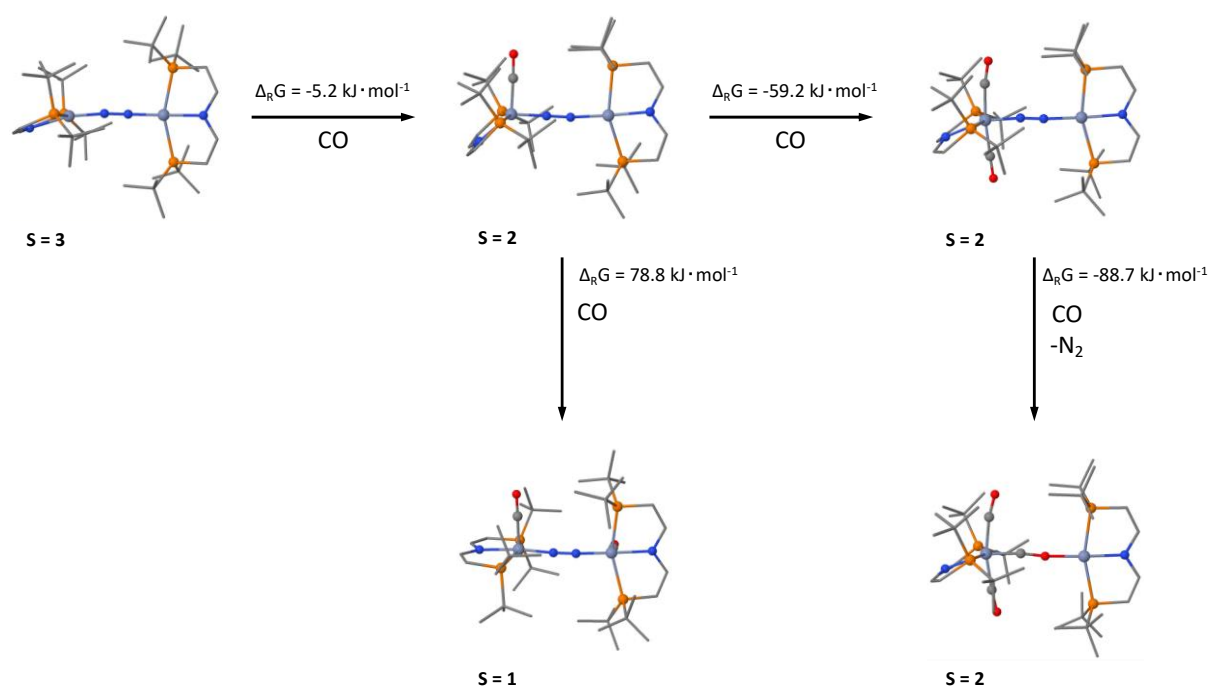
Spin state	PBE(THF)	<S <sup>2</sup> >	ΔE (kJ/mol)	PBE0(THF)	<S <sup>2</sup> >	ΔE (kJ/mol)	ρ <sub>s</sub> (Cr)	ρ <sub>s</sub> (CO)
S = 3	-5473.699154	12.036	176.8	-5474.02201	12.087	187.8	4.54 / 1.05	0.01
BS(3,3) <sup>6</sup>	SCF not converged							
S = 2	-5473.766475	6.033	0.0	-5474.093526	6.038	0.0	3.91 / 0.14	-0.05
S = 1	-5473.727308	2.913	102.8	-5474.045624	3.009	125.8	1.88 / 0.20	-0.07
S = 0	-5473.687152	-	208.3	-5473.978054	-	303.2	-	-

**Table 6.29** Evaluated electronic configurations<sup>305</sup> of **5** and their relative energies and computed (PBE0) Löwdin spin populations of the Cr centers and the bridging N<sub>2</sub> ligand.

Spin state	PBE(THF)	<S <sup>2</sup> >	ΔE (kJ/mol)	PBE0(THF)	<S <sup>2</sup> >	ΔE (kJ/mol)	ρ <sub>s</sub> (Cr)	ρ <sub>s</sub> (N <sub>2</sub> )
S = 3	-5469.910819	12.052	129.5	-5470.238339	12.118	95.1	4.25 / 1.31	0.47
BS <sup>3</sup>	SCF not converged							
S = 2	-5469.960140	6.062	0.0	-5470.274550	6.366	0.0	3.72 / 0.88	-0.45
S = 1	-5469.933373	2.718	70.3	-5470.232327	2.299	110.9	3.25 / -1.05	-0.38
S = 0	-5469.901737	-	153.3	-5470.171289	-	271.1	-	-

**Figure 6.115** Spin density plot (PBE0/def2-TZVPP (COSMO(THF))) of **5** (S = 2 ground state, left side) and **3-CO** (S = 2 ground state, right side).**Table 6.30** Evaluated electronic configurations<sup>305</sup> of **5** and **3-CO** and their relative energies and computed (PBE0) Löwdin spin populations of the Cr centers and the bridging N<sub>2</sub> ligand.

Spin state	PBE(THF)	<S <sup>2</sup> >	ΔE (kJ/mol)	PBE0(THF)	<S <sup>2</sup> >	ΔE (kJ/mol)	ρ <sub>s</sub> (Cr)	ρ <sub>s</sub> (N <sub>2</sub> )
S = 3	-5356.647396	12.157	75.5	-5356.985978	12.627	39.0	3.61 / 2.76	-0.61
BS <sup>3,3</sup>	SCF not converged							
S = 2	-5356.676149	6.089	0.0	-5357.000824	6.446	0.0	3.67 / 0.93	-0.55
S = 1	-5356.659063	3.031	44.9	-5356.975337	3.681	66.9	3.52 / -1.01	-0.53
S = 0	-5356.622872	-	139.9	-5356.899239	-	266.7	-	-



**Scheme 6.1** Calculated free reaction energies and ground state multiplicities of the reaction of **3** with CO (D3BJ-PBE0/def2-TZVPP (Cosmo(THF))).

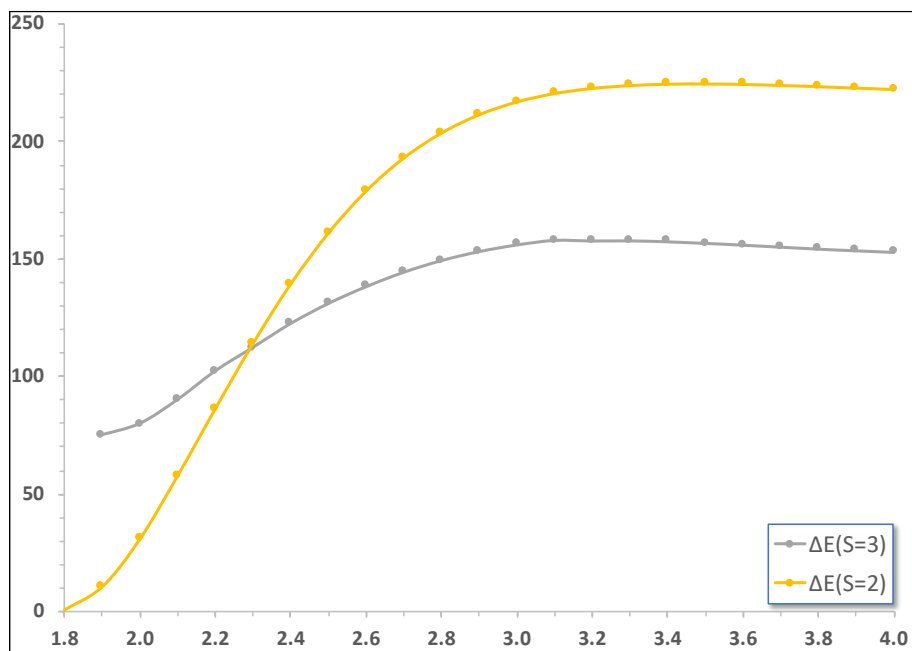


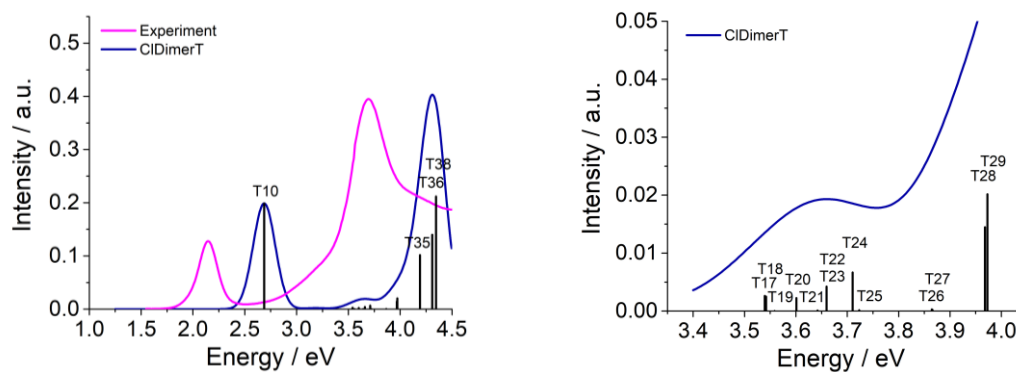
**Figure 6.116** Relaxed surface scan of the CO approach to **3** (RIJ-PBE(D3BJ)/def2-TZVP,def2-SVP energies). At around 2.3 Å, there is a spin change induced by coordination of CO to one Cr-center.



### 6.3.2 TD-DFT calculations for $[(\mu\text{-N}_2)\{\text{ReCl}_2(\text{P}^{\text{r}}\text{PN}^{\text{H}}\text{P})\}_2] 11^{\text{Cl}}$

TD-DFT computations were performed by M. Sc. Severine Rupp (AK Krewald, Technische Universität Darmstadt).

**Computational Details:** ORCA 4.2.1; UKS PBE RI D3BJ Grid7 CPCM(THF); for Re, Cl, N, P, O def2-TZVP def2/J; for C, H def2-SVP def2/J

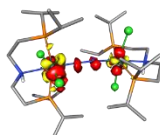
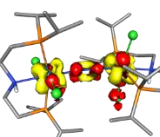
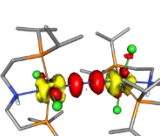
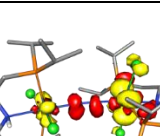
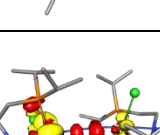
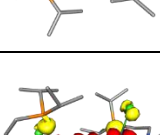
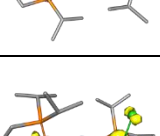
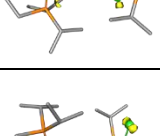


**Figure 6.117** Left: Predicted (blue) and experimental (pink) UV-vis spectrum (PBE0) of the triplet electronic configuration (blue) with the combination of def2-SVP and def2-TZVP basis sets in comparison to the experimental spectrum (magenta) of  $11^{\text{Cl}}$ . Right: Zoom in of the photolytically active region. The highest-intensity transitions are labelled. Computational details: ORCA 4.2.1; UKS PBE0 RIJCOSX D3BJ Grid7 GridX7 CPCM(THF); for Re, Cl, N, P, O def2-TZVP def2/J; for C, H def2-SVP def2/J.

**Table 6.31:** Energies, oscillator strengths and difference densities of the highest-intensity transitions in the triplet spectrum of  $11^{\text{Cl}}$ .

Def2-SVP / Def2-TZVP		
State	E (eV) / $f_{\text{osc}}$	Difference density
10	2.69 / 0.199	
35	4.19 / 0.102	
36	4.31 / 0.140	
38	4.35 / 0.212	

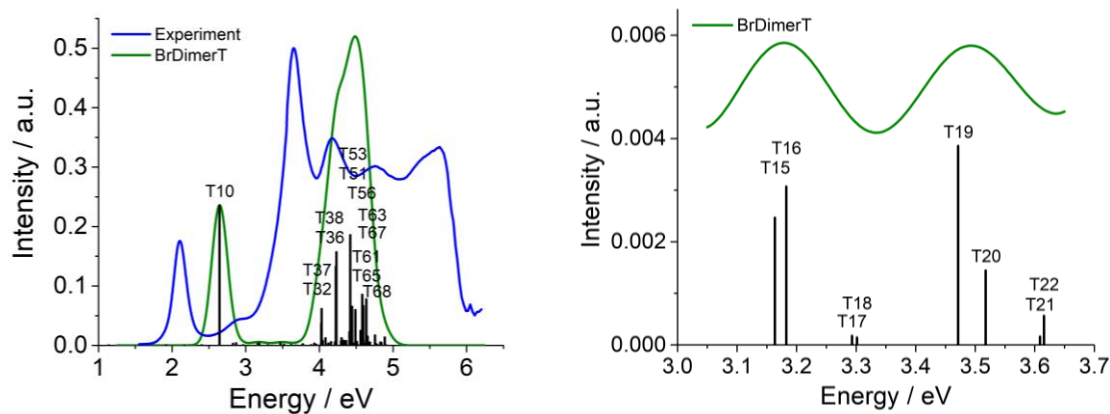
**Table 6.32:** Energies, oscillator strengths and difference densities of the transitions in the active region of the triplet spectrum of **11<sup>Cl</sup>**.

Def2-SVP / Def2-TZVP		
State	E (eV) / $f_{osc}$	Difference density
17	3.54 / 0.003	
18	3.54 / 0.002	
20	3.60 / 0.002	
22	3.66 / 0.004	
23	3.66 / 0.004	
24	3.71 / 0.007	
28	3.97 / 0.014	
29	3.97 / 0.014	

### 6.3.3 TD-DFT calculations for $[(\mu\text{-N}_2)\{\text{ReBr}_2(\text{P}^{\text{r}}\text{PN}^{\text{H}}\text{P})\}_2] \mathbf{11}^{\text{Br}}$

TD-DFT computations were performed by M. Sc. Severine Rupp (AK Krewald, Technische Universität Darmstadt).

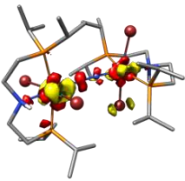
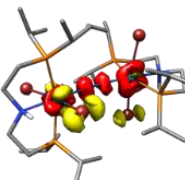
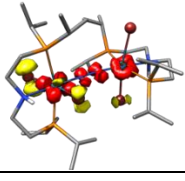
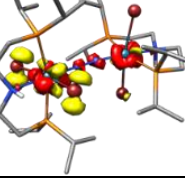
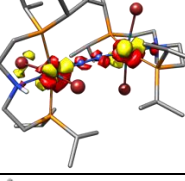
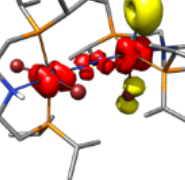
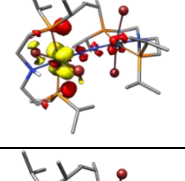
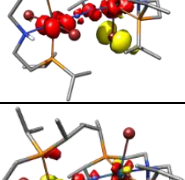
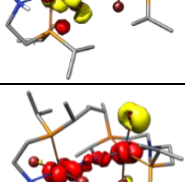
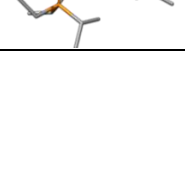
**Computational Details:** ORCA 4.1.2; UKS PBE RI D3BJ Grid7 CPCM(THF); for Re, Br, N, P, O def2-TZVP def2/J; for C, H def2-SVP def2/J



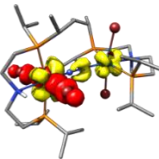
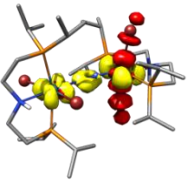
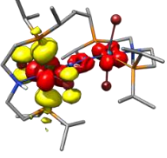
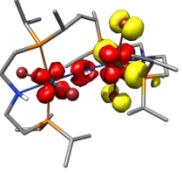
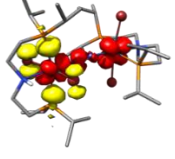
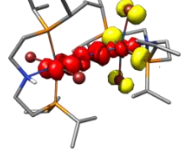
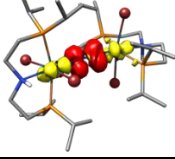
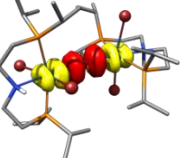
**Figure 6.118 Left:** Predicted (blue) and experimental (green) UV-vis spectrum (PBE0) of the triplet electronic configuration (olive) with the combination of def2-SVP and def2-TZVP basis sets in comparison to the experimental spectrum (blue) of  $\mathbf{11}^{\text{Br}}$ . The highest-intensity transitions are labelled. **Right:** Zoom in of the photolytically active region. Computational details: ORCA 4.2.1; UKS PBE0 RIJCOSX D3BJ Grid7 GridX7 CPCM(THF); for Re, Br, N, P, O def2-TZVP def2/J; for C, H def2-SVP def2/J.

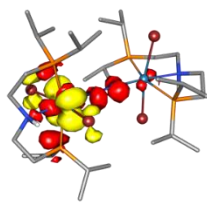
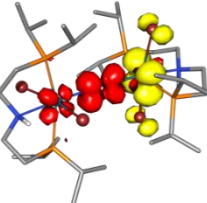
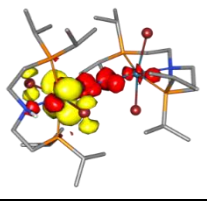
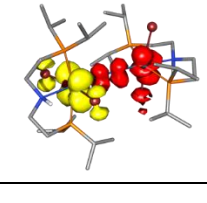
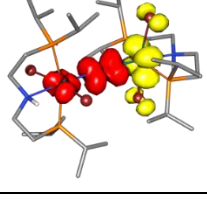
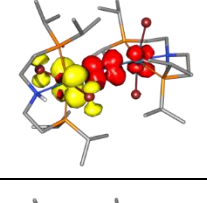
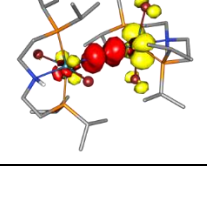
**Table 6.33:** Energies, oscillator strengths and difference densities of the highest-intensity transitions in the triplet spectrum of  $\mathbf{11}^{\text{Br}}$ .

Def2-SVP / Def2-TZVP		
State	E (eV) / $f_{\text{osc}}$	Difference density
10	2.64 / 0.235	
32	4.03 / 0.037	
37	4.03 / 0.061	

36	4.22 / 0.133	
38	4.23 / 0.157	
51	4.42 / 0.186	
53	4.44 / 0.065	
56	4.49 / 0.060	
65	4.56 / 0.025	
61	4.58 / 0.086	
67	4.60 / 0.031	
63	4.60 / 0.066	
68	4.64 / 0.077	

**Table 6.34** Energies, oscillator strengths and difference densities of the transitions in the active region of the triplet spectrum of **11Br**.

Def2-SVP / Def2-TZVP		
State	E (eV) / $f_{osc}$	Difference density
15	3.16 / 0.003	
16	3.18 / 0.003	
17	3.29 / 0.000	
18	3.30 / 0.000	
19	3.47 / 0.004	
20	3.52 / 0.001	
21	3.61 / 0.000	
22	3.62 / 0.001	

Def2-SVP / Def2-TZVP		
State	E (eV) / $f_{osc}$	Difference density
24	3.77 / 0.002	
25	3.78 / 0.002	
27	3.88 / 0.000	
35	3.89 / 0.000	
30	3.93 / 0.003	
31	3.96 / 0.000	
28	4.02 / 0.003	

### 6.3.4 DFT calculations of PCET on nitride complex $10^{\text{Br}}$

DFT calculations were performed by M. Sc. Severine Rupp (AK Krewald, Technische Universität Darmstadt).

Computational details: ORCA 4.2.1; UKS PBE RI D3BJ Grid7 CPCM(THF); for Re, Br, N, P, O, H def2-TZVP def2/J; for C def2-SVP def2/J; Charge: 0

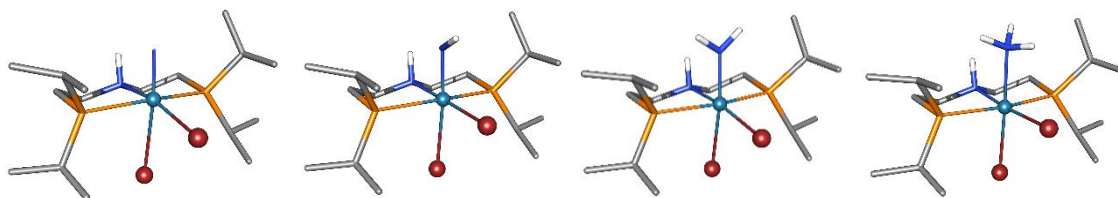


**Figure 6.119** Geometry optimization of all species relevant for ammonia formation of nitride complex  $10^{\text{Br}}$  via PCET.

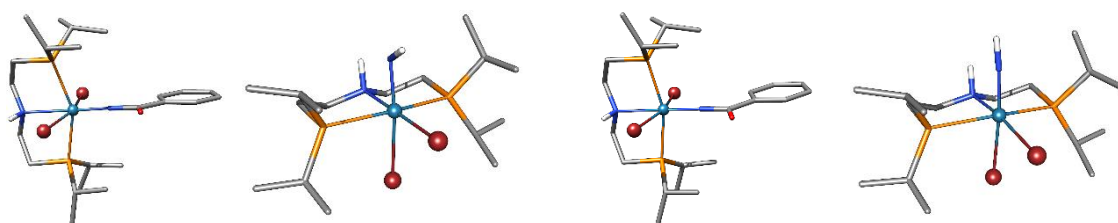
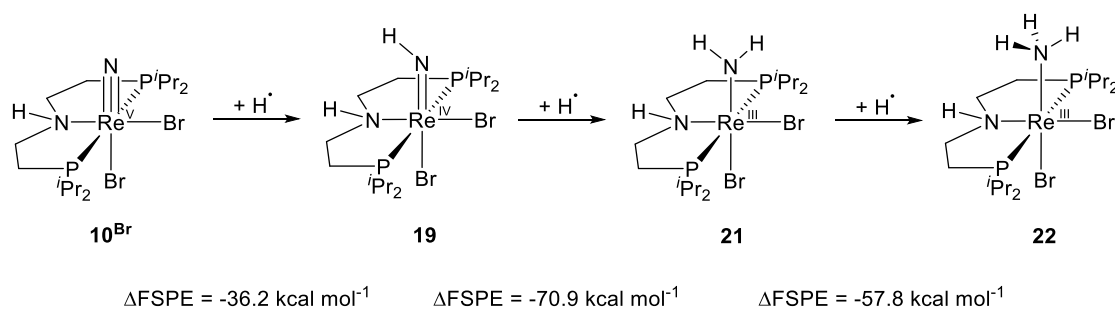
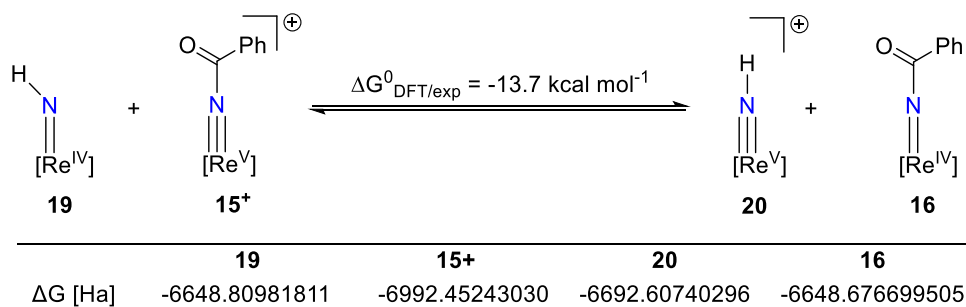


**Figure 6.120** Geometry optimization of all species relevant for the isodesmic reaction of  $15^+$  and  $19$  to  $16$  and  $20$ .



**Scheme 6.2** PCET on nitride complex  $10^{\text{Br}}$ .



**Scheme 6.3** Isodesmic reaction of  $15^+$  and  $19$  to  $16$  and  $20$  and corresponding free energies.

